Transactions of the ASME®

Transactions of the ASME, Journal of Fluids Engineering (ISSN 0098-2202) is published quarterly (Mar., June, Sept., Dec.) by The American Society of Mechanical Engineers, Three Park Avenue, New York, NY 10016. Periodicals postage paid at New York, NY and additional mailing offices.
POSTMASTER: Send address changes to Transactions of the ASME, Journal of Fluids Engineering, c/o THE AMERICAN SOCIETY OF MECHANICAL ENGINEERS, 22 Law Drive, Box 2300, Fairfield, NJ 07007-2300.
CHANGES OF ADDRESS must be received at Society headquarters seven weeks before they are to be effective. Please send old label and new address.
STATEMENT from By-Laws. The Society shall not be responsible for statements or opinions advanced in papers or ... printed in its publications (B7.1, Par. 3).

INDEXED by Applied Mechanics Reviews and Engineering Information, Inc. Canadian Goods & Services Tax Registration #126148048.

Journal of Fluids Engineering

Published Quarterly by The American Society of Mechanical Engineers

VOLUME 123 • NUMBER 4 • DECEMBER 2001

TECHNICAL PAPERS

(Contents continued on inside back cover)

This journal is printed on acid-free paper, which exceeds the ANSI Z39.48-1992 specification for permanence of paper and library materials. ♾™
♻ 85% recycled content, including 10% post-consumer fibers.

TECHNICAL BRIEFS

ANNOUNCEMENTS

Fundamental Analysis on Rotor-Stator Interaction in a Diffuser Pump by Vortex Method

H. Wang
Graduate Student,
Department of Mechanical Engineering,
Kyushu Institute of Technology,
1-1 Sensui-cho, Tobata, Kitakyushu,
804-8550 Japan

H. Tsukamoto
Professor,
Department of Biological Functions and Engineering,
Graduate School of Life Science and Systems Engineering,
Kyushu Institute of Technology,
1-1 Sensui-cho, Tobata, Kitakyushu,
804-8550 Japan

A two-dimensional unsteady flow was calculated within a whole stage of a diffuser pump to investigate pressure fluctuations due to the interaction between impeller and diffuser vanes by using the vortex method, in which vortices shedding from solid boundary were determined by the basic governing equation. The Petrov-Galerkin Method was applied to yield the solutions that satisfy the boundary conditions in an integral sense, and it improved the stability and accuracy of the numerical solutions greatly. A new scheme was also proposed to improve the unsteady pressure evaluation by a boundary integration method in the rotor-stator interaction problem. Moreover, for a more realistic prediction of the pressure fluctuations, the inlet flow was supposed to change with time so that pumping system may balance. The calculated time-varying flow rate, total hydraulic head rise and pressure fluctuations in the vaned diffuser passage, were compared with the measured and calculated ones by other methods. Calculated unsteady pressure fluctuations in the vaned diffuser passage showed good agreement with the experimental data and the CFD calculated ones. [DOI: 10.1115/1.1413242]

Introduction

In a diffuser pump, the centrifugal impeller interferes with its successive diffuser vanes and produces pressure fluctuations downstream of the impeller. These pressure fluctuations may become as large as the total pressure rise across the pump in the case of a small radial gap between the impeller and diffuser vanes [1–4]. These fluctuations not only generate noise and vibration that cause unacceptable levels of stress and reduce component life due to fatigue, but also introduce unfavorable characteristics of pump performance even at or near the design point. Therefore, there is a need to understand the source of unsteadiness (i.e., potential and wake interactions) to control the pressure fluctuations and to improve the overall pump performance and reliability.

Dring et al. [5] proposed two distinct mechanisms of rotor-stator interaction: potential and wake interactions. The potential interaction is a potential flow effect induced by the inviscid interaction because of the relative motion between rotor blades and stator vanes. On the other hand, the wake interaction originates from the impingement and convection of the wakes shed from impeller passages which then move through the successive diffuser passages. These phenomena have been studied extensively in axial-type turbomachines. However, there have been only few studies on the impeller-diffuser interaction in centrifugal pumps.

Some experimental contributions to wake interaction in pumps may be attributed to extensive PIV measurements by Dong et al. [6], and Akin et al. [7], and hot wire measurement by Ubaldi et al. [8], as well as the study in Chu et al. [9,10] and Kaupert and Staubli [11,12]. However, it seems to be difficult to understand the flow phenomena due to rotor-stator interaction from only experimental studies because of the complicated flow structures in pumps. Fortes-Patella et al. [13] presented a 2-D unsteady flow calculation and studied the interaction between the impeller and volute in the volute pump. Bert et al. [14] carried out an unsteady flow calculation in a centrifugal pump using a finite element method. Qin and Tsukamoto [15–17] calculated the pressure fluctuations downstream of a diffuser pump with singularity method. Shi and Tsukamoto [18,19] calculated the pressure fluctuations downstream of an impeller in a diffuser pump using the 2-D and 3-D, unsteady RANS code with standard k-ϵ turbulence models. All of these numerical studies contributed to the understanding of rotor-stator interaction in pumps. However, numerical methods have not yet been developed which result in the efficient and accurate prediction of unsteady flow due to the rotor-stator interaction.

The vortex method can be applied to calculate the pressure fluctuations in such very complicated unsteady flows as that in diffuser pump, since it is grid-free and thus can be easily applied to flows around complex geometry. Moreover, its Lagrangian representation of the evolving vorticity field is well suited to a moving boundary, and the transformation of the governing equations to a non-inertial reference frame is unnecessary. Zhu [20] has calculated the pressure fluctuations due to rotor-stator interaction in a diffuser pump using the vortex method under a constant flow rate condition, but this method cannot be applied to cases of changing operating conditions, such as low capacity range with flow rate fluctuations. In the present study, the authors' vortex method [21] was extended to cases of changing operating points of pump, and the pressure fluctuations due to the rotor-stator interaction in a diffuser pump were calculated.

Numerical Analysis

Flow Model. The unsteady flow in a test diffuser pump shown in Fig. 1 was investigated by calculating the 2-D flow field around the impeller and diffuser vanes shown in Fig. 2. The 2-D unsteady viscous flow analysis was developed by using a vortex method, in which the continuous vorticity field is represented by the bound vortex elements γ_b adjoining the solid boundary, and the vortices γ_w emanating from the trailing edge and boundary layer. Thus, the wake and separated flow which carry concentrations of vorticity are traced by Lagrangian scheme. To satisfy the no flux and no-slip boundary conditions simultaneously in the present calculation, source panels σ are distributed just under the boundary surface. After the vorticity and velocity field are determined, the unsteady pressure field is calculated by the Boundary Element Method.

Unsteady Velocity. As an extension of the well-known Biot-Savart law [22] to 2-D unsteady viscous flow, the velocity $\mathbf{V}(\mathbf{r})$ in a domain S bounded by boundary L can be written as the sum of

Contributed by the Fluids Engineering Division for publication in the JOURNAL OF FLUIDS ENGINEERING. Manuscript received by the Fluids Engineering Division January 8, 2001; revised manuscript received June 29, 2001. Associate Editor: Y. Tsujimoto.

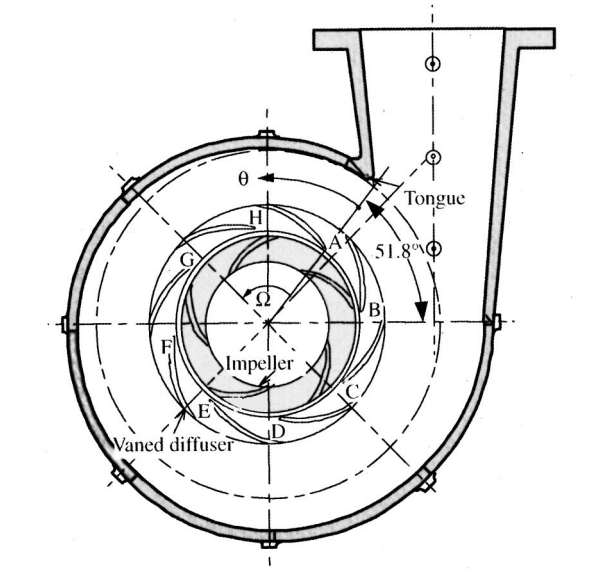

(*a*)

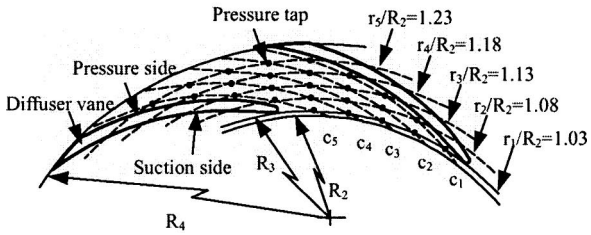

(*b*)

Fig. 1 Schematics of test diffuser pump (*a*) Test pump; (*b*) pressure measurement stations for test vaned diffuser

velocity $\mathbf{V}_S(\mathbf{r})$ induced by all vortex elements in the domain S, and $\mathbf{V}_L(\mathbf{r})$ induced by the absolute motion of the boundary L, that is,

$$\mathbf{V}(\mathbf{r}) = \mathbf{V}_S(\mathbf{r}) + \mathbf{V}_L(\mathbf{r}) \tag{1}$$

where

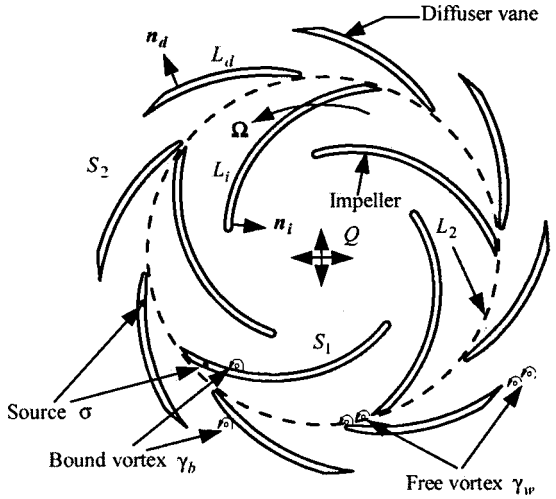

Fig. 2 Mathematical model for calculation

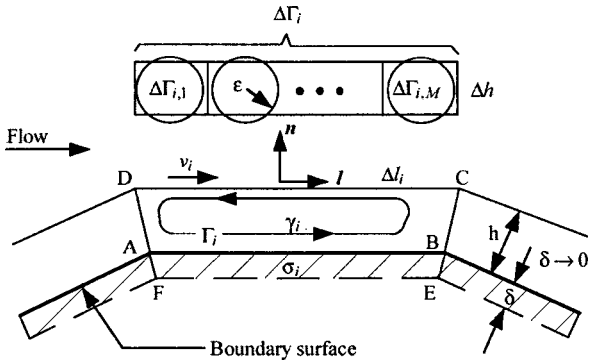

Fig. 3 Panel around solid boundary and nascent vortex elements

$$\mathbf{V}_S(\mathbf{r}) = -\frac{1}{2\pi}\left[\int_S \frac{\omega_0 \times (\mathbf{r}_0 - \mathbf{r})}{|\mathbf{r}_0 - \mathbf{r}|^2} dS_0\right]$$

and

$$\mathbf{V}_L(\mathbf{r}) = -\frac{1}{2\pi}\left[\int_L \frac{(\mathbf{V}_0 \cdot \mathbf{n}_0)(\mathbf{r}_0 - \mathbf{r})}{|\mathbf{r}_0 - \mathbf{r}|^2} dL_0 - \int_L \frac{(\mathbf{V}_0 \times \mathbf{n}_0) \times (\mathbf{r}_0 - \mathbf{r})}{|\mathbf{r}_0 - \mathbf{r}|^2} dL_0\right]$$

Here, $\mathbf{r}_0$ is the position of the vortex elements or boundary elements, and $\mathbf{r}$ is the one where the velocity is being evaluated.

In 2-D unsteady viscous flow past a solid boundary, the absolute motion of the solid boundary, e.g., the rotation of the impeller blade, and inflow condition are generally known, and therefore, $\mathbf{V}_L(\mathbf{r})$ can be obtained easily. The main work is to determine the $\mathbf{V}_S(\mathbf{r})$, that is, the vorticity in the flow field. All the vorticity lies in the following two subregions: a thin layer of fluid adjoining the solid boundary, and free shear layers emanating from the trailing edge and boundary layer, i.e., the wake and separated flow. Thus, instead of integrating over the entire flow field, one can integrate over only two relatively small subregions. Then, velocity $\mathbf{V}_S(\mathbf{r})$ can be rewritten as,

$$\mathbf{V}_S(\mathbf{r}) = \mathbf{V}_b(\mathbf{r}) + \mathbf{V}_w(\mathbf{r}) \tag{2}$$

where $\mathbf{V}_b(\mathbf{r})$ is the velocity induced by the vorticity in the thin layer of fluid adjoining the solid boundary, and $\mathbf{V}_w(\mathbf{r})$ is that induced in the free wake and separated flow.

Therefore, the main problems in vortex methods are how to represent the vorticity in the two small subregions and how to determine its position and strength to satisfy the boundary conditions. There are several important procedures to solve the problems numerically in viscous incompressible fluid flow over a solid boundary.

Boundary Conditions. In the present study, the solid boundary surface is discretized into N panels, and vortex panels of strength γ_i are distributed over each panel with a definite thickness h to represent part of the flow boundary layer as illustrated in Fig. 3. Source panels of strength σ_i are distributed just under the boundary surface so that no flux and no-slip boundary conditions can be satisfied simultaneously. Since the strength of source panels approaches zero as N increases [23], the velocity $\mathbf{V}_B(\mathbf{r})$ due to the source σ as well as vorticity γ is an approximation of $\mathbf{V}_b(\mathbf{r})$ and can be expressed as

$$\mathbf{V}_B(\mathbf{r}) = -\frac{1}{2\pi}\left[\int_L \frac{\sigma(\mathbf{r}_0)(\mathbf{r}_0-\mathbf{r})}{|\mathbf{r}_0-\mathbf{r}|^2}dL_0 - \int_L \frac{\gamma(\mathbf{r}_0)\times(\mathbf{r}_0-\mathbf{r})}{|\mathbf{r}_0-\mathbf{r}|^2}dL_0\right]$$

$$= \sum_{i=1}^{N} (-\sigma_i \mathbf{C}_i + \gamma_i \times \mathbf{C}_i) \tag{3}$$

where $\mathbf{C}_i = (1/2\pi)\int_{L_i}(\mathbf{r}_0-\mathbf{r})/|\mathbf{r}_0-\mathbf{r}|^2 dL_0$, $\gamma_i = \Gamma_i \mathbf{k}/\Delta l_i$, $i = 1,2,...,N$.

The strength of vortex panel in the domain ABCD and source panel ABFE can be determined by the Boundary Element Method, in which there are $2N$ unknowns for a boundary surface discretized by N panels. Requiring the total velocity $\mathbf{V}(\mathbf{r})$ (Eq. (1)) to satisfy the boundary conditions produces an equivalent number of equations. However, there exist additional integral constraints to ensure a unique solution. The conservation of the circulation in the vortex panels around the solid boundary can be expressed by

$$\sum_{i=1}^{N} \Gamma_i(t_j) = \sum_{i=1}^{N} \Gamma_i(t_{j-1}) + \sum \Gamma_{in}(t_{j-1}) - \sum \Gamma_{out}(t_{j-1}) \tag{4}$$

where the second and third terms on the right-hand side of Eq. (4) are the sum of vorticity that flows into the panel ABCD, and the one of vortices shed from the panels, respectively. Here the circulation around each panel can be expressed by the tangential velocity components at boundary CD according to the no-slip boundary condition.

$$\Gamma_i(t_j) = -\Delta l_i \nu_i(t_j) \tag{5}$$

Similarly, the integral of source panels over the boundary surface is zero by continuity, that is,

$$\sum_{i=1}^{N} \sigma_i(t_j)\Delta l_i = 0 \tag{6}$$

Because of the integral constraints in Eqs. (4) and (6), this set of $2N+2$ equations is an over-determined set. The matrix solution for the vortex elements and source panels is formulated via Lagrange multipliers so that $2N$ boundary conditions on velocity can be satisfied in a least-squares sense and the integral constraints can be met exactly.

In order to improve the stability and accuracy of the solution in the present study a Petrov-Galerkin Boundary Method was applied to yield a solution that satisfies the boundary conditions ($\mathbf{V}=0$ on the stationary boundary whereas $\mathbf{W}=0$ on the rotating boundary) in an integral sense as opposed to pointwise [24]. In the Petrov-Galerkin method,

$$\int_L w(x)\mathbf{V}(\mathbf{r})dL = 0 \tag{7}$$

where weighting function $w(x)=1$ on an element and 0 elsewhere. The integral of the velocity $\mathbf{V}(\mathbf{r})$ including $\mathbf{V}_L(\mathbf{r})$, $\mathbf{V}_B(\mathbf{r})$, and $\mathbf{V}_w(\mathbf{r})$ on the discrete boundary surface was evaluated analytically in the Petrov-Galerkin method as given in Appendix A. The stability and accuracy of the solution were improved, especially for the solutions at the leading and trailing edges of the blades.

Vorticity Shedding From Solid Surface. There exist various procedures for evaluating the shedding vortices [20,25–29]. However, the effect of the pressure gradient along the solid surface was neglected in determining the position and rate of the vorticity shedding from the solid surface in the various algorithms of the existing vortex methods. A new procedure for vortices shed from a solid surface was derived directly from the Navier-Stokes equations, and the effect of the pressure gradient along the solid surface was considered in the present study.

Let us consider the strength of the vortices shed from stationary boundary DC of the panel ABCD, expressed in the third term on the right-hand side of Eq. (4). It can be determined by considering the circulation change in a stationary domain outside the panels [21]. Consider now a stationary domain S bounded by L in the 2-D incompressible flow field shown in Fig. 4. The circulation around L can be expressed in the vorticity form of the Navier-Stokes equations, and then the circulation change is

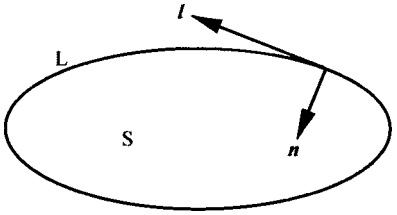

Fig. 4 Circulation change in a domain S

$$d\Gamma/dt = \int_S \partial\omega/\partial t\, dS = \int_S [-(\mathbf{V}\cdot\nabla)\omega + \nu\nabla^2\omega]dS \tag{8}$$

By applying the Gaussian divergence theorem it can be rewritten as

$$d\Gamma/dt = -\oint_L (\nu\nabla\omega)\cdot\mathbf{n}dL + \oint_L (\mathbf{V}\omega)\cdot\mathbf{n}dL \tag{9}$$

The first term on the right-hand side of Eq. (9) represents the circulation change due to the vorticity diffusion on the boundary, whereas the second term represents one due to the convection effect.

Application of the L-directional momentum equation to the integrated functions of Eq. (9) produces

$$(-\nu\nabla\omega + \mathbf{V}\omega)\cdot\mathbf{n} = \partial V_l/\partial t + \partial B/\partial L \tag{10}$$

If the panel boundary DC shown in Fig. 3 is supposed to be a part of the boundary L in Fig. 4, the circulation change due to the vorticity diffusion and convection on the panel boundary DC can be expressed in the above domain S at a given period as

$$\Gamma(t_j) - \Gamma(t_{j-1}) = \int_{t_{j-1}}^{t_j} (d\Gamma/dt)dt = \sum_{i=1}^{i=N} \Delta\Gamma_i \tag{11}$$

where

$$\Delta\Gamma_i = \int_{t_{j-1}}^{t_j}\int_{L_i}^{L_{i+1}} [\partial V_i/\partial t + \partial B/\partial L]dL\,dt \tag{12a}$$

Equation (12*a*) represents that the circulation changes due to the vorticity diffusion and convection on the panel boundary DC consist of two parts: the local acceleration shown in the first term on the right-hand side, and the derivative of the Bernoulli function along the boundary DC. The effect of viscosity will be considered in the calculation of Bernoulli function B as described later.

Vortex Elements Shedding From Rotating Boundary. The circulation change in a given domain rotating with angular velocity Ω can be obtained in the manner similar to the stationary boundary case.

$$\Delta\Gamma_i = \int_{t_{j-1}}^{t_j}\int_{L_i}^{L_{i+1}} [\partial W_l/\partial t + \partial B'/\partial L + (\partial\mathbf{\Omega}/\partial t\times\mathbf{r})\cdot l]dL\,dt \tag{12b}$$

where $B' = B - \mathbf{U}\cdot\mathbf{V}$

Discretization of Shedding Vortex Elements. In a short time increment Δt, the length and vorticity of the nascent vortex element were assumed to equal to those of the respective panel over which it lies. Then, the thickness can be determined by

$$\Delta h_i = h\Delta\Gamma_i/\Gamma_i(t_j) \tag{13}$$

where $\Gamma_i(t_j)$ is the circulation around panel ABCD shown in Fig. 3.

When the thickness Δh_i is positive and thus the vortex is shed from the panel into the flow field, a vortex element is added in the out-domain. When the thickness Δh_i is negative and the vortex elements flow into the panels, on the other hand, no vortex elements are added. The vortex elements that entered the panels in the convection process were ignored in the next calculation step. The effect of the ignored elements was calculated in the second term on the right-hand side of Eq. (4), which was employed to determine the circulation around the panels in the next step.

As illustrated in Fig. 3, in order to avoid the complicated calculation for the nascent rectangular vortex deformation and interference with the complex boundary, M vortex blobs with viscosity radius were used to approximate a rectangular vortex element. Each vortex blob, in which the vorticity is redistributed in Gauss distribution form, is $1/M$ of the rectangular vortex element in area and circulation; that is, in each vortex blob

$$\omega = (\Delta\Gamma_{i,k}/\pi\epsilon^2)\exp(-r^2/\epsilon^2) \tag{14}$$

where $\pi\epsilon^2 = \Delta h_i \Delta l_i/M$ and $\Delta\Gamma_{i,k} = \Delta\Gamma_i/M$; $(k=1,2...,M;\ M = \mathrm{int}(\Delta l_i/h)+1)$. The tangential velocity induced by the vortex blob can be represented as

$$\nu_\theta = (\Delta\Gamma_{i,k}/2\pi r)\{1-\exp(-r^2/\epsilon^2)\} \tag{15}$$

By considering the viscosity diffusion with the core-spreading method [30] in the discrete vortex blobs, in the present study, the time variation of the core radius can be calculated by

$$d\epsilon/dt = c^2\nu/(2\epsilon);\quad c = 2.242 \tag{16}$$

Unsteady Pressure. After the vorticity and velocity field are determined in the above procedures, the unsteady pressure can be calculated according to the calculated velocity and vorticity time to time in the resent 2D flow calculation.

The Boundary Element Method was used to obtain the Bernoulli function B, which is expressed as [31]

$$\begin{aligned}\int\int_S B\cdot\nabla^2 G dS + \int_{L_i+L_d+L_\infty} B\nabla G\cdot\mathbf{n}dL \\ = -\int_{L_i+L_d+L_\infty} \partial\mathbf{V}/\partial t\cdot\mathbf{n}G dL - \nu \\ \times\int_{L_i+L_d+L_\infty} (\nabla G\times\boldsymbol{\omega})\cdot\mathbf{n}dL - \int\int_S \nabla G\cdot(\mathbf{V}\times\boldsymbol{\omega})dS\end{aligned} \tag{17}$$

The acceleration in the first term on the right-hand side of the above equation can be written in the rotational cylindrical coordinates as

$$\partial\mathbf{V}/\partial t = \partial_R\mathbf{W}/\partial t - \nabla(\mathbf{U}\cdot\mathbf{V}) + \mathbf{U}\times(\nabla\times\mathbf{V}) + \partial\boldsymbol{\Omega}/\partial t\times\mathbf{r} \tag{18}$$

From the no-flux boundary condition on the rotating boundary,

$$\int_{L_i} \partial_R\mathbf{W}/\partial t\cdot\mathbf{n}G dL = 0 \tag{19}$$

while on the stationary boundary,

$$\int_{L_d+L_\infty} \partial\mathbf{V}/\partial t\cdot\mathbf{n}G dL = 0 \tag{20}$$

To avoid constructing the mesh for the evaluation of the second and third terms on the right-hand side of Eq. (18), in this study, an inner boundary surface L_2 was set between the rotor and stator as shown in Fig. 2. By employing the Gaussian divergence theorem and the flow continuum equation into Eq. (17), then the following equation can be derived:

Table 1 Values of β_1 and β_2

Locations of P	β_1	β_2
in S_1	1	0
on L_i	0.5	0
on L_2	0.5	0.5
in S_2	0	1
on L_d	0	0.5

* $\iint_S B\cdot\nabla^2 G dS = \beta_1 B' + \beta_2 B$

$$\begin{aligned}\beta_1 B' + \beta_2 B + \int_{L_i} B'\nabla G\cdot\mathbf{n}dL + \int_{L_d+L_\infty} B\nabla G\cdot\mathbf{n}dL \\ = -\int_{L_i} (\partial\boldsymbol{\Omega}/\partial t\times\mathbf{r})\cdot\mathbf{n}G dL + \Omega\int_{L_2} (\partial V_r/\partial\theta)G dL \\ + \int_{L_2} (\mathbf{V}\cdot\mathbf{U})\nabla G\cdot\mathbf{n}dL - \nu\int_{L_i+L_d+L_\infty} (\nabla G\times\boldsymbol{\omega})\cdot\mathbf{n}dl \\ - \int\int_{S_1} \nabla G\cdot(\mathbf{W}\times\boldsymbol{\omega})dS - \int\int_{S_2} \nabla G\cdot(\mathbf{V}\times\boldsymbol{\omega})dS\end{aligned} \tag{21}$$

where the values of β_1 and β_2 at $P(x_p, y_p)$ are shown in Table 1.

The left-hand side of Eq. (21) represents a matrix formulation, which needs to be decomposed on the first several time steps only, if an appropriate time step is set. The right-hand side accounts for the change in impeller rotational speed, the viscosity effect of the vorticity adjacent to the boundary surface, and the flow of volume vorticity. The vorticity field is represented by the bound vortex elements and free vortices, and the free vortex with an invariable circulation is supposed to flow with the velocity at its center point. Thus the volume integrals on the right-hand side of Eq. (21) can be evaluated on the center of the bound vortex elements and free vortices, rather than on a set of convected control points [32].

Instantaneous Total Head Rise and Flow Rate. The instantaneous pump operation is calculated by considering the change in the pump operating point. The total head rise across the pump is defined by the difference of the total hydraulic head between the suction and discharge ports of the pump,

$$H(t) = H_d - H_s(t) \tag{22}$$

The hydraulic head at discharge port H_d was assumed to be $H_d = 0$, so that $H(t)$ can be obtained after the total hydraulic head at suction port $H_s(t)$ has been determined by Eq. (21). The total head rise generated by pumping $H(t)$, balances the elevation head $H_e(t)$, the head loss in the pumping system $H_l(t)$ and the apparent total head difference $H_c(t)$ caused by the inertia of the water contained in pumping system, as the following equation shows:

$$H(t) = H_e(t) + H_l(t) - H_c(t) \tag{23}$$

In the present calculation, it is assumed that the pump delivers no elevation head, so the instantaneous flow rate $Q_i(t)$ can be calculated by

$$H(t) = (l_{eq}/gA_0)dQ/dt + \kappa H_0 Q^2/Q_0^2 \tag{24}$$

where H_0 and Q_0 are the rated total head and flow rates; $A_0 = \pi D_0^2/4$ is nominal flow area; l_{eq} is equivalent pipe length referred to are A_0; and κ is resistance coefficient [33]. At every

Table 2 Specifications of test pump

Rating:		Pump system:	
Q_0	6.21 m^3/min	D_0	0.2 m
H_0	29.2 m	κ	see Table 3
N	2066 min^{-1}	l_{eq}	2 m
Ns	410 m^3/min.m.min^{-1}		
Impeller:		**Diffuser:**	
D_2	250 mm	R_3	129 mm
b_2	41.6 mm	b_3,b_4	45.8 mm
β_5	22.5 Deg.	R_4	162.5 mm
Z_i	5	Z_d	8

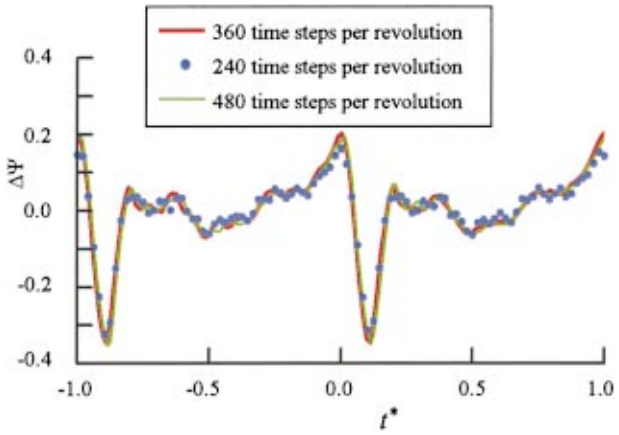

Fig. 5 Effect of time step on pressure fluctuations at station (r_1, c_1) for rated condition

calculation step, the pump operating point is determined in the process of resolving iteratively the instantaneous flow rate and total head rise in Eqs. (21) and (24).

Pump Model and Experimental Data. The test pump is a single-stage diffuser pump with five impeller blades, eight diffuser vanes, and volute casing as shown in Fig. 1(*a*). Its specifications are summarized in Table 2. A comprehensive survey of the instantaneous pressure was made within the diffuser passages by Tsukamoto et al. [4]. The unsteady pressures are measured by semiconductor type pressure transducers installed directly on the pressure taps to prevent the decrease of natural frequency in the pressure measurement systems.

Calculations by Singularity Method and 3D CFD-code. Qin and Tsukamoto [15–17] calculated the pressure fluctuations downstream of a diffuser pump by singularity method. In their 2-D, inviscid and incompressible flow analysis, they set three kinds of vortices for the fundamental analysis on impeller-diffuser interaction: steady bound vortices on the impeller, unsteady bound vortices on the diffuser vanes and free vortices shed from the diffuser vane trailing edges. Shi and Tsukamoto [18,19] calculated the pressure fluctuations downstream of impeller in a diffuser pump by using the 2-D and 3-D unsteady RANS code with standard k-ϵ turbulence models. The CFD code is a commercial software package STAR-CD [34], in which a technique called Arbitrary Sliding Mesh was provided to accommodate the relative motion between the rotor and stator. In their calculations, the unsteady flow was simulated on an unstructured grid with 338,460 nodal points by using the pressure based, fully conservative finite volume method, that is, an implicit first-order scheme for the discretization of the time-dependent term, a third-order scheme QUICK for the convection terms and the central difference scheme for the diffusion terms. The unsteady pressure calculated by the present vortex method will be compared with the one calculated by the singularity method and the 3-D CFD code.

Calculation Condition and Numerical Error. In the present calculation, the thickness of the vortex panels adjoining the solid boundary is assumed to be: $h/D_2 = 2.0/\sqrt{\mathrm{Re}}$. The instantaneous rotational speed $N(t)$ is assumed to be

$$N(t) = N_f(1 - e^{-t/T_{na}}) \tag{25}$$

where $T_{na} = T_0$ was assumed in the present study.

All the computations were conducted on a Workstation VT-Alpha 666 (666 MHz Alpha Processor, 1GB RAM). To determine the sensitivity of numerical results to the magnitude of the time step, the results at 240, 360, and 480 time steps per revolution are compared. The magnitude of the time step has no significant effect on the pressure fluctuations shown in Fig. 5. The sensitivity of the model to the number of surface panels was checked by performing the calculations on two panel systems, one with 45 panels and the other with 60 panels distributed along each blade, as shown in Fig. 6. The numerical results showed that accurate computations are expected from 360 time steps per revolution and 60 panels per blade in the present unsteady calculation, as can be seen in Table 3. Approximately 25,000 vortex elements in the rated operating

Table 3 Calculation condition and statistic values of the calculated result

Case No.	1	2	3	4	5	6
κ	1	0.5	2	1	1	1
N	60	60	60	45	60	60
$T_0/\Delta t$	360	360	360	360	240	480
$\overline{Q}/Q_0$	1.01	1.25	0.78	1.00	1.01	1.01
$\overline{H}/H_0$	1.02	0.79	1.22	1.00	1.02	1.01
$\sigma_Q(\times 10^{-4})$	1.06	2.4	2.2	1.9	2.0	0.96
$\sigma_H(\times 10^{-2})$	1.39	2.48	1.71	1.55	1.17	1.01

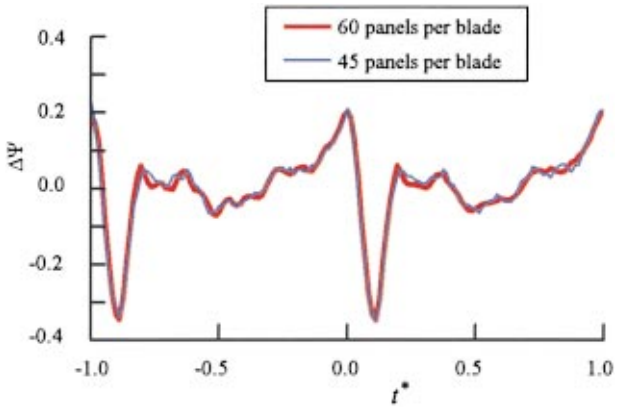

Fig. 6 Effect of panel density on pressure fluctuations at station (r_1, c_1) for rated condition

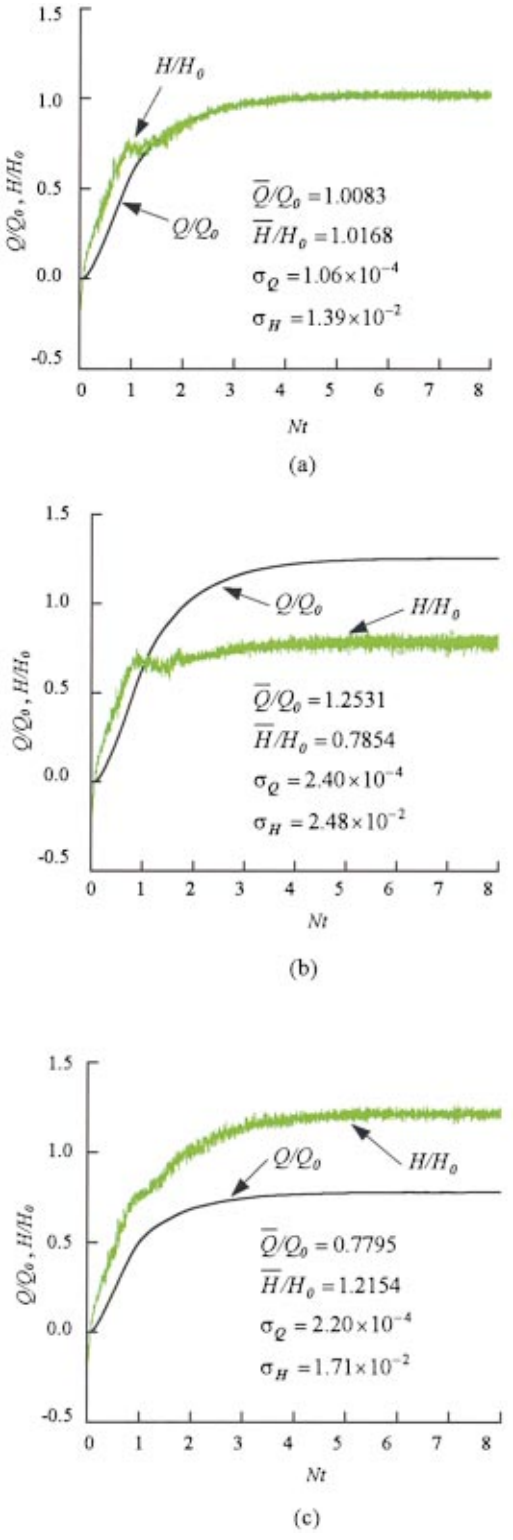

Fig. 7 Time histories of instantaneous flow rate and hydraulic head after starting. (*a*) Case 1(κ=1; rated); (*b*) Case 2 (κ=0.5; overcapacity); (*c*) Case 3 (κ=2; low-capacity)

condition and 30,000 vortex elements in the off-design operating condition were used in the present calculation. Therefore, for the present 2-D calculations,the numerical deviations from the experimental data can be attributed to physical modeling error: (1) 2-D and 3-D difference; (2) difference between numerical calculation

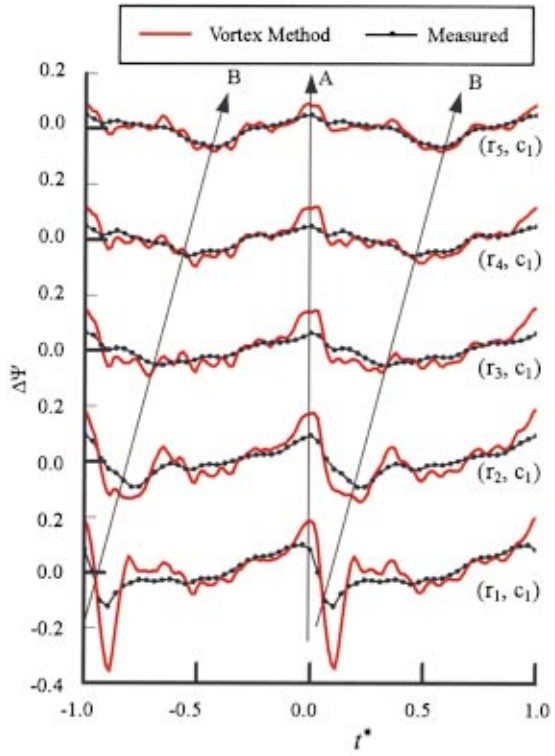

Fig. 8 Time histories of unsteady pressure along c_1 line for Case 1 (κ=1; rated); experimental uncertainty in $\Delta\Psi=\pm 7.1\%$

modeling and real pump modeling; (3) uncertainties in measured data; and (4) discretization error in the vorticity field.

Results and Discussion

Instantaneous Flow Rate and Total Hydraulic Head. Figures 7(*a*), (*b*), and (*c*) show the time histories of the flow rate and total hydraulic head after starting the pump under the rated, overcapacity and low-capacity flow conditions. It can be found that the instantaneous flow rate and total hydraulic head change remarkably at the initial stage after starting the pump and reach their steady values after 6 revolutions of the impeller for the pumping system described in Table 2. The mean values of the instantaneous flow rate and the total hydraulic head in Fig. 7 are the time averaged-values after 6 revolutions of the impeller. The flow in the diffuser pump seems to be the most stable at the rated condition because the calculated standard deviation of instantaneous flow rate and total hydraulic head shown in Fig. 7(*a*) is the smallest among these three cases.

Pressure Fluctuations in the Diffuser Passage. The measured unsteady pressure data presented are phase-averaged in 100 revolutions of the impeller, whereas the calculated data by the present vortex method, the singularity method and the 3-D CFD code are not phase-averaged but instantaneous.

Figure 8 represents the time histories of the calculated and measured unsteady pressure on the pressure taps along c_1 line (see Fig. 1(*b*)) in the diffuser passage at the rated condition. The waveform of unsteady pressure calculated by the present vortex method shows a good agreement with the measured one. The peak of unsteady pressure appears at the instant when the trailing edge of an impeller vane is the closest to the leading edge of a diffuser vane, shown later in Fig. 11(*a*). Since the unsteady pressure at the different radial locations on the c_1 line shows the peak at the same instant as designated by ray A, it is thought to be caused by the change in the relative position of the impeller and diffuser vanes, that is, the effect of the potential interaction. The potential inter-

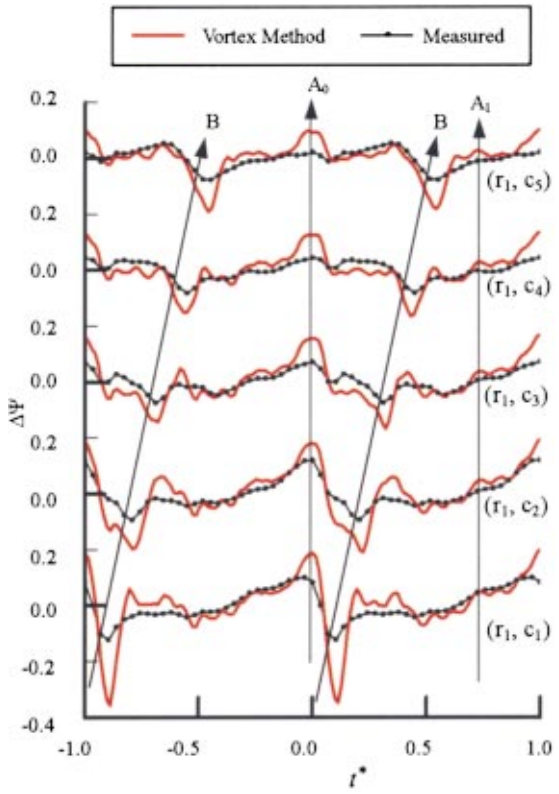

Fig. 9 Time histories of unsteady pressure at diffuser inlet for Case 1 (κ=1; rated); experimental uncertainty in $\Delta\Psi=\pm 7.1\%$

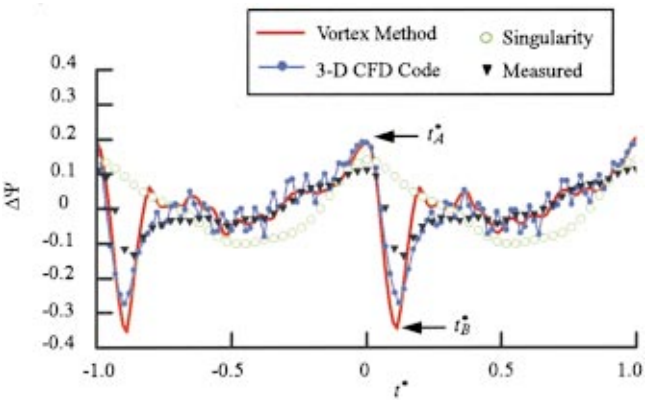

Fig. 10 Time histories of pressure fluctuations at station (r_1, c_1) for Case 1 (κ=1; rated); experimental uncertainty in $\Delta\Psi=\pm 7.1\%$

action is found to be dominant at the inlet because the pressure peak due to the potential interaction decreases at bigger radii in the diffuser passage. On the other hand, the valley of unsteady pressure is due to the gust effect of the impeller blade wake, since it shows a bigger time lag with increasing radii as shown by ray B.

Figure 9 shows the time histories of the unsteady pressure at diffuser inlet $r=r_1$ (see Fig. 1(*b*)) at the rated condition. The calculated waveform agrees well with the measured one. The unsteady pressures are propagating toward the circumferential directions as can be seen in these figures. The pressure peak due to the potential interaction appears at the same instant $t^*=0$ as indicated by A_0, which propagates instantaneously from c_1 to c_5 and decreases from the suction to pressure side in the diffuser passage. It can be found that a similar effect as designed by A_1 appears and propagates from c_5 to c_1 at the instant when the potential interaction occurs at the next diffuser vane near c_5. The amplitude of the pressure fluctuations is greater near the suction side than that near the pressure side. The increase in the unsteady pressure due to the impeller blade trailing edge approaching the diffuser vane leading edge is less than the unsteady pressure drop due to the passing through of the impeller blade trailing edge. Whereas the potential interaction occurs at the same instant on the entire flow field, the effect of wake interaction generates a valley after the passing of the impeller trailing edge through the diffuser leading edge and thus shows a time lag in a pressure valley as designated by ray B.

Figure 10 depicts the time histories of the unsteady pressure coefficient calculated by the present vortex method, singularity method [16,17], 3-D CFD code [19] and as measured on a representative pressure tap (r_1, c_1) at the rated condition. The waveform of unsteady pressure predicted by the present vortex method shows better agreement with the experimental result than the waveform predicted by the singularity method, which comprises only low frequency components, or the 3-D CFD code, which includes much higher frequency components. The amplitude of

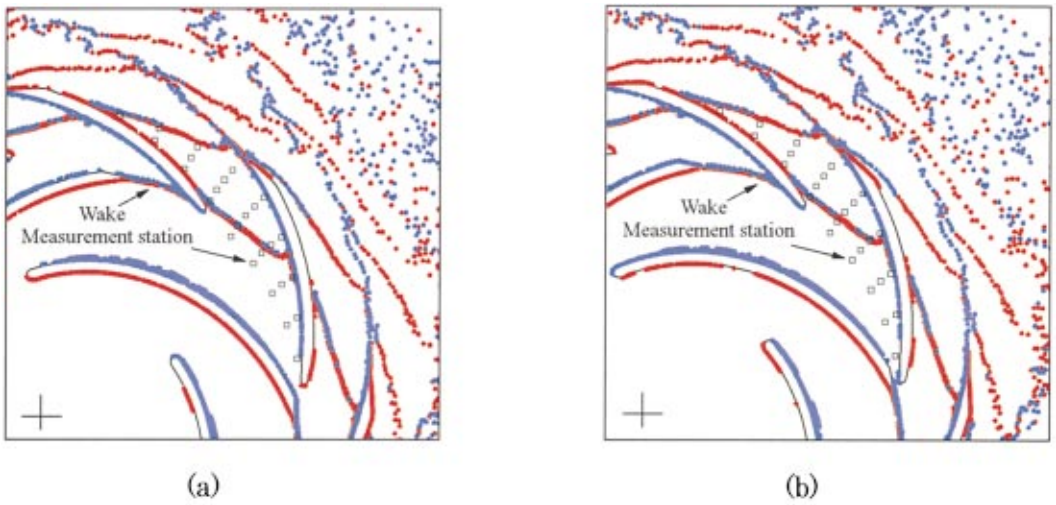

Fig. 11 Vortex pattern and relative position of the rotor to stator for Case 1 (rated). (*a*) At time t^*_A; (*b*) at time t^*_B.

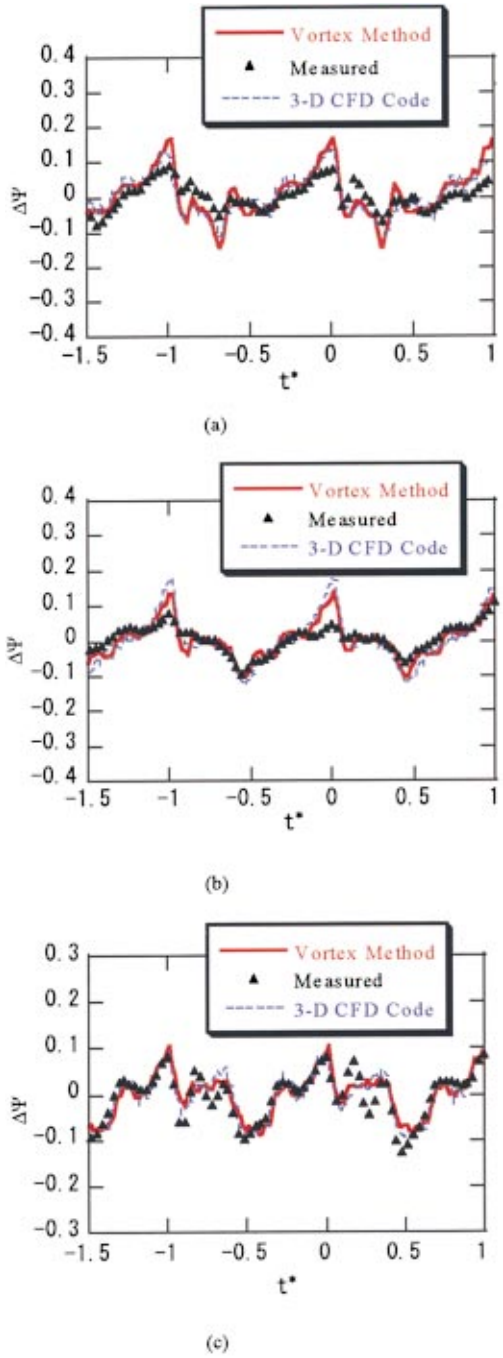

Fig. 12 Time histories of pressure fluctuations for Case 1 (κ=1; rated); Experimental uncertainty in $\Delta\Psi = \pm 7.1\%$. (*a*) Station (r_1, c_3);(*b*) Station (r_2, c_3);(*c*) Station (r_3, c_3).

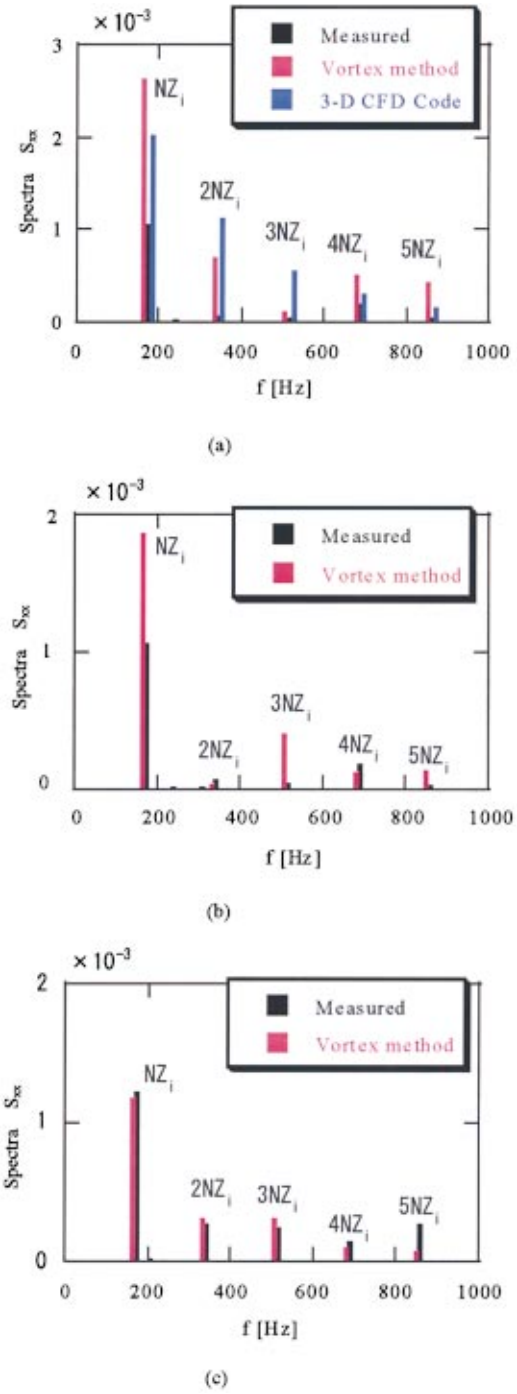

Fig. 13 Pressure fluctuations in frequency domain for Case 1 (κ=1; rated). (*a*) Station (r_1, c_3); (*b*) Station (r_2, c_3); (*c*) Station (r_3, c_3).

the pressure fluctuations predicted by the vortex method or by the 3-D CFD code, however, is bigger than the experimental result and that calculated by the singularity method. The big drop in the pressure fluctuations due to the passing of the impeller blade trailing edge is not predicted by the singularity method because the blade thickness and viscous wake-diffuser interaction are neglected in the calculation. The turbulent model and the numerical error are found to be the reasons why much higher frequency components in unsteady pressure appear in the 3-D CFD code calculation.

Figures 11(*a*) and (*b*) show the vortex pattern in the diffuser passage and the relative position of the rotor to stator at the instant of the unsteady pressure peak and valley on the pressure tap (r_1, c_1), respectively. The big drop in unsteady pressure from peak to valley is caused by the passing of the trailing edge of the impeller blade through the leading edge of diffuser vane. The vortices in the wake shed from the impeller blade trailing edge travel with the main flow from the impeller and are chopped into segments by the diffuser vanes. The vortices in the diffuser passage do not spread over the entire passage but flow in sheet shape at rated condition.

Figures 12(*a*), (*b*), (*c*), and 13(*a*), (*b*), (*c*) depict the pressure fluctuations at the time domain and frequency domain, respectively, on the representative pressure tap (r_1, c_3), (r_2, c_3), and (r_3, c_3) in the diffuser passage at the rated condition. The pres-

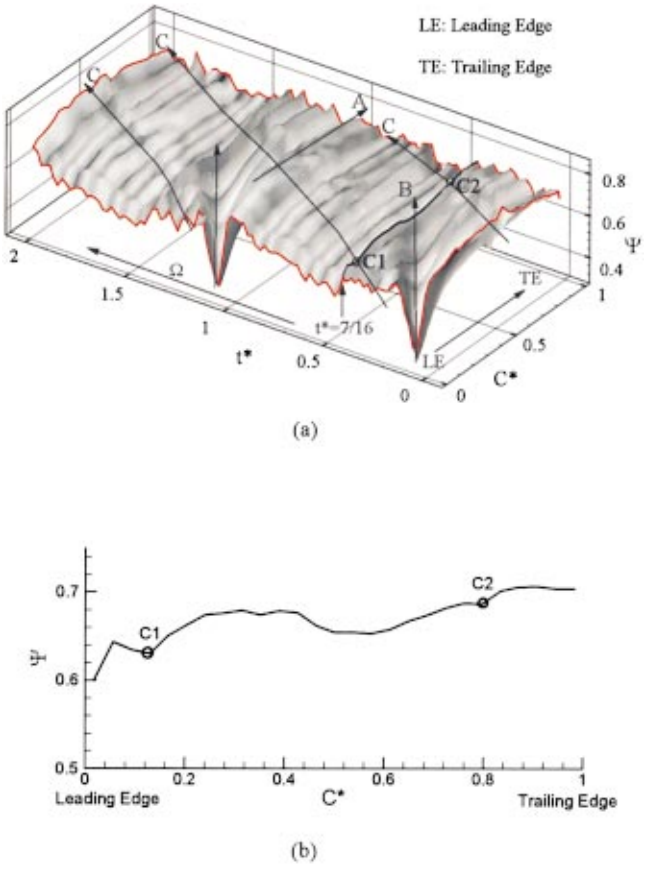

Fig. 14 (*a*) Time histories of unsteady pressure on SS of diffuser vane for Case 1 (rated); (*b*) pressure distributions on SS or diffuser vane at $t^*=7/16$ for Case 1 (rated)

sures calculated by the present vortex method show good agreement with the ones measured and also those predicted by the 3-D CFD code (Fig. 12). The power spectral density function shown in Fig. 13 is extracted from the corresponding data in the time domain shown in Fig. 12 using an external FFT program. The present simulations demonstrate that the unsteady pressure in the diffuser passage fluctuates with the impeller blade passing frequency NZ_i and its higher harmonics. A good agreement can be seen between the measured frequency components and those predicted by the vortex method (Fig. 13).

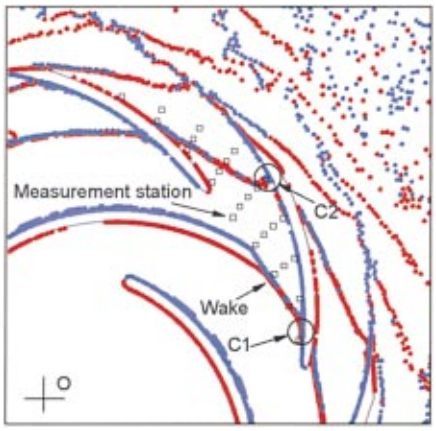

Fig. 15 Vortex pattern at $t^*=7/16$ for Case 1 (rated)

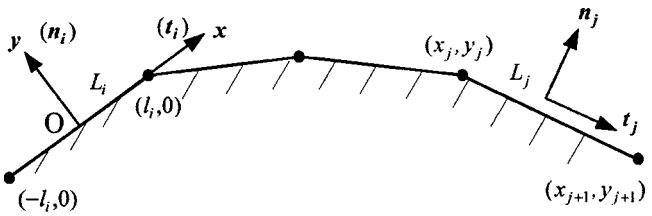

Fig. 16 Local coordinates on boundary

The effects of the rotor-stator interaction are presented in more detail in Fig. 14(*a*), which shows the time histories of unsteady pressure on the suction surface of the diffuser vane at the rated condition. Ray A shows the propagation of pressure peak induced by the potential interaction between the impeller and diffuser vanes, which appears at the same instant as described previously. The pressure valley propagates along the direction of ray B. It is induced by the wake interaction, which is generated at the instant when the trailing edge of impeller blade is passing through the leading edge of diffuser vane. Ray C shows the effect of wake transport from the trailing edge of the impeller vane. The wake shed from the trailing edge of the impeller interacts with the boundary layer of the diffuser vane and affects the pressure on the blade surface. Figure 14(*b*) depicts the unsteady pressure distributions on the suction surface of the diffuser vane at time $t^*=7/16$. Figure 15 shows the vortex pattern at the time corresponding to Fig. 14(*b*). The effect of wake transport can be seen at two locations in Fig. 15, which correspond to the points with a marked pressure drop, $C1$ and $C2$, shown in Fig. 14. The amplitude of the pressure fluctuations due to wake transport is affected by the strength of the wake, and the wake effect is weaker than the potential interaction at the rated condition. While the propagation velocity of the potential interaction is determined by the angular velocity, the effects of wake transport propagate with the flow absolute velocity.

The pressure fluctuations near the diffuser inlet are mainly affected by the potential interaction, while those near the diffuser passage outlet are mainly affected by the wake shed from the impeller blade. The calculations by the singularity method can predict the effect of the potential interaction reasonably, but cannot predict the effect of the wake acceptably. However, the calculations by the present vortex method can predict the effect of the potential interaction as well as the effect of the wake reasonably, as can be seen in Figs. 8–10, 12–15.

Conclusion

A numerical method was developed for a more realistic prediction of the pressure fluctuations due to rotor-stator interaction in a diffuser pump by considering the change in operating point of the pump. The pressure fluctuations were predicted in 2-D unsteady incompressible flow by using a vortex method, in which vortices shed from solid boundary are determined based on the momentum equations. The calculated pressure fluctuations in the diffuser passage were compared with the ones measured as well as calculated by the singularity method and the 3-D CFD code. From the results of the present study, the following conclusions are derived.

1 The potential effect of the wake effect on the pressure fluctuations can be predicted satisfactorily by the present vortex method.

2 Whereas the pressure fluctuations near the diffuser inlet are affected by the potential interaction, the pressure fluctuations near the outlet are predominantly affected by the wake effects due to wake transport.

3 The pressure in the diffuser passage fluctuates with the basic frequency of the impeller blade passing frequency NZ_i and its higher harmonics.

Acknowledgments

The study was supported by the Japanese Ministry of Education, Science and Culture under a grant-in-aid for Scientific Research, No. 09450081. This support is gratefully acknowledged.

Nomenclature

B = Bernoulli function $= p/\rho + V^2/2$
b = passage width
C^* = coordinate of diffuser suction surface measured from leading edge
c = symbol of pressure traverse line
D_2 = impeller diameter
f = frequency
G = Green function
H = total hydraulic head rise across pump
H_0 = rated total head
$H_c(t)$ = apparent total head difference caused by inertia of water in pumping system
H_d = total hydraulic head at discharge port
$H_e(t)$ = elevation head
$H_l(t)$ = total hydraulic loss in pumping system
$H_s(t)$ = total hydraulic head at suction port
κ = resistance coefficient of pumping system
$\mathbf{k}$ = unit vector for z direction in Cartesian system (x,y,z)
l_{eq} = equivalent pipe length
$\mathbf{l},\mathbf{n}$ = unit vector for longitudinal and normal directions on boundary L
L = boundary of concerned domain
N = rotational speed
Nt = number of impeller revolutions after its start $= \int_0^t N(t)dt$
p = static pressure
PS = pressure side
Q = flow rate
Q_0 = rated flow rate
r,θ = cylindrical coordinates
$\mathrm{R_e}$ = Reynolds number $= D_2 V_0/\nu$
S = entire region of concerned domain
SS = suction side
t = time
t^* = nondimensional time $= t/T_i$
T_0 = time required for one revolution of impeller
T_i = time required for one pitch of impeller blade
T_{na} = nominal acceleration time
$\mathbf{U}$ = perpheral velocity
U_2 = peripheral speed of impeller
V_0 = meridian velocity at suction port
$\mathbf{V}$ = absolute velocity
$\mathbf{V}_b(\mathbf{r})$ = velocity induced by thin layer of fluid adjoining solid boundary
$\mathbf{V}_B(\mathbf{r})$ = $\mathbf{V}_b(\mathbf{r})$ approximated in numerical calculation, defined in Eq. (3)
$\mathbf{V}_L(\mathbf{r})$ = velocity induced by absolute motion of boundary L
$\mathbf{V}_S(\mathbf{r})$ = velocity induced by all vortex elements in the entire region of interest
$\mathbf{V}_w(\mathbf{r})$ = velocity induced by wake and separated flow
$\mathbf{W}$ = relative velocity
Z = number of blades
γ = vorticity in thin layer of fluid adjoining solid boundary L
Γ = circulation (anti-clockwise is positive)
ρ = density
σ = source
ν = kinematic viscosity
ω = vorticity
Ω = angular velocity
$\underline{\psi}$ = pressure coefficient $= (p - \rho g H_s)/(\rho U_2^2/2)$
Ψ = steady value of Ψ
$\Delta\psi$ = nondimensional unsteady pressure $= \Psi - \overline{\Psi}$

Subscripts

d = diffuser
i = impeller
1,2 = impeller inlet and outlet
3,4 = diffuser inlet and outlet
∞ = infinite

Appendix A

Let us consider the numerical procedure based on the Petrov-Galerkin method. The integral of velocity $\mathbf{V}(\mathbf{r})$ on the boundary element L_j is written as

$$\int_{L_j} \mathbf{V}(\mathbf{r})dl = \int_{L_j} \{\mathbf{V_B}(\mathbf{r}) + \mathbf{V_w}(\mathbf{r}) + \mathbf{V_L}(\mathbf{r})\}dl \tag{26}$$

From Eq. (3), the first term on the right hand side of the above equation is

$$\int_{L_j} \mathbf{V_B}(\mathbf{r})dl = \sum_{i=1}^{N} \left(-\sigma_i \int_{L_j} \mathbf{C}_i dl + \gamma_i \times \int_{L_j} \mathbf{C}_i dl \right) \tag{27}$$

The integral of $\mathbf{C_i} = (1/2\pi)\int_{L_i} (\mathbf{r}_0 - \mathbf{r})/|\mathbf{r}_0 - \mathbf{r}|^2 dL)$ on the segment L_j contributed by the vortex and source sheet of length $2l_i$ (see Fig. 16) along x axis can be expressed in the Petrov-Galerkin method as follows:

$$\int_{L_j} \mathbf{n_i} \cdot \mathbf{C_i} dl = \sqrt{(1+k^2)} \int_{x_j}^{x_{j+1}} \{\tan^{-1}[(x-l_i)/(kx+b)] - \tan^{-1}[(x+l_i)/(kx+b)]\}dx \tag{28}$$

$$\int_{L_j} \mathbf{t_i} \cdot \mathbf{C_i} dl = \sqrt{(1+k^2)} \int_{x_j}^{x_{j+1}} \{\ln[(x-l_i)^2 + (kx+b)^2] - \ln[(x+l_i)^2 + (kx+b)^2]\}dx \tag{29}$$

where $k = (y_{j+1} - y_j)/(x_{j+1} - x_j)$ and $b = y_j - kx_j$; $(x_j \neq x_{j+1})$, x and y are the tangential and normal field points referenced to the centroid of segment L_i.

Thus, the integral of $\mathbf{V_B}(\mathbf{r})$ on the discrete boundary elements can be obtained analytically. In the similar manner, the second and third term integral on the right hand side of Eq. (26) can be obtained.

References

[1] Arndt, N., Acosta, A. J., Brennen, C. E., and Caughey, T. K., 1989, "Rotor/Stator Interaction in a Diffuser Pump," ASME J. Turbomach., **111**, pp. 213–221.
[2] Arndt, N., Acosta, A. J., Brennen, C. E., and Caughey, T. K., 1990, "Experimental Investigation of Rotor/Stator Interaction in a Diffuser Pump with Several Vaned Diffusers," ASME J. Turbomach., **112**, pp. 98–107.
[3] Brennen, C. E., 1994, Hydrodynamics of Pumps, Concept ETI Inc. and Oxford University Press, pp. 173–218, pp. 261–311.
[4] Tsukamoto, H., Uno, M., Hamafuku, H., and Okamura, T., 1995, "Pressure Fluctuation Downstream of a Diffuser Pump Impeller," The 2nd Joint ASME/JSEM Fluids Engineering Conference, Forum of Unsteady Flow, FED-Vol. 216, pp. 133–138.
[5] Dring, R. P., Joslyn, H. D., Hardin, L. W., and Wagner, J. H., 1982, "Turbine Rotor-Stator Interaction," ASME J. Eng. Power, **104**, pp. 729–742.
[6] Dong, R., Chu, S., and Katz, J., 1992, "Quantitative Visualization of the Flow Within the Volute of a Centrifugal Pump. Part B: Results," ASME J. Fluids Eng., **114**, No. 3, pp. 396–403.
[7] Akin, O., and Rockwell, D., 1994, "Flow Structure in a Radial Flow Pumping System Using High-Image-Density Particle Image Velocimetry," ASME J. Fluids Eng., **116**, pp. 538–544.
[8] Ubaldi, M., Zunino, P., Barigozzi, G., and Cattanei, A., 1996, "An Experimental Investigation of Stator Induced Unsteadiness on Centrifugal Impeller Outflow," ASME J. Turbomach., **118**, pp. 41–54.
[9] Chu, S., Dong, R., and Katz, J., 1995, "Relationship Between Unsteady Flow, Pressure Fluctuations, and Noise in a Centrifugal Pump—Part A: Use of PDV DATA to Compute the Pressure Field," ASME J. Fluids Eng., **117**, Mar., pp. 24–29.

[10] Chu, S., Dong, R., and Katz, J., 1995, ''Relationship Between Unsteady Flow, Pressure Fluctuations, and Noise in a Centrifugal Pump—Part B: Effects of Blade-Tongue Interactions,'' ASME J. Fluids Eng., **117**, Mar, pp. 30–35.
[11] Kaupert, K. A., and Staubli, T., 1999, ''The Unsteady Pressure Field in a High Specific Speed Centrifugal Pump Impeller—Part I: Influence of the Volute,'' ASME J. Fluids Eng., **121**, Sept., pp. 621–626.
[12] Kaupert, K. A. and Staubli, T., 1999, ''The Unsteady Pressure Field in a High Specific Speed Centrifugal Pump Impeller—Part II: Transient Hysteresis in the Characteristic,'' ASME J. Fluids Eng., **121**, Sept., pp. 627–632.
[13] Fortes-Patella, R., Longatte, F., Kueny, J-L., and Croba, D., 1995, ''Numerical Analysis of Unsteady Flow in a Centrifugal Pump,'' ASME Fluid Machinery, FED, Vol. 222, pp. 41–46.
[14] Bert, P. F., Combes, J. F., and Kueny, J. L., 1996, ''Unsteady Flow Calculation in a Centrifugal Pump Using a Finite Element Method,'' XVIII IAHR Symposium on Hydraulic Machinery and Cavitation, Valencia, Spain, pp. 371–380.
[15] Qin, W., 1996, ''Pressure Fluctuations Downstream of Impeller due to Rotor-Stator Interaction in a Diffuser Pump,'' Ph.D. thesis, Kyushu Institute of Technology (in Japanese).
[16] Qin, W., and Tsukamoto, H., 1997, ''Theoretical Study of Pressure Fluctuation Downstream of a Diffuser Pump Impeller—Part 1: Fundamental Analysis on Rotor-Stator Interaction,'' ASME J. Fluids Eng., **119**, pp. 647–652.
[17] Qin, W., and Tsukamoto, H., 1997, ''Theoretical Study of Pressure Fluctuation Downstream of a Diffuser Pump Impeller—Part 2: Effects of Volute, Flow Rate and Radial Gap,'' ASME J. Fluids Eng., **119**, pp. 653–658.
[18] Shi F., and Tsukamoto, H., 1999, ''Numerical Studies of Effects of Flow Rate and Radial Gap on Pressure Fluctuations Downstream of a Diffuser Pump Impeller,'' Proceedings of the 3rd ASME/JSME Joint Fluids Engineering Conference, July 18–23, San Francisco, CA.
[19] Shi, F., and Tsukamoto, H., 2001, ''Numerical Study of Pressure Fluctuations Caused by Impeller-Diffuser Interaction in a Diffuser Pump Stage,'' ASME J. Fluids Eng. **123**, pp. 466–474.
[20] Zhu, B., 1999, ''Study on Application of an Advanced Vortex Method to Unsteady Flow Analysis in Turbomachinery,'' Doctoral thesis, Yokohama National University, Japan.
[21] Wang, H., and Tsukamoto, H., 2000, ''Numerical Analysis of Pressure Fluctuation due to Rotor-Stator Interaction in a Diffuser Pump by Vortex Method,'' The 20th IAHR Symposium, Aug. 6–9, Charlotte, U.S.A.
[22] Wu, J. C., and Thompson, J. F., 1973, ''Numerical Solutions of Time-Dependent Incompressible Navier–Stokes Equations Using an Integro-Differential Formation,'' Comput. Fluids, Vol. 1, pp. 197–215.
[23] Uhlman, J. S., and Grant J. R., 1993, ''A New Method for the Implementation of Boundary Conditions in the Discrete Vortex Method,'' ASME 1993 Fluids Engineering Spring Meeting, Washington, D.C., June, pp. 149–155.
[24] Kempka, S. N., Glass, M. W., Strickland, J. H., and Ingber, M. S., 1999, ''A Galerkin Boundary Element Method for Solving the Generalized Helmholtz Decomposition,'' Third International Workshop on Vortex Flows and Related Numerical Methods. Proceedings, Vol. 7, pp. 205–214.
[25] Sarpkaya, T., 1989, ''Computational Methods With Vortices—The 1988 Freeman Scholar Lecture,'' ASME J. Fluids Eng., **111**, pp. 5–52.
[26] Huyer, S. A. and Grant, J. R., 1996, ''Computation of Unsteady Separated Flow Fields Using Anisotropic Vorticity Elements,'' ASME J. Fluids Eng., **118**, pp. 839–849.
[27] Kamemoto, K., 1995, ''On Attractive Features of the Vortex Methods,'' *Computational Fluid Dynamic Review 1995* (M. Hafez and K. Oshima, eds.), Wiley, NY, pp. 334–353.
[28] Chorin, A. J., 1978, ''Vortex Sheet Approximation of Boundary Layer,'' J. Comput. Phys., **74**, pp. 283–317.
[29] Lenoard, A., 1980, ''Vortex Methods For Flow Simulations,'' J. Comput. Phys., **37**, pp. 289–335.
[30] Kuwahara, K., and Takimi, H., 1973, ''Numerical Studies of Two-Dimensional Vortex Motion by a System of Point Vortices,'' J. Phys. Soc. Jpn., **34**, pp. 247–253.
[31] Uhlman, J. S., 1992, ''An Integral Equation Formation of the Equation of Motion of an Incompressible Fluid,'' Naval Undersea Warfare Center Technical Report 10-086, 15 July.
[32] Marshall, J. S., and Grant, J. R., 1996, ''Penetration of a Blade Into a Vortex Core: Vorticity Response and Unsteady Blade Forces,'' J. Fluid Mech., **306**, pp. 83–109.
[33] Tsukamoto, H., Matsunaga, S., Yoneda, H., and Hata, S., 1986, ''Transient Characteristics of a Centrifugal Pump During Stopping Period,'' ASME J. Fluids Eng., **108**, pp. 392–399.
[34] STAR-CD Documentation, Version 3.0, Computational Dynamics Ltd., London, 1996.

Analysis of Vortical Flow Field in a Propeller Fan by LDV Measurements and LES—Part I: Three-Dimensional Vortical Flow Structures

Choon-Man Jang
e-mail: jang@mech.kyushu-u.ac.jp

Masato Furukawa

Masahiro Inoue

Department of Mechanical Science and Engineering,
Kyushu University,
Fukuoka, Japan

Three-dimensional structures of the vortical flow field in a propeller fan with a shroud covering only the rear region of its rotor tip have been investigated by experimental analysis using laser Doppler velocimetry (LDV) measurements and by numerical analysis using a large eddy simulation (LES) in Part I of the present study. The propeller fan has a very complicated vortical flow field near the rotor tip compared with axial fan and compressor rotors. It is found that three vortex structures are formed near the rotor tip: the tip vortex, the leading edge separation vortex, and the tip leakage vortex. The tip vortex is so strong that it dominates the flow field near the tip. Its formation starts from the blade tip suction side near the midchord. Even at the design condition the tip vortex convects nearly in the tangential direction, thus impinging on the pressure surface of the adjacent blade. The leading edge separation vortex develops close along the tip suction surface and disappears in the rear region of the rotor passage. The tip leakage vortex is so weak that it does not affect the flow field in the rotor. [DOI: 10.1115/1.1412565]

Introduction

Propeller fans with a shroud covering only the rear region of their rotor tips are widely used as cooling fans installed in the outdoor unit of split room air conditioners and in the engine block of automobiles. They have a very complicated vortical flow field near the rotor tip. In addition to compactness, the need for low noise and high efficiency in these systems is rapidly increasing.

It is well known that the vortical flow field near the rotor tip in propeller fans affects their aerodynamic performance and noise characteristics. It was found that the vortical flow field has a close relation to the configuration of the shroud. Parametric studies on the shroud shape, the installation distance between the shroud and the rotor leading edge, and the tip clearance were performed by Fukano et al. [1,2] for a propeller fan. Sato and Kinoshita [3], and Akaike and Kikuyama [4] investigated the behavior of the vortical flow inside and outside of propeller fan rotors using laser Doppler velocimetry (LDV) measurements. They showed that a vortical structure with reverse flow was observed just upstream of the shroud at a low flow rate, and that the system noise could be reduced by controlling the vortical flow near the tip with optimization of the shape of the shroud. Akaike et al. [5] attempted the noise reduction in a cooling (propeller) fan for an automobile radiator by optimizing the axial distance between the fan rotor and the shroud using three-dimensional numerical simulations and experimental measurements. They pointed out that two types of vortex structure were observed near the rotor tip, and the noise level could be reduced by controlling the vortical flow. Longhouse [6] introduced rotating shrouds attached to the rotor tips to reduce the noise caused by the tip leakage vortex. The above studies imply that the vortical flow near the rotor tip is closely related to the aerodynamic performance and noise characteristics of propeller fans.

The role of the tip flow in propeller fans seems to be similar to that of the tip leakage flow in full-ducted fans. Effects of the tip leakage flow in axial fan and compressor rotors have been investigated by a great number of experimental and numerical studies. However, it is difficult to apply these results on the tip leakage flow directly to the tip flow in propeller fans, because in propeller fans considered in these studies only the rear region of the rotor tip is covered by a shroud unlike the full-ducted fans. Structure and behavior of the vortical flow near rotor tip in propeller fans have not been elucidated sufficiently. Although remarkable noise reduction in propeller fans has been achieved in the last two decades, the relation between the vortical flow field and the noise in propeller fans is still unknown.

In the present study consisting of two parts, the vortical flow field in a propeller fan with a shroud covering only the rear region of the rotor blade is analyzed by LDV measurements and a large eddy simulation (LES) to evaluate its structure and unsteady behavior. Moreover, from the point of view of the aeroacoustics in the propeller fan, the relation between the unsteady behavior of vortex structures in the rotor and the pressure fluctuation on the rotor blade is investigated. In Part I, the three-dimensional vortical flow structure in the propeller fan is elucidated.

Experimental Apparatus and Procedures

Test Propeller Fan. The present study was performed in the propeller fan rotor installed in an outdoor unit of room air conditioner, as shown in Fig. 1. The propeller fan is a mixed flow type with inclined angle at the hub. Design specifications of the rotor blade are summarized in Table 1. A flow coefficient (Φ) and a static pressure rise coefficient (Ψ) are defined as

$$\Phi = \frac{4Q}{\pi(D_t^2 - D_h^2)U_t} \tag{1}$$

$$\Psi = \frac{2\Delta P_S}{\rho U_t^2} \tag{2}$$

Contributed by the Fluids Engineering Division for publication in the JOURNAL OF FLUIDS ENGINEERING. Manuscript received by the Fluids Engineering Division April 28, 2000; revised manuscript received July 21, 2001. Associate Editor: P. Bradshaw.

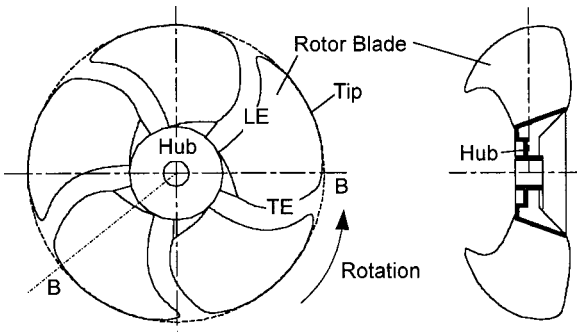

Fig. 1 Schematic view of test propeller fan rotor: Front view (left) and side view (B-B) (right)

Table 1 Design specifications of propeller fan

Flow Coefficient	$\Phi = 0.27$
Pressure Coefficient	$\Psi = 0.22$
Rotor Rotation Frequency	$\Omega = 670$ rpm
Tip Diameter	$D_t = 380$ mm
Hub-Tip Ratio at Rotor Inlet	$\nu = 0.318$
Blade Profile	Circular Arc
Number of Blade	5
Vortex Design	Forced Vortex
Blade Thickness	4 mm (hub), 3 mm (near tip)
Solidity at Tip	0.75
Chord Length at Tip	178 mm
Hub Inclination	20°
Tip Inclination	0°

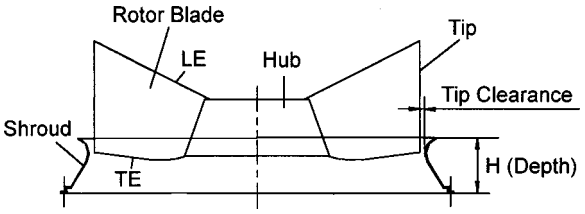

Fig. 2 Configuration of bell-mouth type shroud

where Q is the volume flow rate, ΔP_S is the static pressure rise, U_t is the rotor tip speed, ρ is the density, D_t is the rotor tip diameter, and D_h is the rotor hub diameter at rotor inlet.

The rotor blade has circular arc sections designed according to a quasi-three-dimensional method of Inoue et al. [7]. To obtain the low-noise and high-efficiency propeller fan, the distribution of the blade chord length was optimized using stored (data-based) experimental data of the outdoor unit of room air conditioners. The blade thickness is 4 mm at the hub and 3 mm near the tip, and decreases proportionally from the hub. On the blade edges (leading, trailing and tip edges), there is no blade thickness by rounding off the blade suction side.

Figure 2 shows the configuration of the shroud in the test fan, which is the sectional view. The test shroud is a bell-mouth type covering only the rear region of the fan rotor, which is widely used in the outdoor unit of room air conditioners. It has an inner diameter of 390 mm and a minimum rotor tip clearance of 5 mm (2.8 percent of tip chord). The axial length of the shroud, H in Fig. 2, is 62 mm. Twelve percent of the axial chord at the rear part of the rotor blade is covered by the shroud. Details of the propeller fan are given on a laboratory web site [8].

Figure 3 shows the performance characteristics of the test fan obtained according to the fan performance test standards of JIS B 8330. The efficiency η is defined using the static pressure rise as

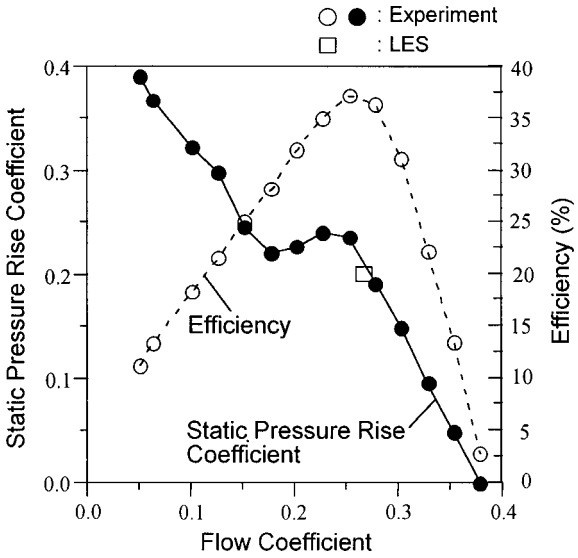

Fig. 3 Total performance of test propeller fan

$$\eta = \frac{Q \cdot \Delta P_S}{T \cdot \Omega} \tag{3}$$

where T is the rotor torque and Ω is the angular velocity magnitude of the rotor. The test fan has the maximum efficiency of 37 percent at the design flow condition, as shown in Fig. 3.

Measuring Procedures and Experimental Uncertainty. Measurements were performed in a system of the outdoor unit of room air conditioner. As shown in Fig. 4, the system consisted of a condenser (heat exchanger), a propeller fan (fan rotor and shroud), and a fan driving motor. Velocity distributions were measured on a meridional plane of the fan rotor. The inflow region consisted of a front inlet and a partial side inlet to maintain a large inlet area. In the present system, the fan driving motor shown in Fig. 4 was installed at the rotor outlet region to keep uniform inlet velocity distributions.

Figure 5 shows the side-sectional view of the experimental apparatus, together with measuring regions. A flow field above 75 percent span, which is shown by A and B in Fig. 5, was measured by a laser Doppler velocimetry (LDV) at the design flow condition (Φ=0.27) with the design rotor rotational speed of 670 rpm. A DANTEC three-dimensional LDV system operating in the back-scattering mode was used to measure the internal flow including the blade passage flow near the rotor tip. The LDV system consisted of a light source, a transmitter, probes, fiber optic cables, a 3-D traverse, and a signal processor. In the LDV measurement, the power of the LEXEL Ar-ion laser was adjusted to 5 W.

One-dimensional and two-dimensional probes for measuring the three-dimensional velocity components were controlled by the

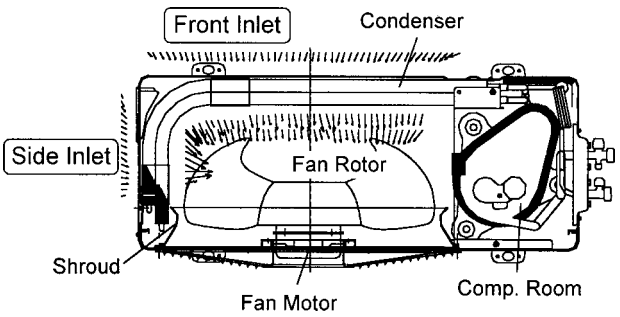

Fig. 4 Top sectional view of experimental apparatus

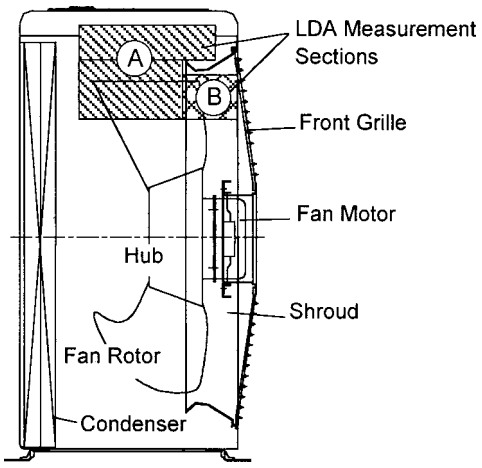

Fig. 5 Side sectional view of experimental apparatus

DANTEC three-dimensional traversing system with traverse resolution of 0.05 mm. The diameter of the front lens of the probes was 85 mm with focal length of 600 mm. The angle between the two probes was kept at 30 degrees. The three-dimensional velocity components were obtained by the single processor based on an auto covariance method.

The fringe count of each component is 28 and the dimension of the measuring volume in the radial, tangential and axial direction is about 271 μm, 278 μm and 290 μm, respectively. In the present measurement of the three-dimensional velocities, the effective data rate is approximately 100 Hz, even though it depends on the measuring positions.

To measure complicated flow fields around the shroud as well as in a rotor blade passage, a measuring section was divided into two blocks: one consisted of regions near the rotor tip and outside the shroud (A in Fig. 5), and the other was a region inside the shroud (B in Fig. 5). The window for LDV measurements was made of plexiglass plate with 0.8 mm thickness and installed on a cover plate just above the region ''A'' in Fig. 5. The seeding was introduced at the entrance of the system using a smoke generator of paraffin oil. The seeding had an average size of 1 μm. The encoder, which had 0.1 degree angular resolution, was installed directly at the fan motor shaft to measure the flow fields phase-locked to the rotor.

Ensemble averaged values were obtained by 30,000 sampling data at each meridional position. The sampling data were determined by preliminary experiments to minimize the experimental uncertainty. Statistical uncertainty could be estimated as stated by Snyder et al. [9]. In the blade passage, the uncertainty of the radial velocity component was 1.7 percent based on the time-averaged absolute velocity, and the uncertainty of the axial and tangential velocity components was lower than the radial one. Relatively high levels of uncertainty are observed near the rotor tip having a strong vortical flow as well as blade surfaces and shroud wall.

Large Eddy Simulation

Numerical Scheme. A large eddy simulation (LES) was executed to investigate the three-dimensional structure and unsteady nature of the vortical flow in the propeller fan. In the present numerical simulation, the flow field was simulated in the frame of reference rotating with the rotor. The numerical method used in the present simulation is outlined in the following.

The filtered compressible Navier-Stokes equations were discretized in space using a cell-centered finite volume formulation and in time using the Euler implicit method. To capture the vortical flow structure sharply, the inviscid fluxes were evaluated by a high-resolution upwind scheme based on a TVD formulation (Furukawa et al. [10]), where a Roe's approximate Riemann solver of Chakravarthy [11] and a third-order accurate MUSCL approach of Anderson et al. [12] with the Van Albada limiter were implemented. In general, most of numerical solvers for incompressible flows are based on artificial dissipative schemes in which the inviscid terms are discretized in central differencing manners with artificial dissipation terms. According to studies on the application of the high-resolution upwind schemes to the Navier-Stokes equations by van Leer et al. [13], and Swanson and Turkel [14], it was found that built-in numerical dissipation terms introduced by the high-resolution upwind scheme using the Riemann solvers such as Roe's (Roe [15]) and Osher's (Osher and Chakravarthy [16]) automatically become much smaller in boundary layers than those introduced by the artificial dissipative schemes so as not to dominate the natural diffusion in boundary layers. This means that the high-resolution upwind schemes using the Riemann solvers have not only shock capturing capability but also excellent boundary layer capturing one.

The viscous fluxes were determined in a central differencing manner with Gauss's theorem. Simultaneous equations linearized in time were solved by a point Gauss-Seidel relaxation method using no approximate factorization (Furukawa et al. [17,18]). To obtain a time-accurate solution, inner iterations, so-called Newton iterations, were introduced at each time step according to Chakravarthy [19]. The scheme was kept second-order-accurate in time by applying the three-point-backward difference approximation to the temporal derivative (Inoue and Furukawa [20]). It should be noted that the present implicit scheme with the relaxation method has no factorization error, thus being stable up to much larger size of time step than implicit schemes with approximate factorization. For the unsteady flow simulation presented in this paper, 25 inner iterations were performed to obtain a highly time-accurate solution at each time step.

In the present large eddy simulation (LES), Smagorinsky's eddy viscosity model [21] with the damping function of van Driest was used to present the subgrid-scale (SGS) stress fields. The subgrid-scale eddy viscosity μ_t is computed by

$$\mu_t = \overline{\rho} l^2 \sqrt{2\widetilde{\Pi}} \tag{4}$$

where

$$\widetilde{\Pi} = \widetilde{S}_{ij}\widetilde{S}_{ij} \tag{5}$$

$\widetilde{S}_{ij}$ is the strain tensor of the resolvable field given as

$$\widetilde{S}_{ij} = \frac{1}{2}\left(\frac{\partial \widetilde{u}_i}{\partial x_j} + \frac{\partial \widetilde{u}_j}{\partial x_i}\right) \tag{6}$$

In Eq. (4) l is the characteristic subgrid length scale, which includes the near-wall effect as follows:

$$l = C_S \Delta \sqrt{(1 - \exp(-y^+/A^+))} \tag{7}$$

where C_S is the Smagorinsky constant (0.1 for this study) and $A^+ = 25$ is the van Driest damping constant. Δ represents the filter width of the computational grid, which was computed as the third root of the computational cell volume (V):

$$\Delta = \sqrt[3]{V} \tag{8}$$

Computational Grids and Boundary Conditions. A composite grid system with structured H-type grids was adopted to represent the complicated configuration of the propeller fan including the shroud. As shown in Fig. 6, the computational domain was divided into two blocks. Block 1 surrounded the rotor, and block 2 was located in the outer region of block 1. The area of the fan inlet was determined equivalently by the whole inlet area of the outdoor unit of room air conditioner including the area of the partial side inlet shown in Fig. 4.

Figure 7 shows computational grids viewed from the top and the front, as well as the perspective view of the grid in block 1. The computational grid of block 1 consisted of 166 cells in the streamwise direction (120 cells on the blade), 86 cells in the span-

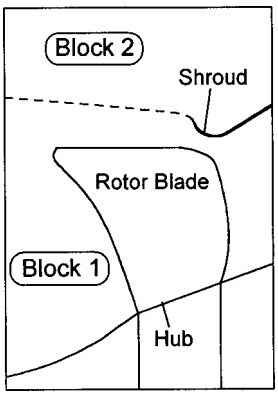

Fig. 6 Meridional view of computational domain

wise direction (61 cells on the blade), and 80 cells in the pitchwise direction. The grid of block 2 consisted of $166\times15\times80$ cells in the streamwise, spanwise and pitchwise directions, respectively. The whole grid system had 1,341,280 cells. The ratio of the minimum grid spacing on solid walls to the blade tip chord length was under 1×10^{-5} to evaluate the viscous fluxes at the walls by applying the no-slip and adiabatic conditions with no wall function method. This minimum grid spacing gave $y^+<2.5$ at the walls. Boundaries of the computational domain were formed by cell interfaces in the cell-centered finite volume approach. In the present scheme, fictitious cells were introduced just outside all the boundaries, and values of conserved variables satisfying boundary conditions were given at the fictitious cells. Using the fictitious cells, numerical fluxes through the boundaries were evaluated in the same way as interior cell interfaces. This treatment of the boundary conditions prevented nonphysical reflections at the inflow and outflow boundaries, because the inviscid fluxes through the boundaries were evaluated according to the approximate Riemann solver in which the signal propagation properties of the Euler equations were simulated.

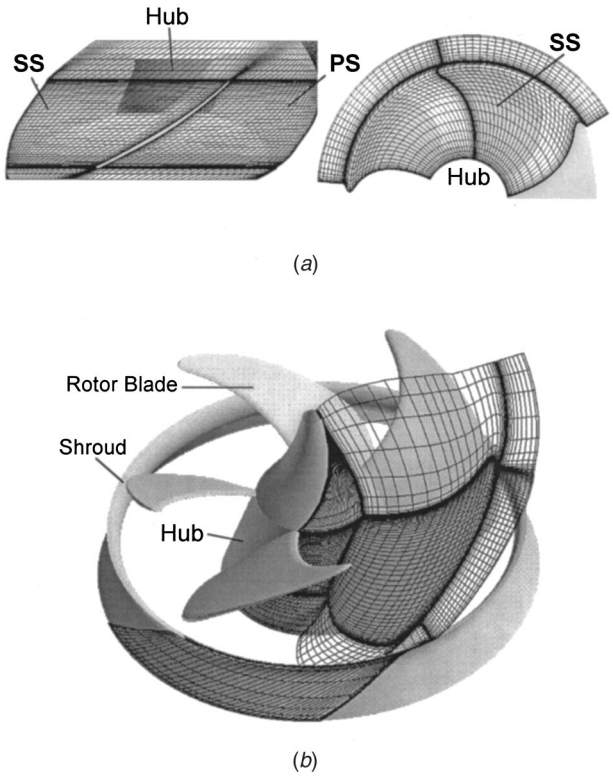

Fig. 7 Computational grid system for block 1 with 50 percent grid density. (*a*) Cross-section views: top view near tip (left) and front view near leading edge (right) (*b*) perspective view.

The conserved variables at the fictitious cells adjacent to the inflow boundary were given by uniform flow conditions upstream of the fan. Meanwhile, for the outflow boundary, the variables except the meridional velocity component at the fictitious cells were set equal to those at interior cells adjacent to the boundary: the profile of the tangential averaged meridional velocity was prescribed by the experimental results, and its magnitude was scaled to the total flow rate imposed. For reducing a computational load, the nonaxisymmetric flow field in the propeller fan installed in the outdoor unit of room air conditioner was simulated by applying a periodic boundary condition in the tangential direction to a single blade passage, taking no account of the partial side inlet (as shown in Fig. 4), the upstream condenser and the downstream grille. The validity of the present simulation will be shown in the following by comparing numerical results of the simulation with experimental ones.

Identification Method of Vortex Cores

To readily understand the vortex structure in the complicated flow field of the propeller fan, a vortex identification method by Sawada [22] was adopted. This method can find the vortex structure clearly in the rotor blade passage. In the Sawada's method, where the vortex axis is identified by a semi-analytic method based on the critical point analysis, the assumption is that the local velocity field can be linearly parameterized in a tetrahedral cell. The streamline equations written in the parameter space become integrable analytically over the cell, and as a result the obtained expression provides the possible vortex centerline. If the vortex center line crosses the cell, the line segment inside the tetrahedral cell is regarded as the fraction of vortex core. Furukawa et al. [23] and Inoue et al. [24] analyzed structures of the tip leakage vortex in an axial compressor rotor using this vortex identification method. In the present study, the vortex identification was performed in the velocity field relative to the rotor.

To analyze the nature of vortices quantitatively, the vortex cores identified according to Sawada's method are colored with a normalized helicity, which is similar to that used by Levy et al. [25]. The normalized helicity is very useful in investigating the nature of vortices, for example detecting the vortex breakdown region and the stagnation point in the vortex core, as shown in compressor rotor flow fields by Furukawa et al. [23,26]. The normalized helicity H_n is defined by

$$H_n=\frac{\vec{\xi}\cdot\vec{w}}{|\vec{\xi}||\vec{w}|} \tag{9}$$

where $\vec{\xi}$ and $\vec{w}$ denote vectors of the absolute vorticity and the relative flow velocity, respectively. It should be noted that the normalized helicity is not defined by the relative vorticity, but by the absolute vorticity, considering that secondary flow fields in turbomachinery rotors are dominated by the component of absolute vorticity along the relative flow direction. The normalized helicity is the cosine of the angle between the absolute vorticity and relative velocity vectors. This means that the magnitude of the normalized helicity tends to unity in the vortex core, and that its sign indicates the swirl direction of the vortex relative to the streamwise velocity component.

Results and Discussion

Analysis of Vortical Flow Structures by LDV Measurements. Meridional velocity vectors and meridional streamlines in a tangentially averaged flow field obtained by the LDV are shown in Fig. 8, which shows only the upper half region of the system. A tip vortex is observed close to the rotor tip and its core is located at 63 percent axial chord from the leading edge. It is

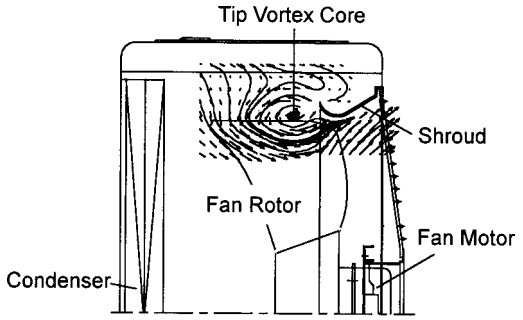

Fig. 8 Tangentially averaged velocity vectors and streamlines on meridional plane (LDV results)

readily seen that a strong inward radial flow in the fore part of the rotor tip and a reverse flow near the leading edge of the shroud are observed. This means that the fluid flows into the rotor passage not only through the rotor leading edge region but also through the fore part of the rotor tip.

Distributions of meridional velocity vectors and meridional streamlines are shown on nine meridional planes in Fig. 9 according to the LDV measurements. The meridional planes are located at intervals of 8 degrees in the tangential direction from the blade suction side to the pressure one, as shown by planes ①-⑨ in Fig. 10. Thick oblique solid lines in Fig. 10 denote the rotor tip sections. The rotor leading edge is located in plane ⑧, and the trailing edge in plane ④. The position of the tip vortex core is determined by the position with minimum kinetic energy in each

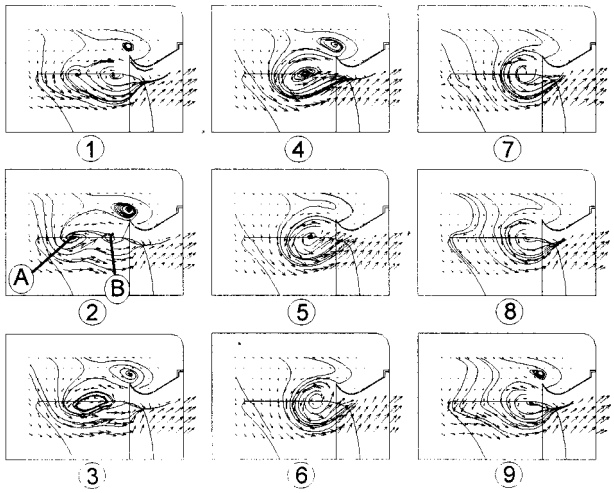

Fig. 9 Tangential distribution of meridional velocity vectors and streamlines (LDV results)

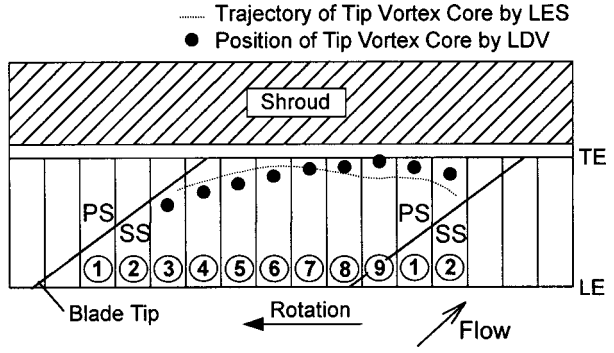

Fig. 10 Trajectory of tip vortex core

meridional plane. The trajectory of the tip vortex core viewed from the shroud is shown by circular symbols in Fig. 10.

The onset of the tip vortex formation is observed near the midchord on the blade tip suction side (A on plane ② in Fig. 9). The tip vortex convects toward the rotor exit from plane ② to plane ⑥. From the midpitch to the pressure side (planes ⑥-⑨), however, the tip vortex convects in the almost tangential direction. The tip vortex is weakened near the pressure surface as shown by B on plane ② in Fig. 9. This implies that the tip vortex impinges on the pressure surface of the adjacent blade. According to Fig. 9, it is found that the tip vortex plays a major role in the flow fields near the rotor tip and has a large blockage effect on the through flow.

Analysis of Vortical Flow Structures in Time-Averaged Flow Field by LES. The large eddy simulation (LES) was applied to the test propeller fan at the design flow condition ($\Phi=0.27$). A nondimensional time step size normalized by the blade tip radius and the inlet sound speed was set to 0.05 in the present unsteady flow calculation by LES. A steady flow solution obtained by the Reynolds-averaged Navier-Stokes (RANS) equations was used as an initial state of the unsteady calculation. The unsteady flow solution of the present LES has a transitional state as will be mentioned in Part II. In the following, three-dimensional structure and unsteady behavior of the vortical flow in the propeller fan are investigated by analyzing the solution for a period of 300 nondimensional time after the transitional state, which corresponds to 6000 time steps (about 9.3 blade passing).

Fujitsu vector parallel supercomputer (VPP700) with 2.2 GFLOPS peak performance per each vector Processing Element (PE) was used for the present study. It took about 750 hours to perform the present LES (whole 16,000 time steps including the transitional state) using 16 PEs.

First of all, numerical results of LES are compared with the results of the LDV measurements to show the validity of the present numerical simulation.

A static pressure rise predicted by LES is compared with the experimental result of the fan performance test. The predicted result of LES at the design operating condition is shown by a rectangular symbol in Fig. 3. It is seen that the predicted pressure rise has a good agreement with the experimental one.

The trajectory of the tip vortex obtained by the LES is presented by a dashed line in Fig. 10 to compare with the experimental result. The position of the tip vortex predicted by the LES corresponds well to that obtained by the LDV measurements. Although for the present numerical simulation the nonaxisymmetric configuration of the experimental apparatus, which has the front inlet and the partial side inlet as shown in Fig. 4, is approximated by the axisymmetric configuration having only the front inlet with the equivalent area, the large-scale vortex structure is found to be captured correctly by the present LES.

Figure 11 shows meridional streamlines and a meridional distribution of the axial momentum flux in a time- and tangentially-averaged flow field of LES. The axial momentum flux is normalized by the momentum flux based on the rotor tip speed. In the figure, the tip vortex is observed near the rotor tip at 62 percent axial chord from the leading edge, which agrees well with the experimental result shown in Fig. 8.

Three-dimensional vortex structures in the time-averaged flow field of LES are shown in Fig. 12, which is a perspective view from the shroud. The vortex cores shown in two blade passages are colored with the normalized helicity defined by Eq. (9). In the figure, a region colored with sky blue denotes the shroud, which covers only the rear part of the rotor. Two main vortex structures are observed near the rotor tip region: the tip vortex (TV) and the leading edge separation vortex (LSV). The tip vortex starts to be formed near the midchord on the suction side of the blade tip and grows nearly in the tangential direction, thus impinging on the pressure surface of the adjacent blade.

The comparisons between the numerical and experimental re-

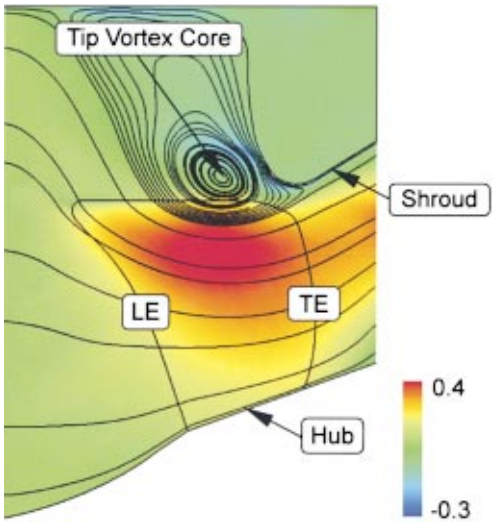

Fig. 11 Tangentially averaged distribution of axial momentum flux and meridional streamlines in time-averaged flow field (LES result)

sults in the time-averaged flow field show that the vortical flow field in the propeller fan is simulated correctly by the present calculation. Consequently, flow phenomena in the fan can be investigated by analyzing the numerical results in detail.

According to the numerical and experimental results shown in Figs. 10 and 12, it is found that the tangential structure of the tip vortex forms a vortex ring surrounding the rotor tips. This structure has a large blockage effect on the through flow (the main flow) in the rotor. However, the tip vortex with the tangential structure induces an axial through flow just under the tip vortex, as well as the inward radial flow in the fore part of the rotor tip and the reverse flow near the leading edge of the shroud, as seen in Figs. 8 and 9. As a result, the axial momentum flux is very large in the interference region between the tip vortex and the main flow, as seen in Fig. 11.

The leading edge separation vortex shown by LSV in Fig. 12 develops close along the suction surface near the tip and disappears in the rear part of the rotor passage. In the midchord region, it convects close under the tip vortex; a reconnection of the leading edge separation vortex to the tip vortex is not observed as will be shown in Figs. 14 and 15.

The vortex structures with the Reynolds-averaged Navier-Stokes (RANS) equations are shown in Fig. 13, which is presented in the same manner as Fig. 12. The RANS equations are solved to calculate the steady flow. In the RANS simulation, the algebraic turbulence model of Baldwin and Lomax [27] was employed to estimate the eddy viscosity. In Fig. 13, the tip leakage

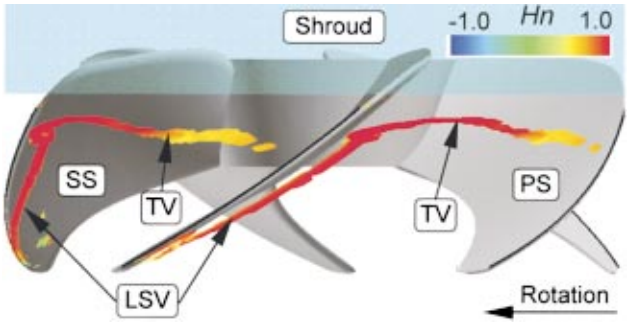

Fig. 12 Vortex cores colored with normalized helicity in time-averaged flow field (LES result)

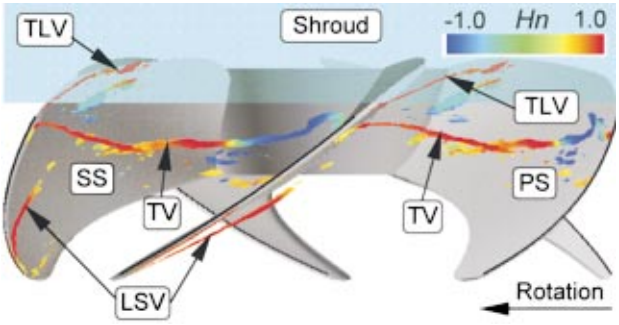

Fig. 13 Vortex cores colored with normalized helicity (RANS result)

vortex (TLV), as well as the tip vortex and the leading edge separation vortex, is observed between the shroud and the rear part of the rotor tip. Compared with the tip leakage vortex in full-ducted axial fans and compressors, however, it is not a main flow feature in the propeller fan. The tip leakage vortex core is hardly visible in the time-averaged flow field of LES shown in Fig. 12.

The tip vortex core has the normalized helicity of about unity from the suction surface to the midpitch region as seen in Figs. 12 and 13. This means that the tip vortex is tightly rolled up and has no abrupt change in its nature on the suction side in the time-averaged flow field. However, the tip vortex core observed in Fig.

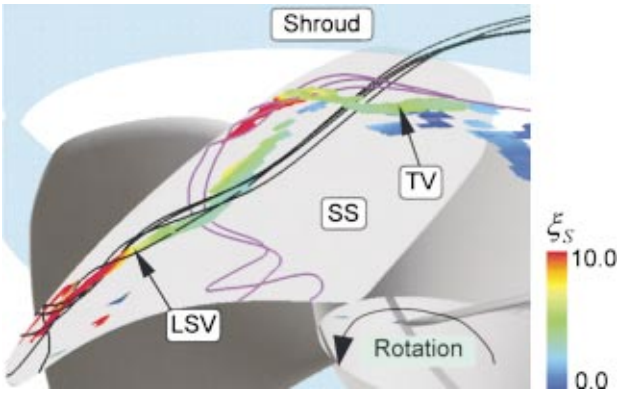

Fig. 14 Instantaneous structures of tip vortex (TV) and leading edge separation vortex (LSV) colored with streamwise absolute vorticity, and streamlines surrounding vortex cores at $t=604$ (LES result)

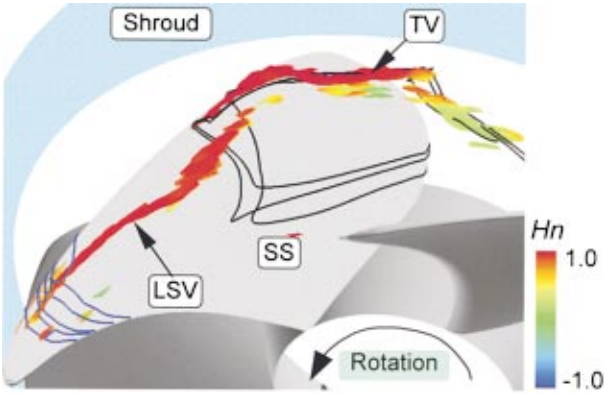

Fig. 15 Instantaneous structures of tip vortex (TV) and leading edge separation vortex (LSV) colored with normalized helicity, and vortex lines surrounding vortex cores at $t=604$ (LES result)

12 disappears near the pressure surface, where the normalized helicity changes rapidly from 1 to −1 along the tip vortex observed in Fig. 13. The disappearance of the tip vortex core and the rapid change in the normalized helicity imply that the tip vortex has significant change in its nature. This behavior of the tip vortex will be discussed in Part II.

Onset of Vortex Structures. To investigate the onset of the vortex structure formation, Fig. 14 shows instantaneous vortex cores at nondimensional time of $t=604$. The figure is a perspective view from an upstream side of the rotor. The vortex cores are colored with the streamwise absolute vorticity ξ_S, which is defined and normalized as

$$\xi_S = \frac{\vec{\xi}\cdot\vec{w}}{2\Omega|\vec{w}|} \tag{10}$$

In the figure streamlines surrounding the vortex cores are presented by purple and black lines. The leading edge separation vortex (LSV), as well as the tip vortex (TV), has the high streamwise vorticity near the suction surface. This indicates that the tip vortex and the leading edge separation vortex are main features associated with the rotor tip. The onset of the leading edge separation vortex occurs close to the leading edge on the rotor tip suction side. This onset results from the fact that the large blockage effect of the tip vortex causes a high incidence condition near the tip even at the design point. The onset of the tip vortex is located on the blade tip suction side at 59 percent axial chord length. Although the leading edge separation vortex convects close under the tip vortex near the midchord of the blade suction surface, no vortex reconnection occurs between the tip vortex and the leading edge separation vortex.

Figure 15 shows vortex lines together with the vortex cores colored with the normalized helicity at $t=604$. The vortex lines emanating from the suction surface boundary layer pass through the vortex cores near the onset of the tip and leading edge separation vortices. It is found that the vortex lines in the tip and leading edge separation vortices link to ones in the suction surface boundary layer. This means that the tip and leading edge separation vortices are formed by the rolling-up of the suction surface boundary layer.

Conclusion

The three-dimensional vortical flow structures in the propeller fan with the shroud covering only the rear part of the rotor tip have been investigated by the experimental measurements by LDV and the numerical analysis by LES. The results are summarized as follows:

1 Three vortex structures are formed near the propeller fan rotor tip: the tip vortex, the leading edge separation vortex and the tip leakage vortex. The tip vortex and the leading edge separation vortex are main flow features formed by the rolling-up of the suction surface boundary layer. The tip leakage vortex is so weak that it does not affect the flow field in the rotor.

2 The tip vortex is so strong that it dominates the flow field near the tip. Its formation starts from the blade tip suction side near the midchord. Even at the design point the tip vortex convects nearly in the tangential direction, thus impinging on the pressure surface near the tip of the adjacent blade. All the tip vortices in the propeller fan form a tangential vortex ring around the rotor tips. The vortex ring induces the strong inward radial flow at the fore part of the rotor tip.

3 The tangential structure of the tip vortex has the large blockage effect near the rotor tip. This blockage effect causes the high incidence condition even at the design point, leading to the onset of the leading edge separation vortex close to the tip. The leading edge separation vortex develops close along the suction surface near the tip and disappears in the rear part of the rotor passage.

Acknowledgments

We would like to thank Dr. K. Saiki for his support of the present numerical analysis by LES. The present research was partially supported by the Ministry of Education, Science, Sports and Culture, Grant-in-Aid for Scientific Research (B), No. 12555049. This support is most gratefully acknowledged.

References

[1] Fukano, T., Fukuhara, M., Kawagoe, K., Hara, Y., and Kinoshita, K., 1990, "Experimental Study on the Noise Reduction of a Propeller Fan, 1st Report, Aerodynamic Characteristics," Trans. Jpn. Soc. Mech. Eng., Ser. B, **56**, No. 531, pp. 3378–3382 (in Japanese).

[2] Fukano, T., Kawagoe, K., Fukuhara, M., Hara, Y., and Kinoshita, K., 1990, "Experimental Study on the Noise Reduction of a Propeller Fan, 2nd Report, Noise Characteristics," Trans. Jpn. Soc. Mech. Eng., Ser. B, **56**, No. 531, pp. 3383–3388 (in Japanese).

[3] Sato, S., and Kinoshita, K., 1993, "Improvement in Performance of Propeller Fans for Outdoor Units of Airconditioners," Proceeding of the 4th Asian International Conference on Fluid Machinery, Vol. 1, pp. 166–170.

[4] Akaike, S., and Kikuyama, K., 1993, "Noise Reduction of Pressure Type Fans for Automobile Air Conditioners," ASME J. Vibr. Acoust., **115**, pp. 216–220.

[5] Akaike, S., Kuroki, S., and Katagiri, M., 1991, "Noise Reduction of Radiator Cooling Fan for Automobile—Three-Dimensional Analysis of the Flow Between the Blades of the Fan-," JSAE (Society of Automotive Engineers of Japan), **22**, No. 3, pp. 79–84 (in Japanese).

[6] Longhouse, R. E., 1978, "Control of Tip-Vortex Noise of Axial Flow Fans by Rotating Shrouds," J. Sound Vib., **58**, No. 2, pp. 201–214.

[7] Inoue, M., Wu, K-C., Kuroumaru, M., Furukawa, M., Fukuhara, M., and Ikui, T., 1984, "A Design of Diagonal Impeller by Means of SCM and Cascade Data," Proceedings of China-Japan Joint Conference on Hydraulic Machinery and Equipment, Vol. 1, pp. 21–30.

[8] http://fluid.mech.kyushu-u.ac.jp/fan/web_propeller_fan.html

[9] Snyder, P. K., Orloff, K. L., and Reinath, M. S., 1984, "Reduction of Flow-Measurement Uncertainties in Laser Velocimeters with Nonorthogonal Channels," AIAA J., **22**, No. 8, pp. 1115–1123.

[10] Furukawa, M., Yamasaki, M., and Inoue, M., 1991, "A Zonal Approach for Navier-Stokes Computations of Compressible Cascade Flow Fields Using a TVD Finite Volume Method," ASME J. Turbomach., **113**, pp. 573–582.

[11] Chakravarthy, S. R., 1986, "The Versatility and Reliability of Euler Solvers Based on High-Accuracy TVD Formulations," AIAA Paper No. 86-0243.

[12] Anderson, W. K., Thomas, J. L., and van Leer, B., 1986, "Comparison of Finite Volume Flux Vector Splittings for the Euler Equations," AIAA J., **24**, No. 9, pp. 1453–1460.

[13] Van Leer, B., Thomas, J. L., and Newsome, R. W., 1987, "A Comparison of Numerical Flux Formulas for the Euler and Navier-Stokes Equations," AIAA Paper No. 87-1104.

[14] Swanson, R. C., and Turkel, E., 1993, "Aspects of a High-Resolution Scheme for the Navier-Stokes Equations," AIAA Paper No. 93-3372-CP.

[15] Roe, P. L., 1981, "Approximate Riemann Solvers, Parameter Vectors, and Difference Schemes," J. Comput. Phys., **43**, pp. 357–372.

[16] Osher, S., and Chakravarthy, S. R., 1983, "Upwind Schemes and Boundary Conditions with Applications to Euler Equations in General Coordinates," J. Comput. Phys., **50**, pp. 447–481.

[17] Furukawa, M., Nakano, T., and Inoue, M., 1992, "Unsteady Navier-Stokes Simulation of Transonic Cascade Flow Using an Unfactored Implicit Upwind Relaxation Scheme With Inner Iterations," ASME J. Turbomach., **114**, pp. 599–606.

[18] Furukawa, M., Saiki, K., and Inoue, M., 1995, "Numerical Simulation of Three-Dimensional Viscous Flow in Diagonal Flow Impeller," Numerical Simulations in Turbomachinery, ASME FED-Vol. 227, pp. 29–36.

[19] Chakravarthy, S. R., 1984, "Relaxation Methods for Unfactored Implicit Upwind Schemes," AIAA Paper No. 84-0165.

[20] Inoue, M., and Furukawa, M., 1994, "Artificial Dissipative and Upwind Schemes for Turbomachinery Blade Flow Calculations," VKI, Lecture Series, No. 1994-06.

[21] Smagorinsky, J., 1963, "General Circulation Experiments with the Primitive Equations. I. The Basic Experiment," Mon. Weather Rev., **91**, pp. 99–165.

[22] Sawada, K., 1995, "A Convenient Visualization Method for Identifying Vortex Centers," Trans. Japan Soc. of Aero. Space Sci., **38**, No. 120, pp. 102–116.

[23] Furukawa, M., Inoue, M., Saiki, K., and Yamada, K., 1999, "The Role of Tip Leakage Vortex Breakdown in Compressor Rotor Aerodynamics," ASME J. Turbomach., **121**, No. 3, pp. 469–480.

[24] Inoue, M., Furukawa, M., Saiki, K., and Yamada, K., 1998, "Physical Explanations of Tip Leakage Flow Field in an Axial Compressor Rotor," ASME paper No. 98-GT-91.

[25] Levy, Y., Degani, D., and Seginer, A., 1990, "Graphical Visualization of Vortical Flows by Means of Helicity," AIAA J., **28**, pp. 1347–1352.

[26] Furukawa, M., Saiki, K., Nagayoshi, K., Kuroumaru, M., and Inoue, M., 1998, "Effects of Stream Surface Inclination on Tip Leakage Flow Fields in Compressor Rotors," ASME J. Turbomach., **120**, No. 4, pp. 683–694.

[27] Baldwin, B. S., and Lomax, H., 1978, "Thin Layer Approximation and Algebraic Model for Separated Turbulent Flow," AIAA Paper No. 78-257.

Analysis of Vortical Flow Field in a Propeller Fan by LDV Measurements and LES—Part II: Unsteady Nature of Vortical Flow Structures Due to Tip Vortex Breakdown

Choon-Man Jang
Masato Furukawa
Masahiro Inoue

Department of Mechanical Science and Engineering,
Kyushu University,
Fukuoka, Japan

The unsteady nature of vortex structures has been investigated by a large eddy simulation (LES) in a propeller fan with a shroud covering only the rear region of its rotor tip. The simulation shows that the tip vortex plays a major role in the structure and unsteady behavior of the vortical flow in the propeller fan. The spiral-type breakdown of the tip vortex occurs near the midpitch, leading to significant changes in the nature of the tip vortex. The breakdown gives rise to large and cyclic movements of the tip vortex, so that the vortex impinges cyclically on the pressure surface of the adjacent blade. The movements of the tip vortex cause the leading edge separation vortex to oscillate in a cycle, but on a small scale. The movements of the vortex structures induce high-pressure fluctuations on the rotor blade and in the blade passage. [DOI: 10.1115/1.1412566]

Introduction

Three-dimensional structures of the vortical flow field in a propeller fan with a shroud covering only the rear region of its rotor tip have been elucidated in Part I. As mentioned in Part I, the tip vortex dominating the flow field in the propeller fan presents a significant change in its nature near the pressure surface. Similar phenomenon has been reported recently in tip leakage vortices of some compressor rotors and has been found to result from the vortex breakdown.

The vortex breakdown was observed in blade rows by pioneer studies of Schlechtriem and Lotzerich [1] and Furukawa et al. [2,3]. Schlechtriem and Lotzerich [1] showed by numerical simulations that the breakdown of the tip leakage vortex caused by the shock-vortex interaction occurred in a transonic axial compressor rotor. Furukawa et al. [2] found that the leakage vortex presented its breakdown even at a design point for a low-speed diagonal compressor rotor with high blade loading. Furukawa et al. [3] showed that the breakdown of the leakage vortex dominated flow fields in a low-speed compressor rotor at near-stall conditions. They also showed that the breakdown yielded substantial changes in the nature of the leakage vortex: large expansion of the vortex and disappearance of the streamwise vorticity concentrated in the vortex core. Unsteady Navier-Stokes flow simulations by Furukawa et al. [4] indicated that the spiral-type breakdown of the leakage vortex caused a cyclic and large movement of the vortex structure.

In general, the vortex breakdown is known as a highly three-dimensional and unsteady phenomenon observed in streamwise slender vortices in external vortical flow and internal swirling flow as in the leading edge vortices over delta wings, the swirling flows in a cylindrical tube and the swirling jet in combustion chambers. Studies of flow fields generated by the vortex breakdown have been reported by many researchers such as Sarpkaya [5,6], Hall [7], Leibovich [8,9], Escudier [10], Brücker and Althaus [11], Brücker [12], and Delery [13]. Although the essential mechanism of the vortex breakdown is not generalized, three types of the breakdown can be distinguished: bubble type and spiral type as well as the transition from the bubble to spiral types (double helix type). The vortex breakdown is characterized by the existence of a stagnation point near the vortex core and the reverse flow downstream of the stagnation point. It is also known that the most distinctive feature of vortex breakdown is the occurrence of the large-scale fluctuation in the vortex structure.

On the other hand, it is well known that turbulence intensity and pressure fluctuation have a close relation with aerodynamic noise generation. In the propeller fan installed in the automotive air conditioners, the turbulence intensity was highest near the rotor tip, where a tip vortex core was formed (Akaike and Kikuyama [14]). It seems that unsteady vortical flow near the rotor tip dominates the generation of noise in propeller fans.

In Part II, the unsteady nature of the vortical flow in a propeller fan is investigated by a large eddy simulation (LES). Effects of the unsteady behavior of the vortex structure on pressure fluctuation in the rotor blade passage are elucidated.

Test Propeller Fan

The present study was performed in a propeller fan with a shroud covering only the rear region of the rotor blade in the outdoor unit of room air conditioner, as shown in Fig. 5 of Part I, which consists of a condenser (heat exchanger), a propeller fan (fan rotor and shroud), and a fan driving motor.

The rotor of the fan has a design flow coefficient of 0.27 and a design static pressure coefficient of 0.22. The hub/tip ratio of the rotor with the tip diameter of 380 mm is 0.318. The rotation frequency of the rotor is 670 rpm at a design condition. The rotor blade has circular arc profile sections designed by a quasi-three-dimensional method of Inoue et al. [15] on a forced vortex operating condition and an axial inlet flow condition. The number of blades is 5, and the blade thickness changes from 4 mm (at rotor hub) to 3 mm (at rotor tip) proportionally. The blade tip section has the solidity of 0.75 and the chord length of 178 mm. Twelve

Contributed by the Fluids Engineering Division for publication in the JOURNAL OF FLUIDS ENGINEERING. Manuscript received by the Fluids Engineering Division April 28, 2000; revised manuscript received July 21, 2001. Associate Editor: P. Bradshaw.

percent of the axial chord at the rear part of the rotor blade is covered by the shroud. The clearance between the shroud and the rotor tip is 5 mm (2.8 percent of tip chord).

Nondimensional Parameters for Analyzing Vortical Flow

To readily understand the nature of the vortex structure in the propeller fan, the vortex core identified by a semi-analytic method based on the critical point analysis (Sawada [16]) was described by nondimensional parameters: the streamwise absolute vorticity, the total pressure loss coefficients, and the normalized helicity.

The total pressure loss coefficient ζ_P is defined as

$$\zeta_P = \frac{\Omega \cdot (r c_\theta - r_1 c_{\theta 1}) - (P - P_1)/\rho}{U_t^2/2} \tag{1}$$

where r is the radius from the axis of rotation, c_θ is the absolute tangential velocity, P is the total pressure, ρ is the density, U_t is the blade tip speed, Ω is the angular velocity magnitude of the rotor, and subscript of 1 denotes the upstream of the rotor.

The streamwise absolute vorticity ξ_S is defined and normalized as

$$\xi_S = \frac{\vec{\xi} \cdot \vec{w}}{2\Omega |\vec{w}|} \tag{2}$$

where $\vec{\xi}$ and $\vec{w}$ denote vectors of the absolute vorticity and the relative flow velocity, respectively.

The normalized helicity H_n is defined as

$$H_n = \frac{\vec{\xi} \cdot \vec{w}}{|\vec{\xi}||\vec{w}|} \tag{3}$$

The magnitude of the normalized helicity tends to unity in the core region of the streamwise vortex, and its sign indicates the direction of swirl of the vortex relative to the streamwise velocity component. In contrast to the streamwise absolute vorticity, distributions of the normalized helicity along the vortex core allow us to analyze the change in the nature of vortex quantitatively, regardless of the decay of the vorticity in the streamwise direction.

In the following, unsteady nature of the vortex structures in the propeller fan is analyzed by the nondimensional parameters mentioned above.

Results and Discussion

Unsteady behavior of the vortical flow, especially the tip vortex in the propeller fan was studied by a large eddy simulation (LES) at the design flow condition of $\Phi = 0.27$. By applying the periodic boundary condition, the flow field in a single blade passage was simulated with the whole grid cells of 1,341,280, which was divided into two blocks to represent the complicated configuration of the propeller fan including the shroud. The matching between block 1 and block 2 was accomplished by the inviscid and viscous fluxes across the boundary between the blocks. The details of numerical scheme, computational grid and boundary conditions were described in the Part I.

A nondimensional time step size normalized by the blade tip radius and the inlet sound speed was set to 0.05. It takes a rotor blade 32.3 nondimensional time (646 time steps) to pass through one pitch. The time resolution of 646 time steps per one blade passing, which corresponds to about 36 kHz, is sufficient to resolve the turbulence in the present propeller fan. A solution obtained by the Reynolds-averaged Navier-Stokes equations was used as an initial state of the unsteady calculation. Figure 1 shows a time history of the rotor torque nondimensionalized by its design value. The figure indicates that the unsteady flow solution has a transitional feature until about nondimensional time of $t = 500$. In the following, the unsteady behavior of the vortical flow in the fan

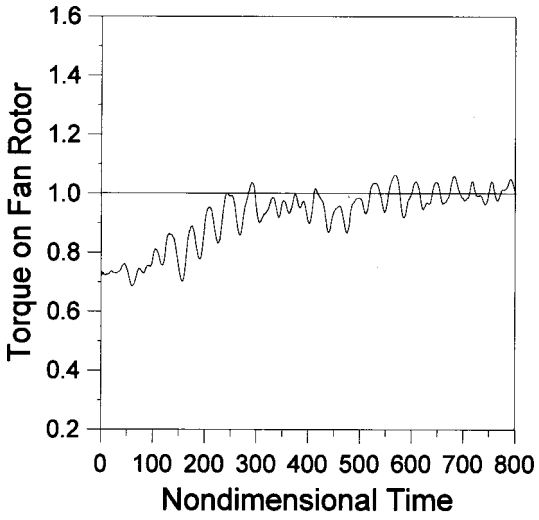

Fig. 1 Time history of torque on rotor blade for LES

is investigated by analyzing the solution for the period of 300 nondimensional time (6000 time steps) from $t = 500$ to $t = 800$ excepting the transitional state.

Turbulence Intensity and Pressure Fluctuation. Figures 2 and 3 show distributions of the turbulence intensity on a meridional plane shown by plane 5 in Fig. 10 of Part I, where the turbulence intensity presents the highest value. Figures 2 and 3 show results of LES and LDV, respectively. The region close to the blade surface, where the LDV measurement is impossible, is represented by a gray zone in Figs. 2 and 3. The turbulence intensity T_i is defined as

$$T_i = \sqrt{\frac{v_r'^2 + v_\theta'^2 + v_z'^2}{3U_t^2}} \tag{4}$$

where, v_r', v_θ', and v_z' denote the velocity fluctuation components in the radial, tangential and axial directions, respectively.

Relatively high turbulence intensity regions shown by A and B in Figs. 2 and 3 are observed close around the blade surface near the rotor tip, especially near the interference region between the tip vortex and the main flow (through flow). It is seen that the level of turbulence intensity agrees between the LDV and LES results. Although there is a little difference in the position of the tip vortex center as shown in Figs. 2 and 3, the two regions having the high turbulence intensity (A and B in Figs. 2 and 3) are in fairly good agreement between the LES and LDV results. It is found that the unsteady flow nature in the propeller fan is captured well by the present LES.

Figure 4 shows the tangentially averaged distribution of the pressure fluctuation predicted by LES. The pressure fluctuation is normalized by a dynamic pressure based on the rotor tip speed as follows:

$$P_f = \frac{\sqrt{p'^2}}{1/2\rho U_t^2} \tag{5}$$

where p' denotes the pressure fluctuation of the resolved field of the LES. Figure 4 indicates that there is a high-pressure fluctuation region under the tip vortex. This region corresponds to the interference region between the tip vortex and the main flow. The above implies that the tip vortex highly fluctuates with time and presents the important noise source.

In the following, the unsteady behavior of the vortex structures near the rotor tip is analyzed by the numerical results of LES.

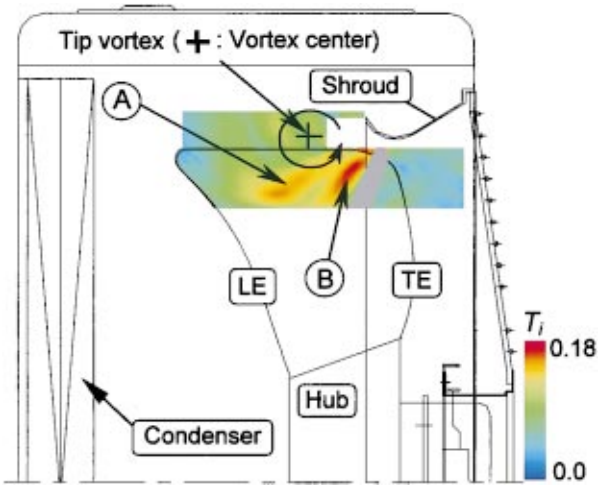

Fig. 2 Turbulence intensity on meridional plane 5 in Fig. 10 of Part I (LES result)

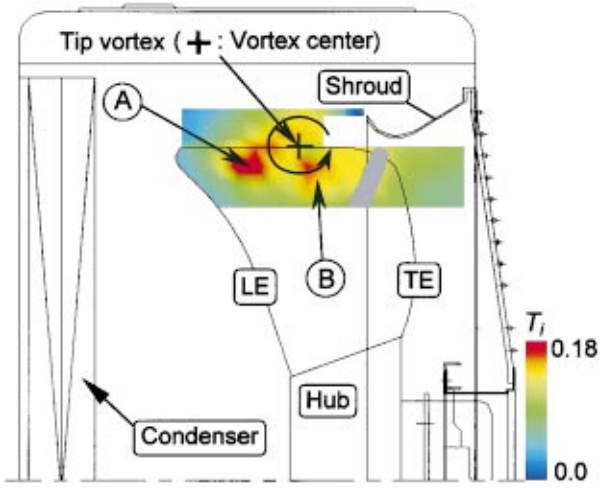

Fig. 3 Turbulence intensity on meridional plane 5 in Fig. 10 of Part I (LDV result)

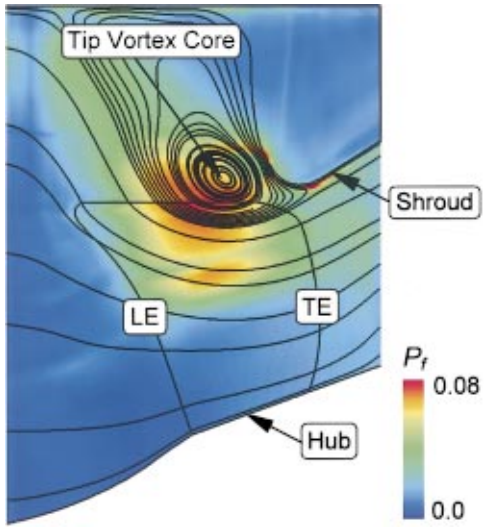

Fig. 4 Tangentially averaged distribution of pressure-fluctuation and meridional streamlines in time-averaged flow field (numerical result by LES)

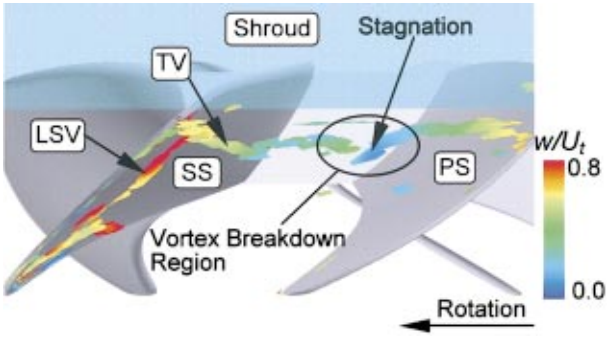

Fig. 5 Distribution of relative velocity along instantaneous vortex cores

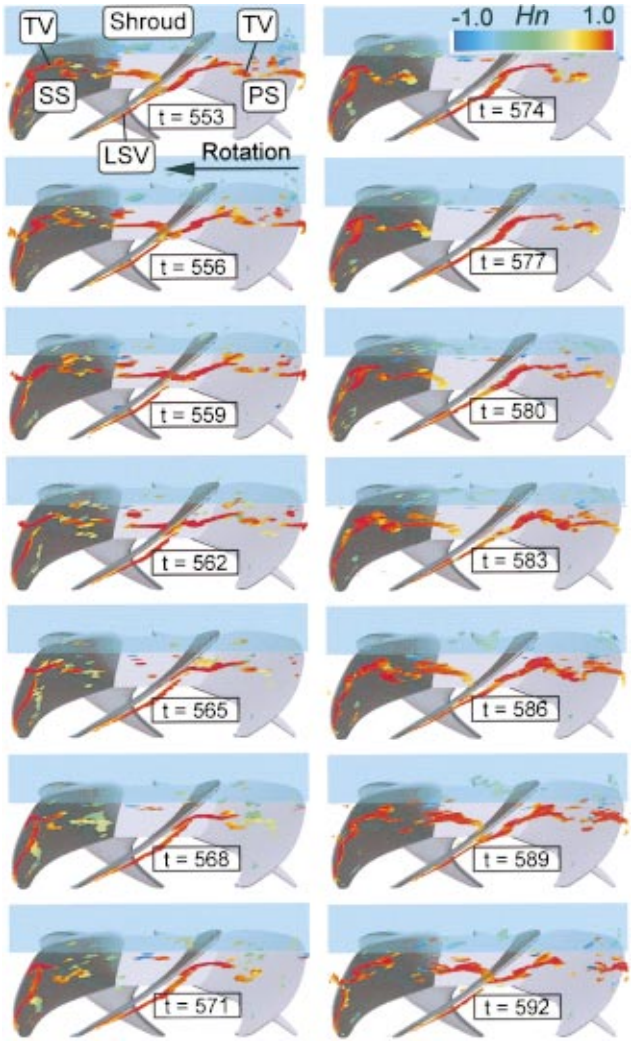

Fig. 6 Unsteady behavior of vortex core structures colored with normalized helicity

Breakdown of Tip Vortex. Although the tip vortex core with high normalized helicity is clearly observed from the blade suction side to the midpitch in the time-averaged flow field obtained by LES, as mentioned in the Part I, it disappears near the pressure surface where the normalized helicity along the tip vortex changes rapidly. The disappearance of the tip vortex core and the rapid change in the normalized helicity imply that there are significant changes in the nature of the tip vortex near the pressure surface.

Figure 5 shows a perspective view of instantaneous vortex core structures, which is the result of LES. The vortex cores are colored with the relative velocity magnitude normalized by the rotor tip speed. Compared with the leading edge separation vortex (LSV), the relative velocity along the tip vortex (TV) is lower. Near the midpitch, the tip vortex core flow is decelerated almost to stagnation, and the tip vortex structure has a large twist. A reverse flow in the direction of the tip vortex axis appears close to the low-velocity region. This flow behavior implies the existence of a stagnation point followed by the reverse flow region in the tip vortex. The existence of the stagnation point in the vortex is the distinctive feature of vortex breakdown (Leibovich [8] and Delery [13]). Therefore, it can safely be said that there is the onset of "vortex breakdown" near the low-velocity region in the tip vortex. It should be realized that the significant changes in the nature of the tip vortex are caused by its breakdown.

Unsteady Nature of Tip Vortex. Unsteady behavior of the vortex structures near the fan rotor tip is shown in Fig. 6 where the vortex cores are colored with the normalized helicity. Each instantaneous view is shown at intervals of three nondimensional time from $t=553$ to 592. The tip vortex (TV) twists and turns violently with time, because its spiral type breakdown occurs near the midpitch. The normalized helicity along the tip vortex core decreases near the pressure surface. This implies that the rolling-up of the tip vortex becomes weak near the pressure surface due to its breakdown. The breakdown of the tip vortex is found to be the spiral type of the breakdown. Moreover, it is clearly observed that the unsteady nature of the tip vortex breakdown causes the unsteady interaction between the tip vortex core and the pressure surface of the adjacent blade. The movement of the leading edge separation vortex (LSV) is much smaller than that of the tip vortex.

It can be understood that an impinging position of the tip vortex on the pressure surface moves around with time, and as a result the onset position of the tip vortex also moves on the rotor tip. The onset position moves in the downstream direction from $t=553$ to $t=568$. At $t=571$, the tip vortex core near the pressure surface disappears due to its breakdown. At the same time, the onset of tip vortex is observed clearly near the suction surface. With time, the tip vortex convects in the tangential direction until $t=586$. At $t=589$, it can be found that the tip vortex structure similar to one at $t=553$ is observed. Like this, the cyclic movement of the tip vortex is also observed at the following time period. The cycle time of the movement is found to be 36 nondimensional time, which corresponds to 0.9 times the blade passing frequency. It should be realized that the cyclic movement of the tip vortex is a self-sustained flow oscillation caused by its breakdown.

Although the movement of the leading edge separation vortex is smaller than that of the tip vortex, the leading edge separation vortex also oscillates cyclically. Its oscillation has a close interaction with that of the tip vortex caused by its breakdown. At $t=553$, the leading edge separation vortex is located close to the suction surface. It goes away from the suction surface while the onset position of the tip vortex moves in the downstream direction from $t=553$ to $t=568$. The leading edge separation vortex has a maximum distance from the suction surface at $t=571$, when the tip vortex core disappears due to its breakdown near the pressure surface. And then, the leading edge separation vortex approaches to the suction surface again. At $t=589$, the leading edge separation vortex is close to the suction surface as shown at $t=553$. The cycle time of the movement of the leading edge separation vortex is also found to be 36 nondimensional times, which is the same cycle as the tip vortex.

The validity of the LES result on the unsteady flow behavior is shown through frequency analyses of fan noise and rotor torque fluctuation. Figure 7 shows a fan noise characteristic measured for the testing configuration, namely, the outdoor unit of room air conditioner with the test fan, heat exchanger, downstream grille, and a driving motor. The frequency is normalized by the blade passing frequency. Noise measurements were carried out in an anechoic chamber where background noise was kept below 18 dB(A). A dominant frequency of 0.9 times the blade passing frequency is distinctly observed in Fig. 7, which corresponds well to the cycle of the tip vortex motion as mentioned above. Figure 8 shows a spectrum analysis of the rotor torque fluctuation obtained by applying a wavelet analysis using the Morlet wavelet to the present LES result. Its power spectrum was determined by a time-averaged absolute modulus of wavelet coefficient of rotor torque fluctuation calculated by LES. In Fig. 8, a dominant frequency of 0.9 times the blade passing frequency is also observed. The experimental and numerical results on the spectrum analyses of the fan noise and the rotor torque, respectively, indicate the same dominant frequency as mentioned above. Needless to say, the variation of rotor torque is caused by a blade loading fluctuation, thus resulting from the pressure fluctuation on the rotor blade. The blade pressure fluctuation, which has a dipole noise source, is a dominant noise source in the propeller fan operating at low Mach number. From the comparison between the experimental and numerical spectrum analyses of the fan noise and the fan rotor

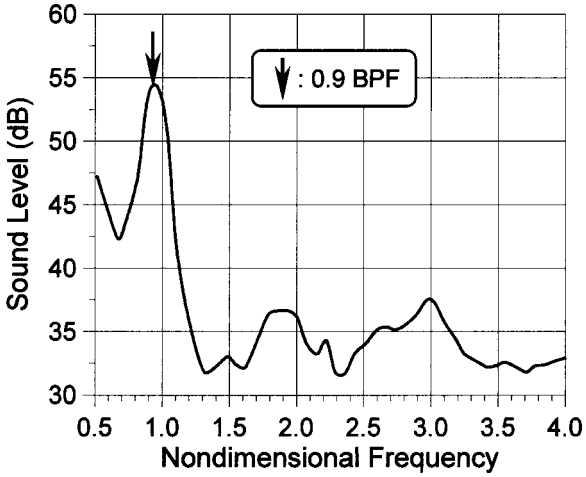

Fig. 7 Fan noise characteristic (Experimental result)

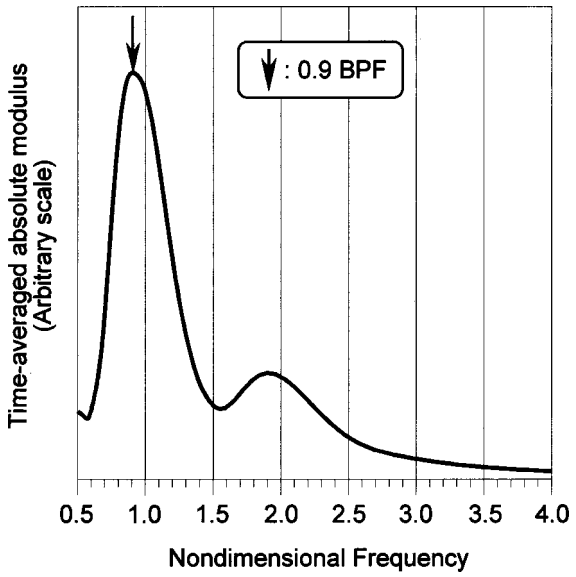

Fig. 8 Spectrum analysis of rotor torque fluctuation (LES result)

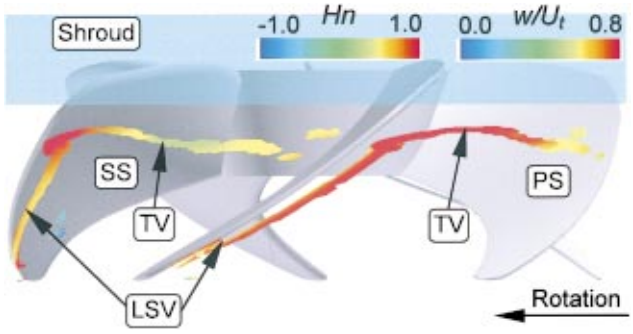

Fig. 9 Vortex cores colored with relative velocity (left passage) and with normalized helicity (right passage) in time-averaged flow field

torque, as shown in Figs. 7 and 8, it can be safely said that the unsteady flow behavior captured by the present LES is reliable.

Effects of Tip Vortex Breakdown on Time-Averaged Flow Field. Figure 9 shows vortex cores colored with the relative velocity magnitude normalized by the rotor tip speed (in left passage) and with the normalized helicity (in right passage) in the flow field averaged from $t = 500$ to 800, which is perspective view from shroud. The tip vortex core is clearly seen from the blade suction side to the midpitch, where the tip vortex convects in the tangential direction and has high normalized helicity in spite of the large movement of the tip vortex as shown in Fig. 6. Near the pressure surface, however, tip vortex core disappears because of the vortex breakdown. It should be noted that the disappearance of the tip vortex core corresponds well to the appearance of the rapid change in the normalized helicity for the steady flow simulation

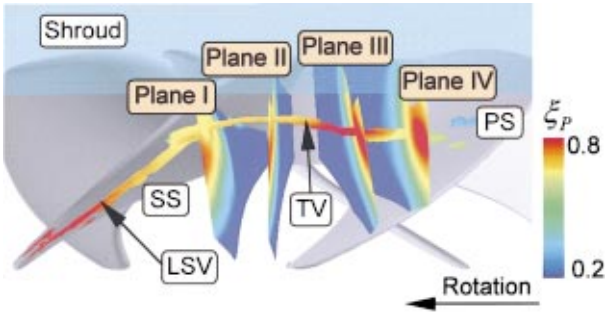

Fig. 10 Distribution of total pressure loss along vortex cores and on planes perpendicular to tip vortex in time-averaged flow field

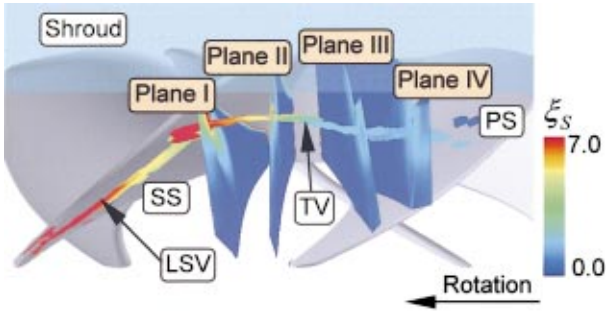

Fig. 11 Distribution of streamwise absolute vorticity along vortex cores and on planes perpendicular to tip vortex in time-averaged flow field

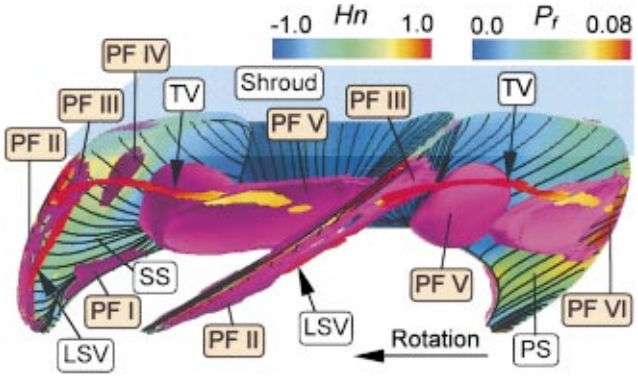

Fig. 12 Isosurface of pressure fluctuation of 0.07 (purple surface), distribution of wall pressure fluctuation (color contours), limiting streamlines (black lines), and vortex cores colored with normalized helicity in time-averaged flow field

result by RANS shown in Part I. In the left passage in Fig. 9 the distribution of the relative velocity magnitude along the tip vortex core indicates that the flow in the tip vortex is decelerated near the midpitch, and then recovered slowly near the pressure surface.

Figure 10 shows time-averaged distributions of the total pressure loss along the vortex cores and on four planes nearly perpendicular to the tip vortex. In the total pressure loss distributions along the vortex cores, the loss production in the tip vortex (TV) is found to become higher near the midpitch (near plane III) where the breakdown of the tip vortex occurs. It is found that the high loss region is spread out to about 30 percent of span from the

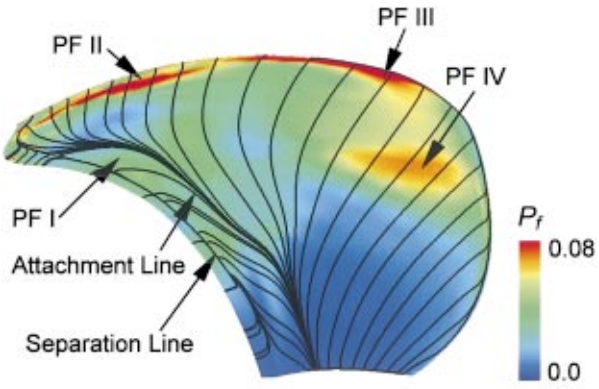

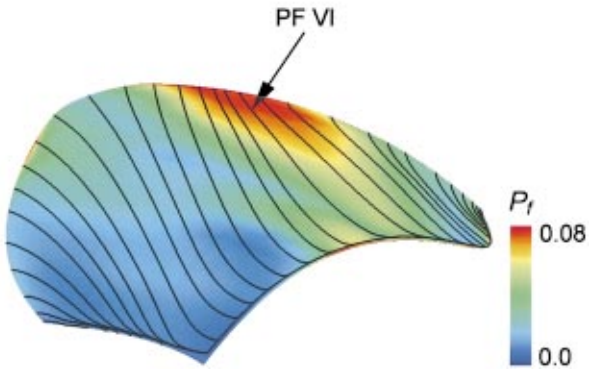

Fig. 13 Pressure fluctuation and limiting streamlines on blade surfaces in time-averaged flow field. (*a*) Suction surface, (*b*) pressure surface

rotor tip. The large spread of the high loss region results from the fact that the large movement of the tip vortex due to the spiral-type breakdown causes its time-averaged structure to expand markedly. It is obvious that the expansion of the time-averaged tip vortex leads to a large blockage effect. The high total pressure loss concentrated around the leading edge separation vortex is decreased gradually in the streamwise direction.

Figure 11 shows time-averaged distributions of the streamwise absolute vorticity along the vortex cores and on the planes, which is presented in the same manner as Fig. 10. The streamwise absolute vorticity in the tip vortex (TV) has a large value near the suction surface and then decreases drastically along the tip vortex, thus being very small near the pressure surface. This corresponds to the fact that the tip vortex structure disappears near the pressure surface. This behavior results from the vortex breakdown. The streamwise absolute vorticity along the leading edge separation vortex core decreases gradually, and is relatively high even near the midchord, because the leading edge separation vortex has no breakdown.

Through the above analysis of the effects of the tip vortex breakdown on the time-averaged flow field, the significant changes are found in the tip vortex behavior near the rotor tip: the drastic decrease in the streamwise vorticity along the vortex core, the large expansion of the vortex and the increase in the loss production along the vortex core.

Pressure Fluctuation Due to Tip Vortex Breakdown. Figure 12 shows a distribution of the pressure fluctuation P_f normalized by a dynamic pressure based on the rotor tip speed, which is defined in Eq. (5). In the figure, purple isosurfaces denote the regions with high-pressure fluctuation of $P_f = 0.07$, and the pressure fluctuation on the rotor blade and the hub is shown by color contours. This figure also shows the vortex core structures (colored with the normalized helicity) and limiting streamlines (black lines) on the blade and hub walls for the time-averaged flow field. A large region with high-pressure fluctuation is observed under the tip vortex as shown by PF V in Fig. 12. This pressure fluctuation results from the large movement of the tip vortex caused by its breakdown. It should be realized that the high-pressure fluctuation brought about by the breakdown appears in the interference region between the tip vortex and the main stream. This region corresponds to the high-pressure fluctuation region in the time- and tangentially averaged flow field shown in Fig. 4. The region PF V in the rotor passage extends to regions PF IV and PF VI on the blade surfaces as seen in Fig. 12. High-pressure fluctuation regions PF II and PF III are caused by the oscillations of the leading edge separation vortex (LSV) and the onset of tip vortex (TV), respectively. A pressure fluctuation PF I on the suction surface is generated by a separation bubble on the suction surface near the leading edge.

Figure 13 shows distributions of the pressure fluctuation on the pressure and suction surfaces of the rotor blade. In the figure, the limiting streamlines are also shown by black lines. Outward radial flows caused by centrifugal effect are observed on the blade surfaces. On the suction surface, there is a separation line followed by an attachment line near the blade leading edge, a separation bubble is formed between the separation and attachment lines.

The high-pressure fluctuation region of PF VI is observed near the tip of the pressure surface where the tip vortex impinges cyclically because of its breakdown as shown in Fig. 6. The cyclic interaction of the tip vortex with the pressure surface causes the movement of the onset position of the tip vortex, thus resulting in the high-pressure fluctuation of PF III near the tip of the suction surface. The high-pressure fluctuation region of PF IV located near the trailing edge of the suction surface results from the unsteady interaction between the tip vortex oscillating and the main flow. The high-pressure fluctuation region of PF II is induced by the oscillation of the leading edge separation vortex interacting with the tip vortex. On the other hand, the intensity of the pressure fluctuation PF I in the separation bubble is much weak as compared with those (PF II, III, IV, and VI) caused by the oscillations of the vortex structures. It is found that the oscillations of the vortex structures caused by the breakdown of the tip vortex give rise to the high-pressure fluctuation.

Conclusions

The unsteady nature of the vortical flow in the propeller fan has been investigated by the large eddy simulation (LES). As a result, the relation between the pressure fluctuation on the blade surfaces and the unsteady behavior of the vortex structures has been elucidated. The results are summarized as follows:

1 The spiral-type breakdown of the tip vortex occurs near the midpitch. It causes the tip vortex to twist and turn violently with time. The effects of the breakdown also cause significant changes in the time-averaged nature of the tip vortex: the drastic decrease in the streamwise vorticity along the vortex core, the large expansion of the vortex and the increase in the loss production along the vortex core.

2 The large and cyclic movement of the tip vortex is the self-sustained flow oscillation due to the vortex breakdown. The movement causes the tip vortex to impinge cyclically on the pressure surface of the adjacent blade, thus resulting in the high-pressure fluctuation near the tip on the pressure surface. The cyclic impingement of the tip vortex gives rise to the movement of the onset position of the tip vortex, leading to the high-pressure fluctuation around the onset position close to the tip of the suction surface.

3 The large movement of the tip vortex caused by its breakdown brings about the high-pressure fluctuation in the interference region between the tip vortex and the main stream. This region extends to the suction surface. The movement of the tip vortex also causes the leading edge separation vortex to oscillate in the same cycle as the tip vortex, leading to the high-pressure fluctuation near the tip in the fore part of the suction surface. However, the scale of the movement of the leading edge separation vortex is much smaller than that of the tip vortex.

4 The unsteady behavior of the tip and leading edge separation vortices dominates the pressure fluctuations in the present propeller fan. The separation bubble on the suction surface near the leading edge causes the lower pressure fluctuation, as compared with the tip and leading edge separation vortices.

Acknowledgments

We would like to thank Dr. K. Saiki for his support of the present numerical analysis by LES. The present research was partially supported by the Ministry of Education, Science, Sports and Culture, Grant-in-Aid for Scientific Research (B), No. 12555049. This support is most gratefully acknowledged.

References

[1] Schlechtriem, S., and Lotzerich, M., 1997, ''Breakdown of Tip Leakage Vortices in Compressors at Flow Conditions Close to Stall,'' ASME Paper No. 97-GT-41.
[2] Furukawa, M., Saiki, K., Nagayoshi, K., Kuroumaru, M., and Inoue, M., 1998, ''Effects of Stream Surface Inclination on Tip Leakage Flow Fields in Compressor Rotors,'' ASME J. Turbomach., **120**, No. 4, pp. 683–694.
[3] Furukawa, M., Inoue, M., Saiki, K., and Yamada, K., 1999, ''The Role of Tip Leakage Vortex Breakdown in Compressor Rotor Aerodynamics,'' ASME J. Turbomach., **121**, No. 3, pp. 469–480.
[4] Furukawa, M., Saiki, K., Yamada, K., and Inoue, M., 2000, ''Unsteady Flow Behavior Due to Breakdown of Tip Leakage Vortex in an Axial Compressor Rotor at Near-Stall Condition,'' ASME Paper No. 2000-GT-0666.
[5] Sarpkaya, T., 1971a, ''On Stationary and Traveling Vortex Breakdowns,'' J. Fluid Mech., **45**, pp. 545–559.
[6] Sarpkaya, T., 1971b, ''Vortex Breakdown in Swirling Conical Flows,'' AIAA J., **9**, No. 9, pp. 1792–1799.
[7] Hall, M. G., 1972, ''Vortex Breakdown,'' Annu. Rev. Fluid Mech., **4**, pp. 195–218.
[8] Leivovich, S., 1978, ''The Structure of Vortex Breakdown,'' Annu. Rev. Fluid Mech., **10**, pp. 211–246.

[9] Leivovich, S., 1984, ''Vortex Stability and Breakdown: Survey and Extension,'' AIAA J., **22**, No. 9, pp. 1192–1206.
[10] Escudier, M., 1988, ''Vortex Breakdown: Observations and Explanations,'' Prog. Aerosp. Sci., **25**, No. 2, pp. 189–229.
[11] Brücker, C., and Althaus, W., 1992, ''Study of Vortex Breakdown by Particle Tracking Velocimetry (PTV) Part 1: Bubble-Type Vortex Breakdown,'' Exp. Fluids, **13**, pp. 339–349.
[12] Brücker, C., 1993, ''Study of Vortex Breakdown by Particle Tracking Velocimetry (PTV) Part 2: Spiral-Type Vortex Breakdown,'' Exp. Fluids, **14**, pp. 133–139.
[13] Delery, J. M., 1994, ''Aspects of Vortex Breakdown,'' Prog. Aerosp. Sci., **30**, No. 1, pp. 1–59.
[14] Akaike, S., and Kikuyama, K., 1993, ''Noise Reduction of Pressure Type Fans for Automobile Air Conditioners,'' ASME J. Vibr. Acoust., **115**, pp. 216–220.
[15] Inoue, M., Wu, K-C., Kuroumaru, M., Furukawa, M., Fukuhara, M., and Ikui, T., 1984, ''A Design of Diagonal Impeller by Means of SCM and Cascade Data,'' Proceedings of China-Japan Joint Conference on Hydraulic Machinery and Equipment, Vol. 1, pp. 21–30.
[16] Sawada, K., 1995, ''A Convenient Visualization Method for Identifying Vortex Centers,'' Trans. Japan Soc. of Aero. Space Sci., **38**, No. 120, pp. 102–116.

Yoshiki Yoshida
Associate Professor
e-mail: yoshida@me.es.osaka-u.ac.jp

Yoshinobu Tsujimoto
Professor

Osaka University, Graduate School of
Engineering Science,
1-3, Machikaneyama, Toyonaka,
Osaka 560-8531, Japan

Dai Kataoka
Engineer,
Kawasaki Heavy Industries, LTD.,
Gas Turbine Division,
Aero Engine Engineering Department,
1-1, Kawasaki, Akashi, Hyogo 673-8666, Japan

Hironori Horiguchi
Research Assistant,
Tokushima University, Mechanical Engineering,
2-1, Minamizyousanzima,
Tokushima 770-8506, Japan

Fabien Wahl
Researcher,
SNECMA, Division SEP,
Direction Grosse Propulsion A Liquides,
Forêt de Vernon BP802,
27208 Vernon Cedex, France

Effects of Alternate Leading Edge Cutback on Unsteady Cavitation in 4-Bladed Inducers

A set of 4-bladed inducers with various amounts of cutback was tested with the aim of suppressing the rotating cavitation by applying alternate leading edge cutback. Unsteady cavitation patterns were observed by means of inlet pressure measurements and high-speed video pictures. It was found that the region with the alternate blade cavitation and asymmetric cavitation were enlarged with the increase of the amount of the cutback. As a result, the region with the rotating cavitation was diminished. At low flow rate, two types of alternate blade cavitation were found as predicted theoretically on 4-bladed inducer with smaller uneven blade length. One of them is with longer cavities on longer blades, and the other is with longer cavities on shorter blades. Switch was observed in these alternate blade cavitation patterns depending whether the cavitation number was increased or decreased. For an inducer with larger amount of cutback, the rotating cavitation and cavitation surge were almost suppressed as expected for a wide range of flow rate and cavitation number, although the cavitation performance was deteriorated. However, we should note that an asymmetric cavitation pattern occurs more easily in inducers with alternate leading edge cutback, and that the unevenness due to the cutback causes uneven blade stress. [DOI: 10.1115/1.1411969]

Introduction

Super-synchronous shaft vibrations were often observed in turbopump inducers for rocket engine (Rosenmann [1], Kamijo et al. [2], de Bernaldi et al. [3], Bordelon et al. [4]). This was attributed to the rotating cavitation with asymmetric pressure pattern rotating faster than the inducer (Kamijo et al. [5], Tsujimoto et al. [6]).

In addition, alternate blade cavitation may occur in inducers with even number of blades. The alternate blade cavitation was reported by several researchers, Goirand et al. [7], Bordelon et al. [4] for four blades, and Huang et al. [8] for two blades, following the observations by Acosta [9] and Iura [10]. Recently, Horiguchi et al. [11] examined theoretically the alternate blade cavitation, and explained the cause of the alternate blade cavitation as follows. When the cavity on blade approaches approximately 65% of the spacing, the flow toward the blade suction surface near the cavity closure interacts with the leading edge of the next blade. This causes the reduction of the angle of incidence to the next blade, and hence the decrease of the cavity on the blade.

The alternate blade cavitation was also observed at a slightly higher inlet pressure than that of the rotating cavitation and cavitation surge onset (Goirand et al. [7]). In the cases with more than two blades, the alternate blade cavitation does not cause shaft vibration since the relative flow is steady and symmetrical.

The motivation of the present study is to reduce the onset range of rotating cavitation by promoting the alternate blade cavitation. For this purpose, the leading edges of 4-bladed inducer are cut back alternately. Unsteady cavitations were observed with the measurements of the inlet pressure fluctuations, and the high-speed video pictures. The experimental results are discussed, and the comparison with the theoretical results is presented.

Test Apparatus

The present experiments were conducted in the Cavitation Test Facility at Osaka University. A detailed description of the test facility can be found in a previous report (Tsujimoto et al. [12]). Here, the description is limited to the tested inducers with alternate leading edge cutback.

Figure 1 shows details of the test section: inducer tip diameter is $D_t = 149.8$ mm ($r_t = 74.9$ mm), and the rotational speed is $n = 4000 \pm 2$ rpm (rotational frequency $f_n = 66.7$ Hz). Tap water was used as the working fluid after degassing. Unsteady cavitations were observed by means of unsteady inlet pressure measurements, and by use of the high-speed video pictures (4500 frames/second), covering a wide range of flow coefficient and cavitation number. The casing is made of transparent acrylic resin, with inner diameter 150.8 mm (i.e., radial tip clearance $s = 0.5$ mm). The inlet pressure fluctuations were measured at four circumferential locations with angular distance of 90 degrees to determine the number of cell patterns and the direction of propagation for the rotating cavitation. A pressure sensor with the resonance frequency of 35 kHz was flush mounted on the casing wall at axial distance 38 mm upstream from the inducer inlet.

In order to examine the effect of alternate leading edge cutback, systematic experiments were carried out. Four inducers were designed and fabricated, as shown in Fig. 2. The inducers have four

Contributed by the Fluids Engineering Division for publication in the JOURNAL OF FLUIDS ENGINEERING. Manuscript received by the Fluids Engineering DivisionMay 22, 2000; revised manuscript received July 11, 2001. Associate Editor: B. Schiavello.

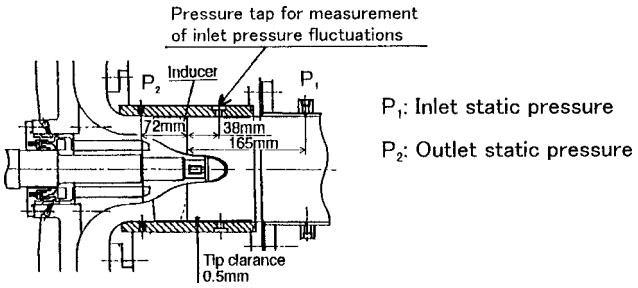

Fig. 1 Inducer cross section and inlet pressure measurement locations

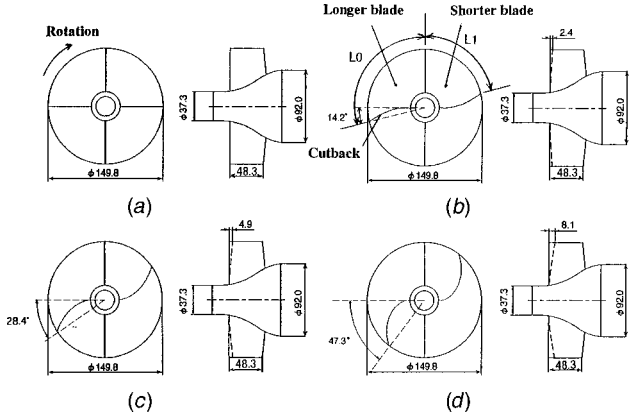

Fig. 2 Sketch of the test inducers, Inducer 0-0 without the cutback and Inducer 0-15, 0-30, 0-50 with the alternate leading edge cutback. (*a*) Inducer 0-0; (*b*) Inducer 0-15; (*c*) Inducer 0-30; (*d*) Inducer 0-50

helical blades with a flat part near the leading edge and a circular arc in the rest of the chord. The inlet blade angle is $\beta_{t1}=7.5$ degrees, and outlet blade angle $\beta_{t2}=9.0$ degrees at the tip. The distribution of the blade angle $\beta(r)$ is satisfied with the helical condition as $r\times\tan\beta(r)=r_t\times\tan\beta_t$ (i.e., spanwise constant pitch). The blade thickness at the tip is 2 mm and the leading edge radius 0.2 mm. Dimensions of the Inducer 0-0, without alternate leading edge cutback (i.e., equal blade length) and with straight radial leading edge, are shown in Table 1. The basic design is the same as for the LE-7 liquid oxygen turbopump inducer except that 3 blades are employed for the LE-7. The design point of the inducer is (design flow coefficient $\phi_d=0.078$, design static pressure rise coefficient $\psi_{sd}=0.120$, and design head coefficient $\psi_d=0.132$).

Uneven blade inducers were produced by cutting back the leading edge of Inducer 0-0 alternately. Since the blade are straight near the leading edge, the inlet blade angle is not changed by the cutback. Amount of the cutback are 14.2, 28.4, and 47.3 degrees at the tip for Inducer 0-15, 0-30, and 0-50 respectively, as shown in Fig. 2. The leading edge curve is obtained by shifting the circumferential location of an involute curve with base radius 26 mm proportionally to the amount of the cutback respectively.

Table 1 Principal dimensions of Inducer 0-0

Number of blades	4
Tip diameter, D_t	149.8 mm
Inlet tip blade angle, β_{t1}	7.5 deg
Outlet tip blade angle, β_{t2}	9.0 deg
Hub/tip ratio at inlet	0.25
Hub/tip ratio at outlet	0.51
Solidity at tip	2.97
Solidity (mean) at hub	2.93
Radial tip clearance, s	0.5 mm
Design flow coefficient, ϕ_d	0.078
Design static pressure rise coefficient, ψ_{sd}	0.120
Design head coefficient, ψ_d	0.132

Pressure Performance

Figure 3 shows the comparison of noncavitating static pressure performance of the tested four inducers. Test cavitation number is $\sigma=0.5$, i.e., $NPSH_A/NPSH_{R3\%}\fallingdotseq 20$. As expected, the present inducers have nearly the same pressure performance. The performance curves have negative slope throughout the flow range, so that no conventional surge nor rotating stall is expected to occur in non-cavitating condition. The design flow rate is $\phi_d=0.078$. The cavitation tests described below are in the flow rate range $\phi=0.055\sim0.09$.

Unsteady Cavitation in Inducer 0-0

First, we examined the unsteady cavitations in Inducer 0-0 as reference. Figure 4 shows the cascade plot of the spectra of the inlet pressure fluctuations for various cavitation number σ, for

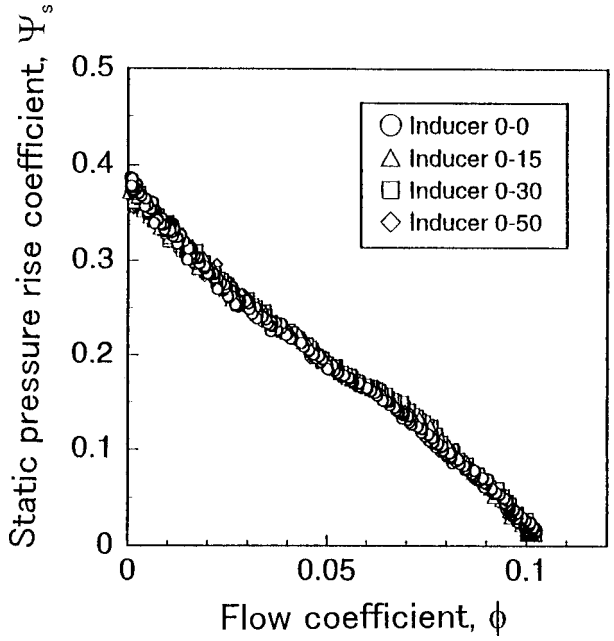

Fig. 3 Static pressure performance curves, for Inducer 0-0, 0-15, 0-30, and 0-50 with noncavitating flow (uncertainty in $\psi_s\pm0.002$, in $\phi\pm0.002$)

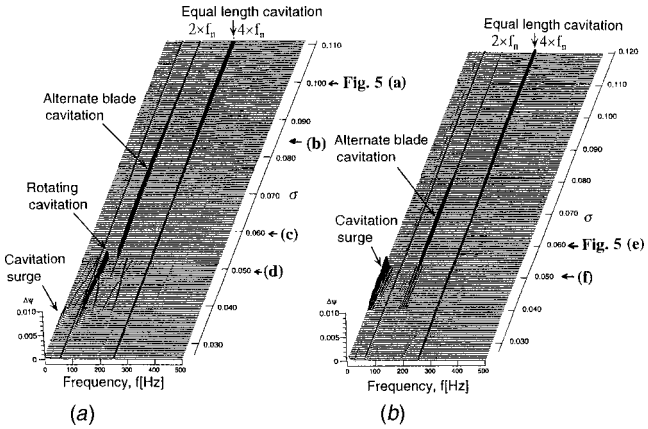

Fig. 4 Spectral analyses of the inlet pressure fluctuations for $\phi=0.080$ and $\phi=0.085$ with Inducer 0-0 (uncertainty in f ±1.5 Hz, in $\sigma\pm0.002$, in $\phi\pm0.002$, in $\psi_s\pm0.0005$), (*a*) $\phi=0.080$; (*b*) $\phi=0.085$

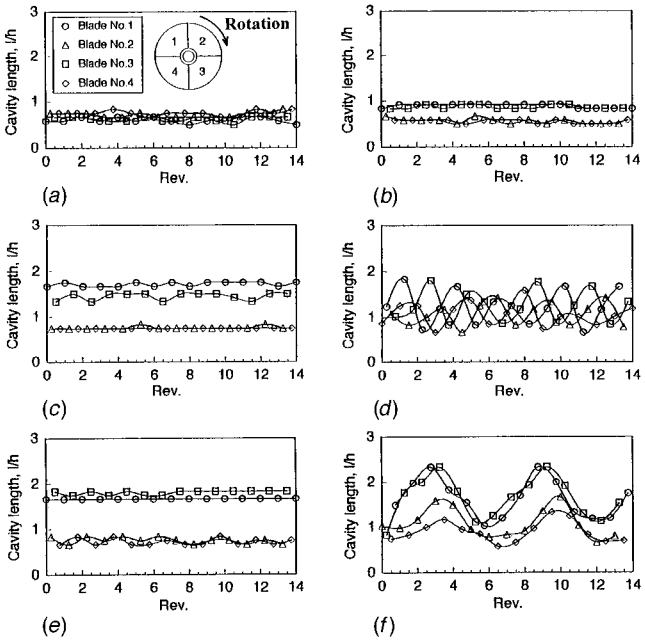

Fig. 5 Changes of the tip cavity length versus shaft rotations for various cavitation numbers, $\phi=0.080$ and $\phi=0.085$ with Inducer 0-0 (uncertainty in l/h±0.05, in Rev.±0.05, in $\phi\pm0.002$, in $\sigma\pm0.002$). (1) Inducer 0-0, $\phi=0.080$. (*a*) Equal length cavitation, $\sigma=0.10$; (*b*) alternate blade cavitation, $\sigma=0.085$; (*c*) alternate blade cavitation, $\sigma=0.060$; (*d*) rotating cavitation, $\sigma=0.050$. (2) Inducer 0-0, $\phi=0.085$. (*e*) Alternate blade cavitation, $\sigma=0.060$; (*f*) cavitation surge, $\sigma=0.050$

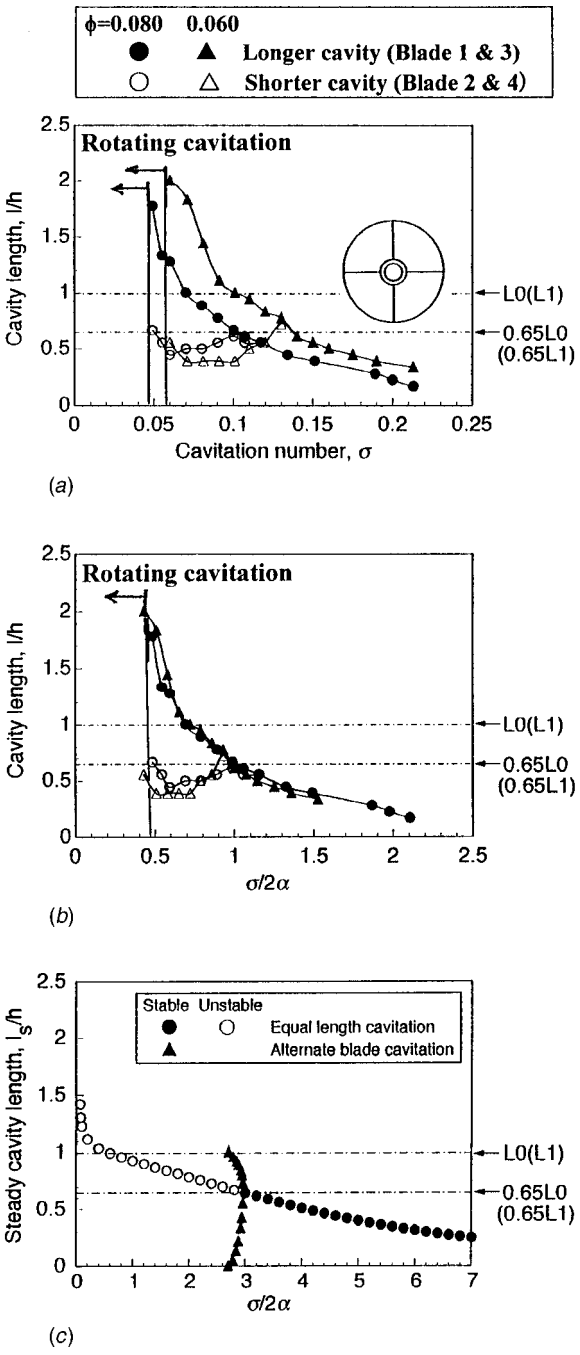

Fig. 6 Variation of the tip cavity length versus cavitation number, σ and $\sigma/2\alpha$ for $\phi=0.060$ and $\phi=0.080$ with Inducer 0-0 (uncertainty in l/h±0.05, in $\phi\pm0.002$, in $\sigma\pm0.002$). (*a*) Cavity length versus cavitation number σ (Experiment, $\phi=0.060$ and $\phi=0.080$); (*b*) cavity length versus $\sigma/2\alpha$ (experiment, $\phi=0.060$ and $\phi=0.080$); (*c*) cavity length versus $\sigma/2\alpha$ (calculation from Horiguchi et al. [11])

Inducer 0-0 with flow coefficient $\phi=0.080$ (Fig. 4(*a*)) and $\phi=0.085$ (Fig. 4(*b*)). Figure 5 shows the plot of cavity length, l/h, at the tip of each blade against the shaft revolutions, rev, observed from the high-speed video pictures, under the condition of the equal length cavitation ($\phi=0.080$, $\sigma=0.10$), the alternate blade cavitation ($\phi=0.080$, $\sigma=0.085$, 0.060, and $\phi=0.085$, $\sigma=0.060$), the rotating cavitation ($\phi=0.080$, $\sigma=0.050$), and the cavitation surge ($\phi=0.085$, $\sigma=0.050$). Figure 6 shows the variation of steady cavity length at the tip against cavitation number, σ (Fig. 6(*a*)), and against $\sigma/2\alpha$ ((cavitation number)/(2×incidence angle (radian))) (Fig. 6(*b*)) along with the calculation results in Fig. 6(*c*) from Horiguchi et al. [11].

For the inducer 0-0, the equal length cavitation appears at higher cavitation number as shown by the $4\times f_n$ component in Fig. 4(*a*) and (*b*). As we decrease the cavitation number, the alternate blade cavitation starts to develop when the cavity length approaches 65% of the spacing. Under the condition with alternate blade cavitation, $2\times f_n$ component appears as shown in Fig. 4(*a*) and (*b*). The critical cavity length (=65% of the spacing) agrees fairly well with the theoretical result as shown in Fig. 6(*c*). This behavior can be explained theoretically (Horiguchi et al. [11,15]) by the interaction of the local flow near the cavity closure with the leading edge of the adjacent blade.

If we reduce the cavitation number further, the longer cavities develop more and exceed the spacing length, while the shorter cavities diminish to a minimum length. As we decrease the cavitation number, the longer cavities grow more and shorter cavity lengths keep almost constant. At flow coefficient $\phi=0.080$, the rotating cavitation starts to appear, when the cavitation number is further decreased less than $\sigma=0.050$, the shorter cavities approach 65% of the spacing again and the longer cavities reach approximately 70% of the chord, C (as shown in Fig. 6(*a*): $l/h\fallingdotseq2.0$, $C/h=2.97$, i.e., $l/C\fallingdotseq0.7$). Under the condition with rotating cavitation, the amplitude of $1.1\sim1.5\times f_n$ component appears as shown in Fig. 4(*a*). Figure 5(*d*) shows clearly the forward propagation of the cavity pattern from blade to blade with one cell. The propagation speed is faster than the inducer rotation, and it approaches the rotational speed of the inducer as we decrease the cavitation number. The propagation speed ratio, Ω_R/Ω, of the present 4-bladed inducer is considerably larger as compared to the 3-bladed inducer (Tsujimoto et al. [12]), as shown in Fig. 7. In this figure, the theoretical results by Watanabe et al. [13] are shown. The theory predicts fairly well the experimental trend re-

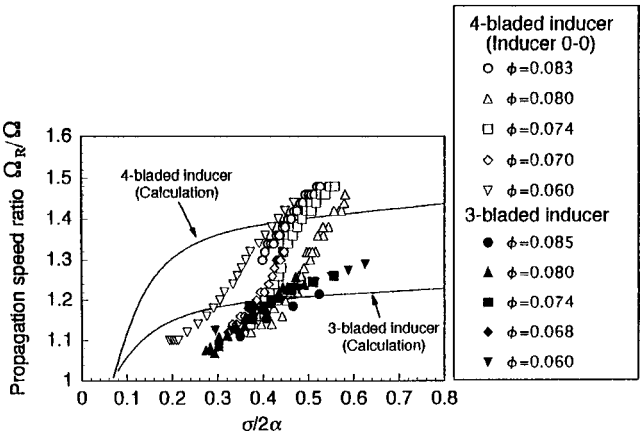

Fig. 7 Comparison between the experimental values and calculated values (Watanabe et al. [13]) for the propagation speed ratio of rotating cavitation showing the effect of number of blades (4-bladed Inducer 0-0 compared with 3-bladed inducer (Tsujimoto et al. [12])) (uncertainty in $\Omega_R/\Omega \pm 0.02$, in $\phi \pm 0.002$, in $\sigma \pm 0.002$)

lated with number of blades. The comparison between theory and experiment is good only for $\sigma/2\,\alpha = 0.2 \sim 0.6$, but the trend is predicted more accurately.

At larger flow coefficient $\phi = 0.085$, the cavitation surge (Fig. 5(f)) with low frequency oscillation of $f = 5 \sim 10$ Hz, as shown in Fig. 4(b), starts to occur at $\sigma = 0.053$ when the shorter cavities approach 65% of the spacing (i.e., 20% of the chord), and the longer cavities 70% of the chord (i.e., 2 times the spacing). Figure 5(f) shows that the longer cavities (on Blade No. 1, 3) and shorter cavities (on Blade No. 2, 4) oscillate with the same frequency ($f = 10$ Hz) but with a small phase difference between the longer and shorter cavities. This cavitation surge with the test 4-bladed inducer can also be understood as the periodical shifts between the alternate blade cavitation and equal length cavitation with low frequency.

Cavity Length Against $\sigma/2\alpha$

Figure 6(a) is a plot of the steady cavity length at the tip, l/h, against the cavitation number, σ, for flow coefficients $\phi = 0.06$ and 0.08. It has been shown by two dimensional linear analysis such as Acosta [14] that the development of cavity length on the cascade is a function of $\sigma/2\alpha$. Figure 6(b) is the plot of the cavity length against $\sigma/2\alpha$ for both flow rates. As expected from the theory, the cavity lengths against $\sigma/2\alpha$ are almost the same for the different angles of α ($= \beta_{t1} - \tan^{-1}(\phi)$; $\alpha = 4.1$ deg for $\phi = 0.06$, and $\alpha = 2.9$ deg for $\phi = 0.08$). We find that the alternate cavitation starts to occur at $\sigma/2\alpha \fallingdotseq 0.9$ with cavity length 65% of the spacing, and the rotating cavitation starts to occur at $\sigma/2\alpha \fallingdotseq 0.5$ with the shorter cavity 65% of the spacing (i.e., 20% of the chord), and the longer cavity approximately 70% of the chord (i.e., 2 times the spacing). From these observations, it could be concluded that the cavity length at the tip plays a significant role for the onset of the alternate blade cavitation, and the unsteady cavitations (rotating cavitation/cavitation surge).

Effect of Alternate Leading Edge Cutback on Unsteady Cavitation

Figure 8 shows the spectra of inlet pressure fluctuations for the tested four inducers, at flow coefficient $\phi = 0.074$ close to the design value. Figure 9 shows the regions of various cavitation patterns against the cavitation number, based on the measurement of the inlet pressure fluctuations and the observation with high-speed video pictures. For the case with alternate leading edge cutback, we call the cavitation with significant difference in cavity length as ''alternate blade cavitation,'' corresponding to a regular pattern of long-short-long-short cavity from one blade to the adjacent one. Under the condition of this alternate blade cavitation, the amplitude of the $2 \times f_n$ component of pressure fluctuations is generally larger than that of the $4 \times f_n$ component.

Figures 8 and 9 show the following effects of alternate leading edge cutback on the unsteady cavitations.

1 The alternate leading edge cutback can enlarge the range of alternate blade cavitation toward low cavitation number, and suppress the rotating cavitation.
2 For larger amount of the cutback, the cavitation surge appears instead of the rotating cavitation.
3 With the alternate leading edge cutback, there appears an ''asymmetric cavitation'' pattern at lower cavitation number.

Figure 10(a) shows the development of the cavity with Inducer 0-30, for $\phi = 0.078$. The cavitation surge starts to occur when the longer cavities on the longer blades approach approximately 70% of the original chord ($l/h \fallingdotseq 2.0$), and the shorter cavities on the shorter blades diminish to almost zero after reaching 65% of the L1. Further reduction in the cavitation number results in ''asymmetric cavitation,'' in which one longer cavity on the longer blade grows further and the other becomes shorter, with no cavities on both shorter blades. The cavity lengths on the blades keep almost

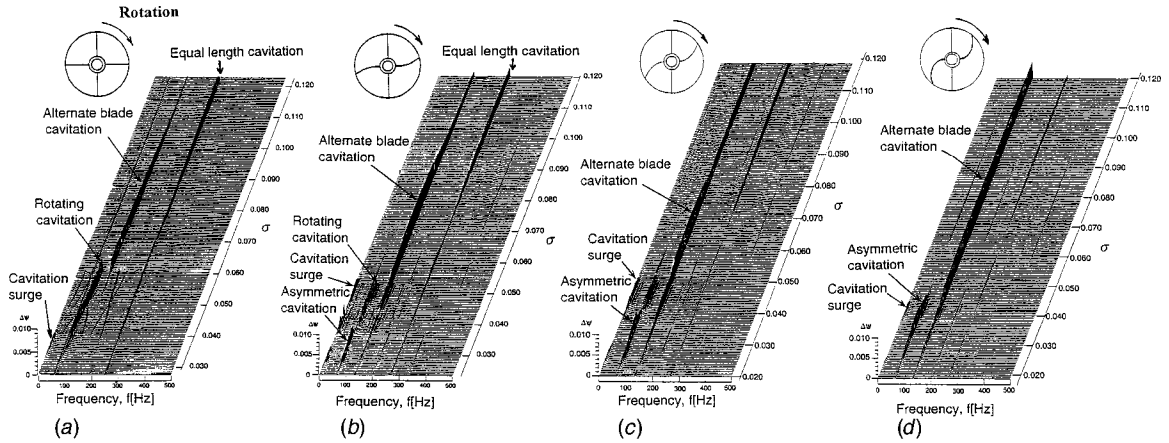

Fig. 8 Spectral analyses of the inlet pressure fluctuations showing the effect of alternate leading edge cutback, for $\phi = 0.074$ with Inducer 0-0, 0-15, 0-30, and 0-50 (uncertainty in f ± 1.5 Hz, in $\sigma \pm 0.002$, in $\phi \pm 0.002$, in $\psi_s \pm 0.0005$), (*a*) Inducer 0-0; (*b*) Inducer 0-15; (*c*) Inducer 0-30; (*d*) Inducer 0-50

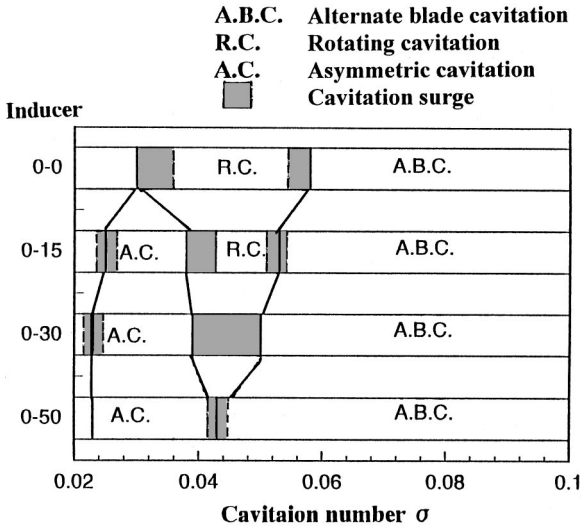

Fig. 9 Comparison of the occurrence regions of various cavitation patterns showing the effect of alternate leading edge cutback, for $\phi=0.074$ with Inducer 0-0, 0-15, 0-30, and 0-50

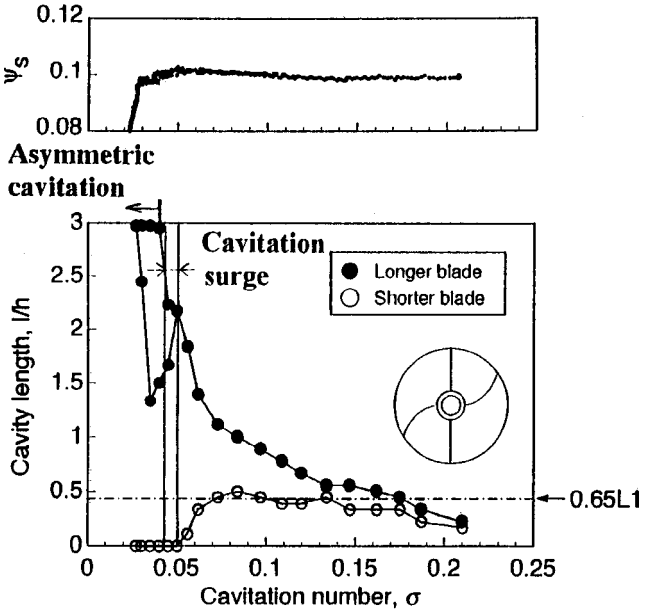

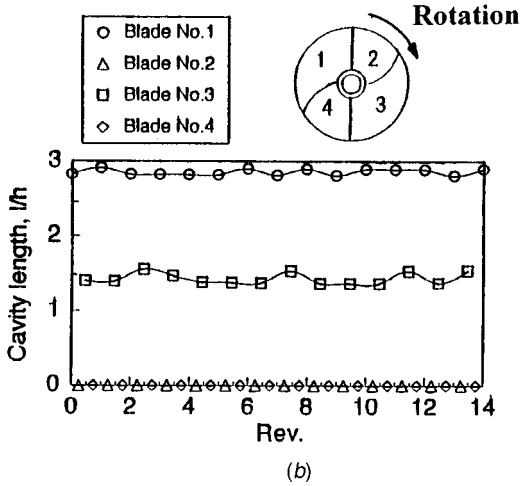

Fig. 10 Variation of the tip cavity length versus cavitation number with the asymmetric cavitation, and changes of the tip cavity length versus shaft rotation under the asymmetric cavitation ($\sigma=0.035$) with Inducer 0-30, for $\phi=0.078$ (uncertainty in l/h±0.05, in ψ_s±0.002, in ϕ±0.002, in σ±0.002, in rev.±0.05). (*a*) $\phi=0.078$; (*b*) $\phi=0.078$, $\sigma=0.035$

constant, as shown in Fig. 10(*b*). The range of asymmetric cavitation extends with increasing of the amount of leading edge cutback, which suppress the rotating cavitation and the cavitation surge.

As a result, with Inducer 0-50, the unsteady cavitation patterns (rotating cavitation and cavitation surge) were almost suppressed, as effect of the enlargement of the range for alternate blade cavitation and asymmetric cavitation, while the cavitation performance was deteriorated as will be mentioned in the last section.

Two Types of Alternate Blade Cavitation

At low flow rate ($\phi\leqq0.065$), two types of alternate blade cavitation were found in the inducers with smaller alternate leading edge cutback (Inducer 0-15 and 0-30), as predicted theoretically by Horiguchi et al. [15]. One of them is with longer cavities on longer blades, and the other is with longer cavities on shorter blades. The former generally occurs and the latter is limited at low flow rate in the present experiments. Photographs of these two alternate blade cavitations in Inducer 0-15 are shown in Fig. 11. Figure 11(*a*) shows that the longer cavities develop on the blades without leading edge cutback. On the contrary, the longer cavities develop on the blades with leading edge cutback as shown in Fig. 11(*b*). In both cases, longer cavities are shown.

In addition, a switch was observed indicating shift between these alternate blade cavitations depending if the cavitation number is increased or decreased. Figures 12(*a*) and (*b*) show the cavity lengths against cavitation number with decreasing and increasing cavitation number in Inducer 0-15 at $\phi=0.06$. Figure 12(*c*) shows the theoretical result to compare with these experimental results.

Decreasing Cavitation Number. Figure 12(*a*) shows the case with decreasing cavitation number. When the cavitation number is large (about $\sigma=0.15$), the cavity lengths on longer blades are longer than those on shorter blades. As we decrease the cavitation number, the cavities on both blades develop more. When the cavities on shorter blades approach 90% of L1 (about $\sigma=0.13$), the cavities on longer blades start to diminish and then the cavities on shorter blades develop more. Here, the change in cavity length occurs continuously. A surge mode oscillation (S.M.O.) (Tsujimoto et al. [12]), whose oscillating frequency (about $f=16$ Hz) is higher than that of the classical cavitation surge (C.S.) ($f=5\sim10$ Hz), appears during this transition. As the cavitation number is further reduced, the cavities on shorter blades develop more and those on longer blades further diminish. When the cavity lengths on longer blades approach 65% of L0 again, the cavities on shorter blades diminish suddenly less than L1, and the cavities on longer blades become larger than L0. Here, the two types of alternate blade cavitation switch discontinuously. At this switching, the static pressure rise coefficient, ψ_s, breaks down slightly. When the longer cavities develop to approximately 70% of the cord ($l/h\fallingdotseq2.0$) and the shorter cavities exceed L1, the classical cavitation surge (C.S.) starts to occur. Under the condition of this cavitation surge, both the longer and the shorter cavities oscillate with the same frequency ($f=5\sim10$ Hz), but with a certain phase difference, just like as shown in Fig. 5(*f*).

Increasing Cavitation Number. Figure 12(*b*) shows the case with increasing cavitation number from smaller value. When we increase the cavitation number from the condition with the classical cavitation surge (C.S.) ($f=5\sim10$ Hz), the alternate blade cavitation with longer cavities on the longer blades occurs in a

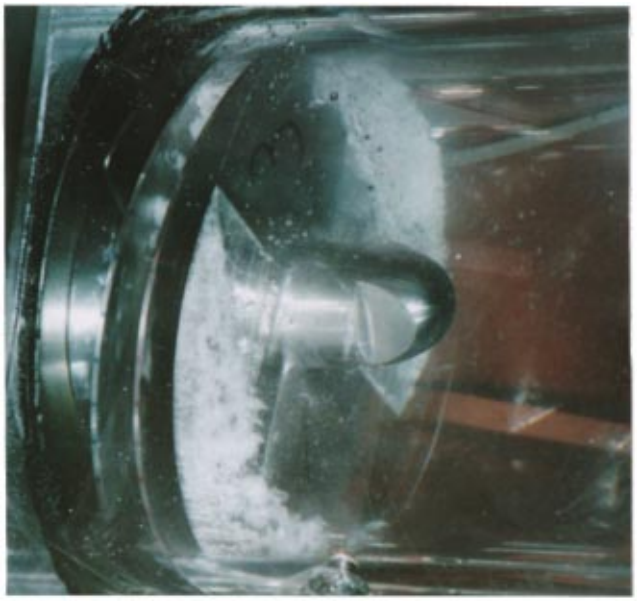

(*a*)

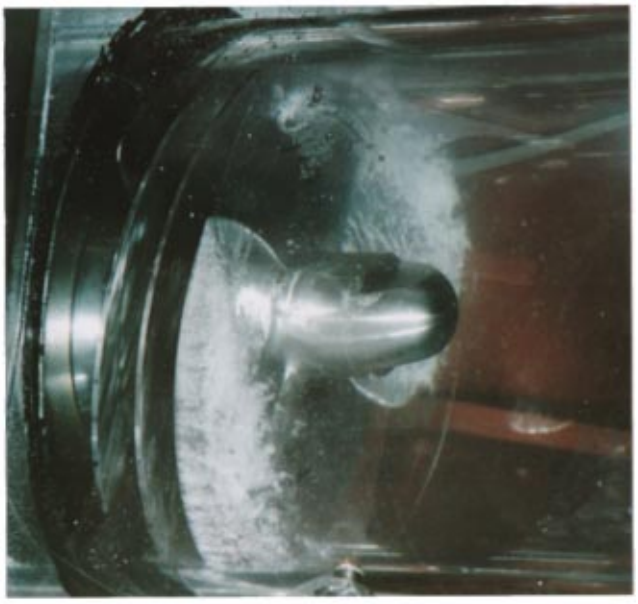

(*b*)

Fig. 11 Photographs of two types of alternate blade cavitation: (*a*) longer cavities on longer blades, and (*b*) longer cavities on shorter blades for $\phi=0.055$, $\sigma=0.060$ with Inducer 0-15 (uncertainty in $\phi\pm0.002$. in $\sigma\pm0.002$). (*a*) Longer cavities on longer blades ($\sigma=0.060$ with increasing cavitation number); (*b*) longer cavities on shorter blades ($\sigma=0.060$ with decreasing cavitation number)

wider range of cavitation number than for the case of decreasing cavitation number. At smaller cavitation number, the cavities on the both blades decrease as the cavitation number is increased. The shorter cavities on shorter blades almost disappear. Then the cavities on shorter blades start to develop. When the cavities on shorter blades develop over 65% of L1, the cavity lengths change discontinuously, and get into another type of alternate blade cavitation with longer cavities on shorter blades. After this switching, a surge mode oscillation (S.M.O.) (about $f=16$ Hz) occurs. The amplitude of pressure fluctuations under the surge mode oscillation is considerably smaller than that under the classical cavitation surge. For the classical cavitation surge at lower cavitation num-

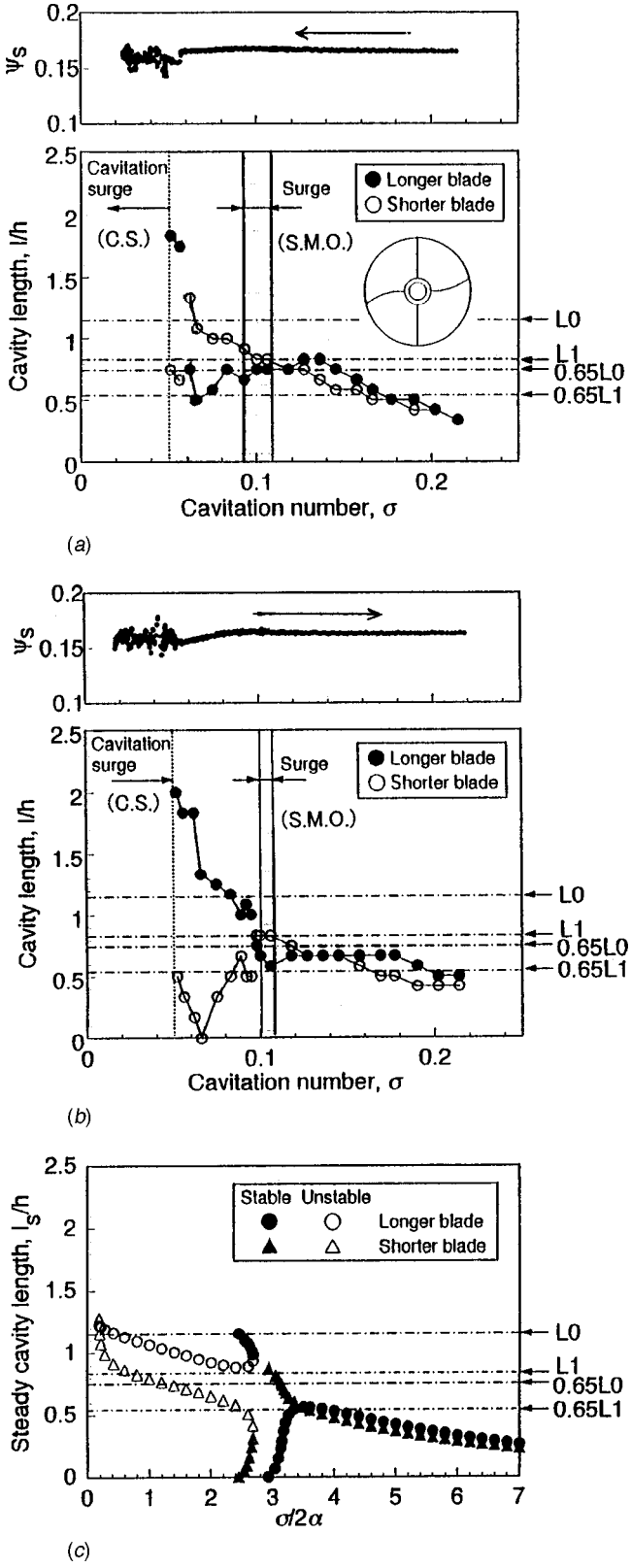

Fig. 12 Switch of the alternate blade cavitation depending if the cavitation number is decreased or increased for $\phi=0.06$ with Inducer 0-15 (uncertainty in l/h±0.05, in $\sigma\pm0.002$, in $\phi\pm0.002$, in $\psi_s\pm0.002$). (*a*) Cavitation number decreasing (experiment); (*b*) cavitation number increasing (experiment); (*c*) calculation (from Horiguchi et al. [15])

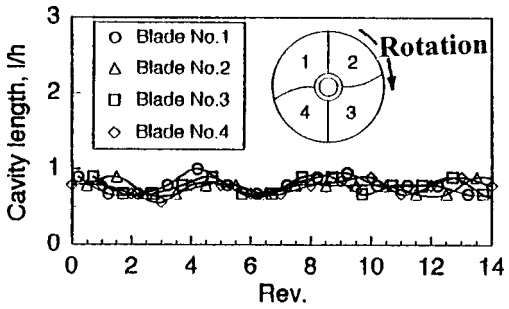

Fig. 13 Change of the tip cavity length versus shaft rotations under the surge mode oscillation (S.M.O., f=16 Hz), for ϕ =0.060, σ=0.10 with Inducer 0-15 (uncertainty in l/h±0.05, in rev.±0.05, in ϕ±0.002, in σ±0.002)

ber, cavity oscillates with $l/h > 1.0$ ($f = 5 \sim 10$ Hz). Under the surge mode oscillation, the cavity oscillates with $l/h < 1.0$ (about $f = 16$ Hz) with smaller amplitude as shown in Fig. 13. If we further increase the cavitation number, the cavities on shorter blades decrease and become shorter than those on longer blades.

Although a comparison with the theoretical results is quite difficult because there is strong hysteresis in present experiments, the theoretical results as shown in Fig. 12(*c*) agree qualitatively with the experimental observations. According to the theoretical calculations, two types of alternate blade cavitation appear and the cavity length switches twice. There exists a region with no stable theoretical solution that corresponds to the abrupt transition observed in the experiments. From these results, it follows that two types of alternate blade cavitation with two switches are caused by the interaction of the local flow near the cavity closure on the shorter/longer blade with the leading edge of the longer/shorter blade respectively.

To examine whether similar switch occurs in the inducer with equal blade length, Inducer 0-0 was tested with increasing and decreasing the cavitation number. However, no switch was found.

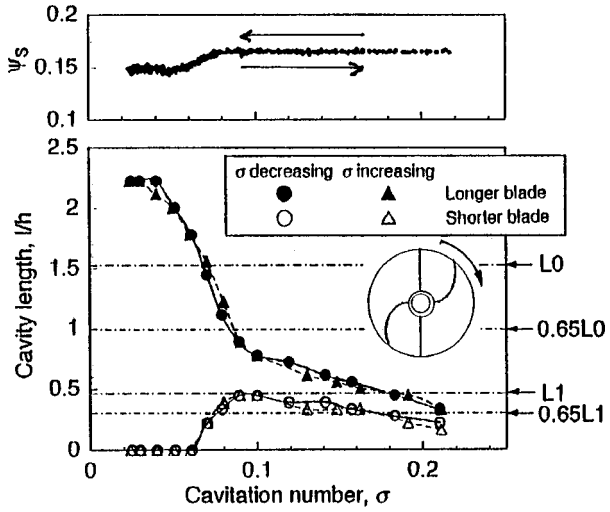

(*a*)

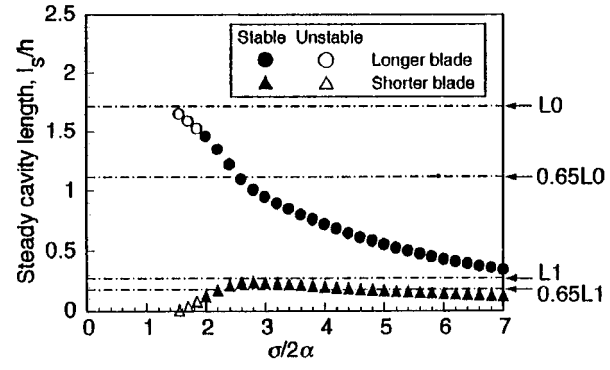

(*b*)

Fig. 14 Variation of the tip cavity length versus cavitation number in Inducer 0-50 with alternate blade cavitation (longer cavities on longer blades) for ϕ=0.060 (uncertainty in l/h ±0.05, in ϕ±0.002, in σ±0.002, in ψ_s±0.002). (*a*) Cavitation number decreasing and increasing (experiment); (*b*) calculation (Equivalent to Inducer 0-65 from Horiguchi et al. [15])

Large Cutback (Inducer 0-50). The results with larger amount of the cutback (Inducer 0-50) are shown in Fig. 14. Significant difference can be seen between Inducer 0-50 and Inducer 0-15 (as shown in Fig. 12). For Inducer 0-50, there exists only one type of alternate blade cavitation throughout the domain of the present test data. To examine if the same switch exists, Inducer 0-50 was tested with increasing and decreasing cavitation number at flow coefficient $\phi = 0.06$. The cavities on longer blades are always larger than those on shorter blades without any switch as shown in Fig. 14(*a*).

As we reduce the cavitation number, the cavity lengths on longer blades approach 65% of L0, while the cavity lengths on shorter blades are kept less than 100% of L1. When the longer cavities exceed 65% of L0, the shorter cavities start to diminish and the pressure coefficient decreases gradually. If we decrease the cavitation number further, the longer cavities approach 100% of L0, and shorter cavities almost disappear. At last, the longer cavities reach approximately 70% of the chord ($l/h \fallingdotseq 2.0$) and then keep their length without oscillation. Figure 14(*b*) shows the theoretical results that corresponds to Inducer 0-65, which has a larger alternate leading edge cutback than that of the experiment Inducer 0-50. The calculation results simulate the experimental observations fairly well, while the cavity becomes unstable at smaller cavitation number. In this case, the cavity on shorter blade is too small to cause the decrease of cavity on longer blade even if it grows to a certain percentage of L1.

Map of Various Cavitations

Figure 15 presents the occurrence region of each cavitation pattern for various amounts of the leading edge cutback in the cavitation performance plots for the case with increasing cavitation number.

With the increase of the amount of cutback, the head breakdown starts to occur at larger cavitation number at high flow rate comparatively. At low flow rate, when strong suction recirculation occurs for ϕ less than 0.07, the static pressure rise coefficient gradually decreases starting from higher cavitation number under the alternate blade cavitation. It was observed that the decrease of the static pressure rise coefficient occurs when the longer cavities on longer blades exceed the spacing L0. Also the pressure coefficient decreases slightly at the asymmetric cavitation onset.

The boundary of the alternate cavitation in Inducer 0-0 is about $\sigma/2\alpha \fallingdotseq 1.0$, while the boundary of the rotating cavitation is $\sigma/2\alpha \fallingdotseq 0.5$ as presented in Fig. 15(*a*). Figure 15(*a*) thru (*d*) shows the following tendencies as to the effects of the amount of cutback on unsteady cavitations:

1 In Inducer 0-15 as compared with Inducer 0-0, the rotating cavitation occurs at smaller cavitation number and the asymmetric cavitation appears before the head breakdown. Cavitation surge (C.S.) appears in a range wider than that of the rotating cavitation.

2 In Inducer 0-30, the range of rotating cavitation disappears, and the cavitation surge is partly suppressed due to the expansion of the range of the asymmetric cavitation.

3 In Inducer 0-50, there is only a small region of the cavitation surge (C.S.) with smaller amplitude of the pressure fluctuations in

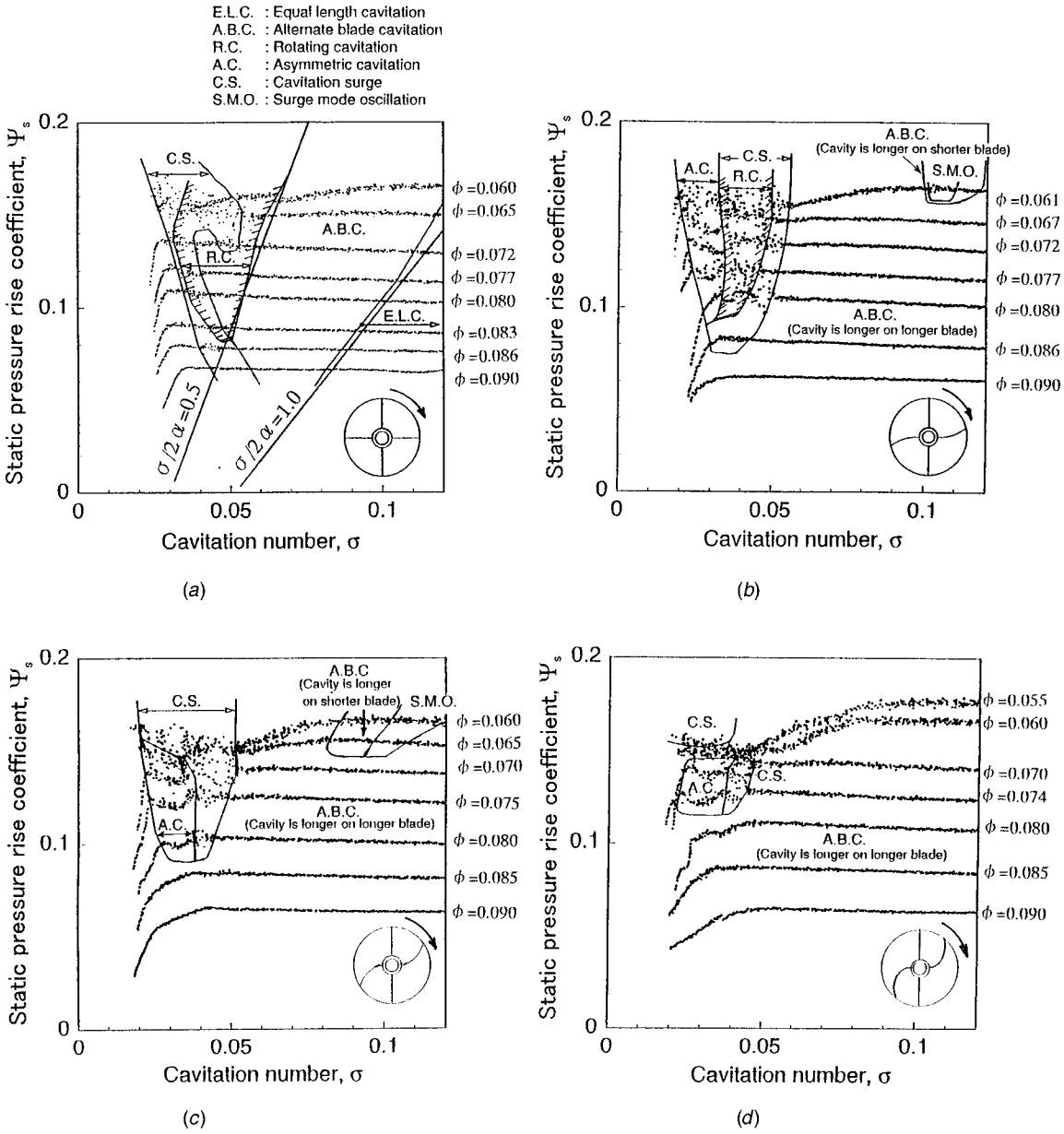

Fig. 15 Cavitation performances and maps showing the occurrence regions of various cavitation patterns for Inducer 0-0, 0-15, 0-30, and 0-50 with increasing cavitation number (uncertainty in $\psi_s \pm 0.002$, in $\phi \pm 0.002$, in $\sigma \pm 0.002$), (*a*) Inducer 0-0; (*b*) Inducer 0-15; (*c*) Inducer 0-30; (*d*) Inducer 0-50

a narrow region with lower flow rates. Unsteady cavitation patterns (R.C., C.S., and S.M.O.) are almost suppressed as expected.

Concluding Remarks

To suppress the rotating cavitation which causes the supersynchronous shaft vibration, 4-bladed inducers with alternate leading edge cutback were examined with various amounts of cutback.

The length of the cavity has an important role on the onset of the unsteady cavitation patterns. The alternate blade cavitation in the inducer with equal length blades starts to appear when the cavity length at the tip approaches 65% of the spacing. As we decrease the cavitation number further, the length of shorter cavities first decrease and then increases. The rotating cavitation and the cavitation surge start to appear when the shorter cavities approach 65% of the spacing again. For inducers with alternate leading edge cutback, the range of alternate blade cavitation was shifted toward low cavitation number, and the asymmetric cavitation appeared at lower cavitation number. Therefore, the region of the rotating cavitation could be diminished by cutting back the leading edge alternately.

For the inducers with small amount of cutback, two types of alternate blade cavitation were observed as predicted theoretically. One of them is with longer cavities on longer blades, and the other is with longer cavities on shorter blades. Switch in these alternate blade cavitation patterns was observed with the increase or decrease of cavitation number. For the case with larger amount of the cutback, the cavities on longer blades are always larger than those on shorter blades. For the inducer with the largest amount of cutback in the present test, the rotating cavitation and cavitation surge were almost suppressed, with the enlargement of the range of alternate blade cavitation and asymmetric cavitation. However, the suction performance was deteriorated by them. We should also note here that: (a) the asymmetric cavitation occurs more easily in

the inducers with alternate leading edge cutback, and (b) the unevenness caused by the asymmetric cavitation could result in uneven blade stress and also synchronous shaft vibration.

Acknowledgments

The authors would like to express their sincere gratitude to Emeritus Prof. A. J. Acosta of Caltech, and Prof. K. Kamijo of Tohoku University who made many valuable suggestions and discussions. They would also like to thank Dr. P. Geai of SNECMA, Division SEP, the late Dr. M. Aoki of Ebara Research Co. LTD, and Mr. T. Kuwabara of NAC Inc. for their continued support and interest. The authors are also deeply grateful to Dr. Bruno Schiavello of Flowserve Pump Division for his extremely helpful and useful comments. Messrs. S. Azuma and T. Arifuku support in conducting the experimental work is also acknowledged. This study is partly supported by the Grand-in-Aid for Science Research of the Ministry of Education, Science, Sports, and Culture.

Nomenclature

C = chord length
D_t = inducer tip diameter
f = frequency of pressure fluctuations
f_n = shaft rotational frequency
h = tip blade spacing, or mean of the tip blade spacing $=(\mathrm{L0}+\mathrm{L1})/2$
l = cavity length at the tip
l_s = steady cavity length
L0 = angular distance at tip between the leading edge of longer blade and that of adjacent shorter blade (see Fig. 2)
L1 = angular distance at tip between the leading edge of shorter blade and that of adjacent longer blade (see Fig. 2)
n = rotational speed (rpm)
p_1 = pressure at inlet (see Fig. 1)
p_2 = pressure at outlet (see Fig. 1)
p_v = vapor pressure
Δp = pressure fluctuation (zero-to-peak)
r = radius
r_t = blade tip radius
s = radial tip clearance
u_t = peripheral speed of inducer tip $=\pi D_t f_n$
v_1 = axial velocity at inducer inlet = flow rate/inlet area
α = incidence angle, i.e., angle between the inlet relative velocity and the blade $=\beta_{t1}-\tan^{-1}(\phi)$
β = blade angle
β_t = tip blade angle (1-inlet, 2-outlet)
σ = cavitation number $=(p_1-p_v)/(\rho u_t^2/2)$
ρ = density
ϕ = flow coefficient $=v_1/u_t$
ϕ_d = design flow coefficient
ψ = head coefficient $=gH/(u_t^2)$ (g = gravity constant, H = head)
ψ_d = design head coefficient
ψ_s = static pressure rise coefficient $=(p_2-p_1)/(\rho u_t^2)$
ψ_{sd} = design static pressure rise coefficient
$\Delta\psi$ = coefficient of unsteady pressure fluctuations $=\Delta p/(\rho u_t^2)$ (zero-to-peak)
Ω = shaft angular velocity
Ω_R = rotating cavitation angular velocity

References

[1] Rosenmann, W., 1965, "Experimental Investigation of Hydrodynamically Induced Shaft Forces with a Three-Bladed Inducer," *Proceedings of the Symposium on Cavitation in Fluid Machinery*, ASME Winter Annual Meeting, pp. 172–195.
[2] Kamijo, K., Yoshida, M., and Tsujimoto, Y., 1993, "Hydraulic and Mechanical Performance of LE-7 LOX Pump Inducer," AIAA Journal of Propulsion and Power, **9**, No. 6, pp. 819–826.
[3] de Bernaldi, J., Joussellin, F., and Von Kaenel, A., 1993, "Experimental Analysis of Instabilities related to Cavitation in a Turbopump Inducer," *The First International Symposium on Pump Noise and Vibrations*, Clamart, France, pp. 1–9.
[4] Bordelon, W. J., Gaddis, S. W., and Nesman, T. E., 1995, "Cavitation Environment of the Alternate High Pressure Oxygen Turbopump Inducer," ASME FED-Vol. 210, pp. 39–46.
[5] Kamijo, K., Shimura, T., and Watanabe, M., 1977, "An Experimental Investigation of Cavitating Inducer Instability," ASME Paper 77-WA/FW-14.
[6] Tsujimoto, Y., Kamijo, K., and Yoshida, Y., 1993, "A Theoretical Analysis of Rotating Cavitation in Inducers," ASME J. Fluids Eng., **115**, No. 1, pp. 135–141.
[7] Goirand, B., Mertz, A-L., Joussellin, F., and Rebattet, C., 1992, "Experimental Investigations of Radial Loads Induced by Partial Cavitation with Liquid Hydrogen Inducer," IMechE, C453/056, pp. 263–269.
[8] Huang, J. D., Aoki, M., and Zhang, J. T., 1998, "Alternate Blade Cavitation on Inducer," JSME International Journal, Series B, **41**, No. 1, pp. 1–6.
[9] Acosta, A. J., 1958, "An Experimental Study of Cavitating Inducer," *Proceedings of the Second Symposium on Naval Hydrodynamics*, ONR/ACR-38, pp. 537–557.
[10] Iura, T., discussion in reference [9].
[11] Horiguchi, H., Watanabe, S., Tsujimoto, Y., and Aoki, M., 2000, "A Theoretical Analysis of Alternate Blade Cavitation in Inducers," ASME J. Fluids Eng., **122**, No. 1, pp. 156–163.
[12] Tsujimoto, Y., Yoshida, Y., Maekawa, Y., Watanabe, S., and Hashimoto, T., 1997, "Observations of Oscillating Cavitations of an Inducer," ASME J. Fluids Eng., **119**, No. 4, pp. 775–781.
[13] Watanabe, S., Sato, K., Tsujimoto, Y., and Kamijo, K., 1999, "Analysis of Rotating Cavitation in a Finite Pitch Cascade Using Closed Cavity Model and a Singularity Method," ASME J. Fluids Eng., **121**, No. 4, pp. 834–840.
[14] Acosta, A. J., 1955, "A note on Partial Cavitation of Flat Plate Hydrofoils," Caltech Hydro Lab. Report No. E-19.9.
[15] Horiguchi, H., Watanabe, S., and Tsujimoto, Y., 2000, "Theoretical Analysis of Cavitation in Inducers With Unequal Blades With Alternate Leading Edge Cutback, Parts I and II," ASME J. Fluids Eng., **122**, No. 2, pp. 412–418, 419–424.

Analysis of the Immediate Boundary Conditions of an Axial Flow Impeller

David A. Johnson
Department of Mechanical Engineering,
University of Waterloo,
Waterloo, Ontario, Canada N2L 3G1

The design and analysis of impellers for mixing applications such as stirred tank reactors (STR) have significant application in many engineering processes. In particular, the evaluation of the turbulent flow boundary conditions immediately around a model impeller has been examined using flow visualization, laser Doppler anemometry (LDA) and particle image velocimetry (PIV). Mean and fluctuating velocities are presented for all three velocity components. Good agreement between LDA and PIV measurements was obtained once an optimized PIV arrangement was defined. Turbulence parameters such as kinetic energy, dissipation, and length scales are estimated from the measurements. Several approaches to evaluating dissipation were used. Triggered PIV measurements were used to evaluate the variation in radial and tangential velocities in the entire planes above and below the impeller at constant axial distances. The size and orientation of the vortices shed from the impeller blade tips and the corresponding regions of high kinetic energy and dissipation indicate the importance of these structures in mixing.
[DOI: 10.1115/1.1412846]

1 Introduction

Engineering applications that require fluid mixing in a confined volume are widespread in the process industries and of significant importance considering energy consumption, mixing quality, dispersion, heat transfer, and reaction. Various methods to accomplish mixing exist and the use of an impeller driven by a rotating shaft to impart energy to the fluid are common. Varying impeller designs exist depending on many parameters such as the fluid(s) to be mixed and volume constraints. Many researchers have evaluated aspects of the impeller/tank arrangement considering the tank geometry and impeller placement (LaFontaine and Shepherd [1], Bittorf and Kresta [2], Hockey and Nouri [3], and many others). The focus here is in quantifying the immediate boundary conditions of the impeller for purposes of impeller performance predictions and as an aid in evaluating computational fluid dynamic (CFD) predictions of this region. Stoots and Calabrese [4] provide detailed mean velocity LDA measurements in the immediate exit region of a Rushton turbine although the instantaneous spatial structure of the vortices is unavailable due to the measurement technique. Discussion of the technique of simultaneous collection of all three velocity components for a Rushton turbine utilizing stereoscopic PIV is presented by Hill et al. [5]. The region in the immediate vicinity of the blade is also the region of trailing vortex formation due to blade passage and these results provide insight to turbulence generation and dissipation. Wu et al. [6] have found the only region of significant dissipation to be the impeller discharge stream in a Rushton turbine. Vortices provide a cyclical input of turbulent energy and account for most of the dispersion according to Ali et al. [7] and Chang et al. [8]. Evaluation of the flow field in this vicinity normally requires some assumptions about the turbulence in order to utilize experimental results. Rao and Broadkey [9] have found the discharge of an impeller to be highly anisotropic. Kresta and Wood [10] make an initial assumption that the flow is locally isotropic and discuss some conditions for this. A review of many approaches to characterizing turbulence and dissipation estimation is provided in Kresta [11].

Contributed by the Fluids Engineering Division for publication in the JOURNAL OF FLUIDS ENGINEERING. Manuscript received by the Fluids Engineering Division December 14, 2000; revised manuscript received August 8, 2001 Associate Editor: A. K. Prasad.

As the primary goal was to evaluate the flow region near the impeller, the far field conditions were not considered. The flow field was examined using flow visualization, laser Doppler anemometry (LDA), and particle image velocimetry (PIV). PIV measurements in an entire tank with resulting lower resolution of the 45 deg pitched blade turbine impeller region are reported in Sheng et al. [12]. A dimensionless group used to characterize the flow is the Reynolds number, $\mathrm{Re_D}$, which is based on the impeller diameter D, the fluid kinematic viscosity ν and the rotational speed of the impeller N ($\mathrm{Re_D}=ND^2/\nu$). In this study, typical values of Reynolds number are $O(10^5)$ depending on rotational speeds providing a fully turbulent flow in the region of the impeller.

2 Experimental Apparatus

A scaled 3 bladed hydrofoil impeller (Hayward Gordon 3AL-39) was utilized with a representative configuration as shown in Fig. 1. It was fabricated using the stereo lithography process and all blades were uniform in design with a blade angle of 39 deg to the horizontal at the hub with decreasing angle to the tip. Because of this manufacturing process the blades were comparatively thick (3 mm), all blade edges were sharp including the blade tips and the blade surfaces were comparatively rough. The outer diameter of the impeller D was 152.4 mm and all other dimensions are scaled from this dimension. The impeller blades are 0.375 D long due to the presence of the hub. The general geometry is detailed in Fig. 2. The unbaffled tank had a square cross section of 3.34 D that was primarily used to avoid optical distortion for the LDA equipment. The origin of the cylindrical coordinate system was the base of the impeller shaft with r and θ as the horizontal coordinates and y as positive upward from the origin. The impeller was mounted 1.0 D above the bottom of the tank. The impeller was driven with a 19 mm solid shaft connected to a variable speed DC motor drive at the top of the tank and no shaft deflection was measured. An optical trigger was mounted on the top of the shaft to provide a pulse output to determine rotational speed and to trigger events in the LDA and PIV equipment although both triggered and constant frequency PIV and LDA measurements were obtained. Water was used as the working fluid with a fixed free surface liquid level of 4D (1.2* tank base dimension) giving a total volume of 0.158 m^3.

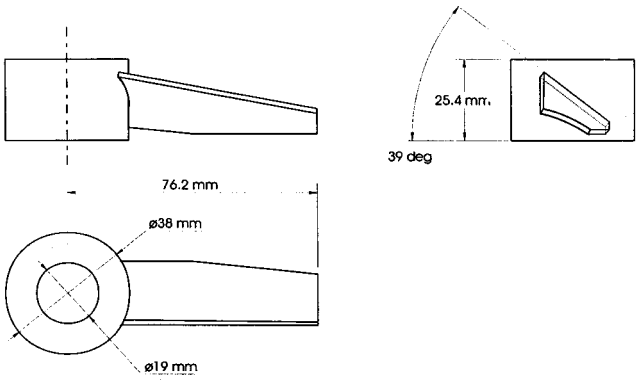

Fig. 1 Impeller configuration- one of three equally spaced blades shown

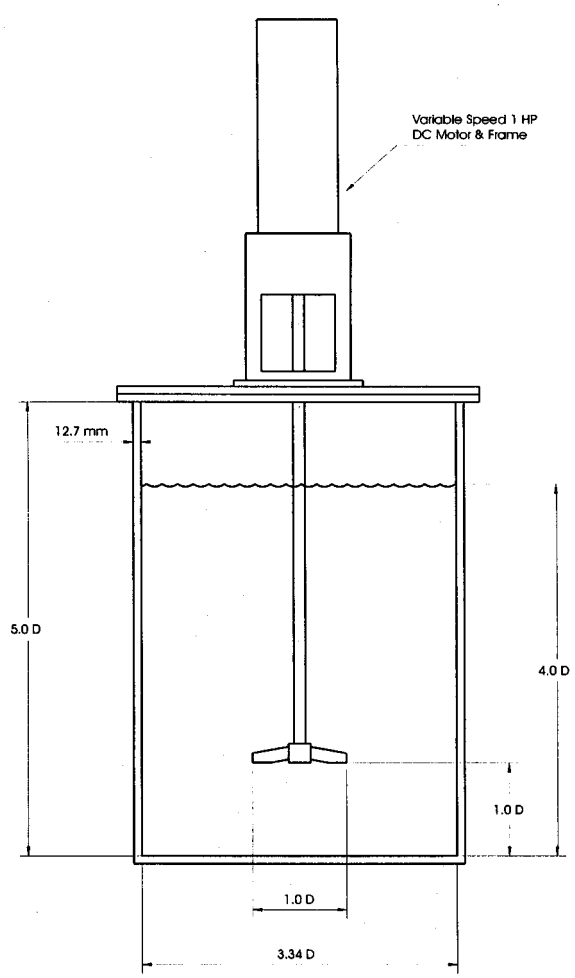

Fig. 2 Experimental configuration all dimensions referenced to the impeller diameter D (0.152 m)

2.1 Flow Visualization. Flow visualizations were undertaken using Fluorescein fluorescent dye and tracer particles with illumination provided by a 300 mW argon ion laser and optics to create a light sheet. Flow visualizations were recorded with a CCD video camera and still photographs were obtained with a 35 mm camera with 400 ASA film.

2.2 Laser Doppler Anemometry. The three velocity components of **V**, the radial, $\mathbf{V}_r$, tangential $\mathbf{V}_\theta$ and axial, $\mathbf{V}_y$ velocities were obtained at predetermined locations with spatial separation of 0.03D with a conventional laser Doppler anemometer operating in forward scatter mode. The system used in the experiments was a conventional two component LDA (Dantec 55X) consisting of a 300 mW argon ion laser, Bragg cell, beam expander, receiving optics and photomultipliers, and counters. In this configuration the measurement volume was approximately 1.100 mm long and 0.064 mm in diameter. Data from the counter processor were transferred to a computer for storage and subsequent analysis. For these measurements, the laser and LDA optics were mounted on a computer controlled three axis traversing stage. Calculations were done to accurately locate the measurement volume within the tank. For the LDA studies the working fluid was seeded with 1.1 μm diameter latex particles although tap water also provided a 10 kHz validated data rate signal. At each measurement location, 40,000 validated velocity measurements were obtained at constant frequencies in the range of 500–2000 Hz.

2.3 Particle Image Velocimetry. The flow through the impeller was illuminated using a double-cavity 120 mJ Nd:YAG laser capable of operating at 10 Hz with a pulse duration of 5 ns. Spherical shaped Pliolite VT particles of diameter ranges of 20–100 μm and specific gravity of 1.03 were used to seed the flow. A Kodak ES 1 K$\times$1 K CCD camera (1008$\times$1018 pixel array) equipped with an 18–108 mm, F/2.5 zoom lens was used to capture the particle images. A 532 nm optical notch filter was attached to the lens to transmit only the laser wavelength light. Numerous orientations of the camera were utilized depending on the region of interest. For example, the camera was positioned perpendicular to a vertical laser sheet or perpendicular to a horizontal light sheet through the use of a front surface mirror imaging from below the clear acrylic tank at 45 deg. In this way an unobstructed view of the $r-\theta$ plane was obtained. With the shaft mounted trigger, it was possible to obtain a large number of instantaneous data at the same circumferential position of the impeller.

Data Acquisition and Processing. The PIV facility was carefully set-up to minimize errors during the data acquisition and processing stages. A measured quantity of the Pliolite VT particles was added to the reservoir tank to ensure a minimum seed particle density of at least 8 particles per interrogation area ($\sim$0.002 grams/liter). A field-of-view of approximately 100$\times$100 mm was used with scaling in the range of 0.09 mm/pixel. The laser pulse delay timing was set with an upper bound of the one-quarter displacement rule for the different image sizes and rotational speeds utilized and was approximately 0.8–1.8 ms for all images. Pulse timing was also decreased to reduce loss of particles due to out of plane motion particularly in the $r-\theta$ plane. 1000 image pairs were acquired at each location for each rotational speed. Due to its thickness ($\sim$2–3 mm), the laser light sheet creates a larger control volume than the comparison LDA probe volume.

The cross-correlation method with interrogation area of 32 $\times$32 pixels and 50% overlap was used to process the images to obtain the velocity vectors resulting in 62$\times$62 vectors per vector map. The Pliolite VT particles gave a good signal-to-noise ratio and the number of outliers was about 1.5%. Therefore only peak validation with a correlation peak signal-to-noise ratio of 1.5 was performed to remove vectors. Individual vector maps were subsequently averaged to provide an averaged flow map and velocity statistics.

2.4 Experimental Uncertainty. For the method used to calculate the $\mathrm{Re_D}$ reported values are $\pm$3% ($\mathrm{Re_D}=77{,}000\pm2160$) using the root sum square method. Variation in the impeller speed is estimated at $\pm$2 rpm. For the LDA measurements at each location 40,000 individual validated velocities were used to calculate the average velocity value giving a random error below 0.5% (Pereira and Sousa, [13]). Velocity measurements made using the laser Doppler anemometer are subject to errors in the location of the probe volume, gradient broadening, and electronic noise giving an uncertainty of less than 2% for averaged velocities

(Johnson, [14]). For the PIV measurements the particles cover approximately six pixels and therefore meet the minimum criterion for centroid location. Random error due to irregular particles, electronic noise, etc. is shown to be small (<0.1 pixel) by Prasad et al. [15] using larger particles and electronic timing errors are estimated to be small. These errors provide an error estimate of less than ± 1 pixel giving a positional error of less than 1%. These values (sub pixel positional accuracy and correspondingly small velocity errors) are in good agreement with Guezennec and Kiritsis [16]. The errors inherent in PIV velocity measurements are estimated to be of the order of 2% (Westerweel [17]).

3 Results and Discussion

3.1 Velocity Measurements. Comparative measurements of average radial V_r and axial V_y velocity obtained with the LDA system and the PIV system are shown in Fig. 3 for $\mathrm{Re_D}=77{,}400$ ($\mathrm{N}=200$ rpm) case. The presented velocities are average velocities taken from untriggered constant frequency LDA (40,000 velocity measurements) and untriggered PIV (1000 image pairs) measurements. All velocities are made dimensionless (*) with the impeller tip speed V_{tip}. The comparative ''control volume'' measurements are obtained from the boundary surrounding the impeller including: a horizontal plane above the impeller parallel to the impeller hub surface for the inlet condition (*inlet* plane), a horizontal plane 0.083D below the impeller parallel to the impeller hub surface for the outlet condition (*outlet* plane) and a cylindrical surface 0.083D from the impeller tip in a vertical plane for the radial velocities (*radial* plane) enclosing the impeller volume. The agreement between the measurement methods is excellent although less than 1000 PIV image pairs gave significantly poorer comparison. The inlet profile shows high velocities near the impeller hub with a peak value of $0.14V_y^*$. The axial exit velocity profile shows a slight upward flow near the impeller hub indicating a region of recirculation directly below the hub. The peak measured average exit axial velocity along this plane is $0.26V_y^*$ occurring at $R^*=0.32$. This value is in good agreement with the results reported by Zhou and Kresta [18] for a fluidfoil turbine (A310) with a much different tank geometry (baffled cylindrical tank with sealed lid) and a tank diameter of 2.1 D suggesting that measurements made close to the impeller may be independent of tank geometry for some cases. The region at $R^*>0.46$ contributes little to the dominant axial flow. The radial velocity profile shows a net flow toward the impeller blade although peak values are low ($V_r^*\sim 0.04$). At the other rotational speeds $\mathrm{Re_D}=155{,}000$ and 232,000 (400 and 600 rpm) very little difference was observed in the dimensionless plots indicative of a fully turbulent flow regime. No appreciable deformation of the tank free surface occurred at these rotational speeds.

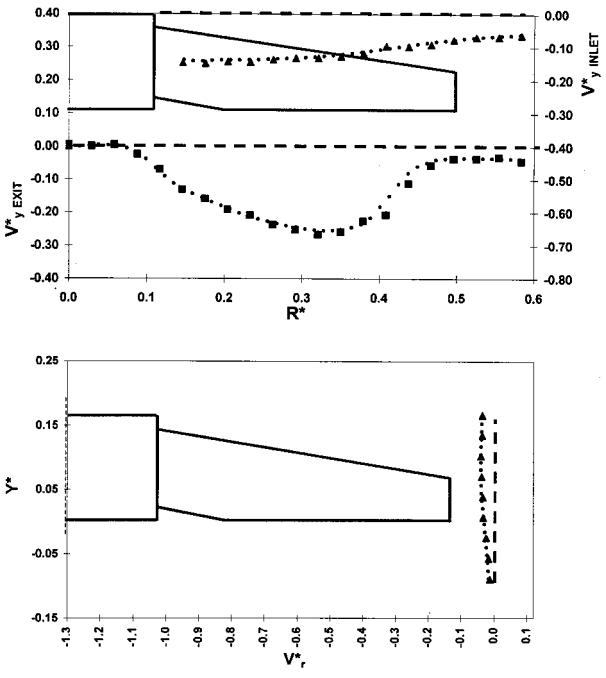

Fig. 3 Average velocities V_r^* and V_y^* in control volume $\mathrm{Re_D}=77{,}000$ ▲LDA measurements ● PIV measurements dashed line indicates location of measurements. Blade schematic included for reference.

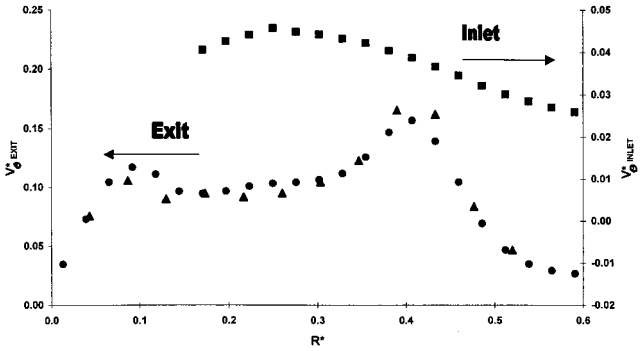

Fig. 4 Average tangential velocities vs R*, V_θ^* inlet at $Y^*=0.167$ (■ PIV-inlet) and exit at $Y^*=-0.083$ (▲ LDA measurements ● PIV measurements), $\mathrm{Re_D}=77{,}000$

Comparative measurements of the average untriggered tangential V_θ obtained with the LDA system and the PIV system are shown in Fig. 4 for $\mathrm{Re_D}=77{,}400$ ($\mathrm{N}=200$ rpm). Measurements were obtained in the same *inlet* plane and *exit* plane as described in the above measurements. LDA measurements were not obtained above the impeller due to the impeller shaft obscuring the forward scatter LDA arrangement. The PIV measurements indicate a swirling inlet flow condition where the tangential velocity V_θ is about 25% of the average axial inlet flow V_y. Peak values of V_θ^* of 0.046 are found at $R^*=0.25$ with decreasing values as R^* increases. These measured values are consistent with flow visualization results that indicated a swirling motion as the impeller intake was approached. Results obtained below the impeller indicate that the two measurement techniques give comparable results. As observed during flow visualization a swirling recirculating area exists directly below the hub extending to the edge of the hub region ($R^*=0.125$). After this region V_θ^* increases slightly to $R^*=0.3$ where a rapid increase in V_θ^* occurs peaking at $R^*=0.41$ after which it decays rapidly. This peak corresponds to a peak in the v_y^* rms velocity. These tangential values are not in significant and are about 40% of the average axial flow values which would be expected in an impeller with a relatively small blade pitch angle. These results are consistent with the blade angle effects found by Ranade and Joshi [19].

3.2 Conservation of Mass. As a test of the validity of the measurement results, the inflow/outflow through the control volume boundaries described above was undertaken. The individual location LDA and PIV measurements were piecewise integrated over the entire control surfaces. The net inflow through the *inlet* control surface amounted to 81.6% of the outflow and the remaining inflow crossed the control volume through the *radial* surface. The measured inflow was 3.5% greater than the measured outflow likely due to measurement uncertainty and the integration method utilized.

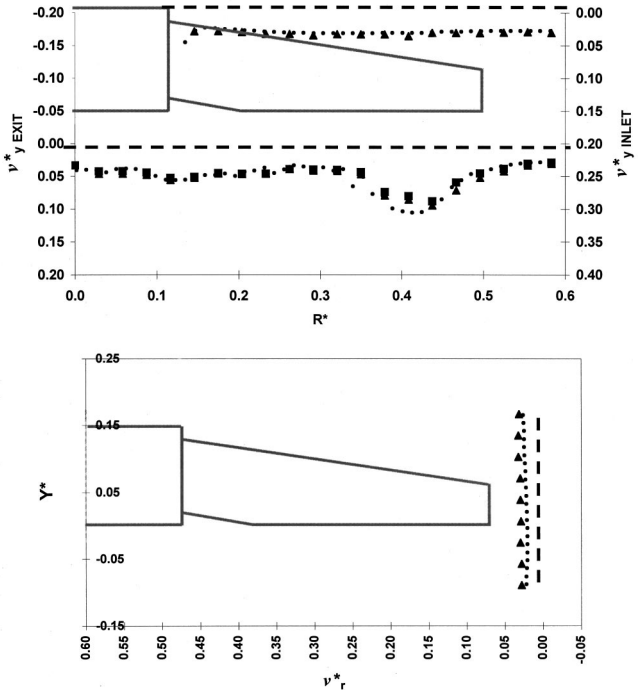

Fig. 5 RMS velocities ν_r^* and ν_y^* in control volume Re_D =77,000 ▲ LDA measurements ● PIV measurements Dashed line indicates location of measurements. Blade schematic included for reference.

3.3 Flow Number. Integrated values of the axial velocity profile below the impeller provided the primary flow number as defined by:

$$N_Q = \frac{\int_0^R V_y 2\pi r dr}{ND^3} \tag{1}$$

A N_Q value of 0.39 was obtained at 200 rpm with a slight increase in N_Q with N. These values are about 12% lower than those found in commercial impellers of the same design likely predominantly due to a large nonpumping hub region (0.25D) and the thick leading and trailing edges, and the rougher surface finish on the lithography prototype.

3.4 Turbulent Velocities and Kinetic Energy. RMS velocities from the LDA and PIV measurements are presented in Fig. 5 in the same arrangement as the average velocities and are made dimensionless (*) with the impeller tip speed V_{tip}. RMS velocities ($\sqrt{\overline{v_r^2}}$, square root of the average of the sum of the squares) are denoted in lower case v_r. The rms velocities presented from untriggered data collection are unfiltered for any frequency and therefore include the effects of blade passage frequencies. There is some discussion in Kresta [11] of the inclusion or exclusion of the effects of blade passage frequency in reporting results. When the axial velocity data is filtered to remove the blade passage frequency the average exit rms velocities for all R^* values drop by 5.8% with one peak rms value 17.1% lower at $R^*=0.467$ suggesting the effect for this impeller is not as pronounced as would be for a Rushton turbine. As expected, the axial inlet rms v_y^* velocities are low and fairly uniform across the entire horizontal plane with values near 0.03. The measured radial rms v_r^* velocities are also uniform and of the same order of magnitude as the axial inlet values. The axial exit rms velocities v_y^* show a minimum rms velocity corresponding to the peak average exit velocity at $R^*=0.32$ and there is a significant distortion of the profile at R^* values greater than this up to the tip of the impeller

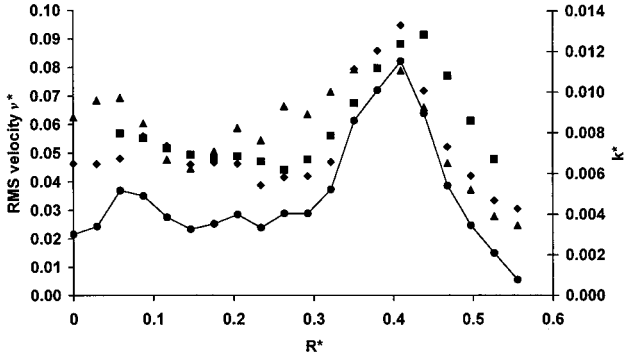

Fig. 6 RMS velocity components (−) vs R* at Y*=−0.083 (▲ ν_r^*, ■ ν_θ^* and ◆ ν_y^* and kinetic energy k* ●) Re_D=77,000

blades. A peak axial rms velocity v_y^* of 0.10 occurs at $R^*=0.42$. This is indicative of high velocity variation in this region which is due to more than blade passage effects and is discussed in a subsequent section.

The exit plane turbulent kinetic energy was calculated using measured turbulent velocity data and from:

$$k^* = \frac{v_r^2 + v_\theta^2 + v_y^2}{2V_{tip}^2} \tag{2}$$

It can be seen in Fig. 6 that all rms velocity components are of approximately the same magnitude with values ranging from 4−10% of the tip speed. Wu and Patterson [20] have also found the magnitude of the rms velocities to be similar in all component directions in a different impeller geometry. As a result of the similarity of rms profiles, the k^* profile mirrors these profiles with a peak value of 0.0115 at $R^*=0.41$. The magnitude of this averaged value is consistent with work from other impeller geometries (Yianneskis et al. [21]). At this peak value the relative turbulence intensity defined by

$$I = \frac{v_y}{V_y} \tag{3}$$

is significant at 29%. I values increase to 60% with increasing R^* ($0.41<R^*<0.55$) due to the low axial mean V_y values in this region. For $0.14<R^*<0.41$ values are around 12% and values below the hub are small (1%).

Reynolds stresses $\overline{v_r v_y}$ and $\overline{v_\theta v_y}$ were measured directly with the two component LDA system. These values are shown in Fig. 7 and indicate a change in sign in the region of the vortex shedding

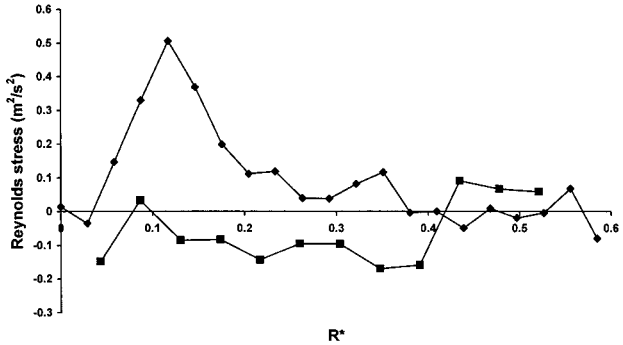

Fig. 7 Measured Reynolds stresses (m^2/s^2) versus R* at Y* =−0.083 Re_D=77,000 (◆ $\overline{v_r v_y}$ and ■ $\overline{v_\theta v_y}$)

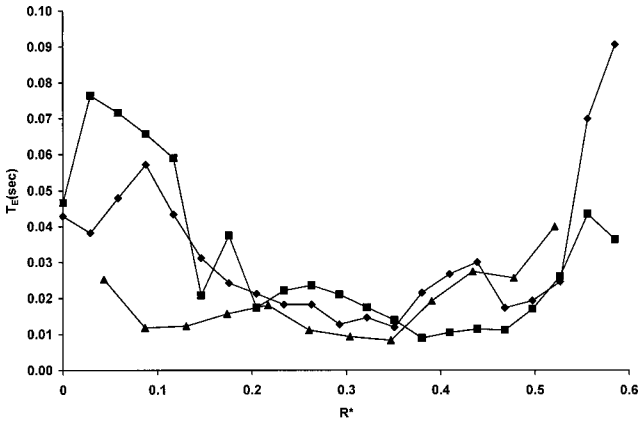

Fig. 8 Integral time scales (s) in r, θ, y directions versus R* at Y*=−0.083 Re_D=77,000 (■ radial, ▲ tangential, ♦ axial)

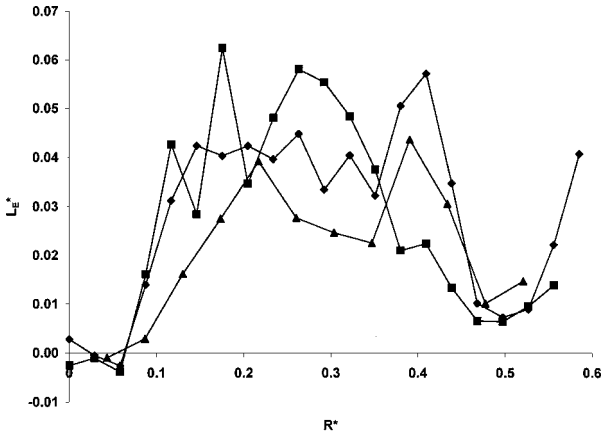

Fig. 9 Integral length scales (−) in r, θ, y directions versus R* at Y*=−0.083 Re_D=77,000 (■ radial, ▲ tangential, ♦ axial)

($R^*=0.41$). These values are somewhat higher than other reported results for a different impeller [10] obtained in an indirect manner.

3.5 Turbulent Scales. The integral time scale T_E was calculated from the LDA data based on the autocorrelation coefficients R_{ii} and is defined as

$$T_E=\int_0^{\tau} R_{ii}(\tau)\,d\tau \tag{4}$$

where integration up to $\tau=0.1$ s is used. Integration of the autocorrelation was performed using the trapezoid rule or Simpsons rule which gave comparable results. Use of this equation implies isotropic turbulence and due to the high turbulence intensities in some flow regions may not be applicable although this approach is widely used in nonisotropic flow conditions [9]. Values of the integral time scale were comparable in all three measured velocity components as shown in Fig. 8. Integral length scales L_E are calculated from the integral time scales and the mean flow velocity based on Taylors frozen hypothesis which assumes that the turbulent structure is fixed in space and is convected by the mean velocity. This would only be justified for homogeneous isotropic turbulence. Normally, the dominant mean velocity would be used but several corrections have been proposed for three-dimensional, high turbulence intensity flows such as the use of a convection velocity V_c (van Doorn as cited in [10])

$$V_c^2=V_y^2+v_y^2+2v_r^2+2v_\theta^2 \tag{5}$$

This correction does not apply over the entire exit plane due to the low turbulence levels below the hub. The determined length scales using the mean axial velocity are in the range of 0.04–0.05 D with peak values at 0.06D (Fig. 9) and should be indicative of the scale of the larger energy containing eddies. Large scale structures shed from the passing blade surfaces as captured using the PIV data (discussed below) are the same order of magnitude (~0.05 D). Application of the convection velocity V_c in the determination of the integral length scale increases the integral length scale by 33% at $R^*=0.41$ although other values from $0.14<R^*<0.38$ are increased by an average of 14% preserving the order of magnitude.

The Taylor microscales λ_f for time were determined from

$$\lambda_f=\sqrt{\frac{-2}{\left.\dfrac{\partial^2 R_{ii}}{\partial\tau^2}\right|_{\tau=0}}} \tag{6}$$

The second derivative of the autocorrelation was evaluated at $\tau=0$ with a fourth-order central difference formula. These microscales for time are shown in Fig. 10 and indicate the time scale of an average energy containing eddy. Micro-length scales λ_g^* are formed using the Taylor time scales and the mean velocity and are made dimensionless with the impeller diameter D (Fig. 11). These length scales in all measured directions are the same order of magnitude (0.005–0.010) with the axial micro-length scale being

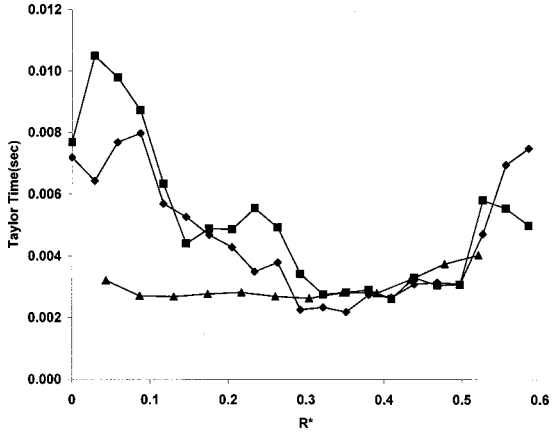

Fig. 10 Taylor time scales (s) in r, θ, y directions versus R* at Y*=−0.083 Re_D=77,000 (■ radial, ▲ tangential, ♦ axial)

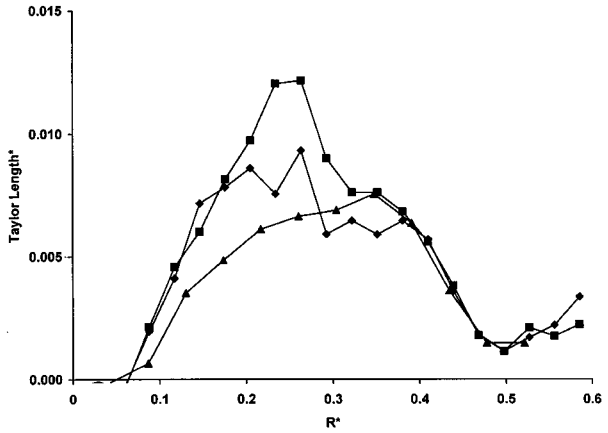

Fig. 11 Taylor length scales (−) in r, θ, y directions versus R* at Y*=−0.083 Re_D=77,000 (■ radial, ▲ tangential, ♦ axial)

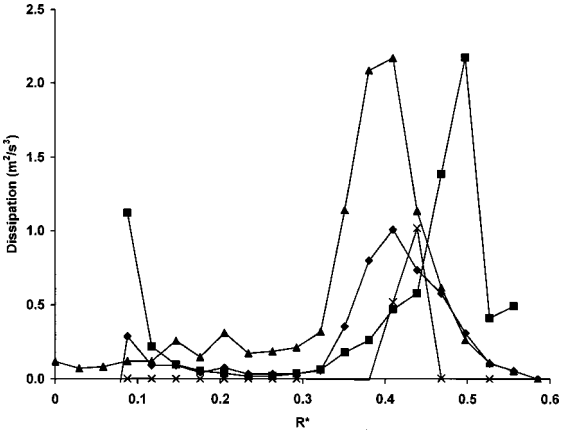

Fig. 12 Dissipation ϵ (m^2/s^3) versus R* at Y*=−0.083 Re_D =77,000 utilizing four methods (■ Eq. (8), ♦ Eq. (9), ▲ Eq. (10), x equation (11))

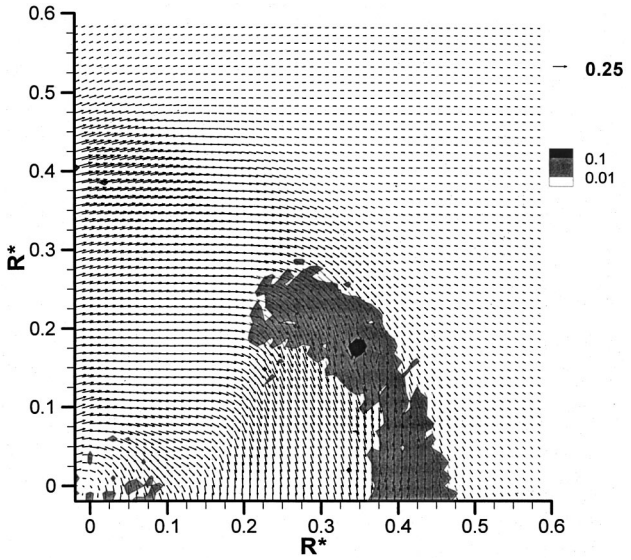

Fig. 13 Dimensionless averaged velocities and contours of k_2^*, r−θ plane at Y*=−0.083 (looking in +y direction) blade located at vertical R* axis rotating counterclockwise triggered PIV data Re_D=77,000 dimensionless reference vector 0.25

1.6 times larger than the other components in the worst case. The similarity of these micro-scales is an indication that the flow may be locally isotropic. The integral scales are approximately an order of magnitude greater than the microscales.

The turbulent Reynolds number as defined by

$$\mathrm{Re}_{\lambda_g} = \frac{k^{1/2}\lambda_g}{\nu} \tag{7}$$

(Hinze [22]) indicates the existence of an equilibrium range in the intermediate scales for $\mathrm{Re}_\lambda > 100$. Re_λ was found to be greater than 100 for the region $0.146 < R^* < 0.44$. In the region past the impeller tip and below the hub Re_λ was found to be small as expected.

3.6 Dissipation. Several methods of evaluating the dissipation ε have been implemented including

$$\varepsilon = 15\nu \frac{v_y}{\lambda_g^2} \tag{8}$$

[22] or the dimensional approach where

$$\varepsilon = A \frac{v_y^3}{L_E} \tag{9}$$

where A is a constant near unity and L_E represents the integral length scale or possibly the scale of the structures created by the impeller. This dimension is the approximate dimension of the trailing vortices shed following the blade passage as discussed in a subsequent section. The use of Eq. (8) is compared to the available dissipation terms measured with two dimensional PIV in Sharp et al. [23] and is found to provide comparable results for studies of a Rushton turbine operating at a comparably low Re.

Another approach is to use the integral time scales determined from the autocorrelation to evaluate the dissipation ε where

$$\varepsilon = \frac{v_y^2}{T_E} \tag{10}$$

The gradient hypothesis was also used to determine the dissipation. It is based on assumptions inherent in the $k-\varepsilon$ turbulence model and has the form

$$\varepsilon = -\frac{0.09k^2}{\overline{v_r v_y}} \frac{\partial V_y}{\partial r} \tag{11}$$

for this analysis [21]. All approaches are shown in Fig. 12 with each method revealing the only location of significant dissipation to be in the region of $R^* = 0.4$. Peak dissipation values of 1–2 m^2/s^3 are consistent with [10] at this distance from the impeller. For comparison, an average energy dissipation rate throughout the tank may be calculated based on the power draw per unit mass [4]. The electrical power draw was measured and found to give unreliable results. The power draw was estimated using a value of the power number N_p

$$N_p = \frac{P}{\rho N^3 D^5} \tag{12}$$

of 0.305 obtained from Jaworski et al. [24] for a common hydrofoil impeller over a wide range of Re. This gives an average energy dissipation rate throughout the tank $\varepsilon_{\mathrm{avg}}$ of 0.006 m^2/s^3, two orders of magnitude below these peak values.

A comparison technique using the measured angular velocity values to determine the power and the resulting power number from the angular momentum balance (moment of momentum equation) using the power equation

$$P = \omega \int_0^R r V_\theta d\dot{m} = 2\pi\omega\rho \int_0^R r V_\theta V_z r dr \tag{13}$$

gave values of $P = 1.00\ \mathrm{kg\,m^2\,s^{-3}}$ at the outlet of the control volume and $P = 0.20\ \mathrm{kg\,m^2\,s^{-3}}$ on the inlet control surface and a power number N_p of 0.26 which is comparable to the reported value obtained by measuring the power draw.

3.7 Spectral Analysis. The equal time interval velocity samples obtained with the LDA were analyzed using Fast Fourier Transform (FFT) spectral analysis to obtain the frequencies present. As expected, the blade passage frequency is the dominant frequency in the spectrum with several harmonics evident. There was no evidence of any low frequency ''global tank circulation'' frequencies found by previous researchers [25] although the close proximity of these measurements to the impeller may preclude the appearance of those frequencies.

3.8 Triggered Measurements. To further insight into turbulence parameters such as kinetic energy and dissipation distribution data was collected with the PIV equipment in a triggered mode utilizing the shaft mounted optical trigger such that each successive image pair was collected at the same impeller position.

3.9 Triggered Kinetic Energy. Figure 13 shows the triggered PIV results obtained in the horizontal *exit* $r\theta$ plane 0.083D

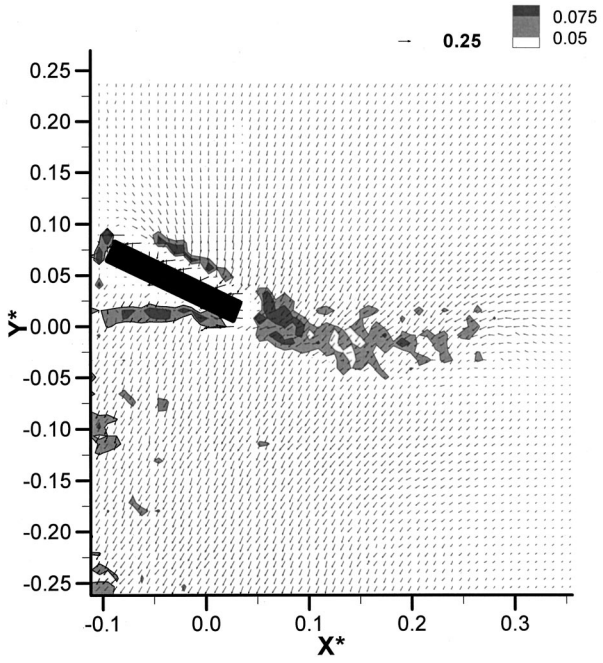

Fig. 14 Dimensionless averaged velocities and contours of k_2^* x−y plane at R*=0.41 blade moving to the left of figure triggered PIV data Re_D=77,000 dimensionless reference vector 0.25

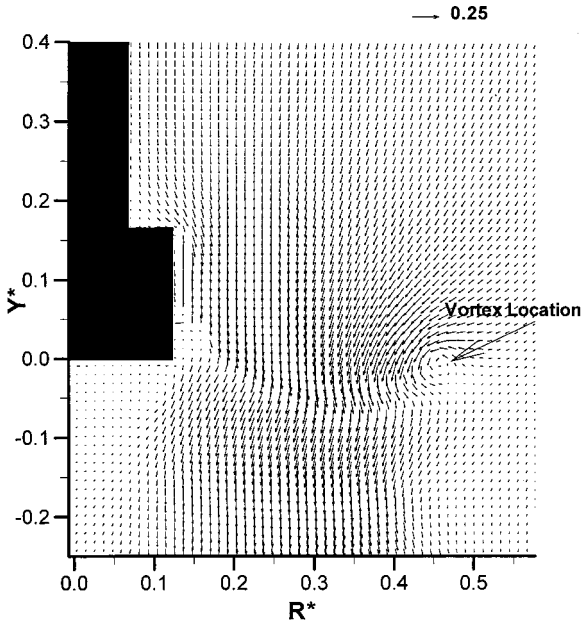

Fig. 15 Dimensionless averaged velocities r−y plane at θ =30° after blade passage (blade moving out of page) triggered PIV data Re_D=77,000 Dimensionless reference vector 0.25

below the impeller looking in the positive y direction. The two measured in-plane rms velocity components (v_r^*, v_θ^*) are represented in this figure forming k_2^* defined similarly to k^* but utilizing only the two measured components, previous results indicate that all rms velocities are the same order of magnitude and therefore total k values should be 50% greater if this assumption is applied. In this configuration one impeller blade is oriented with the positive vertical axis and is rotating counterclockwise. In this plane, below the impeller, the effects of the blade passage are not seen until approximately 41 deg after the blade using the k_2^* contours as a guide. As the contours indicate, the kinetic energy is highly localized, concentrated in a band $0.34 < R^* < 0.48$ with a peak value of k_2^* is 0.155 which occurs at $(R^*, \theta) = (0.389, 63 \text{ deg})$ where θ is measured clockwise from the blade tip. This value is greater than an order of magnitude from the average k^* value presented in Fig. 6 and is consistent with results in [21] for a disk type impeller. This is significant as all the values in the lower contour band of $k_2^* = 0.01$ exceed the total average k^* value found in the untriggered average values shown in Fig. 6. Values outside of this band are low contributing to the lower overall average. Thus, circumferentially averaged values significantly underpredict the level of kinetic energy in the trailing vortex stream.

3.10 Vortex Generation and Location. As a single impeller blade passes through the fluid a pressure differential is created between the pressure side surface upstream and the suction side (back of blade) downstream of the blade. In the case of the open impeller (unshrouded, unconfined) discussed here the pressure differential equalizes through velocity fluctuations once the blade has passed. Evidence of the equalization characterized by flow into the region of the suction side over the pressure side blade surface is shown in Fig. 14. This figure is a planar vertical **xy** image passing through the impeller blade located at $R^* = 0.41$. The light sheet entered the plane from downstream of the blade thus information directly below the blade (in shadow) is less reliable. Only 100 images were averaged to present this data as more images than this removed the detail of the flow trailing the blade. Due to the error associated with obtaining reliable data in areas close to solid surfaces it is difficult to determine if separation on the upper surface of the blade has occurred although k_2^* values are high there (0.107 at (0.003, 0.057)). The peak value of k_2^* is 0.150 which occurs at (0.052, 0.008) in the trailing vortex region corresponding well with the value 0.155 obtained in the $r-\theta$ plane discussed above. There is evidence of significant flow distortion over the top surface of the blunt leading edge. Downstream of the blade there is a wide wake following the blade with an approximate length of two blade chord lengths. In the $r-y$ plane the planar PIV images were indispensable in revealing the existence of a stable vortex trailing the blade passage. Figure 15 shows the average of 1000 triggered PIV image pairs in the $r-y$ plane taken at a constant angular position 30 deg after a blade passage (blades are coming out of the page). It can be seen that this trailing vortex is not in a random location but the center is consistently located at $(R^*, Y^*) = (0.46, -0.009)$ and rotating counterclockwise for all 1000 image realizations. This location is further radially inward than the mean velocity values would suggest indicating the convective radial inflow effects of the wake following the blade passage. In this same plane the remains of the vortex shed from the previous blade passage 150 deg ahead of the image plane is located at $(R^*, Y^*) = (0.42, -0.164)$ and is consistent with the measured mean axial and radial velocities. A vortex (helix) angle γ measured from the horizontal blade position of 13.1 deg was found for the vortex close to the impeller and 12.0 deg for the decaying vortex. This would indicate that the vortex loses some axial velocity further from the impeller although there is more uncertainty in defining the center of the vortex in this location. These values are consistent with the constant vortex angle of 20 deg found in Schäfer et al. [26] for $Re_D = 7300$ and angles of 18–13 deg for $Re_D = 115{,}000$ to 240,000 found in [7] for 45 deg pitched blade turbines. The correlation provided in [26] overpredicts the vortex angle by 40% likely due to the smaller impeller blade angle in this geometry. The corresponding plot of k_2^* is shown in Fig. 16 indicating a similar zone of high kinetic energy in the region of the shed vortex.

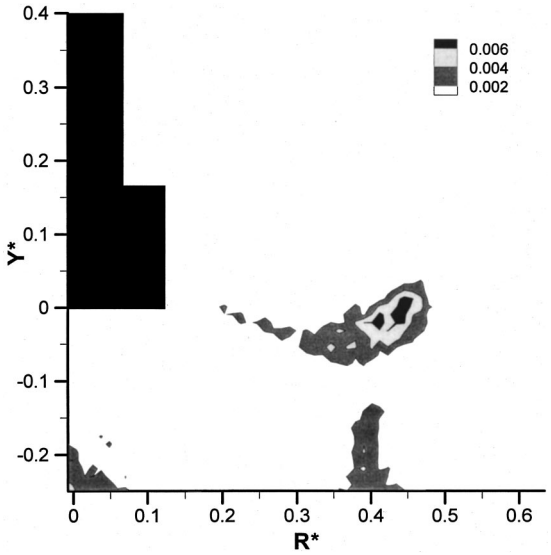

Fig. 16 Contours of k_2^* r−y plane at $\theta=30°$ after blade passage (blade moving out of page) triggered PIV data $Re_D=77{,}000$

4 Conclusions

Detailed measurements of the immediate boundary conditions of a hydrofoil impeller have been obtained for an impeller not previously reported in the literature. All three velocity components have been obtained to provide a complete profile of the flow around the impeller. Utilizing both LDA and PIV techniques agreement in the measured mean velocities is very good for all velocity components. Filtering of the blade passage frequency from the axial LDA data reduced rms velocities by an average of 5.8%. Peak velocities and the shape of the axial velocity profile were found to be in good agreement with other hydrofoil impellers obtained in baffled cylindrical tanks suggesting little influence of tank geometry close to the impeller. Measurements of the tangential velocities above and below the impeller reported here show the importance of this velocity component and the circumferential variation of this velocity. Measured rms velocities and integral time scales in all coordinate directions were found to be similar. Several approaches to determining the integral length scales from the time scales gave comparable results. Predicted macroscales of turbulence such as the integral length scales are in good agreement with previous studies. Microscales for time and length were similar in all directions indicating the flow may be locally isotropic. Several methods of estimating the local dissipation showed only one specific region below the impeller to have significant dissipation. The formation of the vortex is evidenced through a pressure differential creating an inflow condition following the blade passage. High kinetic energy and dissipation levels indicating the primary location of fluid mixing are found only in the region of the trailing vortex with significant blade related cyclical variation. The peak kinetic energy value obtained with triggered measurements was an order of magnitude greater than a circumferentially averaged value showing the importance of the local flow condition. Triggered measurements have shown the creation of a trailing vortex over the blade surfaces and a large scale vortical structure shed from the impeller blade surface and the dimensions and consistent location of these vortices shed from the impeller which are in qualitative agreement with measurements of pitched blade turbines.

Acknowledgments

The author gratefully acknowledges the support of this research through grants from the Natural Sciences and Engineering Research Council of Canada (NSERC) and equipment provided by Hayward Gordon Ltd and assistance with the data collection from Barry Phillips.

Nomenclature

D = impeller diameter (m)
I = relative turbulence intensity (Eq. (3))
k = turbulent kinetic energy (m^2/s^2)
k^* = dimensionless turbulent kinetic energy (Eq. (2))
L_E = integral length scale of turbulence (m)
$\dot{m}$ = mass flow rate (kg/s)
N = rotational speed of impeller (rpm)
N_p = Power number $P/(\rho N^3 D^5)$ (Eq. (12))
N_q = Flow number $Q/(ND^3)$ (Eq. (1))
P = Power transferred to fluid (kg $m^2 s^{-3}$)
r = radial coordinate (m)
R = radius of impeller (m)
R^* = dimensionless radial distance (r/D)
R_{ii} = autocorrelation coefficients
Re_D = Reynolds number ($Re_D = ND^2/\nu$)
Re_λ = turbulent Reynolds number (Eq. (7))
rms = root mean square of turbulent velocity fluctuations (m/s)
T_E = integral time scale of turbulence (s) (Eq. (4))
V = average velocity (m/s)
$\mathbf{V}$ = velocity (m/s)
v = rms velocity (m/s)
V^* = velocity made dimensionless with tip speed (V/V_{tip})
V_{tip} = tip speed of impeller (m/s)
V_c = convection velocity (m/s) (Eq. (5))
x = coordinate (m)
X^* = x/D
y = axial coordinate (m)
Y^* = y/D
γ = vortex angular location from blade position (helix angle) (deg)
ε = dissipation rate/unit mass (Eqs. (8)–(11)) (m^2/s)
θ = angular coordinate
λ = turbulence microscale (Eq. (6))
λ^* = λ/D
μ = dynamic viscosity (kg/ms)
ν = kinematic viscosity (m^2/s)
ρ = fluid density (kg/m^3)
τ = integral time
ω = rotational speed of impeller (rad/s)

References

[1] LaFontaine, R. F., and Shepherd, I. C., 1996, "Particle Image Velocimetry Applied to a Stirred Vessel," Exp. Therm. Fluid Sci., **12**, pp. 256–264.
[2] Bittorf, K. J., and Kresta, S. M., 2000, "Active Volume of Mean Circulation for Stirred Tanks Agitated with Axial Impellers," Chem. Eng. Sci., **55**, pp. 1325–1335.
[3] Hockey, R. M., and Nouri, J. M., 1996, "Turbulent Flow in a Baffled Vessel Stirred by a 60° Pitched Blade Impeller," Chem. Eng. Sci., **51**, pp. 4405–4421.
[4] Stoots, C. M., and Calabrese, R. V., 1995, "Mean Velocity Field Relative to a Rushton Turbine Blade," AIChE J., **41**, pp. 1–11.
[5] Hill, D. F., Sharp, K. V., and Adrian, R. J., 2000, "Stereoscopic Particle Image Velocimetry Measurements of the Flow Around a Rushton Turbine," Exp. Fluids, **29**, pp. 478–485.
[6] Wu, H., Patterson, G. K., and vanDoorn, M., 1989, "Distribution of Turbulence Energy Dissipation Rates in a Rushton Turbine Stirred Mixer," Exp. Fluids, **8**, pp. 153–160.
[7] Ali, A. M., Yuan, H., Dickey, D., and Tatterson, G. B., 1981, "Liquid Dispersion Mechanisms in Agitated Tanks: Part I. Pitched Blade Turbine," Chem. Eng. Comm., **10**, pp. 205–214.
[8] Chang, T. P. K., Sheu, Y. H. E., Tatterson, G. B., and Dickey, D. S., 1981, "Liquid Dispersion Mechanisms in Agitated Tanks: Part II. Straight Blades and Disc Style Turbines," Chem. Eng. Comm., **10**, pp. 215–222.
[9] Rao, M. A., and Broadkey, R. S., 1972, "Continuous Flow Stirred Tank Turbulence Parameters in the Impeller Stream," Chem. Eng. Sci., **27**, pp. 137–156.
[10] Kresta, S. M., and Wood, P. E., 1993, "The Flow Field Produced by a Pitched Blade Turbine: Characterization of the Turbulence and Estimation of the Dissipation Rate," Chem. Eng. Sci., **48**, pp. 1761–1774.

[11] Kresta, S. M., 1998, ''Turbulence in Stirred Tanks: Anisotropic, Approximate, and Applied,'' Can. J. Chem. Eng., **76**, pp. 563–576.
[12] Sheng, J., Meng, H., and Fox, R. O., 1998, ''Validation of CFD Simulations of a Stirred Tank Using Particle Image Velocimetry Data,'' Can. J. Chem. Eng., **76**, pp. 611–625.
[13] Pereira, J. C. F., and Sousa, J. M. M., 1995, ''Experimental and Numerical Investigation of Flow Oscillations in a Rectangular Cavity,'' ASME J. Fluids Eng., **117**, pp. 68–74.
[14] Johnson, D. A., 1988, ''*An Experimental and Numerical Investigation of Turbulent Recirculating Flow Within a Cavity With an Inlet Wall Jet,*'' M. Eng. thesis, McMaster University, Hamilton, Canada.
[15] Prasad, A. K., Adrian, R. J., Landreth, C. C., and Offutt, P. W., 1992, ''Effect of Resolution on the Speed and Accuracy of Particle Image Velocimetry Interrogation,'' Exp. Fluids, **13**, pp. 105–116.
[16] Guezennec, Y. G., and Kiritsis, N., 1990, ''Statistical Investigation of Errors in Particle Image Velocimetry,'' Exp. Fluids, **10**, pp. 138–146.
[17] Westerweel, J., 1997, ''Fundamentals of Digital Particle Image Velocimetry,'' Meas. Sci. Technol., **8**, pp. 1379–1392.
[18] Zhou, G., and Kresta, S. M., 1996, ''Distribution of Energy Between Convective and Turbulent Flow for Three Frequently Used Impellers,'' Trans. Inst. Chem. Eng., Part A, **74**, pp. 379–389.
[19] Ranade, V. V., and Joshi, J. B., 1989, ''Flow Generated by Pitched Blade Turbines I: Measurements Using Laser Doppler Anemometer,'' Chem. Eng. Comm., **81**, pp. 197–224.
[20] Wu, H., and Patterson, G. K., 1989, ''Laser Doppler Measurements of Turbulent Flow Parameters in a Stirred Mixer,'' Chem. Eng. Sci., **44**, pp. 2207–2221.
[21] Yianneskis, M., Popiolek, Z., and Whitelaw, J. H., 1987, ''An Experimental Study of the Steady and Unsteady Flow Characteristics of Stirred Reactors,'' J. Fluid Mech., **175**, pp. 537–555.
[22] Hinze, J. O., 1975, *Turbulence*, McGraw-Hill, NY.
[23] Sharp, K. V., Kim, K. C., and Adrian, R., 2000, ''Dissipation Estimation Around a Rushton Turbine Using Particle Image Velocimetry,'' *Laser Techniques Applied to Fluid Mechanics: selected papers from the 9th Intl. Symp. 1998*, Springer-Verlag.
[24] Jaworski, Z., Nienow, A. W., and Dyster, K. N., 1996, ''An LDA Study of the Turbulent Flow Field in a Baffled Vessel Agitated by an Axial, Down-pumping Hydrofoil Impeller,'' Can. J. Chem. Eng., **74**, pp. 3–15.
[25] Myers, K. J., Ward, R. W., and Bakker, A., 1997, ''A Digital Particle Image Velocimetry Investigation of Flow Field Instabilities of Axial-Flow Impellers,'' ASME J. Fluids Eng., **119**, pp. 623–632.
[26] Schäfer, M., Yianneskis, M., Wachter, P., and Durst, F., 1998, ''Trailing Vortices Around a 45° Pitched Blade Impeller,'' AIChE J., **44**, pp. 1233–1246.

On a General Method of Unsteady Potential Calculation Applied to the Compression Stages of a Turbomachine—Part I: Theoretical Approach

F. Bakir
S. Kouidri
T. Belamri
R. Rey

Laboratoire d' Energetique e de Mechanique des Fluides Interne, Ecole Nationale Superieure d' Arts et Metiers, 151, boulevard de l'Hopital, 75013 Paris, France

An algorithm using the singularity method was developed. It allows taking into account the interaction between fixed and mobile cascades. Its principle is based on the summation of discrete vortices distributed periodically on the rotor and stator profiles. The overall matrix, obtained by applying the boundary conditions, takes into account the complexity of the studied cascade geometry (presence or not of splitter blades, possibly variable pitch of the profiles, etc . . .) To illustrate the interest and the impact of the algorithm, two parametric studies on turbomachines cascade are presented: Planes cascade made up of a rotor and a stator (at the mean radius of an axial fan). Circular cascade made up of impeller and a volute (peripheral cascade of a centrifugal pump).
[DOI: 10.1115/1.1399286]

Introduction

The unsteady phenomena in turbomachines break down into a series of specific problems [1] which we can summarize as follows:

• Those related to the aerodynamic effort on the blade: their origin is in the geometrical irregularities of each blade of the same wheel and in the fluctuations of direction and module of the absolute velocity at the upstream, which is a phenomenon caused by the turbulence [2].
• Those related to the rotor-stator interaction: for a complete stage made up of mobile cascade and a fixed cascade, it is the interaction rotor-stator which can become dominant [3–5]. In the case of a complex blading, the period of the unsteady phenomena corresponds to a full rotation of wheel.

The work of the present paper is a continuation of work already published [6,7] which dealt with the application of the singularity method to the prediction of the steady and unsteady flows in turbomachines. This method is very well adapted to the resolution of the potential flow by synthesizing them as being the superposition of several elementary flows whose solution is known analytically. However, the complexity of current turbomachine cascades, varying from the simple isolate cascade to the case of fixed and mobile multi-cascades, requires more general algorithmic developments taking account of these complex geometries.

When the viscous effects are not very significant (it is the case of the applications presented in Part II), this method restores satisfactory results. In the contrary case a coupling with a model taking into account the effect of boundary layer is necessary.

1 General Algorithm

1.1 Complex Conjugate Velocity Expression for a Rotor-Stator Configuration. The axial stage, shown in Fig. 1, is formed by 4 main rotor blades with 4 splitter blades and 7 blades for the stator. The pitches t_1, t_2, and t_3 can be different for each cascade ($t_1 \neq t_2 \neq t_3$) and also can have variation for the same cascade. For the suggested configuration, the conjugate velocity expression C', induced by the presence of the vortices Γ_j distributed on Z blades in a point M of affix z, is obtained by the summation, according to axis Oy, of all the singularities. These ones are laid out at surface of the profiles of cascade number 1, of the profiles of cascade number 2, then of those of cascade number 3. In the relation (1), the subscripts represent the number of the blade and the superscripts correspond to the cascade:

$$C' = \frac{i}{2\pi}[I_1^1\Gamma_1^1 + I_2^1\Gamma_2^1 + I_3^1\Gamma_3^1 + I_4^1\Gamma_4^1] + \frac{i}{2\pi}[I_1^2\Gamma_1^2 + I_2^2\Gamma_2^2 + I_3^2\Gamma_3^2 + I_4^2\Gamma_4^2] + \frac{i}{2\pi}[I_1^3\Gamma_1^3 + I_2^3\Gamma_2^3 + I_3^3\Gamma_3^3 + \ldots + I_7^3\Gamma_7^3] \quad (1)$$

In a compact form it is:

$$C' = \frac{i}{2\pi}\sum_{s=1}^{3}\left(\sum_{m=1}^{Z^s} I_m^s\Gamma_m^s\right) \quad (2)$$

where s is an indication of cascades number (here 3 cascades) and m is that of the summation on the number of blades constituting each cascade. For an infinite plane cascade, the summation is done from $y \to -\infty$ to $y \to +\infty$. The terms I_m^s become, for example for the first cascade:

$$I_1^1 = \sum_{n=-\infty}^{n=+\infty}\frac{1}{(z - z_1^1 + inh)}$$
$$I_2^1 = \sum_{n=-\infty}^{n=+\infty}\frac{1}{(z - z_2^1 + inh)} \quad (3)$$
$$I_3^1 = \sum_{n=-\infty}^{n=+\infty}\frac{1}{(z - z_3^1 + inh)}$$
$$I_4^1 = \sum_{n=-\infty}^{n=+\infty}\frac{1}{(z - z_4^1 + inh)}$$

Contributed by the Fluids Engineering Division for publication in the JOURNAL OF FLUIDS ENGINEERING. Manuscript received by the Fluids Engineering Division October 1, 1999; revised manuscript received June 6, 2001. Associate Editor: B. Schiavello.

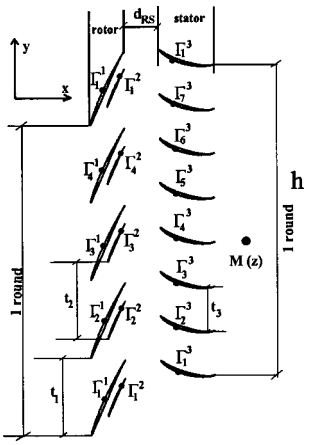

Fig. 1 Position of the singularities

where h is a pitch corresponding to one round. Let us develop the first term of the system (3)

$$I_1^1 = \sum_{n=-\infty}^{n=+\infty} \frac{1}{(z - z_1^1 + inh)} = \sum_{n=-\infty}^{n=+\infty} \frac{\frac{\pi}{h}}{\frac{\pi}{h}(z - z_1^1 + inh) + in\pi}$$

As this summation represents the development in series of the hyperbolic cotangent, we then obtain the final expression:

$$I_1^1 = \frac{\pi}{h} \coth\left(\frac{\pi}{h}(z - z_1^1)\right) \tag{4}$$

By adopting the same development for the other three terms, we obtain the following expressions:

$$I_2^1 = \frac{\pi}{h} \coth\left(\frac{\pi}{h}(z - z_2^1)\right)$$

$$I_3^1 = \frac{\pi}{h} \coth\left(\frac{\pi}{h}(z - z_3^1)\right)$$

$$I_4^1 = \frac{\pi}{h} \coth\left(\frac{\pi}{h}(z - z_4^1)\right)$$

1.2 Generalization of the Method. Let us now suppose that the p cascades are made up of Z^s blades each one (Z^s is unspecified). The expression (2) becomes in this case:

$$C' = \frac{i}{2\pi} \sum_{s=1}^{p} \left(\sum_{m=1}^{Z^s} [I_m^s \Gamma_m^s] \right) \tag{5}$$

with for example:

$$I_m^s = \frac{\pi}{h} \coth\left(\frac{\pi}{h}(z - z_{m,1}^s)\right) \tag{6}$$

where $z_{m,1}^s$ is the position of vortex 1 of the mth blade of the sth cascade. Let k^s be the number of vortices distributed by blade. This number is the same for all the blades of the same cascade but can vary from one cascade to another. The expression (5) can be easily generalized and becomes:

$$C' = \frac{i}{2\pi} \sum_{s=1}^{p} \left(\sum_{m=1}^{Z^s} \left[\sum_{j=1}^{k^s} I_{m,j}^s \Gamma_{m,j}^s \right] \right) \tag{7}$$

with:

$$I_{m,j}^s = \frac{\pi}{h} \coth\left(\frac{\pi}{h}(z - z_{m,j}^s)\right) \tag{8}$$

Note: The expression (7) represents the velocity induced by the jth vortex of the mth blade of the sth cascade in a point M of affix z. It can take into account the effect of an aperiodic geometry (variable blade pitch).

1.3 Velocity Expression. The velocity $\vec{C}$, in any point of the plane, will be defined from the principle of superposition by the following system (9):

$$\vec{C} = \begin{vmatrix} u = Ca + \mathrm{Re}(C') \\ v = Ca \cdot tg\,\alpha_m - \mathrm{Im}(C') \end{vmatrix} \tag{9}$$

in which $\mathrm{Re}(C')$ and $\mathrm{Im}(C')$, respectively, represent the real and imaginary parts of the conjugate velocity C' generated by the vortices sheet attached to each profile.

We introduce the following change of variables:

$$X_{m,j}^s = \frac{\pi}{h}(x - x_{m,j}^s)$$

$$Y_{m,j}^s = \frac{\pi}{h}(y - y_{m,j}^s) \tag{10}$$

along with the following relationship (11):

$$i \coth(Z_{m,j}^s) = \frac{\sin 2Y_{m,j}^s + i \cdot \mathrm{sh}\, 2X_{m,j}^s}{\mathrm{ch}\, 2X_{m,j}^s - \cos 2Y_{m,j}^s} \tag{11}$$

Then the expression (9) becomes:

$$\vec{C} = \begin{vmatrix} u = Ca + \dfrac{1}{2} \displaystyle\sum_{s=1}^{p} \left[\sum_{m=1}^{Z^s} \left(\frac{1}{h}\right) \left[\sum_{j=1}^{k^s} \left[\frac{\sin 2Y_{m,j}^s}{ch\, 2X_{m,j}^s - \cos 2Y_{m,j}^s} \right] \Gamma_{m,j}^s \right] \right] \\ \qquad \pm \kappa \dfrac{\Gamma_{m,moy}^s}{2\Delta s} \cos\delta \\ v = Ca \cdot tg\,\alpha_m - \dfrac{1}{2} \displaystyle\sum_{s=1}^{p} \left[\sum_{m=1}^{Z^s} \left(\frac{1}{h}\right) \left[\sum_{j=1}^{k^s} \left[\frac{sh\, 2Y_{m,j}^s}{ch\, 2X_{m,j}^s - \cos 2Y_{m,j}^s} \right] \Gamma_{m,j}^s \right] \right] \\ \qquad \pm \kappa \dfrac{\Gamma_{m,moy}^s}{2\Delta s} \sin\delta \end{vmatrix}$$

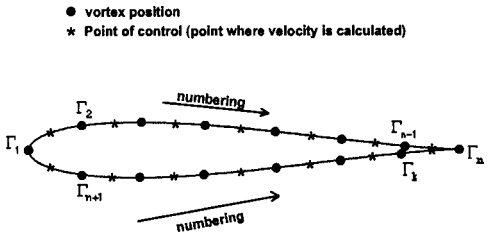

Fig. 2 Discretization of the profile

and can be written in the following final form (12):

$$\vec{C}^s_{m,i} = \begin{cases} \overbrace{u^s_{m,i} = Ca}^{A} + \overbrace{\dfrac{1}{2}\sum_{s=1}^{p}\left[\sum_{m=1}^{Z^s}\left(\dfrac{1}{h}\right)\left[\sum_{j=1}^{k^s} fx^s_{m_{i,j}}\Gamma^s_{m,j}\right]\right]}^{B} \\ \overbrace{\pm\kappa\dfrac{\Gamma^s_{m,i}+\Gamma^s_{m,i+1}}{2\Delta s^s_{m,i}}\cos\delta^s_{m,i}}^{C} \\ \nu^s_{m,i} = Ca\cdot tg\,\alpha_m - \dfrac{1}{2}\sum_{s=1}^{p}\left[\sum_{m=1}^{Z^s}\left(\dfrac{1}{h}\right)\left[\sum_{j=1}^{k^s} fy^s_{m_{i,j}}\Gamma^s_{m,j}\right]\right] \\ \pm\kappa\dfrac{\Gamma^s_{m,i}+\Gamma^s_{m,i+1}}{2\Delta s^s_{m,i}}\sin\delta^s_{m,i} \end{cases} \tag{12}$$

In the system above the second member can be described as:

- the first term (*A*) represents the upstream flow.
- the second term (*B*) represents the influence of the $\Sigma_{s=1}^{p}[Z^s k^s]$ vortices laid out at surface of the *p* cascades. In these terms, the *fx* and *fy* are the influence functions representing the effect of the various singularities.
- the last term (*C*) can be used on the surface of the profile and corresponds to the influence of the vortex on itself, where $\kappa=1$ on the surface of the profiles and $\kappa=0$ everywhere else. Within the framework of our classification (Fig. 2), the sign + will be reserved for the suction side and the sign − for the pressure side.

1–4 Boundary Conditions. The intensity of the vortices sheet must comply with a certain number of boundary conditions corresponding to the physical reality of the flow.

The Zero Normal Velocity Condition. It is the kinematic condition corresponding to the slip of the fluid on the surface of the profiles (Fig. 3):

In absolute motion for a fixed cascade and,

In relative motion for a mobile cascade having a peripheral velocity *U*. This condition can usually be specified with the following equation:

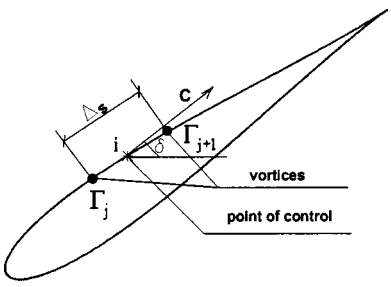

Fig. 3 Parameters of discretization

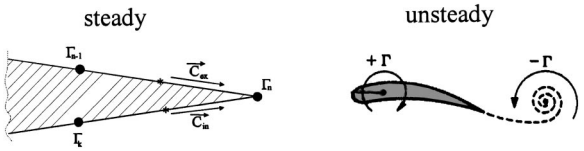

Fig. 4 Kutta condition

$$tg\,\delta(x,y) = \frac{v(x,y)-\lambda U}{u(x,y)} \tag{13}$$

with $\lambda=1$ for a mobile cascade and $\lambda=0$ for a fixed cascade. k^s points of control are defined on the surface of each profile allowing to solve the linear system where Γ^s_m are the unknowns.

By substituting the *u* and *v* expressions of Eq. (12) into Eq. (13) and after development, we obtain:

$$\sum_{s=1}^{p}\left[\sum_{m=1}^{Z^s}\left(\frac{1}{h}\right)\{[tg\ \delta^s_{m,i} fx^s_{m_{i,j}} + fy^s_{m_{i,j}}]\Gamma^s_{m,j}\}\right] = -\lambda U + Ca[tg\,\alpha_m - tg\,\delta^s_{m,i}] \tag{14}$$

Hence the compact form:

$$A_{ij}\Gamma_j = B_i \tag{15}$$

with:

$$A_{ij} = \sum_{s=1}^{p}\left[\sum_{m=1}^{Z^s}\left(\frac{1}{h}\right)(tg\,\delta^s_{m,i} fx^s_{m_{i,j}} + fy^s_{m_{i,j}})\right] \tag{16}$$

$$B_i = -\lambda U + Ca[tg\,\alpha_m - tg\,\delta^s_{m,i}] \tag{17}$$

$$1 \leqslant i \leqslant \sum_{s=1}^{p}[Z^s k^s]$$

$$1 \leqslant j \leqslant \sum_{s=1}^{p}[Z^s k^s]$$

Note

The second member in Eq. (17) can take into account any unsteadiness form of the flow. In fact, the unsteady phenomena corresponding to the internal or external flows, result mainly from:

- Disturbances of the upstream flow (incidence α_m, velocity modulus *Ca*) comparable to certain aspects of the turbulence or wake at the upstream of the studied profile.
- Fluctuations of stagger angle, related to the interaction fluid-structure (aeroelasticity) where the profile deformation and the corresponding force variation are both present.
- Geometrical defects of different blades (pitch, stagger angle, camber)
- Variations of the machine rotational speed which can be expressed as variation of the peripheral velocity *U*
- The rotor-stator interaction.

Thus, we put the second member in a general form depending on time:

$$B_i(x,y,t) = -\lambda U(t) + Ca(x,y,t)[tg\,\alpha_m(x,yt) - tg\,\delta^s_{m,i}(x,y,t)] \tag{18}$$

Kutta Condition

In steady, as in unsteady flow, the system above is undetermined. Then taking into account of the Kutta condition is necessary to arrive at a unique solution.

In steady flow, the pressure side and suction side velocity moduli are equal in the vicinity of the trailing edge (Fig. 4).

In unsteady flow, the difference between the moduli of these velocities is equal to the intensity of the vortex shed at the trailing

edge. This later has sign opposite to the variation of the circulation developing between two consecutive moments. The influence of the vortex shedding was quantified [6]. We show that its influence is weak in the case of the pumps [8]. We do not take into account the influence of the vortex shedding, therefore the unsteady problem is considered as sequence of instantneous steady flow calculations.

Then $\Sigma_{s=1}^{p}[Z^s]$ additional equations respecting the Kutta condition are added to the linear system Eq. (17). Once all the vortices are known, we calculate the velocity field from Eq. (12) and thereafter the pressure field obtained by conservation of the rothalpie ($I=p/\rho+W^2/2-U^2/2=$constant). In the case of a rotor-stator stage the calculation of the pressure in the stator requires the determination of the streamline. A qualitative approximation making it possible to avoid the definition of these streamline is explained in Part II.

1.5 Numerical Accuracy. When the numerical development is treated suitably the method presented here is precise, it merges with an analytical solution. A substantial work on these numerical aspects is detailed in reference [7].

2 Application of the Method to the Aeroacoustic of Axial Fans

2.1 Rotor-Stator Interaction. In order to validate this method, we applied it to the case of an axial machine to determine the velocity and pressure fields within the grid. This application concerns a fan strongly charged and composed of a mobile cascade and stator (N63RS). The geometry of this machine will be described in Part II. The rotor-stator interaction was the subject of several studies [9,10]. This interaction is expressed by the potential effect resulting from the variation of circulation associated with the relative motion between the fixed and mobile cascades or, in other words, with the variation of the axial distance separating the rotor and stator blade (d_{RS}).

Figure 5 shows the evolution of this interaction in the complete stage versus the axial distance d_{RS}. We notice that this interaction is variable from one profile to another and is maximum when the rotor blades are faced to the stator ones. It should be noted that the computational time for such calculation (a position of the rotor/stator stage) on a fast PC lies between 10–15 minutes for all the singularities of 200 vortices/blade.

Figure 6(a) shows, for configuration 2, the relative velocity distribution on the surface of the 4 rotor blades. Here, only the flow distribution close to the trailing edge is affected by the interaction. This phenomenon causes a fluctuation of the force exerted on the blade. This fluctuation is able to constitute a first model to study the aeroelasiticity phenomena [11]. Figure 6(b) represents, under the same conditions, the absolute velocity evolution on the surface of the 7 stator blades. We observe that the interaction involves only the vicinity of the leading edge of the blades.

2.2 Study of Asymmetric Configurations. The developed method can also take into account nonequal pitches for the same cascade. To validate this step, we calculated the pressure fluctuations downstream of the isolated rotor of the previous machine. Three configurations of the rotor cascade were studied:

Case A: The rotor consists of spaced blades of an equal pitch. The near field pressure fluctuations ($Xav=20$ mm) are calculated. The fast Fourier transform of these fluctuations are characterized (Fig. 7), in a dominant way, by a spectrum of lines corresponding to the frequency of the blades passage (133 Hz and multiples).

Case B: In certain cases in order to obtain low acoustic level, the spacing between the blades is made uneven [12]. The pressure spectrum downstream of the rotor is characterized by only one

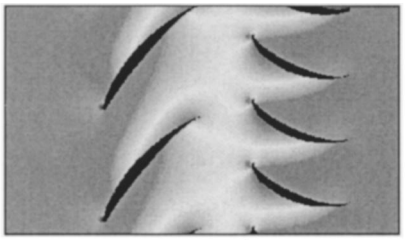

Configuration 1: reduced interaction (d_{RS} = 23 mm)

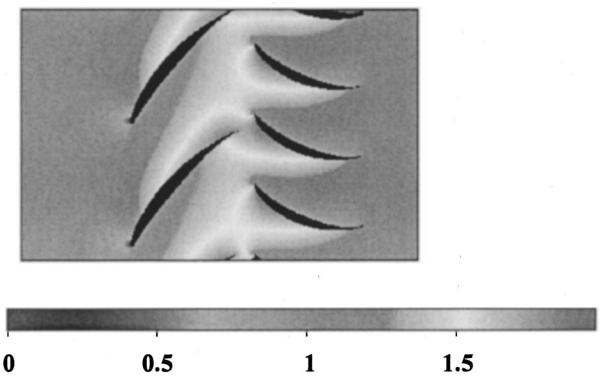

Configuration 2: strong interaction (d_{RS} = 6 mm)

Fig. 5 Absolute velocity field C/C1 calculated in the stage

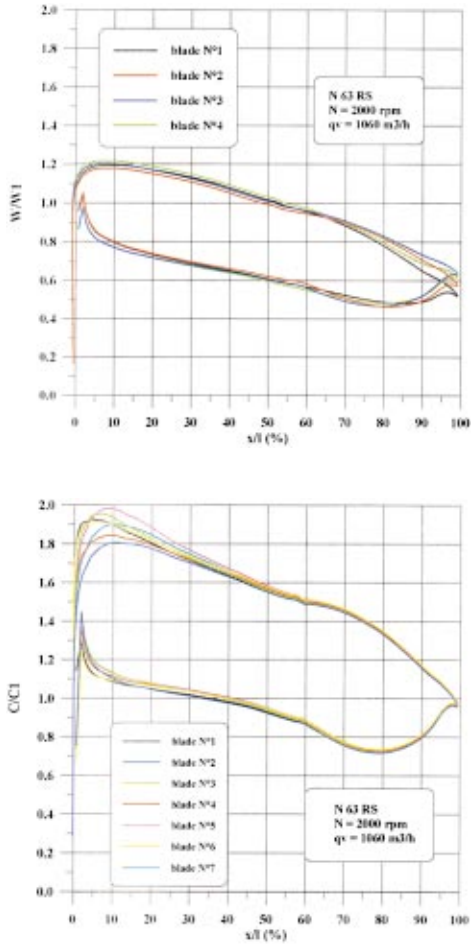

Fig. 6 (*a*) Relative velocity field on the surface of the 4 rotor blades. (*b*) Absolute velocity field on the surface of the 7 stator blades.

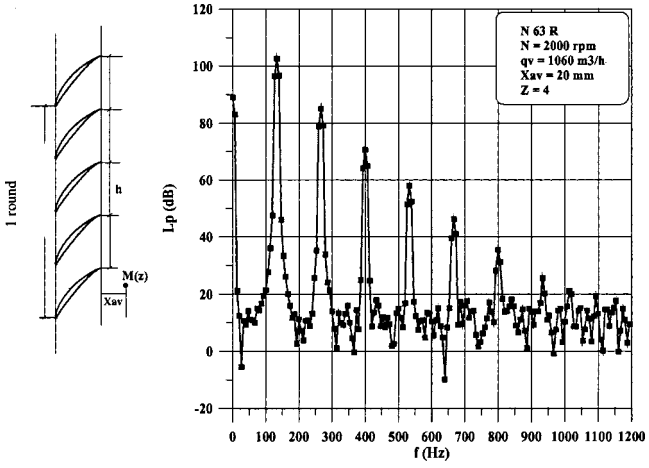

Fig. 7 Geometry with equal pitch (case A)

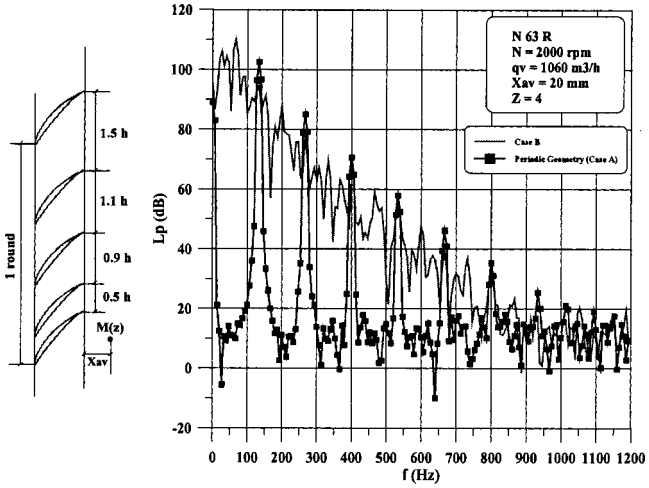

Fig. 8 Strongly aperiodic geometry (case B)

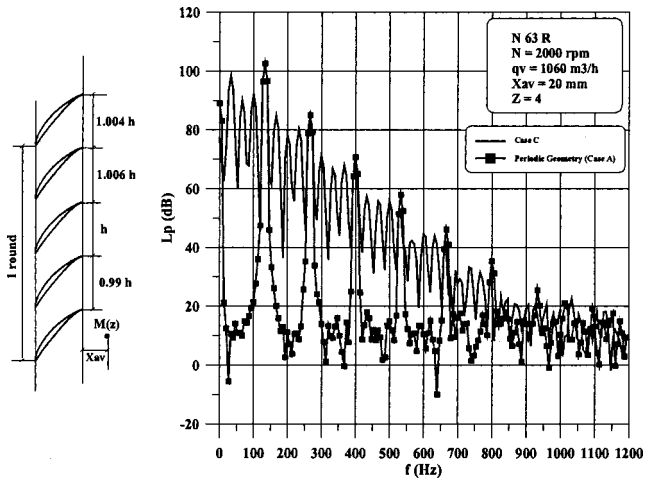

Fig. 9 Pitch deviation lower than 1 percent (case C)

peak corresponding to the rotational speed as shown in Fig. 8. In the same figure, the theoretical pressure spectrum corresponding to case A (periodic geometry) is reported. The characteristic period of the signal corresponds then to one rotation.

Case C: The geometrical machine defects caused by a lack of precision in the blade manufacturing (blade stagger angle, pitch of the profiles etc.) are also the origin of a broadband noise. The effect of manufacturing deviations is added to the upstream flow perturbations in more or less important proportions (Fig. 9).

3 Application on the Impeller Volute Tongue Interaction

We applied this theoretical approach to a peripheral cascade of a centrifugal impeller. The geometry of this machine will be described in Part II. Calculation with annular cascade is facilitated using the transition to the axial cascade by means of a conformal mapping [13] as shown in Fig. 10. The vortex distribution retained for this calculation corresponds to 200 vortices per blade. We obtain a linear system of order 1200×1200 which is resolved within 5 minutes on a fast PC. During this study, our attention was given, in priority, to the influence of the operating conditions and the constructive parameters on the amplitude of the unsteady phenomena. This theoretical study reveals interesting results concerning the impeller-volute interaction.

3.1 Influence of the Flow Rate. At the nominal flow rate, we observe a strong angular asymmetry of the flow pointing out two distinct zones A and B:

Zone A: strongly unsteady flow zone near the volute tongue.

Zone B: quasi-steady zone far away from the volute tongue where the rotor-stator interaction phenomena are reduced.

For an upstream pressure of 1 absolute bar and a rotational speed of 900 rpm, we present, in Fig. 11, the blade to blade pressure field in the impeller for 4 values of the flow rate.

This theoretical model clearly shows the interaction impeller-volute tongue. The kinematics of the flow is different from a channel to the other. The channel close to the volute tongue presents a very important acceleration of the relative speed. This aspect results in:

- a strong depression in particular in the throat and above the nominal flow rate (white color, $qv/qvn=1.2$, Fig. 11).
- the description of the recirculation phenomena (Fig. 12) in particular at partial flow rate even if the viscous effects are not taken into account.

3.2 Influence of the Distance Impeller-Volute Tongue. Always at the nominal flow rate, the distance impeller-volute tongue strongly attenuates this dissymmetry [14]. Figure 13 shows the influence of this radial distance on the blade to blade pressure field (nominal value $d_{RS}=25$ mm and doubled value $d_{RS}=50$ mm) by increasing the radius of the volute tongue R_3.

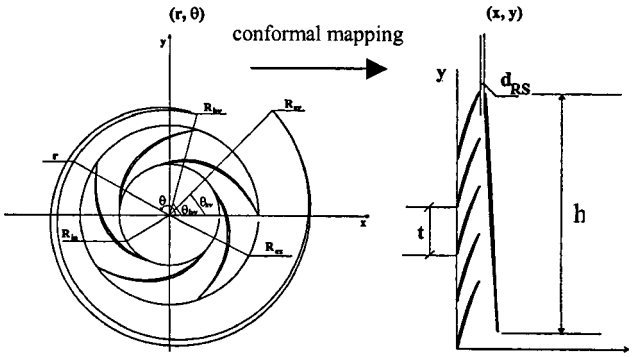

Fig. 10 Conformal mapping of a general cascade to a plane one

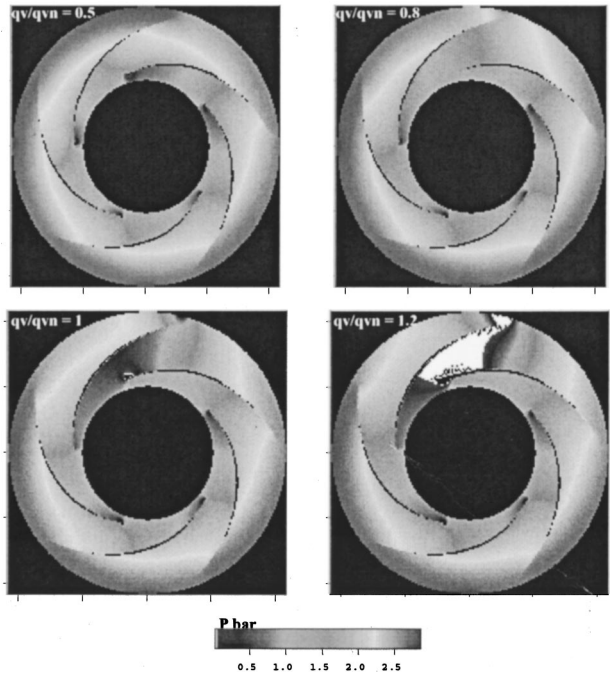

Fig. 11 Blade to blade pressure field (*N*=900 rpm, d_{RS} =25 mm)

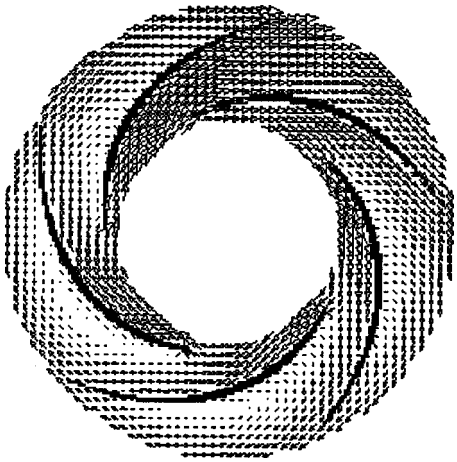

Fig. 12 Relative velocity field in the centrifugal impeller which has a strong angular asymmetric (*qv*/*qvn*=0.5 *N*=900 rpm, d_{RS}=25 mm)

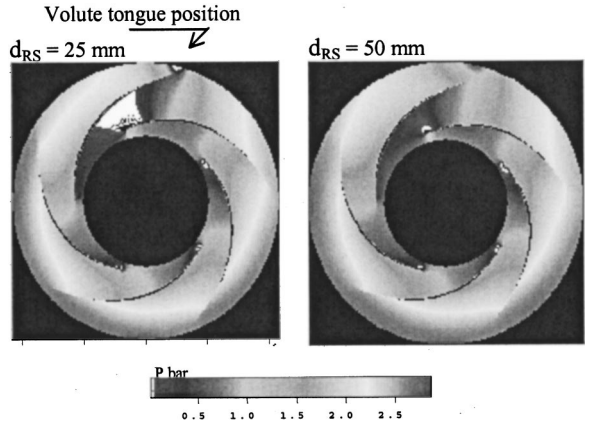

Fig. 13 Influence of the distance impeller-volute tongue (*N* =900 rpm, *qv*/*qvn*=1, p_1=0.5 bar)

Conclusion

The method presented in this paper, fast and widely applicable, permits the determination of the blade to blade flow in the turbomachine rotating cascades with incompressible fluid. Based on the vortices distribution, it allows showing the main physical phenomena of the potential flow, notably the interaction between fixed and mobile cascades. The flexibility of the method permits the analysis of various configurations of cascades: presence or not of splitter blades, uneven pitch between blades, variation of the meridional channel in circular cascade, and other parameters.

Two parametric studies, on cascades of real machines presented in Part II, supplement the theoretical method. The first one relates to a rotor-stator cascade at the average radius of an axial fan. The second one concerns the interaction impeller-volute tongue of the peripheral grid of a centrifugal impeller.

In addition to the facility of use of the method, its power effectively restores certain physical phenomena met in compression machines. Qualitative and quantitative comparisons will be detailed in Part II.

Nomenclature

A_{ij} = matrix of the linear system [$\mathbf{m}^{-1}$]
B_i = second member of the linear system [**m/s**]
C' = conjugate velocity [**m/s**]
C = absolute velocity [**m/s**]
Ca = absolute axial velocity [**m/s**]
Cu = absolute tangential velocity [**m/s**]
d_{RS} = axial rotor-stator distance or radial impeller-volute tongue distance [**m**]
h = one round [**m**]
I = rothalpy [$\mathbf{m^2/s^2}$]
i = imaginary unit in space, $i^2=-1$
Lp = sound pressure level $Lp=20\log(p/2.10^{-5})$ [**dB**]
$M(z)$ = point of the complex plane [**m**]
N = rotational speed [**rpm**]
p_1 = upstream static pressure [**Pa**]
qv = flow rate [$\mathbf{m^3/h}$]
t = cascade Pitch [**m**]
U = peripheral velocity [**m/s**]
W = relative velocity [**m/s**]
W_1 = upstream relative velocity [**m/s**]
Xav = downstream distance between source and microphone [**m**]
z = affix of a point, $x+iy$ [**m**]
Z = cascade profile number
α_m = upstream average flow direction [°]
δ = angle between the segment carrying a vortex and the Ox axis

References

[1] Verdon, J. M., 1993, "Review of Unsteady Aerodynamic Aethods for Turbomachinery Aeroelastic and Aeroacoustic Applications," AIAA J., **31**, pp. 235–250.
[2] Ganz, U., Glegg, S. A. L., and Joppa, P., 1998, "Measurement and Prediction of Broadband Fan Noise," AIAA paper. no 98-2316.
[3] Fleeter, S., Jay, R. L., and Bennett, W. A., 1981, "Wake Induced Time-variant Aerodynamics Including Rotor-Stator Axial Spacing Effects," ASME J. Fluids Eng., **103**, pp. 59–66.
[4] Manwaring, S. R., and Wisler, D. C., 1993, "Unsteady Aerodynamics and Gust Response in Compressors and Turbines," ASME J. Turbomach., **115**, pp. 724–740.
[5] Chung, M. H., and Wo, A. M., 1997, "Navier-Stokes and Potential Calculations of Axial Spacing Effect on Vortical and Potential Disturbances and Gust Response in Axial Compressor," ASME J. Turbomach., **119**, pp. 472–481.
[6] Belamri, T., 1998, "Analyze Aube à Aube de l'Ecoulement Instationnaire Multigrilles par la Méthode des Singualrités-Application aux Turbomachines à Fluide Incompressible," Thèse de Doctorat, Ecole Nationale Supérieure d'Arts et Métiers, Department of Mechanical Engineering, Paris, France (in French).
[7] Belamri, T., Bakir, F., Kouidri, S., and Rey, R., 1999, "Numerical Stability

Conditions in the Calculations of Potential Velocity Field,'' AIAA J., **37**, No. 2, pp. 272–276.
[8] Qin, W., and Tsukammoto, H., 1997, ''Theorical Study of Pressure Fluctuations Downstream of a Diffuser Pump Impeller Part 1: Fundamental Analysis on Rotor-Stator Interaction.'' ASME J. Fluids Eng., **119**, pp. 647–652.
[9] Wo, A. M., Chung, M. H., and Hsu, S. T., 1997, ''Gust Response Decomposition in a Stator-Rotor axial Compressor with Varying Axial Gap,'' J. Propul. Power, **13**, No. 1, pp. 160–165.
[10] Rai, M. M., 1987, ''Navier-Stokes Simulations of Rotor-Stator Interactions using Patched and overlaid Grids,'' AIAA J., **3**, No 5, pp. 387–396.
[11] Berthillier, M., Dupont, C., Chanez, P., and Saurat, F., 1998, ''Réponse Forcée Aéroelastique des Aubes de Turbomachines,'' Revue Française de Mécanique, No. 4, pp. 265–275 (in French).
[12] Wu, S. F., Su, S. G., and Shah, H. S., 1997, ''Modeling of the Noise Spectra of Axial Flow Fans in free Field,'' J. Sound Vib., **200**, No. 4, pp. 379–399.
[13] Bakir, F., Belamri, T., and Rey, R., 1998, ''Theoretical and Experimental Study of the Blade to Blade Flow in a Centrifugal Pump,'' International Journal of Turbo and Jet-Engines, **15**, No. 4, pp. 275–291.
[14] Dong, R., Chu, S., and Katz, J., 1997, ''Effect of Modification to Tongue and Impeller Geometry on Unsteady Flow, Pressure Fluctuations and Noise in a Centrifugal Pump,'' ASME J. Turbomach., **119**, pp. 506–515.

On a General Method of Unsteady Potential Calculation Applied to the Compression Stages of a Turbomachine—Part II: Experimental Comparison

S. Kouidri
T. Belamri
F. Bakir
R. Rey

Laboratoire d' Energetique e de Mechanique des Fluides Interne, Ecole Nationale Superieure d' Arts et Metiers, 151, boulevard de l'Hopital, 75013 Paris, France

Several applications were carried out in order to validate the method presented in Part I. In Part II, two examples of these applications are presented; one relating to the aeroacoustics of the axial fans and the other one to the interaction impeller-volute tongue in a centrifugal pump. The test benches used to study the behavior of these machines are presented. The study of the fan was capable of quantifying the discrete noise associated with the fluctuations in pressure linked to the potential flow. The analysis of the centrifugal pump permitted comparing the theoretical pressure fluctuations with experimental ones measured by various unsteady pressure sensors placed on the impeller shroud and in the volute. The qualitative and quantitative results obtained confirm the interest and the range of the developed algorithm. [DOI: 10.1115/1.1399287]

Introduction

The unsteadiness of the internal flows is at the origin of certain physical phenomena observed in the turbomachines such as aerodynamic noise, unsteady cavitation, and pressure fluctuations. A significant share of the unsteadiness is related to the interaction rotor-stator [1]. The theoretical and experimental control of these aspects is very important in the design and the optimization of these machines.

Several studies on this issue have already been carried out. Two methods were developed: the first one is based on solving the Navier-Stokes equations [2,3]. The second one relies on the singularity method [4], presented in Part I, which allows the calculation of the two-dimensional unsteady flow in the blade cascade. We present in Part II the validation of this approach by applying it to two axial fans and a centrifugal pump tested in the laboratory.

1 Aeroacoustics Behavior of Axial Fans

In accordance with the European standard ISO 5801 [5] describing the rules for performance testing of ducted free inlet and fully ducted fans, a circuit standardized with a 350 mm diameter was installed at ENSAM, Paris (Fig. 1). It was equipped with aerodynamic devices of high precision, including three numerical micromanometers, which are coupled to a system of automatic acquisition and give quick access to the various pressures. A double Pitot tube of Furness type permits to measure the flow rate with 1 percent accuracy. The control of the flow rate of the fan is obtained by using an orifice plate with various diameters.

On the acoustic side, the test bench was equipped with 3 microphonic probes 1/2 in. G.R.A.S with antivent cone and preamplifiers ICP. These microphones are calibrated at each test. The various data are collected and analyzed using a card with format PC ISA supporting a DSP 32 bits in floating point with a resolution of 3201 pts and 4 entries of signal real time.

This set of automatic acquisition and elaboration of the acoustic data allows carrying out the measurements in conformity with the standard ISO 5136 [6] relating to the determination of the acoustic power radiated by fans in duct. The different physical parameters were determined by a method including the averaging of sufficient number of readings at each test point, which achieves a result with an uncertainty on noise level not exceeding 4 percent.

1.1 Rotor-Stator Interaction in an Axial Compression Stage. The stage is composed (Fig. 2) of a mobile cascade and a stator, which are made with NACA 65 profiles. It is designed for the following operating point (machine N 63 RS):

$$qv = 1060\ \mathrm{m^3/h}, \quad \Delta p = 150\ \mathrm{Pa}, \quad N = 2000\ \mathrm{rmp}$$

This relates to a fan strongly charged, which is equipped with profiles with strong camber. The geometrical characteristics of the mobile and fixed cascades, at the average radius of the machine, are shown in Table 1. The rotor-stator interaction was the subject of several studies [7]. In this specific case, the interaction is expressed by the potential effect resulting from the variation of circulation associated with the relative motion between the fixed and mobile cascade. Figure 3 shows the evolution of this interaction in the complete stage versus the axial distance d_{RS}. We notice that this interaction is variable from one profile to another and is maximum when the rotor blades are faced to the stator ones.

The importance of the interaction is underlined qualitatively by a comparison of the global noise emitted by the machine versus the flow rate (Fig. 3). We note that the level of acoustic pressure varies according to the axial distance rotor-stator, d_{RS}, and that when this distance is minimum, the interaction is very significant and gives origin to higher acoustic noise.

In order to validate the results obtained by the calculations based on the developed method, experimental measurements were carried out. The experimental spectrum of the effective near field pressure downstream of the stage was obtained with a microphone placed at the average radius of the stage for $d_{RS} = 23$ mm and $Xav = 20$ mm (gap between the trailing edge and position sensor) and is shown in Fig. 4. The theoretical spectrum was calculated from pressure fluctuations associated with the potential flow and is given in Fig. 5. The comparison of the theoretical amplitude of the discrete frequencies corresponding to the blades passage with corresponding experimental data is satisfactory.

Contributed by the Fluids Engineering Division for publication in the JOURNAL OF FLUIDS ENGINEERING. Manuscript received by the Fluids Engineering Division October 1, 1999; revised manuscript received June 6, 2001. Associate Editor: B. Schiavello.

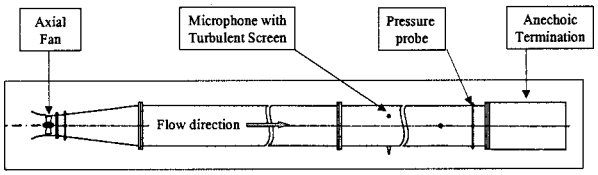

Fig. 1 Aeroacoustic test bench of the centrifugal fan

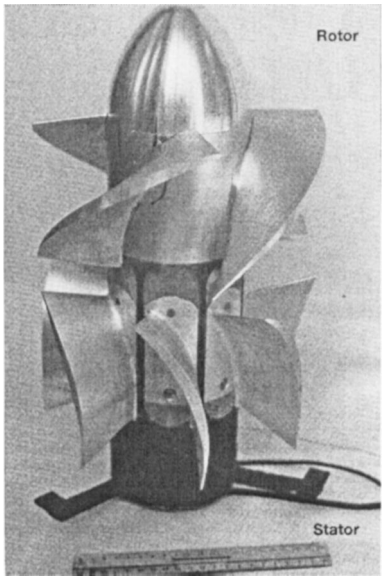

Fig. 2 Fan N 63 RS

Table 1 Data relating to the stage

	Rotor	Stator
Aerodynamic camber Cz∞o	1.580	2.658
Chord l (m)	0.1775	0.1299
Relative maximum thickness e (%)	8	8
Stagger angle γ (°) (from axial)	47.3	21
Solidity	1.288	1.65
Blade number	4	7

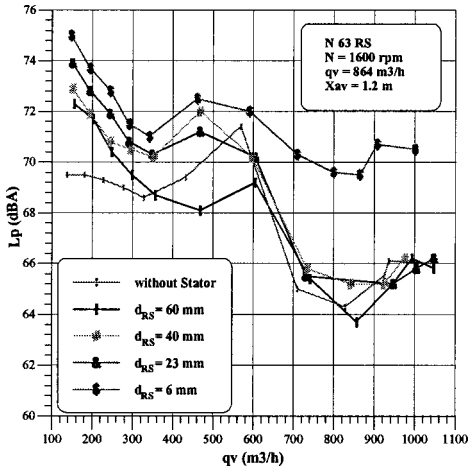

Fig. 3 Global noise measured at 1.2 m downstream of the stage for various axial distances rotor-stator-Machine N63RS at 1600 rpm

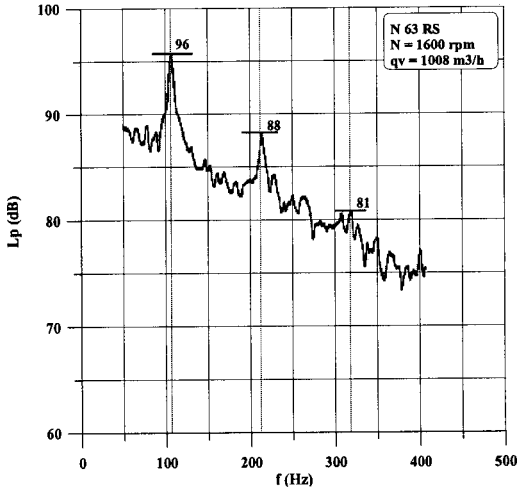

Fig. 4 Spectral analysis: experimental data-Machine N63RS

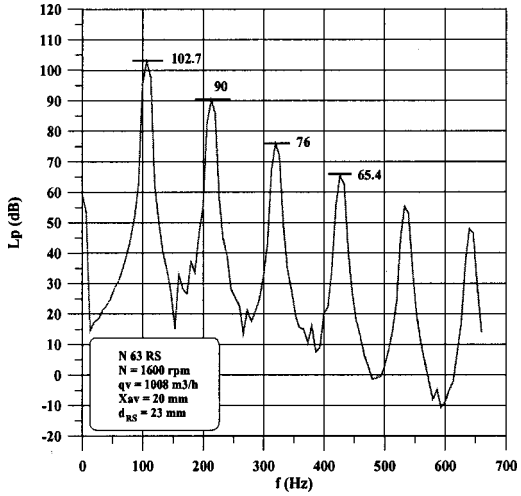

Fig. 5 Spectral analysis: potential calculation-Machine N63RS

1.2 Engine Cooling Fan. For a very different machine (the engine cooling axial fan VB shown in Fig. 6), the method of analysis also permitted calculating in a quantitative way the amplitudes of the pressure fluctuations. Measurement and calculation at 20 mm downstream of the rotor [8], at the average radius, are compared in Fig. 7.

The experimental acoustic spectrum consists of a discrete noise and broadband component mainly due to the turbulence. Calculation presented in Part I does not take into account this phenomenon; consequently, the theoretical signal contains only the dis-

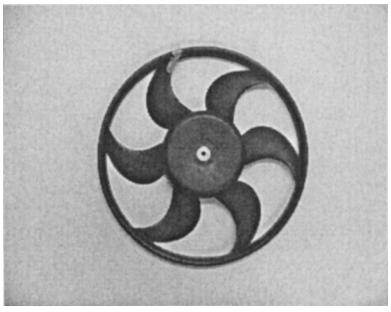

Fig. 6 Fan VB

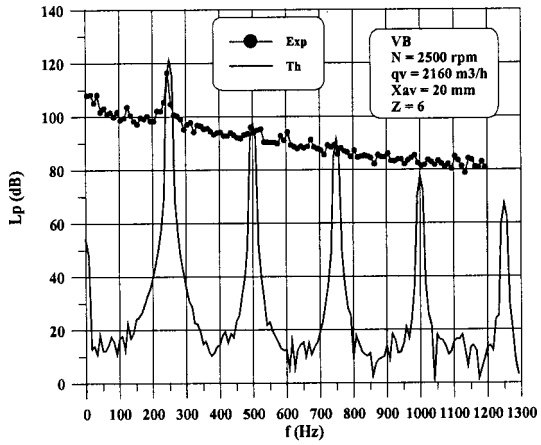

Fig. 7 Comparison theory-experiment

crete spectrum. The comparison of the two spectrums shows good agreements for the first three harmonics. For the others, the comparison is unsuited because of the predominance of the turbulence.

2 Impeller-Volute Tongue Interaction in Centrifugal Pump

2.1 Pump Geometry. Test Rig. To validate the unsteady flow prediction code presented in Part I and to illustrate the influence of the inviscid phenomena on the pressure fluctuations generated by the rotor-stator interaction, we present in this paragraph an experimental study undertaken on a centrifugal pump. The pump, formed by an open impeller and a volute (Fig. 8), is designed for the following nominal point: $N=900$ rpm, $Hn=20$ m, $qv=340$ m^3/h.

The principal constructive parameters are shown in Table 2. Hydraulic layouts of the impeller and the volute were obtained with the computer code HELIOX for design and performance analysis of centrifugal pumps [9].

Experiments were conducted on this pump using the LEMFI pump test rig composed of the following main elements (Fig. 9):

Two storage tanks with capacity of 4 m^3 each, connected by a pipe of 350 mm in diameter. They can be loaded and emptied by means of two electrical control valves.

A liquid ring vacuum pump which regulates the pressure on the free surface inside the storage tanks.

A 45 kW ABB electric motor controlled by a variable frequency drive.

A motoried control valve which serves to control the pump flow rate in a precise manner.

Various measurement instruments and devices:

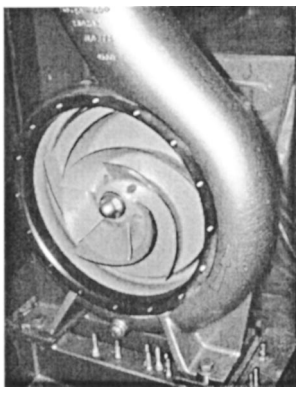

Fig. 8 Centrifugal pump equipped with its volute

Table 2 Principal geometrical parameters of the pump

Specific speed $nsq=\frac{N_{(rpm)}\sqrt{qv_{(m^3/s)}}}{Hn_{(m)}^{0.75}}$	32
Inlet radius at mean streamline R_1 (mm)	75
Outlet radius at mean streamline R_2 (mm)	204
Inlet width b_1 (mm)	86
Outlet width b_2 (mm)	42
Inlet blade angle (from tangential direction) β_1 (°)	20
Exit blade angle (from tangential direction) β_2 (°)	27
Volute tongue radius R_3 (mm)	210
Basic volute width b_3 (mm)	50
Number of impeller Blades Z	5
Chord of the impeller blades (mm)	390

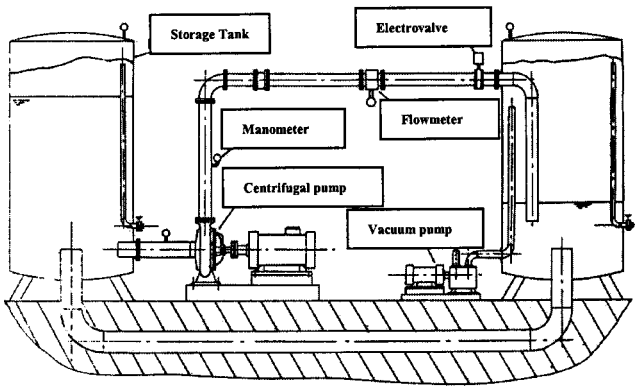

Fig. 9 General diagram of the pump test rig of LEMFI

Electromagnetic flowmeter KROHNE (accuracy 1 percent), placed at the pump outlet.

Manometers using piezoresistive sensors (accuracy 1 percent),

2.2 Position of the Pressure Sensors. On the centrifugal pump, equipped with a transparent front casing wall, 15 dynamic pressure sensors KISTLER brand 601A type were mounted (Fig. 10). Their specifications are: range 0–250 bar, natural frequency >150 kHz.

On the Front Casing Wall. Two sets of positions were used for the sensors mounted on the front casing wall. The θ parameter was used to indicate the angle between the volute tongue and the sensors position or the trailing edge of each blade.

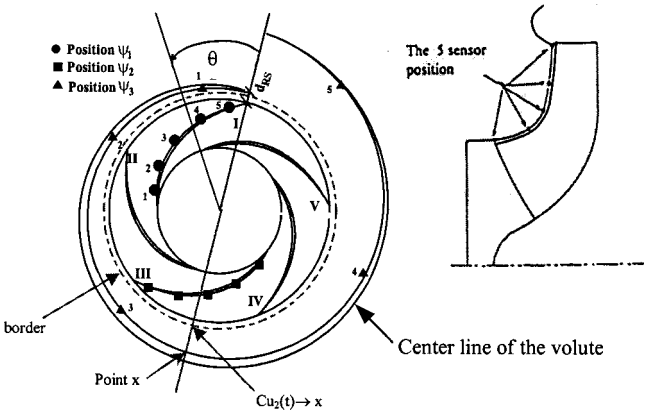

Fig. 10 Position of the dynamic pressure sensors

(a) Position set $\psi 1$: Five sensors were located along a curve close to the mean line of one impeller blade with trailing edge close to volute tongue. The sensor No. 5 is located as near as possible to the blade trailing edge and close to volute tongue.
(b) Position set $\psi 2$: Five sensors were located at 150 deg apart from position set $\psi 1$-sensors in a zone where the unsteady effects, generated by the proximity of the tongue, are minimized.

On the Volute Channel. Position Set $\psi 3$. Five sensors were mounted at the volute channel front surface according to the angular positions given in Fig. 10.

The variations of the blade to blade pressure, as well as the pressure fluctuations in the volute, were measured by these sensors and amplified then treated with a spectrum analyzer (Lecroy 930A). All the signals were identified and stored in a computer for further analysis.

2.3 Asymmetry of the Flow in the Impeller. In the theoretical model the asymmetry of the flowrates among impeller channels is accompanied locally with a cavitation pocket comparable, in amplitude and position, to that one actually observed and photographed under the same conditions of flow rate and rotational speed (Fig. 11).

In the zone A close to the volute tongue, the blade to blade pressure field has a higher amplitude than in the quasi-steady zone B (150 deg a part). The experimental results obtained from the sensors situated at position $\psi 1$ and $\psi 2$, compared each other, confirm this tendency, as shown in Fig. 12 which presents the pressure fluctuations for sensors 2, 3, 4, and 5 at position $\psi 1$ and $\psi 2$.

2.4 Comparison of the Pressure Fluctuations. The measurements of pressure were carried out in cavitating and normal regime for several rotational speeds and various flow rates. From this extensive base of experimental data (600 measurement), we present the comparison of the theoretical and experimental pressures (Fig. 13 and Fig. 14) at the nominal flow rate and 900 rpm for the 5 pressure sensors of the positions $\psi 1$ and $\psi 2$. The theoretical and experimental signals are periodic. In one impeller rotation, we observe five signals, identical for the theoretical ones and slightly different in the experimental case, showing the particular behavior of each of the five blades.

The quality of the comparisons is globally very satisfactory except for the sensors No. 1 and No. 2 located close to the entry of the impeller where we can see a difference in the amplitude. At

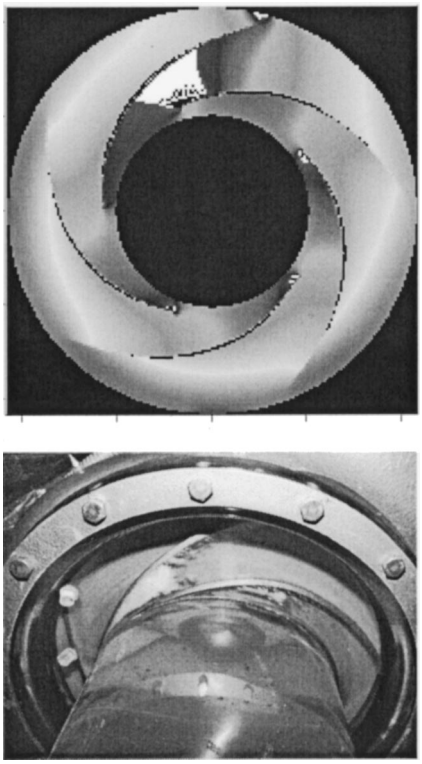

Fig. 11 Photograph of cavitation pocket (d_{RS}=25 mm, qv/qn=1, N=900 rpm, NPSH=6 m)

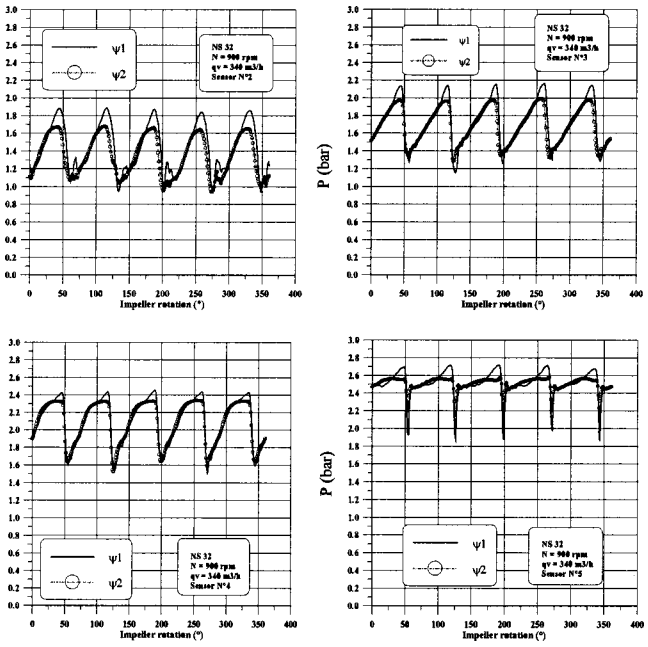

Fig. 12 Comparison of the experimental pressure fluctuations in the blade to blade channels in the zones close and far from the volute tongue (qv/qn=1, N=900 rpm, NPSH=9 m)

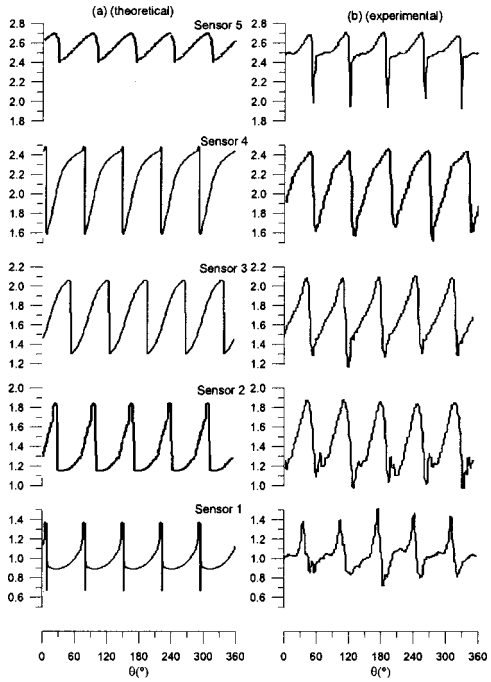

Fig. 13 Theoretical (a) and experimental (b) signals of pressure sensors 1 to 5 of $\psi 1$ (qv/qvn=1, N=900 rpm, NPSH=9 m)

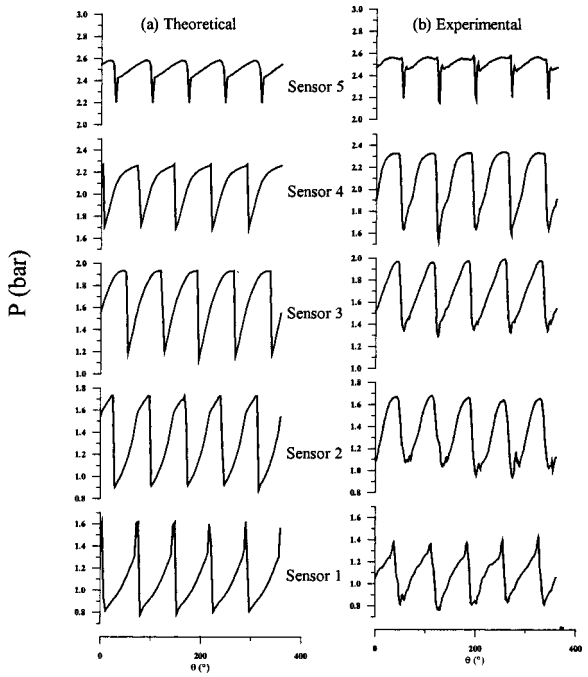

Fig. 14 Theoretical (a) and experimental (b) signals of pressure sensors 1 to 5 of $\psi 2$ ($qv/qvn=1$, $N=900$ rpm, NPSH=9 m)

these positions, the meridional channel cannot be assumed as monodimensionnal and the curvature of the vane is important. In sensor 5 of $\psi 1$ the experimental results show an important peak corresponding to the minimum pressure on the suction side. We also find the same peak but less pronounced in the theoretical results. The rest of the signal presents a good agreement.

2.5 Pressure Fluctuations in the Volute. The time dependent pressure at any point downstream of the impeller is calculated, in potential flow, by the following relation where x is the index of the point considered. We are interested here in the control points located on the volute, and more particularly, at the measurement points on $\psi 3$. The following relationships define the pressure on a streamline.

$$\overbrace{p_x(t)}^{A}=\overbrace{p_1}^{B}+\overbrace{\rho\frac{C_1^2}{2}}^{C}-\overbrace{\rho\frac{C_x^2(t)}{2}}^{D}+\rho U_2 Cu_2(t) \qquad (1)$$

t represents time and C_x the absolute velocity in the volute.

We assume that the total pressure (B term) at the inlet of the pump is steady. The pressure fluctuations at the point x are associated with the local dynamic pressure fluctuations (C term) and the pressure fluctuations (D term) generated by the impeller. By comparing the relative importance of the C term and the D term of right side of Eq. (1), it appears that the pressure fluctuations depend primarily on the tangential velocity fluctuations (D) associated with the passage of the blades (Fig. 15).

Thus, we retain only the term D related with $Cu(t)$ as significant value of $p_x(t)$. To calculate the pressure $pX(t)$ it is necessary to define the streamlines. However, we can qualitatively approximate this calculation by using the value $Cu_2(t)$ obtained at the intersection between a radial line passing through x and the border defined in Fig. 10. A comparison of the measured and calculated pressure fluctuations is presented in Fig. 16 in the form of FFT for sensor No. 1 of the volute (position $\psi 3$).

A difference in amplitude between the theoretical and experimental signals is observed. This difference is related to the approximation defined above and likely viscous effects i.e., pressure

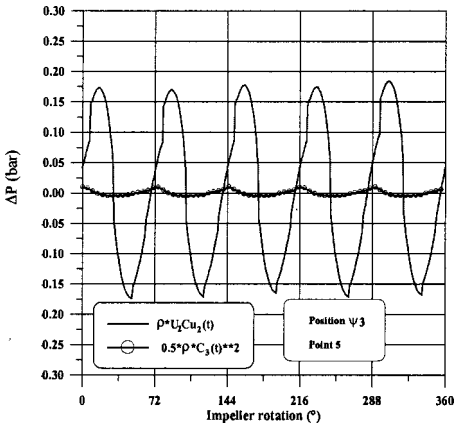

Fig. 15 Theoretical comparison of the local dynamic pressure fluctuations and those generated by the blade passage ($qv/qn=1$, $N=900$ rpm, NPSH=9 m)

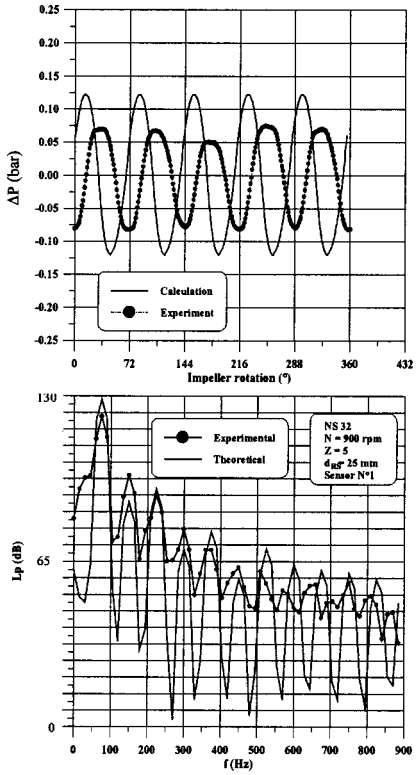

Fig. 16 Temporal signal and spectral analysis of the measured and calculated pressure fluctuations in the point 1 of the volute and $\psi 3$ ($qv/qn=1$, $N=900$ rpm, NPSH=9 m)

loss not described by the potential flow model. The FFT of the signals, on the other hand, highlights the harmonics related to the passing of the blade.

Conclusion

The COSEIX software, based on the model presented in Part I, enabled investigating three applications: An axial fan composed of a rotor-stator stage, an engine fan and a centrifugal pump composed of an impeller and a volute. The three studies highlighted the qualitative and quantitative aspects of the unsteady phenomena linked to the fixed and mobile cascade interaction. The quality of the comparisons at nominal flow rate with the results obtained from the associated experimental studies is generally satisfactory.

The study of the fans was capable to quantify the discrete noise associated with the fluctuations in pressure linked to the potential flow.

The analysis of the centrifugal pump permitted comparing the theoretical pressure fluctuations with experimental ones measured by various unsteady pressure sensors located on the casing front wall in the volute. The instantaneous flow dissymmetry in the impeller even at nominal flow rate was highlighted, with a good agreement concerning the position of the cavitation pockets, caused by the volute interaction.

References

[1] Saren, V. E., 1994, ''Some Ways of Reducing Unsteady Blade Loads Due to Blade Row Hydrodynamic Interaction in Axial Flow Turbomachines,'' Second International Conference EAHE, Pilson, Czech Republic, pp. 160–165.

[2] Chung, M. H., and Wo, A. M., 1997, ''Navier-Stokes and Potential Calculations of Axial Spacing Effect on Vortical and Potential Disturbances and Gust Response in Axial Compressor,'' ASME J. Turbomach., **119**, pp. 472–481.

[3] Rai, M. M., 1987, ''Navier-Stokes Simulations of Rotor-Stator Interactions Using Patched and Overlaid Grids,'' AIAA J., **3**, No. 5, pp. 387–396.

[4] Qin, W., and Tsukammoto, H., 1997, ''Theorical Study of Pressure Fluctuations Downstream of a Diffuser Pump Impeller Part II: Effects of Volute, Flow Rate and Radial Gap.'' ASME J. Fluids Eng., **119**, pp. 653–658.

[5] ISO 5801, Industrial Fans-Performance Testing Using Standardized Airways, 1997 (in French).

[6] ISO 5136, Determination of Sound Power Radiated by Fans and Other Air-Moving Devices-In-Duct Method, 2000 (in French).

[7] Wo, A. M., Chung, M. H., and Hsu, S. T., 1997, ''Gust response decomposition in a stator-rotor axial compressor with varying axial gap,'' J. Propul. Power, **13**, No. 1, pp. 160–165.

[8] Maaloum. A., 1999, ''Etude des Phènomènes Instationnaires Dans les Turbomachines. Application à l'Aéroacoustique des Ventilateurs Axiaux,'' Ph.D thesis, Ecole Nationale Supérieure d'Arts et Métiers, Department of Mechanical Engineering, Paris, France (in French).

[9] Bakir, F., Rey, R., Noguera, R., Massouh, F., and Kouidri, S., 1993, ''Computer Aided Design of Helico-Centrifugal Pumps,'' ASME Pumping Machinery, Vol. 154, pp. 63–74.

Fred Stern
Professor Mechanical Engineering and
Research Engineer
Fellow ASME

Robert V. Wilson
Assistant Research Engineer
Mem. ASME

Iowa Institute Hydraulic Research,
The University of Iowa,
Iowa City, IA 52242

Hugh W. Coleman
Eminent Scholar in Propulsion,
Professor of Mechanical Engineering,
Propulsion Research Center,
Mechanical and Aerospace Engineering
Department,
University of Alabama in Huntsville,
Huntsville, AL 35899
Fellow ASME

Eric G. Paterson
Associate Research Engineer,
Iowa Institute Hydraulic Research,
The University of Iowa,
Iowa City, IA 52242
Mem. ASME

Comprehensive Approach to Verification and Validation of CFD Simulations—Part 1: Methodology and Procedures

Part 1 of this two-part paper presents a comprehensive approach to verification and validation methodology and procedures for CFD simulations from an already developed CFD code applied without requiring availability of the source code for specified objectives, geometry, conditions, and available benchmark information. Concepts, definitions, and equations derived for simulation errors and uncertainties provide the overall mathematical framework. Verification is defined as a process for assessing simulation numerical uncertainty and, when conditions permit, estimating the sign and magnitude of the numerical error itself and the uncertainty in that error estimate. The approach for estimating errors and uncertainties includes (1) the option of treating the numerical error as deterministic or stochastic, (2) the use of generalized Richardson extrapolation for J input parameters, and (3) the concept of correction factors based on analytical benchmarks, which provides a quantitative metric to determine proximity of the solutions to the asymptotic range, accounts for the effects of higher-order terms, and are used for defining and estimating errors and uncertainties. Validation is defined as a process for assessing simulation modeling uncertainty by using benchmark experimental data and, when conditions permit, estimating the sign and magnitude of the modeling error itself. The approach properly takes into account the uncertainties in both the simulation and experimental data in assessing the level of validation. Interpretation of results of validation efforts both where the numerical error is treated as deterministic and stochastic are discussed. Part 2 provides an example for RANS simulations for a cargo/container ship where issues with regard to practical application of the methodology and procedures and interpretation of verification and validation results are discussed.
[DOI: 10.1115/1.1412235]

1 Introduction

Discussion and methodology for estimating errors and uncertainties in computational fluid dynamics (CFD) simulations have reached a certain level of maturity with recognition of importance through editorial policies (Freitas [1]), increased attention and recent progress on common terminology (AIAA, [2]), advocacy and detailed methodology (Roache [3]), and numerous case studies (e.g. [4]). Progress has been accelerated in response to the urgent need for achieving consensus on concepts, definitions, and useful methodology and procedures, as CFD is applied to increasingly complex geometry and physics and integrated into the engineering design process. Such consensus is required to realize the goals of simulation-based design and other uses of CFD such as simulating flows for which experiments are difficult (e.g., full-scale Reynolds numbers, hypersonic flows, off-design conditions). In spite of the progress and urgency, the various viewpoints have not converged and current approaches fall short of providing practical methodology and procedures for estimating errors and uncertainties in CFD simulations.

The present work provides a pragmatic approach for estimating errors and uncertainties in CFD simulations. Previous work on verification (Stern et al. [5]) is extended and put on a more rigorous foundation and combined with subsequent work on validation (Coleman and Stern [6]) thereby providing a comprehensive framework for overall procedures and methodology. The philosophy is strongly influenced by experimental fluid dynamics (EFD) uncertainty analysis (Coleman and Steele [7]), which has been standardized. Hopefully, CFD verification and validation procedures and methodology can reach a similar level of maturity and user variability can reach similar low levels, as for EFD. The work is part of a larger program (Rood [8]) for developing and implementing a strategy for verification and validation of Reynolds-averaged Navier-Stokes (RANS) ship hydrodynamics CFD codes. The program includes complementary CFD and EFD towing-tank investigations and considers errors and uncertainties in both the simulations and the data in assessing the success of the verification and validation efforts. The work also benefited from collaboration with the 21st and 22nd International Towing Tank Resistance Committees (ITTC [9,10]). The procedures proposed in this paper were adopted on an interim basis by the 22nd ITTC and also were recommended and used at the recent Gothenburg 2000 Workshop on CFD in Ship Hydrodynamics (Larsson et al. [11]).

The focus is on verification and validation methodology and procedures for CFD simulations with an already developed CFD code applied without requiring availability of the source code for specified objectives, geometry, conditions, and available benchmark information. The methodology and procedures were developed considering RANS CFD codes, but should be applicable to a fairly broad range of codes such as boundary-element methods and certain aspects of large-eddy and direct numerical simulations. The present work differs in many respects from recent literature. The presentation is relatively succinct with intention for use for practical applications (i.e., industrial CFD) for which numerical errors and uncertainties cannot be considered negligible or overlooked.

Contributed by the Fluids Engineering Division for publication in the JOURNAL OF FLUIDS ENGINEERING. Manuscript received by the Fluids Engineering Division November 4, 1999; revised manuscript received July 10, 2001. Associate Editor: P. E. Raad.

The definitions of errors and uncertainties and verification and validation that are used in any approach need to be clearly stated. The present and Roache [3] definitions for errors and uncertainties are consistent with those used for EFD. The AIAA [2] definitions are from an information theory perspective and differ from those used in EFD, but are not contradictory to the present definitions. The present concepts and definitions for verification and validation are closely tied to the present definitions of errors and uncertainties and equations derived for simulation errors and uncertainties thereby providing the overall mathematical framework. The Roache [3] and AIAA [2] definitions are broader, but not contradictory to the present definitions. The present approach includes both the situations (1) of estimating errors and the uncertainty of those estimates and (2) of estimating uncertainties only. Richardson extrapolation (RE) is used for verification, which is not new; however, the present generalizations for J input parameters and concept of correction factors based on analytical benchmarks, which provides a quantitative metric to determine proximity of the solutions to the asymptotic range, accounts for the effects of higher-order terms, and are used for defining and estimating errors and uncertainties constitute a new approach. The use of quantitative estimates for errors and the use of uncertainties for those estimates also constitute a new approach in verification and validation.

Part 1 of this two-part paper presents the verification and validation methodology and procedures. In Section 2, the overall verification and validation methodology is presented by providing concepts, definitions, and equations for the simulation numerical and modeling errors and uncertainties. In Section 3, detailed verification procedures for estimation of various sub-components of the simulation numerical error and uncertainty are given. In Section 4, validation procedures are given including a discussion of the interpretation of validation results and use of corrected simulation results. Finally, conclusions are provided in Section 5. Part 2 provides an example for RANS simulations for a cargo/container ship where issues with regard to practical application of the methodology and procedures and interpretation of verification and validation results are discussed (Wilson et al. [12]). Present papers are based on Stern et al. [13], which is sometimes referenced for additional details. However, presentation and expanded discussions of verification procedures and implementation were improved based on nearly two years experience with present approach, especially through ITTC community and Gothenburg 2000 Workshop on CFD in Ship Hydrodynamics.

2 Overall Verification and Validation Methodology

In Section 2.1, the overall verification and validation methodology is presented by providing key concepts, definitions, and derivation of equations for the simulation error and uncertainty, as sum and root-sum-square (RSS) of simulation numerical and modeling errors and uncertainties, respectively. The verification and validation equations are derived in Sections 2.2 and 2.3, respectively, where subcomponents of the simulation numerical error are identified and an approach for assessing the simulation modeling uncertainty is presented.

2.1 Concepts and Definitions. Accuracy indicates the closeness of agreement between a simulation/experimental value of a quantity and its true value. Error δ is the difference between a simulation value or an experimental value and the truth. Accuracy increases as error approaches zero. The true values of simulation/experimental quantities are rarely known. Thus, errors must be estimated. An uncertainty U is an estimate of an error such that the interval $\pm U$ contains the true value of δ 95 times out of 100. An uncertainty interval thus indicates the range of likely magnitudes of δ but no information about its sign.

For simulations, under certain conditions, errors can be estimated including both sign and magnitude (referred to as an error estimate δ^*). Then, the uncertainty considered is that corresponding to the error in δ^*. When δ^* is estimated, it can be used to obtain a corrected value of the variable of interest.

Sources of errors and uncertainties in results from simulations can be divided into two distinct sources: modeling and numerical. Modeling errors and uncertainties are due to assumptions and approximations in the mathematical representation of the physical problem (such as geometry, mathematical equation, coordinate transformation, boundary conditions, turbulence models, etc.) and incorporation of previous data (such as fluid properties) into the model. Numerical errors and uncertainties are due to numerical solution of the mathematical equations (such as discretization, artificial dissipation, incomplete iterative and grid convergence, lack of conservation of mass, momentum, and energy, internal and external boundary noncontinuity, computer round-off, etc.). The present work assumes that all correlations among errors are zero, which is doubtless not true in all cases, but the effects are assumed negligible for the present analyses.

The simulation error δ_S is defined as the difference between a simulation result S and the truth T. In considering the development and execution of a CFD code, it can be postulated that δ_S is comprised of the addition of modeling and numerical errors

$$\delta_S = S - T = \delta_{SM} + \delta_{SN} \tag{1}$$

Support for this postulation is provided by using the model value M in definitions for modeling and numerical errors. The simulation modeling error $\delta_{SM} = M - T$ is defined as the difference between the true T and model M values while the simulation numerical error $\delta_{SN} = S - M$ is defined as the difference between the simulation S and model M values. The simulation S and model M values are obtained by numerical and exact solutions of the continuous equations used to model the truth, respectively. Since exact solution of nonlinear equations is seldom possible, approximations are used to replace the continuous modeled equations with discrete ones that are solved algebraically with a CFD code to yield the simulation value S.

The uncertainty equation corresponding to error equation (1) is

$$U_S^2 = U_{SM}^2 + U_{SN}^2 \tag{2}$$

where U_S is the uncertainty in the simulation and U_{SM} and U_{SN} are the simulation modeling and numerical uncertainties.

For certain conditions, the numerical error δ_{SN} can be considered as

$$\delta_{SN} = \delta_{SN}^* + \varepsilon_{SN} \tag{3}$$

where δ_{SN}^* is an estimate of the sign and magnitude of δ_{SN} and ε_{SN} is the error in that estimate (and is estimated as an uncertainty since only a range bounding its magnitude and not its sign can be estimated). The corrected simulation value S_C is defined by

$$S_C = S - \delta_{SN}^* \tag{4}$$

with error equation

$$\delta_{S_C} = S_C - T = \delta_{SM} + \varepsilon_{SN} \tag{5}$$

The uncertainty equation corresponding to error equation (5) is

$$U_{S_C}^2 = U_{SM}^2 + U_{S_C N}^2 \tag{6}$$

where U_{S_C} is the uncertainty in the corrected simulation and $U_{S_C N}$ is the uncertainty estimate for ε_{SN}.

Debate on verification and validation has included discussion on whether errors such as δ_{SN} are deterministic or stochastic, and thus how they should be treated in uncertainty analysis was unclear. In the ''corrected'' approach given by Eqs. (3)–(6), a deterministic estimate δ_{SN}^* of δ_{SN} and consideration of the error ε_{SN} in that estimate are used. The approach is analogous to that in EFD when an asymmetric systematic uncertainty is ''zero-centered'' by inclusion of a model for the systematic error in the data reduction equation and then the uncertainty considered is that associated with the model (Coleman and Steele [7]). In the ''uncorrected''

approach given by Eqs. (1)–(2), any particular δ_{SN} is considered as a single realization from some parent population of δ_{SN}'s and the uncertainty U_{SN} is interpreted accordingly in analogy to the estimation of uncertainties in EFD (with a similar argument for ε_{SN} and U_{S_CN}). Oberkamp and Trucano [14] have criticized Coleman and Stern [6] for treating U_{SN} statistically; however, the present approach is well justified both conceptually and mathematically for reasons just given.

The overall CFD verification and validation procedures can be conveniently grouped in four consecutive steps. The first step is preparation, which involves selection of the CFD code and specification of objectives, geometry, conditions, and available benchmark information. The objectives might be prediction of certain variables at certain levels of validation (e.g., programmatic validation requirements U_{reqd}). The variables can either be integral (e.g., resistance) or point (e.g., mean velocities and turbulent Reynolds stresses) values and the programmatic validation requirements may be different for each variable. The second and third steps are verification and validation, which are described in Sections 2.2 and 2.3. The fourth step is documentation, which is detailed presentation of the CFD code (equations, initial and boundary conditions, modeling, and numerical methods), objectives, geometry, conditions, verification, validation, and analysis.

2.2 Verification. Verification is defined as a process for assessing *s*imulation *n*umerical uncertainty U_{SN} and, when conditions permit, estimating the sign and magnitude δ^*_{SN} of the simulation numerical error itself and the uncertainty in that error estimate. For many CFD codes, the most important numerical errors and uncertainties are due to use of iterative solution methods and specification of various input parameters such as spatial and time step sizes and other parameters (e.g., artificial dissipation). The errors and uncertainties are highly dependent on the specific application (geometry and conditions).

The errors due to specification of input parameters are decomposed into error contributions from iteration number δ_I, grid size δ_G, time step δ_T, and other parameters δ_P, which gives the following expressions for the simulation numerical error and uncertainty

$$\delta_{SN} = \delta_I + \delta_G + \delta_T + \delta_P = \delta_I + \sum_{j=1}^{J} \delta_j \tag{7}$$

$$U^2_{SN} = U^2_I + U^2_G + U^2_T + U^2_P = U^2_I + \sum_{j=1}^{J} U^2_j \tag{8}$$

Similarly, error estimates δ^* can be decomposed as

$$\delta^*_{SN} = \delta^*_I + \sum_{j=1}^{J} \delta^*_j \tag{9}$$

which gives the following expressions for the corrected simulation and corrected simulation numerical uncertainty

$$S_C = S - \left(\delta^*_I + \sum_{j=1}^{J} \delta^*_j \right) = T + \delta_{SM} + \varepsilon_{SN} \tag{10}$$

$$U^2_{S_CN} = U^2_{I_C} + \sum_{j=1}^{J} U^2_{j_C} \tag{11}$$

Verification is based on equation (10), which is put in the form

$$S = S_C + \left(\delta^*_I + \sum_{j=1}^{J} \delta^*_j \right) \tag{12}$$

Equation (12) expresses S as the corrected simulation value S_C plus numerical errors. S_C is also referred to as a numerical benchmark since it is equal, as shown by Eq. (10), to the truth plus simulation modeling error and presumable small error ε_{SN} in the estimate of the numerical error δ^*_{SN}.

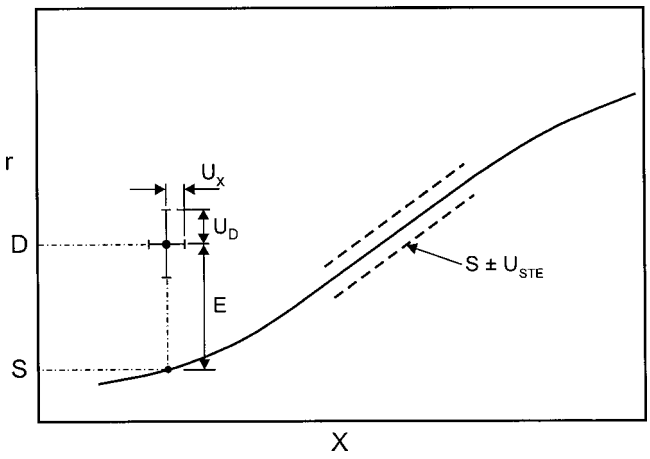

Fig. 1 Definition of comparison error.

2.3 Validation. Validation is defined as a process for assessing simulation modeling uncertainty U_{SM} by using benchmark experimental data and, when conditions permit, estimating the sign and magnitude of the modeling error δ_{SM} itself. Thus, the errors and uncertainties in the experimental data must be considered in addition to the numerical errors and uncertainties discussed in Section 3. Approaches to estimating experimental uncertainties are presented and discussed by Coleman and Steele [7].

The validation methodology of Coleman and Stern [6] which properly takes into account the uncertainties in both the simulation and the experimental data is discussed in this section for both approaches of treating the numerical error as stochastic and as deterministic.

The validation comparison is shown in Fig. 1. The experimentally determined r-value of the (X_i, r_i) data point is D and simulated r-value is S. Recall from Eq. (1) that the simulation error δ_S is the difference between S and the truth T. Similarly, the error δ_D in the data is the difference between D and the truth T, so setting the simulation and experimental truths equal results in

$$D - \delta_D = S - \delta_S \tag{13}$$

The comparison error E is defined as the difference of D and S

$$E = D - S = \delta_D - \delta_S = \delta_D - (\delta_{SMA} + \delta_{SPD} + \delta_{SN}) \tag{14}$$

with δ_{SM} decomposed into the sum of δ_{SPD}, error from the use of *p*revious *d*ata such as fluid properties, and δ_{SMA}, error from *m*odeling *a*ssumptions. Thus E is the resultant of *all* the errors associated both with the experimental data and with the simulation. For the approach in which no estimate δ^*_{SN} of the sign and magnitude of δ_{SN} is made, all of these errors are estimated with uncertainties.

If (X_i, r_i), and S share no common error sources, then the uncertainty U_E in the comparison error can be expressed as

$$U^2_E = \left(\frac{\partial E}{\partial D} \right)^2 U^2_D + \left(\frac{\partial E}{\partial S} \right)^2 + U^2_S = U^2_D + U^2_S \tag{15}$$

or

$$U^2_E = U^2_D + U^2_{SMA} + U^2_{SPD} + U^2_{SN} \tag{16}$$

Ideally, one would postulate that if the absolute value of E is less than its uncertainty U_E, then validation is achieved (i.e., E is "zero" considering the resolution imposed by the "noise level" U_E). In reality, there is no known approach that gives an estimate of U_{SMA}, so U_E cannot be estimated. That leaves a more stringent

validation test as the practical alternative. If the validation uncertainty U_V is defined as the combination of all uncertainties that we know how to estimate (i.e., all but U_{SMA}), then

$$U_V^2 = U_E^2 - U_{SMA}^2 = U_D^2 + U_{STE}^2 \tag{17}$$

where $U_{STE}^2 = U_{SPD}^2 + U_{SN}^2$ is the total estimated simulation uncertainty, as shown in Fig. 1.

If $|E|$ is less than the validation uncertainty U_V, the combination of all the errors in D and S is smaller than the estimated validation uncertainty and validation has been achieved at the U_V level. U_V is the key metric in the validation process. U_V is the validation ''noise level'' imposed by the uncertainties inherent in the data, the numerical solution, and the previous experimental data used in the simulation model. It can be argued that one cannot discriminate once $|E|$ is less than this; that is, as long as $|E|$ is less than this, one cannot evaluate the effectiveness of proposed model ''improvements.'' On the other hand, if $|E| \gg U_V$ one could argue that probably $E \approx \delta_{SMA}$.

Oberkamp and Trucano [14] have criticized Coleman and Stern [6] for fact that U_V excludes U_{SMA}. As already acknowledged, there is no known way for directly estimating U_{SMA}. However, the present approach does provide a more stringent validation metric U_V which sets the level that validation can be achieved as the root sum square of the experimental U_D and the total estimated simulation U_{STE} uncertainties. Additionally, under certain conditions, the simulation modeling error δ_{SMA} itself can be estimated, as further discussed in Section 4. Consideration of Eq. (17) shows that (1) the more uncertain the data (greater U_D) and/or (2) the more inaccurate the code (greater U_{STE}), the easier it is to validate a code, since the greater the uncertainties in the data and code predictions, the greater the noise level U_V. Both Roache [3] and Oberkamp and Trucano [14] have criticized Coleman and Stern [6] for this fact. However, if the value of U_V is greater than that designated as necessary in a research/design/development program, the required *level of validation* could not be achieved without improvement in the quality of the data, the code, or both. Also, if U_{SN} and U_{SPD} are not estimated, but $|E|$ is less than U_D, then a type of validation can be argued to have been achieved, but clearly as shown by the present methodology, at an unknown level.

If the ''corrected'' approach of Eqs. (3)–(6) is used, then the equations, equivalent to Eqs. (14) and (17) are

$$E_C = D - S_C = \delta_D - (\delta_{SMA} + \delta_{SPD} + \varepsilon_{SN}) \tag{18}$$

for the corrected comparison error and

$$U_{V_C}^2 = U_{E_C}^2 - U_{SMA}^2 = U_D^2 = U_D^2 + U_{S_C TE}^2 \tag{19}$$

for the corrected validation uncertainty where $U_{S_C TE}^2 = U_{SPD}^2 + U_{S_C N}^2$ is the total estimated corrected simulation uncertainty, also shown in Fig. 1. Note that S_C and E_C can be either larger or smaller than their counterparts S and E, but U_{E_C} and U_{V_C} should be smaller than U_E and U_V, respectively, since $U_{S_C N}$ should be smaller than U_{SN}.

If there is a programmatic validation requirement, there is another uncertainty U_{reqd} that must be considered since validation is required at that uncertainty level or below. Interpretation of the meaning of the relative magnitudes of E (or E_C), U_{reqd} and U_V (or U_{V_C}) and of the implications on the possibility of estimating δ_{SMA} are discussed in Section 4. Additional discussion is provided in Coleman and Stern [6] on: estimating U_{SPD}; estimating U_D for the data point (X_i, r_i), including both the experimental uncertainty in r_i and the additional uncertainties in r_i arising from the experimental uncertainties in the measurements of the n independent variables $(X_j)_i$ in X_i; and for validation of a CFD code, multiple codes and/or models, and prediction of trends.

3 Verification Procedures

In Section 2, the simulation numerical error and uncertainty were decomposed into contributions from iteration number, grid size, time step, and other parameters in Eqs. (7) and (8). In this section, detailed verification procedures are given for estimation of these contributions through convergence studies (Section 3.1). Iterative (Section 3.2) and parameter (Sections 3.3–3.5) convergence studies are conducted using multiple solutions with systematic parameter refinement to estimate numerical errors and uncertainties. Three convergence conditions are possible: (*i*) monotonic convergence; (*ii*) oscillatory convergence; and (*iii*) divergence and are described in Sections 3.3, 3.4, and 3.5, respectively. For condition (*i*), as already mentioned, errors and uncertainties are estimated using generalized RE. For condition (*ii*), uncertainties are estimated simply by attempting to bound error based on oscillation maximums and minimums. For condition (*iii*), errors and uncertainties cannot be estimated. As discussed below and later in Section 5, there are many issues in estimating errors and uncertainties for practical applications.

3.1 Convergence Studies. Iterative and parameter convergence studies are conducted using multiple (m) solutions and systematic parameter refinement by varying the kth input parameter Δx_k while holding all other parameters constant. The present work assumes input parameters can be expressed such that the finest resolution corresponds to the limit of infinitely small parameter values. Many common input parameters are of this form, e.g., grid spacing, time step, and artificial dissipation. Additionally, a uniform parameter refinement ratio $r_k = \Delta x_{k_2}/\Delta x_{k_1} = \Delta x_{k_3}/\Delta x_{k_2} = \Delta x_{k_m}/\Delta x_{k_{m-1}}$ between solutions is assumed for presentation purposes, but not required as discussed later.

Careful consideration should be given to selection of uniform parameter refinement ratio. The most appropriate values for industrial CFD are not yet fully established. Small values (i.e., very close to one) are undesirable since solution changes will be small and sensitivity to input parameter may be difficult to identify compared to iterative errors. Large values alleviate this problem; however, they also may be undesirable since the finest step size may be prohibitively small (i.e., require many steps) if the coarsest step size is designed for sufficient resolution such that similar physics are resolved for all m solutions. Also, similarly as for small values, solution changes for the finest step size may be difficult to identify compared to iterative errors since iterative convergence is more difficult for small step size. Another issue is that for parameter refinement ratio other than $r_k = 2$, interpolation to a common location is required to compute solution changes, which introduces interpolation errors. Roache [3] discusses methods for evaluating interpolation errors. However, for industrial CFD, $r_k = 2$ may often be too large. A good alternative may be $r_k = \sqrt{2}$, as it provides fairly large parameter refinement ratio and at least enables prolongation of the coarse-parameter solution as an initial guess for the fine-parameter solution.

Equation (12) is written for the *kth* parameter and *mth* solution as

$$S_{k_m} = S_C + \delta^*_{I_{k_m}} + \delta^*_{k_m} + \sum_{j=1, j\neq k}^{f} \delta^*_{j_m} \tag{20}$$

Iterative convergence must be assessed and S_{k_m} corrected for iterative errors prior to evaluation of parameter convergence since the level of iterative convergence may not be the same for all m solutions used in the parameter convergence studies. Equation (20) shows that iterative errors $\delta^*_{I_{k_m}}$ must be accurately estimated or negligible in comparison to $\delta^*_{k_m}$ for accurate convergence studies and that they should be considered within the context of convergence studies for each input parameter. Methods for estimating U_I or δ^*_I and U_{I_C} are described in Section 3.2.2.

With $\delta^*_{I_{k_m}}$ evaluated, S_{k_m} is corrected for iterative errors as

$$\hat{S}_{k_m} = S_{k_m} - \delta^*_{I_{k_m}} = S_C + \delta^*_{k_m} + \sum_{j=1, j\neq k}^{J} \delta^*_{j_m} \tag{21}$$

$\hat{S}_{k_m}$ can be calculated for both integral (e.g., resistance coefficients) and point (e.g., surface pressure, wall-shear stress, and velocity) variables. $\hat{S}_{k_m}$ can be presented as an absolute quantity (i.e., non-normalized) or normalized with the solution as a percentage change; however, if the solution value is small, a more appropriate normalization may be the range of the solution.

Convergence studies require a minimum of $m=3$ solutions to evaluate convergence with respect to input parameter. Note that $m=2$ is inadequate, as it only indicates sensitivity and not convergence, and that $m>3$ may be required. Consider the situation for 3 solutions corresponding to fine $\hat{S}_{k_1}$, medium $\hat{S}_{k_2}$, and coarse $\hat{S}_{k_3}$ values for the *kth* input parameter. Solution changes ε for medium-fine and coarse-medium solutions and their ratio R_k are defined by

$$\begin{aligned} \varepsilon_{k_{21}} &= \hat{S}_{k_2} - \hat{S}_{k_1} \\ \varepsilon_{k_{32}} &= \hat{S}_{k_3} - \hat{S}_{k_2} \\ R_k &= \varepsilon_{k_{21}} / \varepsilon_{k_{32}} \end{aligned} \tag{22}$$

Three convergence conditions are possible:

$$\begin{aligned} &(i)\ \text{Monotonic convergence:} \quad 0<R_k<1 \\ &(ii)\ \text{Oscillatory convergence:} \quad R_k<0^1 \\ &(iii)\ \text{Divergence:} \quad R_k>1 \end{aligned} \tag{23}$$

For monotonic convergence (*i*), generalized RE is used to estimate U_k or δ^*_k and U_{k_C}. Methods for estimating errors and uncertainties for condition (*i*) are described in Section 3.3.

For oscillatory convergence (*ii*), the solutions exhibit oscillations, which may be erroneously identified as condition (*i*) or (*iii*). This is apparent if one considers evaluating convergence condition from three points on a sinusoidal curve (Coleman et al. [15]). Depending on where the three points fall on the curve, the condition could be incorrectly diagnosed as either monotonic convergence or divergence. Methods discussed here for estimating uncertainties U_k for condition (*ii*) require more than $m=3$ solutions and are described in Section 3.4.

For divergence (*iii*), the solutions diverge and errors and uncertainties cannot be estimated. Additional remarks are given in Section 3.5.

Determination of the convergence ratio R_k for point variables can be problematic since solution changes $\varepsilon_{k_{21}}$ and $\varepsilon_{k_{32}}$ can both go to zero (e.g., in regions where the solution contains an inflection point). In this case, the ratio becomes ill conditioned. However, the convergence ratio can be used in regions where the solution changes are both non-zero (e.g., local solution maximums or minimums). Another approach is to use a global convergence ratio R_k, which overcomes ill conditioning, based on the L2 norm of the solution changes, i.e., $\langle R_k \rangle = \|\varepsilon_{k_{21}}\|_2 / \|\varepsilon_{k_{32}}\|_2$. $\langle\ \rangle$ is used to denote an averaged value and $\|\varepsilon\|_2 = [\sum_{i=1}^{N} \varepsilon_i^2]^{1/2}$ denotes the L2 norm of solution change over the N points in the region of interest. Caution should be exercised when defining the convergence ratio from the ratio of the L2 norm of solution changes because the oscillatory condition ($R_k<1$) cannot be diagnosed since $\langle R_k \rangle$ will always be greater than zero. Local values of R_k at solution maximums or minimums should also be examined to confirm the convergence condition based on an L2 norm definition. An alternate approach suggested by Hoekstra et al. [16] is to transform the spatial profile to wave number space and to perform a convergence study on the amplitude distribution of the Fourier modes. In principle, this approach would remove the problem of ill-conditioning of the convergence ratio, R_k.

3.2 Iterative Convergence. The number of order magnitude drop and final level of solution residual (or residual imbalance) can be used to determine stopping criteria for iterative solution techniques. Iterative convergence to machine zero is desirable, but for complex geometry and conditions it is often not possible. Three or four orders of magnitude drop in solution residual to a level of 10^{-4} is more likely for these cases. Methods for estimation of iterative errors and uncertainties can be based on graphical, as discussed below, or theoretical approaches and are dependent on the type of iterative convergence: (*a*) oscillatory; (*b*) convergent; or (*c*) mixed oscillatory/convergent.

For oscillatory iterative convergence (*a*), the deviation of the variable from its mean value provides estimates of the iterative uncertainty based on the range of the maximum S_U and minimum S_L values

$$U_I = \left| \frac{1}{2}(S_U - S_L) \right| \tag{24}$$

For convergent iterative convergence (*b*), a curve-fit of an exponential function can be used to estimate U_I or δ^*_I and U_{I_C} as the difference between the value and the exponential function from a curve fit for large iteration number CF_∞

$$\begin{aligned} U_I &= |S - CF_\infty| \\ \delta^*_{I_{k_m}} &= S - CF_\infty, U_{I_C} = 0 \end{aligned} \tag{25}$$

For mixed convergent/oscillatory iterative convergence (*c*), the amplitude of the solution envelope decreases as the iteration number increases, the solution envelope is used to define the maximum S_U and minimum S_L values in the Ith iteration, and to estimate U_I or δ^*_I and U_{I_C}

$$\begin{aligned} U_I &= \left| \frac{1}{2}(S_U - S_L) \right| \\ \delta^*_{I_{k_m}} &= S - \frac{1}{2}(S_U - S_L), U_{I_C} = 0 \end{aligned} \tag{26}$$

An increase in the amplitude of the solution envelope as the iteration number increases indicates that the solution is divergent.

Estimates of the iterative error based on theoretical approaches are presented in Ferziger and Peric [17] and involve estimation of the principal eigenvalue of the iteration matrix. The approach is relatively straightforward when the eigenvalue is real and the solution is convergent. For cases in which the principal eigenvalue is complex and the solution is oscillatory or mixed, the estimation is not as straightforward and additional assumptions are required.

3.3 Monotonic Convergence: Generalized Richardson Extrapolation. For monotonic convergence, i.e., condition (*i*) in Eq. (23), generalized RE is used to estimate U_k or δ^*_k and U_{k_C}. RE is generalized for J input parameters and concept of correction factors based on analytical benchmarks is introduced. More detailed derivations are provided by Stern et al. [13].

As already mentioned, since Stern et al. [13] there has been nearly two years experience with present approach, especially through ITTC community and Gothenburg 2000 Workshop on CFD in Ship Hydrodynamics. In particular, detailed verification procedures have been the focus of attention (Eca and Hoekstra [18]; Ebert and Gorski [19]). After some background for generalized RE is given, two approaches for estimating errors and uncertainties are presented and are based on (*i*) correction factors proposed in the current paper and (*ii*) factor of safety approach proposed by Roache (1998). Finally, a discussion of fundamental and practical issues for verification is provided.

[1] As discussed in the text that follows, $0<R_k<1$ and $R_k>1$ may also occur for the oscillatory condition.

Background for Generalized RE. Generalized RE begins with Eq. (21). The error terms on the right-hand side of Eq. (21) are of known form (i.e., power series expansion with integer powers of Δx_k) based on analysis of the modified and numerical error equations which is written below as a finite sum (i.e., error estimate) and for the kth parameter and mth solution

$$\delta^*_{k_m} = \sum_{i=1}^{n} (\Delta x_{k_m})^{p_k^{(i)}} g_k^{(i)} \tag{27}$$

n = number of terms retained in the power series, powers $p_k^{(i)}$ correspond to order of accuracy (for the ith term), and $g_k^{(i)}$ are referred to as "grid" functions which are a function of various orders and combinations of derivatives of S with respect to x_k. It is assumed that the power series in Eq. (27) is convergent (i.e., the finite sum convergence to the infinite series value as more terms are included). Substituting Eq. (27) into Eq. (21) results in

$$\hat{S}_{k_m} = S_C + \sum_{i=1}^{n} (\Delta x_{k_m})^{p_k^{(i)}} g_k^{(i)} + \sum_{j=1, j\neq k}^{J} \delta^*_{j_m} \tag{28}$$

Subtraction of multiple solutions where input parameter Δx_k is uniformly refined eliminates the $\delta^*_{j_m}$ terms in Eq. (28) since $\delta^*_{j_m}$ is independent of Δx_k and provides equations for S_C, $p_k^{(i)}$, and $g_k^{(i)}$. This assumes $p_k^{(i)}$ and $g_k^{(i)}$ are also independent of Δx_k. Since each term (i) contains 2 unknowns, $m = 2n+1$ solutions are required to estimate the numerical benchmark S_C and the first n terms in the expansion in Eq. (28) (i.e., for $n=1$, $m=3$ and for $n=2$, $m=5$, etc). The accuracy of the estimates depends on how many terms are retained in Eq. (27), the magnitude (importance) of the higher-order terms, and the validity of the assumption that $p_k^{(i)}$ and $g_k^{(i)}$ are independent of Δx_k. For sufficiently small Δx_k, the solutions are in the asymptotic range such that higher-order terms are negligible and the assumption that $p_k^{(i)}$ and $g_k^{(i)}$ are independent of Δx_k is valid. However, achieving the asymptotic range for practical geometry and conditions is usually not possible and $m>3$ is undesirable from a resources point of view; therefore, methods are needed to account for effects of higher-order terms for practical application of RE. Additionally, methods may be needed to account for possible dependence of $p_k^{(i)}$ and $g_k^{(i)}$ on Δx_k, although not addressed herein. Usually δ^*_k is estimated for the finest value of the input parameter, i.e., $\delta^*_k = \delta^*_{k_1}$ corresponding to the finest solution S_{k_1}.

With three solutions ($m=3$), only the leading-order term of Eq. (27) can be estimated. Solution of the three equations for S_C, $p_k^{(i)}$, and $g_k^{(i)}$ yields estimates for the error $\delta^*_{k_1}$ and order-of-accuracy p_k

$$\delta^*_{k_1} = \delta^*_{RE_{k_1}} = \frac{\varepsilon_{k_{21}}}{r_k^{p_k} - 1} \tag{29}$$

$$p_k = \frac{\ln(\varepsilon_{k_{32}}/\varepsilon_{k_{21}})}{\ln(r_k)} \tag{30}$$

Solving for the first-order term is relatively easy since evaluation of Eqs. (29) and (30) only requires that the $m=3$ solutions are monotonically convergent, even if the solutions are far from the asymptotic range and Eqs. (29) and (30) are inaccurate. With solutions from five systematically refined input parameters ($m=5$), more complicated expressions can be derived to estimate the first two terms of the power series expansion. However, their range of applicability is more restrictive since all five solutions must be both monotonically convergent *and* sufficiently close to the asymptotic range for the expressions to be used.

As previously mentioned, solutions from three values of input parameter where the refinement ratio between the medium and fine input parameters $r_{k_{21}}$ is not equal to that between coarse and medium input parameters $r_{k_{32}}$ can be used to estimate $\delta^*_{k_1}$ from Eq. (29), provided that Eq. (30) for estimating order of accuracy is modified as

$$p_k = \frac{\ln(\varepsilon_{k_{32}}/\varepsilon_{k_{21}})}{\ln(r_{k_{21}})} + \frac{1}{\ln(r_{k_{21}})}[\ln(r_{k_{32}}^{p_k} - 1) - \ln(r_{k_{21}}^{p_k} - 1)] \tag{31}$$

For situations when $r_{k_{21}} \neq r_{k_{32}}$, Eq. (31) is a transcendental equation implicitly defining p_k and must be solved iteratively. If $r_{k_{21}} = r_{k_{32}}$, Eq. (31) degenerates to Eq. (30).

Estimating Errors and Uncertainties Using Generalized RE With Correction Factors. Results from the numerical solution of the one-dimensional (1D) wave and two-dimensional (2D) Laplace equation analytical benchmarks show that Eq. (29) has the correct form, but the order of accuracy is poorly estimated by Eq. (30) except in the asymptotic range. Analysis of the results suggests the concept of correction factors, which provide a quantitative metric to determine proximity of the solutions to the asymptotic range, account for the effects of higher-order terms, and are used for defining and estimating errors and uncertainties. Details are provided in Appendix A.

Multiplication of Eq. (29) by a correction factor C_k provides an estimate for $\delta^*_{k_1}$ accounting for the effects of higher-order terms

$$\delta^*_{k_1} = C_k \delta^*_{RE_{k_1}} = C_k \left(\frac{\varepsilon_{k_{21}}}{r_k^{p_k} - 1} \right) \tag{32}$$

If solutions are in the asymptotic range, correction of Eq. (29) is not required [i.e., $C_k = 1$ so that Eqs. (29) and (32) are equivalent]. For solutions outside the asymptotic range, $C_k < 1$ or $C_k > 1$ indicates that the leading-order term over predicts (higher-order terms net negative) or under predicts (higher-order terms net positive) the error, respectively. The estimate given by Eq. (32) includes both sign and magnitude and is used to estimate U_k or δ^*_k and U_{k_C} depending on how close the solutions are to the asymptotic range (i.e., how close C_k is to 1) and one's confidence in Eq. (32). There are many reasons for lack of confidence, especially for complex three-dimensional flows.

For C_k sufficiently less than or greater than 1 and lacking confidence, U_k is estimated, but not δ^*_k and U_{k_c}. Equation (32) is used to estimate the uncertainty by bounding the error δ^*_k by the sum of the absolute value of the corrected estimate from RE and the absolute value of the amount of the correction

$$U_k = |C_k \delta^*_{RE_{k_1}}| + |(1 - C_k)\delta^*_{RE_{k_1}}| \tag{33}$$

For C_k sufficiently close to 1 and having confidence, δ^*_k and U_{k_c} are estimated. Equation (32) is used to estimate the error δ^*_k, which can then also be used in the calculation of S_c [in Eq. (10)]. The uncertainty in the error estimate is based on the amount of the correction

$$U_{k_C} = |(1 - C_k)\delta^*_{RE_{k_1}}| \tag{34}$$

Note that in the limit of the asymptotic range, $C_k = 1$, $\delta^*_k = \delta^*_{k_1} = \delta^*_{RE_{k_1}}$, and $U_{k_C} = 0$.

Two definitions for the correction factor were developed. The first is based on solution of Eq. (32) for C_k with $\delta^*_{RE_{k_1}}$ based on Eq. (29) but replacing p_k with the improved estimate $p_{k_{est}}$

$$C_k = \frac{r_k^{p_k} - 1}{r_k^{p_{k_{est}}} - 1} \tag{35}$$

Similarly, the second is based on a two-term estimate of the power series which is used to estimate $\delta^*_{RE_{k_1}}$ where p_k and q_k are replaced with $p_{k_{est}}$ and $q_{k_{est}}$

$$C_k = \frac{(\varepsilon_{k_{23}}/\varepsilon_{k_{12}} - r_k^{q_{k_{est}}})(r_k^{p_k}-1)}{(r_k^{p_{k_{est}}} - r_k^{q_{k_{est}}})(r_k^{p_{k_{est}}}-1)} + \frac{(\varepsilon_{k_{23}}/\varepsilon_{k_{12}} - r_k^{p_{k_{est}}})(r_k^{p_k}-1)}{(r_k^{p_{k_{est}}} - r_k^{q_{k_{est}}})(r_k^{q_{k_{est}}}-1)} \tag{36}$$

$p_{k_{est}}$ and $q_{k_{est}}$ are estimates for limiting orders of accuracy of the first and second terms of the error expansion equation (27) as spacing size goes to zero and the asymptotic range is reached. Equation (35) roughly accounts for the effects of higher-order terms by replacing p_k with $p_{k_{est}}$ thereby providing an improved single-term estimate. Equation (36) more rigorously accounts for higher-order terms since it is derived from the two-term estimate with first and second term order of accuracy $p_k^{(1)}$ and $p_k^{(2)}$ replaced by $p_{k_{est}}$ and $q_{k_{est}}$. Equation (36) simplifies to Eq. (35) in the limit of the asymptotic range. Both correction factors only require solutions for three parameter values. The estimated values $p_{k_{est}}$ and $q_{k_{est}}$ can be based either on the assumed theoretical order of accuracy $p_{k_{th}}$ and $q_{k_{th}}$ or solutions for simplified geometry and conditions. In either case, preferably including the effects of grid stretching.

In Appendix A, exact (A) and numerical (S) solutions are used to compare the true simulation error ($A-S$) to (*i*) an uncorrected three-grid error estimate using Eq. (29) and (*ii*) corrected estimates based on Eq. (32) with correction factor defined by Eq. (35) or (36). Correction of error estimates with both definitions of C_k results in improved error estimates. Also, uncertainty estimates using Eq. (33) with correction factor defined by Eq. (35) or (36) are shown to bound the true simulation error ($A-S$), while uncertainty estimates using Eq. (34) are shown to bound the difference between the corrected solution and the truth (S_c-T). Additional testing of expressions for C_k given by Eqs. (35) and (36) is needed and development of improved expressions within the proposed general framework is certainly possible.

Estimating Uncertainties Using Generalized RE With Factors of Safety. In Roache [3], a GCI approach is proposed where a standard three-grid error estimate from RE is multiplied by a factor of safety F_S to bound the simulation error

$$U_k = F_S |\delta^*_{RE_{k_1}}| \tag{37}$$

Note that Eq. (37) with factor of safety differs significantly from Eq. (34). Herein $C_k = C_k(\varepsilon, r_k, p_k, p_{k_{est}}, q_{k_{est}})$, in contrast to Eq. (37) where C_k is a constant referred to as a factor of safety F_S. The exact value for factor of safety is somewhat ambiguous and Roache [3] recommends 1.25 for careful grid studies and 3 for cases in which only two grids are used.

Although not proposed in Roache [3], the factor of safety approach can be used for situations where the solution is corrected with an error estimate from RE. Equation (29) is used to estimate δ^*_k and the uncertainty in that error estimate is given by

$$U_{k_C} = (F_S - 1)|\delta^*_{RE_{k_1}}| \tag{38}$$

With this approach, a fixed percentage of a three-grid error estimate (e.g., 25% $\delta^*_{RE_{k_1}}$ for $F_S = 1.25$) is used to define the uncertainty of the error estimate regardless of how close solutions are to the asymptotic range.

Discussion of Fundamental and Practical Issues. Fundamental and practical issues for verification are discussed in this section. Fundamental issues include convergence of power series equation (27), assumptions that $p_k^{(i)}$ and $g_k^{(i)}$ are independent of Δx_k, and estimating $p_{k_{est}}$. Solution of analytical benchmarks has been used to address some of these fundamental issues while others need further research. Although both correction factor and factor of safety approaches were presented, the authors advocate the use of former. Results from the numerical solution of analytic benchmarks show that the factor of safety approach is overly conservative, especially when the solutions approach the asymptotic range (Appendix A). This is in contrast to the variable correction factor approach proposed in Eqs. (33) and (34), where the uncertainty in the error estimate correctly goes to zero as the asymptotic range is approached because $C_k \to 1$. Admittedly, others have recommended the factor of safety approach, e.g., Eca and Hoekstra [18], although examination of their results as with our own analysis indicates that such estimates are overly conservative.

For practical applications, especially complex flows with relatively coarse grids, solutions may be far from asymptotic range such that some variables are convergent while others are oscillatory or even divergent. Order of accuracy and therefore correction factors and factors of safety may display large variability indicating the need for finer grids. Clearly, more than 3 grids are required to estimate errors and uncertainties for such cases. Eca and Hoekstra [18] suggest a least-squares approach to estimate the error by computing the three unknown parameters from RE when more than three solutions are available. The behavior of the asymptotic range was successfully demonstrated for simpler analytical benchmarks in Appendix A. However, the existence and behavior of the asymptotic range for practical problems has not been demonstrated due to lack of sufficiently refined grids, number of solutions to assess variability, and available resources, among other issues. Another practical issue involves selecting and maintaining appropriate parameter refinement ratio and resources for obtaining solutions with sufficient parameter refinement as well as number of solutions. Lastly, interpretation of results is an issue since, as already mentioned, there is limited experience and no known solutions for practical applications in the asymptotic range for guidance.

The present verification procedures represent the most rational approach presently known. However, alternative strategies for including effects of higher-order terms may be just as viable, e.g., treatment of the power series exponents as known integers as proposed by Oberkampf and investigated by Eca and Hoekstra [18]. Once available, improved verification procedures can be easily incorporated into the present overall verification and validation methodology. These issues are discussed further in Section 5 Conclusions and Recommendations and in Part 2 (Wilson et al. [12]).

3.4 Oscillatory Convergence. For oscillatory convergence, i.e., condition (*ii*) in Eq. (23), uncertainties can be estimated, but not the signs and magnitudes of the errors. Uncertainties are estimated based on determination of the upper (S_U) and lower (S_L) bounds of solution oscillation, which requires more than $m=3$ solutions. The estimate of uncertainty is based on half the solution range

$$U_k = \frac{1}{2}(S_U - S_L) \tag{39}$$

3.5 Divergence. For divergence, i.e., condition (*iii*) in Eq. (23), errors and or uncertainties can not be estimated. The preparation and verification steps must be reconsidered. Improvements in iterative convergence, parameter specification (e.g., grid quality), and/or CFD code may be required to achieve converging or oscillatory conditions.

4 Validation Procedures

In Section 2, an approach for assessing the simulation modeling uncertainty was presented where for successful validation, the comparison error, E is less than the validation uncertainty, U_V given by Eqs. (17) and (19) for uncorrected and corrected solutions, respectively. In this section, validation procedures are presented through discussions in Section 4.1 on interpretation of

validation results and in Section 4.2 on use of corrected simulation results. As previously mentioned, Coleman and Stern [6] provide additional discussion on validation procedures.

4.1 Interpretation of the Results of a Validation Effort. First, consider the approach in which the simulation numerical error is taken to be stochastic and thus the uncertainty U_{SN} is estimated. From a general perspective, if we consider the three variables U_V, $|E|$, and U_{reqd} there are six combinations (assuming none of the three variables are equal):

$$\begin{aligned} &1.\quad |E|<U_V<U_{reqd} \\ &2.\quad |E|<U_{reqd}<U_V \\ &3.\quad U_{reqd}<|E|<U_V \\ &4.\quad U_V<|E|<U_{reqd} \\ &5.\quad U_V<U_{reqd}<|E| \\ &6.\quad U_{reqd}<U_V<|E| \end{aligned} \tag{40}$$

In cases 1, 2, and 3, $|E|<U_V$; validation is achieved at the U_V level; and the comparison error is below the noise level, so attempting to estimate δ_{SMA} is not feasible from an uncertainty standpoint. In case 1, validation has been achieved at a level below U_{reqd}, so validation is successful from a programmatic standpoint.

In cases 4, 5, and 6, $U_V<|E|$, so the comparison error is above the noise level and using the sign and magnitude of E to estimate δ_{SMA} is feasible from an uncertainty standpoint. If $U_V \ll |E|$, then E corresponds to δ_{SMA} and the error from the modeling assumptions can be determined unambiguously. In case 4, validation is successful at the $|E|$ level from a programmatic standpoint.

Now consider the approach in which the simulation numerical error is taken to be deterministic and thus δ^*_{SN} and the uncertainty U_{V_C} are estimated. A similar set of comparisons as those in Eq. (40) can be constructed using $|E_C|$, U_{V_C}, and U_{reqd}. Since E_C can be larger or smaller than E, but U_{V_C} should always be less than U_V, the results for a given corrected case are not necessarily analogous to those for the corresponding uncorrected case. That is, a variable can be validated in the corrected but not in the uncorrected case, or vice versa. For cases 4, 5, and 6 in which $U_{V_C}<|E_C|$, one can argue that E_C is a better indicator of δ_{SMA} than is E, assuming that one's confidence in using the estimate δ^*_{SN} is not misplaced.

4.2. Use of Corrected Versus Uncorrected Simulation Results. As previously stated in Section 3.3, the requirements for correcting the solution are that the correction factor be close to one and that confidence in solutions exist. Since the variability of the order of accuracy cannot be determined from solutions on three grids, confidence is difficult to establish in this case. As a result, caution should be exercised when correcting solutions using information from only three grids.

If a validation using the corrected approach is successful at a set condition, then if one chooses to associate that validation uncertainty level with the simulation's prediction at a neighboring condition that prediction must also be corrected. That means enough runs are required at the new condition to allow estimation of the numerical errors and uncertainties. If this is not done, then the comparison error E and validation uncertainty U_V corresponding to the use of the uncorrected S and its associated (larger) U_{SN} should be the ones considered in the validation with which one wants to associate the prediction at a new condition. (Whether to and how to associate an uncertainty level at a validated condition with a prediction at a neighboring condition is very much unresolved and is justifiably the subject of much debate at this time.)

5 Conclusions

The present comprehensive approach to verification and validation methodology and procedures sets forth concepts, definitions, and equations derived for simulation errors and uncertainties, which provide a well-founded mathematical framework. The approach should have applicability to a fairly broad range of CFD codes, including RANS, Navier-Stokes, Euler, boundary-element methods, and others. However, clearly much more work is needed for other CFD codes (such as large-eddy simulations), additional error sources, and alternative error and uncertainty estimation methods, e.g., single-grid methods and both results for additional analytical benchmarks (especially for nonlinear equations and using stretched grids) for improved definitions of correction factors and estimates of orders of accuracy, and alternative strategies to account for the effects of higher-order terms in RE. Improved verification procedures once available can be easily incorporated into the present overall verification and validation methodology. Furthermore, more experience is needed through application for different codes and geometry and conditions, especially for practical applications.

As mentioned in the Introduction, present verification and validation methodology and procedures were recommended and used at the recent Gothenburg 2000 Workshop on CFD in Ship Hydrodynamics (Larsson et al. [11]). 22 participating research groups from 12 countries and 19 different RANS codes were used for simulations of 3 test cases representing tanker, container, and surface combatant hull forms. Most groups implemented the recommended procedures, but lack of familiarity with the procedures and use of coarse grids led to difficulties. Coarser grid solutions are far from the asymptotic range and show variability such that not all variables display monotonic convergence and oscillatory convergence and even divergence is evident. For monotonic convergence, variability in the estimated order of accuracy was observed for some cases. The current 1 million point grids are clearly insufficient for more complex hull forms such as the tanker and an order of magnitude increase in points may be required to remove variability and achieve monotonic convergence for most variables. In spite of difficulties, the effort was beneficial in enabling quantitative evaluation of levels of verification and validation, increasing familiarity with verification and validation procedures, interpretation of results, and identification of grid requirements for decreasing levels of errors and uncertainties. Careful examination of verification results even for relatively coarse grid solutions provides a road map towards achieving acceptable levels of verification.

Verification and validation methodology and procedures should be helpful in guiding future developments in CFD through documentation, verification, and validation studies and in transition of CFD codes to design through establishment of credibility. Presumably, with a sufficient number of documented, verified, and validated solutions along with selected verification studies, a CFD code can be accredited for a certain range of applications. The contribution of the present work is in providing methodology and procedures for the former, which hopefully will help lead to the latter.

Part 2 provides an example for RANS simulations for a cargo/container ship where issues with regard to practical application of the methodology and procedures and interpretation of verification and validation results are discussed (Wilson et al. [12]).

Acknowledgments

This research was sponsored by the Office of Naval Research under Grants N00014-96-1-0018, N00014-97-1-0014, and N00014-97-1-0151 under the administration of Dr. E. P. Rood. The authors gratefully acknowledge Dr. Rood and other colleagues, especially Prof. W. G. Steele and Dr. H. Raven, who made significant contributions through insightful discussions and comments on early drafts. The recent Masters and Ph.D. theses of

Dr. B. Chen, Mr. G. Dolphin and Dr. S. H. Rhee, all at The University of Iowa, Department of Mechanical Engineering, were helpful both in the development and testing of the present verification and validation methodology and procedures.

Nomenclature

C_k = correction factor
D = benchmark data
E, E_C = comparison error, corrected
p_k = order of accuracy
R_k = parameter refinement ratio
S, S_C = simulation result, corrected
T = truth
U = uncertainty estimate
U_D = data uncertainty
U_E, U_{E_C} = comparison error uncertainty, corrected
U_I = iteration uncertainty
U_P, U_{P_C} = parameter uncertainty (e.g., grid size G and time step T), corrected
U_{reqd} = programmatic validation requirement
U_S, U_{S_C} = simulation uncertainty, corrected
U_{SM} = simulation modeling uncertainty
U_{SMA} = simulation modeling assumption uncertainty
U_{SPD} = simulation uncertainty due to use of previous data
U_{STE}, U_{S_CTE} = simulation total estimated numerical uncertainty
U_{SN}, U_{S_CN} = simulation numerical uncertainty, corrected
U_V, U_{V_C} = validation uncertainty, corrected
Δx_k = increment in *kth* input parameter (e.g., grid size G and time step T)
δ = error
δ^* = error estimate with sign and magnitude
δ_I, δ_I^* = iteration error, estimate
δ_P, δ_P^* = parameter error, estimate
δ_S, δ_{S_C} = simulation error, corrected
δ_{SN} = simulation numerical error
δ_{SMA} = simulation modeling assumption error
ε = solution change
ε_{SN} = error in δ^*

Appendix A. Analytical Benchmarks

The use of analytical benchmarks for development of the concept of correction factors as discussed in Section 3.3 is presented in this Appendix. For analytical benchmarks, the modeling error is zero such that the simulation error is solely due to numerical error. Results are obtained for two analytical benchmarks one-dimensional (1D) wave and two-dimensional (2D) Laplace equations. The results for the 2D Laplace equation were qualitatively similar to those for the 1D wave equation, which are presented. Exact solutions from analytical benchmarks are used to determine the exact simulation numerical error which is compared to estimates from RE, including use of correction factors. More details are provided in Stern et al. [13], including single grid error estimates.

Verification of Analytical Benchmarks. For verification using an analytical benchmark, the simulation error and uncertainty are given by $\delta_S = S - A = \delta_{SN}$ and $U_S^2 = U_{SN}^2$, while the corrected simulation error and uncertainty are given by $\delta_{S_C} = S_C - A = \varepsilon_{SN}$ and $U_{S_C}^2 = U_{S_CN}^2$. Simulations are verified if $|E| = |A - S| < U_{SN}$ and corrected simulations are verified if $|E_C| = |A - S_C| < U_{S_CN}$.

The first-order, linear 1D wave equation models the behavior of a more complicated (nonlinear) partial differential equation. The initial condition is prescribed by a Gaussian function centered at $x = 0.0$. Two discretization techniques were studied: (*i*) first-order (Euler) explicit method with first-order upwind spatial discretization; and (*ii*) a second-order implicit method with second-order central spatial discretization. Since trends from both schemes are similar, only the results from the first-order scheme are presented.

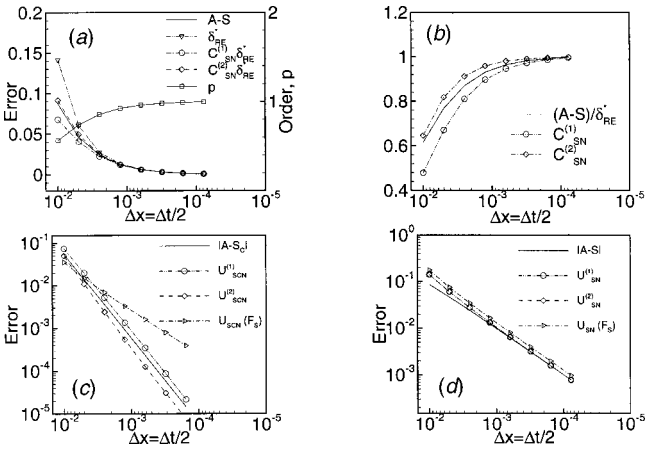

Fig. 2 Verification results for first-order numerical solution of 1D wave equation. (*a*) Comparison of true error $A-S$ to estimates from RE, (*b*) correction factor, and (*c*) comparison of $|A-S_C|$ and U_{SCN}, and (*d*) comparison of $|A-S|$ and U_{SN}.

A combined grid size and time step study was performed where ten solutions were obtained by successively doubling both the grid and time step such that $\Delta t/\Delta x = 0.5$ for all solutions. With this approach, solutions changes are used to estimate total (temporal and spatial) simulation errors and uncertainties. Accordingly, the generic subscript '*k*' appearing in expressions for errors and uncertainties in Section 3.3 is replaced with '*SN*' in this section where appropriate.

Errors, Uncertainties, and Correction Factors. The concept of a multiplication correction factor was introduced in Section 3.3. The correction factor C_k was used to define the numerical uncertainty in Eq. (33) or when conditions permit to improve error estimates in Eq. (32) and to define the uncertainty in that error estimate in Eq. (34). Error and uncertainty estimates given by Eqs. (32)–(34) are tested by numerical solution of analytical benchmarks as well as development of expressions for correction factor.

Figure 2(a) compares the true simulation error E to the three-grid error estimate $\delta^*_{RE_1}$ from Eq. (29) versus step size at one spatial location ($x = 1$ since maximums of numerical error occur there). The three-grid estimate accurately estimates the true error E for smaller step sizes, but over predicts E for larger step sizes. Closer examination reveals that Eq. (29) over estimates the error because Eq. (30) under estimates the order of accuracy, as also shown in Fig. 2(*a*).

Two definitions for C_k were investigated. The first is based on solving equation (32) for C_k with $\delta^*_{RE_{k_1}}$ defined in Eq. (29) but replacing p_k with the improved estimate $p_{k_{est}}$, which is provided by Eq. (35) where $p_{k_{est}}$ is an estimate of the limiting order of accuracy of the first term of the error expansion equation (27). Similarly, the second definition of correction factor is based on estimating $\delta^*_{RE_{k_1}}$ using the first two terms of the powers series and replacing p_k and q_k with improved estimates $p_{k_{est}}$ and $q_{k_{est}}$, which is provided by Eq. (36) where $p_{k_{est}}$ and $q_{k_{est}}$ are estimates for limiting orders of accuracy of the first and second terms of the error expansion equation (27) as spacing size goes to zero and the asymptotic range is reached. With this definition, correction factors approach one in the limit of zero spacing size. The estimated values $p_{k_{est}}$ and $q_{k_{est}}$ can be based either on the assumed theoret-

ical order of accuracy $p_{k_{th}}$ and $q_{k_{th}}$ or solutions for simplified geometry and conditions. In either case, preferably including the effects of grid stretching.

Figure 2(*a*) also compares the true error E to (*i*) an uncorrected three-grid error estimate using Eq. (29) and (*ii*) corrected estimates based on Eq. (32) with correction factor defined by Eq. (35) or (36). Both estimates are closer to E than the uncorrected three grid estimate $\delta^*_{RE_1}$, but for coarser grids $C_k^{(1)}$ is somewhat too small and $C_k^{(2)}$ is slightly too large. Figure 2(*b*) shows the same trends, but directly compares the exact correction factor E/δ^*_{RE} to Eqs. (35) and (36). In this case, $C_k<1$ indicates that the leading-order term over predicts (higher-order terms net negative) the error. However, for the general case, C_k is equally likely to be <1 or >1 depending whether the order of accuracy is approached from below or above, respectively. $C_k>1$ indicates that the leading-order term under predicts (higher-order terms net positive) the error. Thus, for the general case the correction to the leading-term error estimate is equally likely to be positive or negative and can be used to define the simulation numerical uncertainty.

For C_k sufficiently close to 1 and having confidence, δ^*_k and U_{k_C} are estimated. Correction factors $C_k^{(1)}$ and $C_k^{(2)}$ are used to estimate the error δ^*_k in Eq. (32) which can then also be used in the calculation of S_C [in Eq. (10)] and uncertainty U_{k_C} in Eq. (34). Figure 2(*c*) shows a comparison of $|A-S_C|$ and three uncertainty estimates: (*i*) $U^{(1)}_{S_CN}$ defined using $C_k^{(1)}$; (*ii*) $U^{(2)}_{S_CN}$ defined using $C_k^{(2)}$; and (*iii*) U_{S_CN} from a factor of safety approach given by Eq. (38) with $F_S=1.25$. The results show that the uncertainty estimate $U^{(1)}_{S_CN}$ successfully bounds $|A-S_C|$ over the entire range of step sizes and that $U^{(2)}_{S_CN}$ is not conservative enough since $U^{(2)}_{S_CN}<|A-S_C|$. The uncertainty estimate based on the factor of safety approach is not conservative enough for the coarsest two grids and is overly conservative by an order of magnitude for the four finest grids (i.e., when solutions are in the asymptotic range). For C_k sufficiently less than or greater than 1 and lacking confidence, U_k is estimated, but not δ^*_k and U_{k_C}. Correction factors $C_k^{(1)}$ and $C_k^{(2)}$ are used to estimate the uncertainty in Eq. (33) which is compared to factor of safety approach given by Eq. (37). Figure 2(*d*) shows that all three uncertainty estimates successfully bound the true error $|A-S|$ although the factor of safety approach is overly conservative for all grids.

Uncertainty estimates enable a quantitative measure of verification for analytical benchmarks. Figure 2(*c*, *d*) indicates that the present solutions are verified over the chosen range of grid size and time step. As expected, the largest levels of uncertainty are for the coarsest grid size and time step where levels are $(U_k, U_{k_C}) = (15\%, 7.5\%)$.

Eca and Hoekstra [18] also perform verification for the 2D Laplace equation analytical benchmark. Their results are consistent with our own in showing that uncertainty estimates using Eq. (33) always bounded the true error. Unlike our own results, their results indicate that the uncertainty estimate from Eq. (34) failed to bound the difference in the truth and numerical benchmark for some grid triplets when the apparent order of accuracy was estimated to be larger than the theoretical value.

References

[1] Freitas, C. J., 1993, "Editorial Policy Statement on the Control of Numerical Accuracy," ASME J. Fluids Eng., **115**, pp. 339–340.

[2] AIAA, 1998, *Guide for the Verification and Validation of Computational Fluid Dynamics Simulations*, G-077-1998.

[3] Roache, P. J., 1998, *Verification and Validation in Computational Science and Engineering*, Hermosa Publishers, Albuquerque, New Mexico.

[4] Mehta, U. B., 1998, "Credible Computational Fluids Dynamics Simulations," AIAA J., **36**, pp. 665–667.

[5] Stern, F., Paterson, E. G., and Tahara, Y., 1996, "CFDSHIP-IOWA: Computational Fluid Dynamics Method for Surface-Ship Boundary Layers and Wakes and Wave Fields," Iowa Institute of Hydraulic Research, The University of Iowa, IIHR Report No. 381.

[6] Coleman, H. W., and Stern, F., 1997, "Uncertainties in CFD Code Validation," ASME J. Fluids Eng., **119**, pp. 795–803. (Also see "Authors' Closure," ASME J. Fluids Eng., Vol. 120, Sept. 1998, pp. 635–636.)

[7] Coleman, H. W., and Steele, W. G., 1999, *Experimentation and Uncertainty Analysis for Engineers*, 2nd Edition, Wiley, New York, NY.

[8] Rood, E. P., 1996, "Validation Strategy for RANS Computational Ship Hydrodynamics," 2nd International Conference on Hydrodynamics, Hong Kong.

[9] ITTC, 1996, 21st ITTC Proceedings, "Report of the Resistance Committee," Bergen/Trondheim, Norway, September.

[10] ITTC, 1999, 22nd ITTC Proceedings, "Report of the Resistance Committee," Seoul, Korea/Shanghai, China, Sept.

[11] Larsson, L., Stern, F., Bertram, V., 2000, "Gothenburg 2000 A Workshop on Numerical Ship Hydrodynamics," Chalmers University of Technology, Gothenburg, Sweden, Sept.

[12] Wilson, R. V., Stern, F., Coleman, H., and Paterson, E., 2001, "Comprehensive Approach to Verification and Validation of CFD Simulations—Part 2: Applications for RANS Simulation of A Cargo Container Ship," ASME J. Fluids Eng., 123, published in the issue, pp. 803–810.

[13] Stern, F., Wilson, R. V., Coleman, H., and Paterson, E., 1999, "Verification and Validation of CFD Simulations," Iowa Institute of Hydraulic Research, The University of Iowa, IIHR Report No. 407.

[14] Oberkampf, W. L. and Trucano, T. G., 2000, "Validation Methodology in Computational Fluid Dynamics," AIAA Fluids 2000, Paper No. 2549, Denver, CO.

[15] Coleman, H. W., Stern, F., Mascio, A. Di, and Campana, E., 2001, "The Problem with Oscillatory Behavior in Grid Convergence Studies," ASME J. Fluids Eng., **123**, No. 2, pp. 438–439.

[16] Hoekstra, M., Eca, L., Windt, J., and Raven, H., 2000 "Viscous Flow Calculations for KVLCC2 AND KCS Models Using the PARNASSOS Code," Proceedings Gothenburg 2000 A Workshop on Numerical Ship Hydrodynamics, Gothenburg, Sweden.

[17] Ferziger, J. H., and Peric, M., 1996, *Computational Methods for Fluid Dynamics*, Springer-Verlag, New York.

[18] Eca, L., and Hoekstra, M., 2000, "On the Application of Verification Procedures in Computational Fluid Dynamics," 2nd MARNET Workshop.

[19] Ebert, M. P., and Gorski, J. J., 2001, "A Verification and Validation Procedure for Computational Fluid Dynamics Solutions," NSWCCD-50-TR-2001/0006, Hydromechanics Directorate Report, NSWC, Carderock Division, West Bethesda MD 20817-5700.

Robert V. Wilson
Assistant Research Engineer,
Mem. ASME

Fred Stern
Professor Mechanical Engineering and
Research Engineer,
Fellow ASME

Iowa Institute Hydraulic Research,
Department Mechanical Engineering,
The University of Iowa,
Iowa City, IA 52242

Hugh W. Coleman
Eminent Scholar in Propulsion,
Professor of Mechanical Engineering,
Propulsion Research Center,
Mechanical and Aerospace Engineering
Department,
University of Alabama in Huntsville,
Huntsville, AL 35899
Fellow ASME

Eric G. Paterson
Associate Research Engineer,
Iowa Institute Hydraulic Research,
The University of Iowa,
Iowa City, IA 52242
Mem. ASME

Comprehensive Approach to Verification and Validation of CFD Simulations—Part 2: Application for Rans Simulation of a Cargo/Container Ship

Part 2 of this two-part paper provides an example case study following the recently developed comprehensive verification and validation approach presented in Part 1. The case study is for a RANS simulation of an established benchmark for ship hydrodynamics using a ship hydrodynamics CFD code. Verification of the resistance (integral variable) and wave profile (point variable) indicates iterative uncertainties much less than grid uncertainties and simulation numerical uncertainties of about 2%S_1 (S_1 is the simulation value for the finest grid). Validation of the resistance and wave profile shows modeling errors of about 8%D (D is the measured resistance) and 6%ζ_{max} (ζ_{max} is the maximum wave elevation), which should be addressed for possible validation at the 3%D and 4%ζ_{max} levels. Reducing the level of validation primarily requires reduction in experimental uncertainties. The reduction of both modeling errors and experimental uncertainties will produce verified and validated solutions at low levels for this application using the present CFD code. Although there are many issues for practical applications, the methodology and procedures are shown to be successful for assessing levels of verification and validation and identifying modeling errors in some cases. For practical applications, solutions are far from the asymptotic range; therefore, analysis and interpretation of the results are shown to be important in assessing variability for order of accuracy, levels of verification, and strategies for reducing numerical and modeling errors and uncertainties. [DOI: 10.1115/1.1412236]

1 Introduction

Computational fluid dynamics (CFD) is fast becoming an integral tool in the engineering design process as it is applied to increasing complex geometry and physics. As with the use of experimental fluid dynamics (EFD) in making design decisions, assessment of quality of results is imperative, which has accelerated progress on development of verification and validation (V&V) methodology and procedures for estimating numerical and modeling errors and uncertainties in CFD simulations. However, in spite of the progress, the various viewpoints have not yet fully converged and current methodology and procedures are not yet standardized. Case studies are important for evaluating various current V&V approaches and achieving standardization. Mehta [1] provides several case studies following different approaches for a variety of applications. In some cases, large differences in approaches, use of different test cases, and incomplete documentation makes evaluation difficult.

Part 2 of the present two-part paper provides an example case study following the recently developed comprehensive V&V approach presented in Part 1 (Stern et al. [2]). The case study is for a RANS simulation of an established benchmark for ship hydrodynamics using a current ship hydrodynamics CFD code. However, the V&V approach is equally applicable to CFD simulations for other applications in fluids engineering such as aerospace, environmental, and automotive and also should be applicable to a fairly broad range of codes such as boundary element methods and certain aspects of large-eddy and direct numerical simulations. The present papers are based on Stern et al. [3], but with improved presentation and discussion based on nearly two years experience with the present V&V approach, especially through the International Towing Tank Conference (ITTC) community and Gothenburg 2000 Workshop on CFD in Ship Hydrodynamics (Larsson et al.).

The specific objectives of the present work are: (*i*) to provide a documented solution following the methodology and procedures in Part 1; (*ii*) to address practical issues in V&V of CFD simulations for complex geometries (e.g., generation of systematic grids); and (*iii*) to provide analysis and discussion of V&V results for a practical application where interpretation is complicated due to variability in the order of accuracy. Verification and validation methodology and procedures are summarized in Section 2 followed by a description of the CFD code in Section 3. Next, geometry, conditions, and benchmark data are specified in Section 4 with issues related to grid studies for practical applications given in Section 5. V&V results for the total resistance and wave profile are presented in Sections 6 and 7, respectively. Finally, conclusions are given in Section 8.

2 Verification and Validation Methodology and Procedures

The V&V methodology and procedures set forth in Part 1 provide a pragmatic approach for estimating simulation errors and uncertainties. The philosophy is strongly influenced by EFD uncertainty analysis. The present approach allows for treatment of simulation errors as either stochastic or deterministic and properly takes into account uncertainties in both the simulation and the data in assessing the level of validation.

Contributed by the Fluids Engineering Division for publication in the JOURNAL OF FLUIDS ENGINEERING. Manuscript received by the Fluids Engineering Division November 4, 1999; revised manuscript received July 10, 2001. Associate Editor: P. E. Raad.

Methodology. The simulation error δ_S is defined as the difference between a simulation result S and the truth T and is composed of modeling δ_{SM} and numerical δ_{SN} errors ($\delta_S = S - T = \delta_{SM} + \delta_{SN}$) with the corresponding simulation uncertainty given by $U_S^2 = U_{SM}^2 + U_{SN}^2$. For certain conditions, both the sign and magnitude of the numerical error can be estimated as $\delta_{SN} = \delta_{SN}^* + \varepsilon_{SN}$ where δ_{SN}^* is an estimate of the sign and magnitude of δ_{SN} and ε_{SN} is the error in that estimate. The simulation value is corrected to provide a numerical benchmark S_C, which is defined by

$$S_C = S - \delta_{SN}^* \tag{1}$$

with error equation $\delta_{S_C} = S_C - T = \delta_{SM} + \varepsilon_{SN}$ and corresponding uncertainty equation $U_{S_C}^2 = U_{SM}^2 + U_{S_C N}^2$ where U_{S_C} is the uncertainty in the corrected simulation and $U_{S_C N}$ is the uncertainty estimate for ε_{SN}.

Verification is defined as a process for assessing simulation numerical uncertainty U_{SN} and, when conditions permit, estimating the sign and magnitude δ_{SN}^* of the simulation numerical error itself and the uncertainty in that error estimate $U_{S_C N}$. Numerical error is decomposed into contributions from iteration number δ_I, grid size δ_G, time step δ_T, and other parameters δ_P, which gives the following expression for the simulation numerical uncertainty

$$U_{SN}^2 = U_I^2 + U_G^2 + U_T^2 + U_P^2 \tag{2}$$

For situations when the solution is corrected to produce a numerical benchmark S_C, the estimated simulation numerical error δ_{SN}^* and corrected uncertainty $U_{S_C N}$ are given by

$$\delta_{SN}^* = \delta_I^* + \delta_G^* + \delta_T^* + \delta_P^* \tag{3}$$

$$U_{S_C N}^2 = U_{I_C}^2 + U_{G_C}^2 + U_{T_C}^2 + U_{P_C}^2 \tag{4}$$

Validation is defined as a process for assessing simulation modeling uncertainty U_{SM} by using benchmark experimental data and, when conditions permit, estimating the sign and magnitude of the modeling error δ_{SM} itself. The comparison error E is given by the difference in the data D and simulation S values

$$E = D - S = \delta_D - (\delta_{SMA} + \delta_{SPD} + \delta_{SN}) \tag{5}$$

where δ_{SM} has been decomposed into the sum of δ_{SPD}, error from the use of previous data such as fluid properties, and δ_{SMA}, error from modeling assumptions. To determine if validation has been achieved, E is compared to the validation uncertainty U_V given by

$$U_V^2 = U_D^2 + U_{SN}^2 + U_{SPD}^2 \tag{6}$$

If $|E| < U_V$, the combination of all the errors in D and S is smaller than U_V and validation is achieved at the U_V level. If $U_V \ll |E|$, the sign and magnitude of $E = \delta_{SMA}$ can be used to make modeling improvements. For the corrected approach, the equations equivalent to Eqs. (5) and (6) are

$$E_C = D - S_C = \delta_D - (\delta_{SMA} + \delta_{SPD} + \varepsilon_{SN}) \tag{7}$$

$$U_{V_C}^2 = U_{E_C}^2 - U_{SMA}^2 = U_D^2 + U_{SPD}^2 + U_{S_C N}^2 \tag{8}$$

Procedures. The overall CFD V&V procedures can be conveniently grouped into four consecutive steps: preparation, verification, validation, and documentation.

Verification is accomplished through parameter convergence studies using multiple solutions (at least 3) with systematic parameter refinement by varying the kth input parameter Δx_k while holding all other parameters constant. Iterative errors must be accurately estimated or negligible in comparison to errors due to input parameters before accurate convergence studies can be conducted. Changes between medium-fine $\varepsilon_{k_{21}} = \hat{S}_{k_2} - \hat{S}_{k_1}$ and coarse-medium $\varepsilon_{k_{32}} = \hat{S}_{k_3} - \hat{S}_{k_2}$ solutions are used to define the convergence ratio

$$R_k = \varepsilon_{k_{21}} / \varepsilon_{k_{32}} \tag{9}$$

and to determine convergence condition where $\hat{S}_{k_1}$, $\hat{S}_{k_2}$, $\hat{S}_{k_3}$ correspond to solutions with fine, medium, and coarse input parameter, respectively, corrected for iterative errors. Three convergence conditions are possible:

$$\begin{aligned} &(i)\ \text{Monotonic convergence:}\ 0 < R_k < 1 \\ &(ii)\ \text{Oscillatory convergence:}\ R_k < 0 \\ &(iii)\ \text{Divergence:}\ R_k < 1 \end{aligned} \tag{10}$$

For condition (i), generalized RE is used to estimate U_k or δ_k^* and U_{k_C}. For condition (ii), uncertainties are estimated simply by attempting to bound the error based on oscillation maximums S_U and minimums S_L, i.e., $U_k = 1/2(S_U - S_L)$. For condition (iii), errors and uncertainties cannot be estimated.

For convergence condition (i), generalized RE is used to estimate the error $\delta_{RE_{k_1}}^*$ due to selection of the kth input parameter and order-of-accuracy p_k

$$\delta_{RE_{k_1}}^* = \frac{\varepsilon_{k_{21}}}{r_k^{p_k} - 1} \tag{11}$$

$$p_k = \frac{\ln(\varepsilon_{k_{32}} / \varepsilon_{k_{21}})}{\ln(r_k)} \tag{12}$$

Correction of Eq. (11) through a multiplication factor C_k accounts for effects of higher-order terms and provides a quantitative metric to determine proximity of the solutions to the asymptotic range

$$\delta_{k_1}^* = C_k \delta_{RE_{k_1}}^* = C_k \left(\frac{\varepsilon_{k_{21}}}{r_k^{p_k} - 1} \right) \tag{13}$$

where the correction factor is given by

$$C_k = \frac{r_k^{p_k} - 1}{r_k^{p_{k_{est}}} - 1} \tag{14}$$

and $p_{k_{est}}$ is an estimate for the limiting order of accuracy as spacing size goes to zero and the asymptotic range is reached so that $C_k \to 1$. When solutions are far from the asymptotic range, C_k is sufficiently less than or greater than 1 and only the magnitude of the error is estimated through the uncertainty U_k

$$U_k = |C_k \delta_{RE_{k_1}}^*| + |(1 - C_k) \delta_{RE_{k_1}}^*| \tag{15}$$

When solutions are close to the asymptotic range, C_k is close to 1 so that δ_k^* is estimated using Eq. (13) and U_{k_C} is estimated by

$$U_{k_C} = |(1 - C_k) \delta_{RE_{k_1}}^*| \tag{16}$$

Alternatively, a factor of safety approach proposed in Roache (1998) can be used to define U_k and U_{k_C}.

Validation is accomplished through comparison of simulations with benchmark EFD data, including experimental uncertainty estimates U_D. If the three variables U_V, $|E|$, and U_{reqd} (programmatic validation requirement) are considered, there are six combinations. For three cases, $|E| < U_V$ and validation is achieved at the U_V level, but for only one of these $U_V < U_{reqd}$ so that validation is also achieved at U_{reqd}. In these cases, attempting to estimate modeling errors δ_{SMA} is not feasible from an uncertainty standpoint. For the three other cases, $U_V < |E|$ and using the sign and magnitude of E to estimate δ_{SMA} is feasible from an uncertainty standpoint. In one of these cases, $U_V < |E| < U_{reqd}$ so that

validation is successful at the $|E|$ level from a programmatic standpoint. Similar conclusions can be reached using the corrected comparison error and corrected validation uncertainty.

3 RANS CFD Code

Solutions are obtained with CFDSHIP-IOWA, which is a general-purpose, multi-block, MPI-based high-performance, unsteady RANS CFD code (Paterson and Sinkovits, [4]; Paterson et al. [5]; Wilson et al. [6]) developed for computational ship hydrodynamics. The three-dimensional unsteady incompressible RANS equations are solved in either Cartesian or cylindrical-polar base coordinate systems. The grid dynamically conforms to the solution of the exact kinematic free-surface boundary condition. Approximate dynamic free-surface boundary conditions provide boundary conditions for velocity and pressure. For production simulations, Reynolds-stress closure is accomplished using the standard linear stress-strain relationship and a variety of eddy-viscosity models including algebraic Baldwin-Lomax and two-equation k-ω and k-ε models. The solution scheme is based upon the PISO algorithm and is fully implicit. The convective and viscous terms are discretized with second-order upwind and second-order central differences, respectively. Although the code can be run in either steady state or time-accurate mode, a time-marching procedure was used to obtain steady-state RANS solutions for simulations in this paper. The pressure equation is obtained by taking the divergence of the momentum equations. Further description can be found at *http://www.iihr.uiowa.edu/~cfdship* where related references may be found in electronic form.

4 Geometry, Conditions, and Benchmark Data

Steady-state simulations are performed for the Series 60 cargo/container ship. The Series 60 was used for two of the three test cases at an international workshop on validation of ship hydrodynamics CFD codes (CFD Workshop Tokyo [7]). The conditions for the calculations are Froude number $Fr=0.316$, Reynolds number $Re=4.3\times10^6$, and model orientation with zero sinkage and trim. These are the same conditions as the experiments, except the resistance and sinkage and trim tests, as explained next. The variables selected for verification and validation are resistance C_T (integral variable) and wave profile ζ (point variable).

The benchmark data is provided by Toda et al. [8], which was also the data used for the Series 60 test cases at the CFD Workshop Tokyo [7]. The data include resistance and sinkage and trim for a range of Fr for the model free condition (i.e., free to sink and trim). Also, wave profiles, near-field wave pattern, mean velocities, and pressures at numerous stations from the bow to the stern and near wake, all for $Fr=(0.16,0.316)$ and the zero sinkage and trim model fixed condition. The data also include uncertainty estimates, which were recently confirmed/updated by Longo and Stern [9] closely following standard procedures (Coleman and Steele [10]).

The resistance is known to be larger for free versus fixed models. Data for the Series 60 indicates about an 8% increase in C_r for the free versus fixed condition over a range of Fr including $Fr=0.316$ (Ogiwara and Kajatani [11]). The Toda et al. [8] resistance values were calibrated (i.e., reduced by 8%) for effects of sinkage and trim for the present comparisons.

5 Grids Studies With Systematic Refinement

Errors and uncertainties due to grid size are estimated using multiple solutions (at least 3) on systematically refined grids with constant refinement ratio, $r_k=\Delta x_{k_2}/\Delta x_{k_1}=\Delta x_{k_3}/\Delta x_{k_2}$. Although grid doubling ($r_G=2$) is typically used for simplicity, resolving similar physics and meeting near-wall spacing requirements for turbulence modeling can be prohibitively difficult, especially in 3D simulations. A more reasonable refinement ratio of $r_G=\sqrt{2}$ was recommended in Part 1 and is used here. Using $r_G=\sqrt{2}$ has the added benefit that the coarse grid can be easily generated by removing every other fine grid point.

Table 1 Grid dimensions and $y+$ values for grid refinement studies

Grid	*Grid Dimensions*	*Total Number of points*	*y+*
1	*287x78x43*	*876,211*	*0.7*
2	*201x51x31*	*317,781*	*1*
3	*144x36x22*	*114,048*	*1.4*
4	*101x26x16*	*42,016*	*2*

Grid studies were conducted using four grids, which enables two separate three-grid studies to be performed and compared. Grid study 1 (GS1) gives estimates for grid errors and uncertainties on grid 1 using the three finest grids 1–3 while grid study 2 (GS2) gives estimates for grid errors and uncertainties on grid 2 using the three coarsest grids 2–4. Grid dimensions and average y^+ values (for grid points closest to no-slip surface) are given in Table 1 and a comparison of the four grids at the free surface plane is shown in Fig. 1 along with computed wave elevation contours.

With grid refinement ratio $r_G=\sqrt{2}$, only grids 1 and 2 were generated manually using the commercial code GRIDGEN (Pointwise, Inc.). Grids 3 and 4 were obtained by removing every other point from grids 1 and 2, respectively (i.e., the grid spacing of grids 3 and 4 is twice that of grids 1 and 2, respectively). In an effort to keep the exact shape of the leading and trailing edges of the hull surface on all four grids, the single-block grid system is divided into three subblocks. The $j=1$ surface of one of the subblocks is body-fitted and defines the entire no-slip surface of the

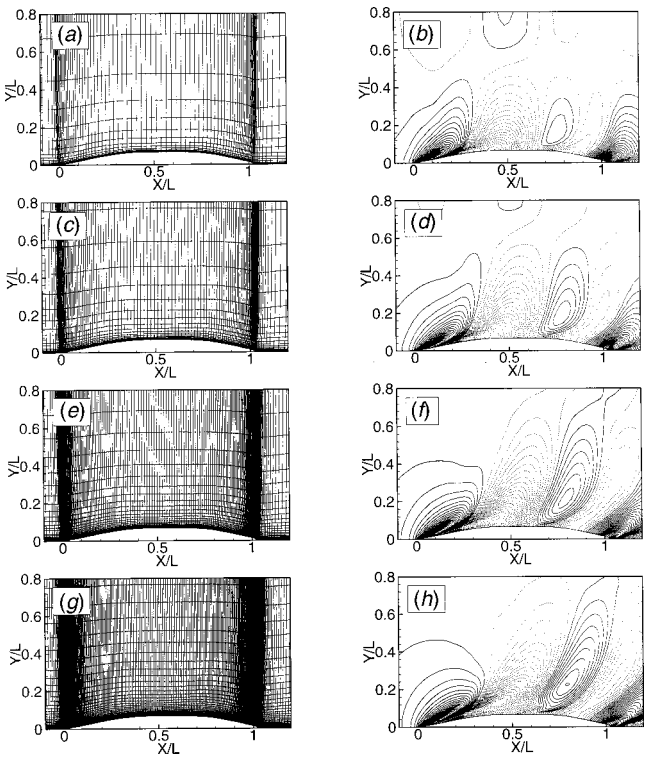

Fig. 1 Grids and computed wave contours on the free-surface plane from verification and validation studies for Series 60: (*a*) and (*b*) coarsest—grid 4; (*c*) and (*d*) grid 3; (*e*) and (*f*) grid 2; and (*g*) and (*h*) finest—grid 1. Ship leading and trailing edges at $x/L=0$ and 1, respectively.

ship from the leading to trailing edges. The $j=1$ surface of the other two subblocks, one upstream and one downstream of the ship hull, defines the symmetry plane using an *H*-type grid topology.

For grid 1 (i.e., finest grid), spacing along the edges of the computational block was controlled by specifying the grid distribution function (e.g., hyperbolic tanh or geometric series), grid spacing at the endpoint(s), and number of points. Grid clustering was used near the bow and stern in the ξ-direction, at the hull in the η-direction, and near the free surface in the ζ-direction. The faces of the subblocks were smoothed using an elliptic solver after which the coordinates in the interior were obtained using transfinite interpolation from the block faces. The three subblocks were then joined into a single block before simulations were performed.

Grid 2 was generated from grid 1 by using the same grid distribution function and by increasing the fine grid spacing Δx_{G_1} at the corners of the blocks and decreasing the number of fine grid computational cells (N_1-1) in each coordinate direction by a factor r_G

$$\Delta x_{G_2} = r_G \Delta x_{G_1} \tag{17}$$

$$N_2 = 1 + (N_1 - 1)/r_G \tag{18}$$

where Δx_{G_1} and Δx_{G_2} are the grid spacing and N_1 and N_2 are the number of points on grids 1 and 2, respectively. Finally, the faces of the blocks for grid 2 were then resmoothed using the elliptic solver and coordinates in the interior were obtained using transfinite interpolation (TFI).

For integer grid refinement ratio, this procedure results in a set of grids with systematic refinement (i.e., constant refinement ratio $r_G = \Delta x_{G_2}/\Delta x_{G_1} = \Delta x_{G_3}/\Delta x_{G_2} = \Delta x_{G_4}/\Delta x_{G_3}$). However, for noninteger refinement ratio r_G, Eq. (18) yields a noninteger grid number N_2 which obviously must be rounded to the nearest integer. This results in a difference in the actual $r_{G_{ACTUAL}}$ and target $r_{G_{TARGET}}$ refinement ratio. In other words,

$$r_{G_{ACTUAL}} = \frac{(N_1-1)}{integer[(N_1-1)/r_{G_{TARGET}}]} \neq r_{G_{TARGET}} \tag{19}$$

where the function "*integer[ ]*" is used to denote rounding of a real number to the nearest integer value.

The actual and target refinement ratios were compared by post-processing grids 1–3. Refinement ratio was computed at grid points along the intersection of the free- and no-slip surfaces which shows an average refinement ratio of $r_G = 1.39$ between grids 1 and 2 and $r_G = 1.44$ between grids 2 and 3. These values vary by 2% from the desired target value of $r_{G_{TARGET}} = \sqrt{2} \sim 1.4142$. However, inclusion of the effects of nonuniform grid refinement ratio for such small differences indicates $<1\%$ S_G differences in the estimates for numerical uncertainties (where $S_G = S_{G_1}$ is the solution on the finest grid), warranting the assumption of uniform grid refinement ratio. Because the volume grid is obtained using TFI from the elliptically smoothed faces of the blocks, larger deviations from uniform grid refinement ratio are possible in the interior.

Subsequent work has developed post-processing tools to automate generation of multiple grids with noninteger grid refinement ratio and to ensure uniform grid refinement ratio between multiple grids (Wilson et al. [11]). With this new procedure, the finest grid is trivially post-processed using a sequence of three, 1D interpolations to yield a medium grid with noninteger grid refinement ratio. This is in contrast to the approach used in this paper as described above for generation of the medium grid, which could become prohibitively difficult and time-consuming for large, multi-block grid systems with complex geometry.

6 Verification and Validation of Integral Variable: Total Resistance C_T

Friction and pressure stresses in the axial direction are integrated over the surface area of the Series 60 and summed to yield the total resistance coefficient C_T. The integration is performed in post processing using a second-order accurate method based on the trapezoidal rule. Results are analyzed and compared for both situations in which simulation numerical uncertainty is taken to be stochastic and U_{SN} estimated and when taken to be deterministic and δ^*_{SN} and U_{S_CN} are estimated for grid studies GS1 and GS2, as discussed in Section 5.

Verification. For verification of the uncorrected solution, U_{SN} is given by Eq. (2), while for the corrected solution, δ^*_{SN} and U_{S_CN} are given by Eqs. (3) and (4), respectively. Since steady-state simulations are performed, only contributions due to iteration number and grid size are considered (e.g., Eq. (2) simplifies to $U^2_{SN} = U^2_I + U^2_G$). The limiting order of accuracy is estimated using the formal order of accuracy of the CFD code (i.e., $p_{k_{est}} = p_{k_{th}} = 2.0$), which is realized for solution of simplified equations with uniform grids. For solution of the RANS equations on non-orthogonal stretched grids, values based on the formal order may be overly optimistic or not certain.

Iterative convergence is assessed through evaluation of the C_T iteration history and L2 norm of solution changes summed over all grid points. Figure 2 shows a portion of the iterative history for grid 1. The portion shown represents a computation started from a previous solution and does not include the total iterative history. Solution change drops four orders of magnitude from an initial value of about 10^{-2} (not shown) to a final value of 10^{-6}. The variation in C_T is about $0.14\% S_1$ (where S_1 is the solution on the finest grid) over the last period of oscillation (i.e., $U_I = 0.07\% S_1$). Iterative uncertainty is estimated as half the range of the maximum and minimum values over the last two periods of oscillation (see Fig. 2(*c*)). Iterative histories for grids 2–4 show iterative uncertainties of about 0.02, 0.03, and $0.01\% S_1$, respectively. The level of iterative uncertainties U_I for grids 2–4 are at least two orders of magnitude less than the corresponding grid uncertainties U_G, whereas the iterative uncertainty for grid 1 is only one order of magnitude smaller than the grid error. For all four grids, the iteration errors and uncertainties are assumed to be negligible in comparison to the grid errors and uncertainties for all four solutions (i.e., $U_I \ll U_G$ such that $U_{SN} = U_G$). Since iterative errors are negligible, correction of solutions for iterative error is not required.

Grid convergence is assessed through multiple C_T solutions on four systematically refined grids with constant refinement ratio (see Section 5). The total resistance C_T values on all four grids are given in Table 2 along with computed solution changes ϵ and benchmark EFD data for comparison. The convergence ratio $R_G(9)$, order of accuracy $p_G(12)$, and correction factor $C_G(14)$ are shown in Table 3. Since $0 < R_k < 1$, both GS1 and GS2 display monotonic convergence as given by condition (*i*), Eq. (10). However, the variability is large, i.e., the order of accuracy for GS1 is much greater than for GS2 and both are greater than $p_{k_{est}} = p_{k_{th}} = 2.0$. As a result, C_G is greater for GS1 than GS2. Although the fact that the order of accuracy does not approach $p_{k_{th}}$ with grid refinement is unexpected, in reality the estimation of $p_{k_{est}}$ for practical applications is not certain, as discussed previously.

Separate verification of the pressure C_P and friction C_F components of $C_T (= C_P + C_F)$ helps explain the variability displayed by p_G for C_T between GS1 and GS2. Note that in model-ship testing following *Fr* scaling, $C_{T_{Ship}} = C_R + C_{F_{ITTC}}$ where the residuary resistance $C_R (= C_{T_{Model}} - C_{F_{ITTC}})$ and $C_{F_{ITTC}}(\mathrm{Re})$ is given by the ITTC model-ship correlation line evaluated for model and full scale Re. Table 2 includes C_P and C_F values along with C_R and $C_{F_{ITTC}}$ for qualitative comparison. C_F comprises

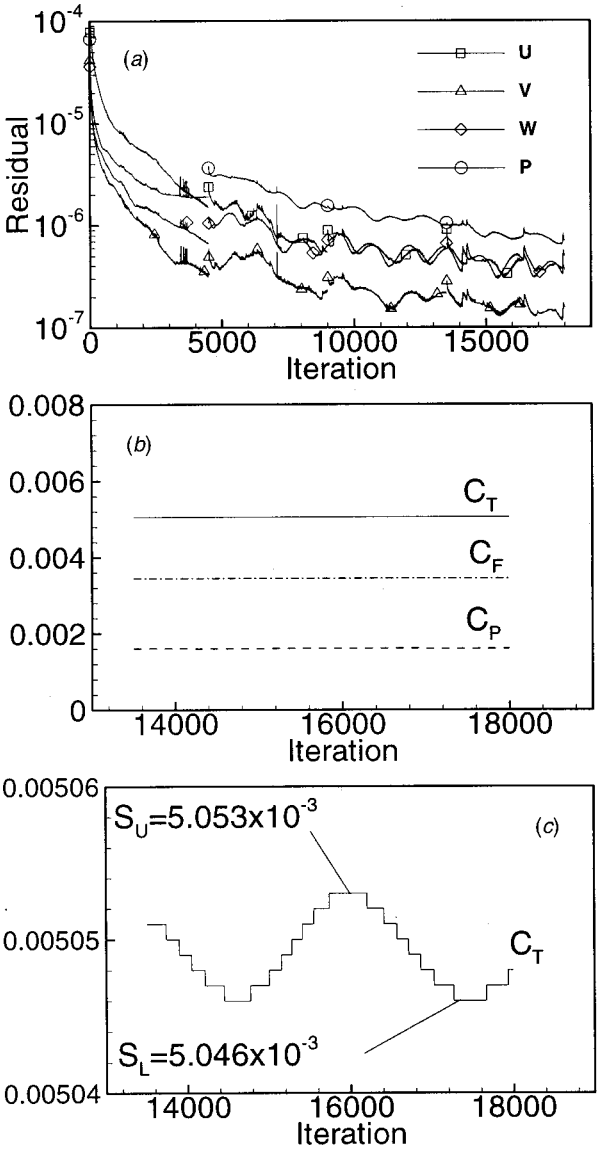

Fig. 2 Iteration history for Series 60 on grid 1: (*a*) solution change, (*b*) ship forces- C_F, C_P, and C_T and (*c*) magnified view of total resistance C_T over last two periods of oscillation

about 70%C_T and is convergent towards $C_{F_{ITTC}}$ (for GS1 within 1%$C_{F_{ITTC}}$). The C_P and C_F convergence ratio R_G, order of accuracy p_G, and correction factor C_G are shown in Table 4. For GS1, C_P is grid independent ($R_G = U_G = 0.0$) so that p_G cannot be estimated and C_F convergent but with $p_G > p_{k_{th}}$. For GS2, both C_P and C_F are convergent but with $p_G \gg p_{k_{th}}$ and $p_G > p_{k_{th}}$, respectively. For C_F, the trends with regard to variability are similar as for C_T but with reduced magnitude. The fact that the C_P is grid independent so that p_G cannot be estimated using RE and C_F is monotonically convergent with $p_G > p_{k_{th}}$ partially explains the variability exhibited in C_T. Such complications should be expected for verification of integral variables comprised of multiple components, especially when components strongly depend on different physics.

Table 2 Grid convergence study for total C_T, pressure C_P, and frictional C_F resistance ($x10^{-3}$) for Series 60

Grid	S_4 *(grid 4)*	S_3 *(grid 3)*	S_2 *(grid 2)*	S_1 *(grid 1)*	*Data*
C_T	6.02	5.39	5.11	5.05	5.42
ε		-10%	-5.2%	-1.2%	
C_P	1.88	1.61	1.60	1.60	$C_B = 2.00$
ε		-14%	-0.6%	0.0%	
C_F	4.14	3.69	3.51	3.45	3.42
ε		-11%	-4.9%	-1.7%	ITTC

% S_1.

Table 3 Verification of C_T($x10^{-3}$) for Series 60

Study	R_G	p_G	C_G
1 (grids 1-3)	0.21	4.4	3.7
2 (grids 2-4)	0.44	2.3	1.3

% S_1

Table 5 shows the estimated grid uncertainty U_G(15), grid error δ_G^*(13), corrected grid uncertainty U_{G_C}(16), and numerical benchmark S_C(1). Uncertainty estimates based on the factor of safety approach are included for comparison. The grid uncertainty is less for GS1 than GS2 and the values (2%S_1 and 7 %S_1, respectively) are reasonable in consideration of the overall number of grid points used. The corrected grid uncertainty is also less for GS1 than GS2, but the difference is smaller than was the case for U_G ($\Delta U_{G_C} \approx 1\% S_1$). Similarly S_C, which according to RE should be grid independent, shows 3% difference when comparing GS1 and GS2. The factor of safety approach provides less conservative estimates, which is contrary to previous experience for analytical benchmarks.

Solutions on the next finer grid with $r_G = \sqrt{2}$ would require 2.4M grid points. U_G would likely be reduced to the current U_{G_C} levels, but with similar or greater levels for U_1 making it difficult to separate iterative and grid uncertainties. Therefore, from a resource point of view it may be sufficient to accept the current corrected solution S_C on the finest grid with associated corrected grid uncertainty U_{G_C}. This conclusion is supported by the overall verification results (i.e., four solutions decrease and converge monotonically with grid refinement and with positive $\delta_G^* > 0$) notwithstanding the variability exhibited in p_G which precludes complete confidence. Nonetheless, additional solutions are desirable for gaining experience and an understanding of the nature of the asymptotic range for practical applications and hopefully such solutions will show reduced variability.

Validation. The comparison error $E = D - S$(5), validation uncertainty U_V(6), experimental data uncertainty U_D, and simulation numerical uncertainty U_{SN}(2) are shown in Table 6. Uncertainty due to the use of previous data U_{SPD} was not considered,

Table 4 Verification of C_P and C_F($x10^{-3}$) for Series 60

Study	C_P			C_F		
	R_G	p_G	C_G	R_G	p_G	C_G
1 (grids 1-3)	0.00	-	-	0.33	3.2	2.0
2 (grids 2-4)	0.04	9.5	26	0.40	2.6	1.5

% S_1

Table 5 Errors and uncertainties for C_T($x10^{-3}$) for Series 60

Grid	C_T uncorrected		C_T corrected			
	U_G (C_G)	U_G (F_S)	δ_G^*	U_{G_C}(C_G)	U_{G_C}(F_S)	S_C
1	2.1%	0.5%	1.2%	0.9%	0.1%	4.99
2	6.7%	5.6%	5.5%	1.1%	1.1%	4.83

% S_1

Table 6 Validation of uncorrected total resistance for Series 60

Grid	E%	U_V%	U_D%	U_{SN}%
1	6.8	3.1	2.5	1.9
2	5.7	6.7	2.5	6.3

%D.

so the validation uncertainty $U_V=\sqrt{U_{SN}^2+U_D^2}$. Note that since iterative uncertainty was found to be negligible $U_{SN}=U_G$ and the data uncertainty was reported to be $U_D=2.5\%D$.

For grid 1, $|E|>U_V$ such that C_T is not validated at the $|E|=7\%D$ level; however, from an uncertainty standpoint, the sign and magnitude of E can be used to estimate δ_{SMA} and make modeling improvements. Further reduction of U_V requires reduction of U_{SN} and U_D since they are of similar magnitude. For grid 2, $|E|<U_V$ such that C_T is validated but at the larger validation uncertainty level of $U_V=6.7\%D$ due to larger U_{SN}. Such large U_{SN} and therefore U_V precludes distinguishing δ_{SMA} from an uncertainty standpoint.

Table 7 is similar to Table 6, but for the corrected comparison error $E_C(7)$, validation uncertainty $U_{V_C}(8)$, and simulation numerical uncertainty $U_{S_CN}(4)$. In this case, $|E_C|>U_{V_C}$ for grids 1 and 2 such that neither is validated at the $U_V=2.6$ and $2.7\%D$ levels, respectively. $U_{S_CN}\ll U_D$ shows that reduction of U_D by one order of magnitude is required to reduce U_{V_C} to the level of U_{S_CN} and leads to the conclusion that the comparison error is largely due to modeling errors (i.e., $E_C\approx\delta_{SMA}$).

The overall conclusion for V&V of resistance is that C_T is not validated on the finest grid due to modeling errors of about $8\%D$. Likely modeling assumptions to consider are approximations of static sinkage and trim, free surface boundary conditions, and turbulence, which should be addressed for possible validation at about the $3\%D$ level. Reducing levels of validation uncertainty primarily requires reduction in experimental uncertainties; since, $U_D(=2.5\%D)>U_{G_C}(=1\%S_1)$.

7 Verification and Validation of a Point Variable: Wave Profile ζ

The wave profile is defined from the computed wave height at the intersection of the free- and no-slip hull surfaces from $0\leqslant x/L\leqslant 1$. Wave elevation contours for the entire free-surface plane are shown in Figs. 1(*b*), (*d*), (*f*) and (*h*) while the wave profile on all four grids is shown in Fig. 3 including qualitative comparison with the benchmark EFD data. To facilitate the comparisons, the solutions from all four grids are interpolated onto the distribution for the data. Results are analyzed and compared for both situations in which simulation numerical uncertainty is taken to be stochastic and U_{SN} estimated and when taken to be deterministic and δ_{SN}^* and U_{S_CN} are estimated for grid studies GS1 and GS2. Both point distributions and profile-averages of errors and uncertainties are discussed for verification and validation of the wave profile.

Verification. Evaluation of convergence ratio $R_G(9)$, order of accuracy $p_G(12)$, and correction factor $C_G(14)$, for point variables can be problematic when solution changes ε_{21_G} and $\varepsilon_{G_{32}}$ both go to zero so that their ratio is ill-defined. To overcome this problem, separate L2 norms of $\varepsilon_{G_{21}}$ and $\varepsilon_{G_{32}}$ are used to define ratios for R_G and p_G, i.e.,

$$\langle R_G\rangle=\|\varepsilon_{G_{21}}\|_2/\|\varepsilon_{G_{32}}\|_2 \tag{20}$$

$$\langle p_G\rangle=\frac{\ln(\|\varepsilon_{G_{32}}\|_2/\|\varepsilon_{G_{21}}\|_2)}{\ln(r_G)} \tag{21}$$

where $\langle\,\rangle$ and $\|\,\|_2$ are used to denote a profile-averaged quantity (with ratio of solution changes based on L2 norms) and L2 norm, respectively.

For verification of the uncorrected solution, Eq. (15) is used to estimate distributions of U_G at each point from the local solution change $\varepsilon_{G_{21}}$, where p_G is estimated from Eq. (21). Similarly, for the corrected solution, $\langle p_G\rangle$ is used to estimate δ_G^* and U_{G_C} at each point using Eqs. (13) and (16), respectively. An L2 norm of point distributions of errors and uncertainties are then used to assess verification levels and to judge if validation has been achieved globally. Iteration errors and uncertainties were found to be negligible in comparison to the grid errors and uncertainties for all four solutions, i.e., $U_I\ll U_G$ such that $U_{SN}=U_G$.

The profile-averaged convergence ratio $\langle R_G\rangle$, order of accuracy $\langle p_G\rangle$, correction factor $\langle C_G\rangle$, global grid uncertainty U_G, and corrected grid uncertainty U_{G_C} are shown in Table 8. Both GS1 and GS2 display monotonic convergence condition (*i*) from Eq. (10), but with $\langle p_G\rangle$ for GS1 greater than that for GS2 and both less than $p_{k_{th}}$, which in this case is consistent with expectations for solutions on stretched, curvilinear grids. The levels of U_G and U_{G_C} for GS1 are 1/2 those for GS2. Variability between GS1 and GS2 is absent and the trends are consistent with expectation. The distributions for U_G and U_{G_C} are discussed next in conjunction with validation.

Validation. Validation results with (U_V,U_{V_C}) and (E,E_C) based on L2 norms of point distributions are discussed first, followed by an examination of the actual point distributions. Profile-

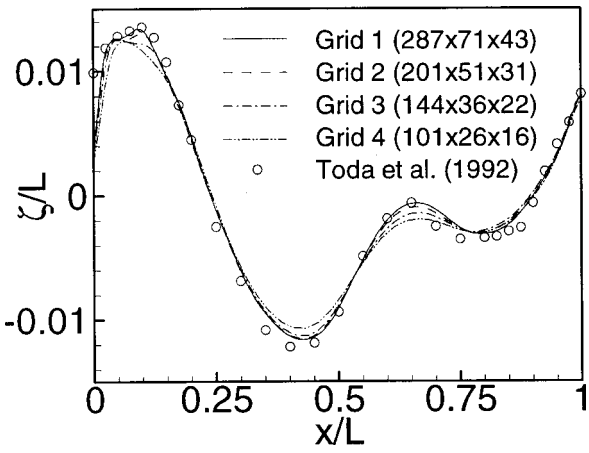

Fig. 3 Grid study for Series 60 wave profile

Table 7 Validation of corrected total resistance for Series 60

Grid	E_C %	U_{V_C} %	U_D %	U_{S_CN} %
1	7.9	2.6	2.5	0.8
2	11	2.7	2.5	1.0

%D.

Table 8 Profile-averaged verification results for wave profile for Series 60

Study	R_G	p_G	C_G	U_G	U_{G_C}
1 (grids 1-3)	0.64	1.3	0.56	2.0%	0.9%
2 (grids 2-4)	0.68	1.1	0.47	4.1%	2.2%

$\%\zeta_{max}$.

Table 9 Profile-averaged validation results for uncorrected wave profile for Series 60

Grid	E%	U_V%	U_D%	U_{SN}%
1	5.2	4.2	3.7	2.0
2	5.6	5.5	3.7	4.1

$\%\zeta_{max}$.

averaged validation results for the uncorrected and corrected wave profile are given in Tables 9 and 10, respectively. Values are normalized with the maximum value for the wave profile $\xi_{max}=0.014$ and the uncertainty in the data is $3.7\%\xi_{max}$. For grid 1, $|E|>U_V$ such that the wave profile is not validated at the $|E|=5.2\%\xi_{max}$ level; however the margin to achieve validation is small, i.e., $<1\%\xi_{max}$. U_D is roughly twice U_{SN}. For grid 2, $E\sim U_V$ such that the solution is nearly validated at $|E|=5.6\%\xi_{max}$ level. U_D and U_{SN} are of similar magnitude.

For grids 1 and 2, $|E|>U_{V_C}$ such that neither is validated at the $|E_C|=5.6\%$ and $6.6\%\xi_{max}$ levels, respectively. Here again, the margin to achieve validation is fairly small (i.e., $<2\%$ and $<3\%\xi_{max}$ for grids 1 and 2, respectively). U_D is roughly twice and four times U_{G_C} for grids 1 and 2, respectively.

Distributions of $(E,\pm U_V)$ and $(E_C,\pm U_{V_C})$ vs. x/L are shown in Figs. 4(*a*, *b*) and 4(*c*, *d*) for grids 1 and 2, respectively. When E is within $\pm U_V$ or E_C is within $\pm U_{V_C}$, the solutions are validated at the levels of U_V or U_{V_C}, respectively. Since U_D is constant the variations in U_V and U_{V_C} are due to variations in U_G and U_{G_C}. In all cases, lack of validation is mainly due to under prediction of wave crests and troughs in the simulations. For grid 1, $U_{V_C}\sim U_D$ since $U_{G_C}\ll U_D$. Although modeling errors are relatively small (2% and $3\%\xi_{max}$ for grids 1 and 2), Fig. 4 clearly indicates where improvements are warranted.

The overall conclusion for V&V of the wave profile is that ξ is not validated due to modeling errors of about $6\%\xi_{max}$; however, in this case, U_V is relatively large compared to E making the margin for reduction in modeling errors small (i.e., $2\%\xi_{max}$). Modeling improvements should be made to increase simulation predictions at crests and troughs so that solutions are validated at about the $4\%\xi_{max}$ level. Reducing the level of validation uncertainty primarily requires reduction in experimental uncertainties; since, $U_D(=4\%\xi_{max})>U_{G_C}(=1\%\xi_{max})$.

Table 10 Profile-averaged validation results for corrected wave profile for Series 60

Grid	E_C %	U_{V_C} %	U_D %	U_{S_CN} %
1	5.6	3.8	3.7	0.9
2	6.6	4.3	3.7	2.2

$\%\zeta_{max}$.

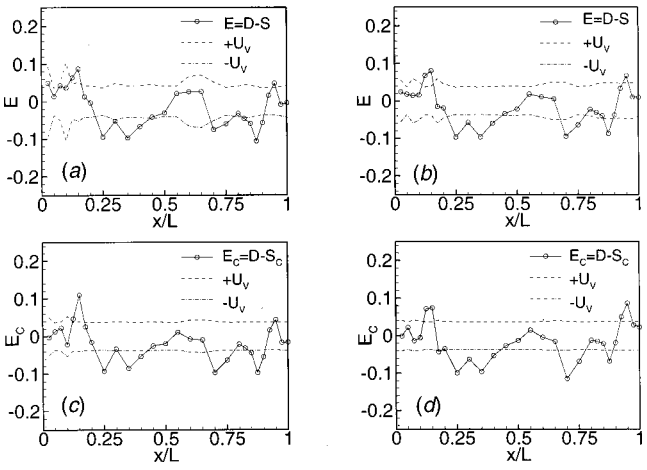

Fig. 4 Validation of wave profile for Series 60: (*a*) and (*b*) grid 1; and (*c*) and (*d*) grid 2. *E* and E_C values are normalized with the maximum value for the wave profile $\zeta_{max}=0.014$

8 Conclusions

In Part 2 of this two-part paper, V&V results were presented for RANS simulation of the Series 60 cargo/container ship, which provides a documented solution following the methodology and procedures presented in Part 1 (Stern et al., [2]). Although there are many issues for practical applications, the methodology and procedures are shown to be successful in assessing levels of verification and validation and identifying modeling errors in some cases. For practical applications, solutions are far from the asymptotic range; therefore, analysis and interpretation of the results is shown to be important in assessing variability for order of accuracy, levels of verification, and strategies for reducing numerical and modeling errors and uncertainties.

Verification of the resistance (integral variable) and wave profile (point variable) indicates iterative uncertainties are much less than grid uncertainties, which are about $2\%S_1$ for the finest grid with 0.9M points. Solutions on the next finer grid with 2.4M points likely will reduce simulation numerical uncertainties to $<1\%S_1$; however, iterative errors may be of similar order making it difficult to separate iterative and grid uncertainties. Therefore, from a resource point of view it may be sufficient to accept the current corrected solution (numerical benchmark) on the finest grid with corrected grid uncertainty $U_{G_C}=1\%S_1$. Validation of the resistance and wave profile shows modeling errors of about $8\%D$ and $6\%\xi_{max}$, which should be addressed for possible validation at the $3\%D$ and $4\%\xi_{max}$ levels. Reducing the level of validation uncertainty primarily requires reduction in experimental uncertainties; since, $U_D>U_{G_C}$. The combination of a reduction of E (through reduction of modeling errors) and U_D will produce verified and validated CFD simulations with low levels of simulation modeling and numerical errors and uncertainties.

Future work will focus on both fundamental and practical V&V issues, especially for applications with complex geometry. Fundamental issues include the convergence of the power series expansion for numerical error, assumptions that the order of accuracy is constant for all solutions, and estimation of the limiting order of accuracy in the definition of correction factor. Issues with practical applications involve observed variability in order of accuracy estimates, existence of the asymptotic range, and generation of multiple grids and solutions with non-integer refinement ratio. The behavior of the asymptotic range was successfully demonstrated in Appendix A of Part 1 for simpler analytical benchmark problems. However, the existence and behavior of the asymptotic range for practical problems has not yet been demonstrated. Such an effort would require solutions on many more grids to properly assess variability in order of accuracy estimates and finer grids to ensure solutions are indeed in the asymptotic range. More experience is needed for additional practical applications and different CFD codes.

Acknowledgments

This research was sponsored by the Office of Naval Research under grants N00014-96-1-0018, N00014-97-1-0014, and N00014-97-1-0151 under the administration of Dr. E. P. Rood.

References

[1] Mehta, U. B., 1998, "Credible Computational Fluids Dynamics Simulations," AIAA Journal, **36**, pp. 665–667.

[2] Stern, F., Wilson, R. V., Coleman, H., and Paterson, E., 2001, "Verification and Validation of CFD Simulations: Part 1—Comprehensive Methodology," ASME J. Fluids Eng., **123**, published in this issue, pp. 793–802.

[3] Stern, F., Wilson, R. V., Coleman, H., and Paterson, E., 1999, ''Verification and Validation of CFD Simulations,'' Iowa Institute of Hydraulic Research, The University of Iowa, IIHR Report No. 407.
[4] Paterson, E. G., and Sinkovits, R. S., 1999, ''Performance, Scalability, and Portability of a MPI-based version of CFDSHIP-IOWA: Results of a NAVO PET Tiger-Team Collaboration,'' 9th DoD HPC Users Group Meeting, Monterey, CA, June.
[5] Paterson, E. G., Wilson, R. V., and Stern, F., 1998, ''CFDSHIP-IOWA and Steady Flow RANS Simulation of DTMB Model 5415,'' Ist Symposium on Marine Applications of Computational Fluid Dynamics, McLean, VA, 19–21 May.
[6] Wilson, R., Paterson, E., and Stern, F., 1998, ''Unsteady RANS CFD Method for Naval Combatant in Waves,'' Proc. 22nd ONR Symposium on Naval Hydro, Washington, DC, August.
[7] CFD Workshop Tokyo 1994, Proceedings, Vol. 1 and 2, 1994, Ship Research Institute Ministry of Transport Ship & Ocean Foundation.
[8] Toda, Y., Stern, F., and Longo, J., 1992, ''Mean-Flow Measurements in the Boundary Layer and Wake and Wave Field of a Series 60 CB=.6 Model Ship—Part 1: Froude Numbers .16 and .316,'' Journal of Ship Research, **36**, No. 4, pp. 360–377.
[9] Longo, J. and Stern, F., 1998, ''Resistance, Sinkage and Trim, Wave Profile, and Nominal Wake and Uncertainty Assessment for DTMB Model 5512,'' Proc. 25th ATTC, Iowa City, IA, 24–25 Sept.
[10] Coleman, H. W., and Steele, W. G., 1999, *Experimentation and Uncertainty Analysis for Engineers*, 2nd Edition, Wiley, New York, NY.
[11] Ogiwara, S., and Kajitani, H., 1994, ''Pressure Distribution on the Hull Surface of Series 60 (C_B=0.60) Model,'' Proceedings CFD Workshop Tokyo, **1**, pp. 350–358.
[12] Wilson, R., Paterson, E., and Stern, F., 2000 ''Verification and Validation for RANS Simulation of a Naval Combatant,'' Preprints of Gothenburg 2000 A Workshop on Numerical Ship Hydrodynamics.
[13] Eca, L., and Hoekstra, M., 2000, ''On the Application of Verification Procedures in Computational Fluid Dynamics,'' 2nd MARNET Workshop.
[14] Roache, P. J., 1998, Verification and Validation in Computational Science and Engineering, Hermosa Publishers, Albuqerque, New Mexico.
[15] Larsson, L., Stern, F., and Bertram, V., 2000, ''Gothenburg 2000 A Workshop on Numerical Ship Hydrodynamics,'' Chalmers University of Technology, Gothenburg, Sweden, Sept. 2000.

Numerical Analysis of Two-Phase Pipe Flow of Liquid Helium Using Multi-Fluid Model

Jun Ishimoto
Associate Professor,
Department of Intelligent Machines
and System Engineering,
Hirosaki University,
3, Bunkyo-cho, Hirosaki 036-8561 Japan
e-mail: ishimoto@cc.hirosaki-u.ac.jp

Mamoru Oike
Associate Professor

Kenjiro Kamijo
Professor

Institute of Fluid Science,
Tohoku University,
2-1-1, Katahira, Aoba-ku,
Sendai 980-8577 Japan

The two-dimensional characteristics of the vapor-liquid two-phase flow of liquid helium in a pipe are numerically investigated to realize the further development and high performance of new cryogenic engineering applications. First, the governing equations of the two-phase flow of liquid helium based on the unsteady thermal nonequilibrium multi-fluid model are presented and several flow characteristics are numerically calculated, taking into account the effect of superfluidity. Based on the numerical results, the two-dimensional structure of the two-phase flow of liquid helium is shown in detail, and it is also found that the phase transition of the normal fluid to the superfluid and the generation of superfluid counterflow against normal fluid flow are conspicuous in the large gas phase volume fraction region where the liquid to gas phase change actively occurs. Furthermore, it is clarified that the mechanism of the He I to He II phase transition caused by the temperature decrease is due to the deprivation of latent heat for vaporization from the liquid phase. According to these theoretical results, the fundamental characteristics of the cryogenic two-phase flow are predicted. The numerical results obtained should contribute to the realization of advanced cryogenic industrial applications.
[DOI: 10.1115/1.1400747]

1 Introduction

Cryogenic flow systems that include two-phase flow are widely used in LNG (Liquefied Natural Gas) plants, aerospace technology, superconductivity technology, and many other engineering applications (Filina and Weisend [1]). Thus, the investigation of the two-phase flow characteristics of cryogenic fluids, such as liquid helium, is very interesting and important not only in the basic study of the hydrodynamics of cryogenic fluid (Van Sciver [2]) but also for providing solutions to problems related to practical engineering applications of cryogenic two-phase flow. Cryogenic fluids are characterized by large compressibility compared with fluids at room temperature such as water, a small difference in density between gas and liquid phases, and a small latent heat of vaporization. These unique characteristics of cryogenic fluids can be utilized to realize high performance in fluid apparatuses, such as the two-phase operation of inducers (Cheremisinoff [3], Kamijo et al. [4], and King [5]).

Although cryogenic fluid flow has been studied for many years, there has been only limited information on the theoretical and experimental study of the basic multiphase hydrodynamic characteristics of the gas-liquid two-phase pipe flow of cryogenic fluids such as superfluid liquid helium (Maki et al. [6], Ishii et al. [7], Ludtke and Daney [8], and Daney [9]). The main reason for the difficulty in the study of cryogenic fluids is that effective formulation, modeling, and numerical procedure of the governing equations for cryogenic two-phase flow with phase change have not been established. Difficulties in the experimental confirmation of cryogenic fluid under a low temperature field and the complete heat insulation of the flow pipe with measuring devices are other reasons. In particular, in the case of liquid helium, as the superfluidity in the low temperature field less than the λ point shows extremely complex phenomena, many difficulties are encountered in the theoretical analysis. To overcome these difficulties, we herein develop a new method for analyzing two-phase flow, based on an advanced mathematical model, which takes the effect of superfluidity of the two-phase cryogenic flow state in the low temperature field into consideration.

In the present study, the two-dimensional characteristics of two-phase flow of liquid helium with phase change in a pipe are numerically investigated to realize the further development and high performance of cooling devices or new cryogenic engineering applications. First, the governing equations of two-phase flow of liquid helium based on the unsteady multi-fluid model are presented, and then several flow characteristics are numerically calculated, taking into account the effect of superfluidity.

2 Numerical Method

In the past few years, the governing equations that represent the gas-liquid two-phase mixture flow of liquid helium have been derived and numerically solved by one of the authors (Ishimoto et al. [10]). As a result, the two-phase flow characteristics with superfluidity have been partially clarified. In the previous analysis of two-phase flow, we used the drift-flux model, which is the analytical model for two-phase mixture flow taking into account the effect of pseudo gas-liquid relative velocity, so the effects of the momentum or energy exchange between gas and liquid phases have not strictly been considered. In the present study on the vapor-liquid two-phase flow of liquid helium, we contrived a new model for analysis, which is based on the unsteady thermal nonequilibrium multi-fluid model by Kataoka [11]. Furthermore, to consider the effects of the evaporation and the condensation on the vapor bubbles, we apply the rapid phase change model to the two-phase flow of liquid helium with superfluidity. The system used in the numerical analysis is schematically depicted in Fig. 1. Applications using cryogenic fluid generally encounter obstacles or complex pipe shapes such as an orifice or a converging-diverging nozzle. Thus, the model used for analysis simulates the two-phase flow of liquid helium passing through the orifice of a vertical cylindrical pipe. The pipe is filled with pressurized liquid helium. Flow immediately occurs when the outlet edge D-C is opened. Liquid helium is continuously introduced via the inlet section A-B, the flow is accelerated at the point of the orifice, and liquid to vapor phase change is induced by a pressure decrease.

Contributed by the Fluids Engineering Division for publication in the JOURNAL OF FLUIDS ENGINEERING. Manuscript received by the Fluids Engineering Division February 17, 2000; revised manuscript received May 23, 2001. Associate Editor: F. K. Wasden.

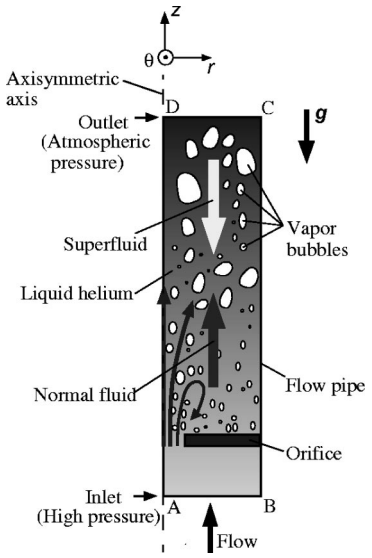

Fig. 1 Schematic of model for numerical analysis

2.1 Governing Equations. In the present numerical formulation of the two-phase flow characteristics of liquid helium, we extend the old two-fluid model by Landau [12] to a new cryogenic vapor-liquid multiphase fluid model for analysis which is based on the unsteady thermal nonequilibrium multi-fluid model of Kataoka [11], Harlow and Amsden [13], and Cook and Harlow [14]. In the numerical model, the cryogenic two-phase flow state can be approximated to that of a homogeneous bubbly flow because the differences in the physical properties such as density, viscosity, and surface tension of the cryogenic fluid between gas and liquid phases are very small compared with the fluid at room temperature. The small difference in the properties between gas and liquid phases is unique to cryogenic fluids. Accordingly, it seems reasonable to assume that the cryogenic two-phase flow pattern is easily formed in the bubbly two-phase flow. In the process of modeling, we consider the effects of superfluidity in two-phase liquid helium, namely, superfluid He II and normal fluid He I are treated as perfect fluid and meta-viscous fluid, respectively. In the calculation, we assume that the property of superfluidity appears when the fluid temperature becomes less than the λ point (temperature at normal fluid to superfluid transition, T_λ, about 2.17 K); however, in the case of temperatures above the λ point, we assume that the superfluid behaves in the same manner as the normal fluid. Here, we consider only the temperature dependence of the superfluid and normal fluid densities; thus, the normal fluid-superfluid transition ratio based on quantum theory is not strictly considered. Furthermore, to consider the effects of the rapid evaporation and condensation of cryogenic fluid, we apply the rapid phase change model of Yamamoto et al. [15], Iriya et al. [16], and Young [17] to the two-phase flow of liquid helium.

The calculation is carried out using the two-dimensional cylindrical coordinate system (r,z). The model for analysis simulates the two-phase flow of liquid helium passing through the orifice of a vertical pipe. In the numerical modeling under this condition, the following assumptions are employed to formulate the governing equations.

1 The two-phase flow is an axisymmetric two-dimensional unsteady laminar pipe flow.
2 The vapor-gas phase is produced by the phase change of the normal fluid.
3 The energy exchange between the liquid and gas phases is taken into account.

For the construction of the two-phase flow characteristics in the present numerical model, it is assumed that the gas phase is homogeneously dispersed in the surrounding liquid phase and that the flow structure will form a bubbly flow.

Under the above conditions, the governing equations of the two-phase flow, taking into account the effect of superfluidity based on the unsteady two-dimensional multi-fluid model, are derived as follows.

The mass conservation equation for a gas phase is

$$\frac{\partial}{\partial t}(\alpha\rho_g)+\nabla\cdot(\alpha\rho_g\mathbf{v}_g)=\Gamma_g, \tag{1}$$

The mass conservation equation for a liquid phase is

$$\frac{\partial}{\partial t}[(1-\alpha)\rho_l)]+\nabla\cdot[(1-\alpha)\mathbf{j}_l]=\Gamma_l, \tag{2}$$

where the liquid phase density, ρ_l, must be comprised of a linear combination of the two components, the density is expressed by the sum of the normal fluid and superfluid components, and ρ_l is defined as follows:

$$\rho_l=\rho_{l(n)}+\rho_{l(s)}. \tag{3}$$

For the two-fluid model, it is assumed that all the temperature dependence in liquid helium densities enter through the variation of the normal fluid density. It is therefore possible to write

$$\frac{\rho_{l(n)}}{\rho_l}=\begin{cases}\left(\dfrac{T_l}{T_{l\lambda}}\right)^{5.6} & \text{for } T_l\leqslant T_{l\lambda}\\ 1 & \text{for } T_l>T_{l\lambda},\end{cases} \tag{4}$$

as the temperature dependence of the normal fluid density (Van Sciver [2]). Because of this strong temperature dependence, the He II is about 99 percent superfluid component at 1.0 K. The total densities of superfluid and normal fluid two components in control volume are conservative in numerical calculation process. Also, the liquid phase momentum flux density $\mathbf{j}_l$ can be written as the sum of each normal fluid and superfluid momentum flux density components, defined as follows:

$$\mathbf{j}_l=\rho_{l(s)}\mathbf{v}_{l(s)}+\rho_{l(n)}\mathbf{v}_{l(n)}. \tag{5}$$

The combined equation of motion for a normal fluid is

$$\begin{aligned}&\frac{\partial}{\partial t}[\alpha\rho_g\mathbf{v}_g+(1-\alpha)\rho_l\mathbf{v}_{l(n)}]+\nabla\cdot[\alpha\rho_g\mathbf{v}_g\mathbf{v}_g+(1-\alpha)\rho_l\mathbf{v}_{l(n)}\mathbf{v}_{l(n)}]\\ &\quad=-\nabla P_l-(1-\alpha)\frac{\rho_l\rho_{l(s)}}{\rho_{l(n)}}S_l\nabla T_l\\ &\qquad-(1-\alpha)\frac{\rho_{l(s)}}{2}\nabla(\mathbf{v}_{l(n)}-\mathbf{v}_{l(s)})^2\\ &\qquad+(1-\alpha)\rho_{l(n)}\mathbf{g}+\nabla\cdot\left\{\mu_T\left[\nabla\mathbf{v}_{l(n)}+(\nabla\mathbf{v}_{l(n)})^T\right.\right.\\ &\qquad\left.\left.-\frac{2}{3}(\nabla\cdot\mathbf{v}_{l(n)})\mathbf{I}\right]\right\}-(1-\alpha)\mathbf{F}_{l(sn)}.\end{aligned} \tag{6}$$

The combined equation of motion for a superfluid is

$$\begin{aligned}&\frac{\partial}{\partial t}[\alpha\rho_g\mathbf{v}_g+(1-\alpha)\rho_l\mathbf{v}_{l(s)}]+\nabla\cdot[\alpha\rho_g\mathbf{v}_g\mathbf{v}_g+(1-\alpha)\rho_l\mathbf{v}_{l(s)}\mathbf{v}_{l(s)}]\\ &\quad=-\nabla P_l+(1-\alpha)\rho_l S_l\nabla T_l+(1-\alpha)\frac{\rho_{l(n)}}{2}\nabla(\mathbf{v}_{l(n)}-\mathbf{v}_{l(s)})^2\\ &\qquad+(1-\alpha)\rho_{l(s)}\mathbf{g}+(1-\alpha)\mathbf{F}_{l(sn)},\end{aligned} \tag{7}$$

where the second terms on the right-hand side of Eqs. (6) and (7) denote the force based on the product of the entropy by the temperature gradient and the third terms denote the effect of momentum energy gradient based on the two-phase superfluid-normal

fluid relative velocity caused by counterflow of the superfluid against the normal fluid. The terms mentioned above are peculiar for liquid helium with superfluidity (Van Sciver [2]). The signs of these terms in Eq. (6) are opposite those in Eq. (7); thus, the forces based on the superfluidity of Eq. (6) act in the direction opposite those of Eq. (7). In this calculation, because the vapor phase is assumed to be produced by the phase change of the normal fluid, the two-phase flow of the superfluid means the mixture flow of the vapor phase produced by the normal fluid and the superfluid. The term $\mathbf{F}_{l(sn)}$ denotes the two-phase superfluid-normal fluid mutual friction interaction term based on the generation of vortex filaments in the superfluid as reported by Donnelly [18], Bekarevich and Khalatnikov [19], Hall and Vinen [20], and Tsubota and Yoneda [21]. Assuming that the flow field is two-dimensional results in the following simplified formula for each component of $\mathbf{F}_{l(sn)}$:

$$F_{l(sn)r} = -A_{GM}\frac{\rho_{l(n)}}{2}[-\omega_{l\theta}v_{l(n)} + \omega_{l\theta}v_{l(s)}] \tag{8}$$

$$F_{l(sn)z} = -A_{GM}\frac{\rho_{l(n)}}{2}[\omega_{l\theta}u_{l(n)} - \omega_{l\theta}u_{l(s)}] \tag{9}$$

$$\omega_{l\theta} = \left(\frac{\partial u_l}{\partial z} - \frac{\partial v_l}{\partial r}\right), \tag{10}$$

where coefficient A_{GM} denotes the mutual friction parameter which has a strong temperature dependence (Kashani et al. [22]). Additionally, μ_T in Eq. (6) denotes the viscosity of the two-phase mixture flow that includes small dispersed bubbles. μ_T was evaluated using the following formula by Einstein for the viscosity of a suspension (Batchelor [23], Tomiyama et al. [24]):

$$\mu_T = (1 + 2.5\alpha)\mu_l \tag{11}$$

where Eq. (11) is mainly applicable in small gas phase volume fraction region. Concerning the viscosity, the present numerical model assumes that superfluid viscosity $\mu_{l(s)} = 0$ and the dissipative interaction is due only to the normal fluid. This assumption corresponds to the physical fact that the superfluid experiences no resistance to flow and therefore no turbulence. The superfluid can flow through a pipe without viscous drag along the boundaries. Equations (6) and (7) are derived by complying the equations of momentum for gas and liquid two-phases.

To consider the effects of additional forces that act on the bubbles and radial expansion of the bubbles, the equation of motion for the gas phase is here replaced with the translational motion of a single bubble (Hinze [25]). The viscous drag forces that act on the bubble in the He II fluids are neglected because of the superfluidity.

The equation of motion for a gas phase is

$$\frac{4}{3}\pi\rho_g R_g^3\frac{d\mathbf{v}_g}{dt} = -\mathbf{F}_P + \mathbf{F}_g - \mathbf{F}_D - \mathbf{F}_{VM} - \mathbf{F}_B + \mathbf{F}_{LM} + \mathbf{F}_{LS}, \tag{12}$$

where each additional force term is derived as follows:

$$\mathbf{F}_P = \frac{4}{3}\pi R_g^3\nabla P_l \tag{13}$$

$$\mathbf{F}_g = \frac{4}{3}\pi R_g^3\rho_g\mathbf{g} \tag{14}$$

$$\mathbf{F}_D = \frac{1}{2}\rho_l C_D|\mathbf{v}_g - \mathbf{v}_l|(\mathbf{v}_g - \mathbf{v}_l)\pi R_g^2 \tag{15}$$

$$\mathbf{F}_{VM} = C_{VM}\cdot\rho_l\frac{4}{3}\pi R_g^3\left[\frac{d}{dt}(\mathbf{v}_g - \mathbf{v}_l) + \frac{3}{R_g}(\mathbf{v}_g - \mathbf{v}_l)\frac{dR_g}{dt}\right] \tag{16}$$

$$\mathbf{F}_B = 6R_g^2\sqrt{\pi\rho_l\mu_l}\int_0^t \frac{\frac{d}{dt}(\mathbf{v}_g - \mathbf{v}_l)}{\sqrt{t-\tau}}d\tau \tag{17}$$

$$\mathbf{F}_{LM} = \pi R_g^3\rho_l(\mathbf{\Omega}_g - \mathbf{\Omega}_l)\times(\mathbf{v}_g - \mathbf{v}_l) \tag{18}$$

$$\mathbf{F}_{LS} = 6.46\frac{\mu_l R_g^2}{\sqrt{|(\mathbf{\Omega}_g - \mathbf{\Omega}_l)|\,\nu_l}}(\mathbf{\Omega}_g - \mathbf{\Omega}_l)\times(\mathbf{v}_g - \mathbf{v}_l) \tag{19}$$

$$\mathbf{\Omega}_l = \frac{1}{2}\nabla\times\mathbf{v}_l, \tag{20}$$

where R_g is the equivalent bubble diameter, $\mathbf{F}_P$ is the force due to the liquid phase pressure gradient, $\mathbf{F}_g$ is the gravitational acceleration force, $\mathbf{F}_D$ is the drag force, $\mathbf{F}_{VM}$ is the virtual mass force considering the expansion of a bubble, and $\mathbf{F}_B$ is the Basset history term which takes into account the effect of the deviation in flow pattern from steady state. $\mathbf{F}_{LM}$ is the Magnus lift force caused by the rotation of the bubble as reported by Rubinow and Keller [26], and Auton ([27,28]). $\mathbf{F}_{LS}$ is Saffman's lift force (Saffman [29]) caused by the velocity gradient of the liquid phase. C_D is the drag coefficient and C_{VM} is the virtual mass coefficient. d/dt is the substantial derivative defined by

$$\frac{d\mathbf{v}_g}{dt} = \frac{\partial\mathbf{v}_g}{\partial t} + \mathbf{v}_g\cdot\nabla\mathbf{v}_g \tag{21}$$

$$\frac{d\mathbf{v}_l}{dt} = \frac{\partial\mathbf{v}_l}{\partial t} + \mathbf{v}_l\cdot\nabla\mathbf{v}_l. \tag{22}$$

The equation for the angular velocity of a bubble is derived as (Dennis et al. [30], Takagi, [31]) follows:

$$\frac{d\mathbf{\Omega}_g}{dt} = \frac{15\mu_l}{R_g^2\cdot\rho_g}(\mathbf{\Omega}_l - \mathbf{\Omega}_g), \tag{23}$$

The energy equation for gas phase is

$$\frac{\partial}{\partial t}(\alpha\rho_g e_g) + \nabla\cdot(\alpha\rho_g e_g\mathbf{v}_g) = -P_g\frac{\partial\alpha}{\partial t} - \nabla\cdot(\alpha P_g\mathbf{v}_g) + \Gamma_g h_g^{(i)} + q_g^{(i)}a^{(i)} - \nabla\cdot(\alpha\mathbf{q}_g) + \alpha\Phi_g. \tag{24}$$

The energy equation for liquid phase is

$$\frac{\partial}{\partial t}[(1-\alpha)\rho_l e_l] + \nabla\cdot[(1-\alpha)\rho_l e_l\mathbf{v}_l] = -P_l\frac{\partial(1-\alpha)}{\partial t} - \nabla\cdot[(1-\alpha)P_l\mathbf{v}_l] + \Gamma_l h_l^{(i)} + q_l^{(i)}a^{(i)} - \nabla\cdot[(1-\alpha)\mathbf{q}_l] + (1-\alpha)\Phi_l, \tag{25}$$

where $h_g^{(i)}$ and $h_l^{(i)}$ are the enthalpy of the gas phase and the liquid phase at the interface, respectively. $a^{(i)}$ is the interfacial area concentration. $\Gamma_g h_g^{(i)}$ and $\Gamma_l h_l^{(i)}$ are the interfacial energy transfer terms due to the liquid-vapor phase change. $q_g^{(i)}$ and $q_l^{(i)}$ are the heat transfer terms of mutual interaction between the vapor and liquid interface. $\mathbf{q}$ is the heat flow vector and Φ is the energy dissipation function, as described below:

$$\mathbf{q}_m = -\lambda_m\nabla T_m, \tag{26}$$

$$\Phi_m = \boldsymbol{\tau}_m:\nabla\mathbf{v}_m, \tag{27}$$

$$\boldsymbol{\tau}_m = \mu_m\left[\nabla\mathbf{v}_m + (\nabla\mathbf{v}_m)^T - \frac{2}{3}(\nabla\cdot\mathbf{v}_m)\mathbf{I}\right], \tag{28}$$

where subscript m denotes the gas phase ($m=g$) or liquid phase ($m=l$).

Assuming that the mass of each vapor bubble and condensed liquid droplet is constant results in the following mass conservation equation for number density, N_k:

$$\frac{\partial}{\partial t}\left(\frac{4}{3}\pi R_k^3 N_k \rho_k\right)+\nabla\cdot\left(\frac{4}{3}\pi R_k^3 N_k \rho_k \mathbf{v}_k\right)=\Gamma_k, \tag{29}$$

$$\begin{cases} k=e: & R_k=R_g, \quad N_k=N_g, \quad \rho_k=\rho_g, \quad \mathbf{v}_k=\mathbf{v}_l, \quad \Gamma_k=\Gamma_g \\ k=c: & R_k=R_l, \quad N_k=N_l, \quad \rho_k=\rho_l, \quad \mathbf{v}_k=\mathbf{v}_l, \quad \Gamma_k=\Gamma_l, \end{cases}$$

where subscript k denotes evaporation ($k=e$) or condensation ($k=c$).

2.2 Constitutive Equations. The drag coefficient, C_D, and the virtual mass coefficient, C_{VM}, are defined as follows (Clift et al. [32]):

$$C_D=\frac{24}{R_B}(1+0.15R_B^{0.687})+\frac{0.42}{1+42500R_B^{-1.16}} \tag{30}$$

$$C_{VM}=0.5 \tag{31}$$

$$R_B=\frac{\rho_l|\mathbf{v}_g-\mathbf{v}_l|D}{\mu_l}. \tag{32}$$

The energy balance condition through the gas and liquid phases interface is expressed by following equations

$$\Gamma_g h_g^{(i)}+q_g^{(i)}+\Gamma_l h_l^{(i)}+q_l^{(i)}=0, \tag{33}$$

where the detailed constitutive equations for interfacial transfer terms in Eq. (33) are given by an empirical formula that is taken from the work of Dobran [33] and Solbrig et al. [34].

It is assumed that the energy transfer is caused by the heat transfer between the isothermal spherical bubble and surrounding liquid. With an assumption of a spherical bubble with equivalent radius R_g, the expression of $a^{(i)}$ is obtained by

$$a^{(i)}=\frac{3\alpha}{R_g}. \tag{34}$$

Assuming that the vapor gas phase follows an ideal gas law and that the relationship between gas phase pressure, P_g, and density, ρ_g, obeys polytropic change, the following equation (Hirt and Romero [35]) results:

$$\rho_g(\kappa_g-1)e_g=[P_g-c_0^2\rho_l(\alpha^*-\alpha)]\alpha^* \tag{35}$$

$$\begin{cases} \alpha\geqslant\alpha_c: & \alpha^*=\alpha \\ \alpha<\alpha_c: & \alpha^*=\alpha_c, \end{cases}$$

where c_0 is the first sound velocity in liquid helium at the initial state ($c_0=236.1$ m/s), and α_c denotes the critical void fraction ($\alpha_c=0.005$). A table of the thermophysical properties of liquid helium by Maynard [36] gives the required physical properties of the liquid phase.

The constitutive equation for gas phase generation density, Γ_g, is defined by the following equation:

$$\Gamma_g=\Gamma_{ge}-\Gamma_{gc}, \tag{36}$$

where Γ_{ge} and Γ_{gc} denote the gas phase evaporation density and gas phase condensation density, respectively. By introducing constitutive equations for Γ_{ge} and Γ_{gc}, we extended the classical nucleation theory for water droplets from subcooled vapor to cryogenic fluid. Namely, Γ_{gk} is assumed to be proportional to the degree of subcooling and superheat. Furthermore, if Γ_{gk} is expressed by the sum of the nucleation rate of the evaporated bubble or the condensed liquid droplet, and also expressed by the increase in mass due to the growth of vapor bubbles and condensed droplets, the following equations for Γ_{gk} are derived (Young [17], Iriya et al. [16], Yamamoto et al. [15]):

$$\Gamma_{gk}=\frac{4}{3}\pi\rho_k I_k R_{k(\mathrm{cr})}^3+4\pi\rho_k\sum_{i=1}^{i_{\max}} N_{ki}R_{ki}^2\frac{dR_{ki}}{dt} \tag{37}$$

$$I_k=\frac{A_c}{1+\Theta}\left(\frac{2\sigma_l}{\pi m^3}\right)^{1/2}\frac{\rho_g^2}{\rho_l}\exp\left(-\frac{4\pi R_{k(\mathrm{cr})}^2\sigma_l}{3k_BT_k}\right)$$

$$\Theta=\frac{2(\kappa_g-1)}{\kappa_g+1}\frac{\Delta h}{\mathcal{R}T_g}\left(\frac{\Delta h}{\mathcal{R}T_g}-0.5\right)$$

$$R_{k(\mathrm{cr})}\approx\frac{2\sigma_l T_s}{\rho_k\Delta h\Delta T}$$

In Eq. (37), R_k is the radius of a bubble or droplet, $R_{k(\mathrm{cr})}$ is the Kelvin-Helmholtz critical nucleate radius, k_B is Boltzmann's constant, I_k is the nuclei generation rate of vapor bubbles or liquid droplets, A_c is the condensation coefficient, Θ is the nonisothermal correction factor, m is the mass of a single molecule of helium, T_s is the saturation temperature, subscript i is the value at each calculation cell. Δh denotes the latent heat which is described by the difference in specific enthalpy between the liquid and gas phases and is defined as $\Delta h=h_l-h_g$, ($h_k=c_{pk}T_k$, $k=g,l$). The temperature difference between saturation temperature and gas phase temperature, ΔT, is defined as $\Delta T=T_s-T_g$. N_{ki} denotes the number density of the generated vapor bubbles or condensed liquid droplets at each calculation cell i. By introducing the formulation of the growth process for bubbles and droplets, we assume that the growth rate of a bubble or droplet is controlled by the rate at which the enthalpy of vaporization or condensation can be conducted away from the bubble and droplets, to the bulk liquid (Moses and Stein [37]). Under that assumption, the equation of the growth process for a single vapor bubble and a condensed droplet is derived as

$$\Delta h\rho_k\frac{dR_{ki}}{dt}=\frac{P}{\sqrt{2\pi\mathcal{R}T_k}}\frac{\kappa_k+1}{2\kappa_k}c_{pk}\Delta T^{(i)}, \tag{38}$$

where $\Delta T^{(i)}$ denotes the interfacial temperature between the vapor phase and the condensed droplet and is derived by the following equation:

$$\Delta T^{(i)}=\left(1-\frac{R_{k(\mathrm{cr})}}{R_{ki}}\right)(T_s-T_g). \tag{39}$$

2.3 Numerical Conditions and Procedure. To construct the numerical conditions for the two-phase liquid helium flow, we refer to the cryogenic two-phase internal flow state of the cavitating He II flow in a venturi channel reported by Maki et al. [6], Daney [9], and to the LE-7 liquid oxygen turbopump for the *H*-II rocket engine reported by Kamijo et al. [4] and Cheremisinoff [3]. The finite difference method is used to solve the set of governing equations mentioned above. In the present calculation, the discrete forms of these equations are obtained using a staggered grid; then a modified SOLA (numerical SOLution Algorithm for transient fluid flow) method of Tomiyama et al. [38] which is superior for the formulation and solution of a gas liquid two-phase flow problem, is applied for the numerical calculation. The liquid phase velocity, $\mathbf{v}_l$, at the location of bubbles is calculated using an area-weighting interpolation method which is used in the SMAC algorithm by Amsden and Harlow [39].

To determine the boundary conditions, nonslip conditions for prescribed normal fluid velocities and free-slip conditions for prescribed superfluid velocities are applied to the sidewall, C-B, in Fig. 1. Also, homogeneous laminar velocity distribution is applied to the inlet cross-sectional area of the flow pipe, A-B, and a continuous outflow condition is applied to the exit section of the pipe, D-C. The mathematical expressions for these boundary conditions are described as follows.

Inlet Section: A-B

Normal fluid component and superfluid component:

$$\mathbf{v}_{l(n)}|_{(\mathrm{in})} = \text{const}, \quad \mathbf{v}_{l(s)}|_{(\mathrm{in})} = \text{const}. \tag{40}$$

Outlet Section: D-C

Normal fluid component and superfluid component:

$$\frac{\partial \mathbf{v}_{l(n)}}{\partial t} + \mathbf{v}_{l(n)m} \frac{\partial \mathbf{v}_{l(n)}}{\partial n_{(\mathrm{DC})}}\bigg|_{(\mathrm{ex})} = \mathbf{0}, \quad \frac{\partial \mathbf{v}_{l(n)}}{\partial t} + \mathbf{v}_{l(s)m} \frac{\partial \mathbf{v}_{l(s)}}{\partial n_{(\mathrm{DC})}}\bigg|_{(\mathrm{ex})} = \mathbf{0}, \tag{41}$$

where $\partial/\partial n_{(\mathrm{DC})}$ denotes the partial derivative of the direction normal to boundary D-C, and $\mathbf{v}_{l(n)m}$ and $\mathbf{v}_{l(s)m}$ denote the normal fluid and superfluid mean velocity at cross sectional area of boundary D-C, respectively.

Sidewall: C-B

Normal fluid component:

$$\mathbf{v}_{l(n)}|_w = \mathbf{0} \tag{42}$$

Superfluid component:

$$\mathbf{v}_{l(s)} \cdot \mathbf{n}_{(\mathrm{CB})}|_w = 0, \quad \frac{\partial}{\partial n_{(\mathrm{CB})}} (\mathbf{v}_{l(s)} \cdot \mathbf{t}_{(\mathrm{BC})})\bigg|_w = 0, \tag{43}$$

Axisymmetric axis: D-A

Normal fluid component and superfluid component:

$$\mathbf{v}_{l(n)} \cdot \mathbf{n}_{(\mathrm{DA})}| = 0, \quad \frac{\partial}{\partial n_{(\mathrm{DA})}} (\mathbf{v}_{l(n)} \cdot \mathbf{t}_{(\mathrm{DA})})\bigg|_w = 0 \tag{44}$$

$$\mathbf{v}_{l(s)} \cdot \mathbf{n}_{(\mathrm{DA})}| = 0, \quad \frac{\partial}{\partial n_{(\mathrm{DA})}} (\mathbf{v}_{l(s)} \cdot \mathbf{t}_{(\mathrm{DA})})\bigg|_w = 0, \tag{45}$$

where $\mathbf{n}_{(\mathrm{DA})}$ and $\mathbf{t}_{(\mathrm{DA})}$ denote the normal and tangential vectors at boundary D-A, respectively, and $\partial/\partial n_{(\mathrm{DA})}$ denotes the partial derivative of the direction normal to boundary D-A.

The initial steady condition of the liquid phase is assumed to be the critical He I state. Next, the initial conditions at the inlet section of the flow pipe are given as follows: $P_{l(\mathrm{in})} = 0.20$ MPa, $\alpha_{(\mathrm{in})} = 0.001$, $e_{l(\mathrm{in})} = 9.351$ kJ/kg, $\kappa_{gs(\mathrm{in})} = 10.21$, $u_{l(n)(\mathrm{in})} = u_{l(s)(\mathrm{in})} = 1.0$ m/s, $v_{l(n)(\mathrm{in})} = v_{l(s)(\mathrm{in})} = 0.0$ m/s, and $N_{k(\mathrm{in})} = 10^4 (\mathrm{m}^3 \cdot \mathrm{s})^{-1}$.

Furthermore, the initial conditions of pressure, P_l, α and e_l at the exit section the flow pipe are given as follows: $P_{l(\mathrm{ex})} = 101.3$ kPa, $\alpha_{(\mathrm{ex})} = 0.9999$ and $e_{l(\mathrm{ex})} = 0.1047$ kJ/kg. For other physical properties (Maynard [36], Van Sciver [2]) used in constitutive equations, $\rho_{l(n)}$, $\rho_{l(s)}$, μ_l, λ_l, S_l, and σ_l are given as a function of temperature.

The interval of each time step is automatically adjusted during the computation to satisfy the CFL condition (Harlow and Amsden [13]). We actually calculated solutions on three different grid densities: 40×130, 60×200 and 80×270 nodes. As a result, we found that each numerical result shows almost the same profiles, and the grid independence of the numerical results was confirmed. Thus, as a compromise between computer memory and accuracy, we chose to use the 60×200 rectangular grid in the r and z directions for the calculations.

2.4 Results and Discussion. Figure 2 shows the numerical results of the transient evolution of the void fraction, α, contour, Fig. 3 shows the instantaneous liquid phase pressure, P_l, contour, Fig. 4 shows the transient evolution of liquid phase temperature, T_l, contour. From Fig. 2, it is clear that the phase change effectively occurs with time and that the gas phase spreads throughout the inner flow pipe. In this numerical calculation, it is assumed that the large gas phase volume fraction region indicates that the small size bubbles are closely aggregated region, and that the downstream flow state keeps very closed bubbly flow in large void fraction region. It is found that the characteristics of superfluidity are conspicuous in the large gas phase volume fraction region where the phase change actively occurs and the pressure gradient actively changes. The effect of superfluidity with He I to He II phase transition is mainly caused by the decrease in liquid

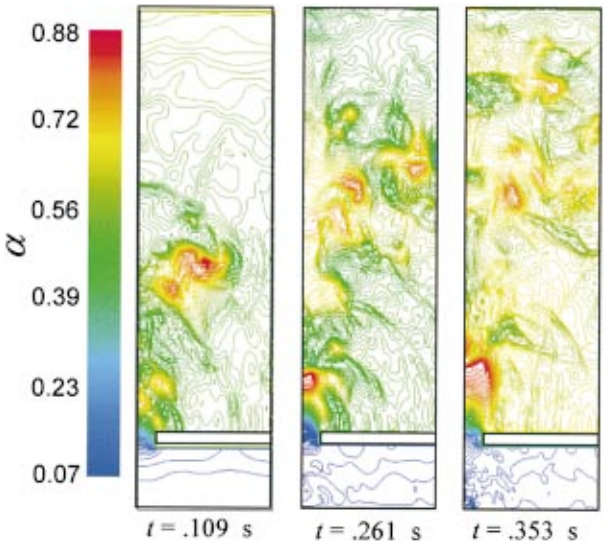

Fig. 2 Time evolution of void fraction distributions

phase temperature or internal energy due to the deprivation of latent heat for vaporization from the liquid phase and the change of the specific heat of the liquid phase with the change of pressure gradient. From Fig. 4, it is especially found that the temperature around the interface between the large gas phase volume fraction region and the liquid phase region decreases with the increase in the phase change. The liquid phase temperature decrease due to the latent heat is characterized by the interfacial energy transfer terms with the phase change in Eqs. (24) and (25). From Figs. 2 and 3, in the region of high volume fraction of the gas phase, the pressure distribution changes markedly because of the normal fluid-superfluid transition due to the momentum terms in Eqs. (6) and (7) that include the temperature gradient term, the momentum energy gradient term based on relative superfluid-normal fluid velocity, and the superfluid-normal fluid mutual friction interaction term. Focusing on Fig. 3, the decrease in the absolute value of the negative pressure gradient and the increase in the absolute value of the positive pressure gradient are found near the downstream region passing through the orifice. Immediately after the flow is initially induced, taking note of the primary feature of the void

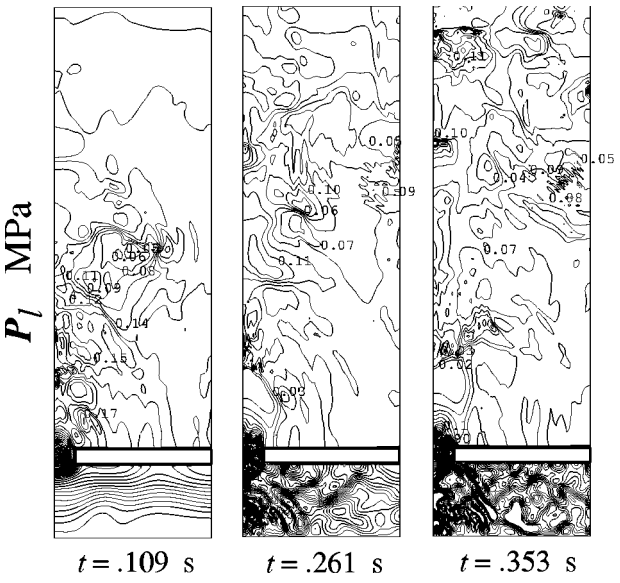

Fig. 3 Instantaneous liquid phase pressure contours

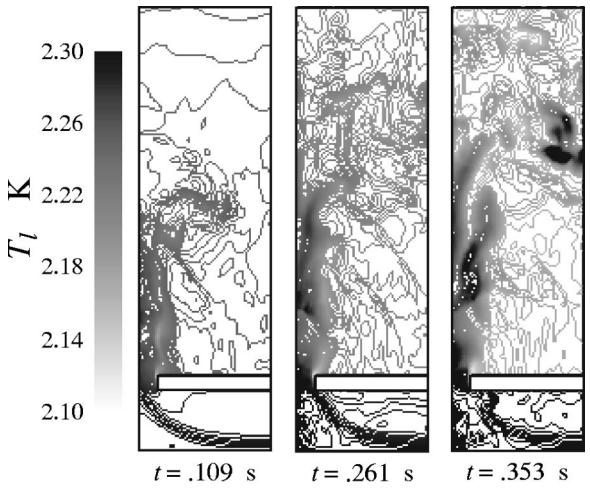

Fig. 4 Time evolution of liquid phase temperature profiles

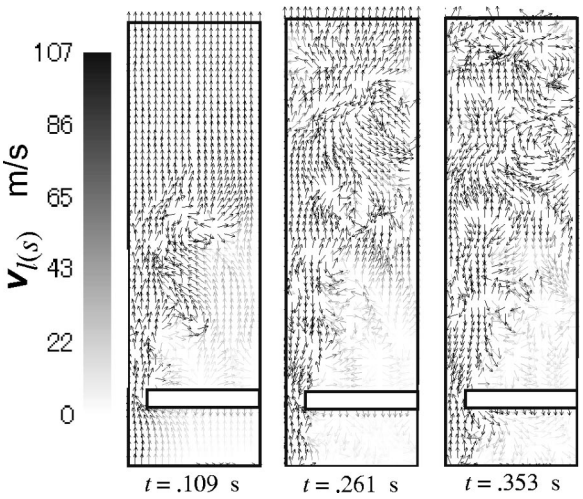

Fig. 6 Instantaneous superfluid velocity vector

fraction profile, the gas phase leaves from a position behind the edge of the orifice and is concentrated downstream of orifice due to the small vortex induced by the He I wake passing through the orifice, based on the effect of the negative pressure gradient. With time, the gas phase rises from the edge of the orifice, and the high volume fraction region of the gas phase moves downstream. It is found that the phase change effectively occurs with time and that the gas phase spreads throughout the inner flow pipe, caused by the decrease in the slip ratio and the gas phase velocity due to the change of both streamwise and transverse pressure gradients based on the superfluidity generation. Another reason for the enhancement of liquid-vapor phase change is that the existence rate of the gas phase spread in the pipe per unit time increases with the increase in the effect of superfluidity. The tendencies of those numerical results for void fraction, pressure, and temperature profiles show qualitatively agreement with the experimental datum of the cavitation in He II flow by Maki et al. [6], and Ishii et al. [7].

Figures 5, 6, and 7 show the instantaneous liquid phase normal fluid velocity component $\mathbf{v}_{l(n)}$, the superfluid velocity component $\mathbf{v}_{l(s)}$, and gas phase velocity $\mathbf{v}_g$ profiles, respectively. In the case of temperatures above the λ point, we assume that the superfluid behaves in the same manner as the normal fluid; thus the profile of $\mathbf{v}_{l(s)}$ similar to the profile of $\mathbf{v}_{l(n)}$ denotes the normal fluid velocity profile. From Figs. 3 and 5, it is found that there is a low-pressure region passing through the central axis of the orifice induced by the acceleration of fluid velocity. From Fig. 5, it can be seen that the magnitude of fluctuation of $\mathbf{v}_{l(n)}$ increases with an increase in streamwise coordinate z just behind the orifice. From a comparison of the results of the two-phase velocity profile between the superfluid component and the normal fluid component, it is clear that the counterflow of the superfluid against the normal fluid occurs in the region where the liquid to vapor phase change actively occurs; and that the velocity vectors between normal fluid and superfluid show different profiles. Immediately after the flow is initially induced, taking note of the primary feature of the liquid phase velocity profile, profiles of $\mathbf{v}_{l(n)}$ and $\mathbf{v}_{l(s)}$ behave similarly; with time, however, especially downstream of the orifice in the high volume fraction region of the gas phase, the difference in velocity profiles is observed due to the counterflow of the superfluid against the normal fluid based on the generation of the superfluidity. It is found that the magnitude of the vortex induced by the He I wake passing through the orifice becomes larger; however, the vortex has a shape different from that of He II because of the small viscosity in normal fluid and counterflow of superfluid. The superfluid counterflow against normal fluid is mainly caused by the momentum terms in Eqs. (6) and (7), i.e., the temperature gradient term and the momentum energy gradient term for superfluid-normal fluid relative velocity. The superfluid counterflow caused by the effect of these momentum terms is conspicuously found when the vaporization with the He I to He II phase transition is generated. Furthermore, it is found that the gas phase is accelerated in streamwise and radial directions, not only by the buoyancy force but also due to the negative liquid phase pressure

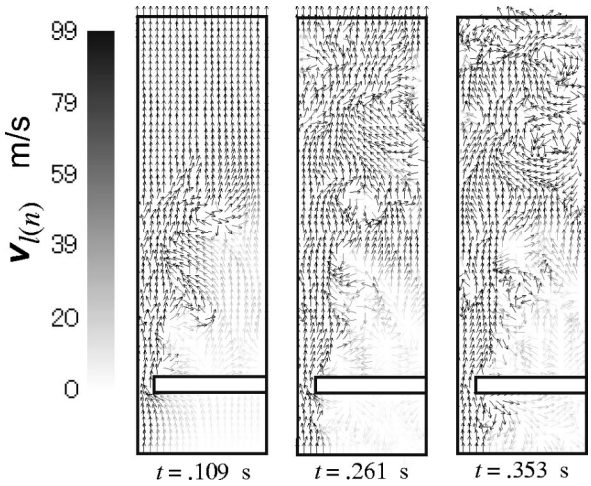

Fig. 5 Instantaneous normal fluid velocity vector

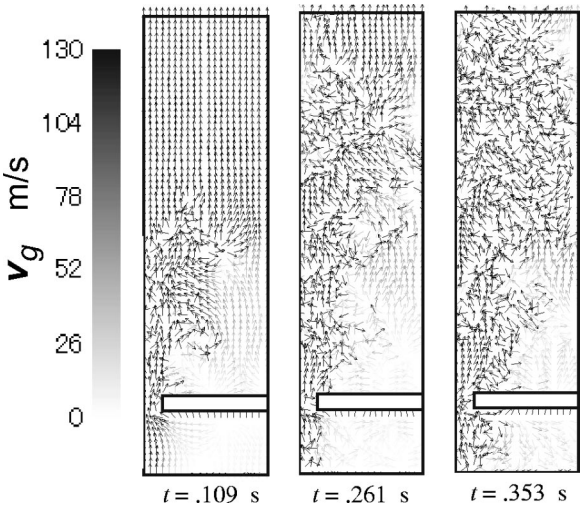

Fig. 7 Instantaneous gas phase velocity vector

gradient and additional lift forces that act on the bubbles. Contrarily, the gas phase is decelerated due to the additional drag forces and positive liquid phase pressure gradient that act on the bubbles. With time, the gas phase motion exhibits diffusing behavior caused by the interaction between the fluid flow of the gas and liquid phases. One of the momentum interactions related to the diffusing behavior is caused by the change of pressure gradient, which acts on the bubbles due to the superfluid counterflow against the normal fluid. The gas phase velocity deceleration rate increases with the increase in the He I to He II phase transition rate due to the decrease in the negative liquid phase pressure gradient or the increase of positive pressure gradient around the interface between gas and liquid phases. The change of the liquid phase pressure gradient for $\mathbf{v}_g$ deceleration with the effect of the spread of the gas phase is caused by the increase of the He II to He I counterflow with phase transition.

3 Conclusion

The axisymmetric two-dimensional characteristics of the vapor-liquid two-phase flow of liquid helium in a pipe were numerically investigated to realize the further development and high performance of cooling devices or new cryogenic engineering applications. First, the governing equations of the two-phase flow of liquid helium based on the unsteady multi-fluid model were presented and several flow characteristics were numerically calculated, taking into account the effect of superfluidity. The main results obtained here can be summarized as follows.

1 It was found that the characteristics of superfluidity are conspicuous in the large gas phase volume fraction region where the phase change actively occurs and the pressure gradient actively changes. Also, the effect of superfluidity with He I to He II phase transition is mainly caused by the decrease in liquid phase temperature or internal energy due to the deprivation of latent heat for vaporization from the liquid phase.

2 The superfluid counterflow against normal fluid caused by the effect of momentum terms based on superfluidity is conspicuously found when the vaporization with He I to He II phase transition is generated. Furthermore, the gas phase diffusing behavior is found with time because of the change of pressure gradient, which acts on the bubbles due to the superfluid counterflow.

Nomenclature

c_p = specific heat at constant pressure
c_v = specific heat at constant volume
D = inner diameter of pipe
e = specific internal energy
$\mathbf{g}$ = vector of gravitational acceleration
h = specific enthalpy
$\mathbf{I}$ = unit tensor
N = number density
P = absolute pressure
R = radius of bubble or droplet
r = radial coordinate
S = specific entropy
T = absolute temperature
t = time
u = velocity component in the r-direction
v = velocity component in the z-direction
$\mathbf{v}$ = vector of velocity
z = streamwise coordinate
α = void fraction
Γ = phase generation density
κ = ratio of specific heat
λ = thermal conductivity
μ = dynamic viscosity
ν = kinematic viscosity
ρ = density
σ = surface tension
θ = azimuthal coordinate
$\boldsymbol{\tau}$ = viscous stress tensor
ω = vorticity
$\boldsymbol{\Omega}$ = angular velocity vector
$\mathcal{R}$ = gas constant
$\mathbf{0}$ = zero vector

Suffixes

c = condensation
e = evaporation
(ex) = exit section of the pipe
g = gas phase
(i) = interface
(in) = inlet section of the pipe
l = liquid phase
(n) = normal fluid
s = saturation
(s) = superfluid
r = component in the r direction
T = transposed matrix
w = wall
z = component in the z direction
λ = λ point
θ = component in the θ direction
0 = initial stationary state

References

[1] Filina, N. N., and Weisend, J. G., 1996, *Cryogenic Two-Phase Flow*, Cambridge University Press, New York, NY, pp. 20–76.
[2] Van Sciver, S. W., 1996, *Helium Cryogenics*, Plenum Press, New York, N.Y., pp. 77–130.
[3] Cheremisinoff, N. P., 1989, *Encyclopedia of Fluid Mechanics Volume 8, Aerodynamics and Compressible Flows*, Gulf Publishing Corp., Houston, Texas, pp. 1039–1061.
[4] Kamijo, K., Yoshida, M., and Tsujimoto, Y., 1993, ''Hydraulic and Mechanical Performance of LE-7 LOX Pump Inducer,'' J. Propul. Power, **9**, No. 6, pp. 819–826.
[5] King, J. A., 1972, ''Design of Inducers for Two-Phase Operation Final Report,'' NASA CR-123555, pp. 1–96.
[6] Maki, K., Ishii, T., Kobayashi, K., and Murakami, M., 2000, ''Visualization and Pressure Variation of Cavitation in He II Flow,'' Journal of the Cryogenic Society of Japan, (in Japanese) **35**, No. 1, pp. 16–21.
[7] Ishii, T., Maki, K., and Murakami, M., 2000, ''Temperature Variation Induced by Cavitation Flow of Liquid Helium,'' *Proceedings of 18th International Cryogenic Engineering Conference*, (in CD ROM).
[8] Ludtke, P. R., and Daney, D. E., 1988, ''Cavitation Characteristics of a Small Centrifugal Pump in He I and He II,'' Cryogenics, **28**, pp. 96–100.
[9] Daney, D. E., 1988, ''Cavitation in Flowing Superfluid Helium,'' Cryogenics, **28**, pp. 132–136.
[10] Ishimoto, J., Oike, M., and Kamijo, K., 2000, ''Two-Dimensional Numerical Analysis of Boiling Two-Phase Flow of Liquid Helium,'' JSME International Journal, Series B, **43**, No. 1, pp. 62–70.
[11] Kataoka, I., 1986, ''Local Instant Formulation of Two-phase Flow,'' Int. J. Multiphase Flow, **12**, No. 5, pp. 745–758.
[12] Landau, L., 1941, ''The Theory of Superfluidity of Helium II,'' Journal of Physics, **V**, No. 1, pp. 71–90.
[13] Harlow, F. H., and Amsden, A. A., 1975, ''Numerical Calculation of Multiphase Fluid Flow,'' J. Comput. Phys., **17**, pp. 19–52.
[14] Cook, T. L., and Harlow, F. H., 1986, ''Vortices in Bubbly Two-Phase Flow,'' Int. J. Multiphase Flow, **12**, No. 1, pp. 35–61.
[15] Yamamoto, S., Hagari, H., and Murayama, M., 2000, ''Numerical Simulation of Condensation around the 3-D Wing,'' Transactions of The Japan Society for Aeronautical and Space Sciences, **42**, No. 138, pp. 182–189.
[16] Iriya, I., Yamamoto, S., and Daiguji, H., 1996, ''Numerical Method for Transonic Viscous Flow Considering Humidity,'' Trans. Jpn. Soc. Mech. Eng., Ser. B, **62**, No. 603, pp. 3854–3859.
[17] Young, J. B., 1992, ''Two-Dimensional, Nonequilibrium, Wet-Stream Calculations for Nozzles and Turbine Cascades,'' ASME J. Turbomach., **114**, pp. 569–579.
[18] Donnelly, R. J., 1993, ''Quantized Vortices and Turbulence in Helium II,'' Annu. Rev. Fluid Mech., **25**, pp. 325–371.
[19] Bekarevich, I. L., and Khalatnikov, I. M., 1961, ''Phenomenological Derivation of the Equations of Vortex Motion in Helium II,'' Sov. Phys. JETP, **13**, No. 3, pp. 643–646.
[20] Hall, H. E., and Vinen, W. F., 1956, ''The Rotation of Liquid Helium II, II. The Theory of Mutual Friction in Unif\ormly Rotating Helium II,'' Proc. R. Soc. London, Ser. A, **238**, pp. 215–234.
[21] Tsubota, M., and Yoneda, H., 1995, ''Dynamics of Quantized Vortices in Rotating Superfluid,'' J. Low Temp. Phys., **101**, No. 3, pp. 815–820.
[22] Kashani, A., Van Sciver, S. W., and Strikwerda, J. C., 1989, ''Numerical Solution of Forced Convection Heat Transfer in He II,'' Numer. Heat Transfer, Part A, **16**, pp. 213–228.

[23] Batchelor, G. K., 1967, *An Introduction to Fluid Dynamics*, Cambridge University Press, New York, NY, pp. 246–255.
[24] Tomiyama, A., Zun, I., Higaki, H., Makino, Y., and Sakaguchi, T., 1997, ''A Three-Dimensional Particle Tracking Method for Bubbly Flow Simulation,'' Nucl. Eng. Des., **175**, pp. 77–86.
[25] Hinze, J. O., 1975, *Turbulence*, 2nd ed., McGraw-Hill, New York, NY, pp. 460–471.
[26] Rubinow, S. I., and Keller, J. B., 1965, ''The Transverse Force on a Spinning Sphere Moving in a Viscous Fluid,'' J. Fluid Mech., **22**, pp. 447–459.
[27] Auton, T. R., 1987, ''The Lift Force on a Spherical Body in Rotational Flow,'' J. Fluid Mech., **183**, pp. 199–218.
[28] Auton, T. R., Hunt, J. C. R., and Prud'homme, M., 1988, ''The Force Exerted on a Body in Invisid Unsteady Non-Uniform Rotational Flow,'' J. Fluid Mech., **197**, pp. 241–257.
[29] Saffman, P. G., 1965, ''The Lift on a Small Sphere in a Slow Share Flow,'' J. Fluid Mech., **22**, Part 2, pp. 385–400.
[30] Dennis, S. C. R., Singh, S. N., and Ingham, D. B., 1980, ''The Steady Flow Due to A Rotating Sphere at Low and Moderate Reynolds Numbers,'' J. Fluid Mech., **101**, Part 2, pp. 257–279.
[31] Takagi, H., 1977, ''Viscous Flow Induced by Slow Rotation of Sphere,'' J. Phys. Soc. Jpn., **42**, No. 1, pp. 319–325.
[32] Clift, R., Grace, J. R., and Weber, M. E., 1978, *Bubbles, Drops, and Particles*, Academic Press, San Diego, CA, pp. 97–141.
[33] Dobran, F., 1988, ''Liquid and Gas-Phase Distributions in A Jet With Phase Change,'' ASME J. Heat Transfer, **110**, pp. 955–960.
[34] Solbrig, C. W., McFadden, J. H., Lyczkowski, R. W., and Hughes, E. D., 1978, ''Heat Transfer and Friction Correlations Required to Describe Steam-water Behavior in Nuclear Safety Studies,'' AIChE Symp. Ser., **74**, No. 174, pp. 100–128.
[35] Hirt, C. W., and Romero, N. C., 1975, ''Application of a Drift Flux Model to Flashing in Straight Pipes,'' Los Alamos Scientific Laboratory Report, LA-6005-MS, pp. 1–16.
[36] Maynard, J., 1976, ''Determination of the Thermodynamics of He II from Sound-Velocity Data,'' Phys. Rev. B, **14**, No. 9, pp. 3868–3891.
[37] Moses, C. A., and Stein, G. D., 1978, ''On the Growth of Steam Droplets Formed in Laval Nozzle Using Both Static Pressure and Light Scattering Measurements,'' ASME J. Fluids Eng., **100**, pp. 311–322.
[38] Tomiyama, A., and Hirano, M., 1994, ''An Improvement of the Computational Efficiency of the SOLA Method,'' JSME International Journal, Series B, **37**, No. 4, pp. 821–826.
[39] Amsden, A. A., and Harlow, F. H., 1970, ''The SMAC Method: A Numerical Technique for Calculating Incompressible Fluid Flows,'' Los Alamos Scientific Laboratory Report, LA-4370.

Predictions of a Turbulent Separated Flow Using Commercial CFD Codes

Gianluca Iaccarino
Center for Turbulence Research,
Stanford University,
Stanford, CA 94305-3030

Numerical simulations of the turbulent flow in an asymmetric two-dimensional diffuser are carried out using three commercial CFD codes: CFX, Fluent, and Star-CD. A low-Reynolds number k-ϵ model with damping functions and the four-equation $\overline{v'^2}-f$ model are used; the first one is available as a standard feature in all the codes, the $\overline{v'^2}-f$ model was implemented using the User Defined Routines. The flow features a large recirculating zone due to the adverse pressure gradient in the diffuser; the $\overline{v'^2}-f$ predictions agree very well with the experiments both for the mean velocity and the turbulent kinetic energy. The length of the separation bubble is also computed within 6 percent of the measured value. The k-ϵ calculations do not show any recirculation and the agreement with the measurements is very poor. The three codes employed show very similar characteristics in terms of convergence and accuracy; in particular, the results obtained using the $\overline{v'^2}-f$ are consistent in all the codes, while appreciable differences are obtained when the k-ϵ is employed. [DOI: 10.1115/1.1400749]

1 Introduction

Computational Fluid Dynamics tools are becoming standard in many fields of engineering involving flow of gases and liquids; numerical simulations are used both in the design phase to select between different concepts and in the production phase to analyze performance. Industrial CFD applications require high flexibility in the grid–generation procedure for complex configurations, short turn around time, and easy–to–use environments. At present, several commercial packages are available for the CFD industrial community; these packages are usually integrated systems which include a mesh generator, a flow solver, and a visualization tool. Often the numerical techniques adopted in these CFD codes are well accepted algorithms published in the open literature; the selection of one technique with respect to others is usually based on robustness and reliability.

There have been few attempts in the literature to compare the performance of these codes; laminar and turbulent test cases have been proposed to several CFD code vendors by the Coordinating Group for Computational Fluid Dynamics, of the Fluids Engineering Division of ASME[1]. A series of five benchmark problems were calculated, with all the mesh generation and simulations performed by the vendors themselves; only two of the problems required turbulent simulations. The first problem is the flow around a square cylinder; the flow is unsteady and all the codes predicted reasonably well the measured Strouhal number. However, poor accuracy resulted in the prediction of the details of the wake flow field. It was also noted that, depending on the code used (and assuming grid-converged results) the *same* k-ϵ model predicted very different results. The reasons for this difference can be different grids, no demonstration of grid convergence, different implementations of the models, and different boundary conditions. It must also be pointed out that the prediction for this problem is strongly affected by the treatment of the stagnation point region. As shown by Durbin [2], the k-ϵ models predict a *spurious* high level of turbulent kinetic energy in this region.

The other turbulent problem reported by Freitas [1] was the three-dimensional developing flow in a 180 degrees bend. In this case all the solutions reported were unsuccessful in predicting the measured data in the bend region and the resolved structure of the flow field was significantly affected by the choice of the turbulence model.

The uncertainties associated with (i) different computational grids, (ii) boundary conditions definition, (iii) convergence, and (iv) numerical schemes do not allow drawing specific conclusions about the codes used, other than the usual conclusion that *further research into more advanced turbulence models for use in commercial CFD codes is required* [1].

In order to carry out a fair comparison between different CFD codes and to establish definitive conclusions on the state–of–the–art of commercial CFD codes, all the differences $(i$-$iv)$ must be fully addressed and, if possible, eliminated. In the present work, an effort has been made to control all these parameters. The codes available for comparison are CFX, Fluent, and Star-CD. The objective is to compare their predictive capabilities for the simulation of a turbulent separated flow. Several turbulence closures (and near-wall treatments) are available in these codes ranging from k-ϵ-type models to full Reynolds stress models. The main focus of the work is on two models: the k-ϵ low-Reynolds model by Launder and Sharma [3] and the $\overline{v'^2}-f$ by Durbin [4]. In addition, results obtained using different closures are reported.

The k-ϵ model is well described in the literature and has been widely used. Its implementation poses some challenges and it requires the solution of two transport equations with numerically stiff source terms. This model is available in all the codes considered and, although it is not expected to be extremely accurate [5], it provides common ground for comparisons between different codes.

The $\overline{v'^2}-f$ model (implemented in a NASA research code) has been already successfully used for simulating separated flows [4], three dimensional configurations [6] and flows with heat transfer [7]. It is rather complex involving the solution of four differential equations (three transport equations plus an Helmotz-type equations).

The test case analyzed in this study is a two-dimensional turbulent flow in a diffuser. Due to the adverse pressure gradient the flow is separated and a large recirculation bubble is generated. This problem has been selected because a very reliable experimental database is available. Moreover, a detailed Large Eddy

Contributed by the Fluids Engineering Division for publication in the JOURNAL OF FLUIDS ENGINEERING. Manuscript received by the Fluids Engineering Division October 16, 2000; revised manuscript received May 21, 2001. Associate Editor: I. Celik.

Simulation study was carried out at the Center for Turbulence Research and the resulting numerical database is also available for comparison [8].

The objective of the paper is to present a detailed and careful comparison of the simulations performed using three commercial CFD codes. Although the flow under investigation is geometrically simple, it is challenging for turbulence modeling and must be considered as a necessary step to evaluate the merits of different approaches. In addition, its simplicity allows to control all the numerical parameters involved in the simulations and to understand the causes of discrepancy between the codes.

The three CFD codes used are briefly introduced in the next section; the turbulence models with the governing equations are presented in Sec. 3, while results and comparison are in Sec. 4.

2 Numerical Method

The steady Navier-Stokes (NS) equations for an incompressible fluid are considered:

$$\frac{\partial u_i}{\partial x_i} = 0 \tag{1}$$

$$u_i \frac{\partial u_j}{\partial x_i} = \frac{\partial}{\partial x_j}\left[(\nu + \nu_t) \frac{\partial u_j}{\partial x_j}\right] - \frac{\partial p}{\partial x_j} \tag{2}$$

where u_i are the mean velocity components, p is the pressure, and ν and ν_t the laminar and turbulent viscosity, respectively. Additional equations for turbulent quantities are considered to compute the eddy viscosity, and are explained in the following section.

All the codes solve the discretized equations in a segregated manner, with the SIMPLE (Semi-Implicit Method for Pressure-Linked Equations) algorithm, or its ''consistent'' variant, SIMPLEC [9], used to achieve the pressure-velocity coupling for stability. In the SIMPLE algorithm, the continuity equation (1) is converted into a discrete Poisson equation for pressure. The differential equations are linearized and solved implicitly in sequence: starting with the pressure equation (predictor stage), followed by the momentum equations and the pressure correction equation (corrector stage). The equations for the scalars (turbulent quantities) are solved after the updating of both pressure and velocity components. Within this loop, the linearized equations for each variable, as they arise, are treated using a linear system solver (i.e., multigrid, Preconditioned Conjugate Gradient, PCG, etc.).

A brief description of the codes is given in the next subsections with emphasis given only to the features required for this study. All the codes allow the implementation of customized models through User Defined Subroutines.

2.1 CFX v4.3. CFX v4.3 is a CFD computer code developed and marketed by AEA Technologies. The code solves the three-dimensional NS equations on structured multiblock grids for both compressible and incompressible flows. Various turbulence models are available ranging from two-equation to complete Differential Reynolds Stress Models (DRSM). CFX uses a SIMPLEC pressure-correction scheme (SIMPLE is also available), and several spatial discretizations which include first-order Upwind Differencing (UD) and QUICK [10]; central differencing is used for the pressure. The linear system arising at each iteration is then solved using a Preconditioned Conjugate Gradient technique.

2.2 Fluent v5.3. Fluent v5.3 is a CFD computer code developed and marketed by Fluent Inc. The code provides mesh flexibility by unstructured meshes. Turbulence closures range from one-equation turbulence model up to DRSM [11].

Fluent employs the SIMPLEC technique and an algebraic multigrid linear system solver to update the solution at each iteration. The QUICK spatial discretization technique is available among others. In particular, a second-order Total Variation Diminishing (TVD) limited discretization for the pressure in the Poisson equation is used [12].

2.3 Star-CD v3.1. Star-CD v3.1 is a CFD computer code developed and marketed by Computational Dynamics Ltd. The code solves the three-dimensional NS equations on unstructured meshes; various linear and non-linear two-equation turbulence models are available [13].

Star-CD uses the SIMPLE technique for velocity-pressure correction and a PCG method to solve the implicit system of equations; several first and high order spatial discretization schemes can be used including QUICK.

3 Turbulence Modeling

Several turbulence models are available in the codes presented in the previous section. Most of them are derived from the standard k-ϵ model [14] with different treatments of the wall region.

The low-Reynolds model of Launder and Sharma [3] and the $\overline{v'^2}-f$ model [4] are the focus of this work, and are described in detail. Additional simulations are performed with the k-ϵ Two-Layer Model [15], the cubic Non-Linear Eddy-Viscosity (NLEV) k-ϵ Model [16], and the Differential Reynolds Stress Model [13].

The Launder and Sharma k-ϵ model is available as a standard option in all the codes (a slightly different damping function is employed in Star-CD). The $\overline{v'^2}-f$ model has been implemented using the User Defined Subroutines in each of the codes.

3.1 Low-Reynolds k-ϵ Model. The k-ϵ model was introduced by Launder and Spalding [14]. The high Reynolds number version is obtained by neglecting all the terms containing the kinematic viscosity. In the proximity of solid walls, viscous effects become important and this assumption no longer holds. Several modifications have been proposed: in the two-layer formulation [15], a simpler model is used close to the wall (usually a one-equation model) and then the eddy viscosity is patched at a certain distance from the wall; both Fluent and Star-CD offer this option. In the damping functions approach [17] algebraic functions are introduced to correct the behavior of turbulent quantities close to the wall. Several different choices are available in the open literature. All the codes have built-in damping function models; in particular, Fluent has six different versions available. In this work, the model introduced by Launder and Sharma [3], which is available in all the codes, was used.

The k-ϵ equations are:

$$u_i \frac{\partial k}{\partial x_i} = P - \epsilon + \frac{\partial}{\partial x_j}\left[\left(\nu + \frac{\nu_t}{\sigma_k}\right)\frac{\partial k}{\partial x_j}\right] - D \tag{3}$$

$$u_i \frac{\partial \epsilon}{\partial x_i} = \frac{f_1 C_{\epsilon_1} P - f_2 C_{\epsilon_2}\epsilon}{T} + \frac{\partial}{\partial x_j}\left[\left(\nu + \frac{\nu_t}{\sigma_\epsilon}\right)\frac{\partial \epsilon}{\partial x_j}\right] + E \tag{4}$$

The eddy viscosity is obtained from

$$\nu_t = C_\mu f_\mu k T \tag{5}$$

The damping functions f_1, f_2, and f_μ, the timescale T and the extra source terms D and E are:

$$f_1 = 1 \tag{6}$$

$$f_2 = 1 - 0.3 e^{-Re_T^2} \tag{7}$$

$$f_\mu = e^{-3.4/(1+0.02\mathrm{Re}_T)2} \tag{8}$$

$$T = k/\epsilon \tag{9}$$

$$D = 2\nu\left(\frac{\partial \sqrt{k}}{\partial x_n}\right)^2 \tag{10}$$

$$E = 2\nu\nu_t\left(\frac{\partial^2 u_i}{\partial x_j x_k}\right)^2 \tag{11}$$

where $\mathrm{Re}_T = k^2/\nu\epsilon$ is the turbulent Reynolds number and x_n is the direction normal to walls.

The damping function f_μ used in StarCD is slightly different from that reported by Launder and Sharma [3]. In order to eliminate this possible cause of discrepancy between the codes, the eddy viscosity in StarCD has been computed using a User-Defined Subroutine according to Eq. (5) with f_μ defined as in (8).

The same constants have been used in all the codes, corresponding to the values reported by Launder and Sharma [3]. The implementation of this model is not straightforward because of the presence of the extra-source terms (10) and (11). In particular, the definition of the direction x_n, the normal to the wall, maybe difficult in general geometries and the evaluation of the second derivatives of the velocity vector (Eq. (10)) is computationally expensive. The presence of the molecular viscosity in the expressions (10) and (11) makes the contributions negligible away from the walls. However, their implementation affects the behavior of turbulent quantities in the viscous-dominated near-wall regions.

3.2 $\overline{v'^2}-f$ Model. The $\overline{v'^2}-f$ turbulence model is an alternative to the k-ϵ model and was introduced to model the near-wall turbulence without the use of exponential damping or wall functions. The model requires the solution of four differential equations: the basic equations for k and ϵ are the same as before (Eqs. (3)-(4)) but with the following definitions:

$$f_1 = 1 + 0.045\sqrt{k/\overline{v'^2}} \tag{12}$$

$$f_2 = 1 \tag{13}$$

$$f_\mu = \overline{v'^2}/k \tag{14}$$

$$T = \max\left[\frac{k}{\epsilon}, 6\sqrt{\frac{\nu}{\epsilon}}\right] \tag{15}$$

$$D = 0 \tag{16}$$

$$E = 0 \tag{17}$$

The additional equations model the turbulence velocity scale $\overline{v'^2}$, and its production, kf:

$$u_i\frac{\partial \overline{v'^2}}{\partial x_i} = kf - 6\overline{v'^2}\frac{\epsilon}{k} + \frac{\partial}{\partial x_j}\left[\left(\nu + \frac{\nu_t}{\sigma_k}\right)\frac{\partial \overline{v'^2}}{\partial x_j}\right] \tag{18}$$

$$f - L^2\frac{\partial^2 f}{\partial x_j \partial x_j} = C_1\frac{(2/3 - \overline{v'^2}/k)}{T} + C_2\frac{P}{k} + \frac{5\overline{v'^2}/k}{T} \tag{19}$$

where L is the length scale, defined as

$$L^2 = C_L^2 \max\left[\frac{k^3}{\epsilon^2}, C_\eta^2\sqrt{\frac{\nu^3}{\epsilon}}\right] \tag{20}$$

The eddy-viscosity damping is provided in this case by the presence of $\overline{v'^2}$ (Eq. (14)) instead of k in Eq. (5). In other words, the amount of damping is controlled by the ratio between $\overline{v'^2}$ and k (instead of the turbulent Reynolds number, Re_t, like in the k-ϵ model) which is a measure of the turbulence anisotropy [4]. The other important feature of the $\overline{v'^2}-f$ model is the nonlocality arising from the solution of an elliptic equation for f.

The $\overline{v'^2}-f$ model has been implemented by the author in the three CFD codes described above. Four additional scalars are solved and the diffusion, source, and convective terms are specified according to Eqs. (3)-(4) and (18)-(19). The eddy viscosity is then computed according to Eq. (5) and used in the mean flow Eqs. (1)-(2).

4 Results

Steady flow in asymmetric, two-dimensional diffuser is considered. This problem was a test-case for the 8th ERCOFTAC/IAHR/COST Workshop on Refined Turbulence modeling in Espoo, Finland, 17-18 June 1999.

The geometry is presented in Fig. 1: the inlet conditions are specified as a fully-developed channel flow at Re=20,000 based on the centerline velocity and the channel height. Separate channel flow simulations were carried out using each code and each turbulence model and the resulting profiles are used as inlet conditions for the simulation of the diffuser.

An experimental database is available from Obi et al. [18] and Buice and Eaton [19]. The data include mean and fluctuating velocities at various stations in the diffuser and skin friction data on both walls. The data can be obtained directly from the Web (www.aero.hut.fi/Ercoftac/ws8/case8_2).

A structured grid consisting of 124×65 points in the streamwise and wall normal direction, respectively, has been used. Strong clustering of the grid points at the walls has been used so that the y^+ of the first grid point away from the wall is everywhere less than 1. A detail of the computational grid in the region close to the connection between the channel and the diffuser is included in Fig. 2.

In Table I a summary of the numerical parameters used for the computations is reported.

In Fig. 3, convergence histories for the all simulations are presented. The residuals have been normalized using their values at the first iteration. The convergence levels reached after 3000 iterations are comparable in all the cases. In particular, slightly lower residuals are obtained using the $\overline{v'^2}-f$ in both Fluent and CFX but not in Star-CD. An extensive analysis of the sensitivity of the convergence history to the numerical parameters (listed in Table 1) was outside the scope of the present work and was not

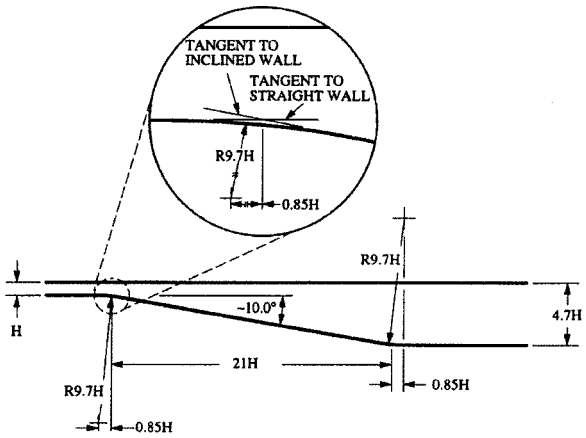

Fig. 1 Asymmetric diffuser geometry

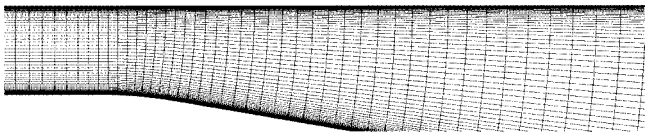

Fig. 2 Computational grid—detail of the channel-diffuser connection

Table 1 Numerical parameters used for the simulations. Legend: U,V: Mean Velocity Components; P: Pressure; TQ: Turbulent Quantities; CD: Central Differencing; UD: Upwind Differencing; TVD: Total Variation Diminishing.

	Spatial Discretization			Pressure Correction	Under-Relaxation		
	U,V	P	TQ		U,V	P	TQ
CFX	QUICK	CD	UD	SIMPLEC	0.65	1	0.6
Fluent	QUICK	TVD	UD	SIMPLEC	0.65	1	0.6
Star-CD	QUICK	CD	UD	SIMPLE	0.70	0.2	0.6

performed. However, the SIMPLEC algorithm used in CFX and Fluent seems to be superior to the standard SIMPLE (also available in the same codes). This technique is not available in Star-CD and the other options available did not give better convergence behaviors. In terms of performance, the unstructured mesh codes (Fluent and StarCD) behaved similarly, with the structured grid code (CFX) being 40 percent faster. The CPU cost of the $\overline{v'^2}-f$ model is about 30 percent more than the k-ϵ model and this is consistent with the fact that two additional differential equations are solved. As it is clear from the Fig. 3, no major differences in terms of convergence speed are observed between the simulations performed using the two turbulence models even if the $\overline{v'^2}-f$ has been implemented as an external customized module.

In Fig. 4 the streamwise velocity contours are reported for the

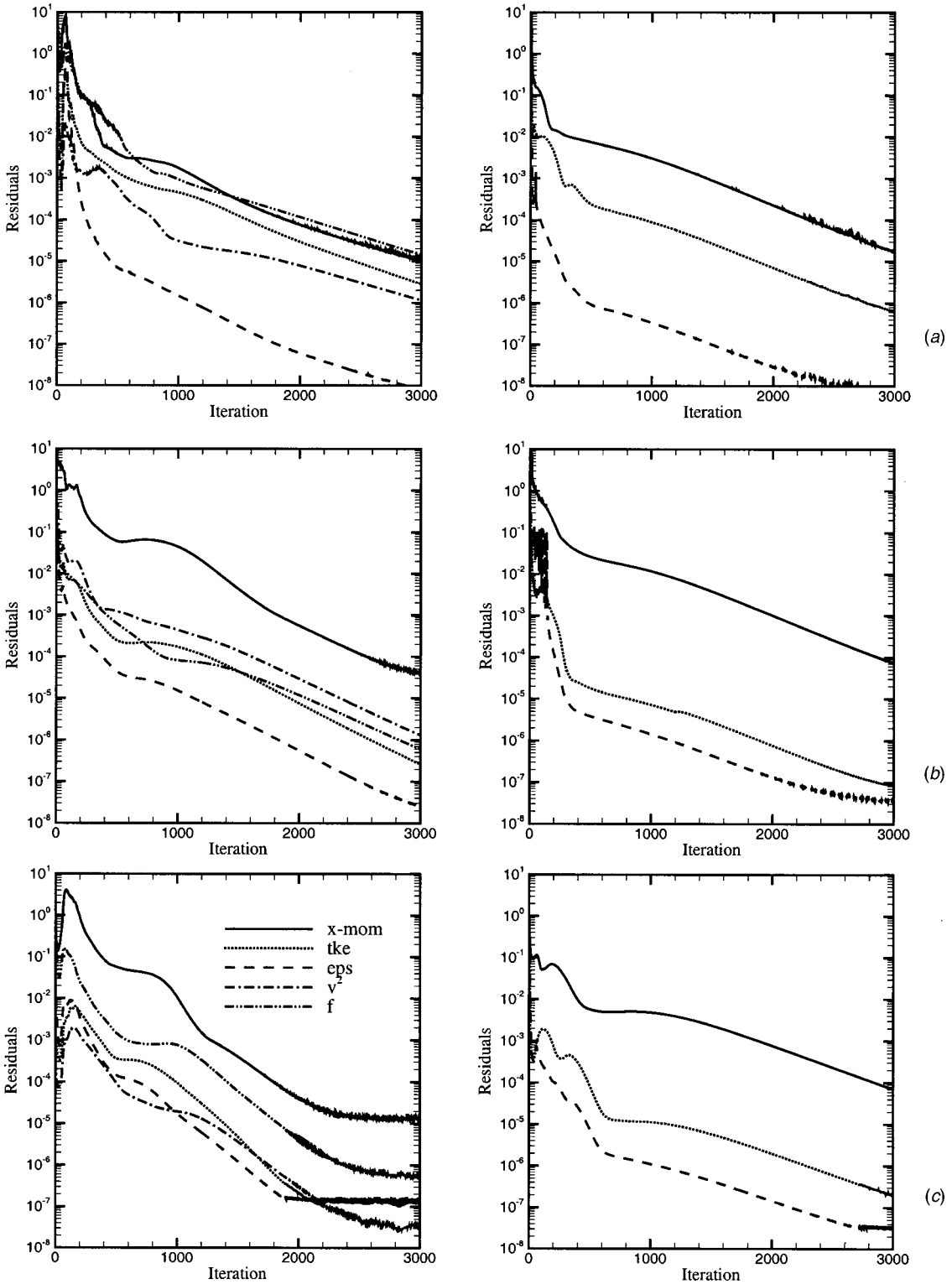

Fig. 3 Convergence history (L_∞ norm). Left column: $\overline{v'^2}-f$ model; right column: low-Reynolds k-ϵ model. (a) CFX v4.3; (b) fluent v5.3; (c) star-CD v3.1.

two models. The results using the $\overline{v'^2}-f$ model show a separation bubble (dashed lines) in qualitative agreement with the experimental findings. This recirculation is not captured by the low-Reynolds k-ϵ model.

The comparison between the computations and the experimental data is reported in Fig. 5 for the streamwise velocity at several stations in the diffuser. The $\overline{v'^2}-f$ results are consistently in good agreement with the measurements for the mean velocity. In par-

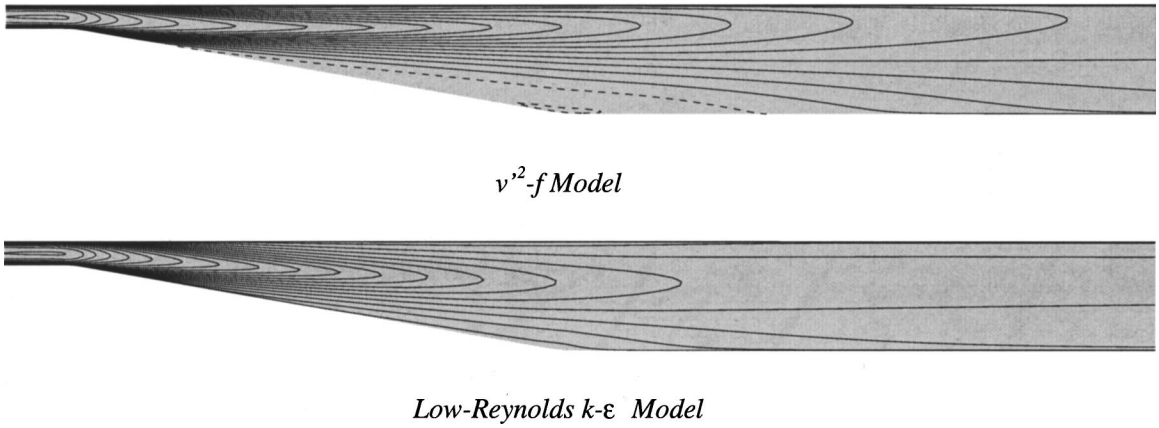

Fig. 4 Mean streamwise velocity—CFX. Contour levels Min=−0.05; max=1.0, Δ=0.05 (dashed lines negative values).

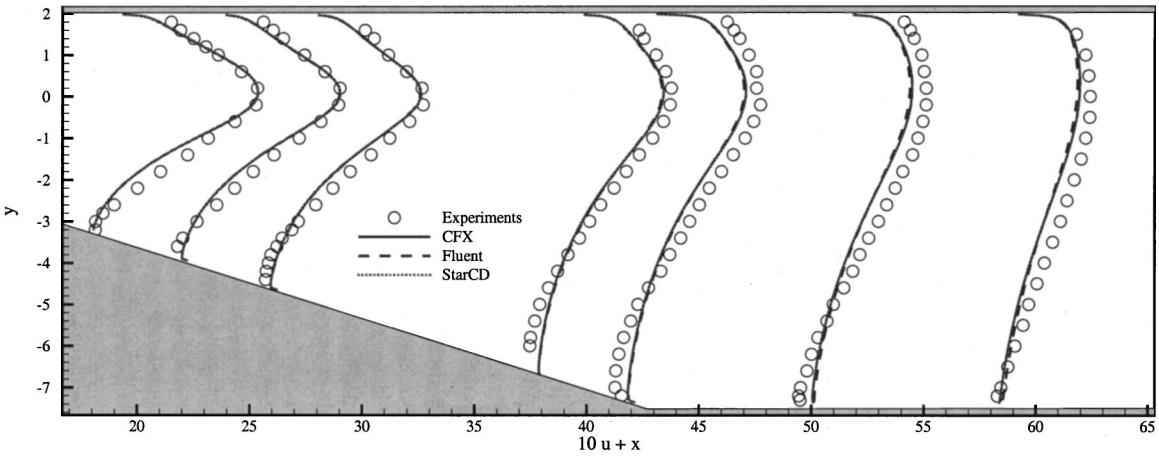

$\overline{v'^2}-f$ *Model*

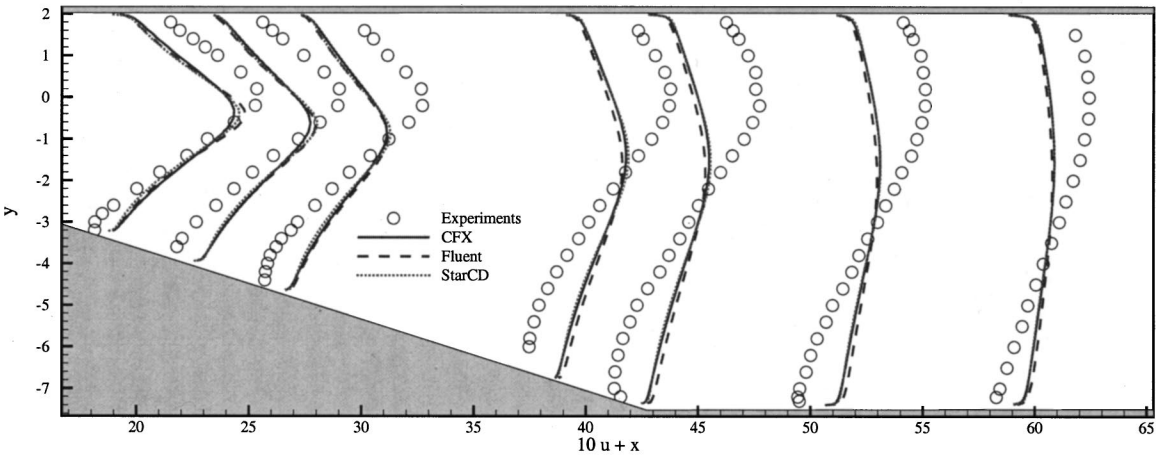

Low-Reynolds k-ε Model

Fig. 5 Streamwise velocity profiles

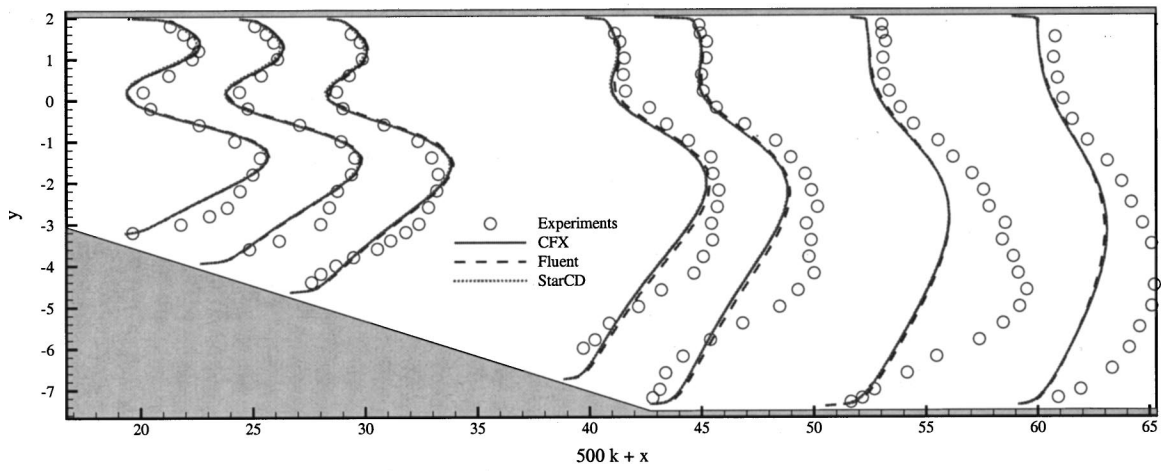

$\overline{v'^2} - f$ *Model*

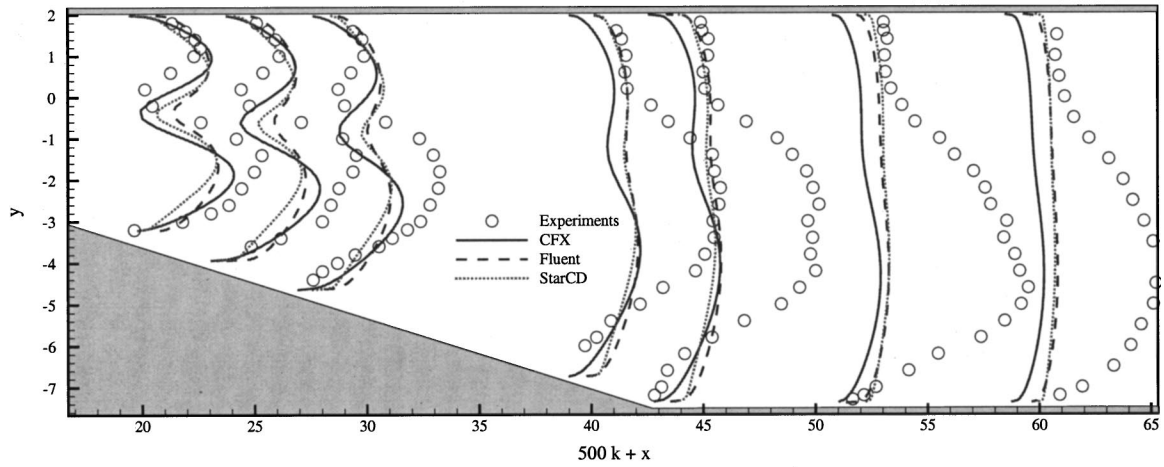

Low-Reynolds k-ϵ Model

Fig. 6 Turbulent kinetic energy profiles

ticular, the separation zone is captured (even if the maximum intensity of the recirculating velocity is underestimated). The predictions using the k-ϵ model are in poor agreement with the data because the model fails to respond correctly to the adverse pressure gradient and misses the separation completely. The comparisons reported in Fig. 6 for the turbulent kinetic energy confirm the quality of the $\overline{v'^2}-f$ predictions as compared to the k-ϵ. The peak of the turbulent intensity is very well predicted by the $\overline{v'^2}-f$ model in the diffuser. However, in the recovery region (after the reattachement) the model underestimates the level of kinetic energy. This is consistent with the $\overline{v'^2}-f$ calculations shown by Durbin [4], the LES results reported by Kaltenbach et al. [8] and with the recent computations presented by Apsley and Leschziner [5] using quadratic and cubic nonlinear k-ϵ models. Possible reasons for this disagreement are the presence of strong three-dimensional effects after the flow reattachement and strong non-equilibrium effects which cannot be correctly accounted for in single–point closures. The results using the k-ϵ model completely fail to capture the asymmetric development of the turbulent kinetic energy and underestimate its magnitude in the diffuser.

The three codes show some differences when the same k-ϵ model is invoked. The disparities are in the mean velocity and especially in turbulent kinetic energy. The very good agreement obtained by using the $\overline{v'^2}-f$ suggests that the differences are not related to the numerical techniques used to discretize the equations but to the implementation of the models. For example, different approximations of the terms in (10)-(11) could lead to the mentioned differences.

In particular, it is worth noting that StarCD and Fluent results are closer to each other (especially for the turbulent kinetic energy) than they are with CFX. This may be related to the fact that both are unstructured mesh codes (whereas CFD is a structured grid solver) and they deal similarly with the issues (mentioned at the end of Sec. 3.1) related to the computation of the cross derivatives in the term D (Eq. (10)) and the evaluation of the wall normal direction. It is also useful to add that the use of the standard f_μ damping function available in StarCD (instead of the one reported in (8)) leads to somewhat different results which no longer agree with the Fluent results.

Finally in Fig. 7 the skin friction coefficients on the lower and upper walls are reported. The separation bubble on the curved wall is indicated by a negative skin friction from $x/H \approx 7$ to $x/H \approx 30$; the $\overline{v'^2}-f$ model predicts the bubble in very close agreement with the experiments. The k-ϵ model fails to predict

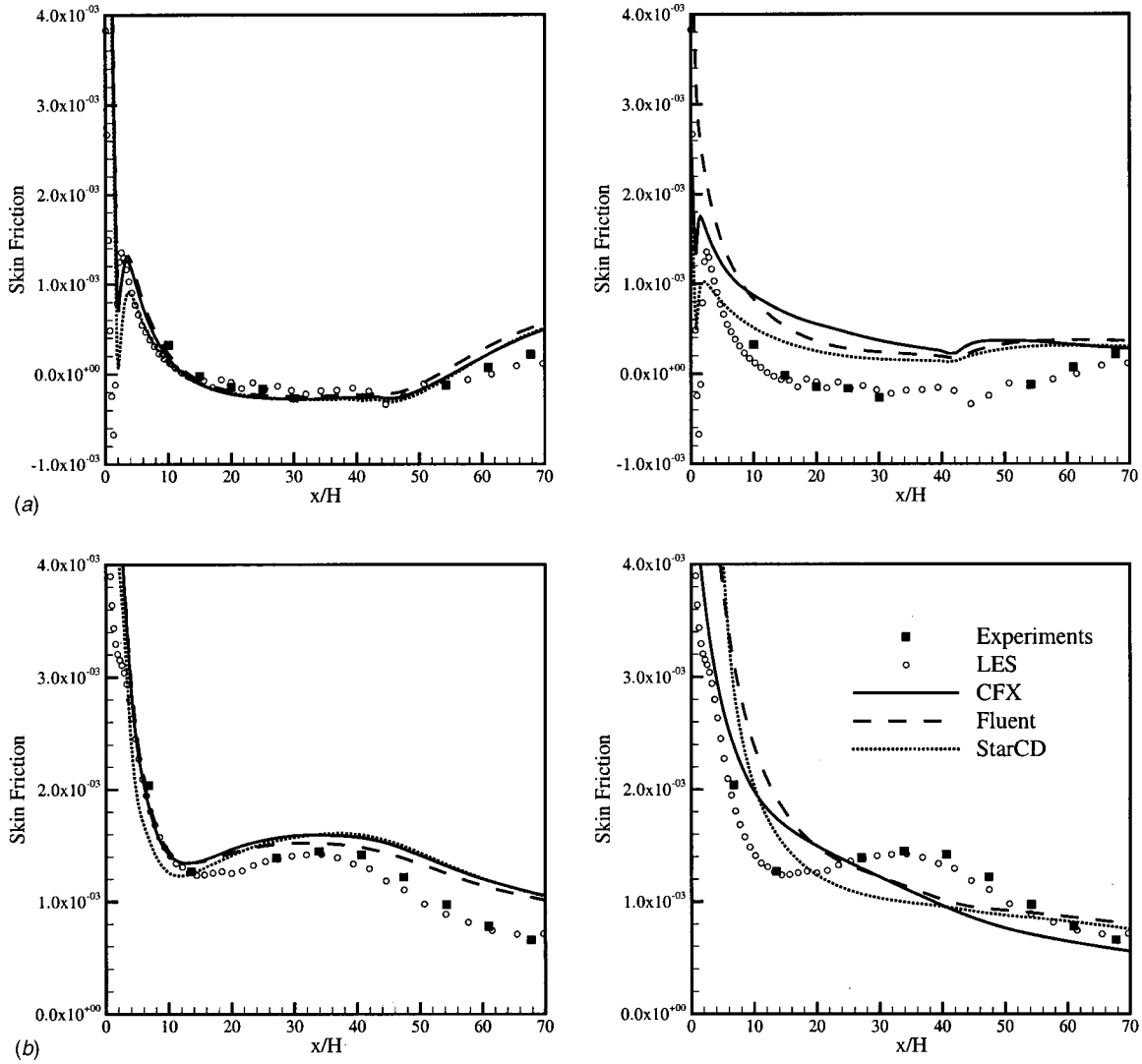

Fig. 7 Skin friction distribution on the diffuser walls. Left column: $\overline{v'^2}-f$ model; right column: low-Reynolds k-ϵ model. (a) Lower wall; (b) Upper wall.

any separation (as already noted). In addition, the three codes predicts quite different friction levels when the k-ϵ closure is employed.

In order to assess the grid sensitivity of the results presented, additional calculations on a refined grid were carried out. The grid was obtained by doubling the number of points in the two directions. The comparison between coarse and fine grid is reported in Fig. 8, in terms of mean flow velocity and turbulent kinetic energy profiles using Fluent and the low-Reynolds k-ϵ model. The results show that a grid converged solution has been reached. Similar comparisons are obtained for the other two codes. In addition, the results obtained using a high-order upwind discretization for the turbulent quantities are also reported on the same plots. The difference, in this case, is very small being the flow dominated by turbulence generation. This conclusion does not apply to more complex situations where the use of high-order differencing for the turbulent equations is mandatory.

The grid convergence study shows that the results obtained are not dependent on the grid and therefore, the differences in the streamwise velocity profiles in Fig. 5 and in the turbulent kinetic energy in Fig. 6, are not directly related to discretization accuracy or to the presence of artificial dissipation. One possible cause of the discrepancy between the codes is the presence of limiters/smoothers in the solution procedure. These operators are usually employed to *enforce* the positivity of selected quantities (turbulent variables, for example) and to improve convergence quality.

Additional simulations are performed using different turbulence models to explore capabilities of the CFD codes tested and the results are presented in Fig. 9. The standard k-ϵ model with the two-layer near-wall treatment gives results which are closely comparable to the predictions presented in Figs. 5 and 6 (using the damping functions). The separation on the bottom wall is not captured and the asymmetry in the turbulent kinetic energy profiles is very small. The two-layer treatment of the near-wall regions is available in both Fluent and StarCD and the results are comparable. On the other hand, the Nonlinear version of the Launder and Sharma k-ϵ model (available only in StarCD) captures the separation and gives a reasonably good representation of the turbulent kinetic energy. The results are in agreement with the experiments and close to the predictions of the $\overline{v'^2}-f$ model. These results are also in agreement with the data reported in the work by Apsley and Leschziner [5].

Finally, results are also presented for calculations with the DRSM model in low-Reynolds number form. This model is available in Fluent (in CFX only a High-Reynolds number version is available). The DRSM predictions do not show the expected improvement with respect to the standard k-ϵ model. This could be partly related to the near-wall treatment based on the two-layer

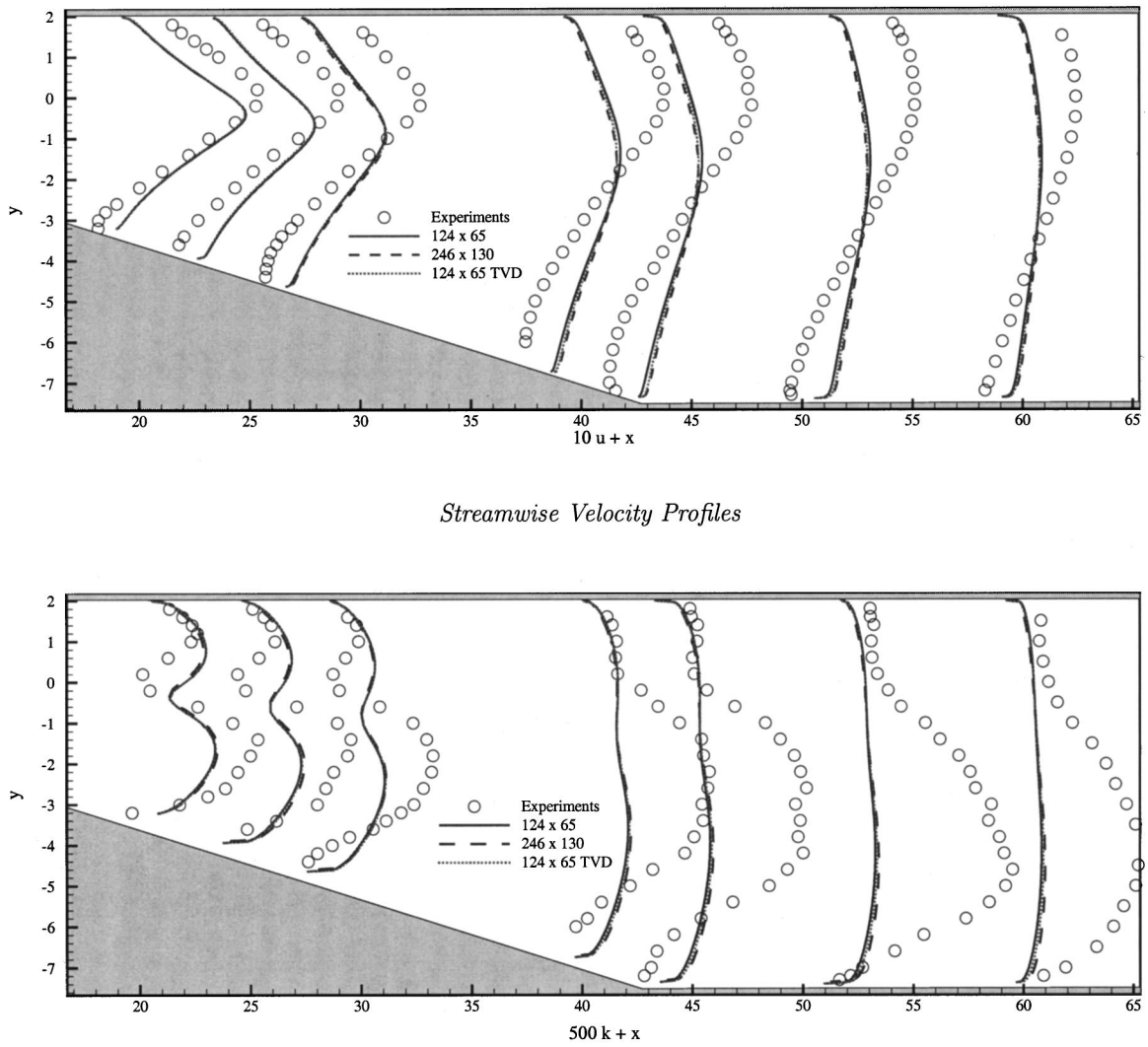

Fig. 8 Grid convergence and differencing scheme dependency—Fluent low-reynolds k-ϵ model

approach. Calculations performed in a similar configuration with the high-Reynolds version of the DRSM in Fluent [11] demonstrated good agreement with the experimental measurements.

It is worth noting that the two-layer k-ϵ required about the same amount of CPU as the Launder and Sharma model presented before and the convergence behavior was very similar. On the other hand, a slight increase in computational time is associated with the NLEV model and 25 percent more iterations were required to achieve the same drop in the residuals. The DRSM simulation required a CPU comparable with the $\overline{v'^2}-f$ one (the number of differential equations to be solved is the same for two-dimensional problems) but almost twice as many iterations were required to achieve convergence.

5 Conclusions

A comparison between three CFD commercial codes, namely CFX, Fluent, and Star-CD, is reported for turbulent flow in a planar asymmetric diffuser. Two turbulence models have been used. The first is the low-Reynolds number k-ϵ model (with Launder and Sharma damping functions) which is available as a standard feature in the codes. The second model is the $\overline{v'^2}-f$ model that has been implemented through the User Defined Routines in the three codes.

The same grid and the same spatial discretization have been used for all the simulations. In addition, a similar iterative procedure based on the SIMPLE technique has been used. In terms of convergence behavior, all the codes reach the steady-state approximately in the same number of iterations, regardless of the turbulence model used. The accuracy of the calculations as compared to the experimental and LES data is very good using the $\overline{v'^2}-f$ model. The length of the recirculation region is captured to within 6 percent and the skin friction on both walls agree reasonably well with the data. The negative velocity in the separation bubble is slightly underestimated. The results using the k-ϵ model do not show any recirculation. The flow is fully attached and this leads to a severe underprediction of the maximum velocity in the diffuser.

An effort was made to control all aspects of the simulations so that the same results were expected using different codes. In particular, the implementation of the $\overline{v'^2}-f$ turbulence model was carried out the same way in the three codes; indeed $\overline{v'^2}-f$ results do show an almost perfect agreement between CFX and Star-CD with Fluent being slightly more dissipative. The results using the k-ϵ model, on the other hand, show strong sensitivity to the code used. The model formulation is exactly the one proposed by Launder and Sharma, but the results are different (especially in terms of turbulent quantities and friction coefficients). This may be due to differences in implementation details which are not specified in the user manuals. In general, the differences between the k-ϵ results are much larger than those obtained using $\overline{v'^2}-f$, suggest-

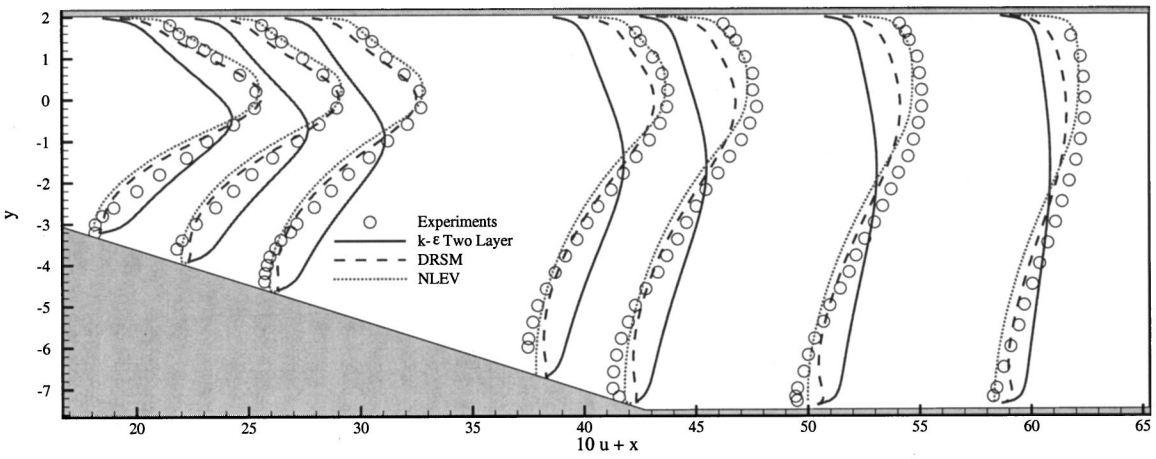

Streamwise Velocity Profiles

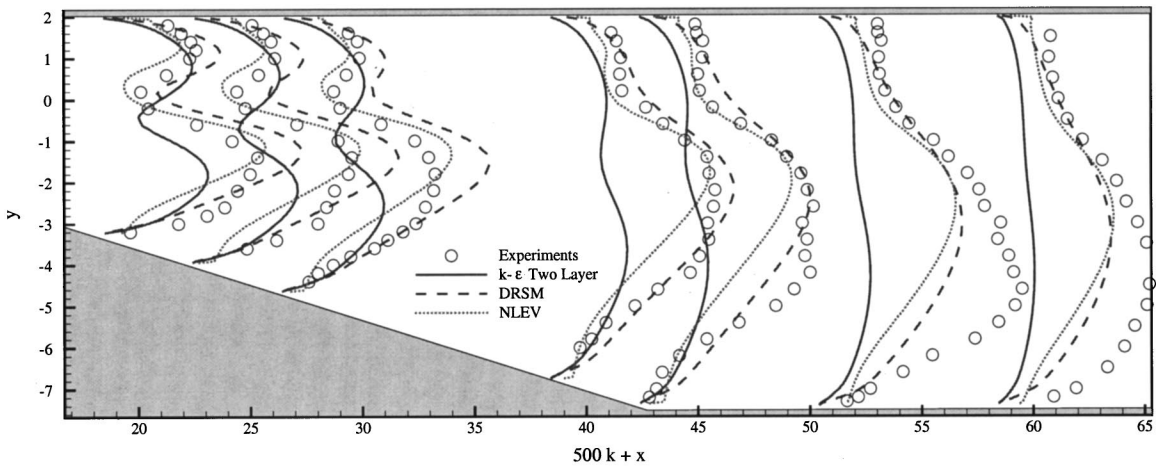

Turbulent Kinetic Energy Profiles

Fig. 9 Results using a differential Reynolds-stress model and non-linear eddy viscosity model

ing that the differences are less due to details of the numerical procedures in the codes than to the implementation of the turbulence models.

Today, one of the challenges in using commercial CFD codes is to choose between several physical/numerical models available. The cross comparison presented in this work proved that the basic numerical techniques (default options) are reliable and deliver the expected performance in terms of accuracy and convergence at least when the computational grid and the boundary conditions are defined carefully. On the other hand, the selection of the correct physical model (in this case the turbulence model) is crucial for the success of the simulations. Using one of the available turbulence models the results were not accurate and, in addition, not reproducible using different codes.

The $\overline{v'^2}-f$ model was implemented in CFX, Fluent, and StarCD *only* using the User Defined Routine feature. Even if the model is rather complex (involving three differential transport equations and a Helmotz-like equation) no particular difficulty was faced by the author. The performance of the codes was not compromised when compared with built-in models, and the expected accuracy level was reached with all the commercial codes tested. This demonstrates that the implementation of a customized physical model in an industrial tool is an available option for CFD practitioners thus shortening the distance between published research work and real–world applications.

Acknowledgments

The author wishes to thank A. Ooi for providing the initial implementation of the $\overline{v'^2}-f$ model in Fluent, and M. Fatica for providing the LES data for the diffuser; in addition, support for the implementation of the $\overline{v'^2}-f$ model was provided by P. Malan (Fluent Inc.), S. Jonnavithula (Adapco Ltd.), and H. Pordal (AEA Technologies Inc.). Discussion with P. Moin, P. Durbin, and G. Medic are appreciated.

References

[1] Freitas, C. J., 1995, "Perspective: Selected Benchmarks From Commercial CFD Codes," ASME J. Fluids Eng., **117**, p. 210–218.
[2] Durbin, P. A., 1996, "On the k-ϵ Stagnation Point Anomaly," Int. J. Heat Fluid Flow, **17**, pp. 89–91.
[3] Launder, B. E., and Sharma, A., 1974, "Application of the Energy-Dissipation Model of Turbulence to the Calculation of Flow Near a Spinning Disk," Lett. Heat Mass Transfer **1**, pp. 131–138.

[4] Durbin, P. A., 1995, ''Separated Flow Computations with the k-ϵ-v^2 Model,'' AIAA J., **33**, pp. 659–664.
[5] Apsley, D. D., and Leschziner, M. A., 2000, ''Advanced Turbulence Modeling of Separated Flow in a Diffuser,'' Flow, Turbul. Combust., **63**, pp. 81–112.
[6] Parneix, S., Durbin, P. A., and Behnia, M., 1998, ''Computation of a 3D turbulent boundary layer using the $\overline{v'^2}-f$ model,'' Flow, Turbul. Combust., **10**, pp. 19–46.
[7] Behnia, M., Parneix, S., Shabany, Y., and Durbin, P. A., 1999, ''Numerical Study of Turbulent Heat Transfer in Confined and Unconfined Impinging Jets,'' Int. J. Heat Fluid Flow **20**, pp. 1–9.
[8] Kaltenback, H. J., Fatica, M., Mittal, R., Lund, T. S., and Moin, P., 1999, ''Study of the Flow in a Planar Asymmetric Diffuser Using Large Eddy Simulations,'' J. Fluid Mech., **390**, pp. 151–185.
[9] Vandoormaal, J. P., and Raithby, G. D., 1984, ''Enhancements of the SIMPLE Method for Predicting Incompressible Fluid Flows,'' Numer. Heat Transfer, **7**, pp. 147–163.
[10] Leonard, B. P., 1979, ''A Stable and Accurate Convective Modeling Procedure Based on Quadratic Upstream Interpolation,'' Comput. Methods Appl. Mech. Eng., **19**, pp. 59–98.
[11] Kim, S. E., 2001, ''Unstructured Mesh Based Reynolds Stress Transport Modeling of Complex Turbulent Shear Flows,'' AIAA Paper 2001-0728.
[12] Barth, T. J., and Jespersen, D., 1989, ''The Design and Application of Upwind Schemes on Unstructured Meshes,'' AIAA Paper 89-0366.
[13] Craft, T. J., Launder, B. E., and Suga, K., 1995, ''A Non-Linear Eddy-Viscosity Model Including Sensitivity to Stress Anisotropy,'' *Proc. 10th Symposium on Turbulent Shear Flows*, **2**, pp. 23.19–23.24.
[14] Launder, B. E., and Spalding, D. B., 1972, *Mathematical Models of Turbulence*, Academic Press, London.
[15] Rodi, W., 1991, ''Experience with two-layer models combining the k-ϵ model with a one-equation model near the wall,'' AIAA Paper 91-0216.
[16] Gibson, M. M., and Launder, B. E., 1978 ''Ground Effects and Pressure Fluctuations in the Atmospheric Boundary Layer,'' J. Fluid Mech., **86**, pp. 491–511.
[17] Speziale, C. G., Abid, R., and Anderson, E. C., 1990, ''A critical evaluation of two-equation models for near wall turbulence,'' AIAA Paper 90-1481.
[18] Obi, S., Aoki, K., and Masuda, S., 1993, ''Experimental and Computational Study of Turbulent Separating Flow in an Asymmetric Plane Diffuser,'' *Proc. 9th Symposium on Turbulent Shear Flows*, pp. 305-312.
[19] Buice, C. U., and Eaton, J. K., 1997, ''Experimental Investigation of Flow Through an Asymmetric Plane Diffuser,'' Report No. TSD-107. Thermosciences Division, Department of Mechanical Engineering, Stanford University, Stanford, CA, USA.

S. K. Dash

M. R. Halder

Department of Mechanical Engineering,
Indian Institute of Technology,
Kharagpur, 721 302, India

M. Peric

Fluiddynamics and Ship Theory Section,
Technical University of Hamburg-Harburg,
Lämmersieth 90, 22305 Hamburg, Germany

S. K. Som

Department of Mechanical Engineering,
Indian Institute of Technology,
Kharagpur, 721 302, India

Formation of Air Core in Nozzles With Tangential Entry

The process of formation of air core and its development with time, inside one cylindrical and one conical nozzle having two tangential entries, has been analyzed experimentally and numerically. Experiments have been carried out using Plexiglas nozzles and water in ambient air; the air core has then been photographed for different nozzles and flow parameters. Numerical simulations have been performed using a finite volume method that employs unstructured grids with cell-wise local refinement and an interface-capturing scheme to predict the shape of the air core. The shape of the air core inside the cylindrical nozzle is found to be helicoidal at steady state for higher inlet velocity, whereas the shape of the free surface remains nearly cylindrical for low inlet velocity. In the conical nozzle, the air core is nearly axisymmetric in experiments. So only two-dimensional simulations are performed; the air core widens at the end of conical section as it approaches nozzle exit. For both nozzles numerical simulation predicts qualitatively and to a large extent also quantitatively the correct shape of the air core and the angle of the spray at the nozzle exit, as verified by comparisons with experimentally observed shapes.
[DOI: 10.1115/1.1412845]

Introduction

Nozzles are used in many practical applications, for example in combustion chambers and spray driers, where it is desired to increase the liquid velocity at the nozzle exit. Normally such nozzles are made conical in shape such that the increase in velocity occurs at the exit plane of the nozzle because of the reduction in cross sectional area. The increased velocity at the nozzle exit can serve two purposes. First, a jet of higher velocity can penetrate a longer distance into the surrounding medium, and second, the higher velocity of liquid jet causes its fragmentation into smaller droplets, thus enhancing evaporation of liquid droplets and mixing of vapor with the surrounding ambience.

The formation and mixing of droplets depends on the spreading of the spray, which in turn is dictated by the jet cone angle at the nozzle exit plane. The jet cone angle also depends on physical properties of the fluid as well as on the geometry of the nozzle. A cylindrical nozzle is much simpler to manufacture than the conical one, however, both cylindrical and conical nozzles cannot produce high spray cone angle at the exit unless initial swirl is imparted to the inlet fluid. In order to achieve this, vane swillers can be used at the nozzle inlet, which again make the manufacturing complicated. Another possibility is to connect a tangential entry port to a cylindrical nozzle, which assures that the liquid exits nozzle with sufficient tangential velocity to form a higher jet cone angle. Such nozzles are much simpler to design and manufacture and find their application e.g., in combustion chambers of aircraft and rocket engines.

In the operation of such type of nozzles, the most interesting phenomenon is the formation of an air core within the nozzle. The fluid enters the nozzle tangentially (having no axial component) so it has a tendency to stick to the outer nozzle wall, causing the pressure at the nozzle center to decrease. When the core pressure falls below the ambient pressure to which the nozzle is discharging, the ambient fluid gets sucked into the nozzle forming an air core. This is true for both cylindrical and conical nozzles. However, while in a conical nozzle the air core remains nearly axisymmetric with increased diameter near nozzle exit, it can attain a complicated helical shape in a cylindrical nozzle so that the jet at nozzle exit does not have a circular but rather an elliptical cross-section.

The development of an air core in a nozzle is a very rapid process, which takes place only for sufficiently high inlet velocity or flow rate. High-speed cameras are needed to capture the air-core formation, which requires a substantial investment. However, it is possible to capture the development of air core in the nozzle numerically, by solving the Navier-Stokes equations along with an equation for the volume fraction of liquid. This shall be demonstrated here for one cylindrical and one conical nozzle by comparing the results of numerical simulations with experimentally observed air core shapes.

Many articles on swirl spray nozzles which describe the air core and spray cone angle both experimentally and theoretically have been published [1–10]. Rizk and Lefebvre [5] have shown the internal flow characteristics in a swirl spray nozzle experimentally and Datta and Som [3] have computed the air core diameter in a two-dimensional axisymmetric conical swirl spray nozzle with the help of the least resistance theory by comparing the pressure drop in the nozzle for different diameters of the preimposed air core. Som and Mukherjee [7] and Som and Biswas [9] have shown the initiation of air core in a swirl nozzle for power law fluids by solving the boundary-layer equations in a conical nozzle through momentum integral method. The air core in their analysis was predicted to be cylindrical and was always over-predicted compared with the experiment. Literature survey shows that—to our knowledge—there are no published results on numerical simulations of air core formation in cylindrical nozzles with tangential entry. The reason is that, methods which allow simulations of two-fluid flow with complicated free-surface patterns have only recently emerged [11–13]. One such method developed by Muzaferija and Peric [13] has been successfully used in this study.

Description of Nozzles and Experimental Setup

Figure 1 shows the geometry of the cylindrical nozzle. The nozzle was made by drilling a centered hole with 4.8 mm diameter and 27 mm deep into a perspex rod 20 mm in diameter and 50 mm long. Two holes with 2.4 mm diameter were drilled so that they entered tangentially into the central hole at its end, as shown in Fig. 1. Extension pipes of inner diameter 2.4 mm were connected to the tangential ports; to each pipe a flexible hose was attached. Water from a supply tank was pumped into the nozzle through

Contributed by the Fluids Engineering Division for publication in the JOURNAL OF FLUIDS ENGINEERING. Manuscript received by the Fluids Engineering Division June 27, 2001; revised manuscript received August 10, 2001. Associate Editor: K. B. M. Q. Zaman.

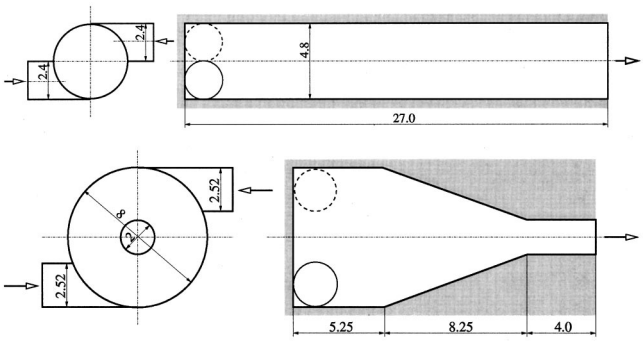

Fig. 1 Geometry of the cylindrical (upper) and conical (lower) nozzle used in experimental and numerical investigations of air-core formation (dimensions are given in millimeters; arrows indicate water flow direction)

these two pipes. Before the water gets bifurcated into the two tangential inlet ports, it was made to pass through a rotameter where the total flow into the nozzle was recorded. The rotameter was calibrated against the direct method of flow measurement by collecting water in tank during a known interval of time to yield an accuracy of more than 98 percent in the measurement of flow. The rotameter was fixed with a valve in its upstream section so that the total flow rate could be controlled. The two branches of the inlet ports were also fitted with two bourdon type pressure gauges to know the inlet water pressure at the entrance to both ports. The pressure gauges were also serving as indicators to make sure that the flow rate is the same through both ports. The pressure gauges were calibrated with a dead weight tester before the experiment.

To start with, the cylindrical nozzle is full of air. When the valves are opened, water enters through the inlet ports into the nozzle displacing the air. It is difficult to observe the initial transient phase expementally without the help of expensive high-speed cameras, because at inlet velocities of the order of 10 m/s, the nozzle is filled with water within a millisecond. Also, there is always initially some air in the pipes so that it takes a second or two to obtain the steady flow. Therefore, only the steady flow patterns have been photographed in the experiment. The shape of the air core can be clearly seen in photographs (Fig. 3). The photographs are scanned and the measurement of the air core is made from a magnified picture obtained from the computer. It should be noted here that the final magnified picture of air core from the computer has three stages of magnification. The air core viewed by normal eye from outside the nozzle appears to be magnified due to the refraction of light through water, nozzle wall and air at the core of the nozzle. The air core was further magnified while taking the photograph. The photograph after being scanned was further magnified in the computer for final measurement. The first stage magnification due to refraction of light from the air core inside the nozzle was taken care of by incorporating a magnification factor determined from the theory of optics by taking the refractive indices of air, water and nozzle material (behaving as a thick curved lens) in to account. The second stage magnification by the camera was known by putting a standard millimeter scale by the side of the nozzle while taking the photograph. The last stage magnification of the scanned photograph was also known from the computer itself. The uncertainty in the measured values of air core diameter was simply the error in the experimental measurements, which was estimated to be below 5percent due to a large magnification of air core compared to the resolution in the linear scale of measurement. The fluctuations in the measurement of air core diameter from different photographs were found to be less than 5percent.

In Fig. 1 the conical nozzle used in experiments is also shown. It has a larger settling chamber, known as swirl chamber, but a smaller exit diameter than the cylindrical nozzle. Air core is formed in both nozzles over a wide range of operating conditions. We shall present here results obtained with inlet velocities in entry ports of 5.313 m/s (conical nozzle) and 11 m/s (cylindrical nozzle). The flow attains a nearly steady state; although some fluctuation in the shape of air core has been observed, it was difficult to quantify. Numerical simulations also indicate that for some flow parameters the air core ''breathes'' after attaining its final shape so that its diameter varies within few percent without significant further changes.

Numerical Solution Methodology

The finite volume method for incompressible viscous flows with free surfaces is described in detail in Muzaferija and Peric [13]; here we describe it only briefly. The starting point are the conservation equations for mass, momentum, and scalar quantities (e.g., energy or chemical species) in their integral from:

$$\frac{d}{dt}\int_{\nu}\rho d\nu-\int_{s}\rho(\nu-\nu_b).\mathbf{n}dS=0 \tag{1}$$

$$\frac{d}{dt}\int_{\nu}\rho u_i d\nu-\int_{s}\rho u_i(\nu-\nu_b).\mathbf{n}dS=\int_{s}(\tau_{ij}.\mathbf{i}-p.\mathbf{i}_i).\mathbf{n}dS+\int_{\nu}\rho b_i d\nu \tag{2}$$

$$\frac{d}{dt}\int_{\nu}\rho\phi d\nu-\int_{s}\rho\phi(\nu-\nu_b).\mathbf{n}dS=\int_{s}\Gamma\nabla\phi.\mathbf{n}dS+\int_{\nu}\rho b_\phi d\nu \tag{3}$$

In these equations, ρ is the fluid density, V is the control volume (CV) bounded by a closed surface S, $\boldsymbol{\nu}$ is the fluid velocity vector whose Cartesian components are u_i, ν_b is the velocity of the CV surface and t is time. Γ represents the diffusion coefficient and b_φ is the volumetric source of the conserved scalar quantity φ, p is the pressure, b_i is the body force in the direction of the Cartesian coordinate x_i, $\mathbf{n}$ is the unit vector normal to S and directed outwards, and τ_{ij} are the components of the viscous stress tensor, including the contribution from an eddy-viscosity turbulence model if the flow is treated as turbulent.

Interface-capturing method and HRIC (High-Resolution Interface Capturing) scheme [13] have been used to simulate the free-surface effects. In addition to the conservation equations for mass and momentum, a transport equation for void fraction of the liquid phase c has been introduced:

$$\frac{d}{dt}\int_{\nu}c d\nu-\int_{s}c(\nu-\nu_b).\mathbf{n}dS=0 \tag{4}$$

The grid extends to both liquid and gas phase; the void fraction c is set equal to 1 for CVs filled by liquid and 0 for CVs filled by gas. Both fluids are treated as a single effective fluid whose properties vary in space according to the volume fraction of each phase, i.e.:

$$\rho=\rho_1 c+\rho_2(1-c),\quad \mu=\mu_1 c+\mu_2(1-c) \tag{5}$$

where subscripts 1 and 2 denote the two fluids (e.g., liquid and gas).

The effects of surface tension at the interface between two fluids are taken into account through a body force as a function of the volume fraction c, which is achieved by introducing the *continuum surface force* (CSF) model [14]. The CSF model uses the smoothed field of c to define a unit vector normal to the interface with the help of the gradient vector of c; the divergence of this unit vector defines the curvature of the interface, κ. The surface tension force and the curvature can thus be expressed as:

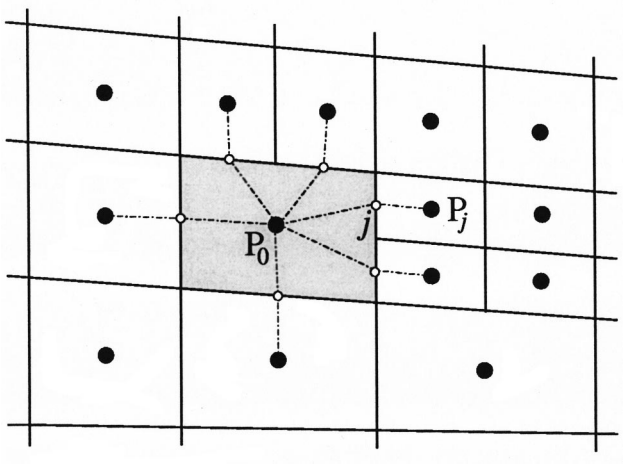

Fig. 2 A control volume in a two-dimensional grid with cell-wise local refinement and the notation used

$$F_\sigma = \int_\nu \sigma K \nabla c dV \quad K = -\nabla . \left(\frac{\nabla c}{|\nabla c|} \right) \tag{6}$$

where, σ is the surface tension coefficient.

The solution domain is subdivided into a finite number of non-overlapping control volumes (CVs); in the center of each control volume lies the computational point at which the known quantities are specified and the unknown variables are to be computed. Local refinement can be used to achieve finer resolution in regions of rapid change of the variables, as indicated in Fig. 2. The control volumes are treated as polyhedra and can have an arbitrary number of neighbors (unstructured grids).

Equations (1)–(3) are applied to each CV and then discretized, leading to one algebraic equation per CV in which variables from immediate neighbors also feature. All integrals are approximated using midpoint rule, i.e., the function to be integrated is evaluated at the center of the integration domain and multiplied by the area, volume, or time interval over which the integration takes place. In order to evaluate the function at the center of the integration domain, one needs to introduce further approximations: interpolation and differentiation. In space, linear interpolation is used, while in time either linear or quadratic shape functions are used. The diffusive fluxes require that the derivatives in the direction normal to CV faces be computed at each cell-face center; these are obtained from linear shape functions with the help of least-squares method or Gauss-theorem. The integration in time is fully implicit (either implicit Euler, which is a first-order method, or three-time-level scheme, which is of second order). The spatial integration is also of either first or second order, depending on the approximation of convected variable in convective fluxes (upwind or central differencing, or a blend of the two). In order to keep the computational molecule limited to cell center node and centers of nearest neighbor cells, *deferred-correction* approach is used: low-order approximations which use only nearest neighbors are used to construct the coefficient matrix, and the difference between the desired approximation and the low-order one is computed explicitly from the values obtained in the previous iteration and added to the source term on the right-hand side of the equation. More details on individual steps in the discretization procedure can be found in Muzaferija and Peric [13].

The algebraic equation obtained at the end in each CV has the following form:

$$a_{P_0} \phi_{P_0} + \sum_{j=1}^{n_j} a_{P_l} \phi_{p_j} = b_{P_0} \tag{7}$$

For the solution domain as a whole, a matrix equation results,

$$A\varphi = b \tag{8}$$

Here, n_j is the number of internal cell faces surrounding cell P_0 and the right-hand side **b** contains source terms, contributions from boundary faces (Dirichlet boundary conditions) and also parts of convective and diffusive fluxes which are for the sake of computational efficiency treated explicitly using deferred correction approach.

In order to calculate the pressure field and to couple it properly to the velocity field, a pressure-correction method of SIMPLE-type is used [15]. Velocities computed from momentum equations using pressure from previous iteration step are corrected to enforce mass conservation, and the correction to cell-face velocity is proportional to the gradient of pressure correction, leading to a Poisson-type pressure-correction equation. Turbulence is taken into account by solving two additional transport equations for turbulent kinetic energy k and its dissipation rate ε and adding an eddy viscosity (computed with help of these two quantities) to the molecular viscosity. When solving the Eq. (4), a special interpolation method is used to compute the cell-face value of the volume fraction c (HRIC-scheme [13]), which is designed to keep the interface sharp (i.e., avoid spreading due to numerical diffusion) and to maintain c bounded (i.e., c is not allowed to become less than zero or greater than unity). This is achieved by blending the upwind and downwind approximations, with blending factor being a function of the local profile of c, the orientation of interface relative to cell face, and the local Courant number.

Equation (7) is obtained for each variable (velocity components, pressure-correction, volume fraction, turbulent kinetic energy, etc.). Due to the nonlinearity of the underlying equations, the solution of the linearized system of algebraic equations (8) is obtained using iterative methods from the conjugate-gradient family (inner iterations). The solution of linear equation systems is repeated in turn for each variable until the non-linear, coupled system is satisfied to a prescribed tolerance.

The computational steps can be summarized as follows:

1 Provide the initial values for the dependent variables (at time t_0).
2 Advance the time by Δt and start *outer* iterations to find the solution at the new time level.
3 Assemble and solve the linearized algebraic equations (*inner* iterations) for the velocity components in turn, employing the currently available mass fluxes and other dependent variables.
4 Assemble and solve the linearized algebraic equations for turbulent kinetic energy k and its dissipation rate ε and obtain turbulent diffusion coefficients, if the flow is turbulent.
5 Assemble and solve the linearized algebraic equations for volume fraction.
6 Update fluid properties according to distribution of volume fraction and turbulence quantities.
7 Return to Step 3 and repeat until the sum of the absolute residuals for all equations has fallen by a prescribed number of orders of magnitude.
8 Return to step 2 and repeat until the prescribed number of time steps is completed.

Inner iterations are stopped when the residual norm has fallen an order of magnitude; for outer iterations, the level of residuals before inner iterations are started is monitored and the solution is assumed to have converged when the residual norm has fallen three to four orders of magnitude. More details on the method are available in [13]. It is implemented in the commercial code Comet [16], which has been used in this study.

Results and Discussion

Experimental Observations. Figure 3 shows the photograph of air core a conical nozzle. The total flow rate was 5.3 $\times 10^{-5}$ m^3/s, which corresponds to the mean velocity in the two

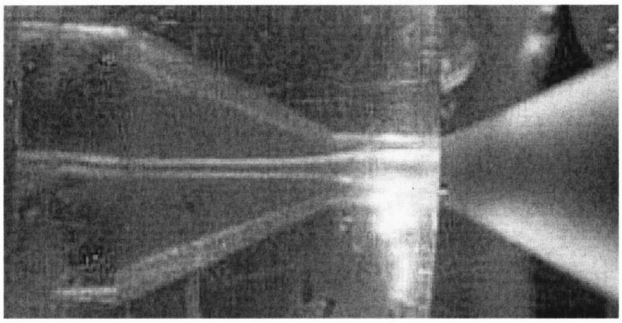

Fig. 3 A photograph of air core in the conical nozzle, also showing the spreading of annular water jet at nozzle exit

tangential inlet ports of 5.313 m/s. The photograph shown in Fig. 3 is representative of a wide range of flow rates. In all cases the air core is nearly axisymmetric; it widens as the conical section ends, remains again nearly cylindrical in the straight part of the nozzle exit hole, and widens again after nozzle exit, where water jet attains a conical form. The spreading of water jet in radial direction is due to the swirl introduced through tangential water entry into the nozzle. Due to the fact that the flow rate is constant in any cross-section, with increasing jet diameter and nearly constant velocity, the thickness of the annular jet sheet reduces, leading eventually to fragmentation into droplets. Jet instability and surface tension play a major role in this process.

The user can control the spreading rate and the size and distribution of droplets by changing the nozzle geometry (diameter ratio between nozzle and settling chamber, length of conical and straight section, nozzle diameter, surface roughness) and the inlet velocity (i.e., for the same flow rate changing the diameter and shape of tangential inlet ports). Higher swirl at inlet leads to a wider opening of the annular water jet.

Figure 4 shows a photograph of the air core obtained in the cylindrical nozzle at the flow rate of $10^{-4}\,m^3/s$, which corresponds to mean velocity in inlet ports of 11 m/s. It can be clearly seen that the air core has a helical shape with some secondary disturbances, unlike in the above case of the conical nozzle where the air core had a smooth, cylindrical surface. The helical shape of the air core has been observed up to an inlet Reynolds number

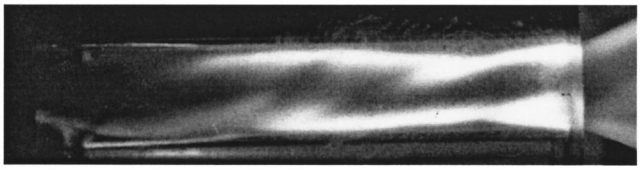

Fig. 4 A photograph of air core in the cylindrical nozzle, showing a helical shape with two main twists and some secondary disturbance

(based on mean velocity and diameter of the inlet port) of 40000, with a maximum of two twists for the same length of the nozzle. However, for low flow rates (below an inlet Reynolds number of 3000), the shape of the air core was nearly cylindrical except in the vicinity of the inlet zone.

Numerical Computations. Since in the case of a conical nozzle the flow appears to be steady with a nearly axi-symmetric air core, a two-dimensional (2D) simulation could be performed. Therefore, the numerical grid has been constructed so that it covers a slice 2 degrees wide with only one cell in circumferential direction (three-dimensional cells are generated because the computer code used requires volumetric cells even when the simulation is two-dimensional). Figure 5 shows part of the grid covering the nozzle and a small distance downstream of its exit; the actual solution domain extended up to 7 millimeters downstream and 8 mm in radial direction away from nozzle exit. Since the flow is swirling, momentum equations have been solved for all three velocity components (axial, radial, and circumferential); however, the condition of zero gradient in circumferential direction allows for a 2D simulation, which greatly reduces the computational cost.

The grid shown in Fig. 5 is the coarse one; another grid has been generated by subdividing each cell of the coarse grid into four finer cells (by halving it in axial and radial direction). The two grids had 5910 and 23640 control volumes (CVs), respectively.

In order to be able to perform a 2D-simulation of the flow in a nozzle whose geometry at inlet is actually three-dimensional, one needs to apply an appropriate approximation at the inlet boundary of the solution domain. To this end a portion of the outer nozzle wall next to its base has been declared inlet (19 CVs from upper left corner, total length 2.4927 mm): at these boundary faces, radial velocity of 0.84566 m/s (inward) and circumferential velocity of 5.313 m/s have been prescribed. The radial component has been set so that the same flow rate is obtained as in the actual geometry; the circumferential velocity has been set equal to the mean velocity in the tangential inlet ports, since this ensures that the same angular momentum enters the nozzle. At the outlet cross-section, constant ambient pressure was prescribed. All other boundaries were treated as no-slip walls.

Although the Reynolds number in the inlet port is above critical (Re=13300, based on mean velocity of 5.313 m/s and pipe diameter of 2.52 mm) and the flow is turbulent there, it is expected that turbulence will not play any important role in the nozzle, due to the stabilizing effect of streamline curvature. Indeed, laminar flow simulation did converge to a steady solution, which would not be possible if the flow were turbulent. Therefore, no turbulence model was used.

Initially, the nozzle is full of air at rest. The start of simulation with prescribed constant inlet velocities corresponds to an instantaneous opening of valve in experiment, which does not quite corresponds to the reality; however, since we are looking for a steady solution, the initial development of flow is of no interest. Therefore, a pseudo-transient simulation has been performed (one outer iteration per time step, so that intermediate solutions are not time-accurate) until a nearly steady-state has been reached. The

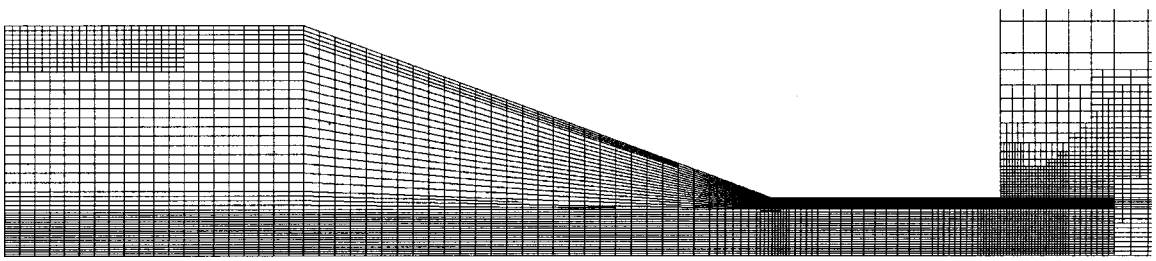

Fig. 5 Numerical grid (coarse) used for the simulation of flow in the conical nozzle, indicating local refinement near inlet, nozzle throat, exit section, and air core region

Table 1 Dimensions of the air core and the jet angle as computed on the two grids

Source	d_1	d_2	α
5910 CV	0.76 mm	1.24 mm	28.4°
23640 CV	0.79 mm	1.26 mm	31.0°
Experiment	0.67 mm	1.15 mm	27°–29°

solution would not come to a complete steadiness due to large vortices in air near exit cross-section. Thereafter, transient computation has been continued for a while, and a small fluctuation in air core size and the angle of water jet have been observed; these were, however, rather small (less than 1%), so the simulation could be stopped. The simulation is then repeated on the refined grid, taking the coarse-grid solution as the initial condition; this way the fine-grid simulation did not take many time steps to reach the steady state (around 1000 steps of 0.001 millisecond).

The results on the two grids—as far as the shape and size of the air core is concerned—differ very little. The main parameters for comparison are: the diameter of air core at nozzle base, d_1, and in the middle of the nozzle exit hole, d_2, and the outer angle of the annular water jet downstream of nozzle, α. The values obtained on the two grids are summarized in Table 1. The values obtained from photographs taken during experiment are also given in Table 1; the reading errors and the fluctuation between different photographs are believed to be below 5%. Based on the difference between the solutions on the two grids, it can be concluded that the discretization errors on the finer grid are small (of the order of 1%), which is probably smaller than the modeling errors (most of all due to the 2D-approximation). All figures below were taken from the fine-grid simulation.

Figure 6 shows computed pressure distribution in the nozzle. It indicates that the pressure is minimum in the core (ca. 8000 Pa below ambient pressure), which is the reason for air being sucked into nozzle. This figure also shows that pressure varies little at the outer diameter, while a very rapid variation takes place near the air core.

Figure 7 shows computed axial velocities in the nozzle. It shows complicated radial profiles of axial velocity within the nozzle: velocity is high near the conical wall, reduces rapidly with wall distance, rises again to its maximum near the free surface and reverses to about the same value in the opposite direction at the symmetry axis. The free surface position can not be identified in this figure, as the axial velocity varies smoothly across it.

Figure 8 shows computed distribution of circumferential velocity component within the nozzle. It attains maximum values near the air core: from the prescribed value at inlet (5.313 m/s) the swirl velocity rises to over 40 m/s at small radii, indicating that the distribution of circumferential velocity resembles that of a potential vortex. At nozzle exit the swirl is still strong with circumferential velocities about 30 m/s.

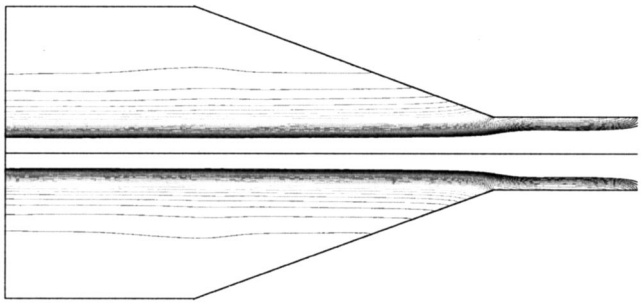

Fig. 6 Computed pressure distribution in the nozzle (lowest at symmetry line, largest at outer wall)

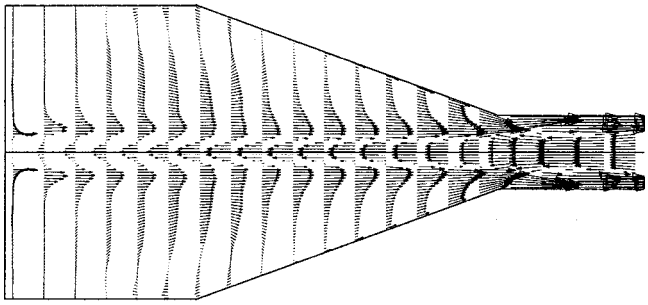

Fig. 7 Computed axial velocity within conical nozzle

Finally, Fig. 9 shows the computed free surface shape in the cross-section through the nozzle. The thickening of the air core at the end of conical section and the spreading and thinning of the annular water jet at nozzle exit are clearly seen; the qualitative agreement with the photograph in Fig. 3 is obvious. As data in Table 1 show, the quantitative agreement is also satisfactory. Test calculation at a higher swirl velocity and the same flow rate showed similar shape and dimensions of the air core, but the angle of the spray has increased, which agrees with experimental observations.

Since the air core shape in the cylindrical nozzle is three-dimensional (3D), here a 3D-simulation had to be performed. The grid used in the simulation is shown in Fig. 10. Here only the flow within nozzle has been computed to save on computing time; it is expected that the spreading of water jet outside nozzle has little effect on the shape of air core inside nozzle. The grid is unstructured with local refinements and has 116 960 CVs.

In this case we have performed a time-accurate simulation of the development of air core, since this could not be observed in experiment due to the lack of sophisticated equipment. The computations, on the other hand, could be performed on a PC with 256 MB of memory and—although they lasted several days—the cost of the numerical analysis is much lower than that of the needed equipment for more detailed experimental analysis. Simulation started with nozzle filled with air at rest; constant inlet velocity

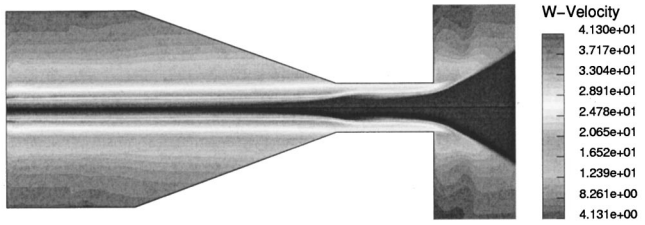

Fig. 8 Computed distribution of circumferential velocity in the nozzle

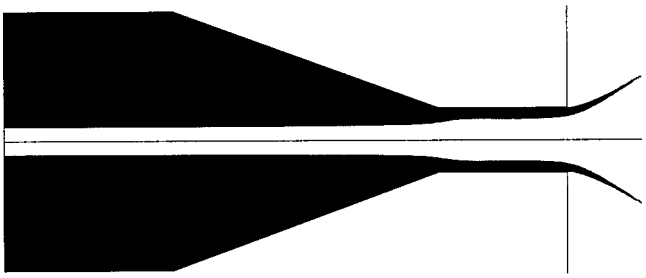

Fig. 9 Computed free surface shape in a cross-section through the conical nozzle

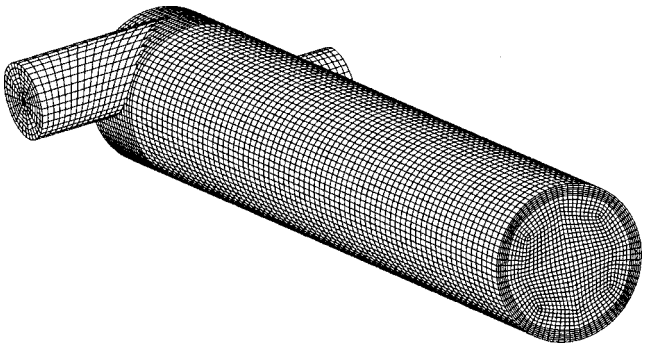

Fig. 10 Numerical grid used to compute the flow in a cylindrical nozzle, also showing distribution of water and air at nozzle exit

equal to the mean velocity in supply tubes has been imposed as the inlet boundary condition, while at outlet the ambient (constant) pressure has been prescribed.

Figure 11 shows distribution of water and air and the velocity vectors in the longitudinal cross-section through the nozzle at four time instants, 1 ms apart (each 500 time steps after the simulation started). Initially, incoming water jets from tangential entry ports fill the nozzle cross-section with water and trap some air at the nozzle base; later on, when low pressure due to spinning is created

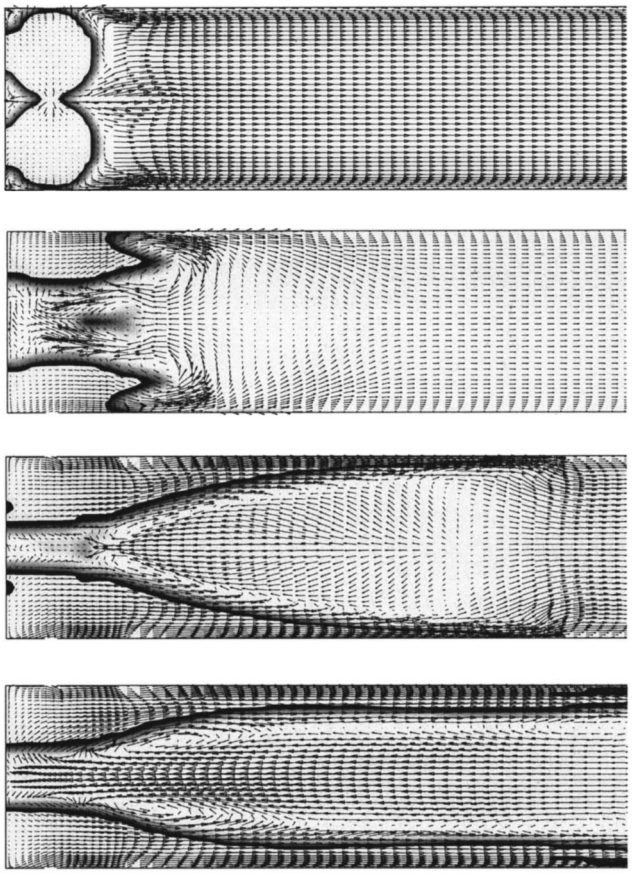

Fig. 11 Development of air core during the filling of the nozzle: distribution of water and air with velocity vectors in a longitudinal cross-section through the nozzle at four time instants, 500 time steps apart.

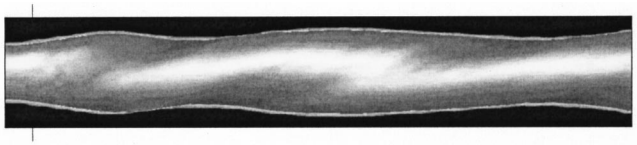

Fig. 12 The computed shape of the air core in a cylindrical nozzle

at symmetry line, air starts flowing into the nozzle from outside and water remains attached to the outer nozzle wall, flowing gradually toward the exit.

These figures show also the complicated flow patterns inside nozzle during the filling process. Several recirculation zones and stagnation regions can be identified, which move as more water flows in. After 2000 time steps, the changes become less pronounced and a nearly-steady state is attained. The air core does not have a cylindrical shape as in the conical nozzle, as the last figure in Fig. 11 shows. The cross-sectional shape of air core is actually elliptical, and the ellipse turns two times as one moves down the nozzle axis. This is clearly seen in Fig. 12, which shows the air core as a three-dimensional object with side lighting, thus showing the helical surface shape. Water fills the space between this core and the outer nozzle diameter.

Comparison with photograph from experiment shown in Fig. 4 revels a remarkable similarity, including the appearance of secondary disturbance superimposed over the primary helical shape. The mean diameter of the air core corresponds also closely to the value observed in experiment.

In another experiment the flow rate was reduced to 9.1×10^{-6} m^3/s. The air core was more or less cylindrical in this case, except the zone very near to the inlet. Near to the inlet the air core has an elliptic cross-section and thereafter it remains cylindrical without any twist. Thus the air core with low inlet velocity, inlet Re$<$3000, does not become helical. As soon as the inlet velocity is increased, the shape of the air core changes and becomes helical again. Numerical simulation for the lower flow rate also produced a cylindrical air core, thus certifying that both qualitative and—at least to some extent—quantitative changes in flow pattern and air core shape can be predicted using the numerical method that has been employed in the present study.

Conclusions

The numerical solution of the Navier-Stokes equations along with the mass and volume fraction conservation equations for both air and water has been shown to provide results for water flows in both conical and cylindrical nozzles which agree both qualitatively and to a large extent also quantitatively with experimental observations. In particular, the shape of air core has been correctly predicted for both nozzles, including a complex twisted 3D-shape in the case of a cylindrical nozzle. Also, the jet spreading angle in the case of a conical nozzle has been correctly predicted, as well as its dependence on the swirl introduced through tangential ports. For cylindrical nozzles the simulation also shows that the air core becomes also cylindrical when the flow rate becomes lower than a certain limiting value.

It has also been demonstrated that 2D-simulations can be successfully performed for nozzles with two tangential entries if the air core is axisymmetric, by employing a suitable simplification of boundary conditions and imposing zero-gradient in circumferential direction. In this way much finer grids can be used (thus eliminating discretization errors) at significant savings in computing times (couple of hours instead of couple of days on a personal computer). The numerical method used here can thus be employed as an engineering tool in the process of nozzle optimization.

Acknowledgments

The first author (SKD) gratefully acknowledges the financial support given to him by the Alexander von Humboldt Foundation for carrying out the numerical work at the Technical University of Hamburg-Harburg, which has made this publication possible. Also, support by the German Science Foundation (DFG) for a visit of M. Peric to IIT in the final stage of preparation of this paper is greatly appreciated.

References

[1] Chang, K. C., Wnag, M. R., Wu, W. J., and Hong, C. H., 1993, ''Experimental and Theoretical Study on Hollow-Cone Spray,'' J. Propul. Power, **9**, No. 1, pp. 28–34.

[2] Chen, S. K., Lefebvre, A. H., and Rollbuhler, J., 1993, ''Factors Influencing the Circumferential Liquid Distribution from Pressure Swirl Atomizers,'' ASME J. Eng. Gas Turbines Power, **115**, pp. 447–452.

[3] Datta, A., and Som, S. K., 2000, ''Numerical Predictions of Air Core Diameter, Coefficient of Discharge and Spray Cone Angle in a Swirl Spray Nozzle,'' Int. J. Heat Fluid Flow, **21**, pp. 412–419.

[4] Kutty, S. P., Narashimhan, M., and Narayanaswamy, K., 1978, ''Design and Prediction of Discharge Rate, Cone Angle and Air Core Diameter of Swirl Chamber Atomizers,'' Proc. *1st Int. Conf. on Liquid Atomization and Spray Systems*, pp. 93–100.

[5] Rizk, N. K., and Lefebvre, A. H., 1985, ''Internal Flow Characteristics of Simplex Swirl Atomizers,'' AIAA J. of Propul. and Power, **1**, No. 3, pp. 193–199.

[6] Rizk, N. K., and Lefebvre, A. H., 1985, ''Prediction of Velocity Coefficient of Spray Cone Angle for Simplex Swirl Atomizers,'' Proc. *3rd Int. Conf. On Liquid Atomization and Spray Systems*, pp. 111C/2/1–16.

[7] Som, S. K., and Mukherjee, S. G., 1980, ''Theoretical and Experimental Investigations on the Formation of Air Core in a Swirl Atomizing Nozzle,'' Appl. Sci. Res., **36**, pp. 173–176.

[8] Som, S. K., 1983, ''Theoretical and Experimental Studies on the Formation of Air Core in a Swirl Spray Atomizing Nozzle Using a Power Law Non-Newtonian Liquid,'' Appl. Sci. Res., **40**, pp. 71–91.

[9] Som, S. K., and Biswas, G., 1984, ''Initiation of Air Core in a Swirl Nozzle Using Power Law Fluids,'' Acta Mech., **51**, pp. 179–197.

[10] Suyari, M., and Lefebvre, A. H., 1986, ''Film Thickness Measurements in a Simlex Swirl Atomizer,'' AIAA J. of Propul. and Power, **2**, No. 6, pp. 528–533.

[11] Lafaurie, B., Nardone, C., Scardovelli, R., Zaleski, S., and Zanetti, G., 1994, ''Modelling merging and fragmentation in multiphase flows with SURFER,'' J. Comput. Phys., **113**, pp. 134–147.

[12] Ubbink, O., 1997, ''Numerical prediction of two fluid systems with sharp interfaces,'' *PhD thesis*, University of London.

[13] Muzaferija, S., and Peric, M., 1999, ''Computation of Free Surface Flow Using Interface-Tracking and Interface-Capturing Methods,'' Chap. 2, O. Mahrenholtz and M. Markiewicz, eds., *Nonlinear Water Wave Interaction*, pp. 59–100, WIT Press, Southampton.

[14] Brackbill, J. U., Kothe, D. B., and Zemaach, C., 1992, ''A continuum method for modeling surface tension,'' J. Comput. Phys., **1**, pp. 335–354.

[15] Patankar, S. V., and Spalding, D. B., 1972, ''A calculation procedure for heat, mass and momentum transfer in three-dimensional parabolic flows,'' Int. J. Heat Mass Transf., **15**, pp. 1787–1806.

[16] Comet User Manual, ICCM Institute of Computational Continuum Mechanics GmbH, Hamburg, Germany (www.iccm.de).

Stability Criteria of the Steady Flow of a Liquid Containing Bubbles Along a Nozzle

A. Crespo

J.García

J. Jiménez-Fernández

Universidad Politécnica de Madrid,
Departamento de Ingeniería Energética y
Fluidomecánica,
José Gutiérrez Abascal, 2, 28006 Madrid, Spain

The steady cavitating flow through a converging-diverging nozzle is considered. A continuum model is assumed with the Rayleigh-Plesset equation to account for the bubble dynamics. A similar problem has been studied previously by Wang and Brennen, and they found that if the upstream gas volume fraction of the bubbles exceeds a critical value there is flashing flow instability. In the present work, a perturbation analysis is made introducing a small parameter, ε, that is the ratio of the initial bubble diameter to the length scale of the nozzle. As a result of this analysis, the critical value of the upstream void fraction is calculated as a function of the several parameters appearing in the problem, and turns out to be very small and proportional to ε^3. A correlation is proposed giving explicitly the functional dependence of this critical value.
[DOI: 10.1115/1.1412564]

1 Introduction

The study of liquid bubbly flows has some interesting applications such as the control of the sound produced by ship propellers or the design of devices to propel high-speed water borne craft; some of these applications are illustrated in more detail by Wijngaarden [1]. The problem may also have a biomedical interest, because the generation of bubbles in the blood is responsible for the submarine sickness and the Caisson disease; besides, the dynamics of cavitation bubbles can be also involved in surgical procedures, like in pulsed-laser angioplasty.

In this work application will be made to study the cavitating flow in a nozzle. Wang and Brennen [2] have studied a similar problem, and Wang [3] has extended the analysis to the case of nonuniform bubble size. They found that two types of solutions could be obtained depending on the upstream volume fraction of bubbles. If this concentration is small enough, the downstream conditions will oscillate with the natural frequency of the bubble, until these oscillations will be damped, and, eventually, the upstream conditions will be recovered. On the other hand, if the upstream bubble concentration is above a threshold value, the bubble radius will increase indefinitely, leading to flashing flow. Wang and Brennen [2] also solved numerically a particular case and gave an analytical expression for the critical bubble size for bifurcation, however, they did not present a general expression for the critical value of the upstream volume concentration of the bubbles. Delale et al. [4] carried out a similar analysis including bubble/bubble interactions, and found solutions similar to those of Wang and Brennen when these interactions were neglected. In a previous work Crespo et al. [5] interpreted this bifurcation in terms of a classical shock structure in a liquid containing bubbles. They also made a preliminary work with application to tubes with a flexible wall.

Here, an asymptotic analysis is presented in terms of a small parameter, ε, that is the ratio of the initial bubble diameter and the nozzle length. Three regions are found along the nozzle: at the entrance there is an *equilibrium region* where the gas and liquid pressures are equal, next there is a *transition region*, and further downstream there is *cavitating region* where the difference in pressure of gas and liquid is large. The transition region that separates the equilibrium and cavitation regions is very thin, and its typical scale divided by the nozzle length tends to zero as $\varepsilon^{6/11}$. It provides the condition to match the solutions in the equilibrium and cavitation regions. The three regions are shown schematically in Fig. 1.

The critical value of the void fraction in the upstream region, α_{1c}, is obtained from *the asymptotic analysis of the cavitating region*, and it turns out to be proportional to ε^3. However, its dependence with the cavitation parameter σ, and the absolute value of the minimum pressure coefficient $|c_{p\,\min}|$, has to be calculated numerically. Further simplifications of the analysis of the cavitating region, reduce the problem to *the solution of a single ordinary differential equation*, and the dependence of α_{1c} with $|c_{p\,\min}|$ is made explicit, but the dependence with $\sigma/|c_{p\,\min}|$ has to be obtained numerically. Finally, a *correlation* is proposed that gives α_{1c} as a function of all the parameters. The results of these three procedures (full asymptotic solution, ODE, correlation) are compared among them, and with those of the numerical solutions of the original set of equations proposed by Wang and Brennen [2], and the agreement is good.

Results for alternative shapes of the nozzles are examined, and the results are qualitatively similar.

2 Equations for the Flow Through a Converging-Diverging Nozzle

The model used here is similar to that presented in Wijngaarden [1]. It is assumed that the bubbles are spherical, and the velocities of liquid and gas are equal, but their pressures are different. The process is steady and quasi unidirectional. The gas density is negligible compared to liquid density. The liquid density is constant. The effect of friction of the fluid with the tube is neglected. The number of bubbles per unit volume of liquid is assumed to be constant. A polytropic law has been assumed to calculate the gas pressure. This last assumption is questionable, as indicated by Watanabe and Prosperetti [6], however, it will be shown that the value of the k exponent is not very relevant for the results of the analysis, particularly for those of the cavitation region presented in Section 5. The problem treated numerically by Wang and Brennen [2] is treated here using an asymptotic approach based on the small parameter:

$$\varepsilon = \frac{2R_1}{L} \ll 1. \tag{1}$$

The following nondimensional variables are used:

Contributed by the Fluids Engineering Division for publication in the JOURNAL OF FLUIDS ENGINEERING. Manuscript received by the Fluids Engineering Division October 4, 2000; revised manuscript received August 8, 2001. Associate Editor: Y. Matsumoto.

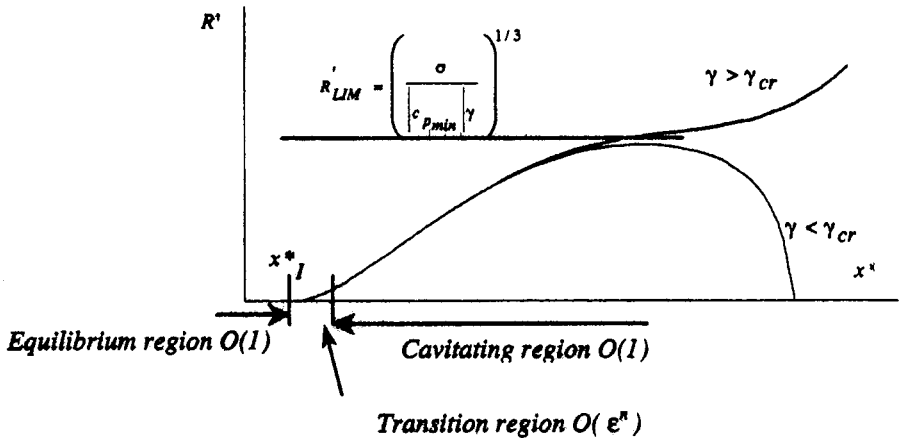

Fig. 1 Schematic showing the evolution of the bubble radius for γ above and below its critical value

$$\mathrm{Re}=\frac{u_1 R_1}{\nu};\quad x^*=\frac{2x}{L};\quad R^*=\frac{R}{R_1};\quad u^*=\frac{u}{u_1};\quad A^*=\frac{A}{A_1} \tag{2}$$

$$c_p=\frac{p-p_1}{\frac{1}{2}\rho_l u_1^2};\quad \sigma=\frac{p_1-p_\nu}{\frac{1}{2}\rho_l u_1^2};\quad \mathrm{We}=\frac{\rho_l u_1^2 R_1}{S}$$

Conservation of mass, momentum, and number of bubbles are expressed by:

$$(1-\alpha)u^*A^*=1-\alpha_1. \tag{3}$$

$$(1-\alpha)u^*\frac{du^*}{dx^*}=-\frac{1}{2}\frac{dc_p}{dx^*}. \tag{4}$$

$$\frac{\alpha}{1-\alpha}\frac{1}{R^{*3}}=\frac{\alpha_1}{1-\alpha_1}. \tag{5}$$

The Rayleigh Plesset equation for radial momentum conservation is:

$$\varepsilon^2\left[R^*u^{*2}\frac{d^2R^*}{dx^{*2}}+u^*\frac{du^*}{dx^*}R^*\frac{dR^*}{dx^*}+\frac{3}{2}u^{*2}\left(\frac{dR^*}{dx^*}\right)^2\right]+\varepsilon\frac{4}{\mathrm{Re}}\frac{u^*}{R^*}\left(\frac{dR^*}{dx^*}\right)+\frac{2}{\mathrm{We}}\left(\frac{1}{R^*}-\frac{1}{R^{*3k}}\right)+\frac{\sigma}{2}\left(1-\frac{1}{R^{*3k}}\right)+\frac{c_p}{2}=0. \tag{6}$$

It will be assumed that the Weber number is large and that the corresponding term in the previous equation is negligible; however it will be retained when reproducing the calculations of Wang and Brennen [2].

3 Equilibrium Region

In a first approximation, if ε is very small, the dynamic terms of Eq. (6) are negligible (then, the pressures of liquid and gas are equal), and the bubble radius is given by:

$$R^{*3k}=\frac{\sigma}{\sigma+c_p}. \tag{7}$$

However, this approximation breaks down when there is cavitation and:

$$\sigma+c_p=0,\ \text{then},\ R^*\to\infty. \tag{8}$$

The point where cavitation starts and condition (8) is satisfied can be easily determined assuming that in the initial equilibrium region, where Eq. (7) holds, α is very small and can be neglected. Then, from Eqs. (3) and (4), the following expression is obtained, (that is really Bernoulli's equation):

$$c_p=1-u^{*2}=1-\frac{1}{A^{*2}}. \tag{9}$$

For the area of the nozzle the following expression is used:

$$\frac{1}{A^{*2}}=1+|c_{p\,\min}|F(x^*) \tag{10}$$

Wang and Brennen [2] give for $F(x^*)$ a sinusoidal shape:

$$F(x^*)=\frac{1}{2}(1-\cos(\pi x^*)),\quad 0<x^*<2,\qquad F(x^*)=0,\quad x^*<0\quad\text{and}\quad x^*>2. \tag{11}$$

An alternative nozzle shape will also be used here using the algebraic expression:

$$F(x^*)=\frac{1}{1+4(x^*-1)^2}. \tag{12}$$

Both shapes satisfy the condition that $F(1/2)=F(3/2)=1/2$, and $F(1)=1$, and $L/2$ is the distance between the two points where F is 0.5.

The position and velocity at the cavitation inception point are given by:

$$F(x_1^*)=\frac{\sigma}{|c_{p\,\min}|}, \tag{13}$$

$$u_1^*=(1+\sigma)^{1/2}. \tag{14}$$

4 Transition Region

This is a narrow region around the cavitation inception point, where the bubble radius is larger than in the previous region, and the dynamic terms in Eq. (6) should be of the same order as the pressure terms. Consequently, the coordinate x^* is changed to Δ, and is scaled as:

$$x^*-x_1^*=u_1^*\varepsilon^n\Delta, \tag{15}$$

and the bubble radius is scaled as:

$$R^*=\bar{R}\varepsilon^{-h}. \tag{16}$$

The exponents n and h are chosen so that the dynamic and pressure terms are of the same order in Eq. (6):

$$h=\frac{2}{2+9k}=\frac{2}{11}(k=1), \tag{17}$$

$$n=\frac{6k}{2+9k}=\frac{6}{11}(k=1). \tag{18}$$

In this region α is still much smaller than one and consequently u^* and c_p will be given by Eq. (9). On the other hand, as the thickness of this region is of order ε^n, much smaller than one, it is possible to approximate u^* and c_p by:

$$u=u_1^*+\left.\frac{du^*}{dx^*}\right|_{x^*=x_1^*} u_1^*\varepsilon^n\Delta+O(\varepsilon^{2n}) \tag{19}$$

$$c_p=-\sigma+\left.\frac{dc_p}{dx^*}\right|_{x^*=x_1^*} u_1^*\varepsilon^n\Delta+O(\varepsilon^{2n}) \tag{20}$$

After making the change of variables given in Eqs. (15) and (16), and using (19) and (20), Eq. (6) becomes:

$$\overline{R}\frac{d^2\overline{R}}{d\Delta^2}+\frac{3}{2}\left(\frac{d\overline{R}}{d\Delta}\right)^2-\beta\Delta-\frac{\sigma}{2}\frac{1}{\overline{R}^{3k}}=0, \tag{21}$$

where,

$$\beta=-\frac{1}{2}u_1^*\left.\frac{dc_p}{dx^*}\right|_{x^*=x_1^*}. \tag{22}$$

In order to obtain Eq. (21) from Eq. (6), only the terms of order ε^n have been retained, and terms containing higher powers of ε have been neglected. The term containing du^*/dx^* in (6) is negligible because is of order ε^{2n}. This also happens with the contribution of the variation of u^* to the other terms of (6). As a matter of fact, u^* could be assumed to be constant, and equal to u_1^* throughout this region, and omit expansion (19). On the other hand, to neglect the viscous term it has to be assumed that the Reynolds number is large enough so that $\mathrm{Re}\gg\varepsilon^{(1-2n)}$; as $2n$ is quite close to one, this condition is expected to be satisfied, even if Re is only moderately large.

For $\Delta\to-\infty$, the solution of Eq. (21) is the equilibrium solution given by Eq. (7):

$$\overline{R}^{3k}=-\frac{\sigma}{2\beta\Delta}, \tag{23}$$

and for $\Delta\to\infty$, the solution of Eq. (21) is:

$$\overline{R}=\sqrt{\frac{8\beta}{33}}\Delta^{3/2}, \tag{24}$$

that is the matching condition for the following region. The transition region represents the classical behavior of a boundary layer. When using outer variables of order one it reduces to a point, located at $x^*=x_1^*$, separating the equilibrium and cavitation regions. On the other hand, when using the inner variable Δ, the behavior of the equilibrium and cavitation regions near $x^*=x_1^*$ is recovered as Δ tends to $\pm\infty$, respectively, see Fig. 1.

5 Cavitation Region

This region extends through the whole nozzle, downstream from the inception point, $x^*>x_1^*$. In this region, $x^*=O(1)$ and $R=O(1/\varepsilon)$, so that the dynamic terms and pressure terms are of the same order in Eq. (6). This means that the bubble radius is of the order of the nozzle length; however, this anomalous situation could be justified because the numerical factors from the calculations are smaller than one, so that the bubble radius turns out to be really smaller than L. From Eq. (5) it is obtained that:

$$R^*\approx\frac{1}{\varepsilon}\to\alpha\approx\frac{\alpha_1}{\varepsilon^3}. \tag{25}$$

Consequently, the expected value of the upstream concentration of gas, α_1, should be very small, $\alpha_1=O(\varepsilon^3)$. In Wang and Brennen [2] the critical value of α_1 is 3×10^{-6}, but no explanation is given for such a small value. The analysis can be carried out taking as new variable $R''=\varepsilon R^*$ in Eqs. (3) to (6), and taking the limit of small ε. In Eq. (5) α_1 can be neglected compared to one and it will become:

$$\frac{\alpha}{1-\alpha}\frac{1}{R''^3}=\alpha_1\varepsilon^{-3}=\gamma_1. \tag{5'}$$

In Eq. (6) terms of $O(1)$ are retained, and then the viscous, surface tension and polytropic terms of Eq. (6) will drop out and,

$$R''u^{*2}\frac{d^2R''}{dx^{*2}}+u^*\frac{du^*}{dx^*}R''\frac{dR''}{dx^*}+\frac{3}{2}u^{*2}\left(\frac{dR''}{dx^*}\right)^2+\frac{\sigma}{2}+\frac{c_p}{2}=0. \tag{6'}$$

Equation (24) has to be used as a matching condition for Eq. (6′) for small values of $(x^*-x_1^*)$. In Eqs. (3), (4), (5′), (6′), and (24), there are only three parameters: γ_1, σ and $|c_{p\,\min}|$ (in Eq. (3) α_1 can also be neglected compared to 1). Then, the critical value of γ_1 for bifurcation should be a function of the two others:

$$\alpha_1\varepsilon^{-3}=(\gamma_1)_{\mathrm{cr}}=f(\sigma,|c_{p\,\min}|). \tag{26}$$

In order to obtain a simpler correlation for the critical conditions, some further simplifying assumptions have been made in Crespo et al. [5]. It can be shown from Eqs. (3) and (4) that:

$$c_p=1-\frac{1}{A^{*2}}-\frac{2\alpha}{(1-\alpha)}+\frac{2\alpha}{(1-\alpha)}\left(1-\frac{1}{A^{*2}}\right)+\int_{-\infty}^{x}\frac{\alpha}{1-\alpha}\frac{2}{A^*}\frac{d}{dx^*}\left(\frac{1}{A^*}\right)dx^*. \tag{27}$$

If it is assumed that α is moderately small and the area variations are also small, or at least that the largest values of α occur at the positions where A^* is equal or close to one, the last two terms in Eq. (27) will be negligible.

The velocity is assumed to take a constant value given by:

$$u^*=\left(1+\frac{|c_{p\,\min}|}{2}\right)^{1/2}. \tag{28}$$

This value corresponds to the square root of the mean of the two values of u^{*2} at the entrance $(u^{*2}=1)$ and at the throat $(u^{*2}=1+|c_{p\,\min}|)$ of the nozzle, for small values of the void fraction. Then, making the change of variables:

$$R^*=\frac{R'}{\varepsilon}\left(\frac{|c_{p\,\min}|}{2}\right)^{1/2}\frac{1}{\left(1+\frac{|c_{p\,\min}|}{2}\right)^{1/2}}, \tag{29}$$

taking Eqs. (27) to (29) into Eq. (6′), and using Eqs. (10) and (5′), it is obtained that:

$$R'\frac{d^2R'}{dx^{*2}}+\frac{3}{2}\left(\frac{dR'}{dx^*}\right)^2+\left(\frac{\sigma}{|c_{p\,\min}|}-F(x^*)\right)-\gamma R'^3=0, \tag{30}$$

where,

$$\gamma=\alpha_1\frac{1}{\varepsilon^3}\left(\frac{|c_{p\,\min}|}{2}\right)^{1/2}\left(\frac{1}{1+\frac{|c_{p\,\min}|}{2}}\right)^{3/2}. \tag{31}$$

In deriving Eqs. (28) and (30), it is assumed that α is small; this is not always true and values of the void fraction as high as 0.20 or 0.25 can be obtained. Then, this assumption has to be further validated by comparing with the results of solving the set of equa-

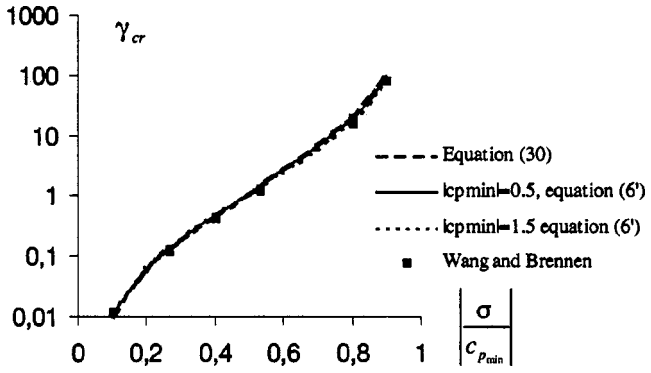

Fig. 2 Variation of the bifurcation parameter as function of $\sigma/|c_{p\,\min}|$, and $|c_{p\,\min}|$. Comparison of the solutions obtained with Eq. (30), the system of equations (3), (4), (5′), (6′), and the original system of equations of Wang and Brennen [2].

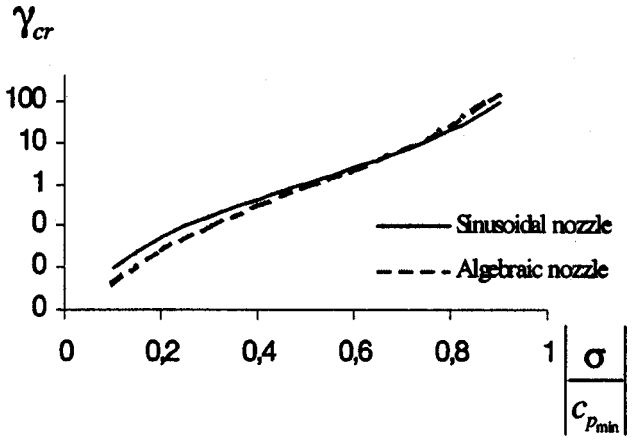

Fig. 3 Comparison of the bifurcation parameter for the two nozzle shapes

tions: (3), (4), (5′), (6′), where α can be finite, or with the original system of equations proposed in Wang and Brennen [2].

Equation (30) has to be solved with the matching condition given by condition (24). As a matter of fact, the solution of Eq. (30) for small values of $(x^*-x_1^*)$, satisfying the conditions that both R' and dR'/dx^* are zero at $x^*=x_1^*$, is:

$$R' = \sqrt{\frac{8}{33}\left.\frac{dF}{dx^*}\right|_{x=x_1}}\,(x^*-x_1)^{3/2}, \tag{32}$$

that coincides with Eq. (24) if it is assumed that u_1^* is given by Eq. (28) instead of Eq. (14). Then, it will not be really necessary to calculate the transition region, and Eq. (30) could be integrated by applying directly the boundary conditions $R'=dR'/dx^*=0$ at $x^*=x_1^*$; although they will not be well justified.

If γ exceeds a critical value $\gamma_{\rm cr}$ the solution of Eq. (30) gives a diverging value of R', otherwise, the value of R' will eventually become very small, as shown schematically in Fig. 1. In Wang and Brennen [2] the bubble oscillates around final equilibrium position when there is no flashing. However, in Fig. 1, the oscillations do not appear because the term associated to the gas compressibility is of smaller order and has been neglected. In Fig. 1 is also presented the corresponding limiting value of R' for the bifurcation, that is obtained equating the last two terms of Eq. (30) (when $F=0$, $A^*=1$), and is similar to that given by Wang and Brennen [2]. The behavior of R'' when solving the whole set of Eqs: (3), (4), (5′), (6′) is similar to that shown in Fig. 1.

From Eq. (30) it can also be seen that, with the previous simplifications, the critical value of γ will only depend on the ratio $\sigma/|c_{p\,\min}|$. This dependence is shown in Fig. 2, for the sinusoidal area distribution of Eq. (11). As expected, as $\sigma/|c_{p\,\min}|$ tends to zero (always cavitating flow) the required value of γ also tends to zero, and oppositely, as it gets close to one the required value of γ tends to infinity, indicating that there is no cavitation. However, this is not exactly true, because for sufficiently large values of γ (of the order ε^{-3}), the upstream value of gas volume concentration, α_1, will be finite and the present theory will not apply. If α_1 is not small the pressure at the end of the equilibrium region will not be given by (9), and, because of the compressibility of the mixture c_p can be smaller than $-|c_{p\,\min}|$, and can be cavitation, even if $\sigma/|c_{p\,\min}|>1$.

When solving the system (3), (4), (5′) and (6′), γ is proportional to ε^{-3} and depends separately on σ and $|c_{p\,\min}|$, as shown in Eq. (26). However, when this dependence is presented in Fig. 2, it can be clearly seen that γ depends mainly on $\sigma/|c_{p\,\min}|$, indicating that the approximations involved in obtaining Eq. (30) (mainly Eq. (28)), are substantially correct.

Finally, in Fig. 2 is also shown the value of γ calculated numerically by Wang and Brennen [2], for $\sigma=0{,}8$, $|c_{p\,\min}|=1$ and $\varepsilon=1/250$. Some other representative values of γ calculated using the same equations of Wang and Brennen [2], are also presented in Fig. 2. In this case the system of Eqs. (3) to (6) has been solved, and γ will depend separately on ε, σ and $|c_{p\,\min}|$, and also on the Reynolds and Weber numbers. A total of 12 cases were solved by combining the following values: $\sigma=0.05$, 0.4, 0.8, 0.9, $|c_{p\,\min}|=0.5$, 1, 1.5, $\varepsilon=1/250$, 1/500 and fixed values of Re=33, We=137. In Fig. 2 there are 4 results for $\sigma/|c_{p\,\min}|=0.8$ giving very similar values of γ. For each respective value of $\sigma/|c_{p\,\min}|=0.266$, 0.4, 0.53 there are also two values of γ that are very similar. The agreement with the previous results obtained both with the system of Eqs. (3), (4), (5′) and (6′), and with the ordinary differential equation (30), is quite satisfactory.

In Fig. 3 are compared the results obtained by solving (30) using the sinusoidal area distribution, given in Eq. (11) with those obtained with the algebraic area distribution (12). It can be seen that the algebraic nozzle gives values of γ that increase more rapidly with $\sigma/|c_{p\,\min}|$, although the difference is not very important, at least qualitatively. Calculations were also repeated for a gaussian nozzle: $F(x^*)=\exp(-2.77(x^*-1)^2)$ (that also satisfies the conditions $F(1/2)=F(3/2)=1/2$, $F(1)=1$) and the results were quite similar to the sinusoidal nozzle.

The following correlation fits the results obtained by solving Eq. (30) with an approximation of 2 percent for $0{,}1<\sigma/|c_{p\,\min}|<0{,}9$:

$$\gamma = C\,\frac{\left(\dfrac{\sigma}{|c_{p\,\min}|}\right)^{m_1}}{\left(1-\dfrac{\sigma}{|c_{p\,\min}|}\right)^{m_2}}. \tag{33}$$

The values of the coefficients are $C=1.18$, $m_1=2.18$, $m_2=2.06$ for the sinusoidal nozzle of Wang and Brennen [2], Eq. (11), and $C=1.05$, $m_1=2.57$, $m_2=2.33$ for the algebraic nozzle of Eq. (12). By combining (31) and (33) the value of $\alpha_{1\,\rm cr}$ can be obtained as a function of the three parameters, ε, σ and $|c_{p\,\min}|$. This correlation is not presented in the figure but it could not be distinguished from the calculations.

6 Conclusions

The flow through a converging diverging-nozzle under cavitating conditions is studied using an asymptotic analysis, in terms of a small parameter. A criterion is obtained for the bifurcation, based on a parameter proportional to the initial void fraction. A correlation is proposed to calculate the minimum initial value of the void fraction that can lead to flashing. Quite small values of

the initial void fraction, of the order of the cube of the small parameter, can lead to infinitely growing bubbles. The most important remaining task, besides completing some aspects of the model, is to compare with experimental results, which are not easily available.

Acknowledgments

This work has been made under the support of the ''Proyecto multidisciplinar de Investigación y Desarrollo, Ref. [11197], de la Universidad Politécnica de Madrid''. We are also very grateful to the reviewers for useful comments and suggestions.

Nomenclature

A = tube cross-sectional area
C = coefficient in correlation
c_p = pressure coefficient
$c_{p\,\min}$ = minimum value of pressure coefficient (that is negative)
$F(x)$ = function giving the nozzle area
h = exponent of ε for R^* in transition region
k = polytropic exponent
L = nozzle length
$m_{1,2}$ = exponents in correlation
n = exponent of ε for x^* in transition region
p = pressure
p_v = vapor pressure
$\underline{R}$ = bubble radius
R = nondimensional radius in the cavitation inception region
R',R'' = nondimensional radius in cavitation region
Re = Reynolds number
S = surface tension
t = time
u = velocity
We = Weber number
x = unidirectional coordinate
α = volume concentration of gas
β = parameter in the cavitation inception region
γ,γ_1 = bifurcation parameter
Δ = nondimensional distance in the cavitation inception region
ε = small parameter$=2R_1/L$
ν = kinematic viscosity
ρ_1 = liquid density
σ = cavitation parameter

Subscripts

1 = upstream conditions for the nozzle
I = point where cavitation starts
cr = critical conditions for flashing

Superscripts

$*$ = nondimensional values

References

[1] van Wijngaarden, L., 1972, ''One-dimensional flow of liquids containing small gas bubbles,'' Annu. Rev. Fluid Mech., **4**, pp. 369–396.
[2] Wang, Y., and Brennen, C. E., 1998, ''One-dimensional bubbly cavitating flows through a converging-diverging nozzle,'' ASME J. Fluids Eng., **120**, pp. 166–170.
[3] Wang, Y., 2000, ''Stability analysis of one-dimensional steady cavitating nozzle flows with bubble size distribution,'' ASME J. Fluids Eng., **122**, pp. 425–430.
[4] Delale, C. F., Schnerr, G. H., and Sauer, J., 2001, ''Quasi-one-dimensional steady-state cavitating nozzle flows,'' J. Fluid Mech., **427**, pp. 167–204.
[5] Crespo, A., García, J., and Jiménez-Fernández, J., 1999, ''One dimensional waves in a liquids containing bubbles flowing along a tube with an elastic wall,'' *IUTAM Symposium on Nonlinear Waves in Multiphase Flow. University of Notre Dame*. July Proceedings pp. 251–260. Fluid Mechanics and its Applications, Vol. 57, Kluwer.
[6] Watanabe, M., and Prosperetti, A., 1994, ''Shock waves in dilute bubbly liquids,'' J. Fluid Mech., **274**, pp. 349–381.

Drag Coefficients of Viscous Spheres at Intermediate and High Reynolds Numbers

Zhi-Gang Feng

Efstathios E. Michaelides

e-mail: emichael@tulane.edu

School of Engineering
and Center for Bioenvironmental Research,
Tulane University,
New Orleans, LA 70118

A finite-difference scheme is used to solve the Navier-Stokes equations for the steady flow inside and outside viscous spheres in a fluid of different properties. Hence, the hydrodynamic force and the steady-state drag coefficient of the spheres are obtained. The Reynolds numbers of the computations range between 0.5 and 1000 and the viscosity ratio ranges between 0 (inviscid bubble) and infinity (solid particle). Unlike the numerical schemes previously implemented in similar studies (uniform grid in a stretched coordinate system) the present method introduces a two-layer concept for the computational domain outside the sphere. The first layer is a very thin one [$O(Re^{-1/2})$] and is positioned at the interface of the sphere. The second layer is based on an exponential function and covers the rest of the domain. The need for such a double-layered domain arises from the observation that at intermediate and large Reynolds numbers a very thin boundary layer appears at the fluid-fluid interface. The computations yield the friction and the form drag of the sphere. It is found that with the present scheme, one is able to obtain results for the drag coefficient up to 1000 with relatively low computational power. It is also observed that both the Reynolds number and the viscosity ratio play a major role on the value of the hydrodynamic force and the drag coefficient. The results show that, if all other conditions are the same, there is a negligible effect of the density ratio on the drag coefficient of viscous spheres. [DOI: 10.1115/1.1412458]

Introduction

Studies by Lovalenti and Brady [1], Mei et al. [2], Mei et al., [3], Feng [4], and Feng and Michaelides [5] have addressed analytically the problems of the unsteady flow and heat transfer of a solid sphere in a viscous fluid, at finite but low Reynolds numbers ($Re<1$). The study by Michaelides and Feng [6] pertains to the motion of spheres of finite viscosity, but is also applicable at very low Reynolds numbers ($Re \ll 1$). Three recent treatises on the subject of droplet and particulate flows [7–9] also address the problem of the motion of solid and viscous spheres in fluids.

Regarding the hydrodynamic force acting on a viscous sphere, there is only a single analytical solution (and one that is occasionally used in practice), which emanates from the classical work by Hadamard and Rybczynski [7,10]. This solution, which is applicable to creeping flows ($Re \ll 1$), yields the following expression for the drag coefficient of a viscous sphere:

$$C_D = \frac{8}{\mathrm{Re}}\left(\frac{3\lambda+2}{\lambda+1}\right) \tag{1}$$

where λ is the viscosity ratio of the internal to the external fluid viscosity, $\lambda = \mu_i/\mu_o$; Re refers to the Reynolds number evaluated with the properties of the outside fluid, $\mathrm{Re} = 2\rho_o U_\infty a/\mu_o$; U_∞ is the velocity of the sphere with respect to the undisturbed fluid; a is the radius of the viscous sphere; and ρ_o is the density of the outside fluid.

Among the earlier solutions on the hydrodynamic forces acting on viscous spheres is the one by Happel and Moore [11]. They derived an asymptotic solution (of the first order) at high Reynolds numbers, which is as follows:

$$C_D = \frac{48}{\mathrm{Re}}\left(1+\frac{3}{2}\lambda\right) \tag{2}$$

Many analytical and numerical solutions for the drag coefficients of solid spheres ($\lambda \to \infty$) or inviscid bubbles ($\lambda = 0$) exist in the literature. However, very few such solutions have been published for the case when the viscosity ratio λ is finite (that is, neither too large, nor close to zero). In this case, the internal flow in the sphere becomes important in the determination of the hydrodynamic force. For a sphere with finite viscosity, both the time-scales associated with the problem, the one for the outside fluid, which is equal to a^2/ν_o, and the one for the inside fluid, which is equal to a^2/ν_i, are important and must be taken into account in the calculations. Because of this, it is impossible to derive a general analytical solution for the drag coefficient of a viscous sphere, except asymptotically. This leaves numerical solutions as the only vehicle to the solution of the problem.

Previous numerical studies on viscous spheres include those by LeClair and Hamielec [12], by Ryvkind et al. [13] who used a finite difference scheme, and by Oliver and Chung [14] who used a hybrid method of series-truncation technique and a finite-difference numerical approximation. All of these methods and their numerical results are limited to low Reynolds numbers (up to a maximum of $\mathrm{Re}=100$) at finite values of the viscosity ratio. A more recent study by El-Shaarawi et al. [15] used the boundary layer approximation to obtain information on the two flow fields, inside and outside the sphere. However, the authors solved only for the frictional part of the drag coefficient and did not calculate the form drag, which is an important component of the hydrodynamic force.

Since applications of droplet flows extend to Reynolds numbers beyond 100, which is the upper limit of the previous studies, we have implemented a novel numerical method to solve the Navier-Stokes equations without any unduly constraining assumptions for the flow inside and outside a viscous sphere. This method may be used at much higher Re but we used it to obtain the drag coefficients up to $\mathrm{Re}=1000$ in the entire range of the viscosity ratio.

It must be pointed out that a viscous sphere becomes elongated (spheroid) at very high Reynolds numbers. For this reason, some of the reported results at the upper limit of Re may not faithfully represent actual spherical drops (unless the surface tension of the

Contributed by the Fluids Engineering Division for publication in the JOURNAL OF FLUIDS ENGINEERING. Manuscript received by the Fluids Engineering Division October 5, 2000; revised manuscript received May 20, 2001. Associate Editor: L. Mondy.

drop is very high and preserves the spherical shape). However, we decided to include these results for two reasons: First, in the absence of better information, these results may serve as a first-order approximation to the drag coefficients of spheroids. Second, in the case of materials with high surface tension the spherical shape is preserved. It must be also pointed out that the numerical technique itself may be used without any modifications to perform similar computations for spheroids.

Governing Equations

1 Conservation Equations. We consider a fluid sphere (a drop) with density ρ_i and viscosity μ_i, rectilinearly translating in a continuous fluid of density ρ_o and viscosity μ_o as depicted in Fig. 1. The undisturbed fluid velocity with respect to the center of the sphere is U_∞. All properties of the sphere will be denoted by the subscript i, while those of the outer fluid will be denoted by the subscript o. The symbol Re is used for the Reynolds number computed with the properties of the external fluid without any subscript, because it is one of the main parameters of the study. The coordinate system is chosen so that the origin is fixed to the droplet center and $\theta=0$ is in the downstream direction.

We use the following dimensionless variables for the radial distance, the stream function and the vorticity components:

$$r=\frac{r'}{a},\quad \Psi=\frac{\Psi'}{U_\infty a^2},\quad \Omega=\frac{\Omega' a}{U_\infty} \tag{3}$$

where r' is the dimensional radial distance, Ψ' is the dimensional stream function and Ω' is a dimensional function related to the z component of the vorticity, ζ', by the following expression:

$$\Omega'=\zeta' r' \sin\theta \tag{4}$$

Hence, the continuity and momentum equations for the internal flow field become:

$$E^2\Psi_i=\Omega_i \tag{5}$$

$$\frac{\mathrm{Re}_i}{2}\sin\theta\left[\frac{\partial}{\partial r}\left(\frac{\Omega_i}{r^2\sin^2\theta}\frac{\partial\Psi_i}{\partial\theta}\right)-\frac{\partial}{\partial\theta}\left(\frac{\Omega_i}{r^2\sin^2\theta}\frac{\partial\Psi_i}{\partial y}\right)\right]=E^2\Omega_i \tag{6}$$

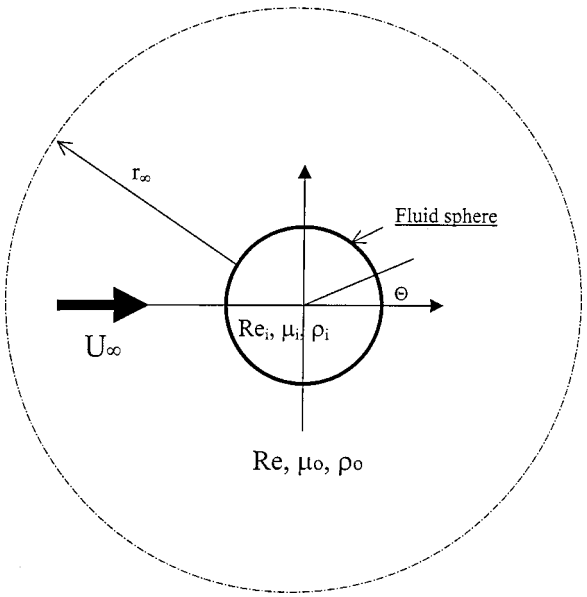

Fig. 1 Schematic diagram of the viscous sphere translating in a fluid.

We also consider a stretched coordinate system for the external flow field introduced by the transformation $r=\exp(y)$ or $y=\ln r$. Hence, the governing equations for the external flow field are:

$$E^2\Psi_o=\Omega_o \tag{7}$$

$$\frac{\mathrm{Re}}{2}e^y\sin\theta\left[\frac{\partial}{\partial y}\left(\frac{\Omega_o}{e^{2y}\sin^2\theta}\frac{\partial\Psi_o}{\partial\theta}\right)-\frac{\partial}{\partial\theta}\left(\frac{\Omega_o}{e^{2y}\sin^2\theta}\frac{\partial\Psi_o}{\partial y}\right)\right]=e^{2y}E^2\Omega_o \tag{8}$$

The operator E^2 is defined in the polar coordinate system as follows:

$$E^2=\frac{\partial^2}{\partial r^2}+\frac{\sin\theta}{r^2}\frac{\partial}{\partial\theta}\left(\frac{1}{\sin}\frac{\partial}{\partial\theta}\right) \tag{9}$$

and in the stretched coordinate system:

$$E^2=e^{-2y}\left(\frac{\partial^2}{\partial y^2}-\frac{\partial}{\partial y}\sin\theta\frac{\partial}{\partial\theta}\left(\frac{1}{\sin}\frac{\partial}{\partial\theta}\right)\right) \tag{10}$$

2 Boundary Conditions. For clarity, the interface will be denoted as $r=1$, when it is approached from inside and as $y=0$, when it is approached from the outside flow field. Hence, the boundary conditions for the stream function and the vorticity may be written as follows:

A. At the center of the viscous sphere:

$$\Psi_i=0,\quad \Omega_i=0\quad at\quad r=0 \tag{11}$$

B. At the fluid-fluid interface,

$$\Psi_i=0,\quad \Psi_o=0\quad at\quad r=1\ \ or\ \ y=0 \tag{12}$$

C. The balance of forces in the tangential direction at the fluid-fluid interface also yields:

$$\lambda\left(\frac{\partial^2\Psi_i}{\partial r^2}-2\frac{\partial\Psi_i}{\partial r}\right)_{r=1}=\left(\frac{\partial^2\Psi_o}{\partial y^2}-3\frac{\partial\Psi_o}{\partial y}\right)_{y=0} \tag{13}$$

D. The continuity of mass in the tangential direction at the interface results in the following expression:

$$\left.\frac{\partial\Psi_i}{\partial r}\right|_{r=1}=\left.\frac{\partial\Psi_o}{\partial y}\right|_{y=0} \tag{14}$$

E. Far from the center of the droplet, at the distance $y=Y$, or $r=e^Y$, the flow is undisturbed and unidirectional. Hence, the values of the functions Ψ and Ω are:

$$\Psi_o=\frac{1}{2}e^{2Y}\sin^2\theta \tag{15}$$

$$\Omega_o=0 \tag{16}$$

Since there are no explicit conditions for the functions Ω_i and Ω_o, we evaluate Ω at the interface from the following expressions:

$$\Omega_i=\left.\frac{\partial^2\Psi_i}{\partial r^2}\right|_{r=1},\quad \Omega_o=\left.\left(\frac{\partial^2\Psi_o}{\partial y^2}-\frac{\partial\Psi_o}{\partial y}\right)\right|_{y=0} \tag{17}$$

Numerical Implementation

Similar studies on the hydrodynamic forces acting on a solid or a viscous sphere [12,13] have used a finite difference method to solve the same set of governing equations. We will refer to this approach as "the conventional approach." From the beginning, it must be pointed out that the conventional approach fails to yield a correct solution for viscous spheres at Reynolds numbers greater than 100. This occurs because a very thin boundary layer of the order of $\mathrm{Re}^{-1/2}$ (or 0.05 sphere radii for Re=400) is formed at the fluid-fluid interface. The conventional approach uses a stretched coordinate system and the previous studies have assumed a computational domain up to $y=5$, usually with 200 total grid points in

the y coordinate. This yields a mesh size at the interface, which is very close to the order of magnitude of the boundary layer thickness. Obviously, such a grid would not capture the details of the boundary layer and, especially, would not compute accurately the derivatives of the vorticity function, Ω, which are needed in the calculation of one of the parts (the form drag) of the drag coefficient (Eqs. (13) and (14) or Eq. (34)). Such a grid would yield inaccurate results for the total force exerted by the fluid and for the drag coefficient. In order to capture correctly the features of the boundary layer and calculate accurately the derivative of Ω by the conventional approach, a grid with 5000 points in the y direction is needed if the conventional method were to be applied. Such an approach would generate a very dense mesh, which would be time-consuming and cumbersome to use, even with today's supercomputers.

A different approach is presented here, which captures the features inside the boundary layer and is not computationally intensive. The basic premise of this approach is to separate the computational domain for the external field into two layers: the first is the boundary layer, whose dimensionless length is $\mathrm{Re}^{-1/2}$. The second layer is the rest of the flow domain. For example, in the case of $\mathrm{Re}=400$, we chose a boundary layer domain of $Y_b=0.05$ with 50 uniformly spaced grid points, thus achieving a mesh size equal to 0.001 of the sphere radius. We also used a mesh of another 150 grid points for the rest of the domain. In order to achieve a smooth transition, the interface of the two layers is nonuniform. Unlike the conventional approach, the mesh size in the proposed method is not necessary to be proportional to the y-direction grid size. Thus, we have found that a grid with approximately 20,000 points for the external flow field is sufficient for our computations.

It must be pointed out that, at high Re, a thin boundary layer is also formed inside the sphere. However, the calculations leading to the drag coefficient of the sphere are not very sensitive to this boundary layer. This is due to the following two reasons: First, the pertinent boundary conditions (Eqs. (13) and (14)) for the internal flow involve only the second order derivatives of the inside stream function and do not involve any derivatives of the vorticity function. Second, the form drag on the sphere depends on the derivative of the vorticity function outside the sphere (Eq. (34)), which corresponds to the third-order derivative of the stream function.

In order to achieve higher accuracy in the computation of the stream function near the interface, we used two cubic polynomials for interpolating the stream function between nearby points on either side of the interface (three rows of grid points in either direction). Thus, the stream function expressions in the vicinity of the fluid-to-fluid interface become:

$$\Psi_i = ay^3 + by^2 + cy + d \tag{18}$$

for the internal flow, and

$$\Psi_o = A(1-r)^3 + B(1-r)^2 + C(1-r) + D \tag{19}$$

for the external flow.

The selection of cubic polynomials for the interpolation the stream function is due to the fact that the numerical method itself is second order and therefore a similar order of interpolation is best to be used. If higher order polynomials were used, some of the coefficients will be indeterminate and certain assumptions would be needed. This would complicate the problem significantly. The calculation of the polynomial coefficients in the last two equations is rather straightforward. From the numerical scheme and the expressions for the grid points on both sides of the interface we have:

$$\begin{aligned} \Psi_{i,0} &= d \\ \Psi_{i,1} &= a\Delta y_1^3 + b\Delta y_1^2 + c\Delta y_1 + d \\ \Psi_{i,2} &= a(\Delta y_1 + \Delta y_2)^3 + b(\Delta y_1 + \Delta y_2)^2 + c(\Delta y_1 + \Delta y_2) + d \end{aligned} \tag{20}$$

and

$$\begin{aligned} \Psi_{o,Ni} &= D \\ \Psi_{o,Ni-1} &= A\Delta r_{Ni}^3 + B\Delta r_{Ni}^2 + C\Delta r_{Ni} + D \\ \Psi_{o,Ni-2} &= A(\Delta r_{Ni} + \Delta r_{Ni-1})^3 + B(\Delta r_{Ni} + \Delta r_{Ni-1})^2 \\ &\quad + C(\Delta r_{Ni} + \Delta r_{Ni-1}) + D \end{aligned} \tag{21}$$

where Δy_i, and Δr_i are the mesh size dimensions between grid point $(i-1)$ to i, and i to $i+1$, respectively.

From the tangential velocity condition at the interface (which is obtained by differentiating the cubic polynomials) we obtain:

$$\left.\frac{\partial \Psi_i}{\partial r}\right|_{r=1} = \left.\frac{\partial \Psi_o}{\partial y}\right|_{y=0} = c = -C \tag{22}$$

The cubic polynomial equations at the interface yield for the needed second derivatives of the stream functions the following expressions:

$$\left.\frac{\partial^2 \Psi_i}{\partial r^2}\right|_{r=1} = 2B \tag{23}$$

$$\left.\frac{\partial^2 \Psi_o}{\partial y^2}\right|_{y=0} = 2b \tag{24}$$

The coefficients a, b, c, d and A, B, C, D may thus be obtained in terms of the stream function at all the grid points. In the case of uniformly distributed grid points, we obtain the following expressions:

$$\Omega_{i,Ni} = \frac{-7\Psi_{i,Ni} + 8\Psi_{i,Ni-1} - \Psi_{i,Ni-2} + 6c\Delta r}{2\Delta r^2} \tag{25}$$

and

$$\Omega_{o,0} \frac{-7\Psi_{o,0} + 8\Psi_{o,1} - \Psi_{o,2} - 6c\Delta y}{2\Delta y^2} - c \tag{26}$$

where c is given by the following expression:

$$c = \frac{\lambda(-7\Psi_{i,Ni} + 8\Psi_{i,Ni-1} - \Psi_{i,Ni-2})\Delta y^2 - (-7\Psi_{o,0} + 8\Psi_{o,1} - \Psi_{o,2})\Delta r^2}{2\Delta r\Delta y[(2\lambda - 3)\Delta r\Delta y - 3(\lambda\Delta y + \Delta r)]} \tag{27}$$

The extension of this method to the two limiting cases of an inviscid bubble and a solid sphere is rather trivial. The final results for the second derivative of the stream function at the interface, which is related to the vorticity, are as follows:

A. For the inviscid bubble, $\lambda = 0$, the tangential shear stress is zero and:

$$\left.\frac{\partial^2 \Psi_o}{\partial y^2}\right|_{y=0} = \frac{-7\Psi_{o,0} + 8\Psi_{o,1} - \Psi_{o,2}}{2\Delta y(1+\Delta y)} \tag{28}$$

B. For a solid sphere, $\lambda=\infty$, which yields $c=0$, and hence,

$$\left.\frac{\partial^2\Psi_o}{\partial y^2}\right|_{y=0}=\frac{-7\Psi_{o,0}+8\Psi_{o,1}-\Psi_{o,2}}{2\Delta y^2} \tag{29}$$

It must be pointed out that Eq. (29) is the same as the expression derived analytically by Briely [16] as a way of expressing the vorticity function at a solid boundary.

For the computations presented in this paper, the value $y_E=5$ (or equivalently, $r_\infty=148.4$) was used in the computations. We arrived at this value of y_E by consulting the literature and performing a validation test for it at the highest values of Re. This value was held constant and did not vary with any of the parameters of the computations. A grid of 180 points has been used in the radial direction (with 50 points reserved for the boundary layer mentioned above) and at least 100 points in the transverse direction. Both parts of the grid outside the sphere are uniform. This type of grid is very dense just outside the sphere and a pictorial representation of it would appear as a thick dark line at the boundary layer. For the domain inside the sphere, 50 grid points in the radial direction have been used for low viscosity ratios ($\lambda<1$) while fewer grid points (40 points) have been used for larger values of λ, because the internal velocities were lower. The number of the transverse points was the same in the internal and the external domains.

We have conducted grid validation calculations by using finer grids with four times as many points and found that the solutions obtained were always within 1 percent of those obtained by the coarser grid. This gave an indication that the grids used are satisfactory for the required computations. The validation by comparison with experimental data and asymptotic solutions (presented in the following section) is another indication of the accuracy of our computations. The convergence criterion for the iterations is chosen, such that the largest relative fractional difference of any quantity, ϕ, between two consecutive iterations is less than 10^{-5}, i.e.,

$$\frac{|\phi^{(n+1)}-\phi^{(n)}|}{\max(|\phi^{(n)}|,1)}\leqslant 10^{-5} \tag{30}$$

Most of the computations were performed in a Pentium MX 300 PC unit operating with the Linux system. The computational times for most of the cases were less than 3 hr.

Results, Validation, and Discussion

1 Expression for the Drag Coefficient. The drag coefficient of the sphere, C_D, is composed of two parts: (a) the contribution resulting from the pressure gradient term, C_{DP}, which is sometimes referred to as the ''form drag;'' and (b) the contribution from friction C_{DF}, which is sometimes referred to as the ''friction drag.'' These two components of the drag force may be expressed as follows:

$$C_{DP}=\int_0^\pi k(a,\theta)\sin(2\theta)d\theta \tag{31}$$

and

$$C_{DF}=\frac{8}{\mathrm{Re}_o}\int_0^\pi\left[\left(\frac{\partial v}{\partial r}-v\right)\sin\theta-2\frac{\partial u}{\partial r}\cos\theta\right]\sin\theta d\theta \tag{32}$$

where $k(a,\theta)$ is the function of the pressure at the surface of the sphere and u and v are the two components of velocity. The pressure function itself is calculated from the following expression:

$$k(a,\theta)=k(a,0)+\frac{4}{\mathrm{Re}}\int_0^\theta\left(\frac{\partial\zeta}{\partial r}+\zeta\right)_{r=1}d\theta-v^2 \tag{33}$$

Hence, it may easily be proven that the form and friction drag components are given as follows:

$$C_{DP}=\frac{4}{\mathrm{Re}}\int_0^\pi\left(\int_0^\theta\frac{1}{\sin\eta}\frac{\partial\Omega_o}{\partial y}d\eta-\frac{\mathrm{Re}}{4}\left(\frac{1}{\sin^2\theta}\frac{\partial\Psi_o}{\partial y}\right)^2\right)\sin(2\theta)d\theta \tag{34}$$

and

$$C_{DF}=\frac{8}{\mathrm{Re}}\int_0^\pi\Omega_o|_{r=1}\sin\theta d\theta \tag{35}$$

The total drag coefficient, C_D, is the sum of these two components.

We performed computations and calculated the stream function, vorticity and velocity fields as well as the hydrodynamic force and the two components of the drag coefficient C_D with Re and λ as parameters. Some of the results of the computations for the stream function and vorticity fields are shown in Figs. 2(*a*), 2(*b*), and 2(*c*). These figures depict the stream function on the top part and the vorticity on the bottom part. The viscosity ratio is the same in all three figures ($\lambda=7$) and the Reynolds numbers are respectively 10, 100, and 500. It is apparent from the stream function results in all the figures that the internal velocity field is that of a well-defined and rather simple recirculating flow. At low Re (Fig. 2(*a*)) the external flow field is also relatively simple. However, at intermediate (Fig. 2(*b*)) and high (Fig. 2(*c*)) Re the external flow field becomes more complex and a recirculation region appears behind the sphere. The presence of the thin boundary layer becomes apparent in the case Re=500 (Fig. 2(*c*)) by the crowding of the streamlines at the interface and by the manifest complexity of the external vorticity field. As expected, the length of the recirculation region increases with Re.

2 Comparisons Between the Conventional Approach and Present Approach. In order to validate and to demonstrate the accuracy and efficacy of the numerical method described in the previous sections, we made a comparison of the results by this method with results derived by following the conventional method and results from the asymptotic solution obtained by Happel and Moore [11]. The latter applies only to low values of the viscosity ratio and was derived asymptotically for high Re. The computations are for $\lambda=0.1$ under the condition, $\mathrm{Re}=\mathrm{Re}_i$, which was invariably used in the previous numerical studies. The computational grids used were 40×120 points for the internal flow field and 180×120 for the external flow field and the results are shown in Table 1.

Two observations are immediately made from the data of Table 1: The first is that the results of the present method agree fairly well with the asymptotic method of Happel and Moore [11] in the entire range of Re. The second is that the results for C_D as derived by the conventional method agree with the results derived by the present method at low values of the Re, but deviate at higher values of this dimensionless number. However, the results for the frictional component, C_{DF}, derived with the two methods are almost identical. This supports the stipulation that the conventional method does not place a sufficient number of points inside the interfacial boundary layer, thus resulting in inaccurate computations of the gradient of the vorticity function and, by extend, of the form drag. The reason for this is that the form drag depends on the derivative of Ω_o (Eq. (34)), which may only be evaluated accurately with a sufficient number of grid points inside the boundary layer. This is clearly illustrated in Fig. 3, which depicts the vorticity function Ω close to the surface of the sphere, as calculated by the two different grids. The parameters for the calculations of this figure are Re=500 and $\lambda=0.1$ and the grid size is 120×40 for the internal and 120×180 for the external domain. The top part of the figure depicts the vorticity function (Ω) computed by the conventional method, while the bottom part depicts the vorticity function computed by the method presented here. It is evident that, while the conventional method predicts fairly accurately the value of the function Ω, it fails to predict with the same accuracy the value of its derivative at the surface of the

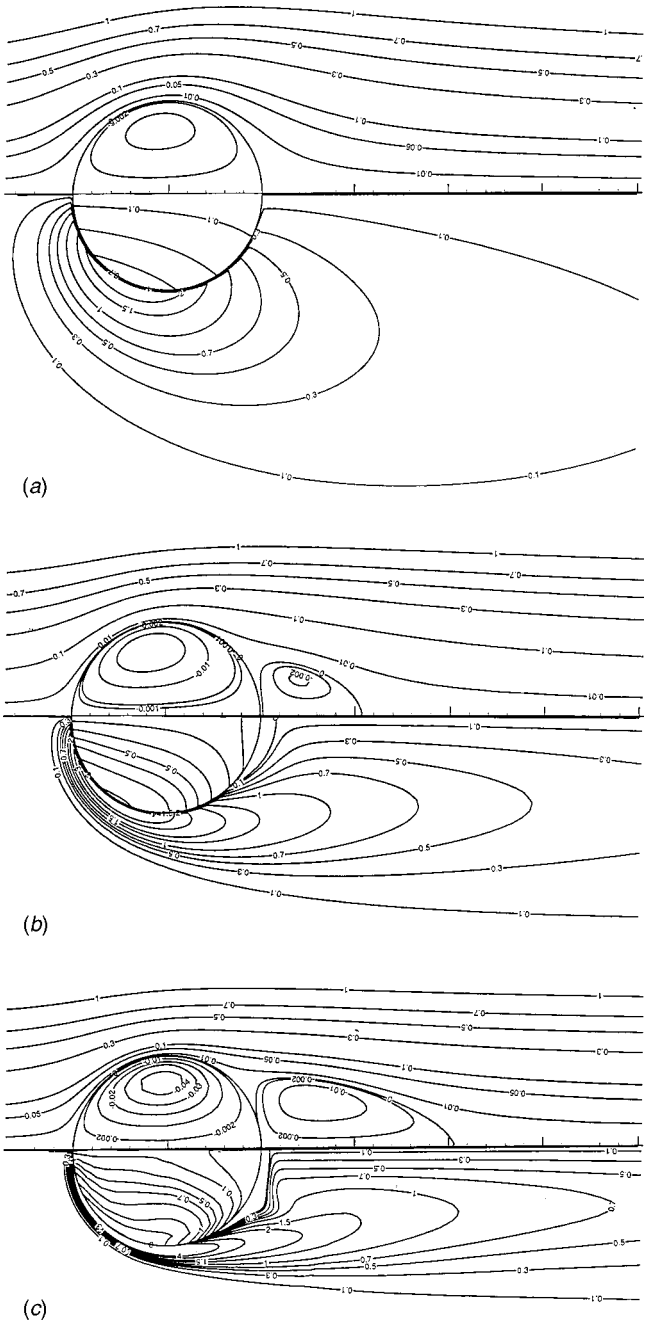

Fig. 2 (*a*) Streamlines and vorticity field for λ=7 and Re=10; (*b*) streamlines and vorticity field for λ=7 and Re=100; (*c*) streamlines and vorticity field for λ=7 and Re=500.

Table 1 Results from two different numerical approaches, and asymptotic solutions at λ=0.1

	Conventional Method			Present Method			Asymptotic Solution
Re\C	C_{DF}	C_{DP}	C_D	C_{DF}	C_{DP}	C_D	C_D
100	0.259	0.180	0.439	0.260	0.161	0.421	0.411
200	0.143	0.117	0.260	0.144	0.089	0.233	0.226
300	0.100	0.096	0.196	0.101	0.062	0.163	0.157
500	0.064	0.079	0.143	0.064	0.040	0.104	0.098
700	0.047	0.070	0.117	0.047	0.029	0.076	0.071
1000	0.034	0.063	0.097	0.034	0.021	0.055	0.051

sphere. Given the trends of Ω and its slope in the two parts of Fig. 3, it is expected that the conventional method would over-predict the values of the form drag and, as a consequence, of the total drag. This is indeed what has been observed with the results of Table 1.

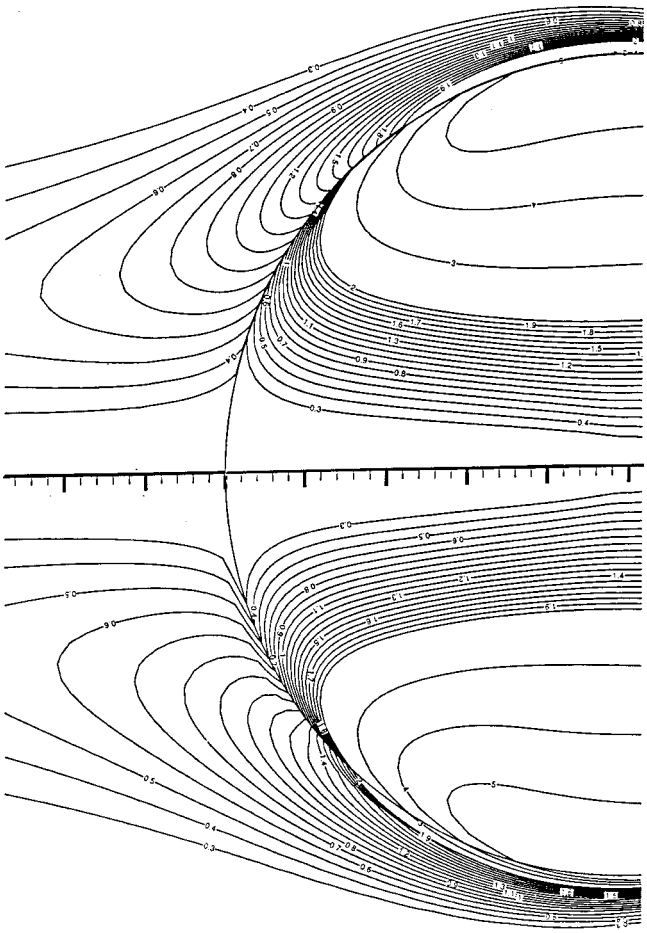

Fig. 3 The vorticity field for Re=500, λ=0.1, with mesh size 120×40 for the internal and 120×180 for the external flow field. The upper half shows the results from the conventional method and the lower half from the method presented here.

3 Validation, Comparisons With Other Data. In order to evaluate the accuracy of our computations, we performed comparisons of our results with those by Rivkind and Ryskin [17] and Rivkind et al. [13] that obtained drag coefficients for viscous spheres up to Reynolds numbers of 100, using the conventional method. These results and the correlation emanating from them have been widely used in engineering practice. The comparison is shown in Table 2. The first number in this table corresponds to the results by Rivkind et al. [13], and the second has been derived by the method presented here. It is obvious that the results (which span the whole range of values for λ and the range of Re≤50) are within 2 percent from those reported in the past. The results deviate at Re=100 with the results of Rivkind et al. [13], which were derived by the conventional method, being higher than the results of our method. The reason for this difference is the manner of calculation of the vorticity gradient at the boundary layer of the

Table 2 Comparison of numerical results for C_D with results by Rivkind et al. [13]

λ \Re	0.5		1		5		10		20		50		100	
0	33.8	33.7	17.5	17.6	4.25	4.28	2.43	2.44	1.41	1.41	0.69	0.69	0.40	0.38
0.333	38.3	38.2	19.9	20.0	4.89	4.96	2.87	2.88	1.71	1.72	0.89	0.88	0.55	0.51
1	42.9	42.6	22.4	22.4	5.65	5.66	3.33	3.34	2.05	2.04	1.12	1.10	0.74	0.68
3	47.4	47.2	24.8	24.8	6.36	6.39	3.80	3.81	2.38	2.37	1.36	1.33	0.94	0.88
∞	52.2	51.8	27.4	27.3	7.05	7.13	4.28	4.30	2.71	2.71	1.58	1.56	1.11	1.10

Table 3 Comparison of drag coefficients of a solid sphere with numerical and experimental data

\Re	10	30	100	200	300	400	500	700	1000	1500	2000
LeClair	4.288	2.110	1.12	0.772	0.632	0.552	--	---	--	--	--
Exper.	4.50	2.20	1.10	0.80	0.65	0.59	0.54	0.48	0.42	0.38	0.36
Present	4.30	2.107	1.103	0.775	0.650	0.579	0.533	0.475	0.427	0.384	0.357

(-- not available)

Table 4 Comparison with the asymptotic solution by Happel and Moore [11]

Re\λ	0		0.5		1	
	Asym. Sol.	Present	Asym. Sol.	Present	Asym. Sol.	Present
100	0.374	0.381	0.506	0.583	0.487	0.674
300	0.140	0.143	0.218	0.230	0.266	0.298
500	0.087	0.090	0.139	0.152	0.179	0.204
700	0.063	0.066	0.103	0.118	0.135	0.159
1000	0.045	0.047	0.074	0.087	0.099	0.124

Table 5 Comparison with the experimental data by Winnikow and Chao [20]

Re	Happel and Moore	Present	Correlation	Experimental
Chlorbenzene droplet in water (λ=0.80, κ=1.107)				
138	0.253	0.459	0.472	0.455
318	0.188	0.259	0.252	0.272
632	0.116	0.152	0.150	0.174
700	0.108	0.141	0.139	0.169
Bromobenzene droplet in water (λ=1.18, κ=1.488)				
245	0.218	0.362	0.355	0.348
299	0.205	0.313	0.308	0.294
539	0.148	0.204	0.202	0.201
596	0.139	0.190	0.188	0.200
Nitrobenzene droplet in water (λ=2.01, κ=1.203)				
246	--	0.441	0.434	0.415
288	--	0.395	0.391	0.350
360	--	0.334	0.337	0.279
M-nitrotoluene droplet in water (λ=2.39, κ=1.157)				
187	--	0.565	0.548	0.642
319	--	0.392	0.391	0.420
506	--	0.289	0.293	0.299

(-- not applicable)

outside interface, as explained above. The agreement of our results with these results up to Re=50 and for all values of λ, is an indication of the validity of our numerical method and the derived results.

We also compared our results for a solid sphere ($\lambda \to \infty$) with one of the first numerical studies performed, the one LeClair and Hamielec [12] and with the experimental data by Elzinga and Banchero [18] where the parameter Re extends to 2000. The comparison of the results is shown in Table 3. A glance at this table proves that there is an excellent agreement of our results with both the numerical study and the experimental data. This is another indication of the validity of the numerical method employed in this study and of the results derived from it.

Another comparison was made of our results with the asymptotic solution by Happel and Moore [11] who used a boundary layer theory. This comparison is made in order to ensure that the trends of our results are in agreement with the asymptotic values. The computations are performed under the condition $\mathrm{Re}=\mathrm{Re}_i$, which is one of the assumptions of the asymptotic solution. The comparison is shown in Table 4.

As with the comparisons above, it is also observed that the results of this study agree very well with the asymptotic solution at the lower values of the viscosity ratio, λ, for all values of Re, but deviate at higher values of λ. Brabston and Keller [19] made the same observation regarding the applicability of the asymptotic solution. It must be recalled that an asymptotic solution yields the trends that should be observed and not the exact values. The fact that the general trends between our study and the asymptotic solution are in agreement, is a further indication of the validity of our results.

A final comparison has been made with the experimental data by Winnikow and Chao [20] that obtained the drag coefficients of several organic-substance droplets in water. This comparison is shown in Table 5. The ''correlation'' column refers to the results of the regression of the numerical results, which is presented in Eqs. (36) and (37) of the next section. The results derived from the asymptotic solution by Happel and Moore are also shown for reference. Although the agreement is not excellent, it is evident that the results of the present study are close to the experimental data and that they fall within the experimental error expected of similar experimental studies.

4 Results for the Drag Coefficients of Viscous Spheres up to Re=1000. Having established the validity of our numerical method and the accuracy of the results obtained by it, we present on Table 6 the results of the friction factor of drops in the range of Reynolds numbers from 0.5 to 1,000 and of the viscosity ratio from 0 (inviscid bubble) to infinity (solid sphere). Table 6 shows the total drag coefficient C_D (third column of each subsection) as well as its two components, the friction (first column) and form (second column) drag coefficients. It is observed that, given a value for the Reynolds number, the drag coefficient is a monotonically increasing function of the viscosity ratio λ. It is also observed that, given a value of the viscosity ratio, the drag coefficient is a monotonically decreasing function of the Reynolds number. Not only the total drag follows these trends, but also its two components, the friction and form drag follow the trends as well. It must also be mentioned that the ratio C_{DF}/C_{DP}, which is equal to 2 in the case of Stokes flow (Re=0), decreases with increasing Re, at constant λ, and for a given value of Re decreases with increasing λ.

5 Correlations for the Drag Coefficients of a Viscous Sphere. Figure 4 is a pictorial representation of the results of Table 6 and shows the total drag coefficient versus the logarithm of the Reynolds number. A glance at this figure proves that, at intermediate and high values of Re, the series of the results in the range $2 \geqslant \lambda \geqslant 0$ exhibit a different behavior from the results for $2 < \lambda < \infty$. For this reason, we separated the range of λ in these two subranges and looked for correlations for the function $C_D(\mathrm{Re},\lambda)$ in terms of the functions $C_D(\mathrm{Re},0)$, $C_D(\mathrm{Re},2)$, and $C_D(\mathrm{Re},\infty)$ by using simple regression techniques. The resulting correlation functions are as follows:

$$C_D(\mathrm{Re},\lambda) = \frac{2-\lambda}{2} C_D(\mathrm{Re},0) + \frac{4\lambda}{6+\lambda} C_D(\mathrm{Re},2) \quad for \quad 0 \leqslant \lambda \leqslant 2, \quad and \quad 5 < \mathrm{Re} \leqslant 1000 \tag{36}$$

and

$$C_D(\mathrm{Re},\lambda) = \frac{4}{\lambda+2} C_D(\mathrm{Re},2) + \frac{\lambda-2}{\lambda+2} C_D(\mathrm{Re},\infty) \quad for \quad 2 \leqslant \lambda \leqslant \infty, \quad and \quad 5 < \mathrm{Re} \leqslant 1000 \tag{37}$$

where the functions $C_D(\mathrm{Re},0)$, $C_D(\mathrm{Re},2)$ and $C_D(\mathrm{Re},\infty)$ are given by the following expressions:

$$C_D(\mathrm{Re},0) = \frac{48}{\mathrm{Re}}\left(1 + \frac{2.21}{\sqrt{\mathrm{Re}}} - \frac{2.14}{\mathrm{Re}}\right) \tag{38a}$$

$$C_D(\mathrm{Re},2) = 17.0\,\mathrm{Re}^{-2/3} \tag{38b}$$

and

Table 6 Drag coefficients of a spherical droplet

Re\λ	0.00			0.25			0.5			0.75		
0.5	22.50	11.28	33.78	24.87	12.46	37.33	26.46	13.25	39.71	27.59	13.79	41.38
1	11.70	5.87	17.57	12.97	6.51	19.48	13.83	6.94	20.74	14.44	7.24	21.68
5	2.809	1.468	4.277	3.165	1.655	4.820	3.408	1.783	5.191	3.585	1.875	5.460
10	1.580	0.861	2.441	1.802	0.988	2.790	1.956	1.074	3.030	2.068	1.138	3.206
20	0.898	0.516	1.404	1.042	0.608	1.650	1.144	0.674	1.818	1.219	0.723	1.942
30	0.645	0.382	1.027	0.758	0.461	1.219	0.839	0.518	1.357	0.899	0.563	1.462
50	0.423	0.262	0.685	0.507	0.323	0.830	0.568	0.371	0.939	0.614	0.412	1.026
70	0.319	0.194	0.512	0.388	0.243	0.631	0.440	0.284	0.724	0.480	0.318	0.798
100	0.236	0.143	0.379	0.291	0.183	0.474	0.333	0.219	0.552	0.366	0.248	0.614
200	0.128	0.078	0.206	0.163	0.103	0.263	0.192	0.125	0.317	0.215	0.145	0.360
300	0.089	0.054	0.143	0.116	0.072	0.188	0.138	0.089	0.227	0.157	0.102	0.259
400	0.068	0.042	0.110	0.090	0.056	0.146	0.109	0.070	0.179	0.124	0.083	0.207
500	0.055	0.034	0.089	0.074	0.047	0.121	0.090	0.058	0.148	0.104	0.069	0.173
700	0.041	0.025	0.066	0.055	0.035	0.090	0.068	0.044	0.112	0.080	0.053	0.133
1000	0.029	0.018	0.047	0.041	0.026	0.067	0.051	0.034	0.085	0.060	0.040	0.100
Re\λ	1			2			3			5		
0.5	28.42	14.22	42.64	30.46	15.23	45.69	31.48	15.74	47.23	32.45	16.22	48.67
1	14.92	7.50	22.42	16.00	8.02	24.02	16.55	8.30	24.85	17.10	8.57	25.67
5	3.717	1.945	5.662	4.036	2.108	6.144	4.198	2.191	6.389	4.362	2.272	6.634
10	2.153	1.186	3.339	2.357	1.298	3.655	2.461	1.354	3.815	2.566	1.408	3.974
20	1.275	0.762	2.037	1.413	0.847	2.260	1.483	0.890	2.373	1.553	0.931	2.484
30	0.945	0.599	1.544	1.056	0.675	1.731	1.113	0.714	1.827	1.168	0.751	1.919
50	0.649	0.448	1.097	0.736	0.514	1.250	0.780	0.552	1.332	0.823	0.589	1.412
70	0.510	0.349	0.859	0.581	0.432	1.013	0.619	0.470	1.089	0.656	0.506	1.162
100	0.392	0.274	0.666	0.457	0.346	0.803	0.489	0.389	0.878	0.520	0.435	0.955
200	0.234	0.163	0.397	0.283	0.221	0.504	0.308	0.262	0.570	0.331	0.315	0.646
300	0.172	0.119	0.291	0.214	0.167	0.381	0.237	0.203	0.440	0.256	0.255	0.511
400	0.138	0.095	0.233	0.176	0.136	0.312	0.197	0.170	0.367	0.215	0.220	0.435
500	0.116	0.080	0.196	0.151	0.116	0.267	0.171	0.148	0.319	0.188	0.196	0.384
700	0.090	0.062	0.152	0.120	0.093	0.213	0.139	0.120	0.259	0.155	0.166	0.321
1000	0.069	0.048	0.117	0.095	0.074	0.169	0.112	0.099	0.211	0.126	0.143	0.269
Re\λ	7			10			20			∞		
0.5	32.98	16.47	49.45	33.40	16.69	50.09	33.96	16.97	50.93	34.54	17.26	51.80
1	17.39	8.71	26.10	17.61	8.82	26.43	17.90	8.97	26.87	18.22	9.13	27.35
5	4.495	2.315	6.760	4.512	2.347	6.859	4.597	2.394	6.991	4.692	2.442	7.134
10	2.619	1.437	4.056	2.660	1.457	4.117	2.717	1.490	4.207	2.779	2.522	4.301
20	1.589	0.952	2.541	1.617	0.967	2.584	1.655	0.991	2.646	1.696	1.013	2.710
30	1.198	0.770	1.968	1.221	0.783	2.004	1.251	0.804	2.055	1.284	0.823	2.107
50	0.845	0.606	1.451	0.862	0.617	1.479	0.885	0.636	1.522	0.910	0.652	1.562
70	0.673	0.525	1.198	0.689	0.535	1.224	0.707	0.554	1.261	0.727	0.567	1.294
100	0.535	0.458	0.993	0.541	0.470	1.011	0.561	0.498	1.059	0.567	0.513	1.090
200	0.340	0.344	0.684	0.347	0.369	0.716	0.355	0.399	0.754	0.358	0.417	0.775
300	0.253	0.307	0.560	0.268	0.317	0.585	0.271	0.355	0.626	0.273	0.377	0.650
400	0.212	0.273	0.485	0.223	0.285	0.508	0.224	0.328	0.552	0.225	0.354	0.579
500	0.194	0.227	0.421	0.194	0.262	0.457	0.194	0.310	0.504	0.194	0.339	0.533
700	0.159	0.196	0.353	0.159	0.234	0.393	0.155	0.288	0.443	0.154	0.321	0.475
1000	0.128	0.172	0.300	0.128	0.211	0.339	0.124	0.269	0.393	0.122	0.305	0.427

$$C_D(\mathrm{Re},\infty)=\frac{24}{\mathrm{Re}}\left(1+\frac{1}{6}\mathrm{Re}^{2/3}\right) \tag{38c}$$

It must be pointed out that the expressions for $C_D(\mathrm{Re},0)$ and $C_D(\mathrm{Re},\infty)$ in (38*a*) and (38*c*) are routinely used correlations for the drag coefficients of bubbles and solid particles. Expression (38*b*) is a simple correlation of our computational results.

In the low range of Re, which is not covered by the above expressions, the following expression is recommended:

$$C_D=\frac{8}{\mathrm{Re}}\frac{3\lambda+2}{\lambda+1}\left(1+0.05\frac{3\lambda+2}{\lambda+1}\mathrm{Re}\right)-0.01\frac{3\lambda+2}{\lambda+1}\mathrm{Re}\ln(\mathrm{Re})$$
$$0\leqslant \mathrm{Re}\leqslant 5 \tag{39}$$

This expression reduces to the Haddamard-Rybszynski solution at Re=0 and to the Oliver and Chung expression for very small Re [14]. The form of the last term of Eq. (39) is derived from the natural next order expansion in terms of Re. Although the intention was to use this expression up to Re=5, we have actually found out that Eq. (39) accurately represents the numerical results up to Re=20.

It must be pointed out that the maximum fractional difference of the correlation functions presented in this section from the computational results is 4.6 percent and the standard deviation of all the fractional differences is 2.1 percent.

The Effect of the Density Ratio

The computations thus far have determined the drag coefficients in terms of two parameters, the viscosity ratio λ and the Reynolds number based on the properties of the external fluid Re. Another parameter that may have an influence on the drag coefficient is the density ratio $\kappa=\rho_i/\rho_o$ or, alternatively, the internal Reynolds number defined as $\mathrm{Re}_i=\mathrm{Re}\,\lambda/\kappa$. For this reason we have made a limited number of computations for the determination of the drag coefficient with κ as a parameter, while Re and λ are kept constant. The results of the computations are shown in Table 7. It is apparent that the effect of the density ratio is minimal since, for given values of λ and Re, a variation of κ by two orders of magnitude results in deviations of C_D, which are less than 2 percent. This observation confirms the implicit assumption made in this study that Re and λ are the main flow parameters the drag coefficient of a viscous sphere depends upon.

As a final note with respect to the effect of the density ratio, we wish to add that when $\lambda\gg 1$ and the parameter κ is large enough to render $\mathrm{Re}_i\gg 10$ (e.g., in the case of a mercury drop in air), one expects that the circulatory motion inside the sphere would break up in two. In this case the interface of the fluid sphere would not be a continuous streamline. A second circulatory motion will take place at the rear part of the viscous sphere leading to a change of the sign of the vorticity function at the separation point. Even in this rather extreme case, we have found by numerical calculations that the effect of the second circulatory motion on the external flow and the drag coefficient is insignificant.

The Effect of Internal Flow on the Drag Coefficients

It was mentioned at the end of the numerical implementation section that a few (40) grid points were used in the radial direction, because the internal flow field does not affect significantly the drag coefficient. We base this assertion on the following observations:

1 The agreement of our results with the experimental data and the asymptotic solutions, which were presented in Tables 1–5.

2 One of the ways to alter the internal flow field is by changing the internal Reynolds number, Re_i. As shown in the previous section, this may be simply accomplished by changing the density of the internal fluid, without changing anything else. However, as it was shown in Table 7, this has almost no effect on the drag coefficient.

3 It is expected that at high Re_i, a thin internal boundary layer will be formed. However, it is not necessary to finely resolve this layer in order to obtain the total hydrodynamic force. This occurs because, for the calculation of the hydrodynamic force it is only necessary to know the value of the vorticity function and its derivative in the outside and not the inside field. Through the boundary conditions these are related to the internal stream function and vorticity, but not to the derivative of the internal vorticity. There-

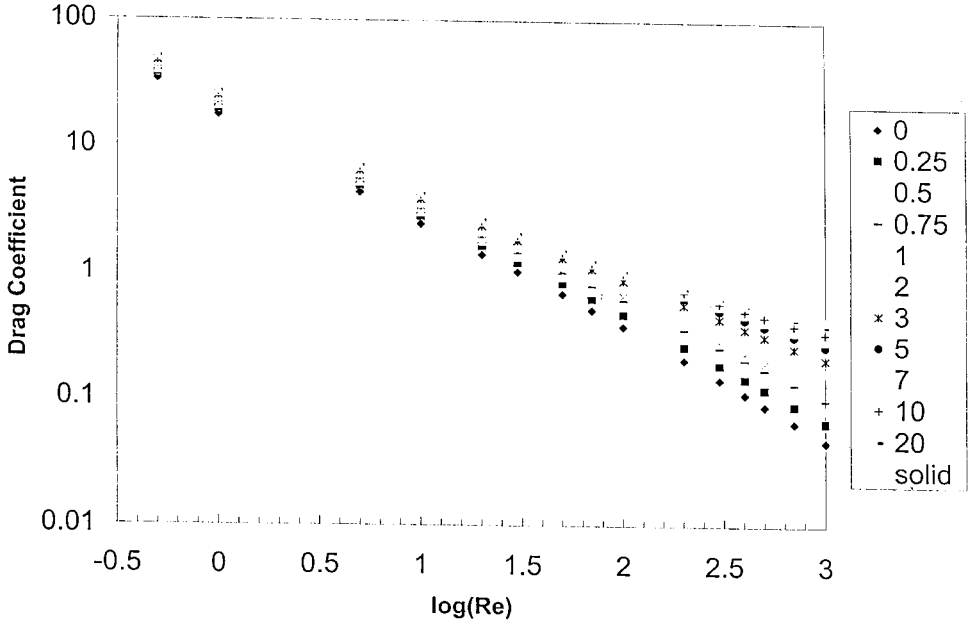

Fig. 4 Drag coefficients for the whole range of λ in terms of log(Re)

Table 7 Drag coefficients at various density ratios

λ	1.0						10.0					
κ	0.1	1.0	10.0	0.25	1.0	2.0	0.1	1.0	10.0	0.1	1.0	10.0
Re	10	10	10	400	400	400	10	10	10	100	100	100
Re_i	1	10	100	100	400	800	1	10	100	10	100	1000
C_D	3.339	3.339	3.336	0.233	0.233	0.236	4.117	4.117	4.117	1.012	1.011	1.000

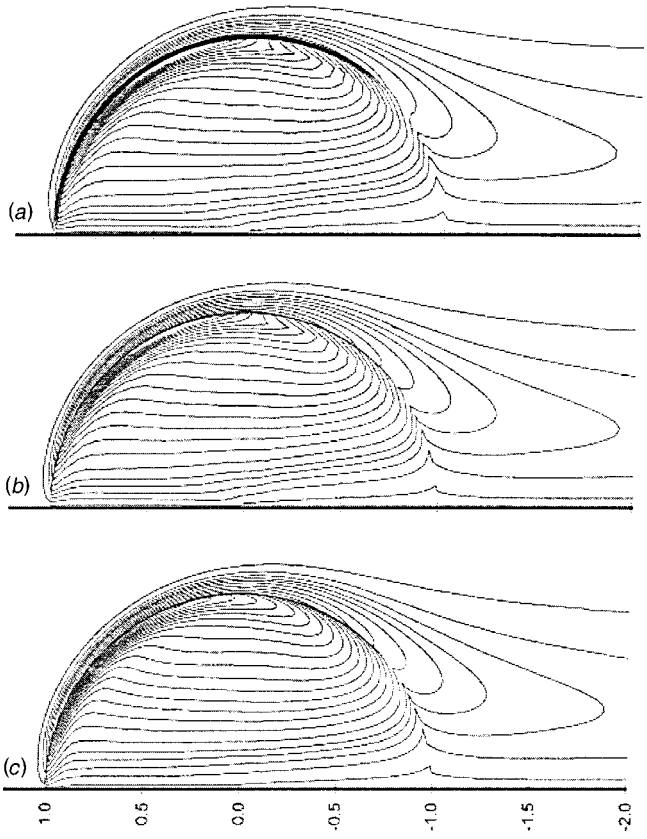

Fig. 5 The effect of the computational grid used on the vorticity field developed at Re=500: (*a*) Conventional method, (*b*) 40 internal grid points, (*c*) 120 internal grid points

fore, if the internal vorticity were calculated with some degree of accuracy, this process would yield an accurate value for the hydrodynamic force and the drag coefficient.

4 In order to prove the above in a practical way we have conducted computations for the internal flow with different mesh sizes in the case Re=500, Re_i=500 and λ=0.1. These computations were performed with as few as twenty internal grid points, with forty points (which is the minimum number of points for the derivation of the of the results of Table 6) and with one-hundred and twenty points, which are sufficient to fully resolve the internal boundary layer. The computed results are shown in Fig. 5, where the vorticity field is depicted under the following conditions: (a) 20 grid points for the internal flow, using the conventional method for the external flow, (b) 20 grid points for the internal flow, using the present method for the external flow, and (c) 120 points for the internal flow, using the present method for the external flow. It is evident that the gradient of the vorticity of the internal flow field is not well computed in Figs. 5(*a*) and 5(*b*). The results for the drag coefficient, in these cases are tabulated in Table 8. A glance at this Table proves that, when the present numerical method is used, the finer resolution of the internal flow field has a very small effect on the value of C_D. This supports the conclusion that the internal boundary layer does not significantly affect the value of the drag coefficient. On the contrary, as it can be seen from a comparison of the results of the conventional method and the present method, the accurate resolution of the external boundary layer is crucial to the accuracy of the results obtained.

Table 8 Internal grid sensitivity analysis for Re=500, Re_i=500, λ=0.1

	C_{DF}	C_{DP}	C_D
Conventional Method 20 grid pts for internal flow	0.0640	0.0739	0.1379
Conventional Method 40 grid pts for internal flow	0.0633	0.0732	0.1365
Present Method 20 grid pts for internal flow	0.0643	0.0396	0.1029
Present Method 40 grid pts for internal flow	0.0637	0.0391	0.1026
Present Method 120 grid pts for internal flow	0.0634	0.0389	0.1023
Asymptotic Solution	N/A	N/A	0.098

A Note on the Deformation of the Droplets at High Re

A central part of the applicability of the results in this manuscript is that at high values of Re the droplet remains spherical or near spherical. Experimental evidence by Winnikow and Chao [20] on the free fall or rise of drops in liquids shows that a liquid drop will remain spherical when the dimensionless Bond number, Bo, which is equal to the ratio We/Fr, is less than or equal to 0.2, that is when:

$$\mathrm{Bo}=\frac{\mathrm{We}}{\mathrm{Fr}}=\frac{g d_{eq}^2|\rho_s-\rho_f|}{\sigma}\leqslant 0.2 \tag{40}$$

The experiments of Winnikow and Chao [20] also show that drops of m-nitrotoluene in water ($\lambda=2.2$) with $d=3.1$ mm remain spherical at Re=506. According to the criterion of Eq. (40), Bo <0.2, calculations show that water droplets in air will maintain their spherical shape at values of Re up to 470. In the case of substances with high surface tension (liquid metals), the corresponding Re would be much larger (up to 1150 for mercury droplets in air).

It is expected that all drops will be slightly deformed when they translate in a viscous fluid. Harper [21] calculated the variation of the droplet drag coefficient as a function of the eccentricity, ε. His results show that, at low values of ε, the drag coefficient augmentation is proportional to the eccentricity. For example, at Re 500 and 1000, an eccentricity of 10 percent results in a 12.3 percent increase of the drag coefficient. From the results of Harper [21] and the analysis of Leal [8] we may conclude that the effect of the drop eccentricity on the drag coefficient is less than 5 percent up to the value $\varepsilon=0.04$ (or 4 percent deformation). If we take this value of ε as the limiting case of the validity of the results for a viscous sphere, then the experiments of Winnikow and Chao [20] reveal that Bo must be less than 0.4 for several organic drops in water and Bo<0.5 for organic and water drops in air. In this case (Bo<0.5) water droplets in air would exhibit drag coefficients close to the one predicted by this study at values of Re up to 970. Hence, one may conclude that at the values of Re used in this study the drops of several substances would retain an almost spherical shape and that the drag coefficients computed would apply to their motion.

Conclusions

Because of the existence of two comparable time scales, it is impossible to derive an analytical solution for the steady-state hydrodynamic force exerted on a viscous sphere at intermediate and high values of the Reynolds number. Only a numerical solution may be obtained, which must also yield the flow fields inside and outside the sphere. A robust numerical technique has been developed that provides information on the two flow fields and accurate results for the drag coefficients of a viscous sphere over the entire range of the viscosity ratio and for Re up to 1000. It was found that both the width of the computational domain and the density of the mesh near the fluid-to-fluid interface are important in determining the accuracy of the computations. Using this numerical technique, the drag coefficients may be calculated in terms of the viscosity ratio and the external Reynolds number. The coefficients obtained by this method are in agreement with the limited amount of experimental data, which are available in the literature, and show the same trends as known asymptotic solutions. The resulting correlations have a standard deviation of the fractional error equal to 2.1 percent. An examination of the effect of the density ratio proves that this parameter is of no importance in the calculation of drag coefficients when the Reynolds number and the viscosity ratio are defined. Also we have found that any internal boundary layer that may be developed does not significantly affect the value of the drag coefficient.

Acknowledgments

This work was partially supported by grants from the NASA and the Louisiana Education Quality Science Fund to Tulane University as well as by a grant from the Office of Naval Research to the Tulane-Xavier Center for Bioenvironmental Research (CBR), for which the authors are thankful.

References

[1] Lovalenti, P. M., and Brady, J. F., 1995, ''Force on a Body in Response to an Abrupt Change in Velocity at Small but Finite Reynolds Number,'' J. Fluid Mech., **293**, pp. 35–46.
[2] Mei, R., Lawrence, C. J., and Adrian, R. J., 1991, ''Unsteady Drag on a Sphere at Finite Reynolds Number with Small Fluctuations in the Free-Stream Velocity,'' J. Fluid Mech., **233**, pp. 613–631.
[3] Mei, R., and Adrian, R. J., 1992, ''Flow past a Sphere with an Oscillation in the Free-Stream and unsteady Drag at Finite Reynolds Number,'' J. Fluid Mech., **237**, pp. 323–341.
[4] Feng, Z.-G., 1996, ''Heat Transfer from Small Particles at Low Reynolds Numbers,'' Sc. D. Dissertation, Tulane Univ.
[5] Feng, Z. G., and Michaelides, E. E., 1998, ''Transient Heat Transfer from a Particle with Arbitrary Shape and Motion,'' ASME J. Heat Transfer, **120**, pp. 674–681.
[6] Michaelides, E. E., and Feng, Z.-G., 1995, ''The Equation of Motion of a Small Viscous Sphere in an Unsteady Flow with Interface Slip,'' Int. J. Multiphase Flow, **21**, pp. 315–321.
[7] Sirignano, W. A., 1999, *Fluid Dynamics and Transport of Droplets and Sprays*, Cambridge Univ. Press, Cambridge.
[8] Leal, L. G., 1992, *Laminar Flow and Convective Transport Processes*, Butterworth-Heineman, Boston.
[9] Kim, S., and Karrila, S. J., 1991, *Microhydrodynamics: Principles and Selected Applications*, Butterworth-Heineman, Boston.
[10] Clift, R., Grace, J. R., and Weber, M. E., 1978, *Bubbles, Drops and Particles*, Academic Press, New York.
[11] Happel, J., and Moore, D. W., 1968, ''The motion of a spherical liquid drop at high Reynolds number,'' J. Fluid Mech., **32**, part 2, pp. 367–391.
[12] Le Clair, B. P., and Hamielec, A. E., 1972, ''A theoretical and experimental study of the internal circulation in water drops falling at terminal velocity in air,'' J. Atmos. Sci., **29**, No. 2, pp. 728–740.
[13] Rivkind, V. Y., Ryskin, G. M., and Fishbein, G. A., 1976, ''Flow around a spherical drop in a fluid medium at intermediate Reynolds numbers,'' Appl. Math. Mech., **40**, pp. 687–691.
[14] Oliver, D. L., and Chung, J. N., 1987, ''Flow about a fluid sphere at low to moderate Reynolds numbers,'' J. Fluid Mech., **177**, pp. 1–18.
[15] El-Shaarawi, M. A. I., Al-Farayedhi, A., and Antar, M. A., 1997, ''Boundary layer flow about and inside a liquid sphere,'' ASME J. Fluids Eng., **119**, pp. 42–49.
[16] Briley, W. R., 1971, ''A numerical study of laminar separation bubbles using the Navier-Stokes equations,'' J. Fluid Mech., **47**, pp. 713–736.
[17] Rivkind, V. Y., and Ryskin, G. M., 1976, ''Flow structure in motion of a spherical drop at intermediate Reynolds numbers,'' Translated from Russian, Fluid Mechanics, **11**, No. 1, pp. 5–12.
[18] Elzinga, E. R., Jr., and Banchero, J. T., 1961, ''Some Observations on the Mechanics of Drops in Liquid-Liquid Systems,'' AIChE J., **7**, No. 3, pp. 394–399.
[19] Brabston, D. C., and Keller, H. B., 1975, ''Viscous flows past spherical gas bubbles,'' J. Fluid Mech., **69**, No. 1, pp. 179–189.
[20] Winnikow, S., and Chao, B. T., 1966, ''Droplet Motion in Purified Systems,'' Phys. Fluids, **9**, pp. 50–61.
[21] Harper, J. F., 1972, ''The Motion of Bubbles and Drops through Liquids,'' Adv. Appl. Mech., **12**, pp. 59–129.

Transcritical Patterns of Cavitating Flow and Trends of Acoustic Level

Wei Gu
Institute of High Performance Computing,
National University of Singapore,
Kent Ridge Crescent,
Singapore 119260

Yousheng He
Department of Engineering Mechanics,
Shanghai Jiao Tong University

Tianqun Hu
Shanghai Ship and Shipping Research Institute

Hydroacoustics of the transcritical cavitating flows on a NACA16012 hydrofoil at a 2/5/8-degree angle of attack and axisymmetric bodies with hemispherical and 45-degree conical headforms were studied, and the process of cloud cavitation shedding was observed by means of high-speed cinegraphy. By expressing the cavitation noise with partial acoustic level, it is found that the development of cavitation noise varies correspondingly with cavitation patterns. The instability of cavitation is a result of cavity-flow interaction, and is mainly affected by the liquid flow rather than by the cavitation bubbles. A periodic flow structure with a large cavitation vortex is observed and found to be responsible for inducing the reentrant-jet and consequent cavitation shedding, and explains the mechanism of periodic cavitation shedding from a new viewpoint. New terms for the three stages, growing, hatching and breaking, are used to describe the process of cavity shedding. [DOI: 10.1115/1.1412233]

Keywords: Cloud Cavitation Shedding, Transcritical, Partial Acoustic Level, Flow Pattern

1 Introduction

Vibratory cavitation always results in vibration and noise, and aggravates the cavitation erosion on materials. Since vibratory cavitations are consistently accompanied by flow unsteadiness, it is difficult to explore the mechanism of the instability of the cavity. When the flow is highly cavitated, the cavitation begins to interact with the main flow so much that the cavity dynamics are complicated by the unsteady flow patterns.

Many types of cavitation patterns, like bubble cavitation, patch cavitation, attached cavitation, partial cavitation, vortex cavitation, band cavitation, cloud cavitation and so forth, have been named based on their appearances or dynamics, and widely studied by many investigators [1–3]. For typical steady cavitating flows such as attached cavitation and supercavitation, the development of the cavitation is often scaled with cavitation number or cavity length, and conceptually classified into three levels: subcavitation, transcavitation and supercavitation. Transcavitating demonstrates the strongest instability. Compared to attached cavitation and supercavitation, transcritical cavitation never has a steady cavity length, and usually generates cloud cavitation in a large scale, resulting in a highly cavitated wake flow downstream. For general flow configurations, it is hard to judge the occurrence of vibratory cavitation only by cavitation number, and no criterion has been established to describe cavitating flows in respective levels of development.

Actually, even an attached cavity is in its state of greatest unsteadiness and turbulence within the closure region [4]. Many methods were employed to explore the structures of cavitating flow. The volume oscillation of axisymmetric cavitation flow was detected by means of vapor impedance measurements [5]. Two-dimensional cavity shedding in large scale was normally investigated with a high-speed camera or video [6,7]. Le, Franc, and Michel [8] measured the fluctuating pressure excited by cloud cavitation, and found that the cavity thickness seemed to affect the reentrant-jet. Kubota and Kato et al. [9] studied the large-scale structure in the cloud cavitation by LDA. Stutz and Reboud [10] also measured the velocity distribution during cavitation shedding. The periodicity of hydrofoil cavitation flow at a small angle of attack was studied by the author [11], and it was found that the Strouhal number plotted against cavitation Reynolds number ($\mathrm{Re}_C=\mathrm{Re}\sqrt{1+\sigma}$) approaches 0.18 when the flow velocity was increased.

Understanding the mechanism of cavitation shedding is of great significance in suppressing the vibration and erosion caused by vibratory cavitation. The cyclic regime of a large vapor structure at the rear of a cavity was described by Knapp [12]. Lush and Peter [13] adopted the instability of the cavity surface as the main cause of cloud cavitation, while Furness and Hutton [14] ascribed the cavitation shedding to the reentrant-jet. Ramamurthy and Balachandar [15] reported the effect of cavitation shedding on the vortex shedding of two-dimensional blunt bodies. Kawanami et al. [16] measured the pressure and made video records of cloud cavitation shedding. Reisman, Wang et al. [17] observed the shock waves in cloud cavitation. Among a good many theories like surface wave, impinging jet and re-entrant jet, the hypothesis of re-entrant jet is regarded as the most possible, but it cannot reasonably explain the periodicity of cavity shedding.

Noise measurement is an effective tool to detect the occurrence of cavitation. Although all kinds of cavitation act as a single or a collection of monopole noise sources, and are always accompanied by remarkable volume fluctuation, a bubble cluster behaves differently from a single vapor bubble in acoustics, mostly in a nonlinear mechanism. In this paper, cavitation noise is measured for three models: a NACA16012 hydrofoil, an axisymmetric body with a hemispherical headform, and a 45-degree conical headform. The trend of noise development is scaled by partial acoustic level and is found to be closely related to the cavitation patterns. This phenomenon will allow a more quantitative definition of cavitation development.

By means of high-speed cinegraphy, the whole process of the forming and shedding of cloud cavitation on the hydrofoil is recorded at different angles of attack. Based on the observations of the 5- and 8-degree angles of attack, it is found that cloud cavitation shedding can be generally divided into three phases: growing, hatching, and breaking. Much attention has been given to the motion of the cloud cavitation, especially at the moments when the cloud cavitation is being shed and is beginning to detach. In con-

Contributed by the Fluids Engineering Division for publication in the JOURNAL OF FLUIDS ENGINEERING. Manuscript received by the Fluids Engineering Division August 12, 1999; revised manuscript received June 6, 2001. Associate Editor: J. Katz.

clusion, an explanation of the mechanism of cloud cavitation shedding is offered from a new viewpoint that the transcritical cavitation is deeply affected by the whole flow structure, and that large vortex cavitation, rather than the reentrant-jet, is more responsible for the cavity shedding.

2 Experimental Setup and Method

2.1 Facilities and Models. Experiments were carried out in the K15 cavitation tunnel of Shanghai Shipping & Ship Research Institute (SSSRI). The 2500 mm long test section is of rectangular form, 600 mm wide and 600 mm high. Turbulence level in the midsection is under 1%. The lower limit of cavitation number could reach as low as 0.2. In order to provide a clear visual quality for cinegraphy, the air content in the tunnel is controlled within $\alpha/\alpha_s = 0.28 \sim 0.33$, measured by a Van Slyke type apparatus.

A hemispherical headform and a 45-degree conical headform are used for studying the axisymmetric cavitation flows. Both headforms are 80 mm in diameter, and have an aspect ratio of about 3.5 from the nose position to the leading edge of the strut, Fig. 1(*a*). Additionally, a NACA16012 hydrofoil with a chord length of 200 mm and an aspect ratio of 3.0 is used to investigate the two-dimensional cavitation flow at three angles of attack (2-, 5-, and 8-degrees), Fig. 1(*b*). No oscillations with fixed frequencies are detected under non-cavitating conditions of this test.

Different patterns of cavitation are obtained by adjusting the pressure independently while the velocity is kept constant.

2.2 Measurement Methods and Setup. A B&K 8100 hydrophone with -205.1 dB sensitivity was employed to measure the noise level of cavitation development. A water-filled plexiglass box, in which the hydrophone is mounted, is attached on one side of observation windows. The hydrophone is placed near where the cloud cavitation is most likely to occur, Fig. 1.

The acoustic signals are separated into high and low frequency components with a band pass. The low frequency components (under 50 Hz) are recorded at a 500 Hz sampling rate, totalling 32 samples, with 1024 points of record length per sample. The high frequency components (6 kHz—100 kHz) are recorded at a 200 kHz sampling rate, with 4096 points of record length and 32 samples. The uncertainty of the frequency measurements is ± 0.25 Hz for the low frequency spectra, and ± 195 Hz for the high frequency spectra.

2.3 Partial Acoustic Level. The sound pressure level is defined by Leighton [18]:

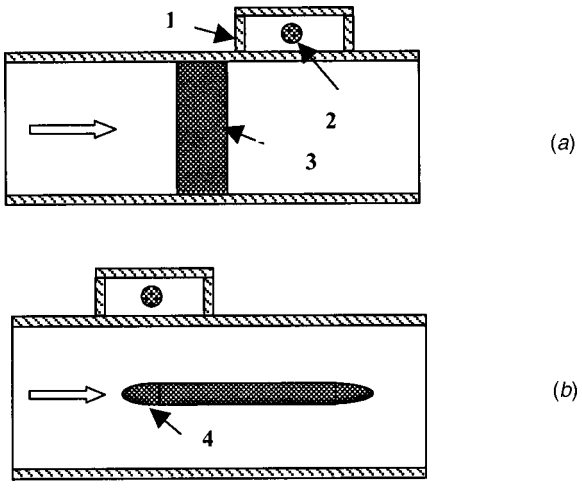

Fig. 1 Models mounted in the water tunnel. (1—Plexiglass box; 2—hydrophone; 3—hydrofoil; 4—headform). (*a*) Hydrofoil; (*b*) axisymmetric bodies.

$$\mathrm{SPL} = 20 \,\mathrm{Log}\frac{p}{p_o} \tag{3}$$

Furthermore, partial acoustic level (PAL) is introduced to scale the variation of acoustic energy within a certain frequency range. PAL is defined as

$$\mathrm{PAL} = 20 \,\mathrm{Log}_{10} \int_{a2}^{a1} s(f)\,df \tag{4}$$

Considering the frequency range detected by the hydrophone, and the frequency range of interest, $a1 = 6$ kHz and $a2 = 100$ kHz are set as the initial and cut-off frequency, respectively. Decreasing $a1$ or increasing $a2$ is found to have no significant effect on the results of PAL. The statistical results of PAL are averages of the 32 samples. The uncertainty of PAL is ± 0.3 dB.

It is assumed that the noise detected in the tunnel is a superposition of the noises generated by the cavitation alone and the non-cavitating flow. For the convenience of comparison, the value of PAL has been reduced by PAL_0, which is measured under non-cavitating flow conditions. Since the main focus of this study is the acoustic trend of transitional cavitation, environmental interference on the hydroacoustics measurement, such as reverberant effects and velocity effects, is not considered.

2.4 High-Speed Cinegraphy. A high-speed cine camera filmed the process of cloud cavitation shedding with 16 mm film at 2000 frames per second. For the hydrofoil cavitation, the flow is recorded in the two-dimensional viewpoint with a vertical illumination from top observation windows. At least 8 cycles of cavity oscillation could be analyzed for two-dimensional hydrofoil cavitation, and a minimum one-second length for axisymmetric cavitation. The sequence of frames provides clear flow details of the forming and shedding of the cloud cavitation. The flow structure is discernible by observing the continuous frames.

3 Transient Feature of Axisymmetric Cavitation Flow

It is already known that cavitation occurs in the region of laminar separation or natural boundary layer transition, thus the boundary layer effect will surely affect the inception and further development [19]. The flow in the vicinity of the shoulder is mainly influenced by the local separated vortex and by the fluctuating pressure above, which play a leading role in producing the cavitation unsteadiness. The characteristics of the boundary layer on the hemispherical headform and the conical headform differ so greatly that the flow transition on hemispherical headform takes place at about $\mathrm{Re}\, 5.0 \times 10^5$, while strong flow separation exists around the shoulder of the conical headform.

(1) Cavitation Appearance on the Hemispherical Headform. Bubble cavitation is the pattern of cavitation inception on the hemispherical headform ($\sigma_i = 0.66$). Under the conditions of the test, the flow develops into a supercritical state when $U = 8$ m/s. Developing patterns, like band cavitation due to laminar separation, are always accompanied by random cavitation shedding in small scales. When the flow is further developed ($\sigma = 0.35, 0.27$), irregular vortical disturbances could be found along the flow interface, and cavitation shedding occurred frequently downstream around the cavity closure, Fig. 2. When supercavitation forms at $\sigma = 0.21$, the main interface becomes smooth and stable.

Due to the unsteadiness and two-phase status in the region between laminar separation and cavity separation [2], the cavity interface on the hemispherical headform has more disturbances than that on the conical headform with a fixed separation position. However, these disturbances neither result in cavity shedding in large scales, nor in fixed frequencies.

(2) Cavitation Appearance on the 45-Degree Conical Headform. The flow separates to form a bubble-ring cavitation as the cavitation number is decreased from the incipient point (σ_i

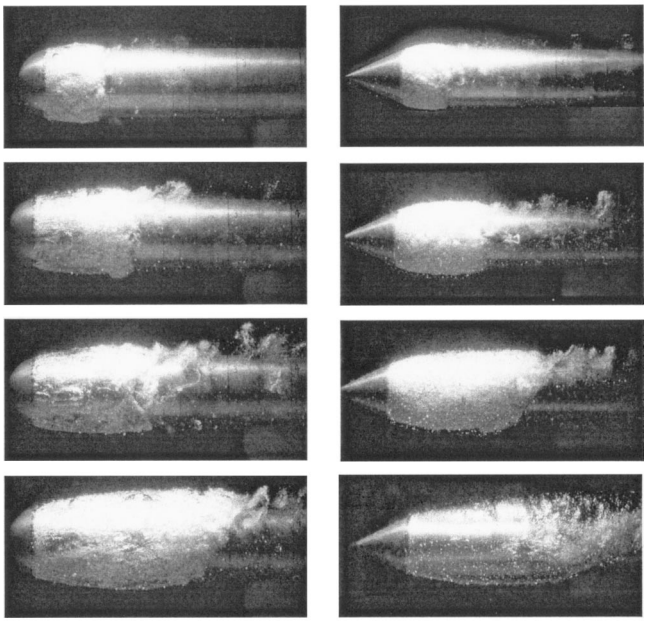

Fig. 2 Cavitation patterns on axisymmetric headforms. Left column: hemispherical headform. From top to bottom (σ =0.35,0.27,0.24,0.21), U=8m/s; Right column: 45-degree conical headform; From top to bottom (σ=0.37,0.33,0.24,0.21), U=8m/s.

=1.48, U=8 m/s). However, the underdeveloped cavitation separated 2-3 mm downstream of the shoulder with a misty interface (σ=0.37), Fig. 2. When the cavitation number is further decreased to σ=0.24 and 0.21, the cavity interface becomes transparent and the position of cavity separation moves upstream to the shoulder point. A limited laminar region is clearly discernible on the cavity interface immediately downstream of the model's shoulder point, and is followed by Tollmien-Schlichting wavy disturbances.

The characteristics of the cavity interface suggest an interaction between the cavitated phase and the liquid. From the state of inception to supercavitation, the cavity interface on the conical headform experiences turbulent separation and reattachment, then laminar separation and turbulent transition. Although disturbances always happen along the interface, especially frequent cavity shedding around the closure region, the global flow pattern remains stable without any periodic oscillations.

(3) Trend of Partial Acoustic Level. Generally, the curves of the PAL of the two headforms ascend steadily with cavitation number. The PAL levels are increased at the higher velocities, Figs. 3 and 4.

In the range of this test, the slope of the PAL (SPAL) for the hemispherical headform changes slightly at around σ=0.27 ~0.30. When σ is above 0.27, SPAL is around 59 dB/σ at U =7.5 m/s and U=8 m/s. Once σ is decreased below 0.27, SPAL becomes steeper at 160 dB/σ, Fig. 3.

The SPAL for the conical headform changes more abruptly when σ drops below 0.3, Fig. 4. When the cavitation number is below 0.30, SPAL varies from 18 dB/σ($0.32<\sigma<0.54$) to 138 dB/σ($\sigma<0.32$) when U=8 m/s, 16.7 db/σ($0.30<\sigma<0.42$) to 150 db/σ($\sigma<0.30$) when U=7 m/s, and 20 db/σ($0.30<\sigma$ <0.40) to 175 db/σ($\sigma<0.30$) when U=6.5 m/s. By comparison, it is found that, when σ is above 0.3 the SPAL of the conical headform is much lower than that of the hemispherical headform at a corresponding range of cavitation numbers. The critical region for the development of cavitation noise from both headforms occurs at a cavitation number of about 0.30–0.32.

The cavities on both headforms turn into transparent vapor layers when σ decreases to 0.27 for the hemispherical headform and to 0.30 for the conical headform. One can easily find that the critical point of SPAL is in agreement with the pattern shift. Additionally, according to the trends of PAL, it is inferred that the bubble type cavitation on the hemispherical headform generates more acoustic contributions than that of a vapor-mixed state on the conical headform. The acoustic trends of the two different flows seem consistent below the critical point after which both flows reach vapor-layer status. This phenomenon implies that the cavitating flow in a vapor layer pattern is a more powerful acoustic source than that of a bubble state, and the bubble type is stronger acoustically than the vapor-mixed type. No eigenfrequencies are detected in the noise spectra of low frequency throughout the test on both headforms.

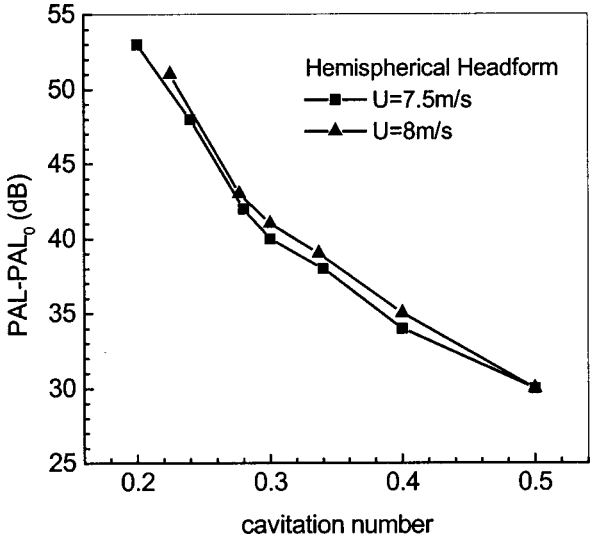

Fig. 3 Trend of partial acoustic level for the cavitation flow on the hemispherical headform

(4) High-Speed Cinegraphy of the Flows on the Headforms. Compared with ordinary photography, dynamic details can be given by high-speed cinegraphy. For the hemispherical headform ($0.21<\sigma<0.35$), irregular cavitation bubbles whose largest visible scale is about 1/5--1/10 of model diameter, are

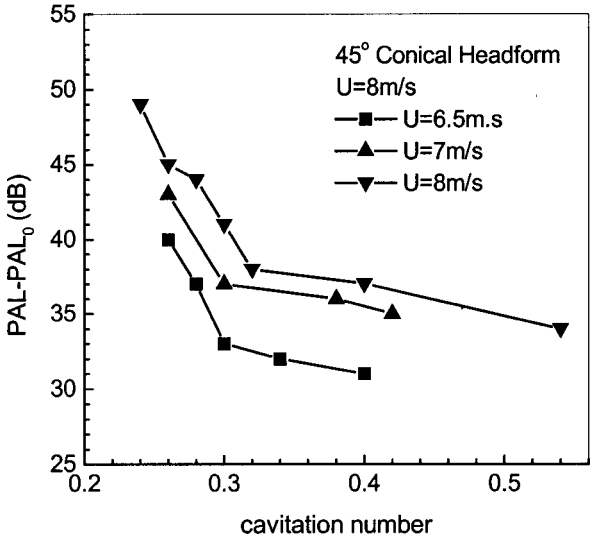

Fig. 4 Trend of partial acoustic level for the cavitation flow on the 45-degree conical headform

always found on the interface. However, for the conical headform ($\sigma<0.30$), cavitation bubbles seem uniform in mini-scale, and the global flow pattern is steady. The random shedding of cavity closure is much less violent than that on hemispherical headform ($\sigma<0.30$). No cavity shedding in large scales or shedding with any fixed frequencies is detected within the record length for either headform.

4 Transient Feature of Hydrofoil Cavitation Flow

Unlike the flows over the axisymmetric bodies, the hydrofoil cavitating flows behave with periodic oscillation as their evident transcritical feature. At a certain angle of attack, transcritical patterns remain unchanged with different flow speeds.

(1) 2-Degree Angle of Attack. Traveling cavitation bubbles are incipient at $\sigma=0.48$ ($U=8$ m/s), and they occupy most of the upper surface on the foil when σ decreases to 0.36. When σ approaches 0.33, the cavity oscillates with a fixed frequency (7.5 Hz), which can be recognized from the noise spectrum in low frequency, shown in Fig. 5. Cavity oscillation disappears if this critical cavitation number is altered. Similar phenomena happen under other velocities from $U=4$ m/s to 8 m/s at the same cavitation number, except for the variations of oscillation frequency. Supercavitation forms when σ is further decreased to 0.28.

The curves of PAL versus cavitation number for different velocities are given in Fig. 6. PAL approaches its maximum when σ holds around 0.33, almost 50 dB higher than that under a noncavitating condition, and 20 dB higher than at the point where supercavitation tends to form. The cavitation number $\sigma=0.28$ and 0.33 become the two critical points where the curves of PAL changed slope. The SPAL remains at 43 dB/σ before the PAL approaches the maximum value for $U=8$ m/s. After supercavitation is formed, the PAL rises with the decreasing cavitation number. Further measurements are not conducted for σ below 0.24 (Fig. 6).

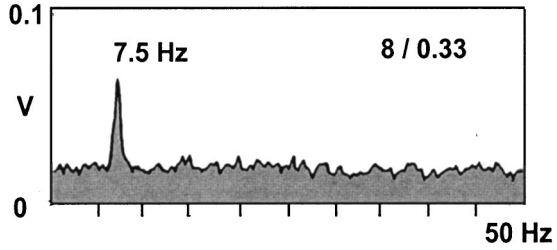

Fig. 5 Noise spectrum in low frequency on the 2-degree a.o.a. NACA16012 hydrofoil ($U=8$m/s and $\sigma=0.33$)

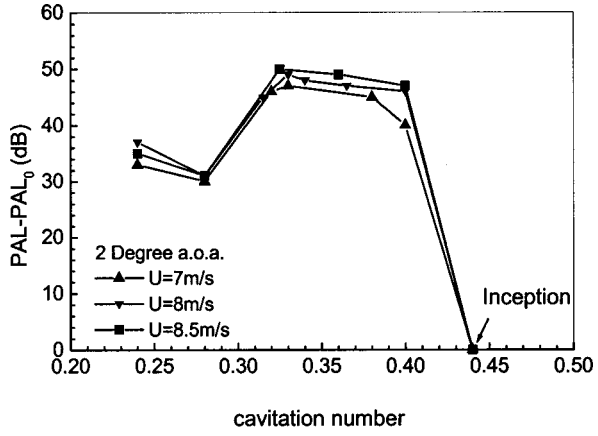

Fig. 6 Trend of partial acoustic level for the cavitation flow on the 2-degree a.o.a. NACA16012 Hydrofoil

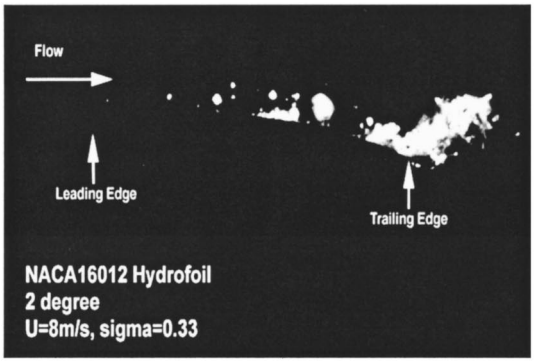

(*a*)

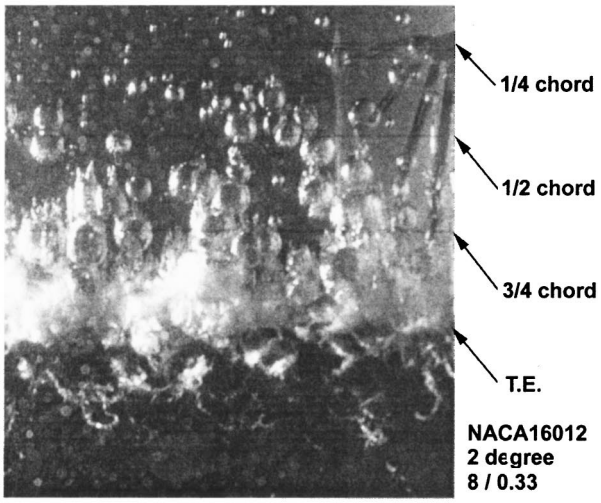

(*b*)

Fig. 7 Pattern of cloud cavitation shedding on the NACA16012 hydrofoil at 2-degree a.o.a. (*a*) Side view (cinegraphic result); (*b*) vertical view

A typical cavity pattern is presented for 2-degree a.o.a. in Fig. 7. The cavity shedding happens in a fixed area, at approximately 80% chord length from the leading edge, and then turns into cloud cavitation once it leaves the foil surface.

(2) 5-Degree Angle of Attack. Sheet cavitation that occurs at a subcritical status at a 5-degree a.o.a. is glossy and has a steady interface. Figure 8 depicts the noise spectra in low frequency when $\sigma=0.60$ and 0.85 at $U=8$ m/s. The eigenfrequency of cavity oscillation can be recognized at 7 Hz and 4.5 Hz, respectively. Amplitudes whose corresponding frequency multiplies the primary frequency are remarkable since stronger vibration is excited at 5-degree a.o.a.

Similar to that at a 2-degree a.o.a., the PAL rises within a critical range of cavitation number, by a maximum of 38 dB higher than at the incipient point when $U=8$ m/s, Fig. 9. The PAL increases at the rate of about 14 dB/σ before approaching the peak value. The PAL for the 5-deg a.o.a. increases gradually before it approaches maximum, while the PAL for the 2-deg a.o.a. intensifies more abruptly after the bubble cavitation is incipient.

It is noticed that the noise level of 2-deg is much higher than that of 5-deg at the same flow speed. The main difference between these two flows is the different cavitation patterns. For the flow at 2-deg a.o.a., traveling bubble cavitation dominates most of the foil surface before it turns into supercavitation. Cavitation noise is mostly emitted by the bubble collapse upon the surface near the trailing edge of the foil. However, for a 5-deg a.o.a., only sheet cavitation exists above the foil surface, and it collapses down-

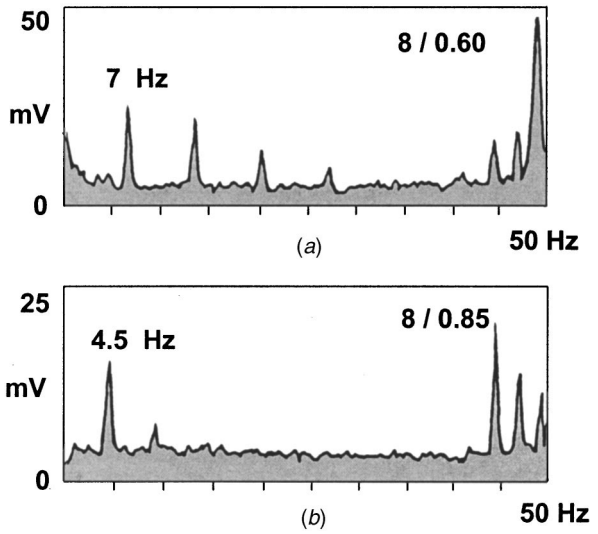

Fig. 8 Noise spectrum in low frequency on the 5-degree a.o.a. NACA16012 hydrofoil (U=8m/s). (*a*) σ=0.60; (*b*) σ=0.85.

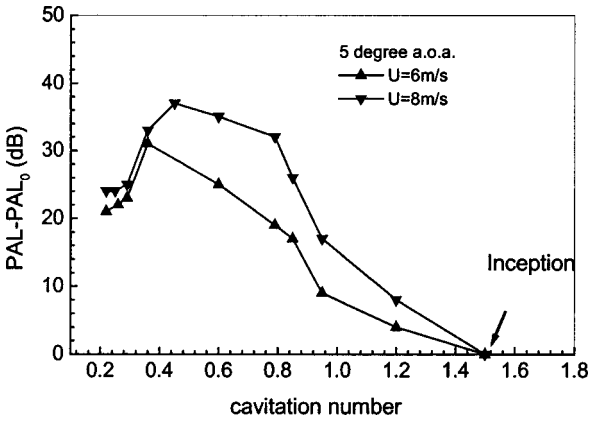

Fig. 9 Trend of partial acoustic level for the cavitation flow on the 5-degree a.o.a. NACA16012 Hydrofoil

stream off the trailing edge rather than upon the foil. Therefore, transcritical cavitation with different patterns yields different levels of cavitation noise.

5 Mechanism of Cloud Cavitation Formation and Shedding

(1) Periodicity of Cavity Oscillation. Figures 10–14 show the periodicity of cavity oscillation, and present the frequency and Strouhal number versus cavitation numbers at varying flow speeds.

At a 5-degree a.o.a., when U=6 m/s to 8 m/s, cavity oscillation exists within $0.35<\sigma<0.85$, and it is evident that the trends of frequency variation are consistent, Fig. 10. But the case of U=4 m/s differs in that the region of instability extends to a higher cavitation number, and its trend is remarkably different from that of U=6 m/s and 8 m/s. Since a cavitation number lower than 0.60 for U=4 m/s is hard to reach within the capability limit of experimental facility, no further information is provided here. In Fig. 12, the Strouhal number is confined within the range of 0.15~0.20, and the curves of Strouhal number versus cavitation number show similar behaviors at other flow speeds.

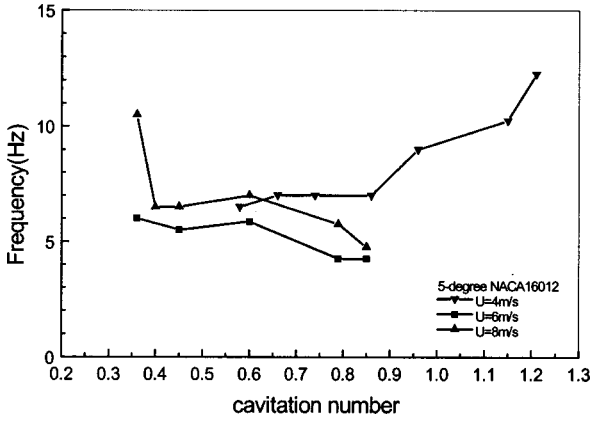

Fig. 10 Frequency of cavity oscillation at 5-degree a.o.a.

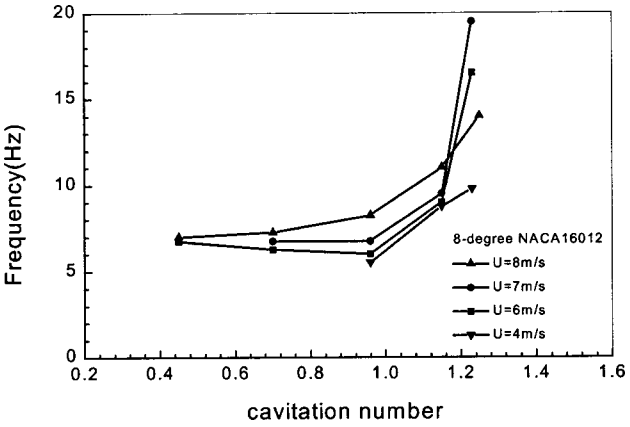

Fig. 11 Frequency of cavity oscillation at 8-degree a.o.a.

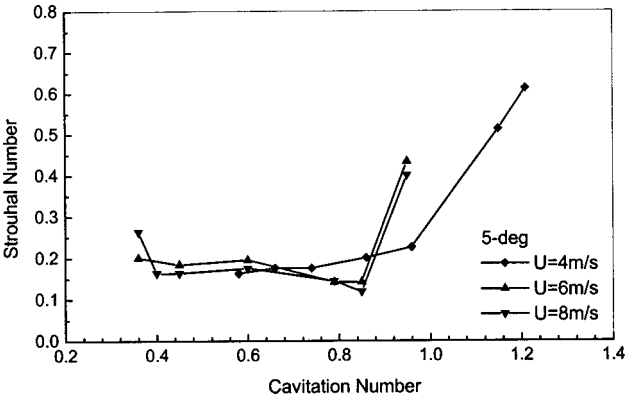

Fig. 12 Strouhal number of cavity oscillation versus cavitation number at 5-degree a.o.a.

For the flow at an 8-degree angle of attack, Fig. 11, the frequency of cavity oscillation versus cavitation number also seems to have a consistent trend, except for a slight difference when U=6 m/s. In the region of cavitation numbers $1.15<\sigma<1.25$, the curves of different velocities intersect in some cases. However, in the range of $0.7<\sigma<1.15$ or lower, frequencies increase steadily with the flow speeds. The Strouhal number tends to be asymptotic to a steady value before the supercavity forms. Also, the Strouhal number seems to be almost constant with the increase of the flow speeds when $\sigma<1.15$, Fig. 13.

Current investigation is focused on the variation of frequency or Strouhal number against cavitation number and flow speed,

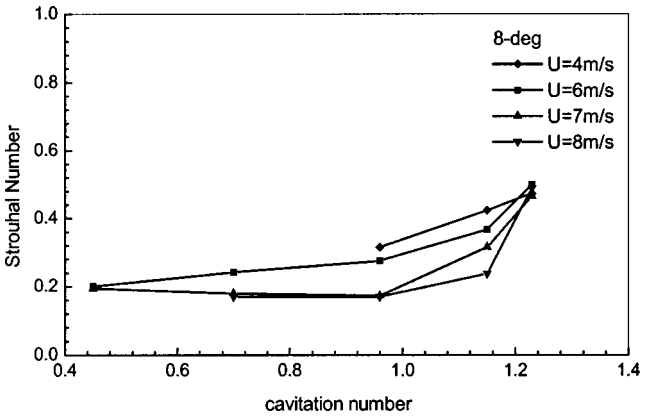

Fig. 13 Strouhal number of cavity oscillation versus cavitation number at 8-degree a.o.a.

thus it might be difficult to compare with other experimental data [6], since most of them only provided an average frequency or Strouhal number, and a different characteristic length is used for calculating the Strouhal number.

(2) Cinegraphic Observation on the Cavity Shedding and Definition of Different Stages. Although cavitation instability usually results in periodic cavity oscillations, the specific process differs in its flow patterns at different angles of attack.

When transcritical cavitation happens in the case of 2-degree a.o.a., bubble cavitation dominates most of the foil surface from the leading edge, while the region downstream of the trailing edge is filled with rarefied vaporous cavitation, Fig. 7(*a*). Limited by the graphic resolution in this small region, the detailed flow structure in cavity shedding is too small to be analyzed, except that the flow seems to be locally separated and vortical at the trailing edge.

In the case of 5-degree a.o.a., cavity growth is clearly observable and scalable before cavity shedding happens, Fig. 14. The transverse cavitation vorticity begins to intensify in the cavity closure after the cavity length stops growing. With the intensification of cavitation vorticity, the cavity closure gradually becomes a cavitated open-wake region. After the cloud cavitation breaks off from the closure, a vapor layer is generated from the leading edge again. The first-order frequencies in acoustic spectra are consistent with the statistical results of cavity cycling counted in the cinegraphy films.

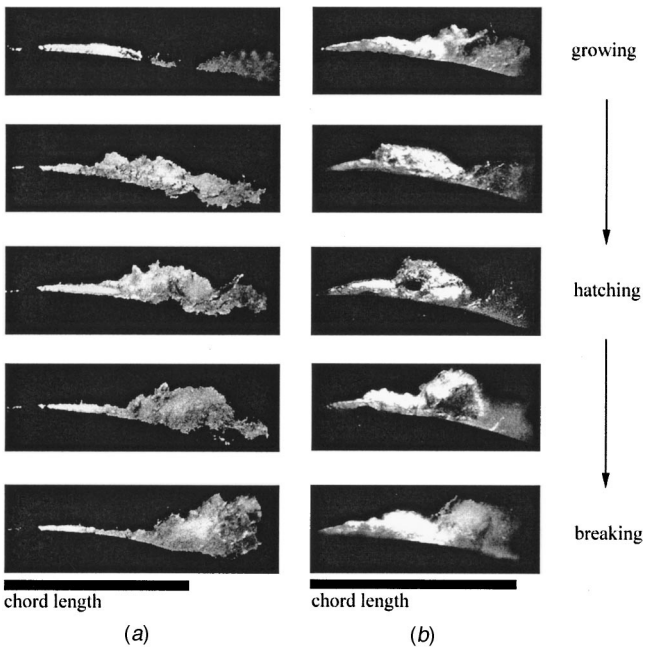

Fig. 14 Typical stages of periodic cloud cavitation shedding on NACA16012 hydrofoil. (*a*) 5-degree a.o.a. $U=7\,m/s, \sigma=0.45$; (*b*) 8-degree a.o.a. $U=7\,m/s, \sigma=1.29$.

In the case of 8-degree a.o.a., violently cavitated vorticity keeps the cavity closure constantly in a highly-cavitated open-wake region. A clear interface only exists near the leading edge. Cavitation vortices that separate from the leading edge accumulate and strengthen at the closure region, until a certain cavitation vorticity triggers the shedding of the cavitated entity. The whole flow recovers so rapidly that it is not until the shed cavity leaves the foil domain that a new cycle has already grown to its former dimension. The reentrant-jets are found in all of the cases at 5- and 8-degree. The details of the behavior of reentrant-jet will be discussed later.

Overall, a cycle of cavity formation and cloud cavitation shedding could be divided into three phases: growing, hatching, and breaking. In the first phase, a cavity mainly grows in length at the beginning of a new cycle. Thereafter the hatching phase takes over, during which cavity thickness develops significantly and the vortices are accumulated and strengthened at the closure. When the largest vortex structure in the closure is built up to a critical intensity, the vortex cavitation begins to detach from the cavity entity with a rolling-up motion, after which the breaking phase finally arrives. Typical frames of each stage are presented in Fig. 14.

(3) Mechanism of Cavity Shedding. Since cavity unsteadiness is not distinct in the flow of axisymmetric bodies, most of the discussions on the mechanism of cloud cavitation shedding are based on the results of hydrofoil cavitation.

It is important to notice that the reentrant-jets do exist in the cases of 5- and 8-degree a.o.a., but they are not triggered before the cavity shedding departs from the closure. This particular phenomenon may be hard to see using vertical cinegraphy. Apparently, different flow configurations create cavitating flows in different patterns. Especially for those strongly separated cavitating flows at 8-degree a.o.a., the cavitation is affected more by the flow environments than the behavior of bubble dynamics. Additionally, compared with the liquid, the density of the cavitated phase is too weak to influence the main flow. Under the circumstances of strong flow separation at higher angles of attack, or even a local separation near the trailing edge at a smaller a.o.a., the main flow will have overwhelming influence over the whole region.

The hypothesis of reentrant-jets is generally accepted as one of the most possible models explaining the mechanism of cavity shedding, and the reentrant-jet is assumed to be the result of flow reattachment. However in this paper, the powerful flow structure is regarded to be more responsible for such a periodic event. In all the cases of the tests, there always exists a flow structure of recirculation (clockwise if the flow is from the left direction) in a certain scale within the cavity closure, but the reentrant-jet only happens a few frames after the moment of cavity shedding. This phenomenon was never mentioned in the former investigations.

A counter flow along the foil surface induced by the flow structure of recirculation stagnates somewhere in the closure region. It does not rush upstream like a jet until the largest cavitating vortex is intensified to a certain extent and then shed leeward. Such a counter flow when it rushes is the so-called reentrant-jet in many observations. Accordingly, the action of cloud cavitation shedding can be divided into two steps: the breaking-off of cavity closure with large vorticity at first, and then the collapse of the remaining attached part due to the arrival of the counter jet.

In conclusion, the mechanism of periodic cavity oscillation is explained in a new way, supported by the cinegraphic observations and the cavitation periodicity dependence on the flow speed. The transcritical features, while resulting from the interaction be-

tween the cavitation and liquid flow, are more affected by the whole flow pattern than by the bubble's behavior. The occurrence of a reentrant-jet is a consequence of the shedding of vortical cavitation structure, and is also the direct reason for the collapse of attached cavitation near the leading edge. On the other hand, shock waves caused by the collapse of the shed cavity is possible at the final moment of the collapse of an attached cavity part.

(4) Understanding the Transcritical Cavitation Noise. Based on the understanding of the mechanism of cavity shedding, the reason why the noise level increases within the transcritical region can be explained. For steady sheet cavitation with rarefied cloud cavitation downstream off the trailing edge, the hydroacoustic noise is much lower than when the cavitation bubble collapses upon the foil surface. The eigenfrequency detected in the noise spectra of low frequency comes from the periodic collapse of cloud cavitation as a monopole acoustic source.

The differences in trends between 2-deg and 5-deg angles of attack can be similarly understood. For the 2-deg a.o.a., because the power emitted by the bubble collapse upon the foil surface is so overwhelming, it accounts for most of the noise level; thus PAL does not increase too much even when the periodicity happens. For the 5-deg a.o.a., sheet cavitation with a vapor-mixed pattern develops gradually with the expanding of the cavitated region. But the slope of the partial noise level grows less abruptly than the slope of the bubble type does at 2-deg a.o.a., because the collection of cloud cavitation collapses downstream off the trailing edge. This trend is in agreement with the results from the headforms.

6 Conclusion

By means of hydroacoustics measurement and high-speed cinegraphy, the transitional patterns and acoustic characteristics of cavitating flow on a two-dimensional hydrofoil and axisymmetric bodies with hemispherical and 45-degree conical headform were studied in this paper. The results are obtained as follows:

1 For the NACA16012 hydrofoil under 2- and 5-degree angle of attack, the partial acoustic level increases when the periodicity of cavitating flow happens, and then decreases until the conditions of supercavitation occur. The efficiency of noise generation of bubble cavitation is much greater than that of attached cavitation in a vapor-mixed state.

2 For the 45-degree conical headform and the hemispherical headform, neither the maximum PAL nor the periodic unsteadiness of cavitation was detected in the test. The slope of the partial acoustic level against cavitation number changes correspondingly with pattern shift. Cavitation in a vapor-layer state emits stronger noise than a cavitating flow does in a bubbly or vapor-mixed state.

3 The periodicity of hydrofoil cavitation flow is found to be closely related to the flow velocity and cavitation number.

4 Based on the high-speed cinegraphic observations on the process of cloud cavitation shedding, it is discovered that more complicated processes are involved to trigger cavitation shedding other than a reentrant-jet. As a result of cavity-flow interaction, the unstable cavitation is mainly caused by the transcritical features of flow separation, in which the flow structures within vortex cavitation are generated periodically. Meanwhile, one cycle of cavity shedding can be divided into three consecutive phases: growing, hatching, and breaking.

Nomenclature

SPL = sound pressure level

$\sigma = P_\infty - P_V / \frac{1}{2} 2 \rho U_\infty^2$ = cavitation number

$\mathrm{Re} = UL/\gamma$ = Reynolds number

PAL = partial acoustic level

PAL_0 = PAL in a non-cavitating state

SPAL = slope of partial acoustic level

P_∞ = static pressure at infinity

P_ν = saturated vapor pressure

ρ = density of water

U = velocity of incident flow

L = characteristic length (chord length of the hydrofoil in this test)

γ = dynamic viscosity

p = sound pressure

p_0 = reference sound pressure ($1 \mu Pa$)

$s(f)$ = spectral density of sound pressure

f = frequency

σ_i = incipient cavitation number

a.o.a. = angle of attack (degree)

$\mathrm{St} = fL/U$ = Strouhal number

References

[1] Arakeri, V. H., and Acosta, A. J., 1976, "Cavitation Inception Observations on Axisymmetric Bodies at Supercritical Reynolds Numbers," J. Ship Res., **20**, pp. 40–50.

[2] Brennen, C., 1970, "Cavity Surface Wave Patterns and General Appearance," J. Fluid Mech., **44**, pp. 33–50.

[3] Acosta, A. J., and Parkin, B. R., 1975, "Cavitation Inception: A Selective Review," J. Ship Res., **19**, No. 4, pp. 193–205.

[4] Holl, J. W., and Carroll, J. A., 1981, "Observations of Various Types of Limited Cavitation on Axisymmetric Bodies," ASME J. Fluids Eng., **103**, pp. 425–433.

[5] Ceccio, S. L., and Brennen, C. E., 1992, "Dynamics of Attached Cavities on Bodies of Revolution," ASME J. Fluids Eng., **114**, pp. 93–99.

[6] Stutz, B., and Reboud, J. L., 1997, "Experiments on unsteady cavitation," Exp. Fluids, **22**, pp. 191–198.

[7] Lush, P. A., and Skipp, S. R., 1986, "High Speed Cine Observations of Cavitating Flow in a Duct," Int. J. Heat Fluid Flow, **7**, pp. 283–290.

[8] Le, Q., Franc, J. P., and Michel, J. M., 1993, "Partial Cavities: Pressure Pulse Distribution Around Cavity Closure," ASME J. Fluids Eng., **115**, pp. 249–254.

[9] Kubota, A., Kato, H., and Yamaguchi, H., 1992, "A New Modeling of Cavitating Flows: A Numerical Study of Unsteady Cavitation on a Hydrofoil Section," J. Fluid Mech., **240**, pp. 59–96.

[10] Stutz, B., and Reboud, J. L., 2000, "Measurements within unsteady cavitation," Exp. Fluids, **29**, pp. 545–552.

[11] Gu, W., 1998, "An experimental Study on the Transient and Periodic Phenomena of Unstable cavitation Flow," Ph.D. thesis, Shanghai Jiao Tong University.

[12] Knapp, R. T., 1955, "Recent Investigations on the mechanism of cavitation and erosion Damage," Trans. ASME, **77**, pp. 1045–1054.

[13] Lush, P. A., and Peter, P. I., 1982, "Visualization of the Cavitation Flow in a Venturi Type Duct Using High Speed Cine Photography," Conference on Operating Problems of Pump Stations and Power Plants, Proceeding of IAHR, Vol. 1, No. 5.

[14] Furness, R. A., and Hutton, S. P., 1975, "Experimental and Theoretical Studies of Two-Dimensional Fixed-Type cavities," ASME J. Fluids Eng., **98**, No. 4, pp. 515–522.

[15] Ramamurthy, A. S., and Balachandar, R., 1992, "Wake and Cavitation Characteristics of Equilateral Prisms at Incidence," J. Fluids Struct., **6**, pp. 671–680.

[16] Kawanami, Y., Kato, H., Yamaguchi, H., Tanimura, M., and Tagaya, Y., 1997, "Mechanism and control of cloud cavitation," ASME J. Fluids Eng., **119**, pp. 778–794.

[17] Reisman, G. E., Wang, Y. C., and Brennen, C. E., 1998, "Observations of shock waves in cloud cavitation," J. Fluid Mech., **355**, pp. 255–283.

[18] Leighton, T. G., 1994, *The acoustic bubble*, Academic Press Inc.

[19] Pan, S. S., Yang, Z. M., and Hsu, P. S., 1981, "Cavitation Inception Tests on Axisymmetric headforms," ASME J. Fluids Eng., **103**, pp. 268–272.

David G. Penn
e-mail: dpenn@Bicron.com

Martin Lopez de Bertodano[1]
e-mail: bertodan@ecn.purdue.edu

Paul S. Lykoudis
e-mail: lykoudis@ecn.purdue.edu
School of Nuclear Engineering,
Purdue University,
West Lafayette, IN 47907

Stephen G. Beus
Bettis Atomic Power Laboratory,
West Mifflin, PA 15122-0079
e-mail: beussg@bettis.gov

Dry Patch Stability of Shear Driven Liquid Films

The breakdown of the liquid film at the wall in annular gas-liquid flow may lead to the formation of a stable dry patch. For the case of heat transfer surfaces this causes a hot spot. Dry patch stability depends on a balance of body and surface forces. In the present study the film is driven by the interfacial shear force and the gravity force is negligible. Hartley and Murgatroyd proposed a model for dry patches of shear driven films based on a balance of surface tension and inertia but the film contact angle had to be adjusted to an unrealistic value to fit the model to experimental data. Murgatroyd later proposed an additional force because the wall and the interfacial shear stresses on the film are unbalanced near the dry patch. The magnitude of the net shear force on the film is determined by a characteristic length, λ, over which this imbalance occurs. However, Murgatroyd did not validate the model with a mathematical solution for the distribution of the shear stresses but determined λ empirically to fit the experimental data. A new computational fluid dynamics (CFD) solution of the flow field in the film around the dry patch has been obtained. The CFD results confirm Murgatroyd's hypothesis, although the details are more complex. In addition new experimental data for adiabatic upward annular air-water and air-ethylene glycol flows provide further validation for Murgatroyd's model.
[DOI: 10.1115/1.1412459]

Introduction

Hartley and Murgatroyd [1], in an early analysis of the break up of a liquid film in annular flow, used a simple balance between surface tension and the inertia of the film to determine the stability of the dry patch. Murgatroyd [2] modified the force balance, adding the force due to the unbalanced shear stresses between the solid-liquid and liquid-gas interfaces. However, this force has not been widely used. In fact, on some occasions, in order to bring Hartley and Murgatroyd's model and experiments into agreement the contact angle has been used as a free parameter (e.g., Hewitt and Lacey [3] used a contact angle of 17 deg to correlate their shear driven film data and Ueda et al. [4] used a contact angle of 15 deg for their falling film data). The present work contains a CFD analysis that validates Murgatroyd's model and that, hopefully, makes the nature of the shear force a little more clear.

It is noteworthy that the force balance approach for the adiabatic case has not been investigated further. However, a significant amount of work has been carried out to study additional forces that appear due to heat transfer for shear driven films (e.g., Zuber and Staub [5] and Chung and Bankoff [6]) and falling films (e.g., Ueda et al. [4] and Hoke and Chen [7]).

Another method to predict the breakup of the liquid film is the energy criterion for the transition from film flow to rivulets. According to this criterion the transition occurs when the sum of the kinetic and surface energies of the rivulets becomes smaller than that of the film (e.g., Saber and El-Genk [8]).

Finally, the stability analysis of the liquid film has received wide attention (e.g., for linear stability see Bankoff [9] and for nonlinear stability see Joo et al. [10]).

Analysis

The force balance model contains the forces that act on a control volume situated along the center streamline of the liquid film leading to the dry patch. A diagram of the film and the control volume are shown in Fig. 1. The liquid film is considered to be symmetric along the dividing streamline (E-G). At point E the liquid film is undisturbed, and has a laminar velocity profile, i.e., Couette flow. Point G is a stagnation point. The liquid film at the edge of the dry patch is characterized by the static liquid-solid contact angle. The gas flow is assumed to produce a uniform shear over the film. This is a good approximation since a typical film thickness is approximately 100 microns, and the resulting change in the gas velocity from the wetted area to the nonwetted area is very small. Furthermore, the effect of the surface waves is neglected.

The adiabatic dry patch model contains four components: liquid inertia, gravity, surface tension, and the shear force.

The liquid inertia effect is due to the change in fluid momentum entering the control volume at point E and exiting through the right side between points E and G (Fig. 1). The fluid enters the control volume fully developed and then curves around the dry patch thus changing its direction and momentum. The inertia "force" per unit width, Δz, is:

$$\frac{F_m}{\Delta z} = \frac{M_{in} - M_{out}}{\Delta z} = \frac{1}{2}\rho_l \int u^2 dy \tag{1}$$

The Couette flow at the entrance of the control volume is given by

$$u(y) = \frac{u_i}{\delta} y \tag{2}$$

where u_i is the liquid velocity at the liquid-gas interface and δ is the film thickness. Substituting Eq. (2) into Eq. (1) and integrating across the film thickness yields

$$\frac{F_m}{\Delta z} = \frac{1}{6}\rho_l \delta u_i^2 \tag{3}$$

The net surface tension force on the control volume is caused by the difference in the x direction component of the surface tension at the two ends of the control volume as shown in Fig. 2. Thus the net surface tension force per unit width over the control volume is:

$$\frac{F_\sigma}{\Delta z} = \sigma(1 - \cos\theta) \tag{4}$$

The gravity term for the control volume is simply:

[1]Corresponding author.

Contributed by the Fluids Engineering Division for publication in the JOURNAL OF FLUIDS ENGINEERING. Manuscript received by the Fluids Engineering Division November 10, 2000; revised manuscript received June 26, 2001. Associate Editor: F. K. Wasden.

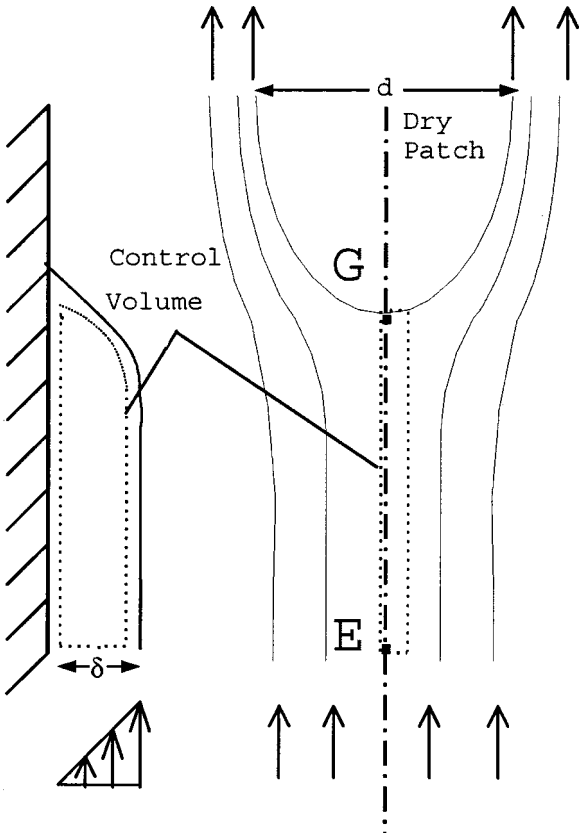

Fig. 1 Dry patch schematic

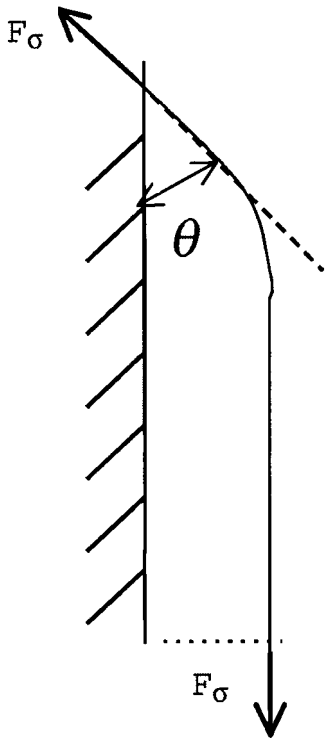

Fig. 2 Surface tension force

$$\frac{F_g}{\Delta z} = \rho_l g \lambda \delta \tag{5}$$

where λ is the length of the control volume in the *x* direction.

The shear force hypothesis relies on the assumption that the viscous shear at the liquid-solid interface goes to zero at the stagnation point. The shear force at the liquid-gas interface remains constant over the entire area of the control volume. The unbalance in the shear results from the difference in the shear at the two interfaces. A graphical representation of the shear forces is shown in Fig. 3. At point E the shear stresses at both interfaces are equal but in opposite directions (i.e., fully developed flow). Approaching the dry patch, the shear at the solid wall decreases and the shear at the gas interface remains constant. This produces a net surface force over the control volume. Murgatroyd assumed the wall shear to be a linear function of *x*:

$$\tau_{sl} = \tau_{gl}\frac{x}{\lambda} \quad for \quad x < \lambda$$

$$\tau_{sl} = \tau_{sl} \quad for \quad x \geq \lambda \tag{6}$$

where λ is the characteristic length over which the shear stresses are not in equilibrium. The shear force is obtained integrating the shear stresses over the control volume surface from G to E:

$$\frac{F_\tau}{\Delta z} = \tau_{gl}\int_0^\lambda \left(1 - \frac{x}{\lambda}\right) dx = \tau_{gl}\frac{\lambda}{2} \tag{7}$$

The total force balance on the liquid film is finally the summation of the four separate forces:

$$\frac{1}{6}\rho_l \delta u_i^2 + \frac{1}{2}\lambda \tau_{gl} = \rho_l g \delta \lambda + \sigma(1 - \cos\theta) \tag{8}$$

If the left-hand side of the equation is dominant then the dry patch will be unstable and will be washed away, if both sides are equal then the dry patch will remain stationary, otherwise the dry patch will grow or move slowly along the solid surface. Equation (8) has an unknown term, λ. In the rest of the paper a relation for it is developed using computational fluid dynamics and experimental data.

One nondimensional number can characterize adiabatic dry patch stability for a fluid with high surface tension, such as air-water flows, when the surface tension force and shear are domi-

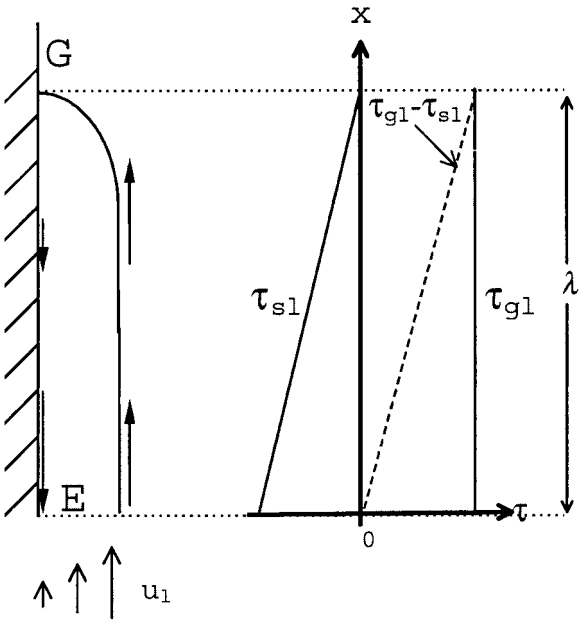

Fig. 3 Shear shear stresses acting on the control volume (τ_{fg}: stress at the liquid gas interface and τ_{fs}: stress at the wall)

nant. If the ratio of these two forces is greater than one then a dry patch should remain stable, so the stability condition is:

$$\pi_\sigma = \frac{\sigma(1-\cos\theta)}{\frac{1}{2}\lambda\tau_{gl}} > 1 \tag{9}$$

CFD Model

A relation for λ is obtained with the aid of the computational fluid dynamics (CFD) code PHOENICS [11]. The flow field of the liquid film is first calculated to determine the viscous stress field so that λ may be found.

To get an accurate solution the geometry of the CFD model should be close to the actual flow. The control volume used for the CFD model is different from that of the analytic model. The grid used is shown in Fig. 4. The flow domain is 30 mm long and 15 mm wide. The width corresponds to half the circumference of the tube. The depth of the film is 0.1 mm. The dry patch is 20 mm wide. Because of symmetry only half of the dry patch is included in the computational domain.

The CFD model is set up so the liquid film has fully developed Couette flow, given by Eq. (2), at the inlet and is uniform in the *z* direction. It is important to note that Eq. (2) corresponds to Couette flow without the effect of gravity. Therefore the present analysis is not valid for those cases where gravity is significant.

The left side of the liquid film is the center streamline leading to the dry patch. This is a plane of symmetry. The right side of the liquid film is also a plane of symmetry since the width of the grid in the *z* direction is 1/2 of the inside diameter of the tube. It is assumed that an actual flow has only one dry patch. The size and shape were estimated from observations made in the laboratory.

The upper surface of the film is the liquid-gas interface. The boundary condition at this surface is a uniform shear stress in the *x* direction. The lower surface of the liquid film is the liquid-solid interface. At this interface there is a no-slip boundary condition.

At the edge of the dry patch, the liquid film flow must turn around it. There is a boundary condition of no flow across this surface. The final boundary is the outlet and here there is no restriction imposed. Therefore the fluid can only enter at the inlet and will only leave at the outlet. The flow slows as it approaches the dry patch and there is a stagnation zone near the point G. The solution of the velocity field can be seen from the velocity vector plot in Fig. 5 and the sketch in Fig. 6. The flow at the bottom of the film actually reverses near the stagnation point, and so does the shear stress (Fig. 7). In the zone upstream of G the net flow is stagnant and since the flow in the upper surface of the film is

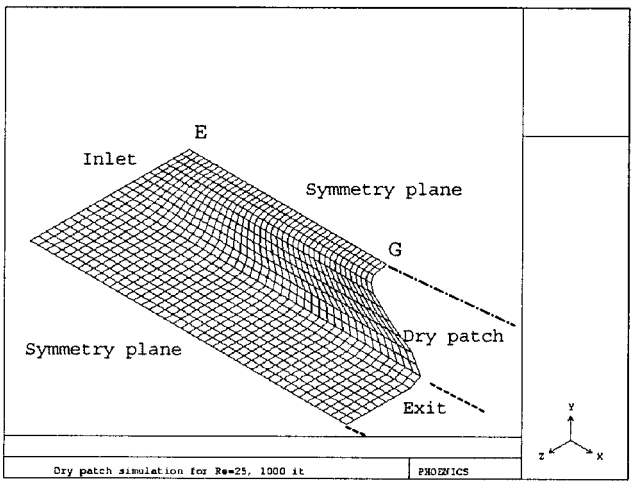

Fig. 4 Body fitted coordinate grid for dry patch CFD calculations

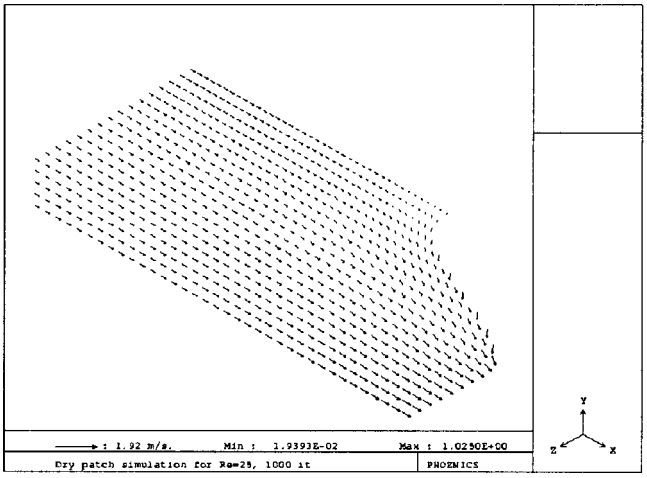

Fig. 5 Velocity vectors showing the film flow pattern around the dry patch

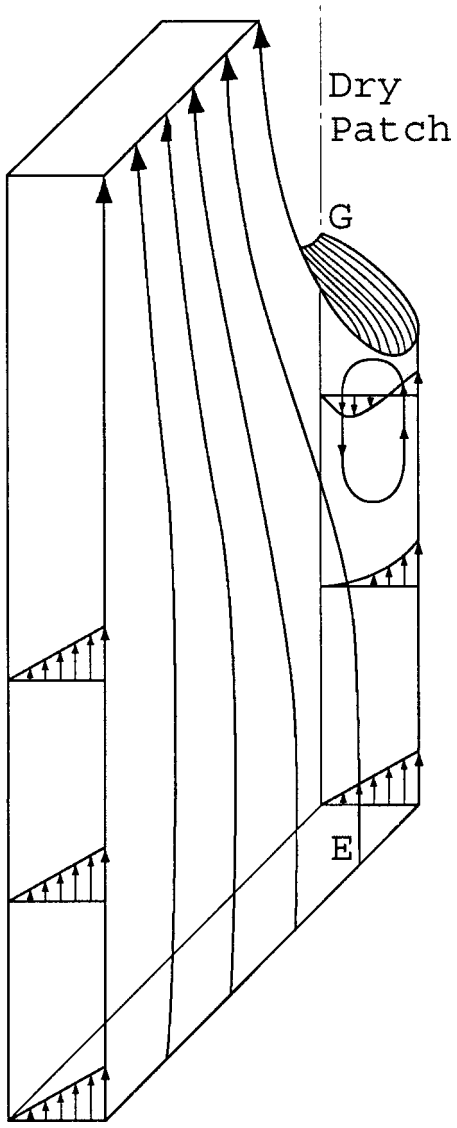

Fig. 6 Schematic of film flow around dry patch

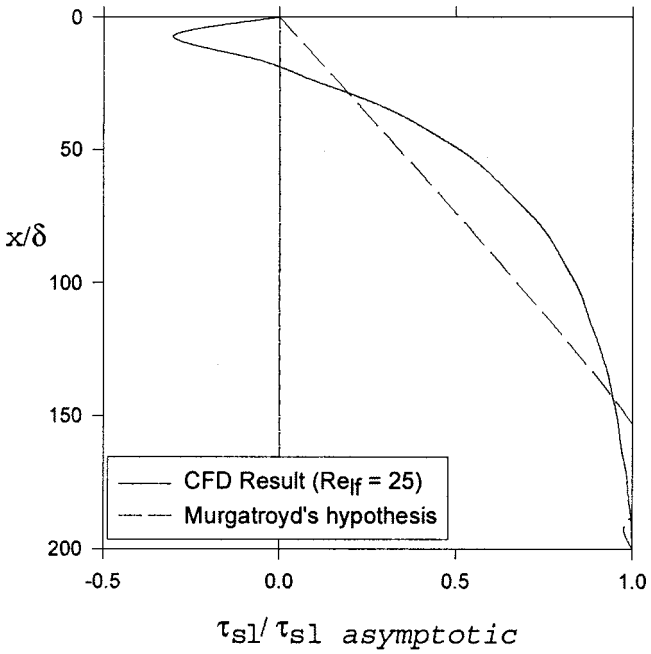

Fig. 7 Shear stress distribution along the dividing streamline

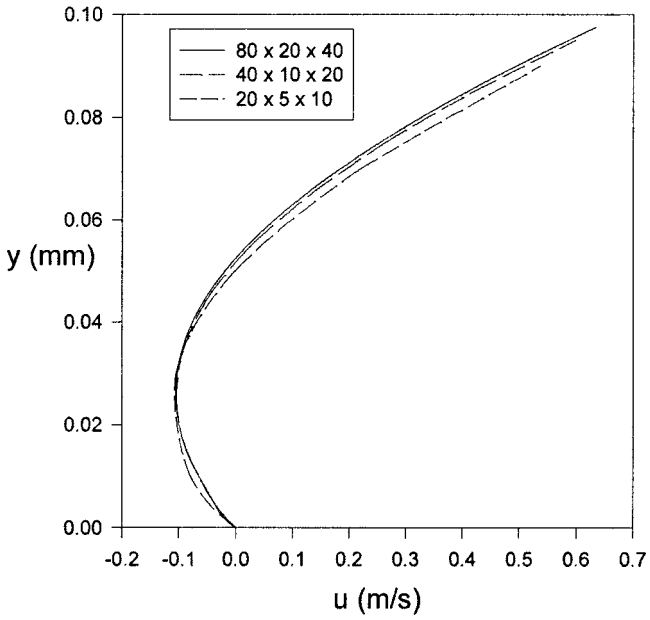

Fig. 9 Convergence test of velocity profile across the film

driven by the uniform shear stress (i.e., the boundary condition) it moves in the positive *x*-direction. Therefore the flow near the wall must move in the negative *x*-direction.

Once the basic flow pattern has been obtained the shear stress distribution along the dividing streamline is calculated. Since the velocity field through the liquid film is known from the CFD solution, and the area of each cell in the mesh is known, the shear force per cell surface area is:

$$F_\tau = -\mu \frac{u_{cell}}{\frac{1}{2}\delta_{cell}} A_{cell}. \tag{10}$$

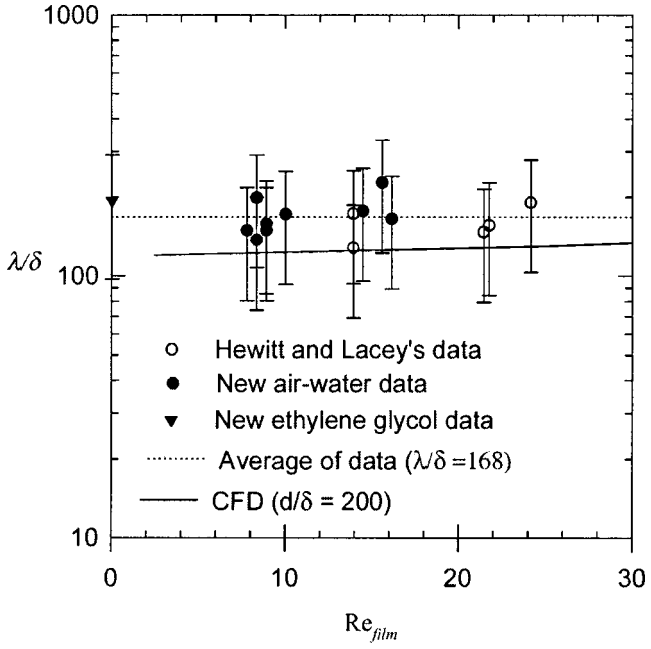

Fig. 8 Relationship of lambda to the film Reynolds number

The resulting stress distribution is shown in Fig. 7. Comparing the result with Fig. 3 it is seen that the hypothetical stress distribution proposed by Murgatroyd is too simple. However, the basic idea that the shear stress at the wall goes to zero at the intersection of the dividing streamline and the line of contact of the dry patch is correct.

The length λ is calculated by integrating the shear stress profile (i.e., summing the individual cell shear stresses along the dividing streamline) at both interfaces starting from the edge of the dry patch and moving upstream. λ is defined as the distance from the edge of the dry patch to the point where the integrated liquid-solid shear force is 1/2 of the liquid-gas shear force. This arbitrary definition is used to match Murgatroyd's model (i.e., Eq. (7)).

This calculation of λ was performed for different Reynolds numbers,

$$\mathrm{Re}_{film} = \frac{\rho_l u_l \delta}{\mu_l}. \tag{11}$$

The solid line in Fig. 8 shows the results of the CFD calculations. The change of λ/δ with the film Reynolds number is small. This means that the inertia of the fluid has little effect so the sensitivity of the model to the Reynolds number is negligible. This is a consequence of the low values of Re over which stable dry patches occur. If dry patches were to occur at higher values of Re then inertia would play a role.

A convergence study was performed on both the number of iterations and the refinement in the mesh spacing. The number of iterations was doubled successively until the solution for λ stopped changing.

Three different grids were generated to test mesh refinement convergence, by doubling the number of cells in each direction. The velocity profile at a location 1 mm from the dividing streamline and 1 mm away from the dry patch is plotted in Fig. 9. This figure shows that the refinement in the mesh spacing from the $40\times10\times20$ grid to the $80\times20\times40$ grid does not produce a substantially improved solution. This is especially true near the liquid-solid interface where the calculation of λ is made. Based on this result all the calculations were performed with the $40\times10\times20$ grid.

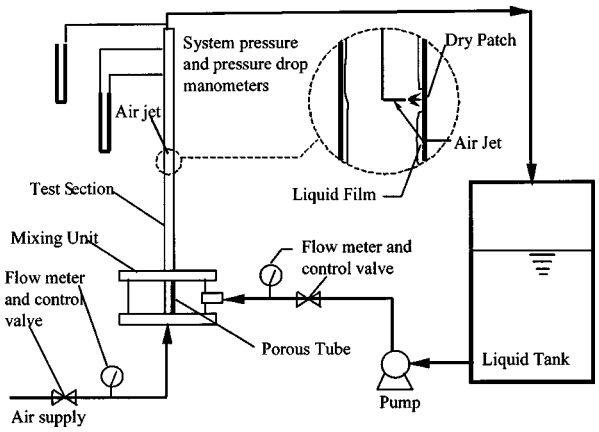

Fig. 10 Schematic of experiment

Experiment

The experiment is similar to Hewitt and Lacey's [3]. A vertical air-water loop, Fig. 10, with a 9.5 mm I.D. test section is used. In this experiment the annular flow is developed in a mixing chamber at the base of the test section. The mixing chamber consists of a porous tube through which the liquid film is injected. The air flows into the porous tube from the bottom. The liquid and gas flow rates are controlled with fine adjustment needle valves and the flow is monitored using standard rotameters. The test section itself is approximately 300 tube diameters long and constructed of clear 9.5 mm I.D. Lexan tubing. The length of the test section assures that the flow will be fully developed at the measurement area. The system pressure and pressure drop across the test section are measured with mercury and water manometers, respectively. The film thickness is measured using a needle attached to the end of a micrometer; the needle is at a 20 deg angle to the tube wall and it enters the test section downstream of the measurement area so it can contact the film without disturbing the flow upstream.

Experiments were carried out with air-water and air-ethylene glycol (properties of water: the surface tension is 0.0735 N/m, the density is 998 kg/m^3 and the viscosity is 1 cp; properties of ethylene-glycol: the surface tension is 0.0484 N/m, the density is 1119 kg/m^3 and the viscosity is 19.9 cp, taken at 20°C from the *CRC Handbook of Chemistry and Physics*, 50th edition). The values of the wetting angle, θ, were measured separately by placing a liquid drop on a lexan sheet and taking a close up photography of the profile of the droplet. The measured values for water and ethylene-glycol were approximately 60 deg. The value for water is in agreement with the data of Chappius [12].

The dry patch is initiated by creating a disturbance to the flow with a small air jet as shown in Fig. 10. The air jet is controlled by an electric solenoid valve and a pressure regulator.

At the beginning of the experiment the tube wall is completely wetted with a film and the gas flow is kept at a moderate value to sustain the annular regime (i.e., j_g is approximately 20 m/s). The liquid flow rate is then reduced and held constant while the gas flow is reduced in small steps to reduce the shear in the film. After each successive reduction of the gas flow the air jet is cycled to create a dry patch. Depending on which forces dominate the flow the dry patch will remain in a stagnant position or the liquid will rewet the surface. If the liquid film will no longer rewet the surface and the dry patch is stagnant then it is considered to be a stable dry patch and the data is recorded.

The experimental data are presented in Table 1 and Fig. 8 along with data from the experiment of Hewitt and Lacey [3]. The values of λ/δ were calculated such that Eq. (8) is satisfied. It is also noted that the shear stress was obtained from the measured pressure drop, and not calculated from the gas velocity. The film thickness given in Table 1 was calculated according to the formula given by Henstock and Hanratty [13] for laminar flow:

Table 1 Dry patch data (Measurements obtained at standard temperature and pressure)

Run	Notes	J_l (m/s)	J_g (m/s)	τ_{sl} (Pa)	δ (m)	Re_{film}	F_m (N/m)	F_g (N/m)	F_σ (N/m)	λ/δ
	Air-water									
1	stationary	0.00655	24.7	5.11	7.81E-05	15.60	0.00208	0.01360	0.03379	227
2	spontaneous	0.00176	25.3	4.09	4.52E-05	4.18				
3	stationary	0.00679	28.1	6.86	6.86E-05	16.16	0.00254	0.00762	0.03379	165
4	spontaneous	0.00164	29.3	4.82	4.02E-05	3.90				
5	stationary	0.00608	28.6	6.72	6.57E-05	14.4	0.00213	0.00749	0.03379	177
6	spontaneous	0.00164	27.0	5.70	3.70E-05	3.90				
7	stationary	0.00351	31.2	8.18	4.52E-05	8.36	0.00103	0.00399	0.03379	199
8	spontaneous	0.00164	31.2	7.16	3.30E-05	3.90				
9	stationary	0.00421	32.5	8.91	4.75E-05	10.03	0.00141	0.00380	0.03379	172
10	spontaneous	0.00164	32.5	8.62	3.01E-05	3.90				
11	stationary	0.00374	35.0	10.95	4.04E-05	8.92	0.00131	0.00252	0.03379	158
12	spontaneous	0.00164	36.0	9.64	2.85E-05	3.90				
13	stationary	0.00374	36.2	12.12	3.84E-05	8.92	0.00138	0.00215	0.03379	149
14	spontaneous	0.00164	36.2	10.81	2.69E-05	3.90				
15	stationary	0.00328	37.8	13.58	3.39E-05	7.80	0.00120	0.00168	0.03379	149
16	spontaneous	0.00211	37.8	13.29	2.75E-05	5.02				
17	stationary	0.00351	37.9	14.75	3.37E-05	8.36	0.00138	0.00152	0.03379	137
18	spontaneous	0.00187	46.5	13.00	2.62E-05	4.46				
2	ethylene glycol	0.00027	37.2	4.71	7.37E-05	0.04	0.00000	0.01146	0.02225	194
27	Hewitts' data	0.00305	20.1	5.12	9.71E-05	24.17	0.00401	0.01768	0.03379	191
28	Hewitts' data	0.00274	22.7	6.24	8.35E-05	21.77	0.00378	0.01067	0.03379	156
36	Hewitts' data	0.00270	22.7	6.63	8.05E-05	21.47	0.00382	0.00934	0.03379	147
47	Hewitts' data	0.00176	25.7	7.09	6.27E-05	13.94	0.00207	0.00667	0.03379	173
58	Hewitts' data	0.00176	30.3	10.56	5.14E-05	13.94	0.00252	0.00331	0.03379	128

$$\frac{\delta\sqrt{\tau_{gl}/\rho_l}}{\nu_l} = 1.414\,\mathrm{Re}_{film}^{0.5} \tag{12}$$

We have also considered Asali et al.'s correlation [14]. The needle probe film thickness data has a lot of scatter and is more or less bounded by these two correlations. Since the average error of the film thickness data with respect to both correlations is similar we had no preference and chose Henstock's correlation. The comparison of Henstock's correlation with the film thickness data produces an average error of 46 percent. This is the largest contribution to the total error shown by the error bars in Fig. 8.

The average value of all the data is $\lambda/\delta = 168$ with a standard deviation of 16 percent and a maximum deviation of 35 percent.

The air-ethylene glycol datum was obtained for further validation of the model at different conditions. Ethylene glycol has a viscosity approximately 20 times that of water (i.e., the film Reynolds number is 20 times smaller) but the liquid density is similar.

Discussion

Table 1 contains the new data together with Hewitt and Lacey's. For the air-water experiment spontaneous dry patch formation was observed at very low liquid flows (i.e., without the air jet). These data are also recorded in Table 1 but they are not analyzed.

The three forces shown in the table are calculated from the measurements. The remaining shear force is obtained by satisfying Eq. (8). Finally, λ/δ is calculated with Eq. (7) given the interfacial shear obtained from the pressure drop measurement. The most significant forces in Eq. (8) for all the data in the table are the shear and the surface tension (i.e., the contributions of the gravity and inertia terms are relatively small).

The magnitude of the inertia force is relatively small for all the air-water data and negligibly small for the ethylene-glycol data. This is in agreement with the small Reynolds number dependence of the CFD results.

The magnitude of the gravity force was never more than 40 percent of the surface tension force for any of the air-water data obtained, and, in general, it was much smaller. This was not true for the ethylene glycol data where the gravity force was greater than the surface tension force for all cases except the one shown in Fig. 8. The reason to discard the rest of the data is that the CFD model does not include the effect of gravity, and therefore the dependence of λ/δ on gravity has not been studied. Based on this the limit of the present theory may be defined by

$$\pi_g = \frac{\rho_l g\,\delta}{\frac{1}{2}\,\tau_{gl}} < 0.4 \tag{13}$$

The CFD results validate Murgatroyd's hypothesis of the shear imbalance and the CFD results for λ/δ are in good agreement with the experimental data. It is important to note that the CFD calculations were performed for a dry patch size of $d = 20$ mm (see Fig. 1) and the results would vary for a different choice. With this limitation in mind it is remarkable that none of the data are far from the particular set of CFD solutions with $d/\delta = 200$. Although the dry patch sizes were not carefully measured in the present experiment, nor in Hewitt and Lacey's, $d/\delta = 200$ is a rough approximation to the observations.

A CFD calculation where d/δ was halved resulted in a value of λ/δ of one half. Therefore, with some caution, it may be stated that λ/δ is proportional to d/δ and the dotted line through the data in Fig. 8 then leads to the final statement that

$$\lambda \cong 0.84d. \tag{14}$$

Conclusion

The present research has shown two separate results on the stability of dry patches of the shear driven liquid film in annular two-phase flow. The first result is the closure of the shear force. Murgatroyd's constitutive relation has been validated, using CFD to simulate the flow, and the length scale needed to correlate the shear force has been shown to be in agreement with the CFD calculations.

The second result is the validation of the model with experimental data for adiabatic air-water and air-ethylene glycol flows. These data show that Murgatroyd's model does predict the stability of dry patches over a wide range of conditions.

Acknowledgment

The financial support of Bettis Atomic Power Laboratory, which made this work possible, is gratefully acknowledged.

Nomenclature

d = dry patch width
D = tube diameter
g = gravity
J = superficial velocity
M = momentum flow
Re_{film} = film Reynolds number
u = liquid velocity
δ = film thickness
θ = contact angle
λ = characteristic length
μ = dynamic viscosity
ν = kinematic viscosity
ρ = density
σ = surface tension
τ_{sl} = wall shear
τ_{gl} = shear at liquid-gas interface

Subscripts

i = interfacial
g = gas, gravity
l = liquid
m = inertial

References

[1] Hartley, D. E., and Murgatroyd, W., 1964, "Criteria for Break-up of Thin Liquid Layers Flowing Isothermally over Solid Surfaces," Int. J. Heat Mass Transf., **7**, pp. 1003–1015.

[2] Murgatroyd, W., 1965, "The Role of Shear and Form Forces in the Stability of a Dry Patch on Two-phase Film Flow," Int. J. Heat Mass Transf., **8**, pp. 297–301.

[3] Hewitt, G. F., and Lacey, P. M. C., 1965, "The Breakdown of the Liquid Film in Annular Two-phase Flow," Int. J. Heat Mass Transf., **8**, pp. 781–791.

[4] Ueda, T., Inoue, M., and Nagatome, S., 1981, "Critical Heat Flux and Droplet Entrainment Rate in Boiling of Falling Liquid Films," Int. J. Heat Mass Transf., **24**, pp. 1257–1266.

[5] Zuber, N., and Staub, F. W., 1966, "Stability of Dry Patches Forming in Liquid Films Flowing over Heated Surfaces," Int. J. Heat Mass Transf., **9**, pp. 897–905.

[6] Chung, J. C., and Bankoff, S. G., 1980, "Initial Breakdown of a Heated Liquid Film in Co-current Two-component Annular Flow: II. Rivulet and Dry Patch Models," Chem. Eng. Commun., **4**, pp. 455–470.

[7] Hoke, B. C., Jr., and Chen, J. C., 1992, "Thermo-capillary Breakdown of Falling Liquid Films," Ind. Eng. Chem. Res., **31**, pp. 688–694.

[8] Seber, H. H., and El-Genk, M. S., 2000, "Determination of the Minimum Thickness of an Isothermal Liquid Film on a Vertical Surface," Proceedings of the 34th National Heat Transfer Conference, Pittsburgh, PA, August 20–22.

[9] Bankoff, S. G., 1971, "Stability of Liquid Flow Down a Heated Inclined Plane," Int. J. Heat Mass Transf., **14**, pp. 377–385.

[10] Joo, S. W., Davis, S. H., and Bankoff, S. G., 1996, "A Mechanism for Rivulet Formation in Heated Falling Films," J. Fluid Mech., **321**, pp. 279–298.

[11] PHOENICS, CHAM, Bakery House, 40 High Street, Wimbledon Village, London SW19 5AU, United Kingdom.

[12] Chappius, J. 1982, *Multiphase Science and Technology*. G. F. Hewitt, J. M. Delhaye, and N. Zuber, eds., Vol. 1, Hemisphere, pp. 387–505.

[13] Henstock, W. H., and Hanratty, T. J., 1976, "The Interfacial Drag and Height of the Wall Layer in Annular Flows," AIChE J., **22**, No. 6, pp. 990–1000.

[14] Asali, J. C., Hanratty, T. J., and Andreussi, P., 1985, "Interfacial Drag and Film Height for Vertical Annular Flow," AIChE J., **31**, No. 6, pp. 895–902.

Solution Structure and Stability of Viscous Flow in Curved Square Ducts

Tianliang Yang[1]

Liqiu Wang

Department of Mechanical Engineering,
The University of Hong Kong,
Pokfulam Road, Hong Kong

The bifurcation structure of viscous flow in curved square ducts is studied numerically and the stability of solutions on various solution branches is examined extensively. The solution structure of the flow is determined using the Euler-Newton continuation, the arc-length continuation, and the local parameterization continuation scheme. Test function and branch switch technique are used to monitor the bifurcation points in each continuation step and to switch branches. Up to 6 solution branches are found for the case of a flow in the curved square channel within the parameter range under consideration. Among them, three are new. The flow patterns on various bifurcation branches are also examined. A direct transient calculation is made to determine the stability of various solution branches. The results indicate that, within the scope of the present work, at given set of parameter values, the arbitrary initial disturbances lead all solutions to the same state. In addition to stable steady two-vortex solutions and temporally periodic solutions, intermittent and chaotic oscillations are discovered within a certain region of the parameter space. Temporal intermittency that is periodic for certain time intervals manifests itself by bursts of aperiodic oscillations of finite duration. After the burst, a new periodic phase starts, and so on. The intermittency serves as one of the routes for the onset of chaos. The results show that the chaotic flow in the curved channel develops through the intermittency. The chaotic oscillations appear when the number of bursts becomes large. The calculations also show that transient solutions on various bifurcation branches oscillate chaotically about the common equilibrium states at a high value of the dynamic parameter. [DOI: 10.1115/1.1412457]

Introduction

Pressure-driven flow in curved ducts is encountered in various practical processes. Flows in separation processes, heat exchangers, and physiological systems represent examples. Therefore, the flow phenomena in the curved ducts have drawn sustained attention. Dean [1] first formulated the problem mathematically under fully developed flow conditions and demonstrated the existence of a pair of counter-rotating vortices as a secondary flow in the curved pipe, known as the Dean Problem in the literature. The Dean problem was studied quite extensively by many researchers after Dean's pioneering work. For example, Stewartson et al. [2] studied the phenomena of boundary-layer collision in a curved duct extensively using numerical method. For a full review of the studies, readers can reference the work of Berger et al. [3], Nandakumar and Masliya [4], Ito [5], and Berger [6]. As the present work aims to understand the multi-solution structures and their stability for a flow inside of the square curved duct, our brief literature review is mainly on flow bifurcation and stability of fully-developed flows. The Dean problem is characterized by a dimensionless parameter called Dean number De, defined as a combination of the Reynolds number and the curvature ratio of the channel σ. It is used to measure the importance of the inertial and centrifugal forces relative to the viscous force. For a certain range of Dean number, the inertial, centrifugal, and viscous forces are of comparable magnitude. Nonlinear effects are thus very strong and flow bifurcations appear. Cheng and Akiyama [7] first mentioned the multi-solution phenomena in the Dean problem. They conducted a laminar forced convection heat transfer study in a loosely coiled curved rectangular duct and proposed that there are dual solutions. Joseph et al. [8] predicted an additional four-vortex secondary flow structure in the curved square duct and Masliyah [9] formed the same solution structure for the case of curved semicircular pipe with a flat outer wall.

Nandakumar and Masliyah [10] investigated the occurrence of dual solutions in curved ducts numerically. They proposed that the two-vortex solution and four-vortex solution coexist. The stability of multiple solutions was not studied. Winters [11] presented a rather comprehensive study of bifurcation structure of fully-developed laminar flows in coiled rectangular duct. They found the $2D$ four-cell flow to be unstable. They also computed the symmetry-breaking bifurcation and the asymmetric solution. However, the calculation in Winters [11] was made only for a relatively small range of Dean numbers. Furthermore, the stability studied by Winters [11] is inconclusive. Daskopoulos and Lenhoff [12] extended the work by Winters [11]. They used an effective numerical algorithm to study the bifurcation structure and found the solution structure obtained much more complicated than that by Winters [11]. In addition to the two-vortex and four-vortex flow structures, symmetric six-vortex and eight-vortex flows were found to co-exist at relatively higher values of Dean number. Because their calculations were conducted in the half a region under the assumption of symmetry, no asymmetric solutions were presented in their work.

The present work adds three new solution branches to the known bifurcation structure. Stability analysis of various solution branches, by a transient calculation method, reveals four kinds of physically realizable fully-developed flows: Stable steady solution, temporally periodic flow from Hopf bifurcation, intermittent flow and chaotic flow. The intermittency and chaotic phenomena are emphasized below based on the following observations: (1) There exists no detail study of the transition from steady

[1]Present Address: Dept. of Mechanical Engr., Univ. of Kentucky, Lexington, KY 40506-0108.

Contributed by the Fluids Engineering Division for publication in the JOURNAL OF FLUIDS ENGINEERING. Manuscript received by the Fluids Engineering Division February 9, 2000; revised manuscript received June 5, 2001. Associate Editor: P. E. Raad.

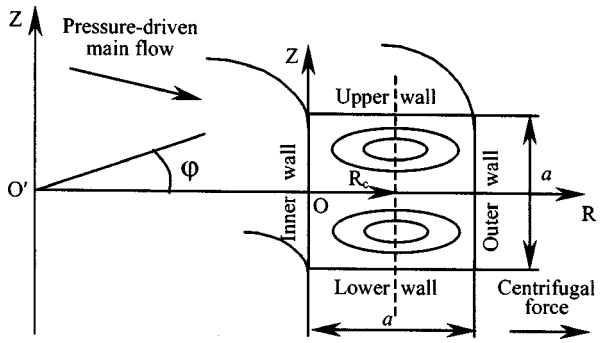

Fig. 1 Physical problem and coordinate system

flow to the temporally chaotic oscillation. (2) The chaotic oscillation feature of channel flows appears not to have been studied before.

Governing Equations and Numerical Algorithm

Governing Equations. Consider the fully developed laminar flow of viscous fluids in a curved square duct (Fig. 1). Properties of the fluid are taken to be constant. The gravitational force is negligible compared with the centrifugal force. In the coordinate system (R, Z, ϕ) as shown in Fig. 1, the governing equations in terms of dimensionless variables are (Cheng et al. [13] and Wang and Cheng [14]):
Continuity equation:

$$\frac{\partial}{\partial r}\{[1+\sigma(r-0.5)]u\}+\frac{\partial}{\partial z}\{[1+\sigma(r-0.5)]v\}=0. \quad (1)$$

Momentum equations

$$\frac{\partial u}{\partial \tau}+u\frac{\partial u}{\partial r}+v\frac{\partial u}{\partial z}-\frac{16w^2Dk^2}{\sigma[1+\sigma(r-0.5)]} =-\frac{\partial p}{\partial r}+\left\{\frac{\partial^2 u}{\partial r^2}+\frac{\partial^2 u}{\partial z^2}+\frac{\sigma}{1+\sigma(r-0.5)}\frac{\partial u}{\partial r} -\frac{\sigma^2 u}{[1+\sigma(r-0.5)]^2}\right\}, \quad (2)$$

$$\frac{\partial v}{\partial \tau}+u\frac{\partial v}{\partial r}+v\frac{\partial v}{\partial z}=-\frac{\partial p}{\partial z}+\left[\frac{\partial^2 v}{\partial r^2}+\frac{\partial^2 v}{\partial z^2}+\frac{\sigma}{1+\sigma(r-0.5)}\frac{\partial v}{\partial r}\right], \quad (3)$$

$$\frac{\partial w}{\partial \tau}+u\frac{\partial w}{\partial r}+v\frac{\partial w}{\partial z}+\frac{\sigma uw}{1+\sigma(r-0.5)} =\frac{1}{1+\sigma(r-0.5)}+\left\{\frac{\partial^2 w}{\partial r^2}+\frac{\partial^2 w}{\partial z^2}+\frac{\sigma}{1+\sigma(r-0.5)}\frac{\partial w}{\partial r} -\frac{\sigma^2 w}{[1+\sigma(r-0.5)]^2}\right\}. \quad (4)$$

Boundary conditions (nonslip, impermeability) may be written, in terms of dimensionless variables, as

$$u=v=w=0 \quad at\ r=0,\ 1 \quad for\ -0.5\leqslant z\leqslant 0.5, \quad (5)$$

$$u=v=w=0 \quad at\ z=-0.5,\ 0.5 \quad for\ 0\leqslant r\leqslant 1. \quad (6)$$

This is a two-parameter problem (σ and Dk). In the present work, we fix the curvature ratio σ at 0.02 (a typically value for cooling systems of rotor drums and conductors of electrical generators) to study the effect of Dk by changing Dk from 0–800.

Numerical Algorithm for Bifurcation Structure. For steady bifurcation structure, we remove the time-dependent terms in Eqs. (1)–(4). The governing Eqs. (1)–(4) are then discretized under the boundary conditions (5) and (6) by a finite volume method which is an adaptation of that in Patankar [15] and Wang and Cheng [14]. Main features of this method include a staggered mesh system, a power-law formulation for the combined effect of convection and diffusion terms, and central difference scheme for source terms and the continuity equation. After this discretization in the flow domain, we obtain a set of nonlinear algebraic equations, the so-called discretization equations, which approximate the governing differential equations (1)–(4) for the boundary conditions (5) and (6). The steady solutions on the single solution branch of the nonlinear algebraic equations are found by using the continuation algorithm together with the Newton iteration method (Rheinboldt [16] and Keller [17]). A test function proposed by Seydel [18,19] is used to detect the bifurcation points on the solution branch during the continuation process. The indirect method of branch switching technique developed by Seydel [18,19], is used to switch branches.

Grid-Dependence Check. The grid dependence was checked by three pairs of grid sizes uniformly distributed in the flow domain. They are 40×40, 50×50, and 60×60. The pair of numbers ($L\times K$) represents the number of grid points used in r- and z-directions, respectively. The bifurcation diagram has no qualitative difference for all three pairs of grid sizes. The quantitative difference between 50×50 and 60×60 grids is also very small for most of the region of interest. The numerical data are shown in Table 1 for eight cases at $Dk=20$, 100, 180, 300, 450, 550, 700, and 800 (all at the primary solution branch S_1), respectively. Three representative properties, namely, Dean number (De), maximum of absolute values of secondary flow stream function ($|\psi|_{max}$) and maximum streamwise velocity (w_{max}), as well as the

Table 1 Variations of De, ψ_{max}, w_{max} and CPU time in seconds with different grids on primary solution branch

$\sigma=0.02,\ Pr=0.7$					
Dk	*Grids*	*De*	$\lvert\psi\rvert_{max}$	w_{max}	*CPU (s)*
20	40×40	19.5	0.880	0.07150	73.5
	50×50	19.5	0.885	0.07153	155.1
	60×60	19.5	0.887	0.07154	301.3
100	40×40	76.5	5.488	0.04938	72.2
	50×50	76.5	5.528	0.04939	157.1
	60×60	76.5	5.546	0.04945	296.4
300	40×40	173.3	8.332	0.03405	73.1
	50×50	173.6	8.386	0.03413	156.3
	60×60	173.8	8.426	0.03419	302.0
450	40×40	234.4	10.733	0.03024	71.7
	50×50	235.0	10.951	0.03037	154.7
	60×60	235.4	10.909	0.03045	301.1
550	40×40	272.8	12.095	0.02867	72.4
	50×50	273.8	12.203	0.02884	158.2
	60×60	274.3	12.246	0.02891	310.7
700	40×40	327.8	13.747	0.02693	72.9
	50×50	329.2	13.836	0.02710	155.9
	60×60	330.1	13.942	0.02718	306.4
800	40×40	362.8	14.622	0.02597	73.1
	50×50	364.6	14.787	0.02615	156.4
	60×60	365.6	14.857	0.02625	291.5

Table 2 Comparison of four representative properties at $Dk=100$, $\sigma=0.02$ with those in Wang and Cheng [14]

Sources	Re	De	$\lvert\psi\rvert_{max}$	w_{max}	θ_{max}
Present work	541.0	76.5	5.528	0.0494	39.7
Wang & Cheng (1986)	542.0	76.6	5.641	0.0496	39.9

CPU time for one continuation step along S_1, are listed in Table 1 for comparison. The computations were carried out on DIGITAL Personal Workstation AU 600. The general trend of these results, as the grid size is decreased, tends to indicate that the solutions for the case of 50×50 grids are accurate to within 1 percent tolerance. We also checked the detailed variations of flow fields on various solution branches for different grid sizes, and found that 50×50 is indeed a reasonably accurate choice for square ducts. To verify the code further, four representative properties obtained by the present work are shown in Table 2 together with those by Wang and Cheng [14] at $Dk=100$, $\sigma=0.02$, where there is only one solution. The results are in good agreement, with a very small difference (less than 2 percent) being due to the different numerical methods used in two studies. It is worth noting that the CPU time increases rapidly as the grid spacing decreases. In order to have a balance between the cost of the computer time and the accuracy of the solution, we carried out all the computations with 50×50 uniform meshes for square ducts.

Stability of the Solutions. For stability, dynamic responses of the multiple steady solutions to finite random disturbances are made. The governing equations with the time-dependent terms are first discretized using the finite volume method mentioned above. The fully implicit method is used because of its superior numerical stability. The discretization equations are then solved by the continuation algorithm together with the Newton iteration method using time as the continuation parameter. The initial condition at $\tau=0$, which also serves as the starting point of the continuation scheme, is formed by the steady solution plus a finite random disturbance. The random disturbance is generated by the product of a random vector (12400) and the maximum percentage of disturbing value over the steady value (4%, 10%, and 15% in the present work). The random vector with the component number equal to that of steady solution vector is produced by the computer in forms of random values from -1 to 1.

Results and Discussion

Solution Structure and Flow Pattern. The solution structure is shown in Fig. 2 using the u-component velocity at (0.9, 0.64) as the state variable and Dk as the bifurcation parameter. This spatial location is chosen because the flow changes most significantly in this region and both symmetric and asymmetric branches are made visible. This fact can be proved by the solution structure using the average parameters [Nusselt number Nu or friction factor (f Re)] as the state variables and Dk as the bifurcation parameter (Yang and Wang [20] and Yang [21]). In Fig. 2, the symmetric and asymmetric solution branches are denoted by S and A, respectively. Among them, branch A_1 is bifurcated from S_1 at the symmetry-breaking bifurcation points ${}_{S1}{}^{A1}$. Branches A_2, A_3, and A_4 are bifurcated from S_2 at three symmetry-breaking bifurcation points ${}_{S2}{}^{A2}$, ${}_{S2}{}^{A3}$, and ${}_{S2}{}^{A4}$, respectively. On each of the solution branches, there are at least one limit point. The name of the limit point is given by An^m or Sn^m (where, n is the serial number of the solution branch and m is the serial number of limit point). For example, $S1^2$ represents the second limit point on the solution branch $S1$. The limit points on each of the solution branches divide the branch itself into several parts. The mth part of branch S_n or A_n is labeled as S_{n-m} or A_{n-m}, respectively. To visualize the details of branch connectivity and some limit points, the locally enlarged state diagrams are also shown in Fig. 2. As Fig. 2 is only 1D projection of N dimensional solution branches, all intersecting points except four bifurcation points should not be interpreted as connection points of branches.

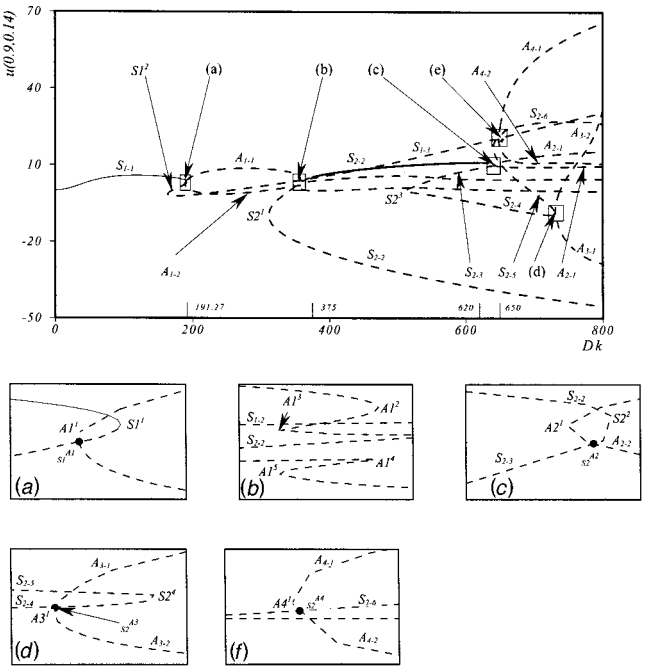

Fig. 2 Solution branches and their connectivity for the flow through the stationary curved duct of square cross-section at $\sigma=0.02$, Pr=0.7 (dimensionless velocity in r direction at $r=0.9$, $z=0.14$ vs. Dk). (a) Connectivity between S_1 and A_1, (b) four limit points on A_1, (c) connectivity between $S2$ and $A2$, (d) connectivity between $S2$ and $A3$, (e) connectivity between $S2$ and $A4$

Among six solution branches, S_1, S_2, and A_1 have been first reported by Winters [11]. Among them, S_{1-n} in the present work matches S_n in the work of Winters (where $n=1,2,3$), S_{2-1} and S_{2-2} in the present work match S_5 and S_4 in the work of Winters [11], respectively. We here reconfirm and extend their findings up to $Dk=800$. While no new limit and bifurcation points are found along S_1 and A_1, four additional limit points (first reported by Daskopoulos and Lenhoff [12]) and three new symmetry-breaking bifurcation points are detected along S_2. In particular, three symmetry-breaking bifurcation points lead to three pairs of asymmetric solution branches A_2, A_3, and A_4.

The secondary flows at $Dk=550$ and $Dk=700$ on each solution branch and at $Dk=180$ on S_{1-1} are shown in Fig. 3 and Fig. 4, respectively. The streamlines are used to illustrate the flow patterns in the figures. On S_{1-1}, the secondary flow is a 2-cell form with two Ekman vortices distributed symmetrically in the duct. On S_{1-3}, the secondary flow is a four-cell state with two Ekman vortices and two Dean vortices [Fig. 3(b), Fig. 4(a)]. Detailed description of the Ekman vortices and Dean vortices can be found in Wang and Cheng [14]. On A_{1-1}, the vortex at the lower part of the duct stretches to the upper part near the outer wall [Fig. 3(c), Fig. 4(b)].

The mirror image of the solution on A_{n-1} about the duct horizontal central-plane yields the solution on A_{n-2} for a given value of Dk ($n=1,2,3,4$). Therefore only secondary flow patterns on the solution sub-branches A_{1-1}, A_{2-1}, A_{4-1} are shown in Fig. 3 and Fig. 4.

The secondary flow becomes a four-cell state with two Ekman vortices and two Dean vortices again on the subbranch S_{2-1} [Fig. 3(d), Fig. 4(c)]. Unlike the four-cell pattern shown in Figs. 3(b) and 4(a), two Dean vortices here stretch spanwise rather radically.

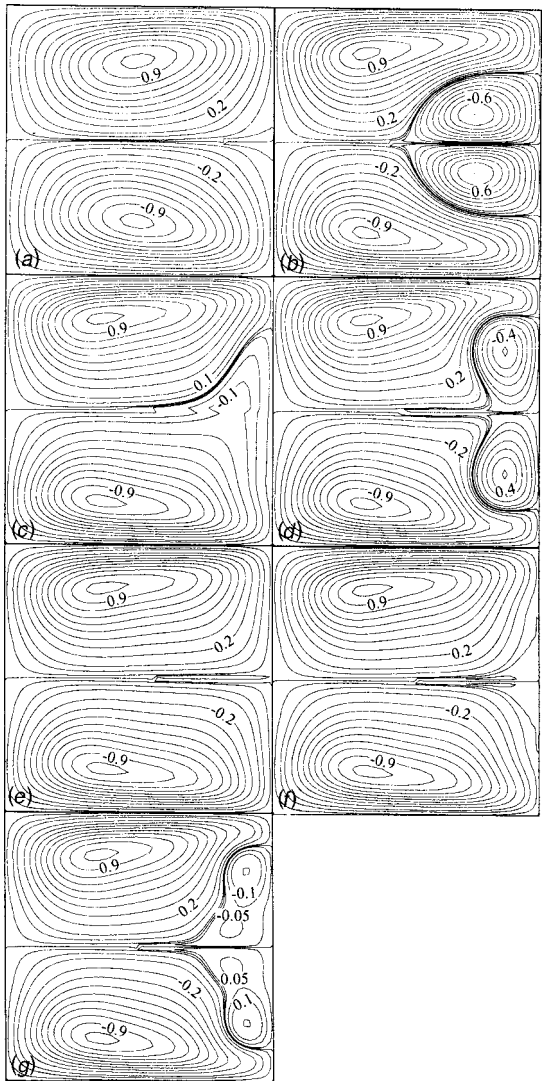

Fig. 3 The flow patterns at $Dk=180/550$, $\sigma=0.02$, Pr$=0.7$. (*a*) $Dk=180$ on $S1_1$, De$=123.4$, (*b*) $Dk=550$, De$=274$ on S_{1-3}, (*c*) $Dk=550$, De$=290$ on A_{1-1}, (*d*) $Dk=550$, De$=279$ on S_{2-1}, (*e*) $Dk=550$, De$=289$ on S_{2-2}, (*f*) $Dk=550$, De$=291$ on S_{2-3} (*g*) $Dk=550$, De$=288$ on S_{2-4}

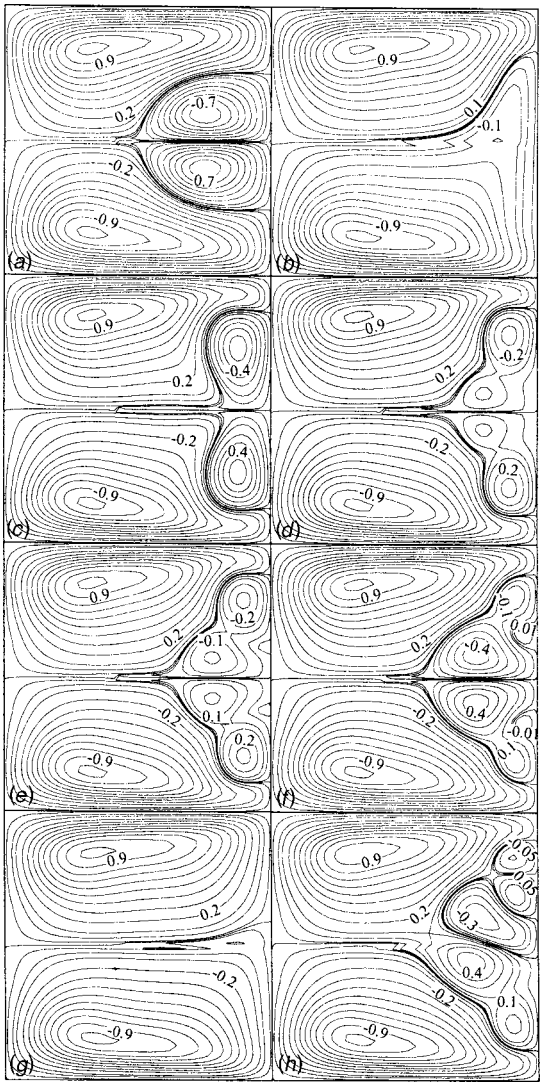

Fig. 4 The secondary flow patterns at $Dk=700$, $\sigma=0.02$, Pr $=0.7$. (*a*) Re$=2328$, De$=329$ on S_{1-3}, (*b*) Re$=2447$, De$=346$ on A_{1-1}, (*c*) Re$=2345$, De$=332$ on S_{2-1}, (*d*) Re$=2402$, De$=340$ on S_{2-4}, (*e*) Re$=2400$, De$=339$ on S_{2-5}, (*f*) Re$=2410$, De$=341$ on S_{2-6}, (*g*) Re$=2448$, De$=346$ on A_{2-1}, (*h*) Re$=2399$, De$=339$ on A_{4-1}

On S_{2-2}, the secondary flow [Fig. 3(*e*)] is a two-vortex patterns state. The flow on S_{2-3} is a weak 4-cell state with a pair of very weak Dean vortices [Fig. 3(*f*)]. The limit point between S_{2-3} and S_{2-4} leads the weakly 4-cell flow on S_{2-3} to a 6-cell state on S_{2-4} with two pairs of Dean vortices along the outer wall [Fig. 3(*g*), Fig. 4(*d*)]. The second pair appears because of the splitting of the original pair. The secondary flow on S_{2-5} is an 8-cell pattern [Fig. 4(*e*)]. Flows on S_{2-6} are also 8-cell state with three pairs of Dean vortices [Fig. 4(*f*)]. The 8-cell structure on S_{2-6} (the third pair of Dean vortices in particular) is stronger than that on S_{2-5}. Because the solution branch A_2 is bifurcated from the two-cell solution on S_{2-2} [Fig. 2], the secondary flow on A_{2-1} [Fig. 4(*g*)] is also a two-cell state. The solution branch A_4 is bifurcated from S_{2-5} with a complex secondary flow pattern. The secondary flow on A_{4-1} [Fig. 4(*h*)] is also complex. There are seven vortices in the cross-section, of which five are near the outer wall region.

Stability of Solutions on Various Branches. Because there is no study on dynamic responses of multiple solutions to finite random disturbances in the literature, a relatively comprehensive transient computation is made to examine the dynamic behavior. It is found that, at $\sigma=0.02$ and Pr$=0.7$, the final dynamic evolution after a short transient period is independent of initial disturbances for all solutions at fixed value of Dk in the region $0\leqslant Dk\leqslant 620$. At any fixed value of Dk in the range $0\leqslant Dk\leqslant 620$, all steady solutions develop, after initial finite random disturbances, to the same final state, i.e., there is no co-existence of two or more stable states in this range within the scope of the present study.

Five subranges are identified with each having distinct dynamic responses to finite random disturbances. The first ranges from $Dk=0$ to $Dk=191.27(S1^1)$, where the finite random disturbances lead all steady solutions at any fixed Dk to a 2-cell steady state on S_{1-1} (solid line in Fig. 2) with the same Dk. The second covers the range $191.27<Dk\leqslant 375$ where all steady solutions evolve to a temporal periodic solution. In the third sub-range $375<Dk\leqslant 620$, the finite random disturbances lead all solutions to a 2-cell steady state on S_{2-2} (solid line in Fig. 2) with the same Dk. The fourth subrange is from $Dk=620$ to $Dk=650$ where the solutions response to the finite random disturbances in the form of temporal oscillation with intermittency, a forecasting signal of chaotic flows. In the last subrange $Dk>650$, any finite random disturbance will deviate the solutions to chaotic oscillation states.

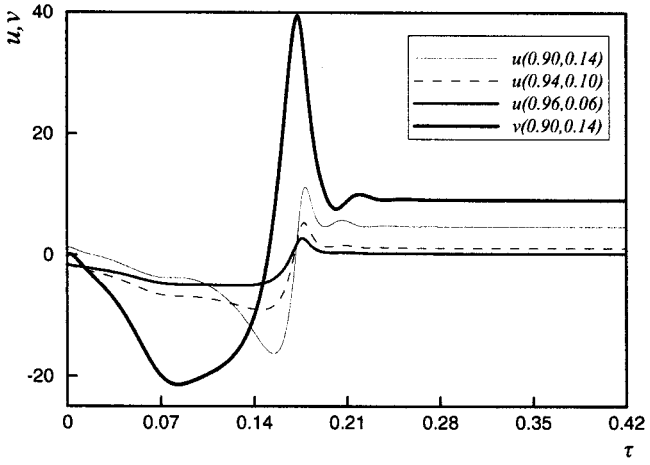

Fig. 5 Typical time evolution process in $0 \leqslant Dk \leqslant 191.27$ at $\sigma = 0.02$, and Pr=0.7: dynamic response of solution on S_{1-2} at $Dk = 180$ to finite random disturbances: evolution to stable steady 2-cell state on S_{1-1}

The first ranges from $Dk = 0$ to $Dk = 191.3$ where S_{1-1} is a stable subbranch. All other subbranches are unstable in this range. The final dynamic evolution of the steady solutions on various subbranches at any fixed Dk is a 2-cell steady state on S_{1-1} with the same Dk. Figure 5 shows the typical dynamic evolution in this region. In the figure, four velocity components $[u(0.9,0.64)$, $u(0.94,0.60)$, $u(0.96,0.56)$, and $v(0.9,0.64)]$ are used to monitor the dynamic evolution of the solution. To facilitate the comparison, we use these four velocity components (either velocity itself or derivation velocity from its initial steady value) in all figures illustrating dynamic responses of the multiple solutions to the finite random disturbances. It is observed that the four velocity components reach the steady states after a short period of time. The secondary flows return to the steady one shown in Fig. 3(*a*), proving that the solutions on S_{1-1} are stable while solutions on S_{1-2} are unstable. Similar to Fig. 5, the dynamic evolution of the solutions on S_{1-3} reach the steady states on S_{1-1} after a short period of time too.

The second subrange covers the $191.3 < Dk \leqslant 375$ where all steady solutions evolve to the periodic flows. For a given Dk, the periodic flows have the unique period and unique oscillation manner. The characteristic of the periodic oscillation does not change regarding to different initial conditions. The typical periodic feature of the dynamic evolution in this region is shown in Fig. 6. The period of the solution is about 0.159 for the case shown in Fig. 6.

In the third subrange $375 < Dk \leqslant 620$, at any fixed Dk, the finite random disturbances lead all solutions on different sub-branches

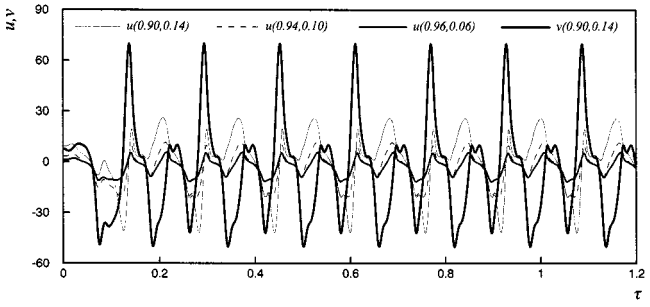

Fig. 6 Typical time evolution process in $191.27 < Dk \leqslant 375$ at $\sigma = 0.02$, and Pr=0.7: dynamic response of solution at $Dk = 300$ on A_{1-1} to finite random disturbances: periodic oscillation (*period*=0.159)

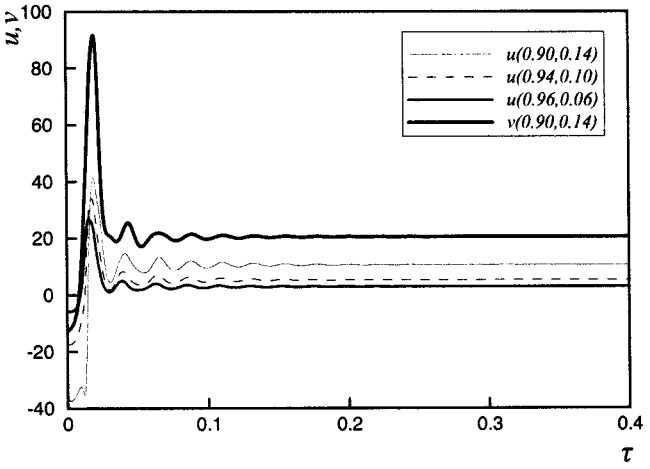

Fig. 7 Typical time evolution process in $375 < Dk \leqslant 620$ at $\sigma = 0.02$, and Pr=0.7: dynamic response of solution at $Dk = 550$ on S_{2-1} to finite random disturbances: evolution to stable steady 2-cell state on S_{2-2}

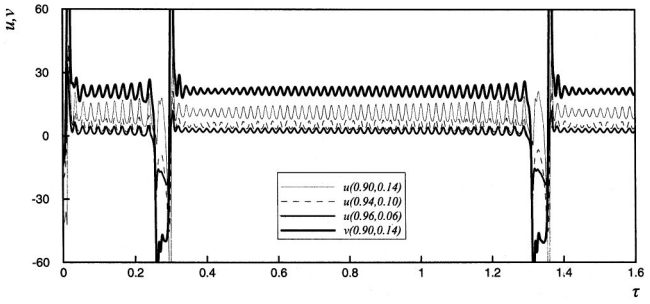

Fig. 8 Typical time evolution process in $620 < Dk \leqslant 650$ at $\sigma = 0.02$, and $Pr = 0.7$: dynamic response of solution at $Dk = 630$ on S_{2-1} to finite random disturbances: intermittency

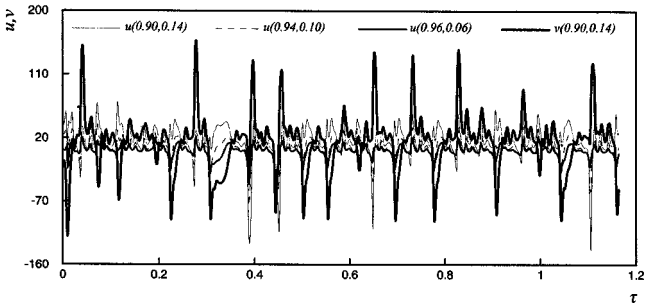

Fig. 9 Typical time evolution process in $650 < Dk \leqslant 800$: dynamic response of the solution at $Dk = 800$, $\sigma = 0.02$, and Pr = 0.7 on A_{3-1} to finite random disturbances: chaotic oscillation

to a 2-cell steady state on S_{2-2}, indicating that the steady solutions on all the other branches are unstable. Figure 7 shows the dynamic evolution of the solution on S_{2-1} at $Dk = 550$ [Fig. 3(*d*)] to steady state on S_{2-2} [Fig. 3(*e*)].

The fourth subrange is $620 < Dk \leqslant 650$ where the solutions on all the solution branches respond to the finite random disturbances in the form of periodic oscillation with intermittency. Figure 8 typifies the dynamic response in this region. The transient flow oscillates periodically around the steady solution on the second branch part S_{2-2} in the most of time. The amplitude of the periodic oscillation becomes larger at larger τ. When the amplitude of periodical oscillation becomes large enough, the oscillation be-

comes no periodic. The intermittency appears as one of routes to chaos (Pomeau and Manneville [22]). After an aperiodic burst, the transient flow returns to a periodic oscillation with relatively smaller amplitude and new periodic phase starts.

In the last subrange $Dk>650$, all solution branches are unstable, any finite random disturbance lead solutions to chaotically oscillating states. The typical chaotic oscillation is shown in Fig. 9. Bursts still appear intermittently. However, the temporal oscillation between two bursts can no longer be regarded as periodic. Flows appear to oscillate chaotically.

Concluding Remarks

The flow bifurcation and stability in the curved square duct have been studied numerically. Governing equations were discretized by using the finite volume method. The Euler-Newton continuation method was used to solve the system of nonlinear algebraic discretized equations. The indirect method was employed to detect bifurcation points and switch the branches during the continuation.

Up to 6 solution branches have been found for $\sigma=0.02$ and $0 \leqslant Dk \leqslant 800$. Three of them are new. The direct transient calculation was made to determine the stability of various solution branches. Five ranges with distinct stability properties have been identified. At any fixed value of Dk in the range $0 \leqslant Dk \leqslant 620$, all steady solutions develop, after the initial finite random disturbances, to the same final state.

Acknowledgment

The financial support from the Research Grants Council of Hong Kong (RGC, Project No: HKU7086/00E), the CRCG and the Outstanding Young Researcher Award of the University of Hong Kong to LW are gratefully acknowledged.

Nomenclature

a = duct width=duct height
c_1 = streamwise pressure gradient ($\partial p/R_c \partial \phi$)
De = Dean number ($\mathrm{Re}\sqrt{\sigma}$)
Dk = modified Dean number ($\sigma a W_1/4\nu$)
p = dimensionless pressure ($P/\rho(\nu/a)^2$)
P = pressure of the fluid
R_c = radius of curvature
Re = Reynolds number ($W_m a/\nu$)
r, z = dimensionless coordinates
R, Z, ϕ = coordinates
t = time
u,v,w = dimensionless velocity components in directions of R, Z, and ϕ ($u=aU/\nu, v=aV/\nu, w=W/W_1$)
U,V,W = velocity components in directions of R, Z, and ϕ
W_1 = representative streamwise velocity ($a^2 c_1 \mu$)
W_m = axial mean velocity
W_{max} = maximum streamwise velocity
μ = viscosity of the fluid
ν = kinematic viscosity of the fluid
ρ = density of the fluid
σ = duct curvature ratio (a/R_c)
τ = dimensionless time
ψ_{max} = maximum of absolute values of secondary flow stream function

References

[1] Dean, W. R., 1927, "The stream-line motion of a fluid in a curved pipe," Philos. Mag., **5**, pp. 673–695.
[2] Stewartson, K., Cebeci, T., and Chang, K. C., 1980, "A boundary-layer collision in a curved duct," Q. J. Mech. Appl. Math., **33**, pp. 59–75.
[3] Berger, S. A., Talbot, L., and Yao, L-S., 1983, "Flow in curved pipes," Annu. Rev. Fluid Mech., **15**, pp. 461–512.
[4] Nandakumar, K., and Masliyah, J. H., 1986, "Swirling flow and heat transfer in coiled and twisted pipes," Advances in Transport Processes, **4**, pp. 49–112.
[5] Itō, H., 1987, "Flow in curved pipes," JSME Int. J., **30**, pp. 543–552.
[6] Berger, S. A., 1991, "Flow and heat transfer in curved pipes and tubes," AIAA 91-0030, pp. 1–19.
[7] Cheng, K. C., and Akiyama, M., 1970, "Laminar forced convection heat transfer in curved rectangular channels," Int. J. Heat Mass Transf., **13**, pp. 471–490.
[8] Joseph, B., Smith, E. P., and Adler, R. J., 1975, "Numerical treatment of laminar flow in helically coiled tubes of square cross section," AIChE J., **21**, pp. 965–974.
[9] Masliyah, J. H., 1980, "On laminar flow in curved semicircular ducts," J. Fluid Mech., **99**, pp. 469–479.
[10] Nandakumar, K., and Masliyah, J. H., 1982, "Bifurcation in steady laminar flow through curved tubes," J. Fluid Mech., **119**, pp. 475–490.
[11] Winters, K. H., 1987, "A bifurcation study of laminar flow in a curved tube of rectangular cross-section," J. Fluid Mech., **180**, pp. 343–369.
[12] Daskopoulos, P., and Lenhoff, A. M., 1989, "Flow in curved ducts: bifurcation structure for stationary ducts," J. Fluid Mech., **203**, pp. 125–148.
[13] Cheng, K. C., Nakayama, J., and Akiyama, M., 1979, "Effect of finite and infinite aspect ratios on flow patterns in curved rectangular channels,"in *Flow Visualization*, Hemisphere.
[14] Wang, L., and Cheng, K. C., 1996, "Flow transitions and combined free and forced convective heat transfer in rotating curved channels: The case of positive rotation," Phys. Fluids A, **6**, pp. 1553–1573.
[15] Patankar, S. V., 1980, *Numerical Heat Transfer and Fluid Flow*, Hemisphere Publishing, New York, pp. 28–30.
[16] Rheinboldt, W. C. 1980, "Solution fields of nonlinear equations and continuation methods," SIAM (Soc. Ind. Appl. Math.) J. Numer. Anal., **17**, pp. 221–237.
[17] Keller, H. B., 1977, "Numerical solution of Bifurcation and nonlinear eigenvalue problems," *Applications of Bifurcation Theory*, Academic Press, New York, pp. 359–384.
[18] Seydel, R., 1983, "Branch switching in bifurcation problems for ordinary differential equations," Numerical Mathematics, **41**, pp. 91–116.
[19] Seydel, R., 1994, *From Equlibrium to Chaos, Practical Bifurcation and Stability Analysis*, Elsevier Science Publishing, New York, pp. 109–304.
[20] Yang, T. and Wang, L., 2000, "Solution structure and stability of viscous flow and heat transfer in curved channels," The 34th National Heat Transfer Conference, Pittsburgh, PA.
[21] Yang, T., 2001, "Multiplicity and stability of flow and heat transfer in rotating curved ducts," Ph.D. thesis, The University of Hong Kong.
[22] Pomeau, Y., and Manneville, P., 1980, "Intermittent transition to turbulence in dissipative dynamical systems," Commun. Math. Phys., **74**, pp. 189–197.

H. A. Dwyer
Department of Mechanical
and Aerospace Engineering
University of California, Davis,
Davis, CA 95616
e-mail: hadwyer@ucdavis.edu

A. Y. Cheer
Department of Mathematics

T. Rutaganira
Department of Mathematics

University of California, Davis,
Davis, CA 95616

N. Shacheraghi
Department of Mechanical
and Aerospace Engineering

University of California, Davis,
Davis, CA 95616

Calculation of Unsteady Flows in Curved Pipes

Highly unsteady three-dimensional flows in curved pipes with significant variation of flow geometry and flow parameters are studied. Using improvements in computational efficiency, detailed knowledge concerning flow structures is obtained. The numerical solutions of the Navier-Stokes equations have been obtained with a variation of the projection method, and the numerical method was enhanced by new algorithms derived from the physics of the flow. These enhancements include a prediction of the flow unsteady pressure gradient based on fluid acceleration and global pressure field corrections based on mass flow. This new method yields an order of magnitude improvement in the calculation's efficiency, allowing the study of complex flow problems. Numerical flow simulations for oscillating flow cycles show that the curved pipe flows have a significant inviscid-like nature at high values of the frequency parameter. The shape of the velocity profiles is strongly influenced by the frequency parameter, whereas the influence of variations on the pipe cross-sectional area is shown to be rather weak. For large values of the frequency parameter the flow history strongly influences the low mass flow part of the cycle leading to highly unusual velocity profiles. The wall shear stress is studied for all the flows calculated. Our results show that wall shear stress is sensitive to area constrictions, the frequency parameter, as well as the shape of the entrance profile.
[DOI: 10.1115/1.1400748]

Introduction

During the past years there have been substantial efforts in solving flow in curved pipes. Some of the papers that have influenced our work are Dean [1], Pedley [2], Berger and Talbot [3], Chung and Hyun [4], Hamakiotes and Berger [5], Karahalois and Panagopoulos [6], Riley [7], Sumida et al. [8], and Yam and Dwyer [9]. However, only recently, with the increasing power of the digital computer, has it been possible to calculate full three-dimensional and time-dependent flows. In this paper, we accelerate these developments with an improved algorithm based on flow physics. Our algorithm is used to calculate a series of important flows that highlight our improvements. We have made our flow parameters similar to those in the excellent study of quasi-three-dimensional flows of Hamakiotes and Berger [5]. In their study, Hamakiotes and Berger [5] solved a fully developed flow in a curved pipe where the fully developed assumption removes the axial coordinate from the problem. With the axial coordinate removed, the influence of entrance and exit conditions cannot be evaluated, and influences of geometric changes cannot be treated. With the development of fully three-dimensional calculations, the range of validity of the work of Hamakiotes and Berger [5] can be assessed, and the important influences of geometry and entrances conditions can be studied. The present paper did not find any evidence of multiple solutions, such as Dennis and Ng [10], Yang and Keller [11], and Hamakiotes and Berger [5], however the nature of our fully three-dimensional are different than the investigation just mentioned.

A major motivation for the present work is its application to problems in physiology. For example, we are quite interested in the implications of our studies for the fluid flow in the aortic arch where early atherosclerotic lesions, important in the development of cardiovascular disease, are found. These lesions are more often found in regions of arterial branching and curvature where the flow field is disturbed. This has motivated the notion that fluid mechanical stresses may act as a localizing factor for the disease. The inability of researchers to precisely and accurately characterize fluid flow in blood vessels has impeded elucidation of the link between fluiddynamics and vascular disease. Thus, a detailed understanding of the time-dependent flow patterns and wall shear stresses are necessary in order to further elucidate the genesis of this process. The present paper is a basic study of fluid flow in this direction, and it's purpose is to serve as a foundation for future studies which will include the realistic geometry of physiological applications.

Contributed by the Fluids Engineering Division for publication in the JOURNAL OF FLUIDS ENGINEERING. Manuscript received by the Fluids Engineering Division October 12, 2000; revised manuscript received June 6, 2001. Associate Editor: P. Bradshaw.

Method of Approach and Analysis

The equations solved in this paper are the time-dependent and incompressible Navier-Stokes equations in control volume form written as:

$$\int\int_A \vec{V}\cdot d\vec{A} = 0 \quad \text{Continuity Equation} \tag{1}$$

$$\int\int\int_V \rho \frac{D\vec{V}}{Dt} dV = -\int\int_A p\, d\vec{A} - \int\int_A \bar{\bar{\tau}}\cdot d\vec{A} \quad \text{Momentum Equations} \tag{2}$$

where $\vec{V}$-is the fluid velocity, p-the dynamic pressure, $\bar{\bar{\tau}}$-the Newtonian stress tensor and ρ-the fluid density. The equations are transformed into a generalized coordinate system in order that we can treat generalized structured grids. These equations are solved using a projection like method (Dandy and Dwyer [12], Pyret and Taylor [13]). The pressure Poisson equation is solved with a matrix free and pre-conditioned version of GMRES (Wigton et al. [14]). However, even with this level of sophistication, the accurate solution of the Poisson equation requires an excessive computational effort. The basic problem appears to be the slow convergence of the pressure field largely caused by the high aspect ratio of the computational cells that result from pipe flows. In order to

have the correct mass flow at each section of the pipe it is necessary to iterate excessively on the Poisson equation leading to a computationally expensive simulation.

In this paper, a new approach to predicting the pressure field is introduced. Exploiting information about the unsteady flow field, this algorithm predicts two accurate pressure corrections:

1 A pressure correction determined by the accelerating flow field in the pipe, and
2 A pressure correction based on the defect or excess of mass at a local pipe cross-section.

With the use of these pressure corrections an order of magnitude improvement in computational efficiency resulted in our calculations.

To illustrate how these pressure corrections are determined, consider a flow into the pipe as shown in Fig. 1 satisfying the Navier-Stokes equations at time t, with mass flow rate $m(t)$. At time $t+\Delta t$ the mass flow increases to $m(t+\Delta t)$. For an incompressible fluid, this causes an increase in the average velocity from $\bar{U}$ to $\bar{U}+\Delta\bar{U}$. This velocity increase must occur at each cross-section of the pipe, since the fluid is incompressible, resulting in an acceleration at each cross-section of $\boldsymbol{acel}=\Delta\bar{U}/\Delta t$. If we assume that the acceleration is associated with a pressure field, we obtain the following relationship in vector form

$$\rho\frac{\Delta\vec{\bar{U}}}{\Delta t}=-\vec{\nabla}p' \quad \text{Pressure Acceleration} \tag{3}$$

where p' is the pressure field that will generate a velocity field of magnitude $\Delta\vec{\bar{U}}$ during a time Δt. For a constant area pipe, this pressure gradient is uniform in the direction of the flow, and it corresponds to a solution of a steady state potential equation with Neumann conditions at the wall and the velocity specified at the exit and inlet.

For an arbitrary shaped pipe, the accelerated flow is assumed to satisfy the following equations

$$\nabla^2\phi=0 \quad with \quad \frac{\partial\phi}{\partial n}=0 \quad on\ solid\ boundaries \tag{4}$$

$$\frac{\partial\phi}{\partial s}=f(x,y,z) \quad at\ the\ pipe\ entrance\ and\ \vec{\nabla}\phi=\vec{V}$$

$$\phi=0 \quad at\ the\ pipe\ exit$$

where n is normal to the wall and s is the streamline direction. The solution can be normalized and made independent of the magnitude of the velocity increase $\Delta\vec{\bar{U}}$. From a physical point of view, this solution corresponds to an assumption that the new flow is irrotational during the time step Δt; however, this irrotational assumption can cause problems at the wall where the zero velocity condition is valid. The use of the pressure field has a direct correlation with boundary layer theory, where the pressure field from a potential flow is used to solve the viscous flow near the wall.

The method can be summarized as follows:

1 Solve the velocity potential flow for the pipe geometry of interest;
2 Normalize and save this solution;
3 Calculate the acceleration pressure field from Eq. (3); and
4 Using this pressure prediction for the acceleration field, solve the Navier-Stokes equations for this time step.

The acceleration pressure field is only an approximation of the pressure field for the Navier-Stokes solution. The remainder of the solution must be obtained from the Poisson equation or other procedures. One procedure to further correct for the pressure field, that we have found to be extremely useful, is a pressure correction based on the average velocity defect at each pipe section. The average velocity defect is defined as

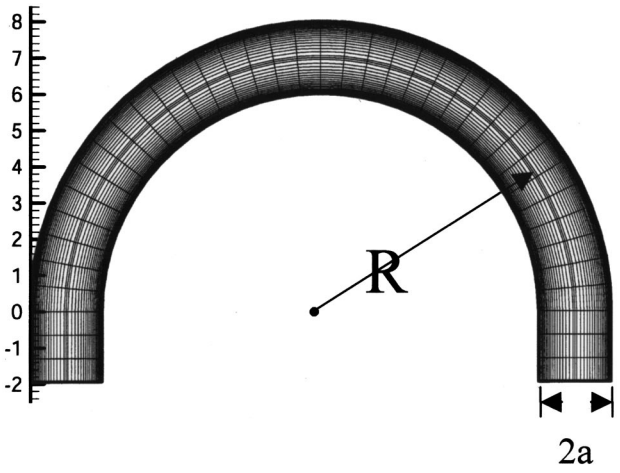

Fig. 1 Mesh system used for the calculations in a curved pipe with circular cross-sections

$$\Delta u'=\left[\left(\int_A\int\vec{V}\cdot d\vec{A}\right)\Big/A_{pipe}-\bar{U}\right] \tag{5}$$

where $\bar{U}$-is the local average velocity and A_{pipe}-is the local pipe area. The local velocity defect can be used to determine a pressure correction using a projection like equation

$$\rho\frac{\Delta\vec{u}'}{\Delta t}=-\vec{\nabla}p''$$

where the solution p'' is the pressure correction based on the local velocity defect in Eq. (5). The overall solution is obtained through the following procedure:

1 Solve the momentum equations with the time dependent pressure term and normal dynamic pressure, $(p+p')$, where p' is obtained from Eq. (3);
2 Determine the local velocity defects and pressure correction, p'';
3 Resolve the momentum equations with the new pressure field, $p+p'+p''$; and
4 Solve and converge the pressure Poisson equation to obtaining the remaining correction to the new pressure field.

The results obtained with this procedure leads to more than an order of magnitude improvement in computational efficiency when compared to using the classical projection method with only the Poisson equation determining the new pressure field. We will now present our investigations of the structure of unsteady pipe flows that will also illustrate these points.

Results

A section of the pipe mesh used in our calculations is presented in Fig. 1. It should be noted that straight pipe sections are added to the entrance and the exit of the curved pipe to limit the interaction of the curved pipe flow with the regions where boundary conditions are applied. The calculations will now be described starting with our validation calculation of steady flow.

(A) Steady Flow in a Curved Pipe, Re=750. We begin with a discussion of steady flow in a curved pipe as shown in Fig. 2. The geometry of the curved pipe and the Reynolds number is chosen to be the same as in the study of Hamakiotes and Berger [5]. A cross section of the pipe geometry is presented in Fig. 1 where the curvature ratio, δ, defined as the ratio of the cross-sectional radius to the curved pipe radius, $\delta=a/R$, is one-seventh, (i.e., $\delta=1/7$). The Reynolds number, $\mathrm{Re}=(\bar{U}D)/\nu$, is taken to be

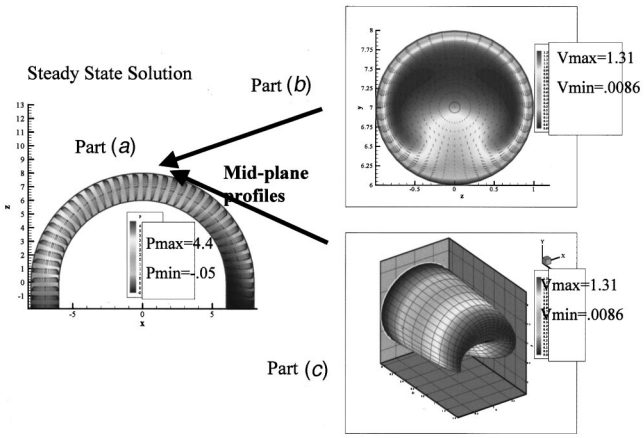

Fig. 2 Steady flow calculations in a curved pipe, Re=750. Part (A)-Symmetry plane pressure contours and velocity vectors. Part (B)-Mid plane primary flow velocity contours and cross-flow velocity vectors. Part (C)-Primary flow velocity shape.

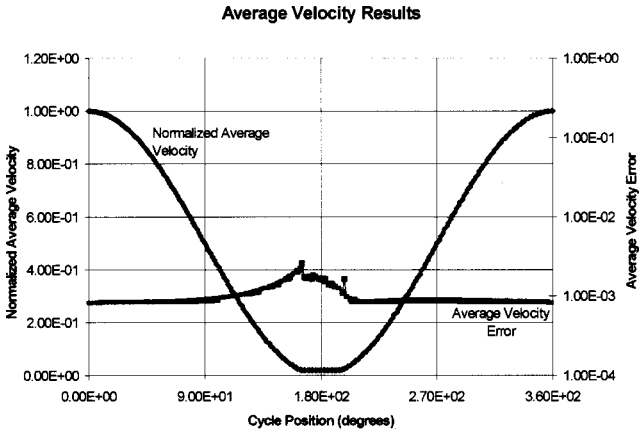

Fig. 3 Cycle average velocity profile and average velocity error

seven hundred and fifty, which effectively determines the Dean number $=\mathrm{Re}\,\delta^{1/2}$. The inflow condition, at the entrance of the pipe, is a uniform flow with a flat velocity profile.

The results, presented in Fig. 2, show three views of the flow: Part (A) shows the normalized velocity vector field and the pressure field in the plane of symmetry of the flow;
Part (B) exhibits the cross-flow vectors and the contour magnitudes of the axial flow for the cross-section located at the middle of the pipe; and
Part (*C*) is the three dimensional representation of the axial flow located at the mid-pipe cross-section. These results are in agreement with the published literature, (Berger et al. [3], Yam and Dwyer [9]) and clearly show the transition of both the velocity and pressure fields from the inlet conditions to a flow dominated by the influence of the curved pipe geometry. The following features should be noted: (a) both the pressure and velocity fields are larger near the outer pipe wall; (b) the cross-flow is down along the outer pipe wall and up towards the pipe center; and (c) the retarded axial flow is near the inner pipe wall. We will refer to these features when discussing the results of other flows calculated in this paper. In particular, it will be shown that highly unsteady flows have a very different character and their solution contains a part that is characteristic of inviscid flows.

Comments on Numerical Accuracy and Convergence

The mesh shown in Fig. 1, 21-radial, 42-periodic, and 41-axial, was the final one chosen to perform the calculations presented in the paper. The minimum mesh that we were able to obtain stable solutions was $11\times22\times21$, however at this resolution there was a serious lack of resolution in the periodic direction. The problem can be seen in Parts (B) and (C) of Fig. 2 by observing the variation of the axial and circumferential flow along the inner section of the pipe. The sharp variations of velocity components require a more refined mesh. In the radial direction we have used a mesh that expanded geometrically from the wall, and a ten percent grid expansion did an adequate job, even with 11 points (a ten percent error in wall shear). We have experimented with the following mesh sizes: $11\times22\times21$, $16\times32\times31$, $21\times42\times41$, and $31\times62\times81$, and we have found that the spatial change in accuracy was less than one percent for the two finest meshes.

The two most computationally expensive parts of our work were the resolution of the time cycle, obtaining a periodic solution, and the convergence of the continuity based Poisson equation. Similar to Hamakiotes and Berger [5] we have found that 240 time steps per cycle gave very good resolution of the accelerations during the cycle, and the variations of peak wall shear between cycles were less than 1 percent after five cycles. We have carried out calculations for 25 cycles, and the variation in peak wall shear between cycles decreased slowly to a value of 0.1 percent. In our fully three-dimensional results with a specific inlet velocity profile, we did not see any evidence of multiple solutions, such as presented by Hamakiotes and Berger [5], Dennis and Ng [10], and Yang and Keller [11].

Even with our acceleration of the convergence of mass continuity with the pressure corrections presented previously, the solution of the Poisson equation required 80 percent of our computational effort. Of course, without the pressure acceleration the computational time increased by an order of magnitude, and the accurate solution of the Poisson equation require 99 percent of the computational time. Some of the quantitative results on the accuracy of the continuity correction will be presented in Figs. 3 and 5.

(B) Unsteady Flow. In general, the flow conditions for this set of calculations are chosen to be similar to the quasi three-dimensional study of Hamakoites and Berger [5], where the pipe geometry is that presented in Fig. 1. The unsteady oscillating inflow condition has the frequency parameter value of $\alpha=15$, where the frequency parameter α is defined as

$$\alpha=a(2\pi f/\nu)^{1/2}$$

In this equation, f is the oscillating flow frequency and ν is the kinematic viscosity of the fluid. The normalized velocity over one cycle $[0,\ 2\pi]$ is plotted in Fig. 3. Each cycle is divided into 240 time steps in our calculations. The base case calculations have mean Reynolds number and amplitude ratio equal to,

$$\mathrm{Re}=(\overline{U}D)/\nu=375 \quad \text{and} \quad \gamma=\overline{U}_{MIN}/\overline{U}_{MAX}=0.95,$$

where $\overline{U}$ is the mean axial velocity averaged over one oscillating cycle, see Fig. 3.

(I) Base Case Calculations: Mean Re=375, $\alpha=15$ and $\gamma=0.95$. As mentioned above, the base case calculations have an oscillating inflow condition. The beginning of the cycle, set at $\phi=0$ deg, corresponds to the maximum velocity of the cycle. The results, presented in Fig. 4, are from the fourteenth cycle of the calculations. Under these conditions, all flow variables have converged to less than 1 percent from previous cycles, and all history effects from the initial conditions have been eliminated.

The results of our base flow calculation, shown in Fig. 4, are divided into two columns. Column one, on the left side of the page, shows the three dimensional axial flow velocity at the pipe mid-section, while the figures on the right column of the page show the pressure contours and the velocity vectors along the symmetry plane of the pipe. The data are plotted at every forty-

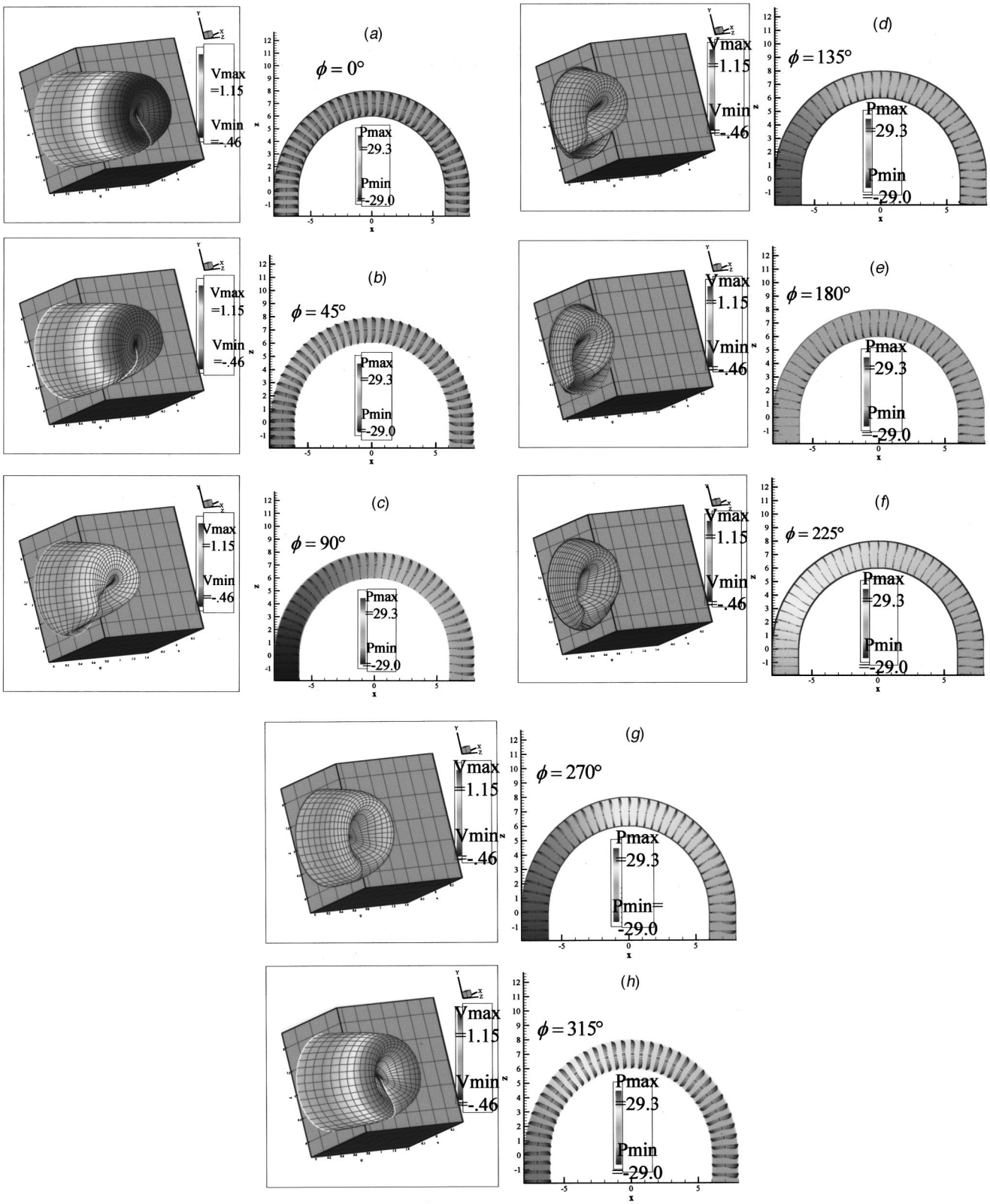

Fig. 4 Pressure contours and axial velocity contours during a complete cycle, Re=375, α=15

five degrees of the cycle. The range for the contour legend values in Fig. 4 is set for the entire cycle, and is not scaled to the local time in the cycle.

The plots in Fig. 4(*a*) correspond to the point of our cycle where the flow is maximum, $\phi = 0$ deg, and the acceleration is zero. Comparing this result to the steady state results presented in Fig. 2, we note that the mean velocity has the same average value in both cases. However, the shape of the velocity profiles is very different. The centrifugal nature of the steady flow profile is not observed in the unsteady calculations. Instead, the flow velocity is

larger near the inner wall than at the center of the pipe. The shape of the profile is the result of the rapid acceleration of the flow to the maximum mean flow. This type of velocity profile was also observed in the work of Hamakiotes and Berger [5], however it does not seem to be widely known within the biofluids research community. The rapid acceleration is essentially inviscid except very near the pipe wall where the no slip condition is applied. This is not unexpected since at a high frequency parameter of $\alpha=15$, the entire cycle time is short compared to viscous wall diffusion times. It is not clear why the fluid near the inner wall has a velocity larger than the pipe center. One reason may be that the essentially inviscid flow has a shorter distance to travel along the inner wall. Another reason could be that it is caused by the fluid ejected by the thin wall boundary layer, which is similar to flow at the entrance of a pipe at elevated Reynolds number (Schlichting [15]) where a similar velocity overshoot can occur. The unsteady flow effects are stronger than the influences of the curved pipe geometry and the flow has a non-centrifugal nature at this value of the frequency parameter. The velocity profiles in Fig. 4(*a*) are almost axisymmetric.

The pressure field plotted in our figures is made dimensionless with the dynamic head, $p=p^*/(\rho\overline{U}^2)$. We note that on the scale of the total pressure change during the entire cycle (sixty dynamic heads), the axial pressure gradient at $\phi=0$ deg, given in Fig. 4(*a*), is rather weak. The magnitude of the pressure loss at $\phi=0$ deg is of the order of four dynamic heads. This result is quite similar to the results for steady flow (see Fig. 2(*a*)). The largest variations in pressure along the pipe occur during the accelerating and decelerating parts of the cycle, near $\phi=90$ deg (Fig. 4(*c*)) and $\phi=270$ deg (Fig. 4(*g*)), respectively.

As the flow decreases in the cycle from $\phi=0$ to $\phi=90$ deg, Figs. 4(*b*) and 4(*c*), we note that at the inner side of the pipe, the velocity profiles become quite retarded. At $\phi=90$ deg the unsteady pressure gradient has reached its maximum unfavorable value and the resulting flow profiles indicate the onset of flow reversal on the bottom wall of the pipe. It appears from these results that the shorter distance over which the pressure differences acts on the inner wall is one of the major factors in the velocity reversal on the inner wall. As the flow decreases to its minimum, Figs. 4(*d*), and 4(*e*), the resulting profiles at the center of the pipe develops into a retarded form, which has very interesting and convoluted positive and negative velocity features. For example at $\phi=180$ deg, the net flow is almost zero, even though there are significant positive flows at the outer pipe wall and negative flows along the inner wall. We note here that these opposite flows are dissipated for lower values of the frequency parameter, since there is more time for viscous influences to act. The positive and negative flows are formed during the deceleration phase of the cycle and they do not dissipate at high values of the frequency parameter.

The acceleration phase of the cycle are shown in Figs. 4(*f*)–4(*h*). The rapid increase of velocity near the pipe walls during this phase is remarkable. At $\phi=270$ deg the unsteady pressure gradient reaches its maximum favorable value, and the minimum velocity occurs at the center of the pipe. This behavior is very similar to those presented by Hamakiotes and Berger [5], but is very different than the steady flow profiles. By the time the cycle reaches $\phi=315$ deg both the inner wall and center flows have significantly recovered from the retarded flow resulting from the deceleration phase of the cycle. However the minimum velocity is still occurring near the center, and this pattern persists until the end of the cycle. It should be mentioned again that this behavior is characteristic of large values of the frequency parameter, and a more traditional flow develops at lower values of the frequency parameter.

(II) Accuracy for the Unsteady Flow Calculations. As described in the methods section, this paper contains new numerical methods for calculating internal flows efficiently. We now present results that highlight the accuracy of our calculations. The

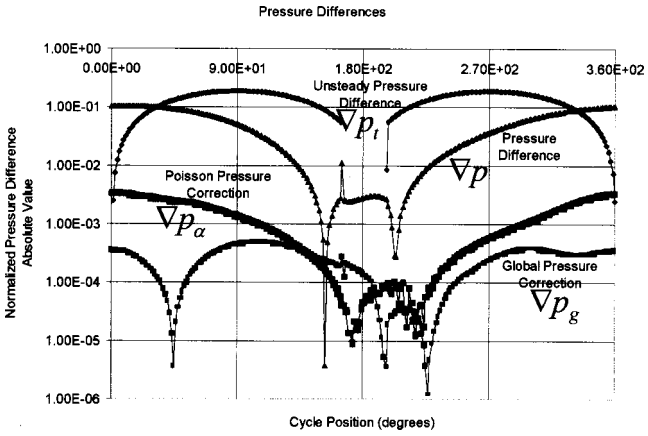

Fig. 5 Analysis of the pressure field during a cycle, Re=375, $\alpha=15$

grid for the curved pipe used in our calculations has mesh sizes of $40\times21\times41$ in the angular, radial and axial directions, respectively. The value of the average velocity error presented in Fig. 3 is define as the quantity

$$abs(\overline{U}(t)_{inlet}-\overline{U}(t)_{mid})/\overline{U}(t)_{inlet},$$

where $\overline{U}$ bar represents the average velocity at the sections indicated in the subscript. This error is small and of the order of one part in a thousand during the entire cycle. This result is obtained with our new algorithm where the unsteady pressure prediction, the global velocity correction, and the solution of the pressure Poisson equation are used. We could further reduce the error in the average velocity and drive the error down to machine zero, but to do so would require iterations on the pressure Poisson equation. This process would require an excessive amount of computational time for accuracy that not is necessary for this problem.

The various contributions to the axial pressure differences are shown in Fig. 5. The four pressure differences plotted are defined as

$$\Delta p=abs(p_{i,j,k+1}-p_{i,j,k})/(\rho\overline{U}^2/2)$$

steady part of pressure gradient

$$\Delta p_\alpha=abs(\alpha_{i,j,k+1}-\alpha_{i,j,k})/(\rho\overline{U}^2/2)$$

contribution of Poisson equation

$$\Delta p_g=abs(p''_{i,j,k+1}-p''_{i,j,k})/(\rho\overline{U}^2/2)$$

pressure error in global mass balance

$$\Delta p_t=abs(p'_{i,j,k+1}-p'_{i,j,k})/(\rho\overline{U}^2/2)$$

unsteady part of pressure gradient

By taking absolute values of these quantities, the reversal of sign of the pressure differences between the accelerating the decelerating parts of the cycle is over-ridden. Again, it should be stated that we have taken pressure differences in the axial direction at the mid-pipe location.

The plots in Fig. 5 are presented at each time step after two iterations of the momentum equations, followed by the solution to the Poisson equation. The results show that the pressure field is dominated by the unsteady pressure difference everywhere except near the maximum velocity part of the cycle (i.e., near $\phi=0$). Analysis of the magnitude of each of the pressure corrections show that the unsteady pressure prediction does a very good job in predicting the new pressure field and accounts for the major portion of the pressure correction in the algorithm. The pressure Pois-

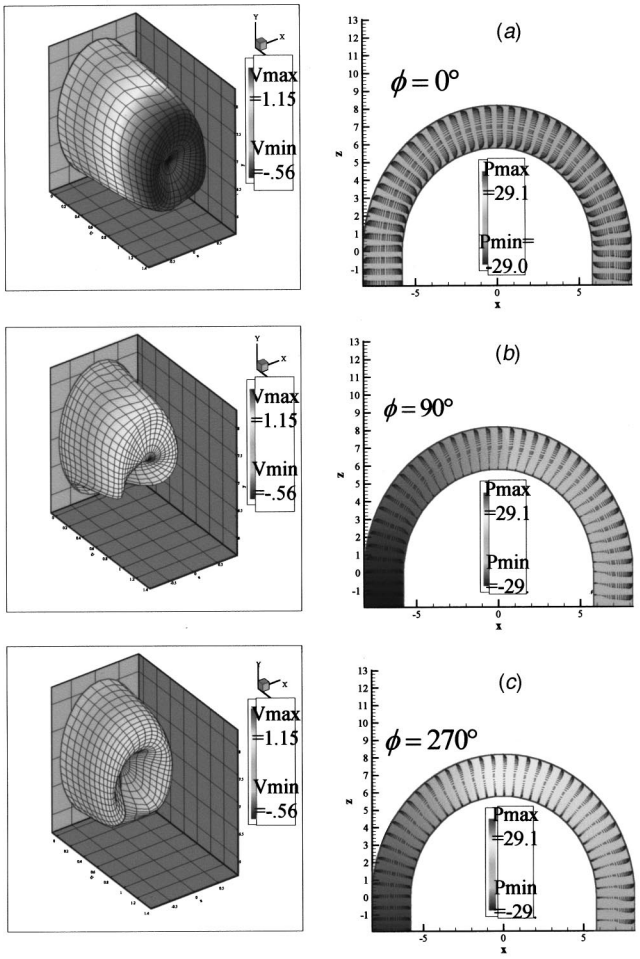

Fig. 6 Pressure contours and axial velocity contours during a complete cycle for an elliptical cross-section, Re=375, $\alpha=15$

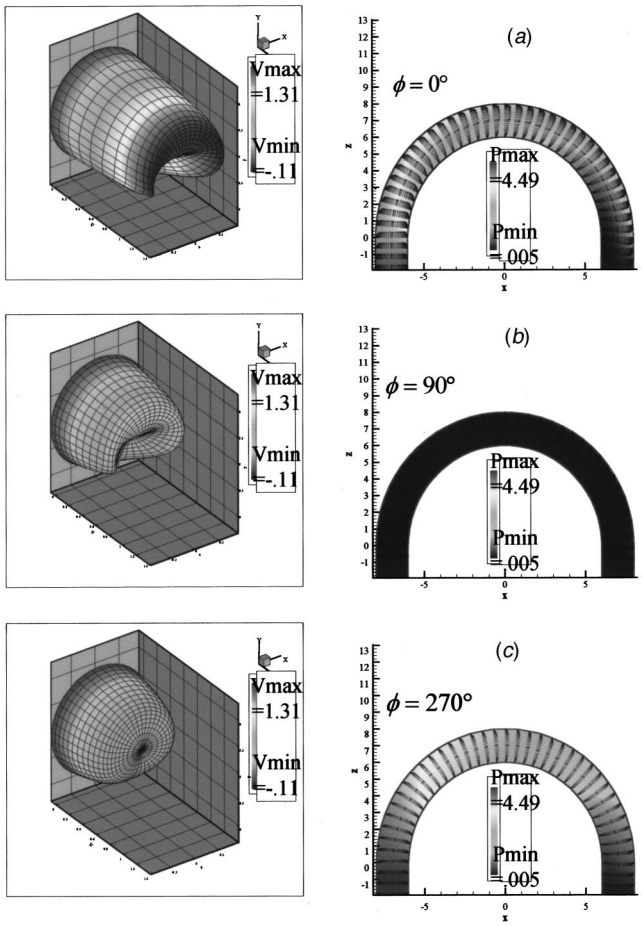

Fig. 7 Pressure contours and axial velocity contours during a complete cycle, Re=375, $\alpha=5$

son equation plays a much smaller role everywhere expect near $\phi=0$. Since the total pressure gradient is the sum of Δp and Δp_t, the accurate prediction of the unsteady pressure field is the reason why we are able to accelerate our algorithms. The global pressure correction shown in Fig. 5 is the pressure error associated with global continuity after the second iteration of the Navier-Stokes equations. The approximate pressure corrections should not be applied more than one or two times, since they do not exactly solve the Navier-Stokes equations. After their application the pressure Poisson equation must be applied to obtain the correct three-dimensional flow field.

It should be mentioned that these new calculations require approximately forty-five minutes per cycle of 240 time steps on a Pentium II 500 PC computer. With this type of speed it is quite easy to calculate ten cycles overnight, and to analyze the data the next day.

C Flow Variations. We will now present some interesting flow variations on our problem. The purpose of these variations is to understand flow physics and to determine the sensitivity of the solution to geometry and frequency parameter.

(I) Variations in Geometry, Elliptical Cross-Section, Re =375, $\alpha=15$. The geometry of the curved pipe was changed to one with an elliptical cross section but with the same area as the round pipe. The ratio of the major to minor axis of the ellipse is 1.44, and the dimensionless values of the radii are 1.2 and 0.833. Some unsteady flow results under similar flow conditions as in the base case calculations are presented in Fig. 6. The plots corresponding to peak flow ($\phi=0$ deg), peak unsteady deceleration ($\phi=90$ deg), and peak acceleration ($\phi=270$ deg) are presented. The first column plots the three-dimensional axial velocity profile at mid-pipe and the second column plots the pressure field and the velocity vector field at the symmetry plane. In general, the characteristics of the flow in the pipe with elliptical cross are similar to those with a round cross-section. This indicates that the effects of the change in the shape of the cross sections are rather small. For a high frequency parameter flow, $\alpha=15$, the flows in both cases, Figs. 4 and 6, are very similar, and they have the same overall pressure range, velocity maximum, and axial velocity profiles. Both flows are dominated by the acceleration pressure gradient. Therefore, from the viewpoint of flow structure, there does not seem to be an obvious advantage or disadvantage to having a curved pipe with elliptical shaped cross sections.

(II) Change in the Frequency Parameter, Re=375, $\alpha=5$. The next flow variation consists of a curved pipe with round cross sections and with a lower frequency parameter, $\alpha=5$. For this value of the frequency parameter, one flow cycle is nine times slower relative to the viscous time scale. The flow results, shown in Fig. 7, are very different when compared to the high frequency parameter flow results in Fig. 4. At the top of the cycle, ($\phi=0$ in Fig. 7(a)), we note that the plots are very similar to the steady state flow presented in Fig. 2, where both the velocity and pressure fields have similar values. These results suggest that this flow is almost locally steady. When the pressure gradient reaches its maximum unfavorable value, ($\phi=90$ deg), the velocity profile has a strong centrifugal flow behavior with no hint of a flow reversal. During the maximum favorable acceleration, ($\phi=270$ deg), the shape of the velocity profile appears to be very

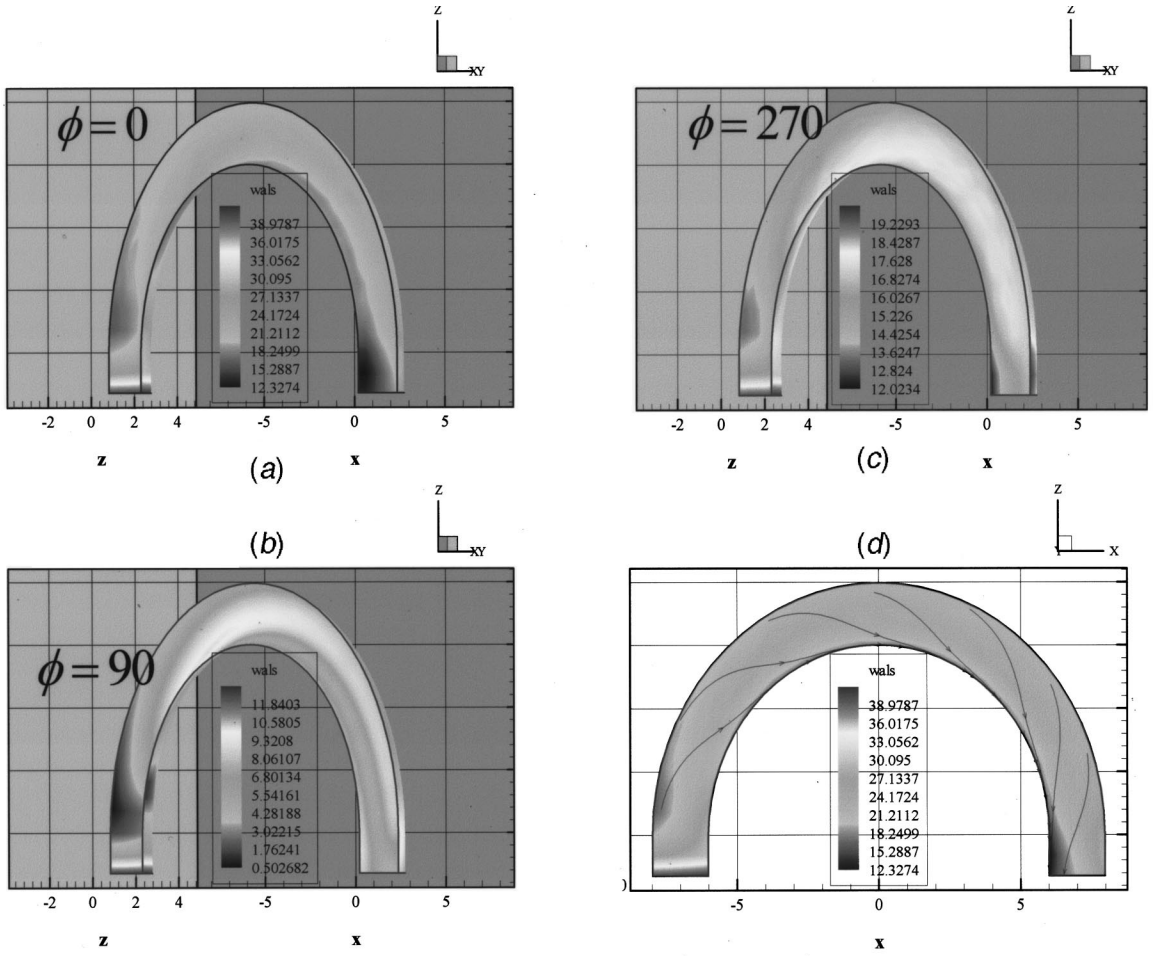

Fig. 8 Wall shear contours during a cycle, Re=375, $\alpha=15$

similar to a local steady pipe flow. That is, the profiles are quite full except in the outflow half of the pipe where a slight centrifugal bias in the flow develops. In general, the main characteristics of flows with high and low values of the frequency parameter differ considerably.

(C) Wall Shear Stress Studies. For many applications, especially in biological flows, the wall shear stress plays a critical role. Early atherosclerotic lesions, for example, are thought to develop preferentially in arterial regions exposed to low and/or oscillatory wall shear stress (Nerem [16], Ku et al. [17], Moore et al. [18], Friedman and Deters [19]). In this section, the wall shear stress distribution of the flows studied and a general discussion of the results obtained are presented. The total wall shear stress is defined as

$$\tau_w = \frac{|\tau_1| + |\tau_2|}{\mu \bar{U}/a}$$

where τ_1 and τ_2 are two orthogonal components of the shear stress on the surface of the wall.

(I) Wall Shear Stress for Base Case Calculations. Figures (8*a*)–(8*c*) show contours of the total wall shear stress at three significant cycle times in the base flow calculations. The base flow has circular cross sections and a frequency parameter value of 15. The contours in Figs. 8(*a*)–8(*d*) are renormalized at each time of the cycle in order to obtain maximum clarity for the presentations. They also give a three-dimensional view of the shear stress as viewed from the interior of one-half of the pipe wall.

The maximum wall shear stress occurs at the maximum inflow part of the cycle $\phi=0$ deg as shown in Fig. 8(*a*) and 8(*d*) and this maximum shear occurs at the pipe entrance. This is due to the flat entrance velocity profile used. It should also be noted that the flow at the inner wall of the entrance retains a high wall shear stress value. Also, on the outer wall, about one diameter in from the entrance, there is an area where the shear stress has a rather low value. This condition is caused by the tendency of the flow to take the shortest path along the inner wall. Near the exit of the pipe, in the area where the curve pipe changes to a straight section, another special interaction of the flow occurs, which tends to increase the wall shear on the outer wall and decrease it on the inner wall. This change in wall shear can be simply explained by the continuation of the centrifugal nature of the flow. The values of the wall shear away from the pipe entrance and at the exit compare quite well to those obtained by Hamakiotes and Berger [5]. The instantaneous surface streamlines plotted in (8*d*) show the same data as Fig. 8(*a*) but viewed from a different angle. It is clear from Fig. 8(*d*) that there are significant cross-flows along the pipe surface.

As the flow decelerates there is a significant decrease in the wall shear. Typical values are shown in Fig. 8(*b*) corresponding to the maximum deceleration point, $\phi=90$ deg of the cycle. In a general sense, the wall shear pattern at this time is similar to that presented for a previous time, $\phi=0$, Fig. 8(*a*) with the exception that the level of wall shear stress is significantly lower. The entrance region of the flow is longer, and as the flow develops, there is a tendency for the wall shear to be higher on the outer wall

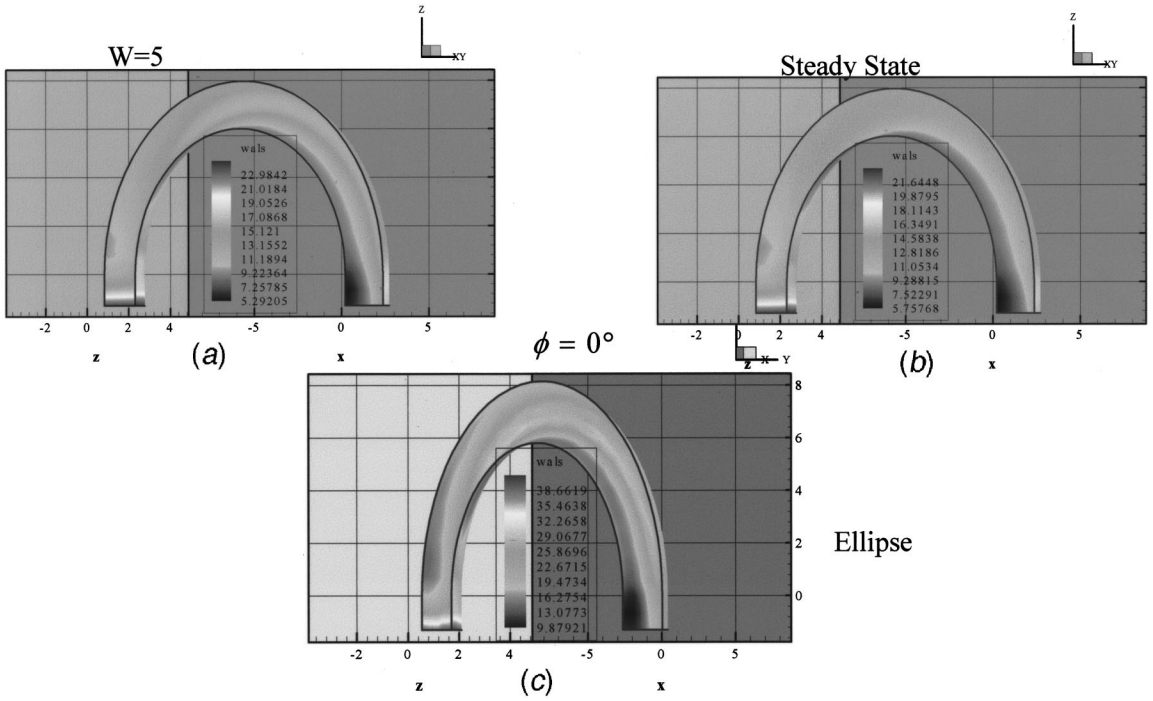

Fig. 9 Wall shear contours at maximum flow for flow variation cases

relative to the inner wall. It should also be noted that the entrance region experiences quite low wall shear values as the flow adjusts to the pipe curvature.

The shear stress distribution during the favorable pressure gradient part of the cycle is shown in Fig. 8(*c*), $\phi = 270$ deg. Again, this distribution has features that are similar to the two previous times presented. The major difference is that the distribution of the wall shear stress is relatively homogeneous and varies by only forty percent over the entire pipe. In fact, if the entrance and exit regions are neglected the wall shear varies by less than ten percent over the entire curved pipe. This rather homogeneous wall shear is a direct reflection of the inviscid acceleration of the flow.

(II) Shear for Cases Where the Flow is Varied From Base Case Calculations. Presented in Fig. 9(*a*) is the wall shear stress distribution for the case where the frequency parameter is five, $\alpha = 5$. The results presented in this figure are for the time when the inflow cycle is at maximum flow (i.e., $\phi = 0$). Just inside of the entrance region, the flow in Fig. 9(*a*) develops larger values of wall shear on the inner wall and smaller values on the outer wall. These results are consistent with the velocity profiles presented in Fig. 7, and they again indicate that the flow is almost quasi-steady. The two most notable differences in the features, when compared to the base case results, are the lower values of wall shear and the development of a pattern that is very similar to that of steady flow in a curved pipe of the same geometry, see Fig. 9(*b*). Comparing this low frequency parameter case with the steady flow case (Fig. 9(*b*)), we note that the maximum wall shear values for both cases have almost the same magnitude, with the unsteady flow case having marginally larger values. We reiterate, based on the comparison between these two cases, flow in a curved pipe with a frequency parameter of five is essentially quasi-steady during the peak velocities in the cycle. However, there are unsteady influence during the deceleration and acceleration parts of the cycle.

The wall shear distribution for the flow with an elliptical cross-section is shown in Fig. 9(*c*) for a high frequency parameter. A comparison of this flow with the base case results (Fig. 8(*a*)), shows that the wall shear patterns and values of total shear are very similar. The only noticeable difference is at the extended entrance region on the outer wall for the elliptical cross-section. Here, the region of lower wall shear on the outer wall is extended further into the curved pipe relative to the base case. Our initial expectations were that larger changes would occur for the case of flow in a curved pipe with elliptical cross-sections, however, as shown in Fig. 9(*c*), the changes that are calculated are quite small relative to the base case.

Summary and Conclusions

In this paper we have successfully calculated a range of fluid flows in curved pipes under highly unsteady flow conditions. Variations include changes in geometry as well as in the frequency parameter. Our calculations give new insight into the structure and nature of these flows. Major findings resulting for our study are:

1 A new and efficient method is developed to calculate time-dependent flows in curved pipes in three-dimensions. The method makes use of the flow physics to predict and correct the time-dependent flow pressure field. This speed up is substantial, and it has reduced the number of iterations for convergence of the pressure field by an order of magnitude. For unsteady flows, fast accurate solutions are also obtained where only one GMRES calculation is required in solving the Poisson equation.

2 The calculations reveal that the flows at high frequency parameters, $\alpha = 15$, exhibit an inviscid-like nature. This effect dominates over the effect of the geometry of the curved pipe that favors a centrifugal nature for the flow. This inviscid like flow is caused and driven by the unsteady pressure field that is required to accelerate the flow. This observation is the key to understanding why the unsteady pressure correction in our algorithms work well for high frequency flows and almost as well for low frequency flows.

3 The effect of changing the cross section of our curved pipe to one with elliptical cross-sections is small for flows at high frequency parameters.

4 During the flow deceleration phase of the cycle, the flow velocity profile becomes quite retarded on the inner pipe wall. These retarded profiles persist throughout the low inflow parts of the cycle.

5 During flow accelerations at high frequency parameter values, the velocity attains its maximum values near the pipe walls with a local minimum near the centerline of the curved pipe.

References

[1] Dean, W. R., 1927, ''Note on the Motion of a Fluid in a Curved Pipe,'' Philos. Mag., **4**, p. 208.

[2] Pedley, T. J., 1980, *The Fluid Mechanics of Large Blood Vessels*, Cambridge University Press.

[3] Berger, S. A., Talbot, L., and Yao, L. S., 1983, ''Flow in Curved Pipes,'' Annu. Rev. Fluid Mech., **15**, p. 461.

[4] Chung, J. H., and Hyun, J. M., 1994, ''Heat Transfer from a Fully-Developed Pulsating Flow in a Curved Pipe,'' Int. J. Heat Mass Transf., **37**, No. 1, pp. 43–52.

[5] Hamakiotes, C. C., and Berger, S. A., 1990, ''Periodic Flows through Curved Tubes,'' J. Fluid Mech., **210**, pp. 353–370.

[6] Karahalois, G. T., and Panagopoulos, A., 1989, ''Oscillatory Flow in a Curve Annular Pipe,'' Phys. Fluids A, **1**, No. 7, pp. 11-4–1111.

[7] Riley, N., 1998, ''Unsteady fully-developed flow in a curved pipe,'' J. Eng. Math., **34**, No. 1-2, pp. 131–141.

[8] Sumida, M., Sudou, K., Wada, H., 1989, ''Pulsating Flow in a Curved Pipe-Secondary Flow,'' JSME Int. J., Ser. II, **32**, No. 4, pp. 523–531.

[9] Yam, Clement, and Dwyer, H. A., 1993, ''Unsteady Flow in a Curved Pipe,'' Fluid Dynamics in Biology, Contemporary Mathematics 141, American Mathematical Society.

[10] Dennis, S. C. R., and Ng, M. C., 1982, ''Dual Solution for Steady Laminar Flow through a Curved Pipe,'' Q. J. Mech. Appl. Math., **35**, p. 305.

[11] Yang, Z., and Keller, H. B., 1986, ''Multiple Laminar Flows through Curved Pipes,'' Appl. Numer. Math., **2**, p. 257.

[12] Dandy, D. S., and Dwyer, H. A., 1990, ''A Sphere in Shear Flow at Finite Reynolds Numbers: Effect of Shear on Particle Lift, Drag, and Heat Transfer,'' J. Fluid Mech., **216**, pp. 381–410.

[13] Pyret, R., and Taylor, T. D., 1983, *Computational Methods for Fluid Flow*, Springer-Verlag.

[14] Wigton, L. B., Yu, N. J., and Young, D. P., 1985, ''GMRES Acceleration of Computational Fluid Dynamics Codes,'' AIAA Computational Fluid Dynamics Meeting, Cinn, Ohio, pp. 67–74.

[15] Schlichting, H., 1968, *Boundary-Layer Theory*, McGraw-Hill, Sixth Edition.

[16] Nerem, R. M., 1992, ''Vascular fluid mechanics, the arterial wall, and atherosclerosis,'' ASME J. Biomech. Eng., **114**, pp. 274–282.

[17] Ku, D. N., Giddens, D. P., Zarins, and C. K., Glagov, S., 1985, ''Pulsatile flow and atherosclerosis in the human cartoid bifurcation,'' Atherosclerosis (Dallas), **5**, pp. 293–302.

[18] Moore, J. E., Xu, C., Glagov, S., Zarins, C. K., and Ku, D. N., 1994, ''Fluid wall shear stress measurements in a model of the abdominal aorta: oscillatory behavior and relationship to atherosclerosis,'' Atherosclerosis (Berlin), **110**, pp. 225–282.

[19] Friedman, M. H., Deters, O. J., 1987, ''Correlation among shear rate measures in vascular flows,'' ASME J. Biomech. Eng., **109**, pp. 25–26.

J. Mi[1]
ARC Research Fellow

G. J. Nathan
FCT Senior Lecturer

D. S. Nobes[2]
Research Fellow

Department of Mechanical Engineering,
The University of Adelaide,
South Australia 5005,
Australia

Mixing Characteristics of Axisymmetric Free Jets From a Contoured Nozzle, an Orifice Plate and a Pipe

The differences in mixing performance between axisymmetric turbulent jets issuing from three common types of nozzle, viz. a contoured (or smooth contraction) nozzle, a sharp-edged orifice and a long pipe, are investigated. The investigation is carried out using both qualitative flow visualizations and quantitative measurements of the centerline passive temperature. It is revealed that the jet issuing from an orifice plate provides the greatest rate of mixing with ambient fluid, while the pipe jet has the lowest rate. Physical insight into the differences is explored using a planar imaging technique and measurements of power spectra of the fluctuating velocity. [DOI: 10.1115/1.1412460]

1 Introduction

Turbulent jets play an important role in many applications, including burners and chemical reactors, by providing a means of mixing different fluids. Three alternative types of nozzle are commonly used to generate practical jet flows, namely, smoothly contracting (*contoured*) nozzles, long pipes, and orifice plates. Most fundamental research on circular (and planar) jets has been performed using contoured nozzles which produce a nearly uniform ''top-hat'' velocity profile and a laminar flow state at the nozzle exit (e.g., Crow and Champagne [1], and Becker et al. [2]). Numerous studies have also been performed on circular jets issuing from a long pipe (e.g., Lockwood and Moneib [3], Pitts [4,5], Richards and Pitts [6]). The exit velocity profile of a long pipe jet is nonuniform, and can be described empirically by a power-law. The boundary layer is also in a fully turbulent state at the pipe exit. By comparison, investigations on circular jets issuing from orifice plates are very limited (Wilson and Danckwerts [7]), possibly because the initial velocity profile and the near-field flow structure are more complex. However, orifice plate nozzles are much easier to manufacture than contoured nozzles, especially when the shape is noncircular. As a result, most investigations on noncircular jets have been performed using orifice plates (e.g., Quinn [8,9], Mi et al. [10], Koshigoe et al. [11], Gutmark and Grinstein [12]).

There has been increasing evidence that the impact of initial conditions on the downstream development of a flow is significant even in the far-field, self-similar region (e.g., Wygnanski et al. [13] and George [14]). However, it is only recently that a direct comparison of the scalar field of jets from a smooth contraction and a long pipe has confirmed that the mixing field throughout the two jets are different (Mi et al. [15]). Clearly, an orifice plate will generate a circular jet with an initial flow condition significantly different from that generated by the other two types of nozzle. It is thus anticipated that the corresponding mixing performance of an orifice jet may also be different.

An extensive literature survey has not revealed any direct comparison of the mixing characteristics of jets issuing from the three types of nozzle described above, although each type of nozzle has been used for independent investigations. Unfortunately, it is not possible to separate the effects of the initial conditions from the effects of experimental errors and those associated with inevitable differences in the surrounding environment, since few previous papers reported full experimental details and measurement uncertainties. Consequently, it is not possible from the literature alone to quantify the difference between mixing characteristics of the circular jets issuing from these three types of nozzle. In this context, we have designed experiments to conduct passive scalar measurements using temperature as a marker and flow visualizations using identical experimental setup and surrounding environment. This minimizes the experimental uncertainty.

The first objective of the present study, therefore, is to provide a direct comparison of the mixing characteristics of jets issuing from a sharp-edged orifice, a contoured nozzle, and a long pipe. The second objective is to explore the physical mechanisms responsible for any differences identified in the comparison.

2 Experiment Details

Full details of the present experimental setup have been provided by Mi et al. [15] so that only a brief description is provided here. The jet facility consists of a vertical, cylindrical plenum chamber with an internal diameter of 80 mm and a length of 900 mm. Filtered and compressed air was supplied through the plenum to a nozzle. Three different types of circular nozzle are employed for the present study. The contoured nozzle has a profile described by the relation $R=40-33\sin^{1.5}(90+9x/8)$, contracting from a diameter of 80 mm to the exit diameter (d) of 14 ± 0.1 mm. Here, x is the axial coordinate originating from the center of the nozzle exit plane. The exit diameter of the sharp-edged orifice plate is also $d=14\pm0.15$ mm. The pipe has an internal diameter of $d=10\pm0.1$ mm and length of 740 mm. For all the jets, the Reynolds number $\mathrm{Re}_d\equiv U_o d/\nu$ is nominally set to 16,000 with an uncertainty of $\pm2\%$, where U_o is the bulk velocity through the nozzle exit and ν is the kinematic viscosity of the fluid.

(a) Temperature and Velocity Measurements. A small passive temperature differential was used to mark the scalar field, following Mi et al. [15]. The jet facility and nozzles were insulated so that a uniform temperature profile was achieved with less than 1.2% variation at the exit plane of any of the nozzles. The exit temperature, T_o, is selected to be 50°C above ambient. Present measurements of temperature were conducted in the range $x/d\leqslant40$ using a cold-wire probe. The probe consists of a short

[1]The Corresponding Author. e-mail: jcmi@mecheng.adelaide.edu.au
[2]Current Address: Optical Sensors Group, Department of Power Engineering and Propulsion, School of Mechanical Engineering, Cranfield University, Cranfield, Bedfordshire MK43 OAL, United Kingdom.

Contributed by the Fluids Engineering Division for publication in the JOURNAL OF FLUIDS ENGINEERING. Manuscript received by the Fluids Engineering Division March 22, 2000; revised manuscript received June 29, 2001. Associate Editor: J. E. Bridges.

length of Wollaston wire (Pt-10%Ph) operated with an in-house constant current (0.1 mA) circuit. At this low current, the sensitivity of the wire to velocity fluctuations was negligible. Two sizes of the wire were used: $d_w = 1.23\,\mu$m for $x/d \leq 5$ (high speed region) and $d_w = 0.63\,\mu$m for $x/d > 5$ (low speed region). The wire length-to-diameter ratio was taken for both cases to be $l_w/d_w \approx 1000$, which is sufficiently large to ignore any possible low-frequency attenuation (Paranthoen et al. [16]).

Present measurements of jet velocities very near to the exit plane of each nozzle and those of velocity power spectra in the shear layers were carried out using a single hot-wire anemometer (5 μm tungsten) probe with an overheat ratio of 1.5. The measurements were conducted in the unheated air jets also at $\mathrm{Re}_d = 16{,}000$. The voltage signals for both temperature and velocity were offset and amplified through the circuits and then digitized by a personal computer with a 12-bit A/D converter. The signals were filtered at a cutoff frequency $f = f_c$ (typically 2.8 kHz) chosen to eliminate high-frequency noise and a sampling frequency of 2 f_c was employed. The record duration was 20–30 seconds, in which typically 110,000 to 310,000 (instantaneous) data points were collected.

Experimental uncertainties in the mean and rms values of temperature and velocity have been estimated based on inaccuracies in the calibration data and the observed scatter in the measurements. They are approximately $\pm 1.5\%$ for the mean temperature, $\pm 2.0\%$ for the rms temperature, $\pm 1\%$ for the mean velocity and $\pm 1.2\%$ for the rms velocity.

(b) Flow Visualizations. Present qualitative flow visualizations were carried out using the Mie scattering technique developed previously by Rosenwig et al. [17] and Becker et al. [18,19]. (A detailed description of the theory and application of this technique was reviewed by Becker [20].) For the present investigation, air, seeded with oil droplets of approximately 0.6 μm, was introduced at ambient temperature through each of the nozzles at $\mathrm{Re}_d = 16{,}000$. Laser pulses of less than 4 ns at 532 nm from an Nd:YAG laser were expanded to form a thin (<0.25 mm) light sheet using a cylindrical lens. The light scattered from the seeded particles was captured by a slow scan, cooled CCD camera which has a two-dimensional array of 576×374 pixel's. The camera was oriented perpendicular to the plane of the light sheet. The images so collected were transferred to the control computer via a GPIB interface, which was also used for communication with, and control of, the detector. A target image was used to provide accurate scaling of the flow.

3 Results and Discussion

3.1 Initial Conditions of Jets From Different Nozzles. Due to the satisfactory insulation, the mean temperature exit profiles from the three nozzles were uniform well within experimental uncertainties, and there was also no significant difference in the rms temperature exit profiles. However, the difference in geometric profile of the three nozzles resulted in significantly different exit velocity profiles, which are presented as follows. The jet exit velocity profiles from the contoured nozzle and the pipe were measured at $x/d \approx 0.05$ while that from the orifice plate was measured at $x/d \approx 0.1$. Figures 1(*a*) and 1(*b*) present radial profiles of the normalized mean (U/U_{cl}) and rms (u'/U_{cl}) of the axial velocity for the three jets. Herein the subscript "*cl*" refers to the quantity obtained at the centerline.

There are distinct differences in the exit profiles of both U/U_{cl} and u'/U_{cl} for the three jets. The radial profile of U/U_{cl} is top-hat in shape for the jet issuing from the contoured nozzle, while that for the pipe jet is well described by the one-seventh power law which relates to a fully-developed pipe flow. The exit profile for the jet from the orifice plate is different again with the highest velocity located toward the edge of the jet. The orifice also generates a vena contracta immediately downstream from the exit plane, so a radially inward velocity component exists at the edge

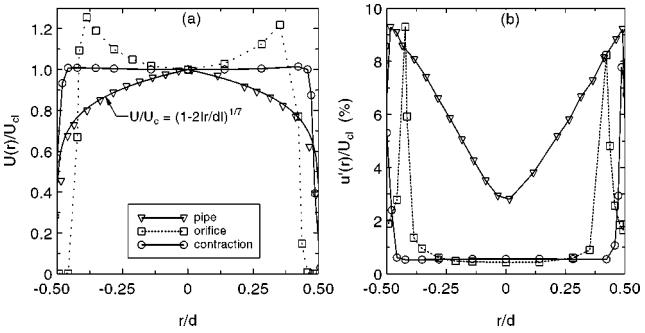

Fig. 1 Radial profiles of velocity mean (U) and rms (u') values obtained at x/d=0.05 in the jets issuing from the contoured and pipe nozzles and at x/d=0.1 in the orifice jet. (*a*) U/U_{cl}; (*b*) u'/U_{cl}.

of the jet. Likewise, differences exist in the initial turbulence profiles of the three jets. For the contoured nozzle, the relative turbulence intensity u'/U_{cl} is low (about 0.5%) in the middle of the jet ($r < 0.45d$) and high (about ~8%) in the thin shear layer at the edge ($r > 0.45d$). For the orifice the turbulence is also relatively low at the center (about 0.4%) and higher at the edges (about ~9%). In contrast, the relative turbulence intensity, u'/U_{cl}, from the pipe is generally much higher throughout the exit plane. It typically varies between 3% ($r = 0$) and 9.5% ($r = d/2$), consistent with data reported by Papadopoulos and Pitts [21].

3.2 Mixing Performance of Jets From Different Nozzles. Figures 2(*a*)–(*c*) show the typical planar images of the instantaneous scalar field of each jet, captured using Mie scattering (Becker [20]), over the region $x/d \leq 18$. The images are scaled to provide the same dimensionless field of each jet to facilitate direct comparison. They were selected from several hundreds of such images for each jet as being representative of the respective mixing fields. The influence of the nozzle type, or more precisely different initial flow conditions (documented above), on turbulent mixing is evident in the images, with significant differences in the distribution of high concentration (i.e., white color in Fig. 2) nozzle fluid. The presence of high concentration nozzle fluid in the jet issuing from the pipe is seen in the central region as far downstream as $x/d \approx 14$, while it is rarely found beyond $x/d \approx 8$ for the other two flows. This suggests that the pipe jet mixes the two streams of fluid least effectively. The images also appear to suggest that the orifice plate produces the jet with the highest mixing rate.

To quantify the differences visually observed above, measurements of the scalar field were performed in each jet over the range $x/d \leq 40$ using a passive temperature differential relative to ambient as a scalar marker. Figures 3 and 4 display the centerline decay of the normalized mean temperature (T_{cl}/T_o) and the centerline variation of the locally normalized rms temperature (θ'_{cl}/T_{cl}), respectively. In order to compare the spreading rates of the jets, we also estimated, from radial profiles of the mean temperature (T), the half-radius, $R_{1/2}$, which is defined as the radial location where $T = T_{cl}/2$. The streamwise variations of $R_{1/2}/d$ for the jets are shown in Fig. 5. The key trends in the present data are consistent with those well established in the literature (e.g., Gouldin et al. [22]; Pitts 1991 [4,5], Richards and Pitts [6], Mi et al. [15]). For $x/d \geq 10$, $R_{1/2}$ varies approximately linearly with x in all the jets. Also, the ratio $T_o/T_{cl}(x)$, see the insert of Fig. 3, exhibits a linear relation with x for $x/d \geq 10$, indicating that $T_{cl}(x) \sim 1/x$ in the region sufficiently downstream from the nozzle.

It is of fundamental interest to note from Figs. 3 and 5 that the jet from the orifice plate clearly demonstrates the highest decay rate of T_{cl} and the widest spreading angle of $R_{1/2}$. This suggests that the orifice jet has the highest rate of entrainment of the cold

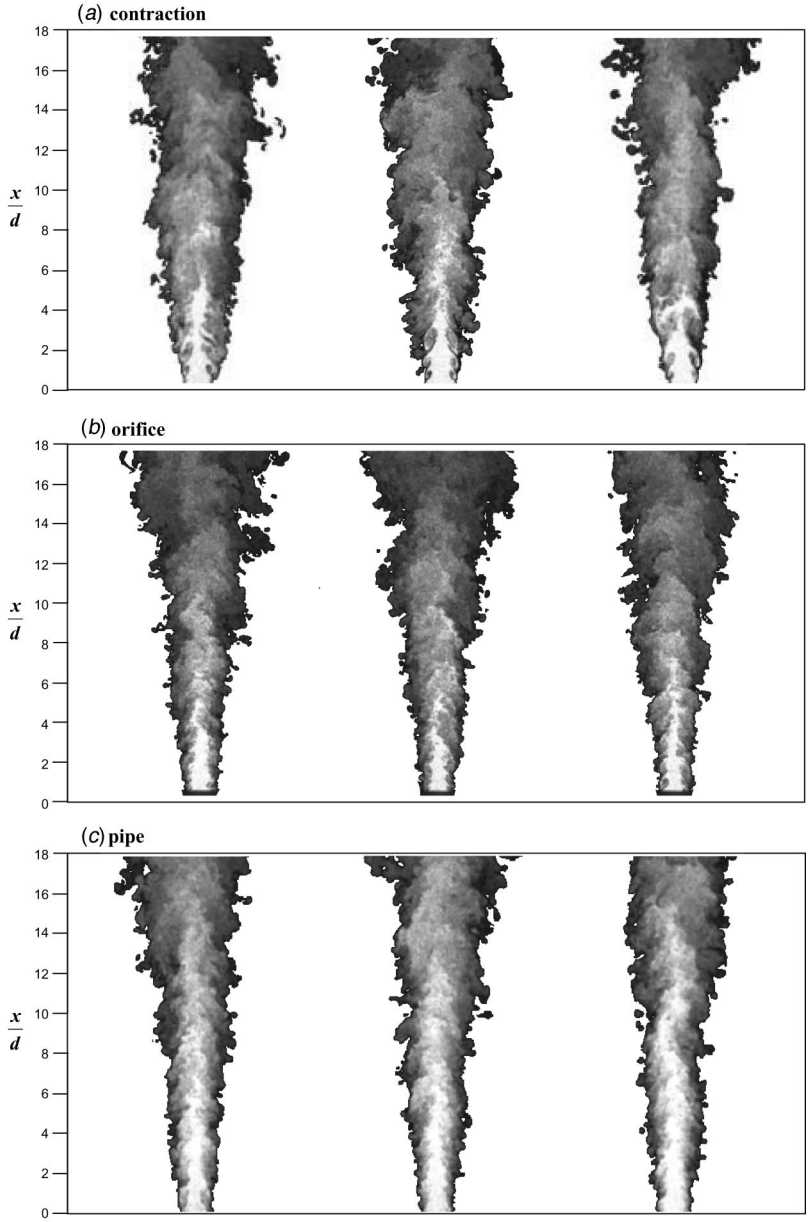

Fig. 2 Instantaneous planar images of the scalar fields of three jets issuing from (*a*) the contoured nozzle, (*b*) the orifice plate and (*c*) the long straight pipe

ambient air fluid. The figures also demonstrate that the pipe jet has the lowest decay rate of T_{cl} and the narrowest spreading angle of $R_{1/2}$. These results are consistent with the trends indicated by the qualitative flow-visualizations (Fig. 2). The results for the pipe jet are also consistent with the findings of Mi et al. [15] from the investigation of the scalar fields of jets from a contoured nozzle and a pipe. That investigation found, both from a review of previous investigations of axisymmetric jets and from direct experiments, that the mean scalar field of a pipe jet decays and spreads at a lower rate than that of a contoured nozzle jet.

Figure 4 shows that the locally normalized rms value θ'_{cl}/T_{cl}, i.e., the relative temperature fluctuation intensity along the centreline, is highest for the contoured nozzle jet and lowest for the pipe jet throughout the measured range. This difference results from different underlying turbulent structure in the three jets, as discussed later.

3.3 Differences in the Mixing Mechanisms of the Jets From the Three Nozzles. Insight into the physical mechanisms responsible for the different mixing rates of the three jets can be obtained from the images of Fig. 2 and the power spectra of the velocity fluctuations shown in Fig. 6. Measurements of the power spectra were performed within the shear layer of each jet at $x/d = 3$. The normalization is taken so that the dimensionless frequency is $f^* \equiv fd/U_{cl}$ and the area under the spectrum curve is unity, i.e., $\int \Phi_u^*(f^*) df^* = 1$.

There are clear differences in the initial underlying flow structure of the three jets (Fig. 2). Well-defined coherent vortical structures are visually evident at $x < 4d$ in the jet from the contoured nozzle. Likewise, coherent structures are also evident along the potential core of the orifice jet, although not as well defined as those from the contoured nozzle. In contrast, there are few coherent structures discernible in the near-field region of the pipe jet. These differences are also reflected by the velocity power spectra, Φ_u, within the shear layer. Figure 6 shows that there is a broad peak in Φ_u for the jets from the contoured nozzle and the orifice plate, reflecting the quasi-periodic passage of coherent structures

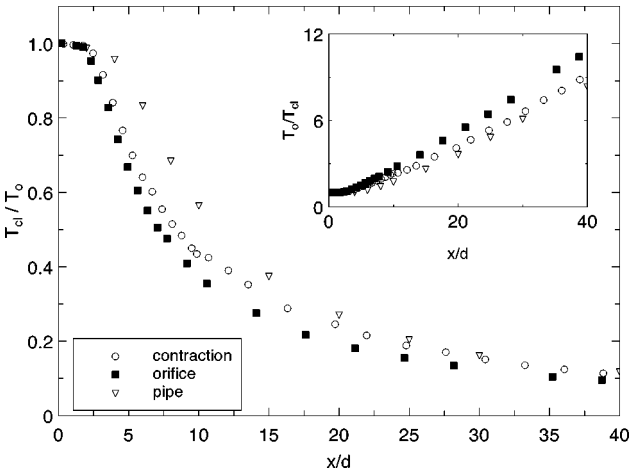

Fig. 3 Normalized centerline mean temperature (T_{cl}) in three axisymmetric jets issuing from a contoured nozzle (○), an orifice plate (■) and a long pipe (▽)

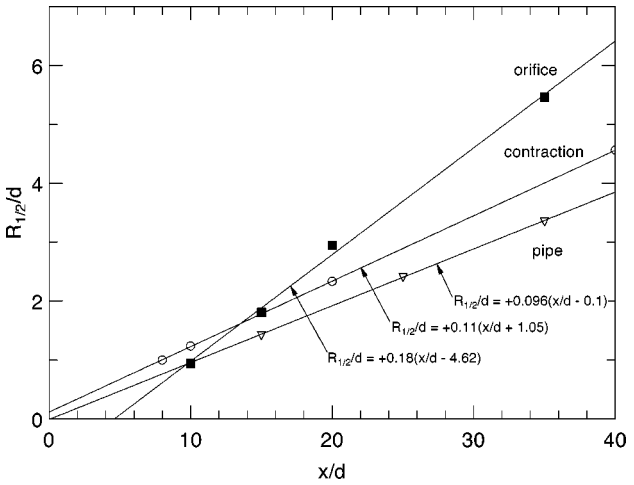

Fig. 5 Streamwise variations of the mean temperature half-widths ($R_{1/2}$) of three axisymmetric jets issuing from a contoured nozzle (○), an orifice plate (■) and a long pipe (▽)

in the near field of the jets. That the structures in the orifice jet are typically not as well defined as those from the contoured nozzle is evidenced by the broader peak in the spectra. The broad peak is seen to be centered at $f^* \approx 0.40$ with the contoured nozzle (which falls within the literature data, 0.3-0.6, as reported by many previous studies such as Crow and Champagne [1] and Ho and Nosseir [23]) and at $f^* \approx 0.70$ with the orifice. This reflects that the coherent structures occur generally at a higher frequency for the orifice jet than for the jet from the contoured nozzle. By comparison, no peak is present in Φ_u for the pipe jet, suggesting that any large-scale structure which may be present in the pipe jet is aperiodic and does not occur regularly.

The differences in θ'_{cl} of the three jets, Fig. 4, are deduced to be a direct result of the initially different underlying structure of these jets. For both the jet from the contoured nozzle and that from the orifice plate, large-scale engulfment of ambient cold air by the highly coherent structures results in a high amplitude of the scalar (temperature) fluctuations, and thus a rapid initial growth of θ'_{cl}. By contrast, for the pipe jet, the apparently reduced large-scale coherent motion leads to a relatively weak engulfment of surrounding cold air into the jet; as a result, the amplitude of the temperature fluctuations in the jet core region is significantly lower. This is also evident in the variation of θ'_{cl}/T_0 as displayed in Fig. 4 as well, with T_0 being a constant ($\approx$50 °C).

The roll-up and pairing processes of large-scale vortex structures of jets issuing from contoured nozzles have been well described in the literature (e.g., Grinstein et al. [24]). This growth mechanism is consistent with the structures observed here in the initial region of the jet from the contoured nozzle (Fig. 2). There is some evidence of related mechanisms in the flow from the orifice plate, although the structures appear to be more complex and to be torn by the high shear rate. In contrast, the different underlying turbulence structure of the pipe jet should exhibit somewhat different growth mechanisms. The near-field mixing mechanisms of the three jets are explored next.

Both the jet from the contoured nozzle and that from the orifice have a thin initial shear layer, with that from the orifice being thinner. Hence, the vorticity is concentrated at the jet edge in both the flows. This has been known to result in the formation of azimuthally coherent vortex rings in jets from contoured nozzles. The subsequent pairing of these structures dominates the initial growth and entrainment of ambient fluid (Grinstein et al. [24]). To our best knowledge, all flow visualizations have been performed

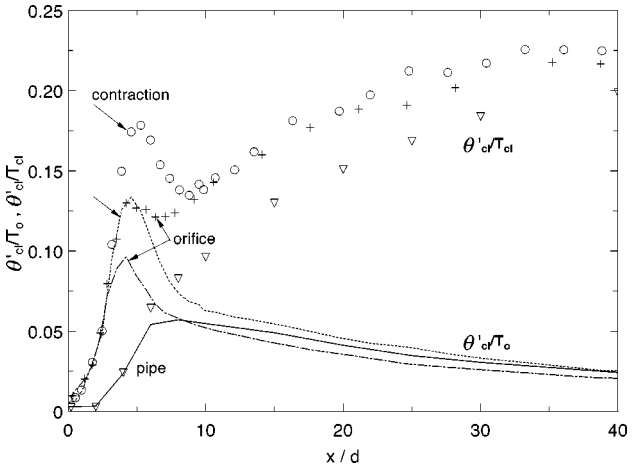

Fig. 4 Normalized centerline rms temperature (θ') in three axisymmetric jets issuing from a contoured nozzle (○), an orifice plate (+) and a long pipe (▽)

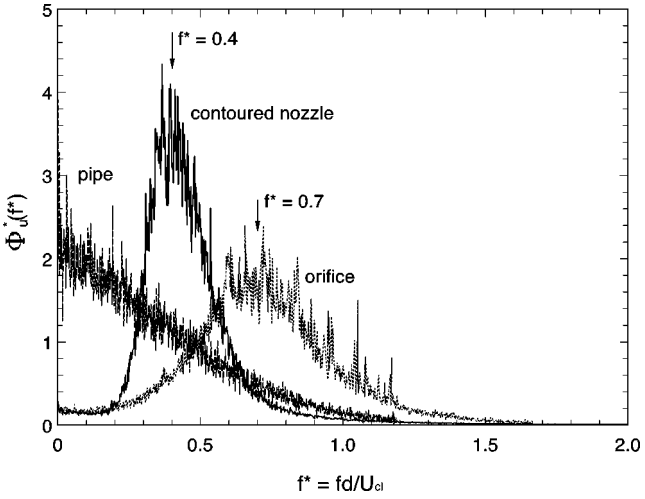

Fig. 6 Power spectra of the velocity fluctuations, Φ_u, obtained at $x/d=3$ in the shear-layers of axisymmetric jets issuing from a contoured nozzle, an orifice plate and a long pipe

on jets exclusively from contoured nozzles to explore the formation mechanism and the pairing of coherent structures. Given that both the jet from the orifice and that from the contoured nozzle appear to exhibit azimuthal coherence (Fig. 2(*a*) and 2(*b*)) and that both have the initial vorticity concentrated near the jet edge, it can be deduced that some of the above features may also be present in the orifice jet.

With increased distance downstream from the nozzle exit, the flow structure in jets from contoured nozzles is known to become increasingly three-dimensional with the streamwise vortices (''ribs'' or ''braids'') playing a controlling role in entraining ambient fluid (e.g., Liepmann and Gharib [25]). Self-induction, vortex stretching, and reconnection, which make the flow structure more three-dimensional, become the dominant fluid-dynamical processes involved in the mixing of these jets (Hussain [26]). These processes are expected to be present also in jets issuing from orifice plates. Importantly, the initial structure of the orifice jet is deduced to be more three-dimensional than that from the contoured nozzle. A strong recirculating separation region is generated both upstream and downstream from an orifice plate. In contrast, there is no upstream separation for a smooth contraction. The orifice jet also has higher initial radial velocity gradients than the smooth contraction, due to the present of the vena contracta. The presence of a thinner initial boundary layer downstream from the sharp-edged orifice plate also implies that it will be more unstable. It follows that the three-dimensionality in the initial flow structure from the orifice is expected to be greater than that from the contoured nozzle. Increased three dimensionality in the orifice jet over the jet from the smooth contraction is consistent with the more poorly defined structures seen in the planar images of the instantaneous flow from the orifice shown in Fig. 2.

The mixing rate from the orifice has been noted above to be significantly higher than that from the contoured nozzle. Increased mixing rates are often associated with increased three-dimensionality of the underlying flow. For example, it has been widely shown that enhancing the three-dimensionality in the shear layer of circular jets leads to increased rates of mixing and entrainment. Previous investigations (e.g., Gutmark et al. [12], Reeder and Samimy [27], Zaman [28], Mi and Nathan [29]) have demonstrated that breaking the axisymmetry, and thus enhancing three-dimensionality, of circular jets by using small tabs at the edge of the contoured nozzle can increase jet mixing substantially. Likewise, there have been many efforts devoted to investigating mixing characteristics of noncircular jets (e.g., Husain and Hussain [30], Ho and Gutmark [31], Miller et al. [32], Mi et al. [10]). Since any variation in the azimuthal curvature of the initial shear layer triggers the self-induced deformation of coherent structures, these noncircular jets have all been found to increase entrainment and mixing rates relative to comparable circular jets.

It is also interesting to consider the difference in the initial vortex motion of the two jets for the higher mixing rate of the orifice jet. While measurements of velocity gradients at the edge of the emerging jet is difficult, it can be inferred from Fig. 1(*a*) and deduced that the maximum velocity gradient in the shear layer is higher for the orifice than for the contoured nozzle. This suggests that the peak vorticity at the edge of the orifice jet might also be higher. We also notice from Fig. 1(*a*) that along the potential core the mean velocity is approximately 25 ~30% higher for the orifice jet than for the contoured nozzle. This implies that the large-scale coherent vortices rolling up from the shear layer of the orifice jet will be convected downstream at a higher speed than those for the contoured nozzle. This deduction is supported by the axial velocity spectra in Fig. 6, in which the mean passage frequency of these vortices at $x/d=3$ in the orifice jet $(0.7U_{\mathrm{cl}}/d)$ is approximately 70% higher than that for the contoured nozzle $(0.4U_{\mathrm{cl}}/d)$. Assuming that the vortex rotation or the circulation is directly related to the entrainment rate, one would expect the orifice jet to grow faster than the jet issuing from the contoured nozzle, as it does (Fig. 5).

By contrast, a broad spectrum of turbulent structures is present in the near field of the emerging jet from the long pipe because the flow is fully developed turbulent pipe flow. The turbulence intensity is significantly higher than the flow either from the contoured nozzle or from the orifice (Fig. 1(*b*)). In addition, the vorticity is distributed throughout the flow rather than being concentrated at the edge of the nozzle. The wide range of wavenumbers can be deduced to overwhelm the natural narrow-band disturbances and therefore disrupt the vortex formation process in the near field (Russ and Strykowski [33]). Together these effects result in a significant reduction of the number of the large-scale coherent structures in the near field of the flow. These deductions are consistent with the measured result that the mixing rate of the pipe jet is found to be lower than that of the other jets.

4 Concluding Remarks

The present study has compared the turbulent scalar mixing characteristics of free turbulent jets issuing from three common types of axisymmetric nozzle: a smooth contraction, a sharp-edged orifice and a long straight pipe. It is found that, not taking into account the pressure-drop issue, the ranking of the nozzle types in terms of mixing rate, in both the near field and developing region, is the orifice, followed by the contoured (or smooth contraction) nozzle and then the pipe. The differences in mixing rates are associated with different underlying turbulent structures in the three jets.

There is evidence of the presence of coherent large-scale structures in both the jets from the orifice and the contoured nozzle. However, the jet from the contoured nozzle results in vortex structures which are visually more coherent, consistent with the higher relative scalar fluctuation intensity. However, the three-dimensionality of the structures in the initial region of the orifice jet is deduced to be higher, based on knowledge of its initial and upstream conditions and comparison with related investigations. Furthermore, while the emerging flow from the pipe may possess some structures, they are poorly correlated and do not occur regularly. As a result, the pipe jet has much weaker large-scale engulfment of the cold ambient fluid, and thus a significantly lower relative scalar fluctuation intensity, than the other two jets.

It is noted that most of previous research has been performed on jets issuing from contoured smooth contraction nozzles. As a result, while the underlying structure of those jets is fairly well understood, the structures of jets issuing from orifice plates and long pipes are poorly understood. It is hoped that the present work will stimulate such investigations. Moreover, further work is required to quantify the link between the higher mixing rate of the orifice jet and the enhanced three-dimensionality of the initial underlying structure.

Acknowledgment

JM and DSN gratefully acknowledge the joint support of the Australian Research Council and Fuel & Combustion Technology Ltd through the Scheme of SPIRT Grants. We appreciate the comments from all three referees, which have strengthened the final draft of this paper.

Nomenclature

- d = nozzle diameter
- d_w = hot/cold-wire diameter
- f = frequency
- f^* = normalized frequency $(\equiv fd/U_{cl})$
- l_w = hot/cold-wire length
- $R_{1/2}$ = half-radius of the mean scalar field, defined as a radial location at which the local mean scalar is half the centerline value
- Re_d = Reynolds number $(\equiv U_o d/\nu)$ based on jet exit diameter and velocity
- T = mean temperature above ambient

T_o = exit mean temperature above ambient
T_{cl} = centerline mean temperature above ambient
U = mean velocity
U_o = exit mean velocity
U_{cl} = centerline mean velocity
u = streamwise fluctuating velocity
u' = root mean square (rms) of u
x = distance measured from the exit
θ' = root mean square (rms) of the temperature fluctuations
Φ_u^* = normalized power spectral density function, or simply spectrum, of the velocity fluctuations

References

[1] Crow, S. C., and Champagne, F. H., 1971, ''Orderly Structure in Jet Turbulence,'' J. Fluid Mech., **48**, pp. 547–591.
[2] Becker, H. A., Hottal, H. C., and Williams, G. C., 1967, ''The Nozzle-Fluid Concentration Field of the Round, Turbulent, Free Jet,'' J. Fluid Mech., **30**, pp. 285–303.
[3] Lockwood, F. C., and Moneib, A., 1980, ''Fluctuating Temperature Measurements in a Heated Round Free Jet,'' Combust. Sci. Technol., **22**, pp. 63–81.
[4] Pitts, W. M., 1991, ''Effects of Global Density Ratio on the Centerline Mixing Behavior of Axisymmetric Turbulent Jets,'' Exp. Fluids, **11**, pp. 125–134.
[5] Pitts, W. M., 1991, ''Reynolds Number Effects on the Centerline Mixing Behavior of Axisymmetric Turbulent Jets,'' Exp. Fluids, **11**, pp. 135–144.
[6] Richards, C. D., and Pitts, W. M., 1993, ''Global Density Effects on the Self-Preservation Behavior of Turbulent Free Jets,'' J. Fluid Mech., **245**, pp. 417–435.
[7] Wilson, R. A. M., and Danckwerts, P. V., 1964, ''Studies in Turbulent Mixing — II. A Hot Air Jet,'' Chem. Eng. Sci., **19**, pp. 885–895.
[8] Quinn, W. R., 1989, ''On Mixing in an Elliptic Turbulent Free Jet,'' Phys. Fluids A, **1**, pp. 1716–1722.
[9] Quinn, W. R., 1992, ''Streamwise Evolution of a Square Jet Cross Section,'' AIAA J., **30**, pp. 2852–2857.
[10] Mi, J., Nathan, G. J., and Luxton, R. E., 2000, ''Centerline Mixing Characteristics of Jets From Nine Differently Shaped Nozzles,'' Exp. Fluids, **28**, pp. 93–95.
[11] Koshigoe, S., Gutmark, E. J., and Schadow, K. C., 1989, ''Initial Development of Noncircular Jets Leading to Axis Switching,'' AIAA J., **27**, pp. 411–419.
[12] Gutmark, E. J., and Grinstein, F. F., 1999, ''Flow Control With Noncircular Jets,'' Annu. Rev. Fluid Mech., **31**, pp. 239–272.
[13] Wygnanski, I., Champagne, F., and Marasli, B., 1986, ''On the Large-Scale Structures in Two Dimensional, Small-Deficit, Turbulent Wakes,'' J. Fluid Mech., **168**, pp. 31–71.
[14] George, W. K., 1989, ''The Self-Similarity of Turbulent Flows and Its Relation to Initial Conditions and Coherent Structures,'' *Recent Advances in Turbulence*, R. E. A. Arndt and W. K. George, eds., Hemisphere, New York, pp. 39–73.
[15] Mi, J., Nobes, D., and Nathan, G. J., 2001, ''Influence of Jet Exit Conditions on the Passive Scaler Field of an Axisymmetric Free Jet,'' J. Fluid Mech., **432**, pp. 91–125.
[16] Paranthoen, P., Petit, C., and Lecordier, J. C., 1982, ''The Effect of Thermal Prong-Wire Interaction on the Response of a Cold Wire in Gaseous Flows (Air, Argon and Helium),'' J. Fluid Mech., **124**, pp. 457–473.
[17] Rosenweig, R. E., Hottel, H. C., and Williams, G. C., 1961, ''Smoke-Scattering Light Measurements of Turbulent Concentration Fluctuation,'' Chem. Eng. Sci., **15**, pp. 111–129.
[18] Becker, H. A., Hottal, H. C., and Williams, G. C., 1963, ''Mixing and Flow in Ducted Turbulent Jets,'' *Ninth Symposium (International) on Combustion*, Pittsburgh: The Combustion Institute, pp. 7–20.
[19] Becker, H. A., Hottal, H. C., and Williams, G. C., 1967, ''On the Light-scattering Technique for the Study of Turbulence and Mixing,'' J. Fluid Mech., **30**, pp. 259–284.
[20] Becker, H. A., 1977, ''Mixing, Concentration Fluctuations, and Marker Nephelometry,'' *Studies in Convection*, Vol. 2, B. E. Launder, ed., Academic Press, New York, pp. 45–139.
[21] Papadopoulos, G., and Pitts, W. M., 1998, ''Scaling the Near-Field Centerline Mixing Behavior of Axisymmetric Turbulent Jets,'' AIAA J., **36**, pp. 1635–1642.
[22] Gouldin, F. C., Schefer, R. W., Johnson, S. C., and Kollmann, W., 1986, ''Nonreacting Turbulent Mixing Flows,'' Prog. Energy Combust. Sci., **12**, pp. 257–303.
[23] Ho, C. W., and Nosseir, N. S., 1981, ''Dynamics of an Impinging Jet. Part 1. The Feedback Phenomenon,'' J. Fluid Mech., **105**, pp. 119–142.
[24] Grinstein, F. F., Glauser, M. N., and George, W. K., 1995, ''Vorticity in Jets,'' Chapter III, *Fluid Vortices*, S. I. Green, ed., Kluwer Academic Publisher, Netherlands, pp. 65–94.
[25] Liepmann, D., and Gharib, M., 1992, ''The Role of Streamwise Vorticity in the Near-Field Entrainment of Round Jets,'' J. Fluid Mech., **245**, pp. 643–68.
[26] Hussain, A. K. M. F., 1986, ''Coherent Structures and Turbulence,'' J. Fluid Mech., **173**, pp. 303–356.
[27] Reeder, M. F., and Samimy, M., 1996, ''The Evolution of a Jet With Vortex-Generating Tabs: Real-Time Visualization and Quantitative Measurements,'' J. Fluid Mech., **311**, pp. 73–118.
[28] Zaman, K. B. M., 1999, ''Spreading Characteristics of Compressible Jets From Nozzles of Various Geometries,'' J. Fluid Mech., **383**, pp. 197–228.
[29] Mi, J., and Nathan, G. J., 1999, ''Effect of Small Vortex-Generators on Scalar Mixing in the Developing Region of a Turbulent Jet,'' Intl. J. Heat & Mass Transfer, **42**, pp. 3919–3926.
[30] Hussain, F., and Husain, H. S., 1989, ''Elliptic Jets. Part 1. Characteristics of Unexcited and Excited Jets,'' J. Fluid Mech., **208**, pp. 257–320.
[31] Ho, C. M., and Gutmark, E. J., 1987, ''Vortex Induction and Mass Entrainment in a Small-Aspect Ratio Elliptic Jet,'' J. Fluid Mech., **179**, pp. 383–405.
[32] Miller, R. S., Madnia, C. K., and Givi, P., 1995, ''Numerical Simulation of Non-Circular Jets,'' Comput. Fluids, **24**, No. 1, pp. 1–25.
[33] Russ, S., and Strykowski, P. J., 1993, ''Turbulent Structure and Entrainment in Heated Jets: The Effect of Initial Conditions,'' Phys. Fluids A, **5**, pp. 3216–3225.

J. Hernández
Professor,
E.T.S. de Ingenieros Industriales,
UNED,
E-28040 Madrid, Spain
e-mail: jhernandez@ind.uned.es

J. López
Assistant Professor

F. Faura
Associate Professor

E.T.S. de Ingenieros Industriales,
Universidad Politécnica de Cartagena,
E-30203 Cartagena, Spain

Influence of Unsteady Effects on Air Venting in Pressure Die Casting

The influence of unsteady effects on the evacuation of air through vents in pressure die casting processes is analyzed. A model is proposed which considers the air flow as one-dimensional and adiabatic, and which retains friction effects. Venting conditions for wide ranges of the relevant dimensionless parameters are analyzed for both atmospheric and vacuum venting systems. The model is solved numerically using the method of characteristics and its results are compared with those obtained for quasi-steady models. It is shown that wide ranges of operating conditions can exist in practical situations, for which unsteady effects, neglected in previous models, are important and must be taken into account to determine the air mass entrapped at the end of the filling process. The selection of parameters which will reduce the amount of trapped air and thus porosity in manufactured parts is also discussed. [DOI: 10.1115/1.1412234]

Introduction

Pressure die casting in horizontal cold chambers is currently the most common process for manufacturing cast components of near-net shape. A die casting machine is shown schematically in Fig. 1. The molten metal is injected into a die cavity from a horizontal shot sleeve in which the metal is pushed by a plunger. The sleeve is partially filled with a volume of molten metal and the plunger then moves the length of the sleeve, which is usually fixed. To reduce air entrapment, the injection process usually consists of slow and fast shot phases. In the slow shot phase, the plunger first forces the molten metal to rise and fill the upper section of the shot sleeve, and then moves at a constant critical speed until the shot sleeve is completely filled with molten metal and the fast phase begins.

The most common defect in this type of die casting is porosity, which limits the integrity of the casting, generally produces low quality casting and makes this type of process only adequate for parts that do not require heat treatment (or welding) to conform to the specified mechanical properties. Among the different mechanisms involved in porosity formation, which have been discussed by different authors (see, e.g., Lindsey and Wallace [1], Campbell [2]), a very important one in pressure die casting is generally the entrapment of air during the injection process. In this process the initial air in the die cavity and in the shot sleeve may be trapped in the molten metal as small air bubbles that will cause porosity when the metal solidifies. The causes of air entrapment are mainly related to operating conditions (e.g., initial filling fraction of the shot sleeve and plunger motion profile), which affect mixing processes during the injection time (see, e.g., Garber [3], Hu et al. [4], Hernández et al. [5]), and to inadequate air venting (Bar-Meir et al. [6]). The design and location of the vents through which the gas is evacuated from the die cavity must, on one hand, reduce the mass of gas remaining in the die at the end of the injection process and, on the other, minimize the need for secondary machining and ensure freezing of the molten metal in the mold.

Bar-Meir et al. [6] reviewed different previous models of air venting, most of which neglect friction in the venting system and assume quasi-steady flow. In some of these models the flow is assumed to be always choked, whereas in others the flow is not choked at all. Karni [7] proposed a model which considers a quasi-steady and adiabatic flow through the vents and retains friction effects. In this model, the gas temperature is assumed constant in the die cavity and both choked and unchoked conditions are considered.

More recently, Bar-Meir et al. [6,8] proposed a quasi-steady model, which assumes that the gas in the die cavity and the shot sleeve undergoes an isentropic evolution, and considers the gas flow through the vents as a Fanno flow. In atmospheric venting, in which the vents are open to the atmosphere, the pressure in the cavity increases continuously and eventually the flow may become choked. The analysis carried out by these authors for atmospheric venting showed that there is a critical vent area, depending on geometry and filling time, below which the ventilation is poor and above which the resistance to gas flow is minimal. For vacuum venting, in which the vents are connected to a vacuum tank, the flow becomes choked almost instantaneously at the beginning of the filling process, and the model proposed by Bar-Meir et al. [6] assumes that the flow is choked throughout the filling process, an assumption which is better justified when the vacuum pressure is very small.

The objective of the research described in this paper was to carry out a systematic study of the influence of unsteady effects, which have been neglected in previous models, on the evacuation of air through vents. An analysis of venting conditions for wide ranges of the relevant dimensionless parameters is presented for both atmospheric and vacuum venting systems using a model which considers the air flow as one-dimensional and adiabatic, and retains friction effects. For vacuum venting, the model can also be applied to cases where both choked and unchoked flow conditions may occur during the filling process. The model is solved numerically using the method of characteristics and the modified Euler predictor-corrector method, and its results are compared with those obtained from the quasi-steady model proposed by Bar-Meir et al. [6,8]. We show that there are wide ranges of operating conditions encountered in practical situations for which unsteady effects are important and must be retained to determine the air mass entrapped at the end of the filling process. We also discuss on the selection of parameters which will reduce the amount of trapped air.

Mathematical Model

Figure 2 shows diagrammatically the simplified model of the venting system which will be considered. The runner and the die cavity are combined and called the cylinder, where it is assumed that the gas is at rest and the values of all parameters at every

Contributed by the Fluids Engineering Division for publication in the JOURNAL OF FLUIDS ENGINEERING. Manuscript received by the Fluids Engineering Division August 12, 1999; revised manuscript received June 11, 2001 Associate Editor: U. Ghia.

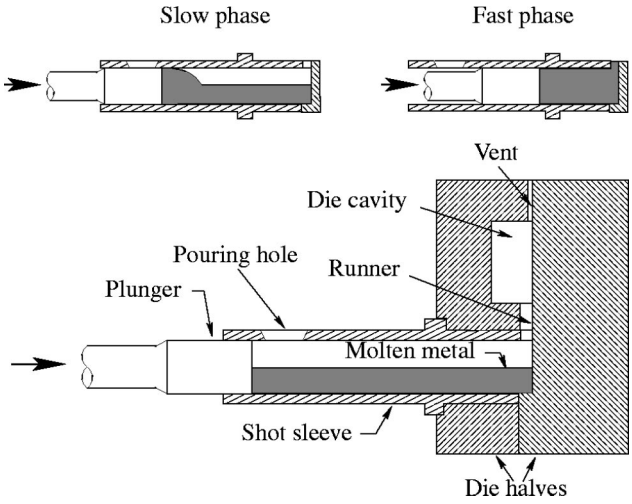

Fig. 1 Schematic representation of a die casting machine

instant are uniform, and that the gas (mostly air) undergoes an isentropic process. It is also assumed that the plunger velocity is constant, and that the volume of air in the cylinder reduces from the initial value $V(0)$ to $V(t)=0$ at $t=t_f$. The omission of the unfilled part of the shot sleeve in the cylinder may be justified by the fact that the plunger speed in the slow phase is usually much lower than in the fast phase. In addition, the assumption of constant plunger speed usually holds true in practice during most of the fast phase. Therefore, although a more complete study could be carried out by considering the existence of different chambers and a variable plunger speed, it is expected that the analysis presented in this work will allow us to take into account the essential characteristics of problems encountered in most situations of practical interest. The initial stagnation density and sound speed in the cylinder are, respectively, $\rho_0(0)$ and $c_0(0)$. The vents are represented by an equivalent straight duct of length L and hydraulic diameter D, with a cross-section of area A. The flow in the duct will be considered as an adiabatic flow with a constant friction coefficient, f. This representation of a vent system requires close estimations of L and f, which in some cases may involve some uncertainty and limit the accuracy of the predictions. The effects of Reynolds and Mach numbers on the friction coefficient are neglected, as in Bar-Meir's model. The adiabatic assumption is appropriate for the very rapid discharge processes that are being analyzed, for which there is little time for significant heat transfer. The flow through the nozzle at the entrance of the duct (Fig. 2) will be considered as isentropic and one-dimensional. It will be assumed that the length of the nozzle is very short when compared with L, so that the flow in the nozzle can also be considered as quasi-steady.

The governing equations for unsteady quasi-one-dimensional flow of a perfect gas (see Shapiro [9]) can be expressed in dimensionless form as follows:

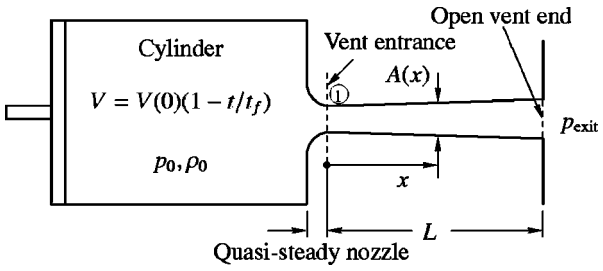

Fig. 2 Schematic representation of the venting system

$$\frac{L}{c_0(0)t_f}\frac{\partial \rho'}{\partial t'} + u'\frac{\partial \rho'}{\partial x'} + \rho'\frac{\partial u'}{\partial x'} + \rho' u'\frac{1}{A}\frac{dA}{dx'} = 0, \tag{1}$$

$$\frac{L}{c_0(0)t_f}\rho'\frac{\partial u'}{\partial t'} + \rho' u'\frac{\partial u'}{\partial x'} + \frac{\partial p'}{\partial x'} = -\frac{\rho' u'^2}{2}\frac{4fL}{D}, \tag{2}$$

$$\frac{L}{c_0(0)t_f}\frac{\partial p'}{\partial t'} + u'\frac{\partial p'}{\partial x'} - \gamma\frac{p'}{\rho'}\left(\frac{L}{c_0(0)t_f}\frac{\partial \rho'}{\partial t'} + u'\frac{\partial \rho'}{\partial x'}\right) = (\gamma-1)\rho'\left(\frac{qL}{c_0^3(0)} + \frac{u'^3}{2}\frac{4fL}{D}\right), \tag{3}$$

where

$$\rho' = \frac{\rho}{\rho_0(0)}, \quad u' = \frac{u}{c_0(0)}, \quad p' = \frac{p}{\rho_0(0)c_0^2(0)}, \quad x' = \frac{x}{L}, \quad t' = \frac{t}{t_f}, \tag{4}$$

γ is the ratio of constant pressure to constant volume specific heats, $A=A(x)$ is the duct cross-sectional area and $q=q(x,t)$ is the heat transfer per unit mass flow rate. As mentioned before, in this work we will take $A=$ constant and $q=0$. The only reason for retaining effects of area change and heat transfer in the equations is that the numerical code developed to solve Eqs. (1)–(3) has been validated by comparing the results with some explicit analytical solutions given by Cai [10] for cases which also include these effects. The dependent variables in Eqs. (1)–(3) are ρ', p' and u'. The initial conditions are $\rho'=1$, $p'=1/\gamma$ and $u'=0$ everywhere at $t'=0$. For subsonic flow, the pressure p_{exit} at duct exit ($x'=1$) is taken equal to $p_0(0)$ for atmospheric venting and to the vacuum pressure for vacuum venting. When the air flow turns backward at the inlet or outlet sections of the vent, which may occur in certain circumstances, the boundary conditions are changed appropriately. To determine the flow magnitudes at duct entrance ($x'=0$), the mass balance in the die cavity is required: $dm/dt + \dot{m} = 0$, where $\dot{m}$ is the mass flow rate out of the cylinder. This equation can be written as

$$(1-t')\frac{d\rho_0'}{dt'} - \rho_0' + \frac{A}{\mathcal{A}}\rho_1' u_1' = 0, \tag{5}$$

where subscript 1 refers to conditions at the end section of the nozzle and

$$\mathcal{A} = \frac{V(0)}{c_0(0)t_f}. \tag{6}$$

The assumption of isentropic air flow in the cylinder provides the additional relationship

$$\frac{p_0'}{\rho_0'^{\gamma}} = \frac{1}{\gamma}. \tag{7}$$

It can be observed from Eqs. (1)–(3) and (5) and from boundary conditions that, for $A=$ constant and $q=0$, the solution of the governing equations in general depends on the following dimensionless parameters: $c_0(0)t_f/L$, $A/\mathcal{A}$, $4fL/D$, $p_{exit}/\rho_0(0)c_0^2(0)$ and γ. The parameter $c_0(0)t_f/L$ represents the ratio between the filling time t_f and the characteristic time $L/c_0(0)$ that a pressure wave takes to travel the vent length. The parameter $A/\mathcal{A}$ can be expressed as the product of the parameter $c_0(0)t_f/L$ and the ratio between vent and cylinder volumes, $AL/V(0)$. As will be shown in the discussion of the results, for any given value of $c_0(0)t_f/L$, the influence of unsteady effects on air conditions in the cylinder will be negligible for sufficiently small volume ratios, $AL/V(0)$, whereas for increasing values of $AL/V(0)$ the wave motion of air in the vent may noticeably affect the pressure in the cylinder, particularly for low values of $c_0(0)t_f/L$, and even produce oscillations in the cylinder pressure for sufficiently large values of

$A/\mathcal{A}$. For large values of $c_0(0)t_f/L$ and $A/\mathcal{A}$, two periods can be distinguished in the filling process: an initial period, during which large-amplitude waves propagate across the vent system, followed by a quasi-steady period, in which the Mach number in the vent flow is determined by the inverse of $A/\mathcal{A}$. For large values of $c_0(0)t_f/L$ and sufficiently low values of $A/\mathcal{A}$, the first term in Eqs. (1)–(3) and the term involving the partial derivative of density with respect to time in Eq. (3) can be disregarded, and the flow in the vent can be considered as quasi-steady. If unsteady effects are neglected, the pressure ratio in the cylinder will vary monotonically according to a law solely determined by the values of $A/\mathcal{A}$, $4fL/D$ and $p_{\text{exit}}/\rho_0(0)c_0^2(0)$. Friction effects in the vent flow are introduced by means of the parameter $4fL/D$, and the effects of the exit pressure intervene through the parameter $p_{\text{exit}}/\rho_0(0)c_0^2(0)$, which relates p_{exit} and the initial pressure in the cylinder and may be relevant in vacuum venting.

Numerical Procedure

The method of characteristics has been used to solve numerically the governing equations, which can be replaced by the following system of characteristic equations (see, e.g., Zucrow and Hoffman [11]):

$$\left(\frac{dt'}{dx'}\right) = \frac{L}{c_0(0)t_f}\frac{1}{u'} \quad \text{(pathline)}, \tag{8}$$

$$\left(\frac{dt'}{dx'}\right)_{\pm} = \frac{L}{c_0(0)t_f}\frac{1}{u' \pm c'} \quad \text{(Mach lines)}, \tag{9}$$

where $c' = (\gamma p'/\rho')^{1/2}$, and the corresponding compatibility equations:

$$dp' - c'^2 d\rho' = (\gamma - 1)\frac{\rho'}{u'}\left(\frac{qL}{c_0^3(0)} + u'\mathcal{F}\right)dx' \quad \text{(along pathlines)}, \tag{10}$$

$$dp' \pm \rho' c' du' = \frac{c_0(0)t_f}{L}\rho'\left[-\frac{1}{A}\frac{dA}{dx'}u'c'^2 \mp c'\mathcal{F} + (\gamma - 1)\times\left(\frac{qL}{c_0^3(0)} + u'\mathcal{F}\right)\right]dt' \quad \text{(along Mach lines)}, \tag{11}$$

where

$$\mathcal{F} = \frac{u'^2}{2}\frac{4fL}{D}. \tag{12}$$

The finite difference grid in the xt plane that has been used is based on the inverse marching method, in which the locations of solution points are specified a priori. The characteristic curves through each solution point are extended rearward to intersect the line of constant time on which the points from previous calculations are located. The characteristic curves between the solution point and the intersection points (initial-data points) are approximated by straight lines. The finite difference equations resulting from the discretization of Eqs. (8)–(11) (see Zucrow and Hoffman [11]) have been solved employing the modified Euler predictor-corrector method. In the predictor step, the coefficients in the finite difference equations are calculated at the initial-data points, where the flow properties are determined from a natural cubic spline interpolation based on previous solution points. In the corrector step, the coefficients are calculated for the average values of the dependent variables along each characteristic curve.

The magnitudes of the flow variables at the duct entrance section can be determined, as a function of the stagnation properties, from the expressions giving ρ_1/ρ_0 and p_1/p_0 as a function of the Mach number at section 1 for an isentropic quasi-steady flow, and additionally, when the nozzle is unchoked, from the compatibility condition of Eq. (11) along the negative characteristic coming from inside the vent. The corresponding discretized equations have been solved using the Newton-Raphson method. To calculate the stagnation properties, Eq. (5) has been solved using the modified Euler predictor-corrector method, with the explicit Euler method as predictor and a trapezoidal formula in the corrector step.

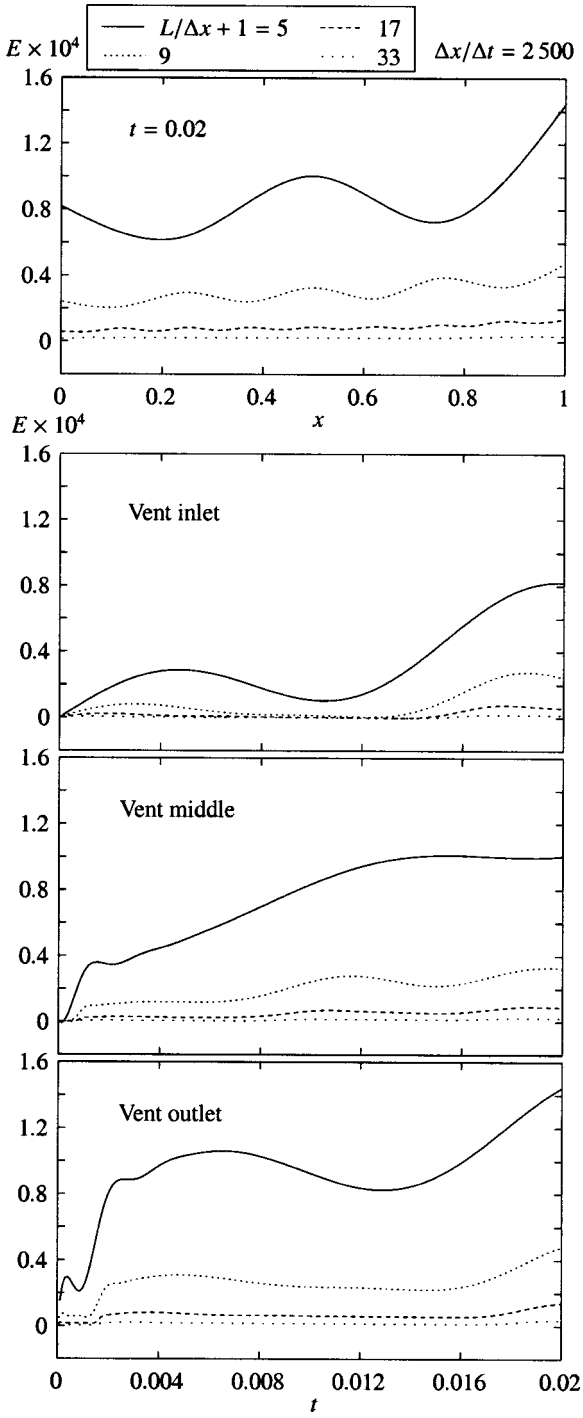

Fig. 3 Validation of the computed results by comparison with the exact solution given by Eq. (16)

For operating conditions in which unsteady effects are negligible, the numerical results of the code have been compared with those obtained by Bar-Meir et al. [6,8], with excellent agreement. In order to check the accuracy of the numerical model, we have extensively compared its results with the different explicit analyti-

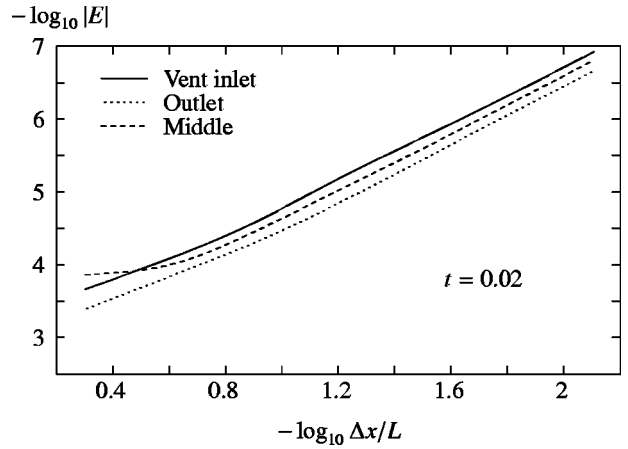

Fig. 4 Results of a grid sensitivity study for the case corresponding to the exact solution of Eq. (16)

cal solutions given by Cai [10]. As an example, Fig. 3 shows the relative error $E=(u-u_{\text{exact}})/u_{\text{exact}}$ between the numerical solutions obtained using different grid sizes for the case of a duct of constant area, A, with constant friction coefficient, f, and

$$q=-\frac{\gamma}{\gamma-1}p_0\frac{\Phi\exp(-\Phi x)[\Phi\exp(-\Phi x)+1]^2}{100(t+0.02)^2\exp(-\Phi x)}-\Phi\left[\frac{\exp(-\Phi x)+1/\Phi}{t+0.02}\right]^3 \tag{13}$$

where $\Phi=f\sqrt{\pi/A}=0.2$, and the following analytical solution given by Cai [10]:

$$p_{\text{exact}}=\text{const}=p_0, \tag{14}$$

$$\rho_{\text{exact}}=\frac{100[(t+0.02)\exp(-\Phi x)]}{(\Phi\exp(-\Phi x)+1)^2}, \tag{15}$$

$$u_{\text{exact}}=\frac{\exp(-\Phi x)+1/\Phi}{t+0.02}, \tag{16}$$

for $0\leqslant t\leqslant 0.02$ and $0\leqslant x\leqslant 1$. The second-order accuracy of the numerical scheme is shown in Fig. 4, which represents the error E as a function of the grid size, Δx, at the inlet, middle and outlet sections of the vent, for $t=0.02$. All the results in Figs. 3 and 4 were obtained using $\Delta x/\Delta t=2500$. The relative difference between the numerical results obtained using grids of 17 and 33 nodes is around 10^{-3}%, and the maximum relative error between the numerical solution obtained with a grid of 33 nodes and the exact solution in Fig. 3 is lower than 10^{-3}%.

Different grids were used to check the grid-dependency of the solution for the cases presented in this paper. An increase in the grid size from 33 to 65 nodes produced differences in the numerical results for the air velocity at $x=L$ and $t=t_f$ (for which the influence of grid size is greatest, as in the case of Fig. 3) of less than 0.4% in the most unfavorable cases. These maximum differences decreased, for example, to around 0.1% for results corresponding to $t=0.95t_f$. We concluded that using 33 nodes along the x coordinate produced nearly grid-independent results for the broad range of conditions presented in this work. The ratio $\Delta x/\Delta t$ was chosen to satisfy the CFL stability condition.

Discussion of Results

Results for the pressure in the cylinder as a function of time obtained with the unsteady model presented in this work are compared in Figs. 5 and 6 with those obtained from the quasi-steady model of Bar-Meir et al. [6,8]. Figure 5 corresponds to atmospheric venting conditions, and Fig. 6 to vacuum venting. Results

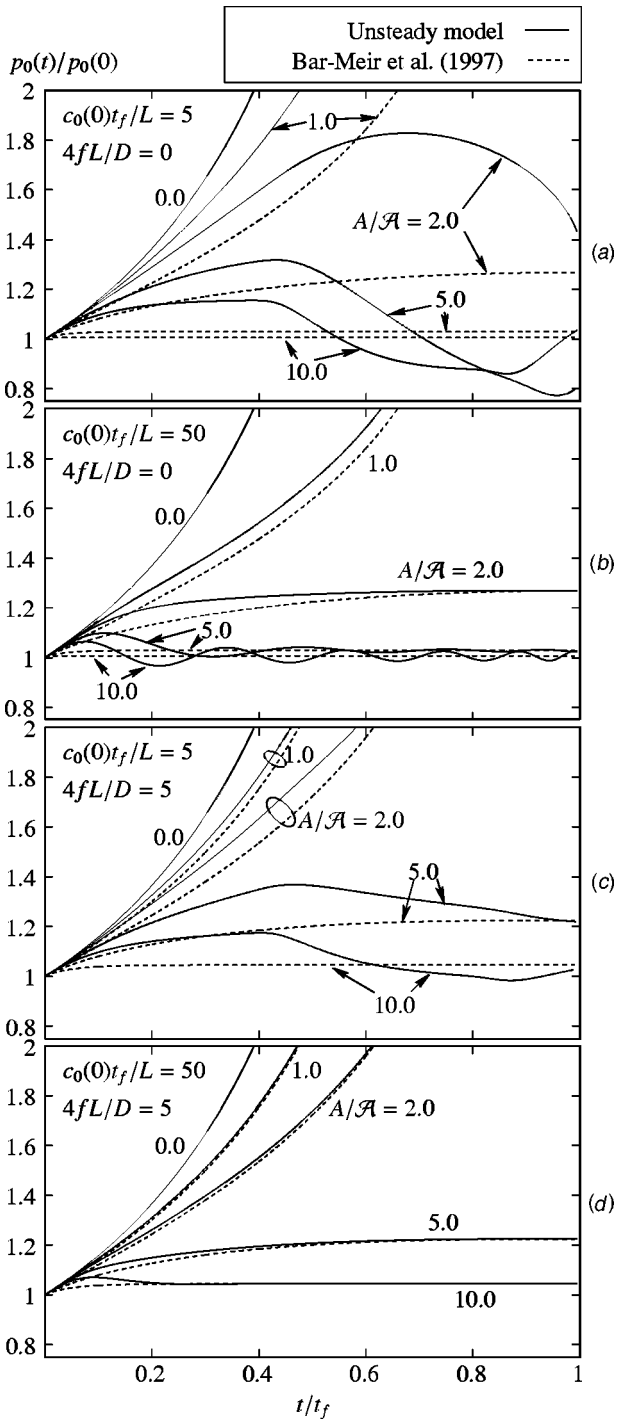

Fig. 5 Effect of vent area values on pressure ratio in the cylinder for two different values of $c_0(0)t_f/L$ and of the friction parameter. Case of atmospheric venting. (*a*) $4fL/D=0$, $c_0(0)t_f/L=5$. (*b*) $4fL/D=0$, $c_0(0)t_f/L=50$. (*c*) $4fL/D=5$, $c_0(0)t_f/L=5$. (*d*) $4fL/D=5$, $c_0(0)t_f/L=50$.

in Figs. 5(*a*–*b*) and 6(*a*–*b*) have been obtained neglecting friction effects, and those of Figures 5(*c*–*d*) and 6(*c*–*d*) correspond to a friction parameter $4fL/D=5$. The parameter $c_0(0)t_f/L$ varies from a value of 5 in Figs. 5(*a*), 5(*c*), 6(*a*), and 6(*c*) to 50 in Figs. 5(*b*), 5(*d*), 6(*b*), and 6(*d*).

In the case of atmospheric venting, it can be observed from Fig. 5 that the influence of unsteady effects on conditions in the cylinder increases as the values of parameters $4fL/D$ and $c_0(0)t_f/L$ decrease and is negligible when the values of $A/\mathcal{A}$ are close to

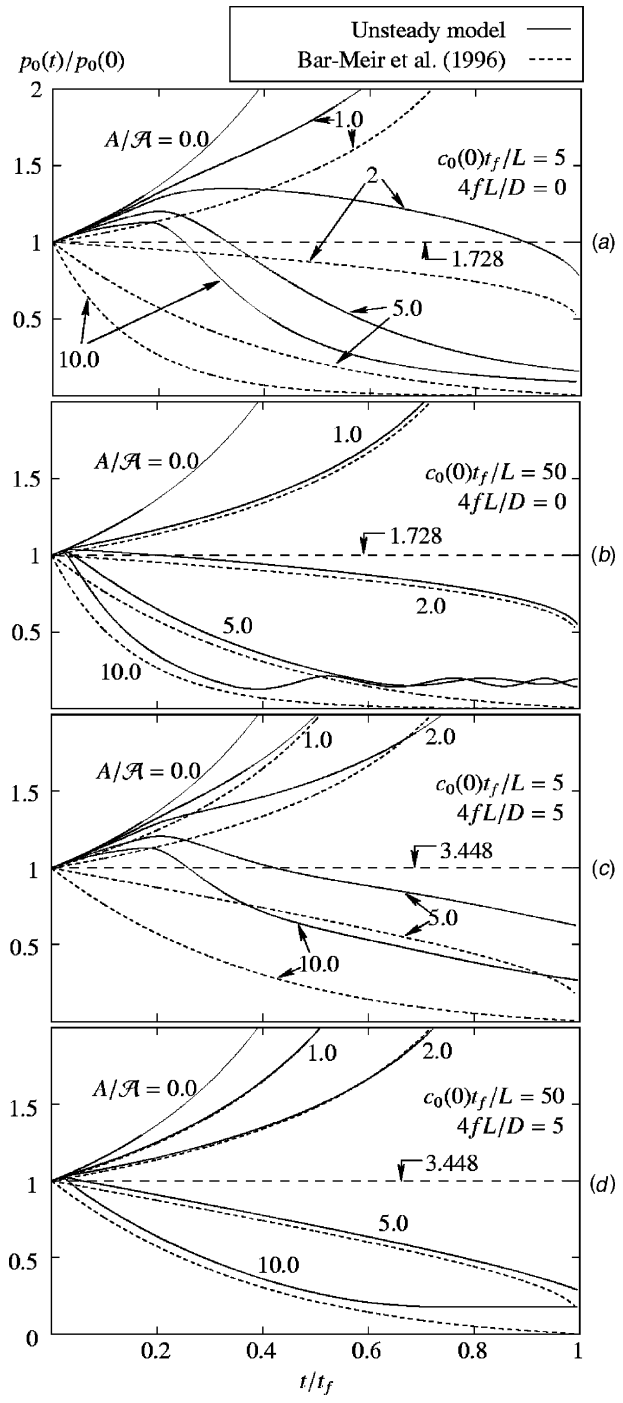

Fig. 6 Effect of vent area values on pressure ratio in the cylinder for two different values of $c_0(0)t_f/L$ and of the friction parameter. Case of vacuum venting. (*a*) $4fL/D=0$, $c_0(0)t_f/L=5$. (*b*) $4fL/D=0$, $c_0(0)t_f/L=50$. (*c*) $4fL/D=5$, $c_0(0)t_f/L=5$. (*d*) $4fL/D=5$, $c_0(0)t_f/L=50$.

zero. At this limit (zero), the variation of the pressure ratio in the cylinder is solely determined by the rate of reduction of the cylinder volume, and so the results of the present model coincide with those obtained with Bar-Meir's model, in which the assumption that the air in the vent system itself has no mass was adopted. For higher values of $A/\mathcal{A}$, unsteady effects make the pressure within the cylinder increase initially at a higher rate than that predicted by the quasi-steady model, and then, for sufficiently high values of $A/\mathcal{A}$ and low values of the friction parameter, the pressure oscillates around the curve predicted by the quasi-steady model. The pressure oscillations in the cylinder are caused by the pressure waves that propagate along the vent and successively reflect at both vent ends. The number of cylinder pressure oscillation cycles during the filling process will depend on the parameters $c_0(0)t_f/L$, $A/\mathcal{A}$ and $4fL/D$. Increasing values of $c_0(0)t_f/L$ will reduce the relative time that pressure waves take to travel the vent length, and therefore will increase the number of oscillation cycles. Increasing values of $A/\mathcal{A}$ will cause an increase in the amount of air, relative to the air mass in the cylinder, leaving the cylinder when the successive expansion and compression waves reach the die cavity. The larger the value of $A/\mathcal{A}$, the smaller the number of pressure waves required to reach the die cavity to produce the pressure oscillations in the cylinder, and, consequently, the higher the number of pressure oscillation cycles in the cylinder during the filling process. In the absence of friction, for sufficiently large values of $A/\mathcal{A}$ the number of cycles would be determined solely by $c_0(0)t_f/L$.

It can be observed from Fig. 5 that, for increasing values of $c_0(0)t_f/L$, the results of the unsteady model become closer to those of the quasi-steady model proposed by Bar-Meir et al. [8], as is to be expected. Notice that, for $c_0(0)t_f/L=50$, $4fL/D=5$ and large $A/\mathcal{A}$ values, quasi-steady flow conditions are reached after an initial period, during which unsteady effects have a slight influence. When friction is low, for values of $c_0(0)t_f/L$ above those of Fig. 5 and large values of $A/\mathcal{A}$, a quasi-steady period can also be reached following an initial period in which large-amplitude waves propagate across the vent and whose duration decreases as $c_0(0)t_f/L$ increases.

By comparing Figs. 5(*a–b*) and 5(*c–d*) it can also be observed that friction effects produce an appreciably higher increase of pressure in the cylinder for both quasi-steady and unsteady cases, and an attenuation of unsteady effects. Typical values of the friction parameter $4fL/D$ can range between 0.5 and 50 (Bar-Meir et al. [8]), and those of parameter $c_0(0)t_f/L$ can typically vary between 5 and 50. Thus, unsteady effects may be very important in some practical situations, and must be taken into account for a proper design of the venting system.

It should be pointed out that in a poorly-designed vent system the required vent area may be very large, and so the hypothesis of uniform conditions and air at rest in the cylinder may not hold. In these situations, which are more likely to occur for large values of $A/\mathcal{A}$ and low values of $c_0(0)t_f/L$, not only Bar-Meir's model but also the present one are inadequate.

For vacuum venting conditions, considerations similar to the previous ones for atmospheric venting can be made in view of Fig. 6. As already mentioned, the pressure in the cylinder and everywhere in the vent is initially equal to $p_0(0)$. At $t=0$, the end of the vent is instantaneously connected to a vacuum tank, where the pressure is assumed constant with time. The flow then becomes choked very rapidly. For low values of $A/\mathcal{A}$, the pressure evolution in the cylinder is very similar to that for the case of atmospheric venting. This also occurs for higher values of $A/\mathcal{A}$ during an initial period of time, which is longer for low values of parameter $c_0(0)t_f/L$; after this period, the pressure increases more slowly and then begins to decrease. In this case, too, as is to be expected, unsteady effects become less important for large values of $c_0(0)t_f/L$. However, for sufficiently large values of $c_0(0)t_f/L$ and $A/\mathcal{A}$, the pressure in the cylinder may become close to the vacuum pressure and oscillate around it (Fig. 6(*b*)). The pressure oscillations in the cylinder are also caused in this case by the pressure waves travelling along the vent. For such cases, the effects of friction lead to the pressure in the cylinder decreasing more slowly and, as in the case of atmospheric venting, prevent the above oscillations (Fig. 6(*d*)). Notice that in the quasi-steady model of Bar-Meir et al. [6] the flow is assumed to be choked at any time, which requires a very small vacuum pressure for large values of $A/\mathcal{A}$. In this work we have considered a vacuum pressure of $0.167p_0(0)$, and therefore the flow may be unchoked, not only at the beginning of the filling process, but also

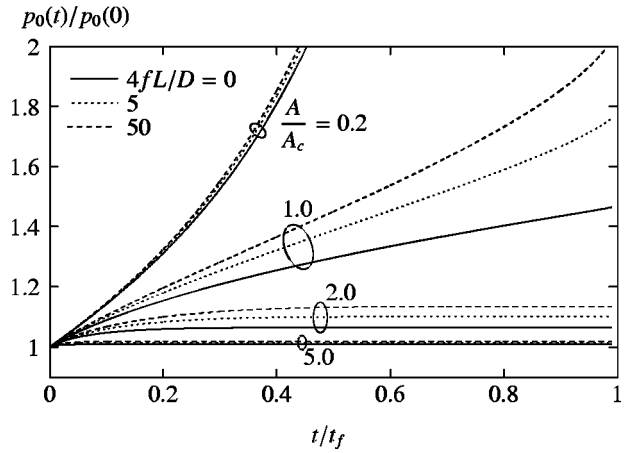

Fig. 7 Effect of friction on the pressure ratio in the cylinder, for atmospheric venting and quasi-steady conditions, and different values of the vent area ratio A/A_c

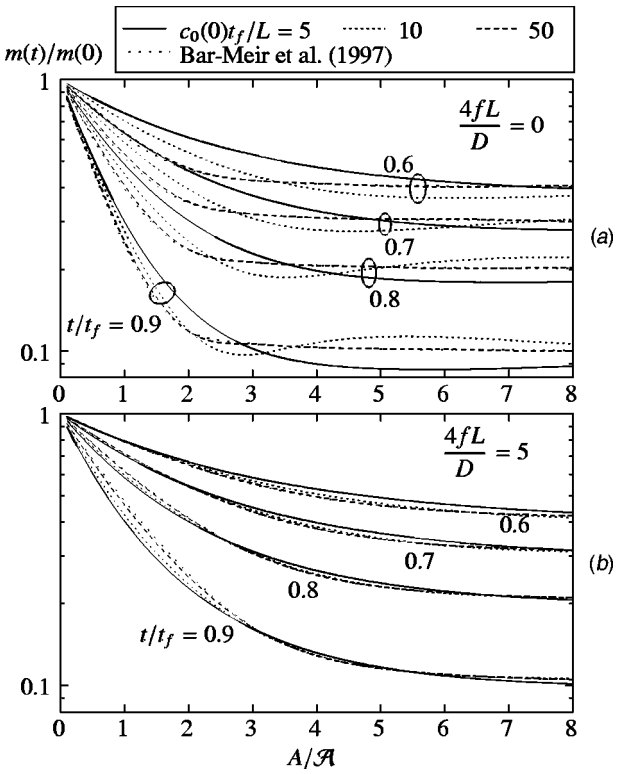

Fig. 8 Effect of the area ratio $A/\mathcal{A}$ on the mass ratio of air remaining in the cylinder at various dimensionless times, t/t_f, for atmospheric venting and different values of $c_0(0)t_f/L$. (*a*) $4fL/D=0$. (*b*) $4fL/D=5$

for sufficiently large values of t/t_f, particularly for large values of $c_0(0)t_f/L$ and $A/\mathcal{A}$ and low values of $4fL/D$. Comparison of the results in Figs. 5 and 6 reveals the effect of vacuum venting versus atmospheric venting. In vacuum venting, an additional substantial reduction in the pressure in the cylinder can usually be attained and, therefore, as will be discussed below, in the mass of residual air. It can be deduced from Figs. 5 and 6 that this is especially true when $A/\mathcal{A}$ is large and the friction effects are low, and that the advantages of using vacuum venting are less evident in poorly-designed vent systems. It should also be pointed out that when unsteady effects are substantial, the actual reduction of pressure in the cylinder is not as high as that predicted by quasi-steady models.

Bar-Meir et al. [6] have shown that, when the flow is choked from the start of the filling process, as is assumed in their quasi-steady model for vacuum venting, the following vent area makes the pressure in the cylinder remain constant with time:

$$A_c = \frac{\mathcal{A}}{M_{\max}\left(1+\frac{\gamma-1}{2}M_{\max}^2\right)^{(\gamma+1)/2(1-\gamma)}}, \tag{17}$$

where $M_{\max}$ is the maximum Mach number at the vent inlet for a Fanno flow. Under these choked conditions, they have also shown that $p_0(t)/p_0(0)$ only depends on A/A_c. For atmospheric venting and quasi-steady conditions, Bar-Meir et al. [8] have studied the effects of A/A_c on the pressure development and on the residual air mass in the cylinder, considering the influence of parameter $4fL/D$ to be quite small. This approximation is more adequate for sufficiently large or low values of A/A_c, for which $p_0(t)/p_0(0)$ depends solely on A/A_c, whereas for intermediate values of A/A_c of around one, $p_0(t)/p_0(0)$ also depends on $4fL/D$, as shown in Fig. 7. In this work we have used $\mathcal{A}$, instead of A_c, to nondimensionalize the vent area in order to show explicitly the influence of the friction parameter, on which A_c depends through $M_{\max}$ (Eq. (17)). For the cases of Figs. 6(*a*-*b*) and 6(*c*-*d*), $A/A_c=1$ corresponds to values of $A/\mathcal{A}$ equal to 1.728 and 3.448, respectively, for which the corresponding curves have been drawn with dashed lines.

For atmospheric venting conditions and for $4fL/D$ values of 0 and 5, respectively, Figs. 8(*a*) and 8(*b*) show the mass ratio of air remaining in the cylinder at different dimensionless times, t/t_f, as a function of the dimensionless vent area, $A/\mathcal{A}$, for different values of the parameter $c_0(0)t_f/L$. It can be observed that results for $c_0(0)t_f/L=50$ are very close to those of the quasi-steady model of Bar-Meir et al. [8], which have also been represented in Fig. 8. Notice that, for this quasi-steady conditions, the air mass within the cylinder at a given t/t_f decreases with $A/\mathcal{A}$, although above a more or less defined critical $A/\mathcal{A}$ ratio, which does not depend on t/t_f, it remains approximately constant. This behavior was already found and discussed by Bar-Meir et al. [8], and may be explained in view of Fig. 5, which shows the decreasing influence of the $A/\mathcal{A}$ ratio on the pressure ratio in the cylinder as $A/\mathcal{A}$ increases. This happens for any value of the friction parameter, although the critical area ratio increases with $4fL/D$. For $4fL/D=0$, the critical area ratio can be taken as equal to 2. For increasing friction effects, the slope of the curve depicting $m(t)/m(0)$ as a function of $A/\mathcal{A}$ is less pronounced, and the critical area ratio becomes less clearly defined, although for $4fL/D=5$ we can consider that it takes on a value of around 4. Despite the above mentioned slight dependence of $m(t)/m(0)=f(A/A_c)$ on $4fL/D$, the two values of the critical area indicated correspond approximately to a sole value of $A/A_c=1.2$, which coincides with that given by Bar-Meir et al. [8] for $4fL/D=5$.

In the case of unsteady conditions, the air mass in the cylinder may not decrease monotonically with $A/\mathcal{A}$ when this value is sufficiently high (Fig. 8(*a*)). The nonmonotonic variation of the air mass in the cylinder which appears in some cases represented in Fig. 8(*a*) is a reflection of the already mentioned oscillating behavior of the pressure inside the cylinder and of the fact that each of the curves represented in this figure corresponds to a given moment in time. For example, in Fig. 5(*a*), for $t/t_f=0.9$, the pressure (and so the mass of air) in the cylinder for $A/\mathcal{A}=5$ is less than the pressure corresponding to a value of $A/\mathcal{A}=10$. It can be observed in Fig. 8(*a*) that the optimum area ratio for which the air mass in the cylinder is minimum, or above which the air mass remains approximately constant, increases with decreasing $c_0(0)t_f/L$ and t/t_f. In the cases represented in Figs. 8(*a*) and 8(*b*) (except for $4fL/D=5$, $t/t_f=0.6$ and $c_0(0)t_f/L=5$, in the range of $A/\mathcal{A}$ shown in the figure), it can be observed that a range of values of $A/\mathcal{A}$ can be found, for which the air mass remaining in

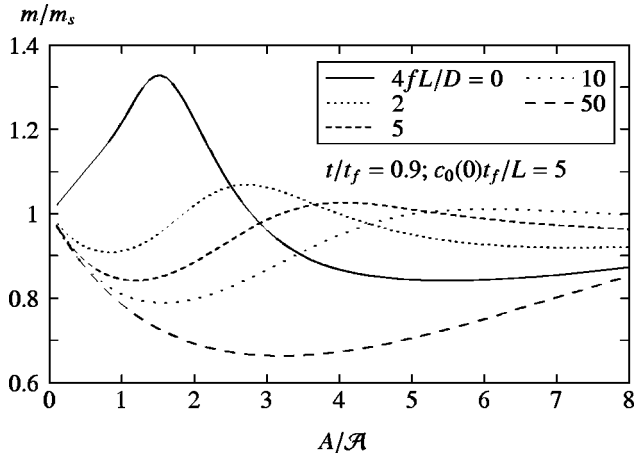

Fig. 9 Effect of the area ratio $A/\mathcal{A}$ on the ratio between the residual air mass in the cylinder at $t/t_f=0.9$, as predicted by the unsteady model for $c_0(0)t_f/L=5$, and that predicted by the model of Bar-Meir et al. [8] for atmospheric venting and different values of the friction parameter

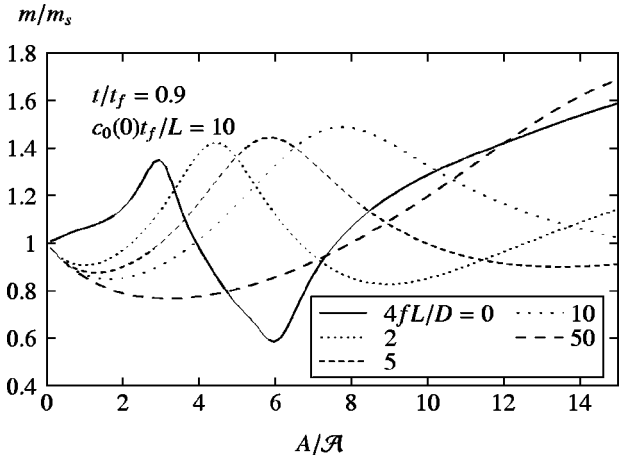

Fig. 11 Effect of the area ratio $A/\mathcal{A}$ on the ratio between the residual air mass in the cylinder at $t/t_f=0.9$, as predicted by the unsteady model for $c_0(0)t_f/L=10$, and that obtained assuming quasi-steady conditions ($c_0(0)t_f/L=500$), for vacuum venting and different values of friction parameter

the cylinder is lower than that corresponding to the critical area for the quasi-steady case. The dependence of the optimum area ratio on t/t_f introduces an additional uncertainty in the selection of an appropriate vent area when the instant at which the molten metal reaches the vent inlet cannot be predicted a priori.

Figure 9 has been prepared to show with more detail the influence of unsteady effects on the mass of air remaining in the cylinder for atmospheric venting. In this figure we represent the ratio between the residual air mass in the cylinder predicted by the unsteady model and that predicted by the quasi-steady model as a function of $A/\mathcal{A}$, for $t/t_f=0.9$, $c_0(0)t_f/L=5$ and different values of the friction parameter. The value of $t/t_f=0.9$ has been taken as a representative value of the time at which the molten metal reaches and blocks the vent. Although important unsteady effects exist for values of A below the critical area, as can be seen in Fig. 8, those which exist in a range of areas around and above the critical area are of greater practical interest. For each value of $4fL/D$, the critical area corresponds to a value of $A/\mathcal{A}$ close to that of the local maximum which can be observed to exist in the corresponding curve of Fig. 9 (for $4fL/D=50$ the maximum is located outside the range of $A/\mathcal{A}$ shown in the figure). It can be observed that the unsteady effects lead to m being greater than m_s for areas slightly greater than the critical and lower than m_s for even greater areas. The variations in m with respect to m_s around the critical area are approximately 25 percent, 7 percent and 3 percent for $4fL/D=0$, 2 and 5, respectively. From the above, it can be deduced that vent areas greater than the critical area pre-

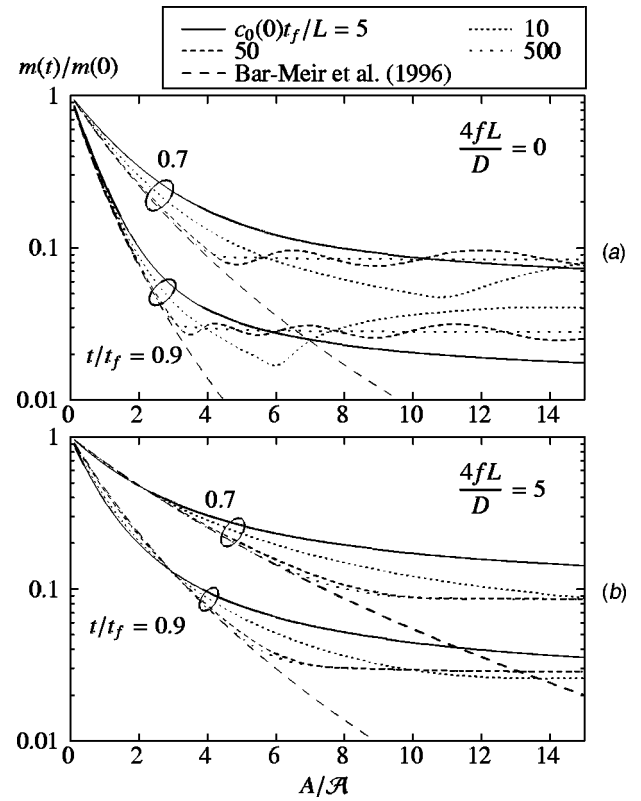

Fig. 10 Effect of the area ratio $A/\mathcal{A}$ on the mass ratio of air remaining in the cylinder at various dimensionless times, t/t_f, for vacuum venting and different values of $c_0(0)t_f/L$. (*a*) $4fL/D=0$. (*b*) $4fL/D=5$

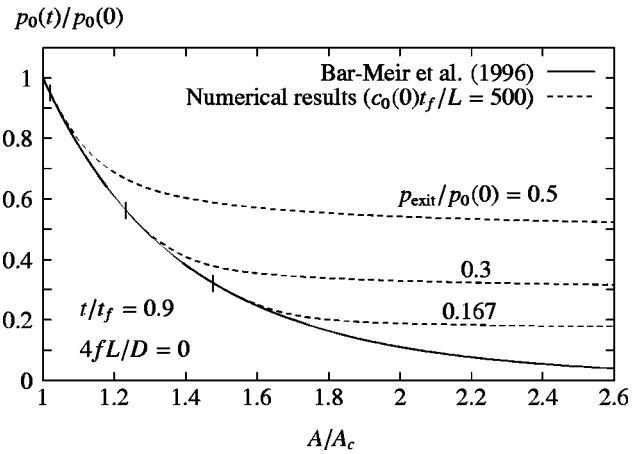

Fig. 12 Effect of vacuum pressure on the pressure ratio in the cylinder at $t/t_f=0.9$ as a function of the vent area ratio A/A_c, predicted by the numerical model for $c_0(0)t_f/L=500$ and by the model of Bar-Meir et al. [6]

dicted by the quasi-steady model give rise to substantial additional reductions in the residual air mass in the cylinder, particularly when friction is low.

Results similar to those of Figs. 8 and 9 are presented in Figs. 10 and 11 for vacuum venting conditions. Notice that, for the reasons explained above, the results for $c_0(0)t_f/L=500$ in Fig. 10, which can be considered as quasi-steady, only coincide with those of the quasi-steady model of Bar-Meir et al. [8] for sufficiently small values of $A/\mathcal{A}$. Also notice that, as occurs for atmospheric venting, for quasi-steady conditions there is a critical vent area above which the residual air mass in the cylinder remains approximately constant. This critical area, besides increasing with $4fL/D$ for a given vacuum pressure, as in atmospheric venting, also depends on t/t_f, decreasing as this parameter increases. For $t/t_f=0.9$ and $p_{\text{exit}}/p_0(0)=0.167$, for example, the critical area ratios for $4fL/D=0$ and 5 are around 3 and 6, respectively, values which correspond to a sole value for A/A_c of around 1.8. The minimum mass of air which can be trapped in the cylinder at a given moment decreases as the vacuum pressure decreases and is reached for venting areas equal to or above the critical area, which, in turn, increases as the vacuum pressure decreases. This can be seen in Fig. 12, which shows the dimensionless pressure in the cylinder as a function of A/A_c for different vacuum pressures and $t/t_f=0.9$. The solid line corresponds to the results of Bar-Meir et al. [6], which are valid for sufficiently low vacuum pressures, and the dashed lines represent numerical results for $c_0(0)t_f/L=500$, which can be considered as corresponding to quasi-steady conditions (results for quasi-steady conditions can also be obtained by numerical integration of the differential equation proposed by Bar-Meir et al. [8] to calculate pressure evolution in the cylinder for atmospheric venting, using the appropriate initial and boundary conditions). Note that, in principle, it is obviously possible to attain pressure values in the cylinder and so of the residual air mass as low as is wished if vacuum pressures are sufficiently low and by choosing a suitably large vent area for the vacuum pressure selected. In practice, the restrictions mentioned in the introduction limit the area of vents.

For unsteady conditions, a comparison of Figs. 8 and 10 shows that the results for vacuum venting are qualitatively similar to those obtained for atmospheric venting, although the unsteady effects in the former are much more important than in the latter particularly in the case of high $4fL/D$ values. This can be seen in greater detail in Fig. 11, which corresponds to a value of $c_0(0)t_f/L=10$ even greater than in Fig. 9, for which the unsteady effects would in principle be less important. Note that the local maximum of m/m_s for each value of $4fL/D$ is reached for a $A/\mathcal{A}$ ratio close to the critical value corresponding to the quasi-steady case. At these maxima, the unsteady effects increase the residual mass of air in the cylinder by 30 percent (when there is no friction) to almost 50 percent for $4fL/D=10$. This means that it may be necessary to use vent areas substantially above the critical areas determined using quasi-steady models in order to reduce the mass of residual air in the cylinder.

Conclusions

The flow through venting systems in pressure die casting processes has been analyzed using an unsteady model for both atmospheric and vacuum venting conditions. The numerical results of the model agree very well with the results of previous quasi-steady models for conditions for which unsteady effects are negligible, as expected. The results of the model have also been extensively compared with some explicit analytical solutions of 1-D unsteady compressible flows with friction and heat transfer effects, and a very good degree of agreement has been found. The results presented in this work show that, for broad ranges of operating conditions, unsteady effects must be taken into account in the selection of design parameters in order to minimize the amount of trapped air and thus porosity in manufactured parts. For sufficiently low values of $c_0(0)t_f/L$, within ranges which are encountered in practical operating conditions, it has been found that unsteady effects can substantially affect the mass of air remaining in the die cavity at a given time. As a consequence, the minimum vent area which provides good ventilation, and above which the residual air mass in the cylinder is not appreciably further reduced (and even increases in some cases), can be considerably higher than the critical area predicted by previous quasi-steady models. The unsteady effects are, in general, higher for vacuum venting conditions and, in the case of vent areas around the critical area corresponding to quasi-steady conditions, may increase the amount of residual air by as much as 50 percent or even more. For atmospheric venting, unsteady effects for vent areas around the critical value corresponding to quasi-steady conditions are lower than those for vacuum venting, particularly when friction effects in the vent are large, although in sufficiently unsteady conditions and when friction is low they may be decisive in choosing appropriate vent areas. This analysis and the results obtained make it possible to establish useful criteria for designing venting systems for use in die casting processes.

Acknowledgments

The authors gratefully acknowledge the support of the Spanish Comisión Interministerial de Ciencia y Tecnología (CICYT) under grants TAP97-0489 and PB98-0007, and the CICYT and the European Commission under grant 1FD97-2333.

Nomenclature

A = cross-sectional area of vent
A_c = area defined in Eq. (17)
$\mathcal{A}$ = area defined in Eq. (6)
c = sound speed
E = relative error between the numerical solution and the exact solution of Eq. (16), $[(u-u_{\text{exact}})/u_{\text{exact}}]$
f = friction coefficient
$\mathcal{F}$ = dimensionless parameter defined in Eq. (12)
D = hydraulic diameter of vent
L = equivalent length of vent
M = Mach number
$M_{\max}$ = maximum Mach number at vent inlet for a Fanno flow
m = air mass in the cylinder
p = pressure
p_{exit} = pressure at vent exit
t = time elapsing from the moment the molten metal enters the runner
t_f = filling time of the cylinder
u = velocity
V = air volume in the cylinder
x = coordinate along the vent
Δx = size of the computational grid
γ = specific-heat ratio
ρ = air density

Subscripts

0 = conditions in the cylinder (runner and die cavity)
1 = conditions at vent inlet
s = quasi-steady conditions

Superscripts

$'$ = dimensionless magnitude

References

[1] Lindsey, D., and Wallace, J. F., 1972, "Effect of Vent Size and Design, Lubrication Practice, Metal Degassing, Die Texturing and Filling of Shot Sleeve on Die Casting Soundness," *Transactions of 7th SDCE International Die Casting Congress and Exposition*, Chicago, IL, paper 10372, 1–15.
[2] Campbell, J., 1991, *Castings*, Butterworth-Heinemann, Oxford.
[3] Garber, L. W., 1982, "Theoretical Analysis and Experimental Observation of Air Entrapment During Cold Chamber Filling," Die Casting Engineer, May-June, pp. 14–22.
[4] Hu, J., Ramlingam, S., Meyerson, G., Eckert, E. R. G., and Goldstein, R. J.,

1992, ''Experiment and Computer Modelling of the Filling Flows in Pressure Die Casting,'' *ASME/CIE Design*, San Francisco, CA, Vol. 1, 401–410.
[5] Hernández, J., López, J., Gómez, P., and Faura, F., 1999, ''Influence of Non-Hydrostatic and Viscous Effects on Shot Sleeve Wave Dynamics in Die Casting Injection,'' *Proceedings of the 3rd ASME/JSME Joint Fluids Engineering Conference. Forum on Advances in Free Surface and Interface Fluid Dynamics*, FED-Vol. 248, San Francisco, CA.
[6] Bar-Meir, G., Eckert, E. R. G., and Goldstein, R. J., 1996, ''Pressure Die Casting: A Model of Vacuum Pumping,'' ASME J. Manuf. Sci. Eng., **118**, 259–265.
[7] Karni, Y., 1991, ''Venting Design in Die Casting: An Analytical Approach,'' *NADCA Congress and Exposition*, Detroit, MI, paper G-T91-OC2.
[8] Bar-Meir, G., Eckert, E. R. G., and Goldstein, R. J., 1997, ''Air Venting in Pressure Die Casting,'' ASME J. Fluids Eng., **119**, 473–476.
[9] Shapiro, A. H., 1954, *The Dynamics and Thermodynamics of Compressible Fluid Flow*, The Ronald Press, New York.
[10] Cai, R., 1998, ''Some Explicit Analytical Solutions of Unsteady Compressible Flow,'' ASME J. Fluids Eng., **120**, 760–764.
[11] Zucrow, M. J., and Hoffman, J. D., 1977, *Gas Dynamics*, Wiley, New York.

Joseph L. Morton
Graduate Research Assistant,
Department of Mechanical & Aerospace Engineering & Engineering Mechanics,
University of Missouri, Rolla, MO 65409
e-mail: jmorton@umr.edu

Nancy Ma
Assistant Professor of Mechanical & Aerospace Engineering,
Department of Mechanical & Aerospace Engineering,
North Carolina State University, Raleigh, NC 27695
Assoc. Member ASME
e-mail: nancy_ma@ncsu.edu

David F. Bliss
Physicist,
e-mail: bliss@rl.af.mil

George G. Bryant
Ceramic Engineer,
e-mail: bryant@maxwell.rl.plh.af.mil

U.S. Air Force Research Laboratory,
Hanscom Air Force Base, MA 01731

Diffusion-Controlled Dopant Transport During Magnetically-Stabilized Liquid-Encapsulated Czochralski Growth of Compound Semiconductor Crystals

During the magnetically-stabilized liquid-encapsulated Czochralski (MLEC) process, a single compound semiconductor crystal is grown by the solidification of an initially molten semiconductor (melt) contained in a crucible. The melt is doped with an element in order to vary the electrical and/or optical properties of the crystal. During growth, the so-called melt-depletion flow caused by the opposing relative velocities of the encapsulant-melt interface and the crystal-melt interface can be controlled with an externally applied magnetic field. The convective dopant transport during growth driven by this melt motion produces nonuniformities of the dopant concentration in both the melt and the crystal. This paper presents a model for the unsteady transport of a dopant during the MLEC process with an axial magnetic field. Dopant distributions in the crystal and in the melt at several different stages during growth are presented.
[DOI: 10.1115/1.1411968]

Introduction

Since molten semiconductors are excellent electrical conductors, a magnetic field can be used to control the dopant distribution in the crystal, which depends on the convective and diffusive transport of the dopant in the melt. Electronic and optical devices are manufactured on single-crystal wafers from ingots of semiconductor crystals. Since the performance of any device depends strongly on the uniformity of the local dopant concentration in the wafer on which it is produced, a major objective during the solidification of any semiconductor is to minimize dopant segregation in the crystal. Hurle and Series [1] and Walker [2] reviewed the literature on the use of magnetic fields during the bulk growth of semiconductor crystals.

The characteristic ratio of the electromagnetic (EM) body force to the viscous force is Ha^2, where $\mathrm{Ha}=BR(\sigma/\mu)^{1/2}$ is the Hartmann number, B is the magnetic flux density of the magnetic field, R is the characteristic dimension of the melt, σ is the electrical conductivity of the melt, and μ is the dynamic viscosity of the melt. Since the ratio of σ to μ is enormous for virtually all molten semiconductors, even a weak magnetic field gives $\mathrm{Ha}=500$ or 1,000 for a typical crystal growth system, so that the EM damping can easily stabilize the melt motion. Bliss et al. [3,4] were the first to use magnetic stabilization to produce 8-cm-diameter twin-free indium-phosphide (InP) crystals.

In order to provide an EM suppression of the melt motion where the dopant transport is dominated by diffusion, the species transport Péclet number, $\mathrm{Pe}_g=U_gR/D$, must be extremely small, where U_g is the characteristic velocity of the magnetically damped melt motion, while D is the diffusion coefficient for the dopant in the molten semiconductor. Since typical values of D are 1 to 2×10^{-8} m^2/s, it is currently not practical to produce a magnetic flux density which is large enough to eliminate melt motion due to buoyant convection, rotationally-driven flow, etc. [5]. It is more practical to use a moderate magnetic field to tailor the melt motion in order to achieve dopant uniformity in the crystal. At each stage during the growth of a crystal by any process, there are infinitely many ways to tailor the strength and configuration of the externally applied magnetic field, the rotation rates of the crystal and crucible, the distribution of heat flux into the melt, the radiative and conductive heat losses from the melt, etc., so that models which accurately predict dopant distribution in an entire crystal are needed to facilitate process optimization.

In the present study, we treat the species transport of iron (Fe) in an InP melt during the magnetically-stabilized liquid-encapsulated Czochralski (MLEC) process with a uniform, steady, axial magnetic field. In a pair of studies, Ma and Walker [5,6] presented an asymptotic treatment which substantially reduced the computational requirements needed to simulate dopant transport in a magnetic field, and thereby provided the first predictions of dopant composition in the entire crystal in a model problem. Using this method, Hirtz and Ma [7] investigated the effect of magnetic field orientation on dopant transport and found that an axial magnetic field produces a crystal with less radial segregation. Recently, Ma and Walker [8] applied this to vertical Bridgman crystal growth with a steady magnetic field. In the present paper, we apply this approach to the MLEC process with so-called melt-depletion flow. We refer to the melt motion caused by the opposing relative motions of the encapsulant-melt interface and crystal-melt interface as melt-depletion flow which drives convection of dopant. Because this flow occurs in any Czochralski process even in the absence of natural or forced convections, this is the Czhochralski equivalent of ''diffusion-controlled growth'' which occurs in directional solidification or Bridgman growth in the limiting case where there is no natural or forced convection.

Contributed by the Fluids Engineering Division for publication in the JOURNAL OF FLUIDS ENGINEERING. Manuscript received by the Fluids Engineering Division October 5, 2000; revised manuscript received July 10, 2001. Associate Editor: L. Mondy.

Melt Motion

This paper treats the unsteady, axisymmetric species transport of iron in an indium-phosphide melt during the liquid-encapsulated Czochralski process with an externally-applied, uniform, steady, axial magnetic field $B\hat{\mathbf{z}}$. Here, B is the magnetic flux density while $\hat{\mathbf{r}}$, $\hat{\theta}$ and $\hat{\mathbf{z}}$ are the unit vectors for the cylindrical coordinate system. An axial magnetic field preserves the axisymmetry of the crystal while a transverse or horizontal uniform magnetic field produces deviations from axisymmetry in the melt composition, leading to undesirable rotational striations in the crystal. Bryant et al. [9] showed that nonuniform magnetic fields are not beneficial for compound semiconductors. Our dimensionless problem is sketched in Fig. 1. The coordinates and lengths are normalized by the crucible's inner radius R, so that γ is the dimensionless crystal radius, and $b(t)$ is the dimensionless depth of the melt. This study uses the bulk approximation which assumes that the crystal-melt and encapsulant-melt interfaces lie in the same horizontal plane at $z=b(t)=b_0-\gamma^2 t$. The crystal-growth velocity is the sum of the velocity at which the crystal is moved upward and the velocity at which the crystal-melt interface moves downward. Here, b_0 is the initial dimensionless melt depth.

Before solidification begins, phosphoric gas is bubbled at high pressure through the indium melt, and indium and phosphorus fuse to form the compound InP. A layer of boron oxide (B_2O_3) encapsulates the melt to prevent escape of the volatile component (P). A single crystal seed is lowered through the B_2O_3 which initiates solidification. Once the crystal has grown to the desired diameter, the crystal is pulled vertically upward at a rate which maintains this diameter. The melt is housed by a quartz crucible which is structurally supported by a graphite susceptor as shown in Fig. 1. For a typical process, $R=4.7$ cm [4].

In the present paper, we treat only one component of the flow, namely the so-called melt-depletion flow. In a reference frame moving with the crucible, the fluid at the encapsulant-melt interface moves downward at a rate $-db/dt$ while the fluid at the crystal-melt interface moves vertically upward at the pull velocity, causing a melt motion which is referred to as the melt-depletion flow. Here, time t is normalized with R/U_g, where U_g is the constant velocity of the crystal-melt interface. This terminology arises because the crystal-melt interface acts as a porous boundary with suction. During growth, there is typically rotationally-driven flow associated with rotations of the crystal and the crucible [10], and the effect of these rotations and of the buoyant convection on the dopant transport will be investigated in a future study. Without a magnetic field, the natural and forced convections are vastly larger than the melt-depletion flow. With a magnetic field, the EM damping suppresses these convections and dramatically reduced their magnitudes so that they become comparable to the melt-depletion flow and even smaller than the melt-depletion flow for some larger field strengths and in some regions of the melt even for weaker field strengths. For example, with melt-depletion flow and buoyant convection with a moderate field strength, during early stages of growth the buoyant convection dominates everywhere except near the interfaces where the melt-depletion flow is large. At later stages, the melt depth is smaller so the buoyant convection is weaker and the melt-depletion flow can dominate most of the melt.

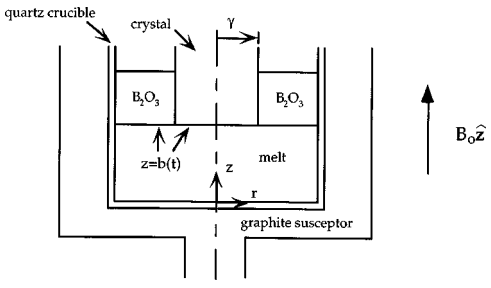

Fig. 1 Magnetically-stabilized liquid-encapsulated Czochralski crystal growth with a uniform, steady, axial magnetic field and with coordinates normalized by the crucible's inner radius

The electric current in the melt produces an induced magnetic field which is superimposed upon the applied magnetic field produced by the external magnet. The characteristic ratio of the induced to applied magnetic field strengths is the magnetic Reynolds number, $R_m=\mu_p\sigma U_g R$, where μ_p is the magnetic permeability of the melt. For all crystal-growth processes, $R_m \ll 1$ and the additional magnetic fields produced by the electric currents in the melt are negligible.

In the Navier-Stokes equation, the characteristic ratio of the EM body force term to the inertial terms is the interaction parameter, $N=\sigma B^2 R/\rho U_g$, which varies as B^2. For a sufficiently strong magnetic field, N is large so that inertial terms are negligible. In a recent study, Ma and Walker [11] investigated the role of inertia on the melt motion during MLEC growth, and determined the errors associated with neglect of inertial effects for field strengths between 0.1 and 0.9 T. For MLEC growth of InP, they found that inertia is totally negligible for $B \geqslant 0.5T$.

For inertialess flow, the melt-depletion flow is governed by

$$-\nabla p+\mathbf{j}x\hat{\mathbf{z}}+\mathrm{Ha}^{-2}\nabla^2\mathbf{v}=0, \tag{1a}$$

$$\nabla\cdot\mathbf{v}=0, \tag{1b}$$

$$\nabla\cdot\mathbf{j}=0, \tag{1c}$$

$$\mathbf{j}=-\nabla\phi+\mathbf{v}x\hat{\mathbf{z}}, \tag{1d}$$

where $\mathbf{v}(r,\zeta,t)=v_r\hat{\mathbf{r}}+v_z\hat{\mathbf{z}}$ is the dimensionless velocity of the melt normalized by U_g, p is the dimensional pressure normalized by $\sigma B^2 U_g R$, $\mathbf{j}$ is the electric current density normalized by $\sigma U_g B$, ϕ is the electric potential function normalized by $U_g BR$. Here, $\zeta=-1+2z/b(t)$ is a rescaled axial coordinate so that $-1 \leqslant \zeta \leqslant +1$ for all time.

In an asymptotic solution for $\mathrm{Ha}\gg 1$, the melt is divided into an inviscid core, Hartmann layers with an $O(\mathrm{Ha}^{-1})$ thickness adjacent to the bottom crucible wall at $\zeta=-1$ and adjacent to the crystal-melt and encapsulant-melt interfaces at $\zeta=+1$. The encapsulant is so viscous that $v_r=0$ at the encapsulant-melt interface. The Hartmann layers have a simple, local, exponential structure, which matches any radial core or parallel layer velocities at $\zeta=+1$, which satisfies the no-slip conditions at the crucible's surface, and the crystal-melt interface and the encapsulant-melt interface, and which indicates that v_z in the core or parallel layer is $O(\mathrm{Ha}^{-1})$ at $\zeta=\pm 1$. For magnetic field strengths of interest, this parallel layer is not actually thin as assumed in the formal asymptotic expansion for $\mathrm{Ha}\gg 1$. While a formal asymptotic analysis for $\mathrm{Ha}\gg 1$ is not appropriate, the numerical solution of the inertialess Navier-Stokes equation with all viscous terms is not necessary. The Hartmann layers represent an extremely small fraction of the melt depth and have a simple exponential structure. Therefore, we use a composite core parallel-layer solution which does not assume that the parallel-layer thickness is small. We discard the viscous terms $\mathrm{Ha}^{-2}\partial^2\mathbf{v}/\partial z^2$ in the Navier-Stokes equation, and we relax the no-slip conditions at $\zeta=\pm 1$ because they are satisfied by the Hartmann layers which are not part of the composite solution.

For our axisymmetric flow, there is no azimuthal electric field, and there is a radial EM body force due to the azimuthal electric current and the axial magnetic field. The streamfunction is governed by

$$\mathrm{Ha}^{-2}\frac{\partial}{\partial r}\left\{\frac{1}{r}\frac{\partial}{\partial r}\left[r\frac{\partial}{\partial r}\left(\frac{1}{r}\frac{\partial\psi}{\partial r}\right)\right]\right\}-\frac{4}{b^2}\frac{1}{r}\frac{\partial^2\psi}{\partial\zeta^2}=0, \tag{2a}$$

where

$$v_r=\frac{2}{b}\frac{1}{r}\frac{\partial\psi}{\partial\zeta}, \tag{2b}$$

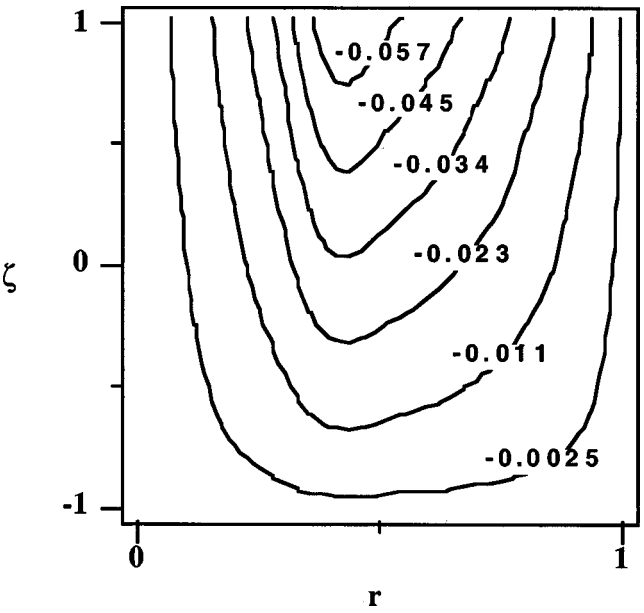

Fig. 2 Streamlines for melt-depletion flow for $\gamma=0.4$, b $=0.6348$, Ha$=2{,}748$, and $U_g=5.556\ \mu$m/s

$$v_z=-\frac{1}{r}\frac{\partial\psi}{\partial r}. \tag{2c}$$

In a typical process, the crystal grows at a rate of $U_g=20$ mm/hr or 5.556 μm/s, which is so small that it is appropriate to treat the melt-depletion flow as quasi-steady, i.e., to neglect inertial effects [12]. The boundary conditions along the crystal-melt and encapsulant-melt interfaces are [12]

$$\psi=-\frac{1}{2}(1-\gamma^2)r^2, \quad \text{at } \zeta=+1, \quad \text{for } 0\leqslant r\leqslant\gamma, \tag{3a}$$

$$\psi=-\frac{1}{2}\gamma^2(1-r^2), \quad \text{at } \zeta=+1, \quad \text{for } \gamma\leqslant r\leqslant 1. \tag{3b}$$

We use a Chebyshev spectral collocation method to solve Eq. (2*a*) with Eqs. (3*a*) and (3*b*) at $\zeta=+1$, the no-slip condition along the crucible's vertical wall, and no-penetration conditions along the crucible's walls. A Galerkin method is used to avoid a Gibb's phenomena associated with the discontinuity in the streamfunction at $r=\gamma$ and $\zeta=+1$. We use Gauss-Lobatto collocation points in r and ζ, and a sufficient number of collocation points in order to resolve all velocity gradients.

The streamlines for the melt-depletion flow are shown in Fig. 2. for $\gamma=0.4$, $b_0=0.6348$, Ha$=2{,}748$ and $U_g=5.556\ \mu$m/s, where the minimum value of the streamfunction is -0.0659. For the results presented in Fig. 2, 31 collocation points in the radial direction and 31 collocation points in the axial direction are enough points to give accurate numerical results. The present inertialess results are certainly appropriate for Ha$=2{,}748$ for which $B=2\ T$ [11]. For a constant growth rate, the minimum value of the streamfunction is constant for all stages of growth. The melt-depletion flow is spread over almost the entire volume of the melt with axially downward flow for $\gamma\leqslant r\leqslant 1$, radially inward flow everywhere, and axially upward flow for $0\leqslant r\leqslant\gamma$. When the electrically-conducting fluid flows radially across the vertical magnetic field, it generates an induced magnetic field which drives an azimuthal electric current which in turn flows across the magnetic field, creating an EM body force which opposes the radial velocity. Since there is no EM body force opposing flow along magnetic field lines, the flow along the magnetic field lines is elongated, so that there is melt-depletion flow over the entire melt.

Dopant Transport

Before solidification begins, the dopant concentration is uniform, and this initial value is used to normalize the concentration C, so that $C(r,\zeta,t=0)=1$. Once crystal growth starts, the crystal rejects dopant into the local melt for $k_s<1$, leaving a dopant-rich region near the crystal-melt interface. Here, k_s is the segregation coefficient which is the ratio of the local dopant concentration in the crystal to that in the melt at any point on the interface. The dimensionless equation governing this dilute species transport is

$$\frac{\partial C}{\partial t}+\mathbf{v}\cdot\nabla C=\mathrm{Pe}_g^{-1}\nabla^2 C, \tag{4}$$

where $\mathbf{v}$ is the dimensionless melt-depletion velocity. The boundary conditions for the crystal-melt and encapsulant-melt interfaces are

$$\frac{2}{b}\frac{\partial C}{\partial\zeta}=\mathrm{Pe}_g(1-k_s)C, \quad \text{at } \zeta=+1, \quad \text{for } 0\leqslant r\leqslant\gamma, \tag{5a}$$

$$\frac{\partial C}{\partial\zeta}=0, \quad \text{at } \zeta=+1, \quad \text{for } \gamma\leqslant r\leqslant 1, \tag{5b}$$

where $\mathrm{Pe}_g=U_gR/D$ is the growth Péclet number. The boundary conditions along the bottom and vertical crucible walls are

$$\frac{\partial C}{\partial\zeta}=0, \quad \text{at } \zeta=-1, \tag{6a}$$

$$\frac{\partial C}{\partial r}=0, \quad \text{at } r=1. \tag{6b}$$

Solutions for the dopant concentrations in the Hartmann layers show that the changes in the conditions (5) and (6*a*) due to the Hartmann layers are smaller than the $\mathrm{O(Ha^{-1})}$ terms which are neglected in the melt motion solutions [5]. Therefore, the Hartmann layers can be ignored in the species transport problem.

We use a Chebyshev spectral collocation method for the convective and diffusive terms in Eq. (4) with Gauss-Lobatto collocation points in r and ζ. We use a sufficient number of collocation points in order to resolve the concentration gradients near $\zeta=\pm 1$ and the velocity gradients near $r=1$. For the time derivative in Eq. (4), we use a second-order implicit time integration scheme from $t=0$ to a t which is slightly less than b_0/γ^2, and use a large enough number of time steps such that the results do not change by increasing the number of time steps.

At the beginning of crystal growth, the melt concentration, normalized with the initial uniform concentration, is $C(r,\zeta,t=0)=1$. Thus the amount of dopant initially in the melt is obtained by integrating across the melt's volume giving a total concentration equal to πb_0. We verify that the sum of the dopant concentration in the melt and in the crystal is equal to πb_0 at each time step.

Assuming that there is no diffusion of dopant in the solid crystal and that the density of the solid and liquid are the same, the dopant distribution in the crystal $C_s(r,\Xi)$, normalized by the initial uniform dopant concentration in the melt, is given by

$$C_s(r,\Xi)=k_sC\left(r,\zeta=+1,t=\frac{b_0-\gamma^2\Xi}{\gamma^2}\right), \tag{7}$$

where $k_s=0.001$ for indium-phosphide doped with iron [13]. Here, $\Xi=\mathrm{b_0}/\gamma^2$ corresponds to the first-grown part of the crystal at $t=0$ while $\Xi=0$ corresponds to the last-grown part of the crystal.

Results and Discussion

For dopant transport with only melt-depletion flow, the constant-concentration curves in the melt at various times and those in the crystal are presented in Figs. 3 and 4, respectively, for $\gamma=0.4$, $b_0=0.6348$, Ha=2,748, $U_g=5.556\ \mu$m/s, and $k_s=0.001$, for which $Pe_g=13.0556$ and the time to grow a crystal is 3.9675. In Fig. 3(*a*), 5% of the crystal has grown when $t=0.1984$, and the maximum value of the concentration is 4.3870. Most of the constant-concentration curves are concentrated in a region near the crystal-melt interface while the remainder of the melt is at its initial uniform concentration $C=1$. Without the melt-depletion flow, the constant-concentration curves would be much more rounded. The melt-depletion flow's upward motion below the crystal-melt interface opposes the diffusion of dopant away from the interface and thus flattens the constant-concentration curves. The minimum dopant concentration in the melt remains at $C=1$ until nearly 10% of the crystal has grown.

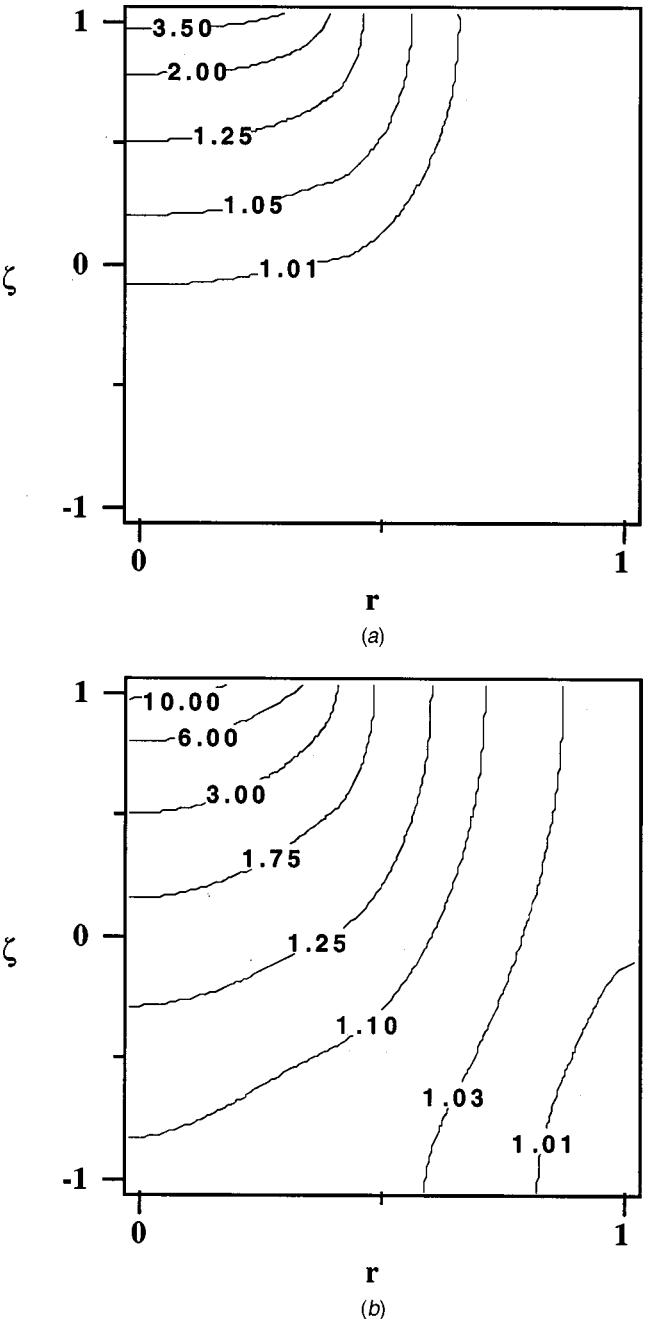

Fig. 3 Contours of the concentration in the melt C(r,ζ,t) for $\gamma=0.4$, b=0.6348, Ha=2,748, $U_g=5.556\ \mu$m/s, and $k_s=0.001$: (*a*) C(r,ζ,t=0.1984), (*b*) C(r,ζ,t=0.7935)

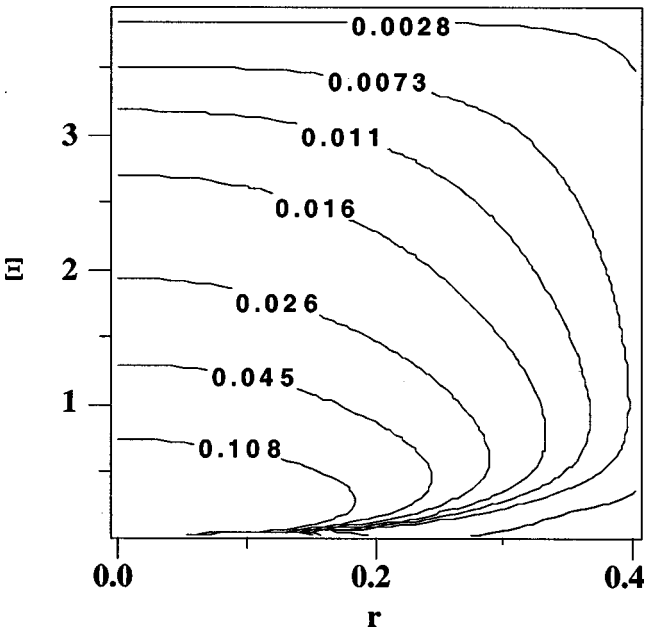

Fig. 4 Contours of the concentration in the crystal $C_s(r,\Xi)$ for $\gamma=0.4$, $b_0=0.6348$, Ha=2,748, $U_g=5.556\ \mu$m/s, and $k_s=0.001$

We use the asymptotic limit for the melt-depletion flow for $Ha\gg 1$ to help understand the transport in the melt at later stages during the growth. For $Ha\gg 1$, (1) the bottom of the crucible moves vertically upward with velocity γ^2 in a reference frame moving with the crystal-melt and encapsulant-melt interfaces, and (2) the melt can be divided into subregions: an inner inviscid core below the crystal-melt interface, an outer inviscid core region below the encapsulant-melt interface, $O(Ha^{-1})$ Hartmann layers adjacent to the crystal-melt and encapsulant-melt interfaces at $\zeta=+1$ and adjacent to the crucible's bottom at $\zeta=-1$,$O(Ha^{-1/2})$ parallel layer adjacent to the vertical crucible wall at $r=1$, and an $O(Ha^{-1/2})$ free shear layer at $r=\gamma$ beneath the crystal edge [14]. In the inner core region for $0\leqslant r\leqslant\gamma$, the radial and axial velocities are

$$v_r(r)=-\frac{r}{2b}(1-\gamma^2),\quad \text{for } 0\leqslant r\leqslant\gamma \text{ and } -1\leqslant\zeta\leqslant+1, \tag{8a}$$

$$v_z(\zeta)=\frac{1}{2}(1-\gamma^2)(\zeta+1),\quad \text{for } 0\leqslant r\leqslant\gamma \text{ and } -1\leqslant\zeta\leqslant+1. \tag{8b}$$

In the outer core region for $\gamma\leqslant r\leqslant 1$, the radial and axial velocities are

$$v_r(r)=\frac{\gamma^2}{2b}\left(r-\frac{1}{r}\right),\ \text{for } \gamma\leqslant r\leqslant 1 \text{ and } -1\leqslant\zeta\leqslant+1, \tag{9a}$$

$$v_z(\zeta)=-\frac{\gamma^2}{2}(\zeta+1),\ \text{for } \gamma\leqslant r\leqslant 1 \text{ and } -1\leqslant\zeta\leqslant+1. \tag{9b}$$

The maximum radial velocity is equal to $(1-\gamma^2)/(2b)$ and increases as b^{-1}.

Near $r=0$, the rejected dopant must diffuse only axially because the solidification is uniformly rejecting dopant back into the melt for early stages of growth. The large axial velocity opposes the diffusion of rejected dopant, so that the concentration remains

high. The dopant rejected near $r=\gamma$ diffuses axially and radially. The axial diffusion is also opposed by the strong axial velocity but Eq. (8*a*) indicates that the radial diffusion is against a relatively weak inward velocity for larger values of b for early stages of growth. Once the dopant diffuses past $r=\gamma$ near $\zeta=+1$, the dopant diffuses axially downward with a small axial velocity as indicated by Eq. (9*b*). Thus this dopant diffuses downward into the outer core and the concentration is small near $r=\gamma$ and $\zeta=+1$, causing more radial diffusion near $r=\gamma$. Thus, a diffusion boundary layer quickly develops near $r=0$, and the crystal concentration rises rapidly as Ξ decreases from its maximum value, as shown in Fig. 4. On the other hand, the rejected dopant near $r=\gamma$ diffuses outward and downward into the outer core, so that no diffusion boundary layer develops at $r=\gamma$, and the crystal concentration remains near k_s for a long decrease in Ξ. This is reflected in the $C_s=0.0073$ contour in Fig. 4, which dramatically curves downward near $r=\gamma$. The outer core is almost well-mixed so that the rejected dopant spreads quickly over the far away melt.

As growth continues, the axial velocities near the interfaces remain constant, but the maximum radial velocity increases as b^{-1}. Since the dopant concentration near $r=0$ is higher than the concentration near $r=\gamma$, the rate of dopant rejection is higher near the centerline than near the periphery of the crystal as reflected in Eq. (5*a*). This leads to a larger concentration gradient near the crystal-melt interface and thus increases diffusion in the radial direction. However, this diffusion is opposed by a larger radial inflow as r increases from $r=0$ to $r=\gamma$, so that dopant accumulates and a diffusion boundary layer develops near $r=\gamma$. The dopant that diffuses downward can diffuse increasingly faster with depth because v_z decreases as ζ, i.e., v_z varies from $(1-\gamma^2)$ at the crystal-melt interface to zero at the crucible bottom in the inner core as indicated by Eq. (8*b*). Near $r=\gamma$, the dopant which diffuses radially to the outer core can easily diffuse axially because of the small downward axial melt motion, leading to the almost vertical constant-concentration curves in Fig. 3(*b*). In Fig. 3(*b*) 20% of the crystal has grown at $t=0.7935$, and the minimum and maximum melt concentrations are 1.005 and 11.99, respectively. Some dopant has entered the outer core but this is a rather small amount of dopant in the large volume of the outer core, so that the concentration in the outer core is still close to $C=1$ and the concentration gradients are small.

During latter stages of growth, higher concentration levels lead to increasingly larger dopant rejection at the crystal-melt interface near $r=0$ due to the higher inward radial velocities coupled with the constant upward axial velocities. Near $r=\gamma$, concentration values remain relatively smaller leading to higher radial non-uniformity in the melt at the crystal-melt interface. This radial non-uniformity is reflected in Fig. 4 for the latter grown sections of the crystal, where the concentration values near $r=0$ are roughly 15 times larger than the concentration values near $r=\gamma$. In contrast, the concentration at $r=0$ at $\Xi=3.5$ is only 2.75 times higher than the concentration at $r=\gamma$.

Conclusions

During the magnetically-stabilized liquid-encapsulated Czochralski growth of compound semiconductors, convective dopant transport due to melt-depletion flow creates undesirable radial non-uniformity in the crystal's dopant concentration.

While this paper treats the melt-depletion flow alone, the dopant transport is also significantly affected by other melt motions. For example, radio-frequency induction heating used to keep the semiconductor molten creates buoyant convection which also drives convection of dopant. Future research will include the effects of these other melt motions in order to support experiments in a search for the optimal growth conditions.

Acknowledgments

This research was supported by the National Aeronautics and Space Administration under grant NAG8-1817, and by the U.S. Air Force Office of Scientific Research. The calculations were performed on the SGI Origin2000 at the National Center for Supercomputing Applications at the University of Illinois at Urbana-Champaign.

Nomenclature

- b = dimensionless melt depth
- B = magnetic flux density of the uniform, steady, axial magnetic field
- b_0 = dimensionless initial melt depth
- C = dimensionless concentration in the melt
- C_s = dimensionless concentration in the crystal
- D = diffusion coefficient for the dopant in the molten semiconductor
- Ha = Hartmann number; square root of the characteristic ratio of the electromagnetic body force to the viscous force
- $\mathbf{j}$ = dimensionless electric current density
- k_s = segregation coefficient
- N = interaction parameter; characteristic ratio of the electromagnetic body force to the inertial force
- p = dimensionless pressure
- Pe_g = species transport Péclet number; characteristic ratio of the convection of species to the diffusion of species
- r = dimensionless radial coordinate
- $\hat{\mathbf{r}}$ = unit vector in the radial direction
- R = crystal radius
- R_m = magnetic Reynolds number
- t = dimensionless time
- U_g = constant velocity of the crystal-melt interface
- $\mathbf{v}$ = dimensionless melt velocity
- v_r = dimensionless radial velocity of the melt
- v_z = dimensionless axial velocity of the melt
- z = dimensionless radial coordinate
- $\hat{\mathbf{z}}$ = unit vector in the axial direction
- γ = dimensionless radius of the crystal
- ζ = dimensionless rescaled axial coordinate in the melt
- $\hat{\theta}$ = unit vector in the azimuthal direction
- μ_p = magnetic permeability of the melt
- Ξ = dimensionless axial coordinate in the crystal
- π = 3.14159 radians
- ρ = density of the melt
- σ = electrical conductivity of the melt
- ϕ = dimensionless electric potential function
- ψ = dimensionless streamfunction in the melt

References

[1] Hurle, D. T. J., and Series, R. W., 1994, "Use of a magnetic field in melt growth," *Handbook of Crystal Growth*, D. T. J. Hurle, ed., Elsevier Science Publishers, Vol. 2A, pp. 261–285.

[2] Walker, J. S., 1999, "Models of Melt Motion, Heat Transfer, and Mass Transport during Crystal Growth with Strong Magnetic Fields," *The Role of Magnetic Fields in Crystal Growth, Progress in Crystal Growth and Characterization of Materials*, K. W. Benz, ed., Elsevier Science Publishers, Vol. 38, pp. 195–213.

[3] Bliss, D. F., Hilton, R. M., Bachowski, S., and Adamski, J. A., 1991, "MLEK Crystal Growth of (100) Indium Phosphide," J. Cryst. Growth, **20**, pp. 967–971.

[4] Bliss, D. F., Hilton, R. M., and Adamski, J. A., 1993, "MLEK Crystal Growth of Large Diameter (100) Indium Phosphide," J. Cryst. Growth, **128**, pp. 451–456.

[5] Ma, N., and Walker, J. S., 1997, "Dopant Transport during Semiconductor Crystal Growth with Magnetically Damped Buoyant Convection," J. Cryst. Growth, **172**, pp. 124–135.

[6] Ma, N., and Walker, J. S., 1997, "Validation of Strong Magnetic Field Asymptotic Models for Dopant Transport in Semiconductor Crystal Growth," J. Cryst. Growth, **180**, pp. 401–409.

[7] Hirtz, J. M., and Ma, N., 2000, "Dopant transport during semiconductor crystal growth. Axial versus transverse magnetic fields," J. Cryst. Growth, **210**, pp. 554–572.

[8] Ma, N., and Walker, J. S., 2000, "A Model of Dopant Transport during Bridg-

man Crystal Growth with Magnetically Damped Buoyant Convection,'' ASME J. Heat Transfer, **122**, pp. 159–164.
[9] Bryant, G. G., Bliss, D. F., Leahy, D., Lancto, R., Ma, N., and Walker, J. S., 1997, ''Crystal Growth of Bulk InP from Magnetically Stabilized Melts with a Cusped Field,'' IEEE *Proceedings of the International Conference on Indium Phosphide and Related Materials*, Hyannis, Cape Cod, MA.
[10] Ma, N., Walker, J. S., Bliss, D. F., and Bryant, G. G., 1998, ''Forced convection during liquid encapsulated crystal growth with an axial magnetic field,'' ASME J. Fluids Eng., **120**, pp. 844–850.
[11] Ma, N., and Walker, J. S., 2001, ''Inertia and Thermal Convection during Crystal Growth with a Steady Magnetic Field,'' AIAA Journal of Thermophysics and Heat Transfer, **15**, pp. 50–54.
[12] Hjellming, L. N., and Walker, J. S., 1987, ''Melt Motion in a Czochralski Puller with an Axial Magnetic Field: Motion due to Buoyancy and Thermocapillarity,'' J. Fluid Mech., **182**, pp. 335–368.
[13] Hurle, D. T. J., 1993, *Crystal Pulling from the Melt*, Springer-Verlag, New York.
[14] Hjellming, L. N., and Walker, J. S., 1988, ''Melt Motion in a Czochralski Crystal Puller with an Axial Magnetic Field: Uncertainty in the Thermal Constants,'' J. Cryst. Growth, **87**, pp. 18–32.

Joon Mo Yang[1]

Chih-Ming Ho

Mechanical and Aerospace Engineering Department, University of California, Los Angeles, Los Angeles, CA 90095

Xing Yang

Yu-Chong Tai

Electrical Engineering Department, California Institute of Technology, Pasadena, CA 91125

Micromachined Particle Filter With Low Power Dissipation

Microfilters for collecting micron-size airborne biological agents are designed and fabricated using a micro-electro-mechanical-system (MEMS) fabrication technology. The thickness of the microfilter ranges from 1 μm–3 μm, and the hole diameter from 5 μm–12 μm. Iterations between experimental and numerical studies are carried out to attain efficient microfilter designs with low pressure drop. Two orders of magnitude reduction of viscous power consumption have been achieved. A design rule of the filter in a low Reynolds-number range was first derived from numerical simulations. Highly accurate measurements of the three-dimensional (3-D) geometry, side-wall profile, and diameter of the micron-size holes are critical in validating and modifying the design rule. The effect of the surface slip is found to be small in the tested Knudsen-number range.
[DOI: 10.1115/1.1399285]

Introduction

Filtering is a common method of collecting particles suspended in air, and the MEMS fabrication technology enables us to make a filter with micron-size openings to separate minute particles from the air [1–5]. The filter is a thin membrane with perforations that are smaller than the diameters of the targeted particles. The thickness of the reported microfilters ranges from 1–3 μm, and the hole diameter from 10 nm–12 μm. Kittilsland et al. [1] fabricated a filter that consisted of two silicon membranes with holes. By changing the membrane separation distance, they fabricated filters for particles down to 50 nm (0.05 μm). van Rijn and Elwenspoek [2] and van Rijn et al. [3] presented a microfilter, having a silicon nitride membrane with uniformly sized pores. The deflection and maximum load of the microfilter were investigated in their study. Yang et al. [4] developed a robust MEMS-based filter that has a micron-thick silicon-nitride membrane coated with Parylene, and they showed that the fracture aerodynamic loading can reach 4 psi (28 kPa) with the Parylene coating. Chu et al. [5] designed and fabricated silicon micropore filters using a sacrificial oxide removal technique. Their special design and fabrication technique enabled them to control pore sizes in the tens of nanometers range with the pore size uniformity within 10 percent. Tu et al. [6] presented a bulk-micromachined, direct-bonded silicon nanofilter that can remove particles as small as 44 nm. By pressuring N_2 at 20 psi (138 kPa), they achieved a flow rate as high as 1.8 l/min/cm^2.

The interesting range of the particle size in this study is 5–15 μm. For detecting airborne biological agents, we need to be able to detect the suspended bio-agents at very low concentrations. In other words, a large amount of air needs to be filtered per unit time. Fast flow through micron-size holes suffers high viscous dissipation. Therefore, efficient designs of the microfilters become critical for lowering the power requirement [7]. The power requirement for the filter is the product of the pressure drop through the microfilter and the volumetric flow rate. Therefore, in order to reduce the power consumption, the pressure drop through the microfilter should be extensively studied and correctly predicted.

The empirical formulas for obtaining the pressure drop have been previously established for the conventional screens or filters. As an example, a formula for the pressure drop through two-layer weaving screens was proposed by Wieghardt [8], and Derbunovich et al. [9] suggested a formula for perforated plates. It should be noted that the Reynolds number of the flow through a microfilter ranges from 1–50. Here, the Reynolds number is defined as $U_{in}d/\beta\nu$, where U_{in} is the inlet velocity, d is the hole size, β is the opening factor of the microfilter (area of holes/total area), and ν is the kinematic viscosity of the air. The velocity passing through the opening is U_{in}/β. However, all the formulas, for the conventional screens or filters were established for a much higher Reynolds number (typically$\gg$50). Therefore, the pressure drop predicted from the empirical formula established for the conventional screen cannot be applied for estimating the pressure drop through the microfilter [4].

At a low Reynolds number range, the creeping flow solution can be used to predict the pressure drop. The creeping flow for an infinitely thin orifice was theoretically studied by Sampson [10]. According to his study, the pressure drop through an orifice is dependent upon the flow rate, the hole diameter, and the viscosity of the fluid. Dagan et al. [11] obtained analytic solutions in the case of an orifice with a finite thickness. They showed that a simple approximate expression, obtained by assuming Poiseuille flow through the orifice and Sampson's solution outside, showed good agreements with the exact solution. Tio and Sadhal [12] carried out analytical studies of the Stokes flow through an infinitesimally thin plate with a periodic array of circular apertures. The geometry as well as the Reynolds number of their study was closer to that of the microfilter in the present case. However, the effect of a finite thickness on the pressure drop was not shown in their study.

Experimental study of the low Reynolds number flow through micron-size hole can be found in Hasegawa et al. [13] and in Yang et al. [4]. Hasegawa et al. carried out experimental and numerical studies for the flow through very small orifices in water flow. The diameter of their study ranged from 8.8 μm to the order of 1 mm. Yang et al. [4] showed, from both the measurement in air flow and the two-dimensional numerical calculation, that the pressure drop through the microfilter was very sensitive to the opening factor.

In the paper by Yang et al. [4], the measured data followed the trend of the numerical formula, but the measured pressure drop was observed to be much lower than that predicted by the Navier-Stokes equation with a no-slip boundary condition at the wall. The deviation could be partly attributed to the micro-fluidic phenomena [14]. When the Knudsen number is high ($\gg$0.01), the surface slip should be taken into consideration [15–17]. Here, the Knudsen number is defined as the ratio between the mean free path of the molecules and the length scale of the flow device (hole diameter of the microfilter in the present study). However, the Knudsen number in the present experiment is not high enough to make the difference between experimental and numerical data. The present

[1]Current affiliation: Nanogen, Inc., 10398 Pacific Center Court, San Diego, CA 92121. E-mail: jyang@nanogen.com

Contributed by the Fluids Engineering Division for publication in the JOURNAL OF FLUIDS ENGINEERING. Manuscript received by the Fluids Engineering Division June 2, 2000; revised manuscript received May 20, 2001. Associate Editor L. Mondy.

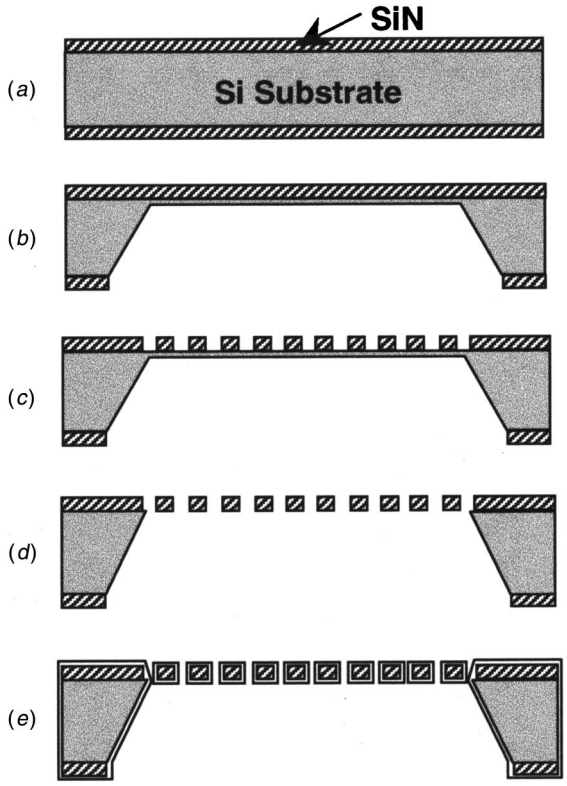

Fig. 1 Fabrication process for the membrane particle filters: (*a*) membrane (SiN) deposition (LPCVD), (*b*) KOH etching of Si wafer, (*c*) Hole patterning (RIE), (*d*) KOH etching of Si wafer, and (*e*) Parylene C deposition

authors believe that the geometry of the microfilter should be precisely characterized prior to taking the micro-fluidic phenomena into consideration.

The objective of the present study is to design and fabricate an efficient microfilter with low pressure drop. In addition, we carried out precise measurements of the geometry of the microfilter and performed a three-dimensional numerical simulation in order to accurately predict the viscous power dissipation in the collection process of micron-size particles.

Microfilter

Fabrication of the microfilter is based on the MEMS technology. A detailed description of the fabrication process is shown in Fig. 1 and Yang et al. [4]. Figure 2 shows the microfilter obtained by the micromachining process. The fabricated microfilter is 10.9 mm×10.9 mm and is composed of a filtering region and a solid frame (see Fig. 2(*a*)). The filtering region, comprising an array of micron-size holes, is an 8 mm×8 mm membrane with a thickness of 1–3 μm. The frame region is a silicon wafer with a thickness of 500 μm. Depending on the mask used in the reactive ion etching (RIE) process, various hole shapes, such as circles (Fig. 2(*b*)), hexagons (Fig. 2(*c*)), and rectangles (Fig. 2(*d*)), are perforated.

As shown in Fig. 3, the hole diameter (d), the spacing between the holes (s), and the thickness (t) determine the geometry of the microfilter. The opening factor (β) can be calculated from the hole diameter, the spacing between the holes, and the hole shape. Normally, d and s can be determined from the mask in the RIE process. However, in the case of the microfilter with Parylene coating, the hole diameter (d) should be measured after the coating is applied.

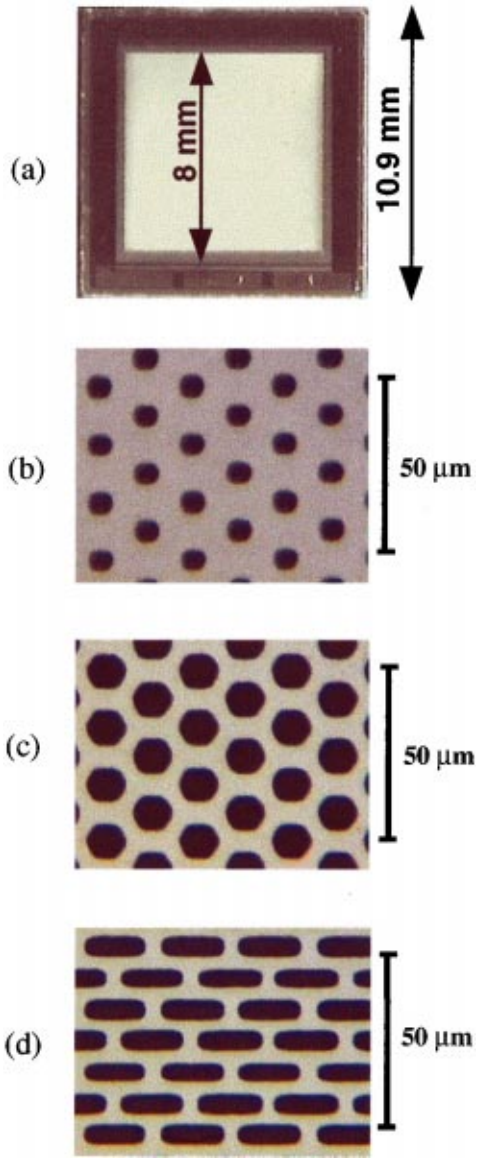

Fig. 2 Photographs of the fabricated microfilters: (*a*) photograph of the entire microfilter, (*b*) filtering region with circular holes, (*c*) filtering region with hexagonal holes, and (*d*) filtering region with rectangular holes

Measurements of Pressure Drop

The pressure drop through the microfilter is measured in a small wind tunnel designed and built for this purpose. The wind tunnel consists of inlet section (bell-mouth and pre-filter), settling chamber, contraction, test section, diffuser, and suction fan [4]. The total length of the wind tunnel is approximately 70 cm. The test section is 30 cm long with a cross section of 8 mm×8 mm. The cross-sectional area of the test section is determined so that the nonfiltering region of the microfilter will not be exposed to the test section of the wind tunnel. A notch into which a microfilter can be inserted is placed 15 cm downstream from the contraction. At the inlet of the wind tunnel, a prefilter is inserted to prevent dust from clogging the microfilter during the measurement.

The flow rate is determined by measuring the static pressure both upstream and downstream from the contraction of the wind tunnel. Solving both the continuity and the Bernoulli equations, the volumetric flow rate (Q) can be calculated as

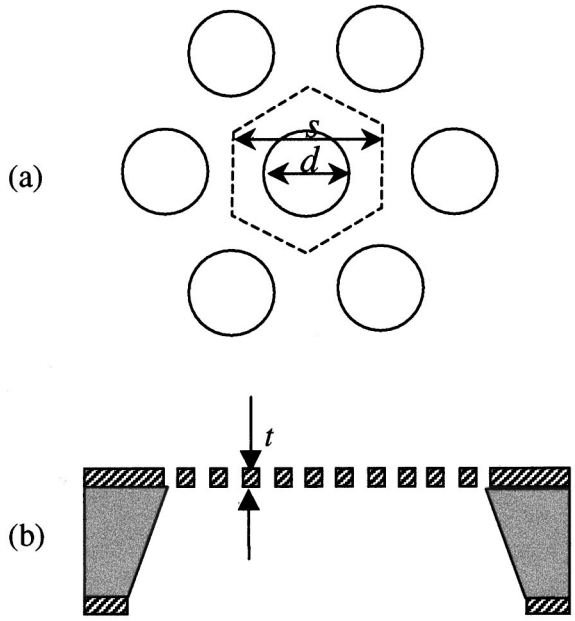

Fig. 3 Geometrical factors in the microfilter: (*a*) front and (*b*) side views

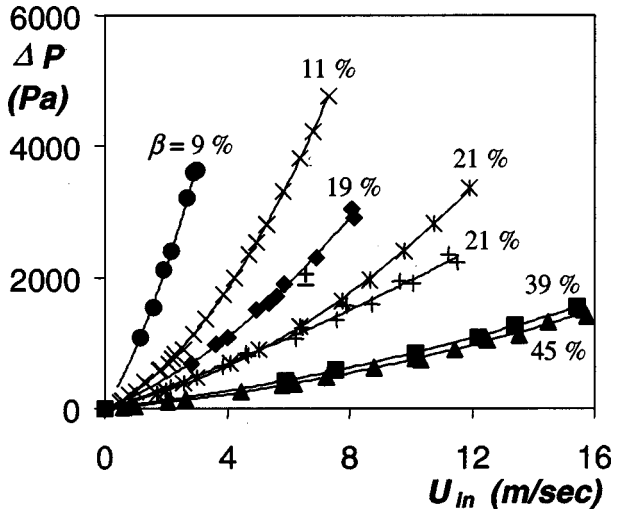

Fig. 4 Measured pressure drop as a function of the inlet velocity for various microfilters. Each line represents second-order fitting curve. For dimensions of each microfilter, see Table 1. (Uncertainties $\Delta P = \pm 2$ percent, Uncertainties $U_{in} = \pm 3.5$ percent).

$$Q = U_2 A_2 = A_2 \sqrt{\frac{2(P_1 - P_2)}{\rho(1 - A_2^2/A_1^2)}}, \tag{1}$$

where U is the average velocity across the cross section, A is the area of the cross section, ρ is the density of air, P is the pressure, and subscripts 1 and 2 represent, respectively, the location upstream and downstream from the contraction. The static pressure upstream and downstream from the contraction is measured by using a differential pressure transducer with a resolution of 0.01 Pa (MKS Baratron). The method of measuring the flow rate is verified by comparing the flow rate determined from Eq. (1) with that measured using a total pressure probe in the test section of the wind tunnel. Therefore, U_2 in Eq. (1) are used as the inlet velocity (U_{in}) throughout this paper. In order to measure the pressure drop through the microfilter, pressure tappings are made both 10 mm upstream and downstream from the microfilter. The pressure drop is measured by using a manometer with a resolution of 1.5 Pa.

Figure 4 shows the measured pressure drop as a function of the inlet velocity for various microfilters fabricated in the present investigation. Table 1 shows the microfilters that were fabricated and tested in this study. It can be seen that by increasing the opening factor from 9 percent to 45 percent, the pressure drop can be reduced by order of magnitude, which will reduce viscous power dissipation significantly.

Three-Dimensional Numerical Simulation

A 2-D numerical simulation of flow through micro openings was performed in a study by Yang et al. [4]. It provided a correct trend but not an accurate prediction of magnitude. We proceed to carry out a 3-D numerical calculation with circular or hexagonal holes. Figure 5 shows the computational domain and the boundary conditions. As shown in Fig. 2 and Fig. 3, the microfilter comprises an array of small holes. Since in the case of the microfilters with circular or hexagonal holes, the boundary between the holes has a hexagonal shape (Fig. 3(*a*)), the microfilter can be regarded as a conglomeration of small hexagonal regions. Therefore, the hexagonal domain with one hole as shown in Fig. 5(*a*) represents the flow field around the microfilter. Yang et al. [4] simplified the 3-D calculation domain to an axisymmetric domain, as shown Fig. 5(*b*). In the axisymmetric domain, the spacing between the holes (s) was determined so that the opening factor (β) would be the same as that in the 3-D domain. Figure 5(*c*) shows the computational domain near the hole in both cases (Fig. 5(*a*) and (*b*)).

Numerical calculations are carried out for both the 3-D and the axisymmetric domains. For the numerical calculations, we assume a laminar flow in a low Reynolds-number range. For the boundary conditions, we use the no-slip boundary condition at the wall, a symmetry boundary condition ($df/dn = 0$, where f is the arbitrary variable and n is the normal vector) at the boundary between the holes, and the uniform velocity far upstream and downstream of the hole (Fig. 5(*a*) and (*b*)). A Computational Fluid Dynamic Research Corporation (CFDRC) software is used to perform calculations.

We perform numerical calculations for various geometric factors (β, d, and t) and inlet velocities (U_{in}) for both the 3-D and the axisymmetric domains. The ranges of the parameters in the calculation are as follows:

$$5 \text{ percent} < \beta < 45 \text{ percent}$$

$$0.08 < t/d < 0.65,$$

$$1 < U_{in} d/\beta\nu < 100.$$

The nondimensional pressure drop ($K = 2\Delta P/\rho U_{in}^2$) should depend upon the aspect ratio (t/d), the opening factor (β), the Reynolds number (Re) and the shape of the hole (hexagonal or circular in this study). Dagan et al. [11] suggested that the pressure drop for the creeping flow through an orifice with a finite thickness can be expressed as follows:

$$\Delta P = \frac{\mu Q_1}{(d/2)^3}\left[\frac{16}{\pi}\left(\frac{t}{d}\right) + 3\right]. \tag{2}$$

Table 1 Microfilters shown in Figs. 4, 16, and 17

Symbol	Hole shape (size in μm)	Thickness (μm)	Opening factor (%)
●	circle (5.4)	3	9
×	circle (10.6)	1	11
◆	circle (8.2)	3	19
+	rectangular (3 x 18)	3	21
✳	hexagon (8.2)	3	21
■	rectangular (5 x 20)	1	39
▲	hexagon (12)	1	45

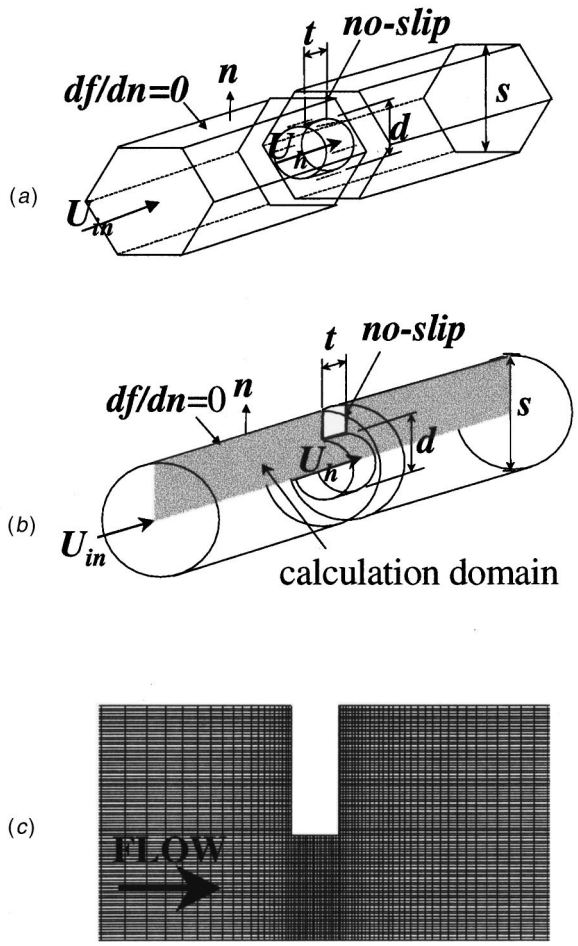

Fig. 5 Calculation domain and boundary conditions for numerically predicting the pressure drop through the microfilter: (*a*) a 3-D domain, (*b*) a simplified axisymmetric domain [4], and (*c*) a magnified region around the hole

Here, Q_1 is the volumetric flow rate through one hole. Dagan et al.'s formula is the case when $\beta \to 0$. Tio and Sadhal [12] considered the creeping flow through a thin membrane with an array of holes. Their solution can be described as

$$\Delta P = \frac{3\mu Q_1}{(d/2)^3}[1 - f(\beta)], \tag{3}$$

where $f(\beta) = \sum_{i=1}^{\infty} a_i \beta^{(2i+1)/2}$ with $a_1 = 0.3389$, $a_2 = 0.1031$, $a_3 = 0.0558$ and $a_4 = 0.0364$ in the case of a hexagonal array of circular holes. van Rijn and Elwenspoek [2] combined Eq. (2) and Eq. (3) and suggested that the creeping flow solution for the pressure drop through a microfilter with a finite thickness can be expressed as follows:

$$\Delta P = \frac{3\mu Q_1}{(d/2)^3}\left[\frac{16}{3\pi}\left(\frac{t}{d}\right) + 1\right][1 - f(\beta)]. \tag{4}$$

In this study, we assume that the nondimensionalized formula can be expressed as

$$K = \frac{\Delta P}{(1/2)\rho U_{in}^2} = \beta^{-2}\left[\frac{16}{\pi}\frac{t}{d} + 3\right]\left[C_1 \frac{\beta \nu}{U_{in} d} + C_2\right]. \tag{5}$$

The constants, C_1 and C_2, are determined so that all the calculated results are collapsed onto a single curve regardless of the dimensions of the microfilters:

Table 2 90 percent confidence intervals of the estimated parameters in Eq. (6)

Estimated parameter	90 % confidence interval
10.7	± 0.16
0.27	± 0.022

$$K = \frac{\Delta P}{(1/2)\rho U_{in}^2} = \beta^{-2}\left(\frac{16}{\pi}\frac{t}{d} + 3\right)\left(10.7\frac{\beta \nu}{U_{in} d} + 0.27\right). \tag{6}$$

Confidence intervals for the determined constants (C_1 and C_2) in Eq. (6) are calculated based on the paper by Donaldson and Schnabel [18], and the 90 percent confidence interval of each constant is shown in Table 2.

The formula is shown in Fig. 6 with some of the calculation results. For comparison, the 2-D numerical formula proposed by Yang et al. [4],

$$K = \frac{\Delta P}{(1/2)\rho U_{in}^2} = \beta^{-2}\left(\frac{t}{d}\right)^{0.28}\left(73.5\frac{\beta \nu}{U_{in} d} + 1.7\right), \tag{7}$$

Dagan et al.'s solution, Eq. (2), and the creeping flow solution for the microfilter, Eq. (4), in the case when $\beta = 20$ percent and $\beta = 45$ percent, are also shown in Fig. 6. The pressure drop predicted by the creeping flow solution decreases as the opening factor increases. It is interesting to note that both 3-D (open symbols and solid line) and axisymmetric (dashed line) calculations collapse onto a single curve. Furthermore, it can be seen that the effect of the hole shape (hexagonal or circular) is very small (e.g., compare the circular symbols with the triangular symbols in Fig. 6).

Equation (6) shows that the pressure drop coefficient varies inversely as the second power of the opening factor (β), while the other factors (t/d and Reynolds number) affect the pressure drop to the first power. Thus, increasing the opening factor is the most effective way to reduce the power consumption. However, the fracture strength decreases when the opening factor is increased.

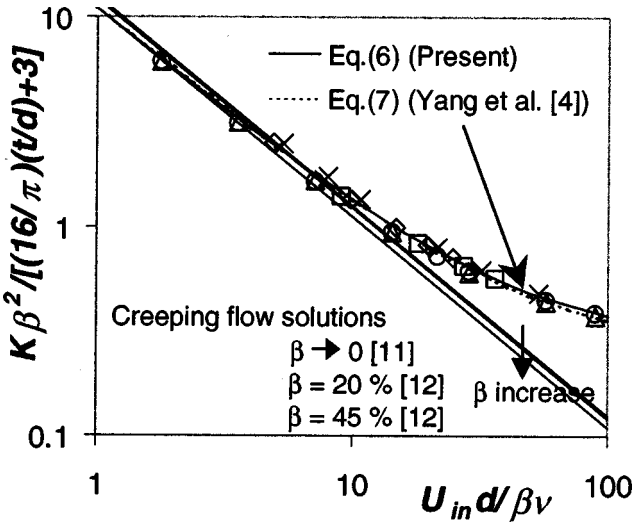

Fig. 6 A nondimensionalized formula obtained from numerical calculations based on the calculation domain shown in Fig. 5. Some of the calculated results are shown as symbols: ○ − d = 12 μm, hexagonal, t = 1 μm, β = 45 percent, Δ − d = 12 μm, circular, t = 1 μm, β = 45 percent, □ − d = 7.8 μm, hexagonal, t = 3 μm, β = 19 percent, x − d = 8 μm, circular, t = 3 μm, β = 20 percent, ◇ − d = 4.8 μm, circular, t = 3 μm, β = 7 percent.

Table 3 Dimensions of microfilters in Fig. 7, Fig. 11, Fig. 14, and Fig. 15

	d (μm)	s (μm)	t (μm)	β (%)	Kn	Membrane
FILTER I	12	18	1	45	0.0057	SiN
FILTER II	8.2	18	3	19	0.0084	Parylene
FILTER III	5.4	18	3	9	0.0127	Parylene

Since the Parylene coating substantially increases the strength [4], it is feasible to make a filter with a large opening factor.

Experimental Validation

Three filters with opening-factor ranging from 9 percent to 45 percent (Table 3) were chosen to validate and improve the empirical formula. All of the microfilters shown in Table 3 have an array of either circular or hexagonal holes. Filters II and III are obtained from the deposition of the Parylene C over the same base filter (Filter I). The spacing between the holes is 18 μm for all three microfilters. The experimental data were found not to fit the 2-D simulation (see Fig. 7), which also had been observed by Yang et al. [4]. There may be two reasons for the mismatch: the surface slip in microflows and/or the measurements of the filter geometry. We will investigate the effects of these two possibilities with the 3-D computational results.

Knudsen Number Effect. In the present case, the Knudsen numbers of the three filters range from 0.0127–0.0057 (Table 3). It is known that the no-slip boundary condition will not hold when the Knudsen number reaches approximately 0.01. Maxwell suggested that the zero wall velocity should be replaced by:

$$u_w = \pm \frac{2-\alpha}{\alpha} Kn \left. \frac{du}{d(y/d)} \right|_w , \tag{8}$$

where α is the accommodation constant ($0<\alpha<1$). Solutions for rarefied gas flow in rectangular and circular cross-sections [16,17] showed that empirical values for α lie between 0.9 to 1.0.

The slip boundary condition was applied in the 3-D code, and its effect on the pressure drop is shown in Fig. 7. The slip boundary condition reduces the pressure drop as expected, and the extent to which it does increases slightly with increasing Knudsen number. However, even after the correction with the surface slip, there are large discrepancies especially in the case of Parylene-coated microfilters (Fig. 7(*b*) and (*c*)), because the Knudsen number is not high enough to make the differences between the measured (Fig. 4) and the calculated pressure drop (Eq. (6)).

Measurements of the Filter Geometry. The viscous dissipation occurs as the flow passes through the micro opening. Therefore, the accuracy of predicting the power dissipation depends on a precise measurement of the hole geometry, which includes the thickness of the filter, the diameter of the filtering hole, and the profile of the hole passage.

The thickness of the microfilter can be measured by using an alphastep and by taking a scanning-electron-microscopic (SEM) picture of a microfilter after purposely breaking the filter (see Fig. 8). The vertical resolution of the alphastep used in this investigation is 0.005 μm, and the measured thickness of Filter III is 2.99 μm. In the measurement using the SEM picture, the thickness is determined by comparing the SEM picture of the filter (Fig. 8(*c*)) with that of 1 μm-resolution grid as shown in Fig. 8(*a*), and the thickness of Filter III is found to be approximately 3.2 μm in this case.

The diameter of the hole is critical because it appears in all three terms in the formula (Eq. (6)). The nominal diameter in the three filters tested here varies from 5–12 μm. Optical methods are used in order to obtain high resolution. We used two different instruments for this purpose: a SEM and a piezo-electrically driven optical-interferometer-type surface profiler (WYKO surface profiler). An image of the filtering hole taken directly by the SEM is shown in Fig. 9(*a*). The hole diameter can be determined by comparing the SEM picture of the microfilter with that of the 1-μm-thick resolution grid (Fig. 8(*a*)).

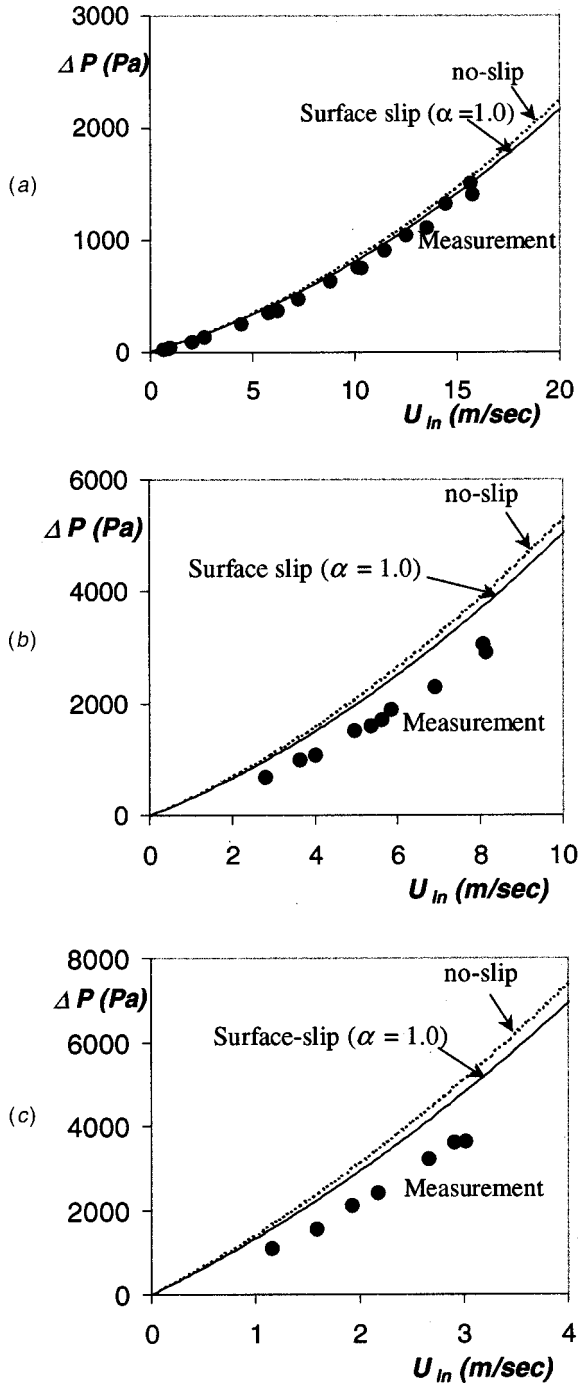

Fig. 7 Comparison of the measured and the calculated pressure drop and the effect of slip boundary condition (α=1.0): (*a*) Filter I, (*b*) Filter II, and (*c*) Filter III. (Uncertainties ΔP = ±2 percent, Uncertainties U_{in} = ±3.5 percent).

Parylene coating is translucent, which could present a difficulty when an optical method is used. In order to avoid this difficulty, the microfilter is coated with 1000-Å gold. Then the surface is profiled by a WYCO surface profiler, with a lateral resolution of approximately 10 nm (0.01 μm). The image taken by using the WYKO surface profiler is shown in Fig. 9(*b*).

Figure 9 shows that the holes are not truly round and are not exactly the same size. We measured the ''diameter'' at eight cir-

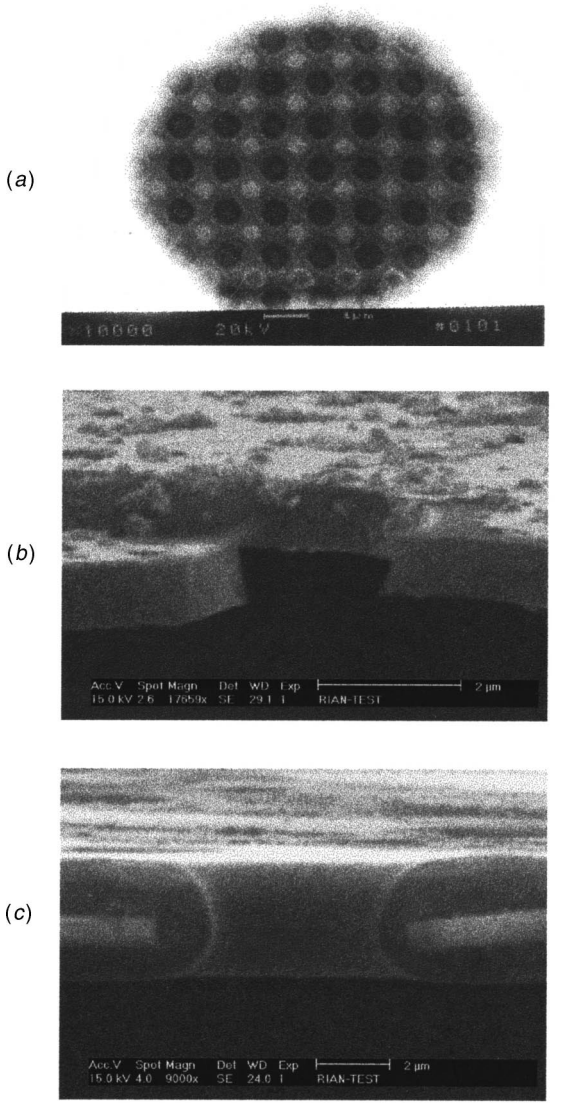

Fig. 8 A SEM picture of (*a*) a 1-μm-thick resolution grid, (*b*) a silicon nitride membrane, and (*c*) a Parylene coated membrane for measuring the thickness of the microfilter and the side-wall profile of the filtering hole

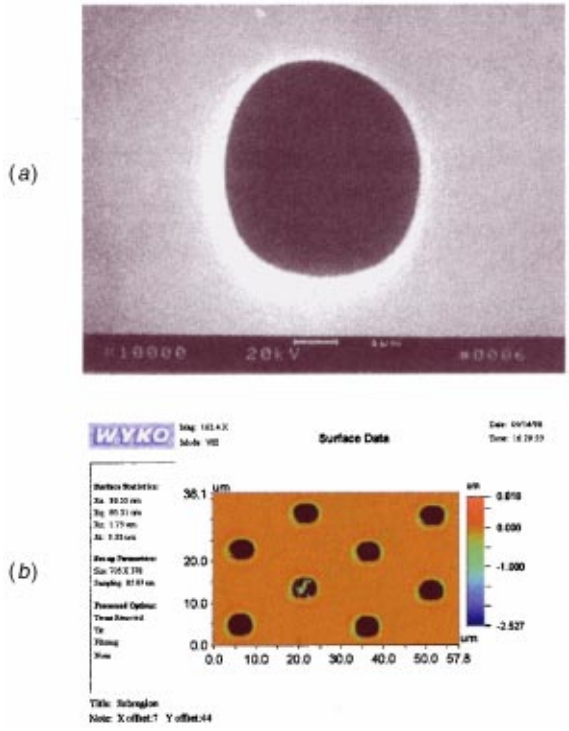

Fig. 9 Images taken for measuring the hole size of the microfilter: (*a*) a SEM picture of one hole and (*b*) an image of the filtering holes from WYKO surface profiler

cumferential directions in one hole, and obtained the average value. The diameters of 100 holes were measured in this way. The distribution of the hole size can be expressed as a histogram ($P(d)$) which is defined as

$$P(d) = \frac{N_d}{N_{\text{total}}}. \tag{9}$$

Here, N_{total} is the total number of the holes measured, and N_d is the number of the holes whose size is $d \pm \Delta d$, where $\Delta d/d = 0.02$. Figure 10 shows the distribution of the hole diameter for a Parylene-coated microfilter (Filter III) obtained from the WYKO images. It can be seen that the diameter is not uniform over the membrane. In this figure, the average diameter and the standard deviation are, respectively, 5.4 μm and 0.5 μm.

The pressure drops of the microfilters with the measured diameters as a function of the free steam velocity are shown in Fig. 11. In order to know the sensitivity of the hole diameter in the pressure drop prediction, the pressure drops with diameters of only one standard deviation (0.5 μm) smaller were calculated and plotted (dashed line in Fig. 11). In these cases, the spacing between the holes is kept constant (18 μm). Even though the difference of the hole diameter is only 0.5 μm from the measured values, the difference in the calculated pressure drops is very large. The difference increases as the hole diameter decreases, because the percentage of the uncertainty increases. When the spacing between the holes is constant, the opening factor depends only on the hole diameter, which makes the calculated pressure drop differ greatly according to the hole size measurement. The sensitivity study shows clearly that an accurate measurement of hole diameter is very important in correctly predicting the pressure drop through the microfilter.

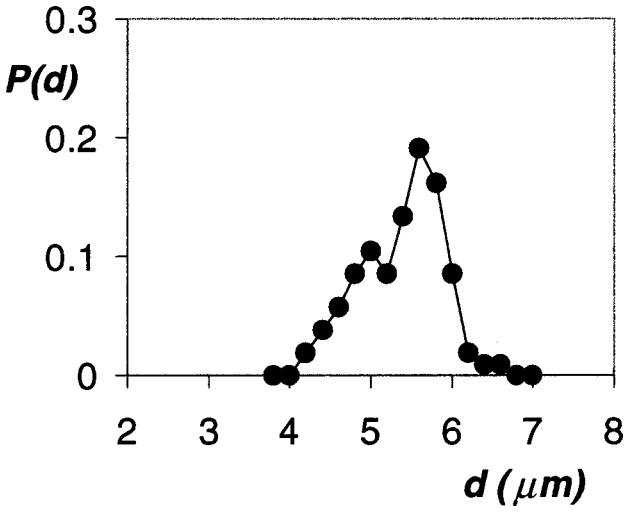

Fig. 10 Probability density function (PDF) of the hole diameter obtained from the images using the WYKO surface profiler ($d_{\text{avg}} = 5.4$ μm)

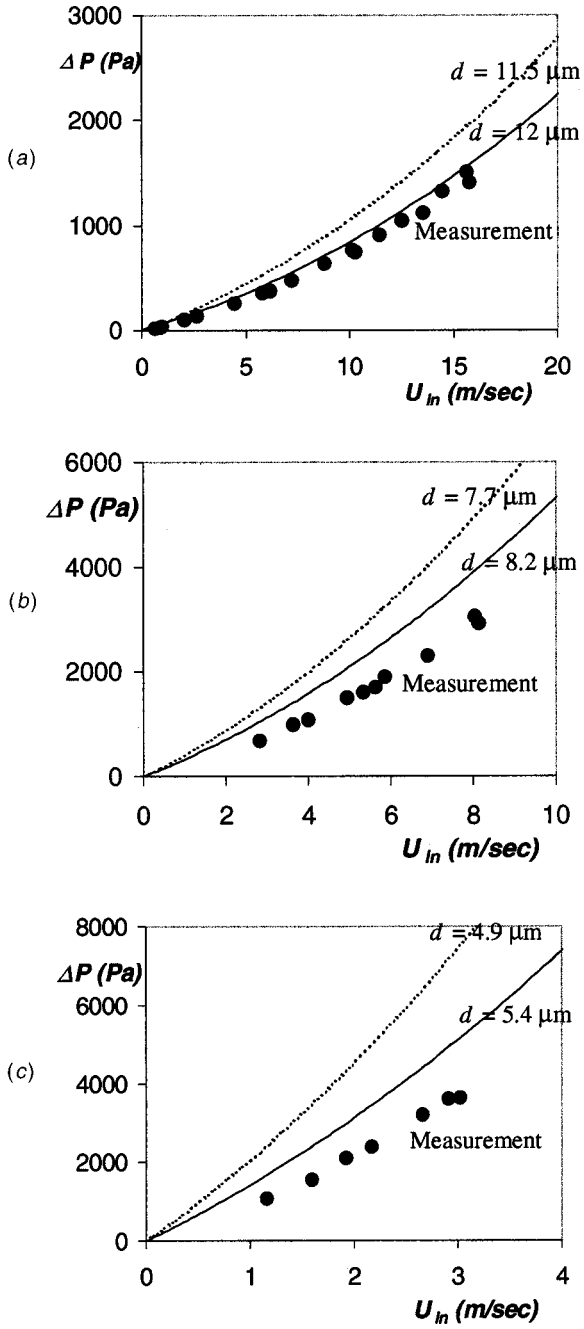

Fig. 11 Comparison of the calculated pressure drop with 0.5 μm error in the measurement of the hole diameter for (*a*) Filter I, (*b*) Filter II, and (*c*) Filter III. (Uncertainties $\Delta P = \pm 2$ percent. Uncertainties $U_{in} = \pm 3.5$ percent).

It should be noted that in Fig. 11 there are still large discrepancies between the measured and calculated pressure drops. The side-wall profile is the next issue to be examined. Reactive ion etching (RIE) is used to etch away the silicon nitride membrane to make the filtering holes. The RIE process is normally used for anisotropic etching, and ideally it would provide a straight side-wall of the filter hole, as is being assumed in the numerical simulation (Fig. 5(*c*)). Figure 8 shows SEM pictures of the cross sections of the microfilters, which are broken at the hole location. Figures 8(*b*) and 8(*c*) show, respectively, the silicon nitride membrane (Filter I) and the Parylene coated membrane (Filter II or Filter III). It can be seen that the side-wall profile of the hole is not straight, which indicates that the side-wall profile shown in

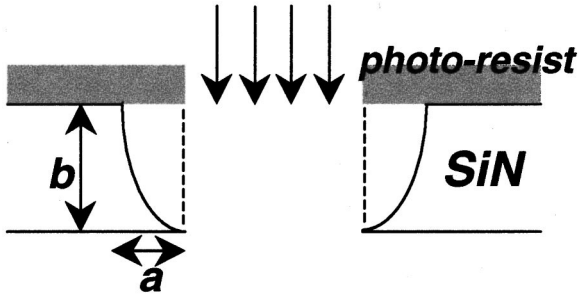

Fig. 12 Side-wall profile of the filtering hole generated by the RIE process (*a*/*b*=0.5; dashed line is ideal case, solid line is real case)

Fig. 5(*c*) should be re-modeled. It has been reported that the side-wall profile generated by the RIE process is not straight [19–21]. May et al. [21] have studied the side-wall profile obtained by the RIE process and showed that the internal profile depends on various plasma parameters. In this study, the internal profile of the hole is observed to be an elliptical shape, and a/b is found to be 0.5 [see Figs. 8(*b*) and 12]. Based on this consideration, we reconstruct a computational domain based on the side-wall profile for the silicon nitride membrane, as shown in Fig. 13(*a*). Figure 13(*b*) shows a computational grid of the side-wall profile, after the Parylene C is conformally deposited on the surface of the silicon nitride membrane.

The numerical results, which are shown in Fig. 14, indicate that the side-wall profile of the filter hole has a strong effect on the pressure drop. This effect becomes more important as the hole size decreases. After the slip boundary condition is taken care of, accurate pressure drops can be predicted with precisely modeled hole diameters and side-wall profiles (Fig. 14).

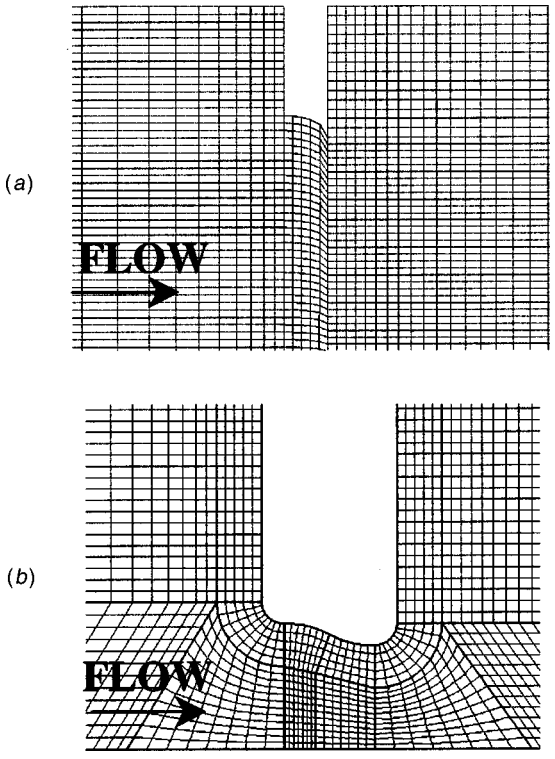

Fig. 13 Computational domain determined from the SEM picture shown in Fig. 8 for (*a*) a silicon nitride membrane and (*b*) a Parylene coated membrane

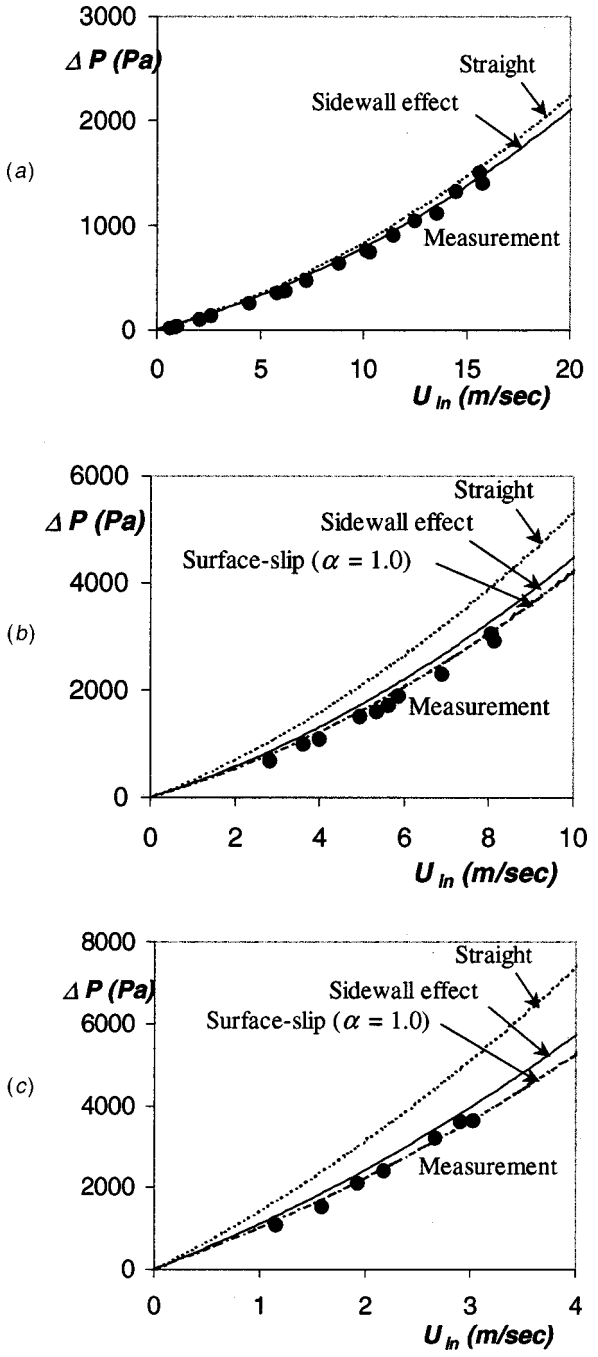

Fig. 14 Comparison between the measured and the calculated pressure drop after the side-wall profile is taken into consideration for (*a*) Filter I, (*b*) Filter II, and (*c*) Filter III. (Uncertainties $\Delta P = \pm 2$ percent, Uncertainties $U_{in} = \pm 3.5$ percent).

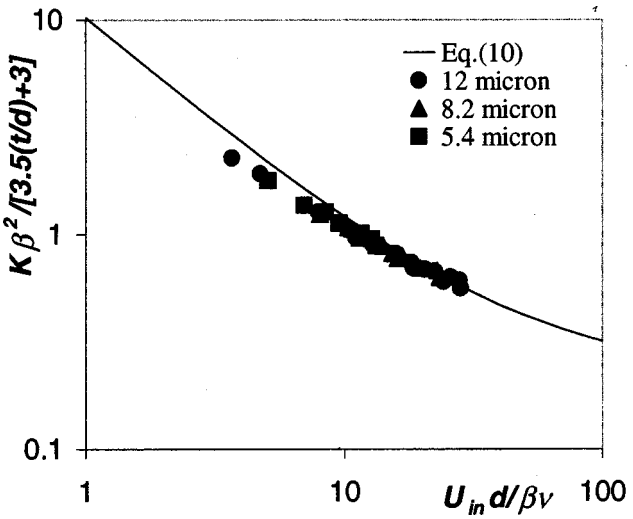

Fig. 15 A nondimensionalized formula, which is established based on the geometry shown in Fig. 13 and a comparison with the measured pressure drop. (Uncertainties $K\beta^2/[3.5(t/d)+3] = \pm 7.8$ percent, Uncertainties $U_{in}d/\beta\nu = \pm 3.9$ percent).

$$K = \frac{\Delta P}{(1/2)\rho U_{in}^2} = \beta^{-2}\left(3.5\frac{t}{d}+3\right)\left(10.0\frac{\beta\nu}{U_{in}d}+0.22\right). \quad (10)$$

The formula is shown in Fig. 15 with the measured data for the three kinds of filters given in Table 2. Confidence intervals for the four constants (3.5, 3, 10.0, and 0.22) in Eq. (10) are calculated [18], and the 90 percent confidence interval of each constant is shown in Table 4. It can be seen that the design formula is in fairly good agreement with the experimental data.

The power required for filtering a certain amount of flow rate (P_{required}) is plotted in Fig. 16 for the microfilters designed and fabricated in the present investigation. The power requirements vary widely. In designing a low-power microfilter, the particle size (d) is a given requirement. Increasing the opening factor is the key for achieving the low power requirement. With a given hole size, the opening factor is determined by how much the spacing between the holes can be decreased and still have enough strength. By using the Parylene coating with a thickness of a few microns, Yang et al. [4] achieved a fracture strength of 4 psi (28 kPa), which is more than 10 times the dynamic head of the highest operating speed (approximately 2 kPa) in the present experiment (see Fig. 4).

On the other hand, a microfilter with rectangular holes can provide a higher opening factor at a given targeted particle size. Figure 17 shows the power requirements for two filters with the same particle threshold but with a different opening factor. In this figure, the opening factor of a filter with a rectangular hole is 39 percent. According to the fitting curve (solid line in Fig. 17), the power needed to filter 20 liter-per-min of air through a 1-cm^2-area

An Accurate Design Formula and Low Power Filter

Based on the issues discussed in the previous section, the design formula is rederived. Although it is still based on a 3-D numerical simulation, the surface slip, the distribution of the accurately measured hole diameters and the side-wall profiles are considered. Calculations are carried out and nondimensionalized so that all the nondimensionalized pressure drops will collapse onto a single curve with respect to the Reynolds number. The formula has the same functional dependence on β, t/d, and Re as that in Eq. (6), but the coefficients are smaller than those in Eq. (6), *i.e.*,

Table 4 90 percent confidence intervals of the estimated parameters in Eq. (10)

Estimated parameter	90 % confidence interval
3.5	± 0.54
3	± 0.15
10.0	± 0.14
0.22	± 0.061

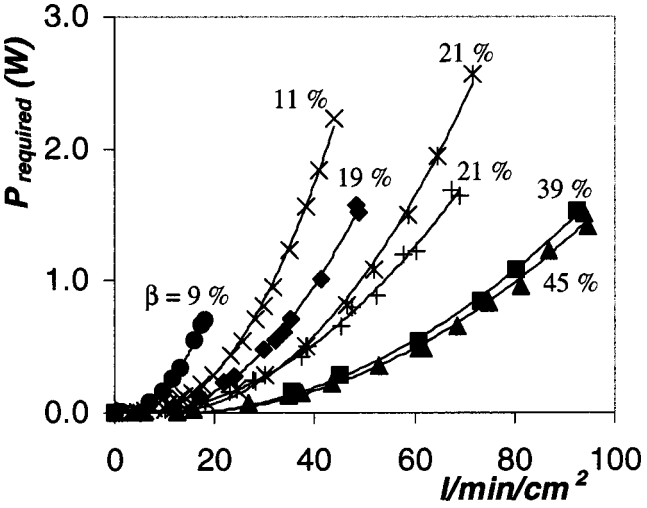

Fig. 16 Power required to sustain a desired flow rate as a function of the flow rate per unit area. See Table 1 for dimensions of each microfilter. Here, each line represents the curve fit of each data set. (Uncertainties $P_{required} = \pm 6.4$ percent, Uncertainties $U_{in} = \pm 3.5$ percent).

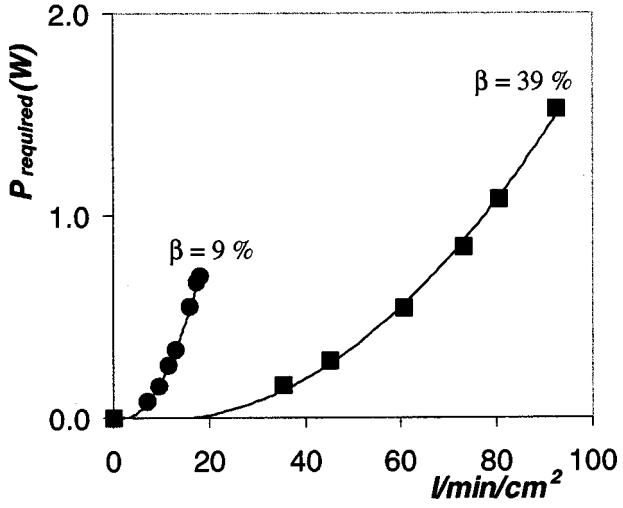

Fig. 17 Comparison of the power requirement with the same particle threshold (5 μm) but different opening factors. See Table 1 for dimensions of each microfilter. Here, each line represents the curve fit of each data set. (Uncertainties $P_{required} = \pm 6.4$ percent, Uncertainties $U_{in} = \pm 3.5$ percent).

microfilter is only 0.03 W. A filter of the same particle threshold but with only a 9 percent opening factor will require 1 W at the same flow rate.

Conclusion

For filtering air through micron-size holes at large flow rate, tens or hundreds of liter-per-minute, high-velocity shear is experienced. The viscous dissipation and, therefore, the power requirement can be extremely high. Numerical simulation is used for deriving a formula for guiding the design of the microfilters. Iterative modifications between experiments and numerical simulation are essential for establishing a design rule. Extremely accurate measurements of the diameter and the side-wall profile of the hole are critical in modifying and reaching a design rule that can provide accurate prediction in power dissipation. The power dissipation is found to be a function of the opening factor, the ratio of the filter thickness to the hole diameter, and the Reynolds number. The power is inversely proportional to the second power of the opening factor. Therefore, increasing the opening factor under the structure strength limit is a key issue. By using a thin coating of Parylene, the fracture strength can be significantly increased. Two orders of magnitude decrease in the power dissipation has been achieved between the first generation and the most recent microfilters fabricated for this investigation. The pressure drops in this experiment are found to be sensitive to slight changes of boundary condition, which suggests opportunities of developing a passive control technique for reducing the pressure drop.

Acknowledgments

This work is supported by the DARPA MICROFLUMES program managed by the Naval Ocean Systems Center (Contract N66001-96-C-83632). The authors would like to thank Dr. Fan-Gang Tseng, Ms. Ellis Meng, and Mr. John D. Mai for their assistance with the measurement of the hole diameter. Ms. Joan George's help in editing the manuscript is greatly appreciated.

Nomenclature

A = cross-sectional area
a = geometrical factor in side-wall profile of the filtering hole
b = geometrical factor in side-wall profile of the filtering hole
d = hole diameter of the microfilter or targeted particle size (particle threshold)
f = arbitrary variable or arbitrary function
K = pressure drop coefficient: $\Delta P/(1/2)\rho U_{in}^2$
Kn = Knudsen number: λ/d
n = wall normal vector
N_d = the number of holes the size of which is d
N_{total} = the total number of holes whose sizes are measured
P = pressure or probability density function (PDF)
P_{required} = power requirement
Q = flow rate
Q_1 = flow rate through one hole
Re = Reynolds number: $U_{in}d/\beta\nu$
s = spacing between the holes in a microfilter
t = thickness of the microfilter
u = velocity
U = average velocity across the cross section
U_h = velocity through the hole: U_{in}/β
U_{in} = inlet velocity
u_w = velocity at the wall
y = wall normal direction
Δd = resolution in determining the PDF of the hole diameter
ΔP = pressure drop
α = accommodation constant
β = opening factor of the microfilter (equals area of holes/total area)
λ = mean free path of the air
ρ = density of the air
ν = kinematic viscosity of the air

Subscripts

1 = upstream
2 = downstream

References

[1] Kittilsland, G., Steme, G., and Norden, B., 1990, "A Submicron Particle Filter in Silicon," Sens. Actuators A, **23**, pp. 904–907.
[2] van Rijn, C. J. M., and Elwenspoek, M. C., 1995, "Micro Filtration Membrane Sieve with Silicone Micro Machining for Industrial and Biomedical Application," Proceedings of IEEE the Eighth Workshop on Micro Electro Mechanical Systems, Amsterdam, the Netherlands, pp. 83–87.
[3] van Rijn, C. J. M., van der Wekken, M., Hijdam, W., and Elwenpoek, M. C., 1997, "Deflection and Maximum Load of Microfiltration Membrane Sieves

Made with Silicon Micromachining,'' J. Microelectromech. Syst., **6**, pp. 48–54.
[4] Yang, X., Yang, J. M., Tai, Y.-C., and Ho, C.-M., 1999, ''Micromachined Membrane Particle Filters,'' Sens. Actuators A, **73**, pp. 184–191.
[5] Chu, W.-H., Chin, R., Huen, T., and Ferrari, M., 1999, ''Silicone Membrane Nanofilters from Sacrificial Oxide Removal,'' J. Microelectromech. Syst., **8**, pp. 34–42.
[6] Tu, J. K., Huen, T., Szema, R., and Ferrari, M., 1999, ''Filtration of Sub-100 nm Particles Using a Bulk-Micromachined, Direct-Bonded Silicon Filter,'' Journal of Biomedical Microdevices, **1**, pp. 113–119.
[7] Ho, C.-M., Huang, P.-H., Yang, J. M., Lee, G.-B., and Tai, Y.-C., 1998, ''Active Flow Control by Micro Systems,'' FLOWCON, International Union of Theoretical and Applied Mechanics (IUTAM) Symposium of Mechanics of Passive and Active Flow Control, Gottingen, Germany, pp. 18–19.
[8] Wieghardt, K. E. G., 1953, ''On the Resistance of Screens,'' Aeronaut. Q., **4**, pp. 186–192.
[9] Derbunovich, G. I., Zemskaya, A. S., Repik, Ye. U., and Sosedko, Yu. P., 1984, ''Hydraulic Drag of Perforated Plates,'' Fluid Mech.-Sov. Res., **13**, pp. 111–116.
[10] Sampson, R. A., 1891, ''On Stokes's Current Function,'' Philos. Trans. R. Soc. London, Ser. A, **182**, pp. 449–518.
[11] Dagan, Z., Weinbaum, S., and Pfeffer, R., 1982, ''An Infinite Solution for the Creeping Motion Through an Orifice of Finite Length,'' J. Fluid Mech., **115**, pp. 505–523.
[12] Tio, K.-K., and Sadhal, S. S., 1994, ''Boundary Conditions for Stokes Flows Near a Porous Membrane,'' Appl. Sci. Res., **52**, pp. 1–20.
[13] Hasegawa, T., Suganuma, M., and Watanabe, H., 1997, ''Anomaly of Excess Pressure Drops of the Flow Through Very Small Orifices,'' Phys. Fluids, **9**, pp. 1–3.
[14] Ho, C.-M., and Tai, Y.-C., 1998, ''Micro-Electro-Mechanical Systems (MEMS) and Fluid, Flows,'' Annu. Rev. Fluid Mech., **30**, pp. 579–612.
[15] Harley, J. C., Huang, Y., Bau, H. H., and Zemel, J. N., 1995, ''Gas Flow in Micro-Channels,'' J. Fluid Mech., **284**, pp. 257–274.
[16] Ebert, W. A., and Sparrow, E. M., 1965, ''Slip Flow in Rectangular and Annular Ducts,'' ASME J. Basic Eng., **87**, pp. 1018–1024.
[17] Sreekanth, A. K., 1968, ''Slip flow through long circular tubes,'' *Rarefied Gas Dynamics*, Academic Press, pp. 667–680.
[18] Donaldson, J. R., and Schnabel, R. B., 1987, ''Computational Experience With Confidence Regions and Confidence Intervals for Nonlinear Least Squares,'' Technometrics, **29**, pp. 67–82.
[19] Pelka, J., Weiss, M., Hoppe, W., and Mewes, D., 1989, ''The Influence of Ion Scattering on Dry Etch Profiles,'' J. Vac. Sci. Technol. B, **7**, pp. 1483–1487.
[20] Daubenspeck, T. H., and Sukanek, P. C., 1990, ''Development of Chlorofluorocarbon/Oxygen Reactive Ion Etching Chemistry for Fine-Line Tungsten Patterning,'' J. Vac. Sci. Technol. B, **8**, pp. 586–595.
[21] May, P. W., Field, D., and Klemperer, D. F., 1993, ''Simulation of Sidewall Profiles in Reactive Ion Etching,'' J. Phys. D: Appl. Phys., **26**, pp. 598–606.

J. Baker

T. Oliver

University of Alabama
Tuscaloosa, AL 35487-0276

L. Lin
Universal Energy System, Inc.,
Dayton, OH

R. Ponnapan
AFRL/PRPG,
Wright-Patterson AFB, OH 45433-7251

J. Leland
University of Dayton Research Institute,
Dayton, OH 45469-0102

Correlations of Critical Froude Number for Annular-Rimming Flow in Rotating Heat Pipes

The behavior of flow within a rotating finite length cylinder has been investigated. For low rotational speeds, the flow is characterized by a non-uniform thickness i.e., rimming flow. Above a critical rotational speed, the flow transitions to annular flow. Correlations developed from the experimental data are presented for the three regimes: onset of annular flow, complete annular flow, and collapse of annular flow. The correlation for the collapse of annular flow compared well with a previously presented, theoretically developed correlation. Given that the heat transfer characteristics of rotating heat pipes depend upon the film thickness of the fluid charge, the correlations presented here will be valuable in determining regular operating conditions. [DOI: 10.1115/1.1411967]

1 Introduction

As in a stationary heat pipe, a rotating heat pipe (RHP) consists of a hollow cylinder. This hollow cylinder may be conceptually divided into three characteristic regions: the evaporator, the adiabatic, and the condenser. In the evaporator region, heat is transferred from the surroundings to the RHP. The fluid in the evaporator region is transformed from a liquid to a vapor via the exchange of latent energy. The resulting vapor generation creates an area of higher pressure in the evaporator region of the RHP. This pressure differential is the mechanism by which the vapor flows from the evaporator region through the adiabatic region to the condenser region. The principal phenomenon in the adiabatic region is the counter-flow transport of the liquid and vapor. In the condenser region, energy is removed from the RHP and is transferred to the surroundings. This results in condensation of the vapor. A small internal taper, along with the rotation of the RHP, produces the centrifugal forces that pumps the condensate back to the evaporator region. A RHP is able to dissipate relatively large heat fluxes at a relatively constant temperature due to the thermodynamic nature of the phase change process.

Gray [1] was the first to propose a rotating heat pipe as a means of transporting large amounts of energy. In Daniels and Al-Jumaily [2], an experimental and theoretical investigation of RHP performance was presented. To theoretically predict the behavior in the condenser region, a modified ''Nusselt-type'' analysis was employed. Unlike previous investigations, consideration of drag on the film-wise condensate by the counter-flowing vapor was included. Drag forces at the liquid-vapor interface were obtained by assuming a friction factor relation. The experimental investigation recorded temperature distributions and heat transfer rates for various speeds and operating conditions. The rate of heat transfer and the temperature distributions across the RHP were found to be directly related to the size of the operating charge (mass of fluid in the heat pipe). The authors observed that the size of the charge is directly proportional to the thickness of the condensate film, e.g., to the film heat transfer resistance. The authors also noted that while there was a theoretically optimal charge size, the charge size should be of sufficient mass to avoid burnout after critical heat flux is reached.

For smaller diameter heat pipes a simple friction factor assumption may not be valid. Faghri et al. [3] developed a more accurate estimate of shear stress and vapor velocity profiles by modeling only the vapor phase of the fluid within a small diameter RHP. Their model, unlike previous investigations, considered the vapor flow over the entire heat pipe as a single domain instead of modeling each of the RHP regions separately. The incompressible Navier-Stokes equations were solved using the finite difference method. Constant properties were assumed throughout the vapor field. Evaporation and condensation of the fluid were modeled by specifying blowing and suction velocities in the evaporator and condenser regions, respectively. In this investigation, it was found that centrifugal forces resulted in a movement of the maximum velocity (at a given location along the centerline) away from the centerline. At higher rotational speeds the flow was observed to reverse at the centerline. The flow reversal became more prominent at increasing speeds and was expected to eventually envelope the evaporator region. As a result of the above phenomenon, radial velocity was positive in the evaporator region and negative in the condenser region. Axial velocity was nearly linear across the radius but was affected by the blowing and suction sections of the heat pipe. The predicted friction factor was significantly affected by rotation at low Reynolds numbers because phenomena in the condenser section were said to propagate upstream. Predicted wall shear stresses increased with rotational speed and were more substantial in the condensation section than the evaporator section.

A further improvement to the above mentioned model was presented in Harley and Faghri [4]. Here a numerical simulation of the vapor phase, similar to that used by Faghri et al. [3], was coupled with the Nusselt type analysis of Daniels and Al-Jumaily [2]. This allowed for both the vapor pressure drop and the increased interfacial shear stress that resulted from the counter-flowing vapor and liquid to be included in the analysis. The coupling of heat conduction in the pipe wall was also included in the investigation although a fixed heat flux was defined at the outer wall interface. Results from the computational model were compared to experimental data presented in Daniels and Al-Jumaily [2]. As in the previous model, a reversal of the vapor core was observed along the length of the RHP. Evaporative blowing was observed to counteract centrifugal forces and therefore reduced the extent of flow reversal. The reversal of the flow in the vapor core was observed to increase in the adiabatic and condenser sections. Throughout the time-dependent analysis, the vapor core was

Contributed by the Fluids Engineering Division for publication in the JOURNAL OF FLUIDS ENGINEERING. Manuscript received by the Fluids Engineering Division July 6, 2000; revised manuscript received June 5, 2001. Associate Editor: P. E. Raad.

nearly isothermal and exhibited only a small axial pressure drop. The appearance of rotational effects in the vapor lagged behind the initial application of rotation and resulted in a nonlinear radial variation of the axial velocity. The nonlinear nature of the axial vapor velocity increased as the flow moved from the evaporator to the condenser section. This indicated that the RHP did not exhibit the solid body rotation that had been assumed in previous studies. The study also concluded that a nonzero axial flow velocity existed at the liquid-vapor interface. This nonzero flow condition resulted in a higher liquid-vapor interfacial shear stress compared to previously reported values.

Several experimental investigations have been undertaken with the aim of determining if it is feasible to use RHPs in high-speed turbomachinery applications [5–11]. Low speed testing of RHPs designed for high speed applications indicate that increased rotational speeds lead to increased heat transport and decreased pipe temperature variations [12]. However, RHP performance has been observed to be relatively sensitive to the external method of cooling the condenser region. In a similar study, Ponnappan et al. [13] investigated the impact of different working fluids (and therefore different thermophysical properties) on high-speed RHP performance. Using water and methanol as the working fluids, it was determined that substances with higher heat capacities increased the overall heat transfer capacity of a RHP. It was also determined that RHPs with a fixed heat flux input to the evaporator region produced higher heat transfer capacities for higher rotational speeds, regardless of the fluid used. One notable point of interest from an implementation point of view was the formation of a non-condensable gas within the RHP when water was used in a stainless steel RHP. During operation of the RHP, the noncondensable gas was observed to migrate to the condenser region of the RHP. This effectively ''shut down'' part of the working area of the condenser, limiting heat pipe performance. When a noncondensable gas was not present, a nearly isothermal wall condition was observed for the optimal operating conditions.

The above investigations have assumed that, for a specified position along the length of the rotating heat pipe, the thickness of the liquid layer is constant in the radial direction. During start-up conditions, or operating conditions below a certain critical rotational speed, this is not the case. Rimming flow may be defined as the existence of a nonuniform radial film thickness in a rotating device due to the interaction of wall shear stress, centrifugal force, and gravity. Figure 1 gives a schematic representation of rimming flow and the transition to annular flow above a certain critical rotational speed. Note that while the figure shows rimming flow wetting the entire perimeter of the cylinder, during the experiments this was not always the case. After the collapse of annular flow, the degree to which the fluid wetted the perimeter of the rotating cylinder depended upon the rotational speed of the cylinder. This fact has definite implications with regard to the performance of rotating heat pipes during actual operating conditions.

Ruschak and Scriven [14] theoretically investigated rimming flow behavior for three limiting cases: acceleration due to gravity approaching zero, cylinder rotational speed approaching infinity, and cylinder radius approaching infinity. Under the assumptions of steady, two-dimensional, viscous flow with a free surface, the theoretical solutions predicted that the maximum film thickness was insensitive to the fluid loading. The authors also noted that all the limiting cases led to solid body rotation but through different mechanisms.

Lin and Groll [15] investigated the conditions that lead to the collapse of annular flow in a rotating heat pipe. A perturbation analysis was used to theoretically predict the critical Froude number for collapse of annular flow. From the theoretical model, the critical Froude number was found to be

$$\mathrm{Fr}=\frac{3}{(1-D)^2} \tag{1}$$

which is a modified version of the criterion presented in Phillips [16]. The modification introduced in Eq. (1) was to account for the experimentally observed, three-dimensional variation of the film thickness in the axial direction near critical conditions. For a loading of $D<0.06$, the above criterion accurately predicted the collapse of annular flow. For a loading of $D>0.1$ the theoretical prediction underestimated the experimentally observed critical Froude number. The fact that the two-dimensional theoretical analysis did not account for the experimentally observed appearance of axial waves (for large values of the loading parameter) was used to explain this discrepancy.

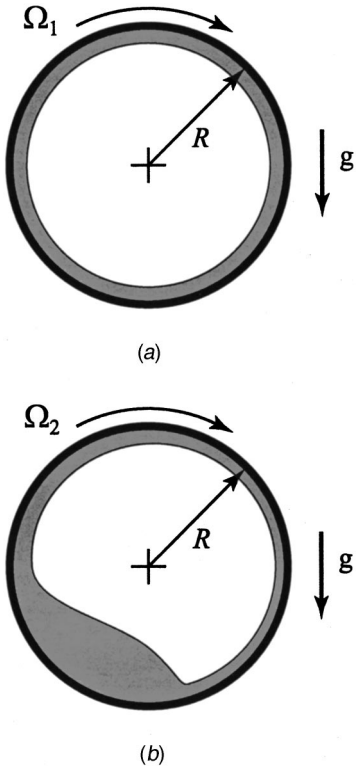

Fig. 1 A schematic representation of (a) annular flow and (b) rimming flow with $\Omega_2<\Omega_c<\Omega_1$

Rotating heat pipes have been proposed as a means of thermal management for next generation turbo-machinery applications. Heat transfer characteristics for rotating heat pipes are directly related to the liquid film thickness. Predicting the transition from rimming flow to annular flow, and the conditions for the collapse of annular flow, is therefore critical to predicting performance characteristics of such devices. Since the principles involved in the onset and collapse of annular flow in a rotating heat pipe are the same as those for a cylinder without taper, this effort has focused upon critical behavior in a hollow cylinder filled with a specified charge of water. For the data presented in this paper, there was no heating or cooling of the cylinder. This investigation has focused only on the hydrodynamic interaction as a means of explaining the discrepancies between previously reported theoretical models and experimental rotating heat pipe data. In Section 2, the experimental apparatus and the procedure used to determine critical Froude numbers are presented. An analysis of the measurement uncertainty and the experimental error is given in Section 3. Results and experimentally determined correlations for conditions corresponding to: the onset of annular flow, complete annular flow throughout the cylinder, and the collapse of annular flow are presented and discussed in Section 4. Closing remarks and conclusions as to the stability characteristics of flow in a rotating cylinder are stated in Section 5.

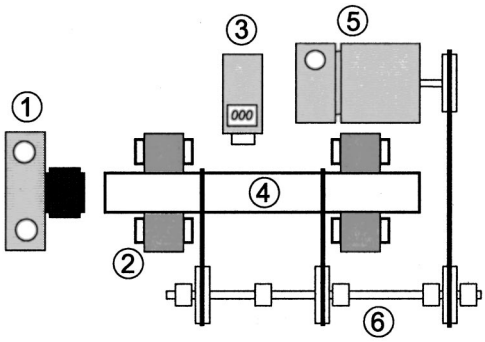

1. 35 mm single reflex camera
2. roller bearing system
3. optical tachometer
4. hollow acrylic cylinder with liquid charge
5. variable speed motor and controller
6. shaft/pulley/bearing system

Fig. 2 A schematic diagram of the experimental test cell

2 Experimental Apparatus and Procedure

A schematic diagram of the experimental test cell is presented in Fig. 2. A 35 mm single reflex camera was used to photograph the behavior of the fluid in the clear acrylic cylinder. The dimensions of the different acrylic cylinders used in this investigation are listed in Table 1. Water was used as the working fluid for all the experiments and the charge corresponding to each cylinder is also shown in Table 1. Water was used as the charging fluid since it has been used as the working fluid for previous rotating heat pipe research and has been used in actual heat pipes. In the present investigation, other fluids were not considered because previous research indicates that the Froude number is the appropriate dimensionless parameter and thus thermophysical properties such as viscosity, surface tension, etc. are not as critical. Once the corresponding liquid charge was placed in the cylinder, the cylinder was permanently sealed by gluing an acrylic disk on the end of the cylinder. The cylinder rested on 4 roller bearings and was held in place as a results of the position of the shaft/pulley/bearing system. A variable speed motor, connected to the cylinder via the shaft/pulley/bearing system, was used to control the rotational speed of the cylinder. An optical tachometer was used to determine the rotational speed of the cylinder.

The following procedure was used to obtain the critical values of the rotational speed corresponding to the onset of annular flow, complete annular flow, and collapse of annular flow. Once a respective cylinder was fixed in place, a test run was made to determine the order of magnitude for each of the conditions of interest. Once this was accomplished, the cylinder was brought to rest. When the motion of the fluid subsided from this initial run, the rotational speed of the cylinder was slowly increased and several photographs of rimming flow at several rotational speeds were taken. The rotational speed was then slowly increased until annular flow was initially observed. Again, a photograph was taken at the point of the initial onset of annular flow and the rotational speed corresponding to this point was recorded. At this point it should be noted that annular flow always occurred near the end of the cylinder with rimming flow in the middle of the cylinder. The rotational speed of the cylinder was again increased until annular flow was observed throughout the cylinder. This rotational speed, corresponding to complete annular flow, was recorded. At this time, the rotational speed of the cylinder was decreased until annular flow collapsed and once again rimming flow was observed. After each cylinder was tested, it was removed and another cylinder was tested. This procedure continued until each cylinder was tested at which time a new series of tests were conducted.

Table 1 Cylinder dimensions and fluid loading

R_o (cm)	L (cm)	V_f (mL)
3.8	61.12	100
	60.96	500
	61.12	1000
2.5	60.96	100
	61.12	500
	60.96	700
1.2	61.12	75
	61.12	100
	61.12	150

3 Uncertainty and Error Analysis

Twenty tests were conducted on each cylinder and for each of these tests the rotational speed corresponding to the onset of annular flow, complete annular flow, and the collapse of annular flow was recorded. The maximum and minimum standard deviations for each of these cases is presented in Table 2. As one can see from Table 2, the maximum standard deviation for all the cases was less than one percent of the average values. From this, we conclude that the repeatability of the experimental data was acceptable.

A simple measurement uncertainty analysis [17] was conducted on the data to determine the accuracy of the Froude number, Fr, and the loading parameter, D. The uncertainty in the measurement of the cylinder length and inner radius was ± 0.794 mm. The uncertainty in the angular speed was ± 0.5 rpm. The uncertainty in the volume of the fluid charge was ± 5 mL. The uncertainty in the total volume of the cylinder was calculated and was found to be: ± 116 mL ($R = 3.8$ cm cylinder), ± 76 mL ($R = 2.5$ cm cylinder), and ± 37 mL ($R = 1.2$ cm cylinder). The uncertainty in the Froude number and the loading parameter is shown relative to the experimental data in Figs. 3, 4, and 5. The measurement uncertainty in the Froude number ranged from approximately 2.1 percent to 6.6 percent of the calculated values while the measurement uncertainty in the loading parameter ranged from 4.2 percent to 14.8 percent of the calculated value.

4 Results and Discussion

At the onset of annular flow, the fluid would transition from annular flow at the ends of the rotating cylinder to rimming flow in a region occupying the center of the cylinder. As the rotational speed increased, this region of rimming flow would decrease until annular flow was observed throughout the rotating cylinder. The transition from the onset of annular flow to complete annular flow occurred in a range of about 100–500 rpm depending upon the cylinder diameter. Once annular flow was established, the well-known hysteresis associated with the collapse of annular flow was observed. Unlike the onset of annular flow, which occurred at the

Table 2 Standard deviation of observed behavior

	RPM / σ_{max}	RPM / σ_{min}
Onset of Annular Flow	2423 / 11	719 / 1.9
Complete Annular Flow	1406 / 9.1	2584 / 2.5
Collapse of Annular Flow	799 / 6.1	339 / 0.7

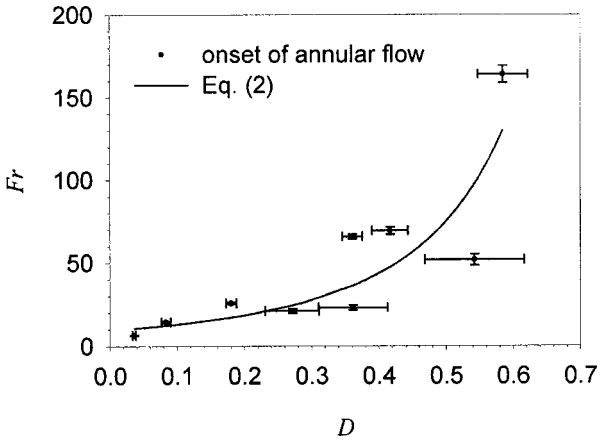

Fig. 3 A plot of critical Froude number for onset of annular flow

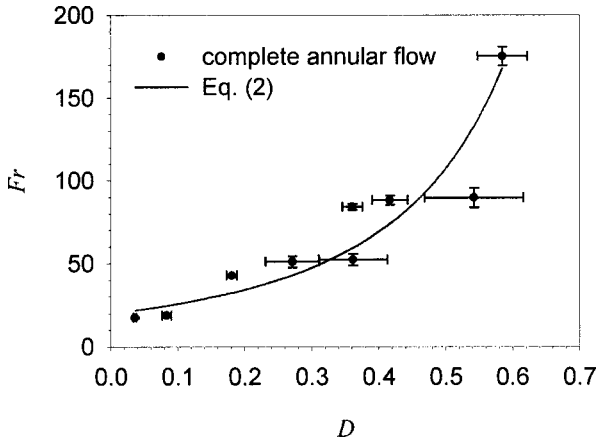

Fig. 4 A plot of critical Froude number for annular flow throughout cylinder

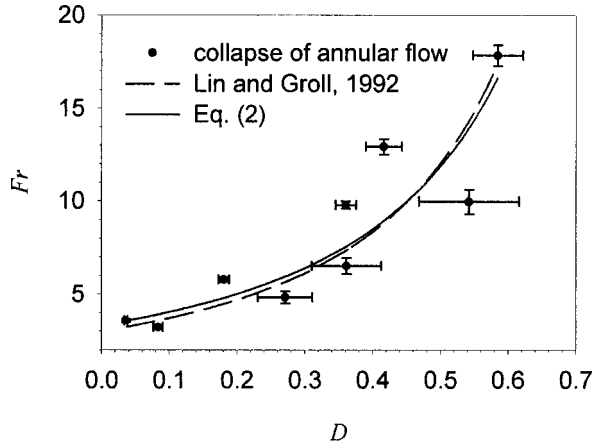

Fig. 5 A plot of critical Froude number for collapse of annular flow

ends of the cylinder and expanded in an axial direction toward the middle of the cylinder, the collapse of annular flow occurred simultaneously throughout the cylinder. For the larger values of the loading parameter, the collapse of annular flow typically occurred at an rpm value that was an order of magnitude less than the rpm value corresponding to the initial observance of complete annular flow in the cylinder. Actual rotating heat pipes have rotational speeds on the order of 200 rpm to 1200 rpm with high-speed rotating heat pipes reaching as high as 30,000 rpm. For the data presented here, the range of rotational speeds was on the order of 300 rpm to 2500 rpm. From this it can be concluded that the rotational speeds investigated in this effort are well within the range for typical rotating heat pipes and would be in the startup range for high-speed rotating heat pipes.

Table 3 Coefficients and correlation coefficient for Eq. (2)

	C_1	C_2	R^2
Onset of Annular Flow	9.60	-2.967	0.7850
Complete Annular Flow	20.03	-2.421	0.8763
Collapse of Annular Flow	3.32	-1.833	0.8309

In Fig. 3, experimentally observed Froude numbers corresponding to the onset of annular flow as a function of the loading parameter are presented. A correlation for the onset of annular flow is also plotted on Fig. 3. This correlation is of the form

$$\mathrm{Fr} = C_1(1-D)^{C_2} \tag{2}$$

where the coefficients associated with the onset of annular flow are given in Table 3. In Eq. (2) the Froude number is defined as

$$\mathrm{Fr} = \frac{\Omega^2 R}{g} \tag{3}$$

where the orientation of the gravitational acceleration relative to the rotating cylinder is identified in Fig. 1. The form of the correlation was chosen to be of the same functional form as that developed in Lin and Groll [15]. Similar plots for conditions corresponding to annular flow throughout the cylinder and to the collapse of annular flow are presented in Fig. 4 and Fig. 5, respectively. Coefficients for the correlations predicting the existence of annular flow throughout the cylinder and the collapse of annular flow are also presented in Table 3. Note that a plot of Eq. (1) is presented in Fig. 3 to allow for comparison between the experimental correlation developed during this investigation and the theoretical prediction of Lin and Groll [15] for the collapse of annular flow. Table 3 also provides a listing of the coefficients of determination for the corresponding experimentally determined correlations.

As can be seen from Fig. 5, the experimental data and the experimentally determined correlation compared favorably with the theoretically developed correlation presented in Lin and Groll [15]. Note that in Lin and Groll [15] the theoretical expression under-predicted the experimentally observed collapse of annular flow for values of the loading parameter greater than 0.05. This discrepancy was attributed to the existence of axial periodicity in the liquid interface. This discrepancy occurred despite the fact that the theoretical model of Lin and Groll [15] was a modification of a previous two-dimensional model. Their modification was intended to account for the three-dimensional variations and gave a value of $C_2=2$ in Eq. (2). It should also be noted that the experimental data presented here was produced without heating the cylinder while the experimental data in Lin and Groll [15] was produced using an actual glass heat pipe. The theoretical model of Lin and Groll [15] was based upon a purely hydrodynamic analysis and thus one would expect that their theoretical model would be more appropriate for the results presented here as compared to results from an actual heat pipe. As can be seen from Table 3, the coefficients of the experimental correlation developed in this investigation are almost exactly those predicted by Lin and Groll [15] i.e., the coefficient associated with Eq. (1).

From the plots of the experimental data, one can see that the experimental data does follow the functional relationship given by Eq. (2) considerably well. The variability in the experimental data could be the results of the increased uncertainty in the values of the loading parameter for larger values of the loading parameter. The variability in the experimental data for larger loading parameters is responsible for the relatively low values of the coefficient of determination shown in Table 3. Note from the correlations that annular flow throughout the cylinder should occur for a Froude number of about twice that corresponding to the onset of annular flow, for a given loading parameter. Also note that, as implied above, once annular flow has been fully established the Froude number can be decreased nearly an order of magnitude before the collapse of annular flow will occur, for a given loading parameter.

5 Concluding Remarks

Results of an experimental investigation examining the stability of flow in a rotating cylinder have been presented. Experimental correlations, in terms of the Froude number and the loading parameter, have been developed to predict the onset of annular flow, the existence of annular flow throughout a finite length cylinder, and the collapse of annular flow. The correlation for the collapse of annular flow compares well with a previously presented theoretical correlation. Curve fits of the experimental data indicate that critical behavior associated with flow in a rotating cylinder follows the functional form of the above-mentioned theoretical correlation. Given the observed behavior at the onset of annular flow, additional investigation into the impact of the ''tube radius to length'' seems warranted. The flows examined here have direct application to rotating heat pipes. The experimentally determined correlations may provide valuable information regarding acceptable operating conditions. Care should be exercised, however, as previously presented data indicates that models developed using a purely hydrodynamic analysis may significantly under-predict behavior involving energy transfer as well.

Acknowledgments

This work was sponsored by the Air Force Research Laboratory's Power Division, through Universal Energy System, Inc. The authors would like to thank T. Huynh, M. Bell, and D. Murphy for their assistance in the construction and data acquisition phases of this effort.

Nomenclature

C = coefficients of experimental correlations
D = fluid loading parameter, $D = V_f / V$
Fr = Froude number, $\mathrm{Fr} = \Omega^2 R/g$
g = acceleration due to gravity
L = length of cylinder
R^2 = coefficient of determination
RHP = rotating heat pipe
R_o = inner radius
rpm = revolutions per minute
V = volume of the cylinder
V_f = volume of the fluid charge
σ = standard deviation
Ω = angular velocity

Subscripts

c = critical
f = fluid
max = maximum
min = minimum

References

[1] Gray, V. H., 1969, ''The Rotating Heat Pipe—A Wickless Hollow Shaft for Transferring High Heat Fluxes,'' ASME Paper No. 69-HT-19.
[2] Daniels, T. C., and Al-Jumaily, F. K., 1975, ''Investigations of the Factors Affecting the Performance of A Rotating Heat Pipe,'' Int. J. Heat Mass Transf., **18**, pp. 961–973.
[3] Faghri, A., Gogineni, S., and Thomas, S., 1993, ''Vapor Flow Analysis Of An Axially Rotating Heat Pipe,'' Int. J. Heat Mass Transf., **36**, No. 9, pp. 2293–2303.
[4] Harley, C., and Faghri, A., 1995, ''Two-Dimensional Rotating Heat Pipe Analysis,'' ASME J. Heat Transfer, **117**, pp. 202–208.
[5] Ponnappan, R., He, Q., Baker, J., Myers, J. M., and Leland, J., 1997, ''High Speed Rotating Heat Pipe: Analysis and Test Results,'' 10th International Heat Pipe Conference, Stuttgart, Germany.
[6] Ponnappan, R., He, Q., and Leland, J. E., 1997, ''Test Results of a High Speed Rotating Heat Pipe,'' AIAA Paper No. 97-2543.
[7] Ponnappan, R., Leland, J. E., and Beam, J. E., 1996, ''Comparison of Performance Results for Water and Methanol Rotating Heat Pipes,'' AIAA Paper No. 96-0477.
[8] Ponnappan, R., and Leland, J. E., 1995, ''High Speed Rotating Heat Pipe for Aircraft Applications,'' SAE 951437, Aerospace Atlantic Conf., Dayton, OH.
[9] Ponnappan, R., Leland, J. E., and Beam, J. E., 1994, ''Thermal Management Issues of Rotors in Rotating Electrical Machines,'' SAE 942184, Aerotech '94, Los Angeles, CA.
[10] Ponnappan, R., and Leland, J. E., 1994, ''Rotating Heat Pipe for Cooling of Rotors in Advanced Generators,'' AIAA Paper No. 94-2033.
[11] Streby, M. A., Ponnappan, R., Leland, J. E., and Beam, J. E., 1996, ''Design and Testing of a High Speed Rotating Heat Pipe,'' Paper No. 96301, IECEC-96, Washinton, DC.
[12] Ponnappan, R., and Leland, J. E., 1994, ''Rotating Heat Pipe for Cooling of Rotors in Advanced Generators,'' AIAA Paper No. 94-2033.
[13] Ponnappan, R., Leland, J. E., and Beam, J. E., 1996, ''Comparison of Performance Results for Water and Methanol Rotating Heat Pipes,'' AIAA Paper No. 96-0477.
[14] Ruschak, K. J., and Scriven, L. E., 1976, ''Rimming Flow of liquid in a Rotating Horizontal Cylinder,'' J. Fluid Mech., **76**, Part 1, pp. 113–125.
[15] Lin, L., and Groll, M., 1992, ''Critical Conditions for Collapse of Annular Flow in a Rotating Heat Pipe with Cylindrical Wall,'' Adv. in Heat Pipe Science & Tech., Proc. 8th Intl. Heat Pipe Conf., pp. 452–456.
[16] Phillips, O. M., 1960, ''Centrifugal Waves,'' J. Fluid Mech., **7**, pp. 340–352.
[17] Holman, J. P., 1994, *Experimental Methods for Engineers*, McGraw-Hill, New York, pp. 49–56.

C. L. Zhang
e-mail: clzhang@mail.sjtu.edu.cn

G. L. Ding
Professor
e-mail: glding@mail.sjtu.edu.cn

Institute of Refrigeration and Cryogenics,
Shanghai Jiaotong University,
Shanghai 200030, China

Modified General Equation for the Design of Capillary Tubes

In order to improve the design efficiency of capillary tubes, capillary tube models have been developed. Yilmaz and Ünal presented a general approximate analytic equation for the design of adiabatic capillary tubes. In this work, the Yilmaz-Ünal equation was analyzed in detail and some problems were found. Consequently, a modified general equation was developed and verified by theoretical and experimental data.
[DOI: 10.1115/1.1411970]

1 Introduction

The capillary tube is widely used as a throttling device in the small vapor refrigeration equipment such as household refrigerators and freezers, dehumidifiers, and room air conditioners. It is simple, reliable, and inexpensive. In addition, the pressure-equalizing characteristic of a capillary tube makes a low starting torque of compressor. Most used diameters of capillary tubes are between 0.6 and 2.0 mm, and most used lengths are between 0.5 and 5 m.

A number of research works have been carried out since 1940 on capillary tubes both in theory and experiment [1]. Especially in the past ten years or so, the capillary characteristics have been widely studied with new alternative refrigerants. Because the selection of the proper diameter and length of a capillary tube for a given application is largely a trial-and-error process, computer models have been developed in several ways.

The most established model of capillary tubes is distributed-parameter model. Many researchers such as Kuehl and Goldschmidt [2], Li et al. [3], Escanes et al. [4], Bittle and Pate [5], Chung [6], Sami and Tribes [7], and Jung et al. [8] developed this kind of capillary model and gave acceptable prediction accuracy against experimental data. Because of the general mechanism in modeling, the distributed-parameter model is suitable for performance prediction of new working fluids flowing through capillary tubes. However, the computation of the distributed-parameter model is time-consuming, especially in the case of refrigeration system simulation and optimization. In addition, the program skill of the model is somewhat difficult for most engineers.

Empirical correlations are used for simple prediction in engineering applications. This kind of model is obtained by the multivariable regression method. In recent years, Bansal and Rupasinghe [9], Bittle et al. [10], Chen et al. [11], Melo et al. [12], and Jung et al. [8] presented several dimensional or dimensionless empirical correlations. These correlations are simple and wieldy. Their accuracy is acceptable in the range of regression. However, if the calculating conditions are out of the regressive range, the error of calculating results cannot be forecasted. Furthermore, the coefficients of correlations are not all the same for different refrigerants. Thus, for new refrigerant, the existing correlations cannot be used for prediction without verification. Generally speaking, coefficients of the selected correlations need be rebuilt on the basis of experimental data or results calculated by some advanced distributed-parameter model.

Differing from the two above models, Yilmaz and Ünal [13] first presented an approximate analytic equation for the design of capillary tubes. Because the general equation is an integral result of the basic governing equations, a few simple steps in calculation are needed. It can be used both in theoretical analysis and in engineering calculation. However, some problems were found in our work with the equation. In this paper, problems in the Yilmaz-Ünal equation are analyzed and the modified equation is given.

2 Analysis on the Yilmaz-Ünal Equation

To set up the fundamental model of refrigerant flowing through an adiabatic capillary tube, several assumptions are applied.

- One-dimensional homogeneous flow assumption is generally adopted because of the very high flow velocity in such small tube diameters.
- The gravity effect and the entrance pressure loss are negligible owing to their slight influence under most operating conditions and incomplete information for evaluation.
- The metastable flow is not considered. One reason is that this work focuses on solving the numerical problems found in Yilmaz and Ünal's work. In order to compare the method presented in our work with that by Yilmaz-Ünal under the same conditions, it had better omit metastable flow as done by Yilmaz and Ünal. Another reason is the error resulting from this assumption can be accepted in engineering. Bittle and Pate [5] found that omitting metastable flow would underpredict the mass flow rate less than 6 percent while Kuehl and Goldschmidt [2] found the assumption would result in the length error up to 25 percent or so. According to our calculation, 25 percent length error corresponds to about 9 percent mass flow rate error under typical conditions.

Consequently, the governing equations are as follows:

$$-\mathrm{d}p = G^2 \mathrm{d}\nu + \frac{f}{2d} G^2 \nu \mathrm{d}L \tag{1}$$

$$\frac{\mathrm{d}\left(h + \frac{1}{2}G^2\nu^2\right)}{\mathrm{d}L} = 0 \tag{2}$$

Here, are p the pressure, ν the specific volume, h the specific enthalpy, G the mass flux, f the friction factor, d the inner diameter, L the length of the capillary tube.

Yilmaz and Ünal [13] assumed that the process in capillary tube is isenthalpic. In other words, Eq. (2) can be reduced as

$$\frac{\mathrm{d}h}{\mathrm{d}L} = 0 \tag{3}$$

To solve the differential Eq. (1) in two-phase region, Yilmaz and Ünal combined the equation

$$\nu = \nu_l + \frac{h_r - h_l}{r}(\nu_v - \nu_l) \tag{4}$$

with the Clausius-Clapeyron equation,

$$\ln\frac{p}{p_r} = \frac{r}{R}\left(\frac{1}{T_r} - \frac{1}{T}\right) \tag{5}$$

Contributed by the Fluids Engineering Division for publication in the JOURNAL OF FLUIDS ENGINEERING. Manuscript received by the Fluids Engineering Division November 3, 2000; revised manuscript received June 25, 2001. Associate Editor: Y. Matsumoto.

and obtained a simple approximate function between ν and p.

$$\nu^* = 1 + k_a(1/p^* - 1) \tag{6}$$

where, $p^* = p/p_r$, $\nu^* = \nu/\nu_r$, r and R are the evaporation latent heat and the gas constant, respectively. The slope of Eq. (6), k_a is a dimensionless parameter. In the subscripts, l and ν denote the saturated liquid and saturated vapor, respectively, and r means the reference point. In the opinion of Yilmaz and Ünal, the reference point is the crossing point of the isenthalpic line and the saturated liquid line in the pressure-enthalpy diagram.

To obtain the dimensionless parameter k_a, Yilmaz and Ünal [13] calculated numerically for different refrigerants and gave a relation as follows:

$$k_a = 2.62 \times 10^5 / p_r^{0.75} \tag{7}$$

Equation (7) is not dimensionless. Yilmaz and Ünal [13] had tried to obtain a dimensionless expression, but the accuracy got worse.

Substituting Eq. (7) into Eq. (1) and taking integral, one can obtain the equation developed by Yilmaz and Ünal [13] as follows:

$$L^* = \ln\left(\frac{p^*}{k_a + (1-k_a)p^*}\right) - \frac{1}{k_b(1-k_a)}\left\{p^* - 1 - \frac{k_a}{1-k_a}\ln[k_a + (1-k_a)p^*]\right\} \tag{8}$$

where,

$$k_b = \nu_r G^2 / p_r \tag{9}$$

$$L^* = \frac{fL}{2d} \tag{10}$$

In the process of integral, the friction factor f is considered as constant and related to the average dynamic viscosity of two-phase region. One relation built by numerical method calculates the average dynamic viscosity.

Summing up the work of Yilmaz and Ünal [13], one can conclude that the key of the work is Eq. (6), the simple approximate function between ν and p in two-phase region. We test the equation with different refrigerants and find good linearity between ν^* and $1/p^*$ under the commonly encountered conditions. The correlation coefficient is larger than 0.99. Because of the good degree of approximation, we continue to use this equation in the work.

When we use the Yilmaz-Ünal equation in deeper calculation, however, we are restricted by some potential problems in the equation.

First, the dimensionless parameter k_a is calculated by a dimensional empirical correlation (7). It is somewhat unreasonable. Furthermore, to obtain accurate empirical correlation needs numerous trial-and-error calculations, but validity of the correlation is limited by the range and accuracy of the regressive data. Strictly speaking, it cannot be extrapolated beyond the range of regressive data.

Second, Yilmaz and Ünal [13] defined the reference point of Eq. (6) as the crossing point of the isenthalpic line and the saturated liquid line in the pressure-enthalpy diagram. However, when the quality inlet condition occurs, as shown in Fig. 1, one cannot directly calculate the capillary tube length L_{12} with Eq. (8) because the reference point does not exist within the actual throttling process. For this case, the method used by Yilmaz and Ünal [13] was calculating the length L_{32} and L_{31}, respectively (point 3 as the reference point) and then $L_{12} = L_{32} - L_{31}$. Besides the increase of calculation quantity and error, this method has severe hidden trouble in theory. Due to the nonlinearity in two-phase flow, the capillary tube length cannot be simply added or subtracted. It could lead to abnormal fault in calculation.

To understand the problem clearly, one can consider the following special case. When the inlet state is (p_3, h_3), if the choked pressure p_{ch} at capillary tube exit is higher than the pressure p_1,

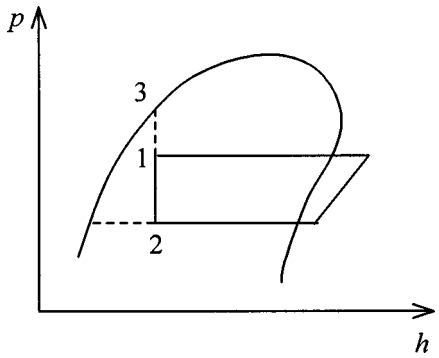

Fig. 1 Schematic of throttling process

then the flow in the capillary tube is choked whether p_1 or p_2 is the evaporating pressure, in other words, the evaporating pressure lower than p_{ch} does not influence on the capillary tube flow. Thus $L_{32} = L_{31}$, namely, $L_{12} = 0$. Calculation fails. Because Yilmaz and Ünal did not consider the choked flow in capillary tubes, an abnormal result $L_{32} < L_{31}$, namely, $L_{12} < 0$ will occur under the same condition, so calculation fails also. If the choked pressure p_{ch} is between p_1 and p_2, the abnormal result $L_{12} < 0$ also possibly occurs without taking the choked flow into account. Only if the choked pressure p_{ch} is lower than p_2, in other words, the choked flow does not occur in capillary tubes, the abnormal faults in calculation could be completely avoided.

Third, as mentioned above, Yilmaz and Ünal [13] did not consider the choked flow in capillary tubes. In fact, the choked flow in capillary tube is most encountered in practical refrigeration application. Consequently, to warrant the physical facticity of calculated results and avoid the above abnormal faults in calculation, the choked flow needs to be considered.

All in all, Yilmaz and Ünal [13] presented a successful approximate relationship, Eq. (6) between ν and p in two-phase region. It gives a simple integral approach to the differential equation (1). However, some details are not considered deeply. In this work, the modification is discussed and a modified result is given.

3 Modification of the Yilmaz-Ünal Equation

First, to reasonably deal with the quality inlet condition as shown in Fig. 1, the location of the reference point should be reset. According to the above analysis, the proper reference point should be located on the actual process line. By comparison, the inception point of two-phase region is a good choice, because two kinds of reference points will overlap each other under the subcooled inlet condition and Eq. (6) will be still valid. When the refrigerant enters the capillary tube under the quality inlet condition, as shown in Fig. 1, the new reference point is point 1, but the old reference point is point 3. Is Eq. (6) still applicable to this case? We simply prove it as follows.

As shown in Fig. 1, according to the definition by Yilmaz and Ünal, Eq. (6) is valid between the points 3-1 and between the points 3-2. $p_r = p_3$, $\nu_r = \nu_3$. Especially, for point 1, we have

$$\nu_1^* = 1 + k_a(1/p_1^* - 1) \tag{11}$$

Substituting Eq. (11) into Eq. (6), we obtain one similar to Eq. (6)

$$\nu^* = 1 + k_a'(1/p^* - 1) \tag{12}$$

where new reference point is used. $p_r = p_1$, $\nu_r = \nu_1$, and

$$k_a' = \frac{k_a/p_1^*}{1 + k_a(1/p_1^* - 1)} \tag{13}$$

As one part of line 3-2, the pressure and specific volume on the line 1-2 fit in with Eq. (12). Therefore, if we define the inception point 1 of two-phase region as the new reference point, Eq. (12) is

effective whether liquid or quality inlet conditions are encountered. In addition to the reference point, the difference between Eq. (12) and Eq. (6) is the slope. The relationship between k_a and k_a' is described by Eq. (13).

To get a general relation of the slope k_a', we do not try to find an accurate dimensionless correlation, but use a simple approach as follows. As for the linear equation (12), its slope k_a' can be determined by any two points on the line. Besides the inception point 1 of two-phase region, only one point is needed. Obviously, the simplest choice is the end point 2 of two-phase region. As a result,

$$k_a'=(\nu_2^*-1)/(1/p_2^*-1) \tag{14}$$

where ν_2^* is dependent on p_2^* and the inlet enthalpy because of the isenthalpic assumption.

Although the empirical correlation may be of good accuracy in the regressive range, the regressive range also restricts its use and the regression needs numerous trial-and-error calculations. On the contrary, Eq. (14) can be used without restrictions. To get better accuracy in calculation of k_a', we use a mid-point formula similar to that in numerical integral or differential. Let

$$k_a'=(\nu_m^*-1)/(1/p_m^*-1) \tag{15}$$

where

$$p_m^*=(1+p_2^*)/2 \tag{16}$$

ν_m^* is the specific volume relevant to p_m^*. It can be determined by p_m^* and the inlet enthalpy in an isenthalpic process.

Substituting Eq. (12) into Eq. (1) and taking integral, one can obtain the same result as Eq. (8) except k_a. k_a is replaced by k_a'.

Finally, to warrant the physical facticity of calculated results, the choked flow in a capillary tube is considered. If the choked flow is considered, then when the evaporating pressure falls lower than the choked pressure, the mass flux will reach the choked value and will no longer change. If not, the mass flux will unreasonably decrease along with the evaporating pressure drop. To judge whether the flow is choked, we use a simple criterion, namely the mass flux through the capillary tube is not larger than the corresponding choked mass flux. One can derive the expression of the choked mass flux G_{ch} from the definition of local sonic velocity (Chisholm [14]).

$$G_{ch}=\left[\frac{x_{out}}{G_{ch,\nu}^2}+\frac{1-x_{out}}{G_{ch,l}^2}\right]^{-1/2} \tag{17}$$

where

$$\frac{1}{G_{ch,\nu}^2}=\frac{\nu_\nu-\nu_l}{s_\nu-s_l}\frac{\mathrm{d}s_\nu}{\mathrm{d}p}-\frac{\mathrm{d}\nu_\nu}{\mathrm{d}p} \tag{18}$$

$$\frac{1}{G_{ch,l}^2}=\frac{\nu_\nu-\nu_l}{s_\nu-s_l}\frac{\mathrm{d}s_l}{\mathrm{d}p}-\frac{\mathrm{d}\nu_l}{\mathrm{d}p} \tag{19}$$

s is the specific entropy.

According to Eqs. (17)–(19), the choked mass flux is dependent on refrigerant thermodynamic properties and the outlet quality that can be solved along the isenthalpic line. For the purpose of simple calculation, Eqs. (18) and (19) can be calculated by the curve-fitting polynomials.

4 Friction Factor and Viscosity Equations

To calculate the present model, the friction factor along a capillary tube need to be evaluated, which relates to the evaluation of the dynamic viscosity, especially in the two-phase region.

4.1 Friction Factor Equation. For the convenience of comparison, we use the Churchill equation [15] for friction factor calculation, which is cited by many researchers including Yilmaz and Ünal [13].

$$f=8[(8/\mathrm{Re})^{12}+1/(A+B)^{3/2}]^{1/12} \tag{20}$$

$$A=\{2.457\ln(1/[(7/\mathrm{Re})^{0.9}+0.27(\varepsilon/d)])\}^{16} \tag{21}$$

$$B=(37530/\mathrm{Re})^{16} \tag{22}$$

where Reynolds number $\mathrm{Re}=G\cdot d/\mu$. μ is the dynamic viscosity. If the relative roughness ε/d is unknown, a recommended value 3.27×10^{-4} [13] could be used in Eq. (21).

4.2 Two-Phase Viscosity Equation. The two-phase friction factor is calculated using Eq. (20) with a Reynolds number that is based on the two-phase dynamic viscosity, μ_{TP}. In the literature, three models of the two-phase viscosity are often used as follows.

The Cicchitti model [16]:

$$\mu_{\mathrm{TP}}=x\mu_\nu+(1-x)\mu_l \tag{23}$$

The McAdams model [17]:

$$\frac{1}{\mu_{\mathrm{TP}}}=\frac{1-x}{\mu_l}+\frac{x}{\mu_\nu} \tag{24}$$

The Dukler model [18]:

$$\mu_{\mathrm{TP}}=\frac{x\nu_\nu\mu_\nu+(1-x)\nu_l\mu_l}{x\nu_\nu+(1-x)\nu_l} \tag{25}$$

Evaluating the three models under the same refrigerant state one can find that the Cicchitti model and the Dukler model gives the maximum and the minimum value of two-phase viscosity, respectively, while the McAdams model gives the middle one. Therefore, the minimum mass flow rate of a capillary tube will be predicted with the Cicchitti model, while the maximum and the middle value will be predicted with the Dukler model and the McAdams model, respectively.

In this paper, we mainly choose the Cicchitti model like Yilmaz and Ünal so as to compare the Yilmaz and Ünal work with the authors' modification under the same conditions. Additionally, capillary calculation with the McAdams model and the Dukler model are also done.

4.3 Average Viscosity Along Two-Phase Region. In calculation of the integrated equation (8), the average viscosity along the whole two-phase region is needed. Generally, the average viscosity can be considered as a weighted average of the inception and end values of two-phase region.

$$\overline{\mu}_{\mathrm{TP}}=w\mu_1+(1-w)\mu_2 \tag{26}$$

where w is the weight.

To determine the weight w, an optimization process is introduced. The optimized function is

$$\min_{0\leqslant w\leqslant 1}\left\{\sum_j\ [G_j(\overline{\mu}_{\mathrm{TP}})-G_{j,\mathrm{dpm}}]^2\right\} \tag{27}$$

where $G_j(\overline{\mu}_{\mathrm{TP}})$ is the mass flux calculated by the present model in which the average viscosity is defined by Eq. (26). $G_{j,\mathrm{dpm}}$ denotes the mass flux calculated by an advanced distributed-parameter model which is similar to that built by Bittle and Pate [6]. j is a counting number for different operating conditions of capillary tubes. Under the commonly encountered operating conditions as shown in Table 1, numerical results of the mass fluxes through adiabatic capillary tubes are used in Eq. (27) to find the optimal weight w. As a one-dimensional optimization problem, the golden section method is used.

The resultant optimal value of weight w is quite different for the above-mentioned three two-phase viscosity models. For the Cicchitti model, the McAdams model, and the Dukler model, the optimal weights are 0.90, 0.55, and 0.40, respectively. Although Eq. (26) is the simplest way to calculate the average viscosity in two-phase region, the effect that will be shown in Section 6 is gratifying.

5 Algorithm

Modification of the Yilmaz and Ünal work in two-phase region has been discussed above. For the purpose of integrality of the capillary tube model, the calculation of liquid region length is needed. Because the liquid density can be assumed as constant and independent of the pressure, the length of liquid region can be simply derived from the governing equations.

$$L_l = \frac{2d\Delta p_l}{G^2 f_l \nu_l} \tag{28}$$

where the pressure drop Δp_l is the pressure difference between inlet and flashpoint. If one takes metastable liquid region into account, Eq. (28) is also available.

Based on the above-mentioned model of adiabatic capillary tubes, one can predict the mass flux or the mass flow rate according to the given operating conditions, or determine the tube length by the desired mass flow rate under especial operating conditions. Whichever evaluation one does, an iterative process cannot be avoided because one needs to judge if the choked flow will occur at exit of a capillary tube.

Different from the existing algorithms, we combined the choked flow judgment with the initial value of mass flux in iterative process. The details of our algorithm for predicting the mass flux or the mass flow rate of an adiabatic capillary tube are shown in Fig. 2. The algorithm is a simple and stable dichotomy. Here we assume at first that the flow at capillary exit is just choked and the outlet pressure equals to the evaporating pressure. Therefore the initial value of mass flux can be determined by Eq. (17) and avoided assigning an arbitrary value that may lower the efficiency of iterative evaluation. On the other hand, only one time is needed for the choked flow judgment in the algorithm.

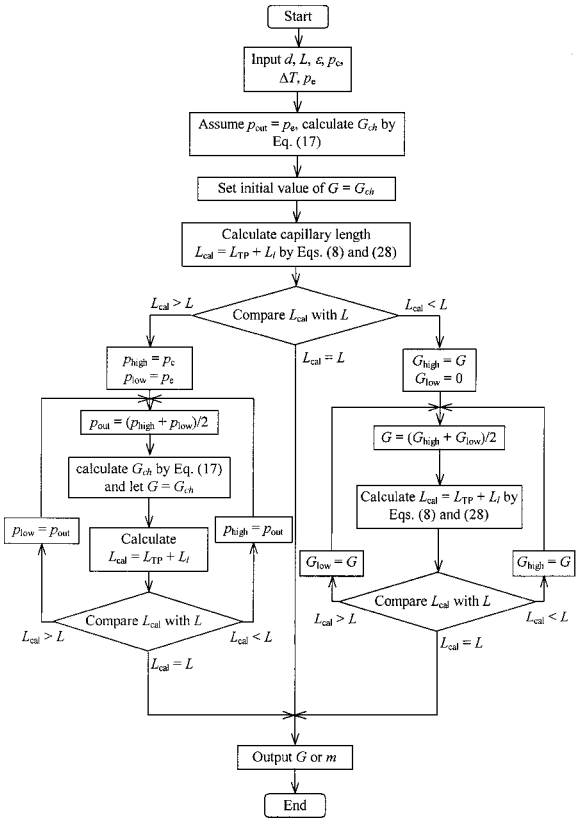

Fig. 2 Computer model flow chart

6 Theoretical and Experimental Verification

Theoretical and experimental data are used to verify the modified general equation. On the one hand, the Yilmaz-Ünal equation and the present equation are compared with the advanced distributed-parameter model in calculation of mass flux under the commonly encountered conditions. On the other hand, experimental data in open literatures are used for case study.

First of all, the Yilmaz-Ünal equation, the present equation and the advanced distributed-parameter model are used to calculate the mass fluxes of capillary tubes under the commonly encountered operating conditions as shown in Table 1. All the friction factors are calculated by the Churchill equation and the Cicchitti viscosity model for comparison under same conditions.

As shown in Table 1, 4800 cases ($=5\times10\times4\times(4+4)\times3$) of each refrigerant are calculated and more than 95 percent cases are choked. The working fluids are refrigerant CFC-12 and its main substitutes HFC-134a and HC-600a. The three refrigerants are very representative because not only are they commonly used in refrigeration and air-conditioning plants, but also they are different in thermodynamic properties. The thermodynamic properties of CFC-12 are similar to those of HFC-134a, but distinct from those of HC-600a. The deviations of mass fluxes are shown in Table 2. Here, the average deviation (Ave. Dev.) is defined as

$$\text{Ave. Dev.} = \frac{1}{4800}\sum_{j=1}^{4800}\frac{|G_j - G_{j,\text{dpm}}|}{G_{j,\text{dpm}}}\times 100\,\text{percent} \tag{29}$$

The maximum deviation (Max. Dev.) is defined as

$$\text{Max. Dev.} = \max_{1\le j\le 4800}\left\{\frac{|G_j - G_{j,\text{dpm}}|}{G_{j,\text{dpm}}}\times 100\,\text{percent}\right\} \tag{30}$$

As shown in Table 2, the average deviations between the Yilmaz-Ünal equation and the distributed-parameter model fall into 2~6 percent, which is acceptable in engineering application. But the maximum deviations reach 90 percent or so except for calculation faults. It indicates that the Yilmaz-Ünal equation is not always satisfactory in a wide range. By comparison, the present equation coincides with the distributed-parameter model well. The average deviations between them fall to 0.2 percent or so; meanwhile, the maximum deviations are less than 4 percent. The deviations before and after modification are obviously reduced. Because less empirical components are utilized relative to the Yilmaz-Ünal equation, the present equation is a good approximation for the distributed-parameter model in a wider range. Furthermore, there are 20 failures in calculation with the Yilmaz-Ünal

Table 1 Distribution of operating conditions

d [mm]	L [m]	T_c [°C]	ΔT [°C]	x_{in}	T_e [°C]
0.5, 1.0, 1.5, 2.0, 2.5	0.5, 1.0, 1.5, 2.0, 2.5, 3.0, 3.5, 4.0, 4.5, 5.0	24, 36, 48, 60	5, 10, 15, 20	0, 0.1, 0.2, 0.3	−40, −10, 20

Table 2 Capillary mass flux deviations between approximate equations and distributed-parameter model with the Cicchitti viscosity model [percent]

	Yilmaz-Ünal equation		The present equation	
Refrigerant	Ave. Dev.	Max. Dev.	Ave. Dev.	Max. Dev.
CFC-12	5.62	88.41	0.20	3.25
HFC-134a	2.05	87.46	0.21	3.99
HC-600a	3.65	85.90	0.19	3.87
Failure times	20		0	

Table 3 Capillary mass flux deviations between present equation and distributed-parameter model with different viscosity models [percent]

	Cicchitti model		McAdams model		Dukler model	
Refrigerant	Ave. Dev.	Max. Dev.	Ave. Dev.	Max. Dev.	Ave. Dev.	Max. Dev.
CFC-12	0.20	3.25	0.18	6.20	0.38	5.82
HFC-134a	0.21	3.99	0.64	9.87	0.68	9.66
HC-600a	0.19	3.87	0.34	13.39	0.65	10.80

equation. The reason has been discussed in Section 2 of the paper. By comparison, there is no failure in calculation with the present equation.

In addition, relative deviations of capillary mass flux between the present equation and the advanced distributed-parameter model are evaluated with different viscosity models. As shown in Table 3, although effects of the McAdams model and the Dukler model are somewhat worse than that of the Cicchitti model, the deviations are also acceptable in engineering. The Yilmaz-Ünal equation is not included here because only the Cicchitti viscosity model was used in their investigation.

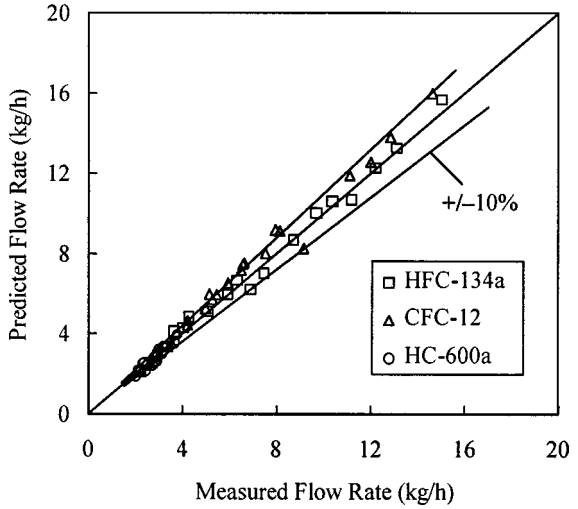

Fig. 3 Melo et al. [12] data versus predictions

To examine the applicability of the present equation, we use it to predict the experimental data of capillary tubes in open literatures. Some results are shown in Figs. 3–5.

The experimental data in Fig. 3 are from Melo et al. [12]. Melo et al. made precise measurement for the inner diameters and roughness of capillary tubes. Thus the uncertainty in measurement can be weaken to a great extent. The predictions are shown in Fig. 3 to compare within ±10 percent of the experimental data.

The experimental data in Fig. 4 are from Wijaya [19] cited by Yilmaz and Ünal [13]. The present equation gives an underprediction of the flow data by 0 to 15 percent. It agrees with the correlation developed by Bittle et al. [10].

The experimental data in Fig. 5 are from Li et al. [3]. The present equation overpredicts these data by 0 to 8 percent.

From the above-mentioned comparisons, one can see that the present equation yields good predictions to the experimental data. The deviations may be considered to be reasonable and satisfactory on account of the simplicity of the present method.

If a metastable length correction is included in the model, the prediction results could accord better with the experimental data, especially with the Wijaya data in Fig. 4. On the other hand, the Melo et al. data and the Li et al. data were taken on capillary tubes with pressure tap holes, which have the effect of decreasing the normal metastable effect seen in unmodified capillary tube. Therefore the prediction effect will be kept. Finally, from the point of view of algorithm, the metastable correction is easy to be included in the liquid region calculation of the existing algorithm.

7 Conclusions

A modified analytical method is developed on the basis of the Yilmaz-Ünal equation (Yilmaz and Ünal [13]). For the design of capillary tubes, it is more reliable and applicable than the Yilmaz-Ünal equation. Under an extensive range of operating conditions, the maximum deviations of mass fluxes given by the present equation and the advanced distributed-parameter model fall into 4 per-

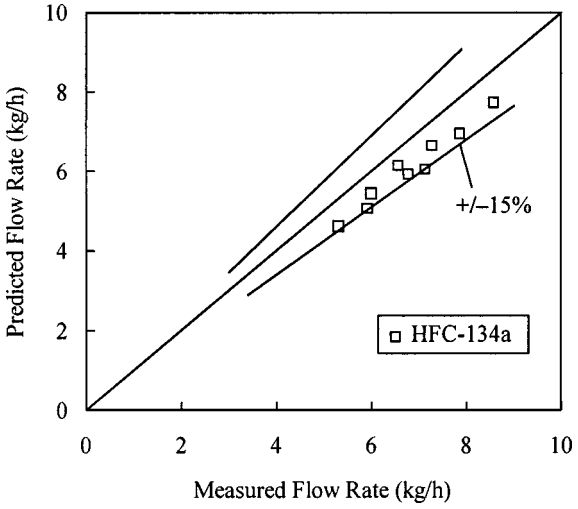

Fig. 4 Wijaya [19] data versus predictions

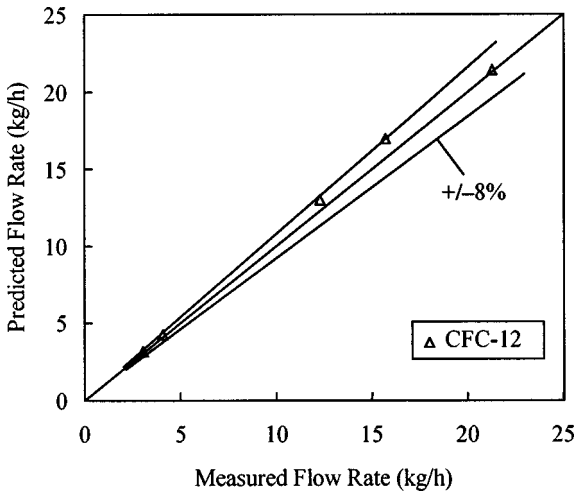

Fig. 5 Li et al. [3] data versus predictions

cent, and the average deviations are only 0.2 percent or so. In addition, the comparisons between our method and the experimental data in open literatures are also satisfactory.

Acknowledgment

This work was supported by the State Key Fundamental Research Program under the contract No. G2000026309.

Nomenclature

A = defined in Eq. (21)
B = defined in Eq. (22)
d = capillary tube inner diameter
f = friction factor
G = mass flux
h = specific enthalpy
k_a = defined in Eq. (7)
k_a' = defined in Eq. (14) or (15)
k_b = defined in Eq. (9)
L = capillary tube length
m = mass flow rate
p = pressure
r = specific latent heat
R = gas constant
Re = Reynolds number
s = specific entropy
T = temperature
v = specific volume
w = weight defined in Eq. (26)
x = quality
Δp = pressure drop
ΔT = subcooling of the liquid
ε = roughness
η = dynamic viscosity

Subscripts and Superscripts

c = condensing parameter
cal = calculating value
ch = choked flow
dpm = distributed-parameter model
e = evaporating parameter
in = inlet
l = liquid or saturated liquid
m = mid-point or mean value
out = outlet
r = reference point
TP = two-phase region
v = saturated vapor
1 = inception point of two-phase region, as shown in Fig. 1
2 = end point of two-phase region, as shown in Fig. 1
3 = crossing point of the isenthalpic line and the saturated liquid line in the pressure-enthalpy diagram, as shown in Fig. 1
* = dimensionless parameter
– = average value

References

[1] ASHRAE, 1988, *ASHRAE Handbook*—1988 *Equipment*, American Society of Heating, Refrigerating and Air-Conditioning Engineers, Inc., Atlanta, pp. 19.21-19.30.
[2] Kuehl, S. J., and Goldschmidt, V. W., 1991, ''Modeling of Steady Flows of R-22 through Capillary Tubes,'' ASHRAE Trans., **97**, Part 1, pp. 139–148.
[3] Li, R. Y., Lin, S., and Chen, Z. H., 1990, ''Numerical Modeling of Thermodynamic Non-Equilibrium Flow of Refrigerant through Capillary Tubes,'' ASHRAE Trans., **96**, Part 1, pp. 542–549.
[4] Escanes, F., Perez-Segarra, C. D., and Oliva, A., 1995, ''Numerical Simulation of Capillary-Tube Expansion Devices,'' Int. J. Refrig., **18**, pp. 113–122.
[5] Bittle, R. R., and Pate, M. B., 1996, ''A Theoretical Model for Predicting Adiabatic Capillary Tube Performance with Alternative Refrigerants,'' ASHRAE Trans., **102**, Part 2, pp. 52–64.
[6] Chung, M., 1998, ''A Numerical Procedure for Simulation of Fanno Flows of Refrigerants or Refrigerant Mixtures in Capillary Tubes,'' ASHRAE Trans., **104**, Part 2, pp. 1031–1042.
[7] Sami, S. M., and Tribes, C., 1998, ''Numerical Prediction of Capillary Tube Behavior with Pure and Binary Alternative Refrigerants,'' Appl. Therm. Eng., **18**, pp. 491–502.
[8] Jung, D., Park, C., and Park, B., 1999, ''Capillary Tube Selection for HCFC22 Alternatives,'' Int. J. Refrig., **22**, pp. 604–614.
[9] Bansal, P. K., and Rupasinghe, A. S., 1996, ''An Empirical Correlation for Sizing Capillary Tubes,'' Int. J. Refrig., **19**, pp. 497–505.
[10] Bittle, R. R., Wolf, D. A., and Pate, M. B., 1998, ''A Generalized Performance Prediction Method for Adiabatic Capillary Tubes,'' HVAC&R Research, **4**, pp. 27–43.
[11] Chen, S. L., Liu, C. H., and Jwo, C. S., 1999, ''On the Development of Rating Correlations for R134a Flowing through Adiabatic Capillary Tubes,'' ASHRAE Trans., **105**, Part 2, pp. 75–86.
[12] Melo, C., Ferreira, R. T. S., Neto, C. B., Goncalves, J. M., and Mezavila, M. M., 1999, ''An Experimental Analysis of Adiabatic Capillary Tubes,'' Appl. Therm. Eng., **19**, pp. 669–684.
[13] Yilmaz, T., and Unal, S., 1996, ''General Equation for the Design of Capillary Tubes,'' ASME J. Fluids Eng., **118**, pp. 150–154.
[14] Chisholm, D., 1983, *Two-Phase Flow in Pipelines and Heat Exchangers*, Longman Inc., New York, pp. 77–91.
[15] Churchill, S. W., 1977, ''Frictional Equation Spans All Fluid Flow Regions,'' Chem. Eng., **84**, No. 24, pp. 91–92.
[16] Cicchitti, A., Lombardi, C., Silvestri, M., Soldaini, G., and Zavattarelli, R., 1960, ''Two-Phase Cooling Experiments—Pressure Drop, Heat Transfer, and Burnout Measurements,'' Energ. Nucl. (Milan), **7**, pp. 407–425.
[17] McAdams, W. H., Wood, W. K., and Bryan, R. L., 1942, ''Vaporization inside Horizontal Tubes-II-Benzene-Oil Mixtures,'' Trans. ASME, **64**, pp. 193.
[18] Dukler, A. E., Wicks, M., and Cleveland, R. G., 1964, ''Frictional Pressure Drop in Two-Phase Flow–Part A and B,'' AIChE J., **10**, No. 1, pp. 38–51.
[19] Wijaya, H., 1992, ''Adiabatic Capillary Tube Test Data for HFC-134a,'' *Proc. The IIR-Purdue Refrigeration Conference*, West Lafayette, Ind., Vol. 1, pp. 63–71.

Three-Dimensional Swirl Flow Velocity-Field Reconstruction Using a Neural Network With Radial Basis Functions

J. Pruvost

J. Legrand[1]
e-mail: jack.legrand@gepea.univ-nantes.fr

P. Legentilhomme

GEPEA, University of Nantes,
CRTT-IUT, BP 406,
F-44602 Saint-Nazaire Cedex, France

For many studies, knowledge of continuous evolution of hydrodynamic characteristics is useful but generally measurement techniques provide only discrete information. In the case of complex flows, usual numerical interpolating methods appear to be not adapted, as for the free decaying swirling flow presented in this study. The three-dimensional motion involved induces a spatial dependent velocity-field. Thus, the interpolating method has to be three-dimensional and to take into account possible flow nonlinearity, making common methods unsuitable. A different interpolation method is thus proposed, based on a neural network algorithm with Radial Basis Functions. [DOI: 10.1115/1.1412847]

1 Introduction

Except for simple cases having analytical representations, a flow-field is often described as a discrete distribution of hydrodynamical specific characteristics. For example, experimental measurements provide only local information. Interpolation schemes, like linear or cubic interpolation, are thus usually employed in fluids engineering to determine unknown values at desired positions, as for pathlines determination for instance. The same problem arises if special hydrodynamical features have to be determined, like stress-fields or vorticity-fields, that imply the use of derivative approximation with finite difference methods. Results are then biased by the systematic error induced by the method. A way to improve the determination of such results is to employ a fitting function of the hydrodynamical features evolutions. This solution provides a continuous mathematical expression, which can be then employed to calculate values at unknown locations. If the mathematical function is chosen derivable, special hydrodynamical features, like stress-fields or vorticity-fields, can then be easily deduced without adding approximation of derivative schemes. For example, Marshall and Grant [1] have developed a Lagrangian vorticity collocation method where a polynomial fitting is used to determine a continuous vorticity-field using local values defined on a nonuniform grid, allowing the exact differentiation of the vorticity-field which is needed to calculate a viscous diffusion term. But, naturally, the accuracy of such a method depends on the ability of the retained function to fit the local values distribution.

When the flow becomes complex and three-dimensional, hydrodynamical features can be characterized by nonlinear evolutions. If the flow exhibits a great spatial dependency, polynomial fitting or common interpolation schemes are then not adapted, because a large amount of data is requested to accurately represent the flow in the entire geometry. Another method based on a neural network representation is proposed in this study. By considering nonlinear evolutions, such technique appears interesting to reconstruct complex flows, such as the three-dimensional swirling flow investigated here. The neural network method will provide a continuous mathematical expression of the flow-field, by representing it as a sum of Gaussian functions, each function being derivable, that allows further calculation of specific hydrodynamical features involving differentiation.

For example, swirling flows are often used in chemical engineering for the design of new hydrocyclones or heat exchangers [2]. By involving a three-dimensional motion and increasing turbulent intensities, such flows appear as an efficient way to enhance transport phenomena, like mass or heat transfer [3–5]. But the generated hydrodynamics remains difficult to fully characterize, owing to the spatial dependency of the flow-field [6–9]. A tangential inlet can be used to induce a stationary swirling flow in tubes or annular geometries with a rather simple design [2–10]. The swirl motion is achieved at the inlet of the device and then decays freely along the flow path (Fig. 1). Hydrodynamic characteristics are not only a function of the radial position, but also depend on the axial location, due to the free decay of the swirl intensity, and on the angular position, the flow generated not being axisymmetric. Thus, a full characterization of the flow requests a high amount of experimental data, especially when local measurement techniques are employed, like laser Doppler anemometry or hot-wires techniques [11]. A previous study has shown the interest of spatial measurement techniques, like the Particle Image Velocimetry (PIV), which allows faster investigation by measuring the instantaneous velocity-field in a designed area [10]. But two problems remain: (i) the obtained velocity-field is not continuous, (ii) the acquisition area remains limited and a complete investigation of the flow-field would request numerous measurement areas.

Thus, an experimental investigation can require a very long time to obtain a sufficient amount of data. Because neural networks can express nonlinearities, they seem an efficient tool for the reconstruction of data linked to multiple parameters, and thus an interesting alternative solution to common interpolation schemes. Neural networks with Radial Basis Functions are especially designed for this particular kind of application [12–14]. This method can thus be employed to determine a mathematical expression of the flow-field defined on the entire geometry, using only a small amount of experimental local measurements. To evaluate the accuracy of this interpolating technique, a large set of data has first been measured using PIV technique. Next, the set has been divided into two parts: the first being used by the neural network in order to reconstruct the velocity-field during the learning step, and the second to estimate the reconstruction efficiency by comparing values obtained with the neural method to experi-

[1]Author to whom correspondence should be addressed.

Contributed by the Fluids Engineering Division for publication in the JOURNAL OF FLUIDS ENGINEERING. Manuscript received by the Fluids Engineering Division October 25, 2000; revised manuscript received May 15, 2001. Associate Editor: J. S. Marshall.

mental measurements. The number of data requested to achieve an accurate calculation of the continuous flow-field has been determined.

2 Experimental PIV Investigation

In a previous work, we have shown that a usual PIV technique can be used to characterize the main characteristics of a swirling decaying flow induced by a tangential inlet in an annular geometry. The three components of the velocity and turbulent intensity have been investigated. The main features of the experimental investigation are described in details by Pruvost et al. [10].

It has been shown that, by allowing spatial investigation, PIV measurements appear to be well-adapted to this particular flow, which was found to be very complex and space dependent. But, to fully characterize hydrodynamics in the geometry under study, a large set of data is needed. Furthermore, because the employed PIV system allows the simultaneous acquisition of only two velocity components, two series of measurements are requested to determine the complete velocity-field: the first allows acquisition of axial and radial components of the velocity vector and the second, the circumferential one. For the last series, the measurements cannot be done for several radial positions simultaneously, contrary to axial and radial velocity components acquisitions. The measurement time is thus greatly increased to obtain an accurate spatial characterization of each velocity component, especially for the circumferential one.

The hydraulic test rig used for experimental investigation is described by Pruvost et al. [10]. It consists of an annular test section (Fig. 1) made of two concentric Plexiglas tubes having a total length of 1.5 m. The internal radius of the outer cylinder, R_0, is 50 mm, the outer radius of the inner tube, R_i, being 20 mm. The diameter of the tangential inlet is 30 mm, equal to the annular gap width, e, corresponding to pure swirling flow according to Legentilhomme and Legrand [4]. The outlet of the annulus is of axial type, so as not to disturb the flow. For all experimental measurements, the water flow rate is $Q=1.27\ \mathrm{m}^3/\mathrm{h}$ corresponding to a mean axial velocity in the annulus, $\overline{U}$, of 5 cm/s and a Reynolds number, Re, equal to 3000, where Re is calculated by:

$$\mathrm{Re}=\frac{2e\overline{U}}{\nu} \tag{1}$$

The PIV Dantec system used consists of a Spectra Physics Model 2020 laser source with an emission wavelength of 488 nm for a maximum emission power of 5 Watt. The laser beam is shutter gated to induce laser light pulses and a thin light sheet is generated by means of an optical lens. The electro-optical shutter is synchronized with a CCD camera Double Image 700, the camera sensor includes 768×484 light-sensitive pixels. Tracer particles are of TiO_2 type. A representation of the experimental test rig set with the PIV measurement technique is shown in Fig. 2. Additional parameters of the PIV set-up can be found in Pruvost et al. [10].

To investigate the neural network reconstruction capacity, a large set of experimental data has been collected. The reconstruction accuracy is analyzed from the influence of two parameters: the number of values requested along the axial direction to represent the decrease of the swirl intensity and the number of needed

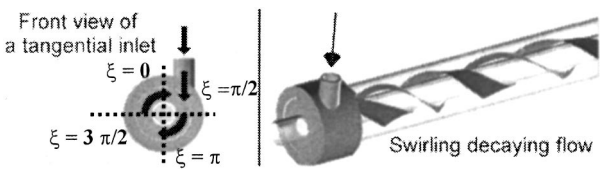

Fig. 1 Schematic representation of the tangential inlet and the swirling decaying flow

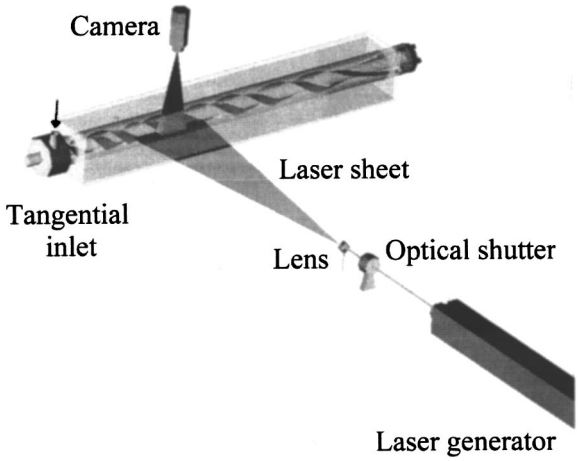

Fig. 2 Experimental set-up for flow-field investigation using PIV measurement method

angular positions to characterize the asymmetric behavior of the flow. Measurements positions for mean components are defined in Table 1(a) and 1(b), and in Table 1(c) for turbulent intensities. The measurement of the circumferential velocity component and the evaluation of turbulent intensities requesting longer time of investigation measurements were made for only three angular positions. This particular point will be discussed further. The various investigated axial positions show a nonuniform distribution of the velocity-field. Thus, the number of axial locations has to be increased near the inlet where the flow is found to be very spatial dependent, and then spaced out for locations further in the annulus where inlet disturbances vanish.

3 Neural Network Reconstruction Method

3.1 Global Method. Neural networks are used in various research areas, and applications can be found in fluid engineering, because of the ability of such methods to represent complex phenomena making them useful for the prediction of dynamic features of unsteady flow-fields, for instance [15]. Another particular application is data interpolation. A special kind of neural network is devoted to this purpose: neural network with Radial Basis Functions (RBF) [16]. The use of functions with local spatial influence like RBF instead of the common sigmoidal functions improves their spatial representation capacity, thereby enabling this kind of networks to interpolate any kind of a priori unknown function depending on n-parameters [17]. In this study, each hydrodynamical characteristic to be approximated, named V, is spatial-dependent, and thus a function of the three spatial coordinates x, r, and ξ.

RBF are directly linked to the function approximation theory [18]. In fact, with mathematical formulation, the goal of RBF is to find the best approximation $F(E,P)$ of a function $f(P)$ which depends on a set of N-parameters $P=(p_1,p_2,p_3,\ldots,p_N)$, E being a set of fitting parameters to determine. Because $f(P)$ can be of any type, the exact solution cannot always be provided, but an approximated solution can always be found, when $F(E,P)$ is expressed as a weighted-sum of elementary functions of a base $\Phi=\{\phi_i\}_{i=1}^m$. If weights are named $W=\{W_i\}_{i=1}^m$, $F(E,P)$ can be expressed by the following equation:

$$F(E,P)=\sum_{i=1}^{m} W_i\phi_i(P) \tag{2}$$

This expression can be represented using a neural network architecture. This kind of net has three layers:

Table 1 Distribution of the number of axial positions experimentally investigated. (*a*) Measurement of axial and radial mean velocity components (first series); (*b*) measurement of circumferential mean velocity component (second series); (*c*) measurement of turbulent intensities.

Measurement area (mm)	185<x<225 20<r<50	225<x<265 20<r<50	265<x<305 20<r<50	305<x<345 20<r<50	345<x<385 20<r<50	385<x<425 20<r<50	425<x<465 20<r<50
Position $\xi = 0$	22	22	22	22	22	22	22
Position $\xi = \pi/2$	22	22	0	0	0	0	0
Position $\xi = \pi$	22	0	22	22	22	22	22
Position $\xi = 3\pi/2$	22	22	22	22	22	22	22

Measurement area (mm)	545<x<585 20<r<50	585<x<625 20<r<50	625<x<685 20<r<50	785<x<725 20<r<50	885<x<925 20<r<50	1085<x<1125 20<r<50	1460<x<1500 20<r<50
Position $\xi = 0$	22	22	22	22	22	22	22
Position $\xi = \pi/2$	0	22	22	22	22	22	22
Position $\xi = \pi$	22	22	22	22	22	22	22
Position $\xi = 3\pi/2$	0	22	0	0	0	22	22

(*a*)

Measurement area (mm)	185 < x < 1500
Position $\xi = 0$	14
Position $\xi = \pi/2$	14
Position $\xi = 3\pi/2$	14

(*b*)

	T_x and T_r	T_ξ
Measurement area (mm)	185 < x < 1500	185 < x < 1500
Position $\xi = 0$	6	6
Position $\xi = \pi/2$	3	6
Position $\xi = 3\pi/2$	6	6

(*c*)

1 An input layer, where the set of function parameters P is given to the net, with one unit per parameter. In this study, the goal function is $V(x,r,\xi)$ and the net is thus defined with three input units (x,r,ξ),
2 An output layer, with one unit, corresponding to the function to reconstruct $f(P)$, which is in this case $V(x,r,\xi)$,
3 A hidden layer, of m-units with activation function $\phi_i(x,r,\xi)_{i=1,m}$, where the parameter m has to be found.

The neural network principle is rather simple: for given values in input, corresponding to a location (x,r,ξ) in the geometry, the net has to provide the desired response, $V(x,r,\xi)$. Neural networks are interconnected, as shown in Fig. 3. The input signal is directly given to each unit of the hidden layer activated by a function chosen in Φ: each unit calculates $\phi_i(x,r,\xi)_{i=1,m}$. Results are next transferred using weight-links to the output units, where they are finally summed. Thus, this kind of structure is the exact representation of Eq. (2).

With the right set of functions Φ, the objective function named $V_{app}(x,r,\xi)$, can be interpolated. Local functions, as one of gaussian type, have been retained because they can approximate any kind of function [19], and they remain derivable for further investigation of hydrodynamical feature deduced from differentiation. For the three-dimensional reconstruction, this kind of function is defined as follows:

$$\phi(x,r,\xi) = \exp\left(-\frac{(x-C_x)^2}{\tau_x^2} + \frac{(r-C_r)^2}{\tau_r^2} + \frac{(r\xi-C_\xi)^2}{\tau_\xi^2} \right) \quad (3)$$

where C and τ are, respectively, centers and radii associated to each direction of the reconstruction problem. To obtain a homo-

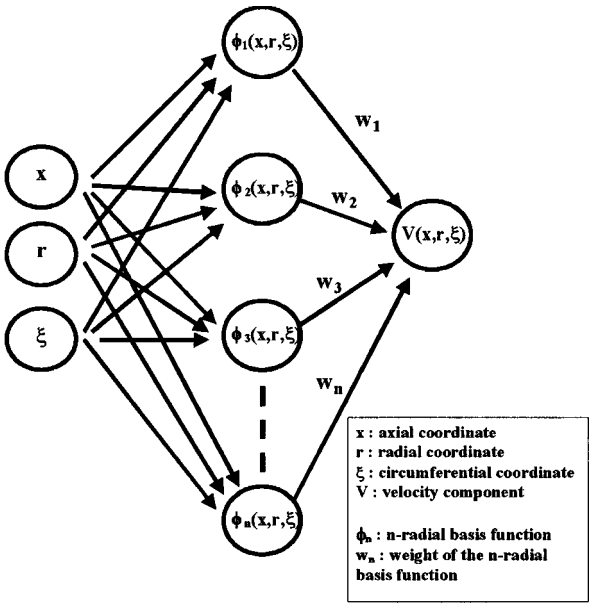

Fig. 3 Neural network architecture

geneous formulation, the circumferential coordinate ξ has been expressed as the product of the radial position by the circumferential one in Eq. (3). Thus, the objective is to find the best approximation $V_{app}(x,r,\xi)$ of $V(x,r,\xi)$:

$$V(x,r,\xi) \approx V_{app}(x,r,\xi) = \sum_{i=1}^{m} W_i \exp\left(-\left(\frac{(x-c_{x_i})^2}{\tau_{x_i}^2} + \frac{(r-c_{r_i})^2}{\tau_{r_i}^2} + \frac{(r\xi - c_{\xi_i})^2}{\tau_{\xi_i}^2} \right) \right) \quad (4)$$

where C_{ji} and τ_{ji} are, respectively, centers and radii of the ith neuron in the hidden layer of size m in direction j.

A solution of Eq. (4) is obtained by minimizing the following function, called the cost function:

$$E_1 = \sum_{i=1}^{p} [V_i(x,r,\xi) - V_{app_i}(x,r,\xi)]^2 \quad (5)$$

where p is the size of the subset of a given hydrodynamical characteristic V used for the net learning step.

But, minimizing only the function E_1 is an ill-posed solution because, when interpolating data, the objective function has to represent both available and unknown data. Accurate results are not necessarily obtained if only Eq. (5) is employed, and especially if original data are noisy, as for PIV measurements. This is the so-called ''representation problem.'' This shortcoming is solved by estimating the neural net capacity to find accurate values where no experimental data are available and by introducing an additional regularization term in Eq. (5) [20,21]:

$$C = E_1 + \lambda \varphi(W) \quad (6)$$

where λ is the regularization parameter and φ a function to define.

In this study, the estimator employed is the Cross Validation or CV described in Wahba [22]. To determine the CV-value, experimental data employed during the learning step are divided into two parts. Each part is used in turn to determine the neural net parameters, while the remaining amount of data is employed to calculate the error between net results and experimental values using Eq. (6). Next, the mean of reconstruction errors gives an estimation of the neural net accuracy, CV, which has to be minimized.

To allow CV calculation, function φ has to be defined in Eq. (6). An overall review of such functions can be found in Poggio et al. [23]. The chosen function is related to experimental data by assuming noise to be equally shared between all data [18]. The final cost function to be minimized is thus:

$$C = \sum_{i=1}^{p} [V(x,r,\xi) - V_{app}(x,x,\xi)]^2 + \lambda \sum_{j=1}^{m} (w_j)^2 \quad (7)$$

Dedicated algorithms are available to solve this nonlinear problem of finding the best solution $V_{app}(x,r,\xi)$. Each net parameter is determined during the learning step. This step can be divided into two successive parts: the neural net architecture design, and the weight-values determination. Both are well-known and a complete description can be found in Orr [24]. In this application, weight-values are calculated following the ''standard ridge regression'' algorithm and the neural net is designed using the ''forward selection'' scheme [24], which presents an incremental construction of the neural network structure: each unit of the hidden layer is added step by step, until the net can provide the requested response. After the learning step, when a new value is presented to the net, its response is close to the desired one: the net is thus able to reconstruct and interpolate data.

In this study, experimental values are obtained for different locations ($185\,\text{mm} < x < 1500\,\text{mm}, 20\,\text{mm} < r < 50\,\text{mm}, 0 < \xi < 2\pi$). Learning values are first transformed in order to follow a normal statistical distribution (zero mean and variance one) to prevent numerical approximation problem during the learning step due to the use of data having different order of magnitude.

Table 2 Initial values in the neural network of activation function radii

	Mean velocity measurement		
	U_x	U_r	U_ξ
Axial direction	0.5	0.3	0.5
Radial direction	0.4	0.3	0.4
Circumferential direction	0.5	0.4	0.5

	Turbulent intensity measurement		
	T_x	T_r	T_ξ
Axial direction	0.5	0.5	0.5
Radial direction	0.6	0.6	0.6
Circumferential direction	0.5	0.5	0.5

3.2 Learning the Neural Network. Algorithms of ''standard ridge regression'' and ''forward selection'' are implemented using Matlab software on a personal computer Pentium II 333 MHz. To initialize the neural network method, only radii of activation functions ϕ have to be previously defined. They are arbitrarily initialized to give an a priori good representation of the desired evolution. Though this step is not essential because these values will be next optimized during the neural network learning step, computation-time can be decreased in this way. Initial values of radii are given in Table 2.

3.3 Evaluation Criteria of the Neural Network Accuracy. The initial set of experimental data is divided into two parts. The first is used during the learning step and the second, containing remaining data, is next employed to evaluate the reconstruction accuracy. For each experimental value, the three coordinates are given as input to the net, and the result is next calculated and compared with the experimental data. To evaluate the neural network reconstruction accuracy, two parameters are calculated: a mean error criterion Err_{abs} and a more sensitive parameter giving an evaluation of the error distribution around its mean value, the associated root mean square τ_{err}, defined by:

$$\text{Err}_{abs} = \frac{1}{n} \sum_{i=1}^{n} |V_{app_i} - V_i| \quad (8)$$

$$\tau_{err} = \left(\frac{1}{n} \sum_{i=1}^{n} (|V_{app_i} - V_i| - \text{Err}_{abs})^2 \right)^{1/2} \quad (9)$$

where n is the total number of experimental values available for a given hydrodynamical characteristic V.

Although error of reconstruction is fully determined using these two parameters, neural network accuracy is not well represented. Error is indeed evaluated by comparing the neural network result to the experimental one, which presents experimental uncertainty. Thus, having null values of error does not mean a perfect reconstruction, but only that experimental uncertainty is fully integrated to the neural network reconstruction, making results biased too. Values calculated following Eq. (8) and Eq. (9) are thus not fully representative of the reconstruction accuracy and, because the measured velocity-field cannot be experimentally noise free, they can be considered only as estimators.

Finally, three kinds of data sets are defined: (i) the total set of size n, called the generalization set, used to estimate the reconstruction accuracy on the entire geometry, (ii) the learning set of size p, composed of values used during the learning step and which is a part of the generalization set, and (iii) the test set of size n-p, composed of values not employed in the learning set. By changing the size of the learning and of the test sets, the

minimum number of requested values can be deduced. The test set will be used to evaluate the neural network interpolation accuracy for unknown locations.

4 Results and Discussion

4.1 Validation of the Neural Method. Neural network method efficiency depends on data employed during the learning step. As it often appears, increasing the size of the learning set will improve the resulting accuracy. But another parameter is the distribution of data employed. For example, in the particular case of the swirling decaying flow, the velocity-field has been found asymmetric and not established along the axial coordinate. Thus, before using the neural network method to reconstruct hydrodynamical characteristics, interpolation accuracy has been first evaluated following two parameters: (i) the number of experimental values needed to represent swirling flow evolution along the axial coordinate, and (ii) the number of angular positions requested to represent the flow asymmetry following the circumferential coordinate. Axial mean velocity representation has been chosen for this preliminary evaluation because of its important dependence on spatial coordinates. The mean distribution of axial velocity deduced from the average of PIV measurements was thus employed during the learning step (see Section 4.2 for the averaging procedure applied to PIV acquisitions).

4.1.1 Axial Coordinate Influence. The effect of the number of axial positions has been studied in order to determine the size of the learning set to interpolate the flow-field with accuracy. The learning step was performed on five sets containing different numbers of data representing the distribution of the mean axial velocity. Efficiency was next estimated using the generalization set and the test set. Results are given in Fig. 4.

Figure 4 shows that a minimal error of 0.46 cm/s is obtained, but as indicated in Section 3.3, error free values cannot be reached, because an experimental uncertainty about 10 percent of the mean axial velocity is included in reference data. This value, which corresponds to the experimental error, represents the limit of the method efficiency. These results reveal the number of experimental data necessary to reach an accurate reconstruction of the axial velocity component. An experimental set of 19096 values has been measured, but as shown in Fig. 4, only 2000 values are needed. Increasing the size of the learning set does not provide any improvement in neural reconstruction.

4.1.2 Influence of the Number of Angular Positions. Because the swirling flow induced by a tangential inlet is not axisymmetric, experimental measurements have to be repeated for several angular positions. The influence of the number of angular positions given for the neural network learning step has been studied in order to show if neural method was able to represent the flow asymmetry and to determine the number of circumferential positions requested to obtain accurate results.

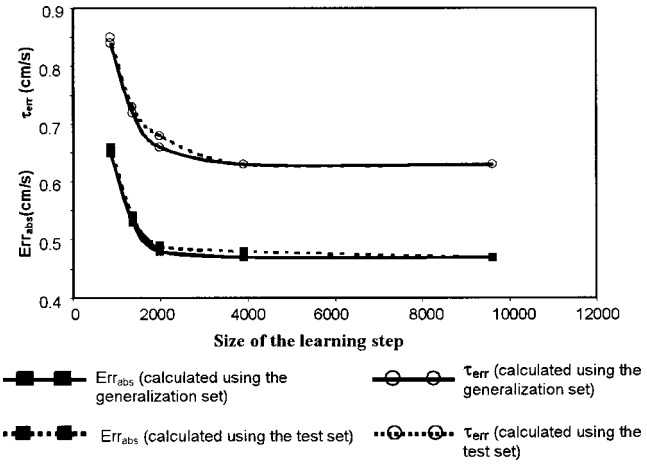

Fig. 4 Influence of the size of the learning set of data on the neural network reconstruction efficiency

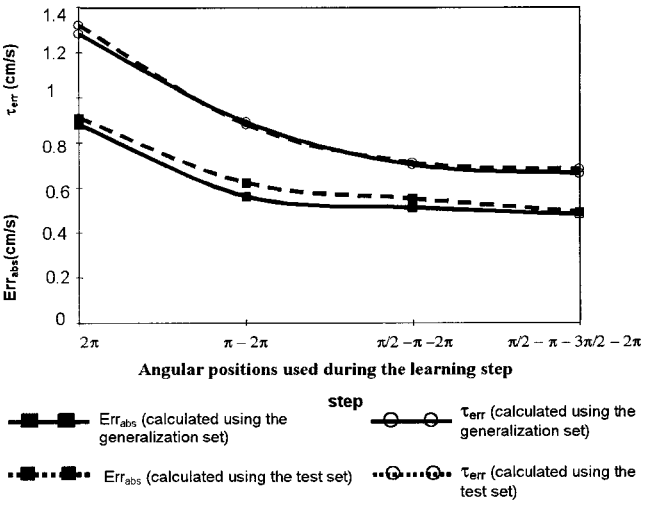

Fig. 5 Influence of the number of angular positions of the learning set of data on the neural network reconstruction efficiency

Reconstruction efficiency as a function of the number of angular positions is shown in Fig. 5. The number of angular positions experimentally investigated appears to be sufficient to give a good representation of the flow asymmetry. Values of τ_{err} can be considered as minimal using only three angular positions. These results show the efficiency of the neural method, which is able to represent nonlinear evolutions of the swirling flow asymmetry. With this method, only little information is needed to allow an efficient reconstruction of the data evolution.

4.2 Hydrodynamical Parameters Reconstruction. As shown by previous results, the number of measured data is sufficient to obtain an efficient reconstruction of the spatial evolution of hydrodynamical parameters. The neural network will be used in this section to reconstruct mean velocities and turbulent intensities of the flow-field. Mean velocities and turbulent intensities employed in the learning step are obtained with PIV technique. The averaging procedure of instantaneous PIV acquisitions is described as follows:

$$U_x=\frac{1}{N}\sum_{i=1}^{N} u_{x_i}, \quad U_r=\frac{1}{N}\sum_{i=1}^{N} u_{r_i}, \quad U_\xi=\frac{1}{N}\sum_{i=1}^{N} u_{\xi_i} \tag{10}$$

$$T_x=\frac{\sqrt{\frac{1}{N}\sum_{i=1}^{N}(u_{x_i}-U_x)^2}}{\overline{U}}, \quad T_r=\frac{\sqrt{\frac{1}{N}\sum_{i=1}^{N}(u_{r_i}-U_r)^2}}{\overline{U}}, \quad T_\zeta=\frac{\sqrt{\frac{1}{N}\sum_{i=1}^{N}(u_{\xi_i}-U_\zeta)^2}}{\overline{U}} \tag{11}$$

To achieve a statistically stable mean spatial distribution of experimental hydrodynamical quantities, $N=200$ instantaneous acquisitions were used for mean values, and $N=1000$ for turbulent intensities, for each of the investigated position, listed in Table 1.

The neural network method has next been applied for each flow characteristic. Figure 6 shows the reconstruction obtained for each investigated angular position for the three mean components of the velocity, whereas Fig. 7 is dedicated to turbulent intensities

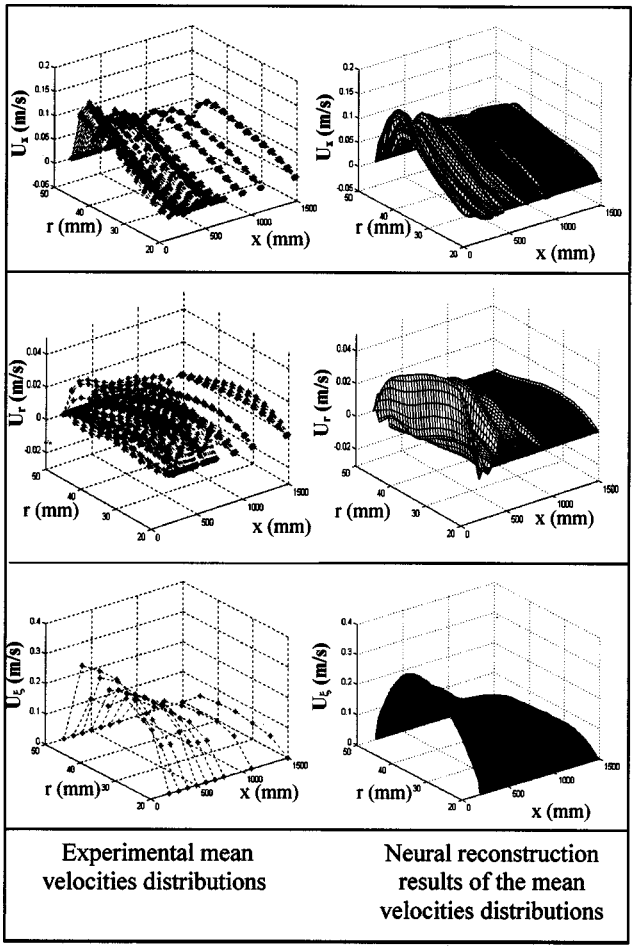

Fig. 6 Mean velocity reconstruction. (*a*) Axial component; (*b*) radial component; (*c*) circumferential component

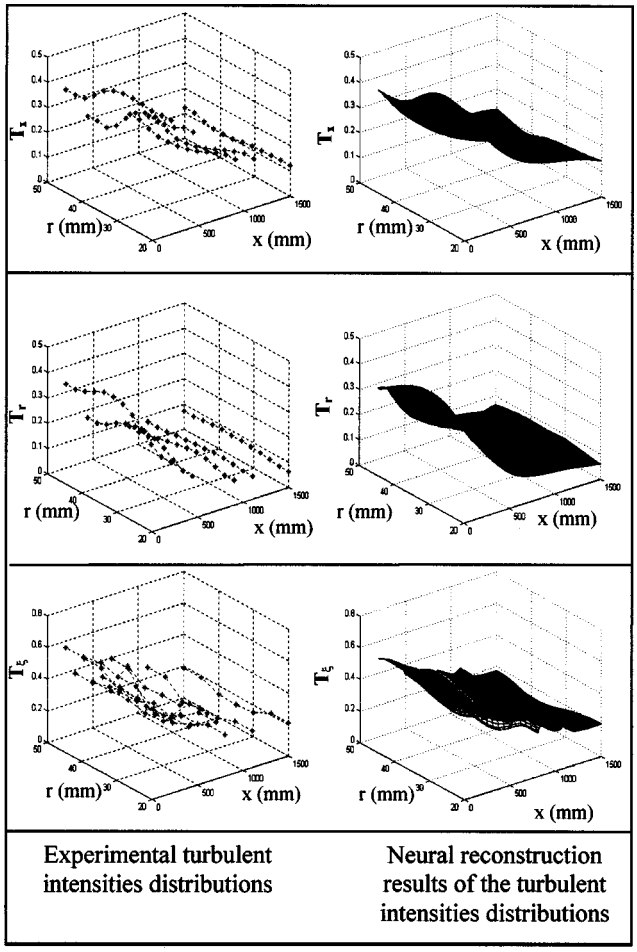

Fig. 7 Turbulent intensity reconstruction. (*a*) Axial component; (*b*) radial component; (*c*) circumferential component

characteristics. The neural network is able to represent their spatial evolution efficiently and to give a good representation of the main features of the swirling flow as its asymmetric behavior and the free decay of the swirling motion along the axial coordinate. Thus, this method appears as a universal approximation tool, which is able to reconstruct any kind of data and hydrodynamical feature. This is confirmed by final errors Err_{abs} obtained for each component of the velocity-field (see Table 3).

Following Eq. (4), the neural network results are the exact representation of a sum of elementary continuous functions. After the learning step, when neural network is defined, a continuous expression of each hydrodynamical parameter is obtained. Any location in the investigated geometry can be provided to the net input, a solution will be determined in output. Two examples of velocity-field deduced from initial PIV measurements are compared with the neural network results. These examples are given in Fig. 8 for two plane projections, in the axial-radial (Fig. 8(*a*)) and radial-circumferential one (Fig. 8(*b*)). Neural network results have been obtained by providing a set of some locations corresponding to a finest mesh than the one used for PIV measurements. These results show the neural method interest which transforms the discrete velocity-field experimentally measured into a mathematical expression defined on the whole domain, despite the very complex behavior of the swirling decaying flow. Thanks to the neural network method, hydrodynamical characteristics are now determined at any location in the studied geometry.

Table 3 Error criteria Err_{abs} for each reconstructed hydrodynamical characteristic

Mean velocity components		
U_x	U_r	U_ξ
0.47 cm/s	0.22 cm/s	0.35 cm/s

Turbulent intensity components		
T_x	T_r	T_ξ
0.021	0.023	0.015

5 Conclusion

A neural network method using RBF has been used to express hydrodynamical parameters obtained using PIV on the entire geometry of an annular test-cell involving a swirling decaying flow induced by a tangential inlet. The neural method being able to express nonlinear evolutions of a three-dimensional flow, this kind of technique appears to be an efficient tool to accurately represent any hydrodynamical characteristics of this complex flow, as well for the three components of the mean velocity as for turbulent intensity. This universal approximation behavior is very interesting when no a priori idea of what kind of evolution has to be obtained. Results show that this method can be used where hydrodynamical conditions are found to be very disturbed and three-dimensional. But the neural network is not restricted to this particular flow and the algorithm remains adaptive. For example, it can be simplified either for two-dimensional flows, giving the net only two inputs, or adapted to complex nonstationary flows. In the

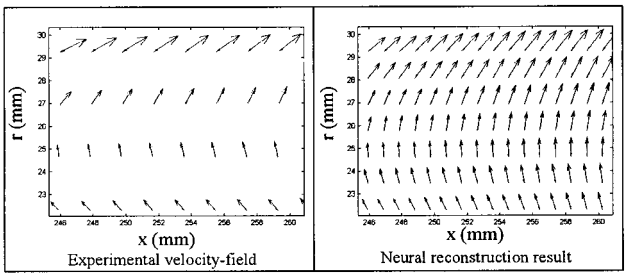

(*a*)

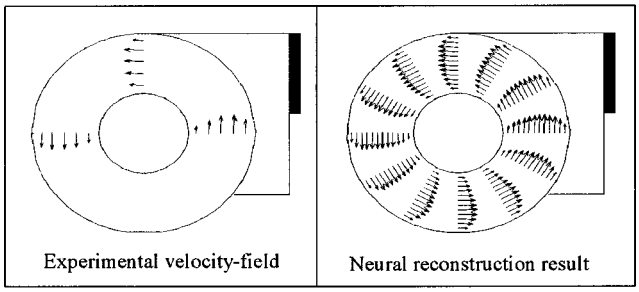

(*b*)

Fig. 8 Examples of velocity-field reconstruction. (*a*) Axial-radial plane projection ($\xi=0$); (*b*) Radial-circumferential plane projection (x=205 mm)

latter case, the neural network has four inputs (three for the spatial coordinates, and one for the time dependency). Assuming that the number of experimental data is sufficient, the neural network will give accurate results, this method being able to reconstruct any function depending on *n*-parameters. Thus, this technique is interesting when complex data base have to be interpolated, and especially experimental data which present measurements uncertainty, neural networks with RBF functions being found to be robust interpolating methods when data are noisy. But the comparison presented in this study between experimental measurements and neural network results does not allow a conclusion about the noise influence on the reconstruction efficiency, because the exact flow-field is unknown. This could be achieved by a further study where, for instance, results of a CFD simulation would be used instead of experimental PIV measurements. Reconstruction accuracy could then be determined as a function of an artificial noise added to CFD results.

The second main advantage of such neural network is to provide a derivable mathematical expression of each hydrodynamical feature valid for the whole domain. This is helpful, for example, for the determination of boundary conditions in CFD simulations using local experimental measurements, or for the calculation of additional hydrodynamical information of the flow, like stress-fields, vorticity-fields or pathlines. When values are locally defined, derivative methods are requested, which implies the use of numerical approximation scheme (finite difference techniques). Defining the flow-field on the whole domain by means of a derivable mathematical function will prevent the employment of such methods. Therefore, the use of this neural method seems an interesting tool for flow-field data post-processing, especially for three-dimensional flows, where common numerical methods are difficult to apply. In conclusion, such a technique provides two main advantages: it reduces the investigation time by decreasing the number of requested experimental measurements, and it leads to a better understanding of the flow-field by allowing the numerical determination of pertinent hydrodynamical characteristics.

Nomenclature

C_{in} = center of the n-gaussian activation function associated to the *i*-direction of the reconstruction problem
Err_{abs} = error criterion for neural reconstruction efficiency evaluation (m/s)
Q = flow rate in the annulus (m^3/s)
R_i = external radius of the inner cylinder (m)
Re = $2e\overline{U}/\nu$. Reynolds number (Eq. (1))
R_0 = internal radius of the outer cylinder (m)
T = turbulent intensity (Eq. (11))
$\overline{U}$ = $Q/(\pi(R_0^2-R_i^2))$: average velocity in the annulus (m/s)
U = mean velocity (m/s)
V = generic hydrodynamical characteristic to be reconstructed
V_{app} = neural approximation of V
W = set of weights in the neural network
e = thickness of the annular gap (m)
r = radial position with respect to the annulus axis (m)
u = instantaneous velocity (m/s)
x = axial position with respect to the tangential inlet (m)
w_n = weight of the *n*-radial basis function
ξ = circumferential position with respect to the tangential inlet axis (radians)
Φ = base of elementary functions
ϕ_n = elementary function of activation from the *n*-neuron in the hidden layer
λ = regularization parameter
ν = kinematic viscosity of water (m^2/s)
τ_{err} = root mean square of error provided by the neural network (m/s)
τ_{in} = radius of the n-gaussian activation function associated to the *i*-direction of the reconstruction problem

Subscripts

x = axial component of mean velocity, velocity fluctuation or turbulent intensity
r = radial component of mean velocity, velocity fluctuation or turbulent intensity
ξ = circumferential component of mean velocity, velocity fluctuation or turbulent intensity

References

[1] Marshall, J. S., and Grant, J. R., 1997, "A Lagrangian vorticity collocation method for viscous, axisymmetric flows with and without swirl," J. Comput. Phys., **138**, pp. 302–330.
[2] Gupta, A., Lilley, D. G. and Syred, N., 1984, *Swirl Flow*. Energy and Engineering Sciences Series, Abacus Press.
[3] Legentilhomme, P., and Legrand, J., 1990, "Overall mass transfer in swirling decaying flow in annular electrochemical cells," J. Appl. Electrochem., **20**, pp. 216–222.
[4] Legentilhomme, P., and Legrand, J., 1991, "The effects of inlet conditions on mass transfer in annular swirling decaying flow," Int. J. Heat Mass Transf., **34**, pp. 1281–1291.
[5] Legentilhomme, P., Aouabed, H., and Legrand, J., 1993, "Developing mass transfer in swirling decaying flow induced by means of a tangential inlet," Chem. Eng. J., **52**, pp. 137–147.
[6] Aouabed, H., Legentilhomme, P., Nouar, C., and Legrand, J., 1994, "Experimental comparison of electrochemical and dot-paint methods for the study of swirling flow," J. Appl. Electrochem., **24**, pp. 619–625.
[7] Aouabed, H., Legentilhomme, P., and Legrand, J., 1995, "Wall visualization of swirling decaying flow using a dot-paint method," Exp. Fluids, **19**, pp. 43–50.
[8] Legrand, J., Aouabed, H., Legentilhomme, P., Lefèbvre, G., and Huet, F., 1997, "Use of electrochemical sensors for the determination of wall turbulence characteristics in annular swirling decaying flows," Exp. Therm. Fluid Sci., **15**, pp. 125–136.
[9] Farias Neto, S. R., Legentilhomme, P., and Legrand, J., 1998, "Finite-element simulation of laminar swirling decaying flow induced by means of a tangential inlet in an annulus," Computer Methods in Applied Mechanics and Engineering, **165**, pp. 189–213.
[10] Pruvost, J., Legrand, J., Legentilhomme, P., and Doubliez, L., 2000, "Particle Image Velocimetry investigation of the flow-field of a 3D turbulent annular swirling decaying flow induced by means of a tangential inlet," Exp. Fluids, **29**, No. 3, pp. 291–301.

[11] Shi, R. X., and Chehroudi, B., 1994, ''Velocity characteristics of a confined highly turbulent swirling flow near a swirl plate,'' ASME J. Fluids Eng., **116**, pp. 685–693.
[12] Hardy, R. L., 1971, ''Multiquadratic equations of topography and other regular surfaces,'' J. Geophys. Res., **76**, pp. 1905–1915.
[13] Franke, R., 1982, ''Scattered data interpolation: tests of SOE method,'' Math. Comput., **38**, pp. 181–200.
[14] Renals, S., and Rowher, R., 1989, ''Phoneme classification experiments using radial basis function,'' Proceedings of the International Joint Conference on Neural Networks 1, Washington D.C., June, pp. 461–467.
[15] Faller, W. E., Schreck, S. J., and Helin, H. E., 1995, ''Real-time model of three-dimensional dynamic reattachment using neural networks,'' J. Aircr., **32**, No. 6, pp. 1177–1182.
[16] Powell, M. J. D., 1987, *Radial basis functions for multivariate interpolation: a review. Algorithms for Approximation*, J. C. Mason and M. G. Cox edition, Clarendon Press, Oxford.
[17] Poggio, T., and Girosi, F., 1990, ''Networks for Approximation and Learning,'' Proc. IEEE, **78**, No. 9, pp. 1481–1497.
[18] Moody, J., 1992, ''The effective number of parameters: an analysis of generalization and regularization in nonlinear learning systems,''Advances in Neural Information Processing Systems 4, Morgan Kaufmann Publishers, San Mateo, pp. 847–854.
[19] Chen, T., and Chen, H., 1995, ''Approximation capability to functions of several variables, nonlinear functionals, and operators by radial basis function neural networks,'' IEEE Trans. Neural Netw., **6**, No. 4, pp. 904–910.
[20] Craven, P., and Wahba, G., 1979, ''Smoothing noisy data with spline functions,'' Numerische Mathematik , **31**, pp. 377–403.
[21] Grimson, W. E. L., 1981, *From images to surfaces*, MIT Press, Cambridge, MA.
[22] Wahba, G., 1977, ''Practical approximate solutions of linear operators equations when the data are noisy,'' Journal of Numerical Analysis, **14**, pp. 651–667.
[23] Poggio, T., Jones, M., and Girosi, F., 1995, ''Regularization Theory and Neural Networks Architectures,'' Neural Comput., **7**, No. 2, pp. 219–269.
[24] Orr, M. J. L., 1995, ''Regularization in the selection of radial basis function centers,'' Neural Comput., **7**, pp. 602–623.

Alternative Models of Turbulence in a Porous Medium, and Related Matters

D. A. Nield
Associate Professor,
Department of Engineering Science,
University of Auckland,
Private Bag 92019, Auckland, New Zealand
e-mail: d.nield@auckland.ac.nz

Recently published papers involving two distinct models of turbulence in a porous medium are discussed, together with related matters including inertial effects, lateral momentum transfer and spin-up, nonlinear drag, and the detection of the onset of turbulence.
[DOI: 10.1115/1.1413246]

1 Introduction

After mentioning several of their papers in which turbulent transport equations for porous media were developed based on the generalized Volume Averaging Theory (VAT) for highly porous media, Travkin et al. [1] wrote (page 2), ''Antohe and Lage [2] presented a two-equation ... turbulence model for incompressible flow within a fluid saturated and rigid porous medium that is the result of incorrect procedures.'' It is regrettable that Travkin et al. did not find room in their paper to explain why they considered those procedures to be incorrect, and the reader is left to guess that any procedures that are not based on VAT must be incorrect. Travkin et al. [1] proceeded to derive their own form of the kappa-epsilon equations, displayed as their Eqs. (35) and (37). These complicated equations contain various integrals, and there is no indication in the paper of how closure is to be completed, despite the claim (page 6) that ''closure examples are given.'' In a signed review of an earlier version of this paper, Dr Travkin argues that his complicated equations are correct, and therefore that the approximate equations of other people must be wrong. It appears that he does not appreciate that in order to make practical progress it is necessary to make approximations. In his review, Dr Travkin admits that he has been unable to solve completely the closure problem for the VAT equations.

A more informative treatment of the matter is that by Nakayama and Kuwahara [3]. On page 427 they wrote:

''Recently, two distinct two equation turbulence models have been established for turbulent flows in porous media. Antohe and Lage [2] chose to carry out the Reynolds averaging over the volume-averaged macroscopic equations to derive two-equation turbulence model equations, whereas Masuoka and Takatsu [4] derived a macroscopic turbulence transport equation by spatially averaging the turbulence transport equation of the two-equation turbulence model. Antohe and Lage [2] examined their model equations for the turbulence kinetic energy and its dissipation rate, assuming a unidirectional fully-developed flow through an isotropic porous medium. Their model demonstrates that the only possible steady state solution for the case is ''zero'' macroscopic turbulence kinetic energy. This solution should be re-examined, since the macroscopic turbulence kinetic energy in a forced flow through a porous medium must stay at a certain level, as long as the presence of porous matrix keeps generating it. (The situation is analogous to that of turbulent fully-developed flow in a conduit.) Also, it should be noted that the small eddies must be modeled first, as in the case of LES (Large Eddy Simulation). Thus we must start with the Reynolds averaged set of the governing equations and integrate them over a representative control volume, to obtain the set of macroscopic turbulence model equations. Therefore, the procedure based on the Reynolds averaging of the spatially averaged continuity and momentum equations is questionable, since the eddies larger than the scale of the porous structure are not likely to survive long enough to be detected. Moreover, none of these models has been verified experimentally.''

Nakayama and Kuwahara [3] go on to describe their own work:

''The macroscopic turbulence kinetic energy and its dissipation rate are derived by spatially averaging the Reynolds-averaged transport equations along with the $k-\varepsilon$ turbulence model. For the closure problem, the unknown terms describing the production and dissipation rates inherent in porous matrix are modified collectively. In order to establish the unknown model constants, we conduct an exhaustive numerical experiment for turbulent flows though a periodic array, directly solving the microscopic governing equations, namely, the Reynolds-averaged set of continuity, Navier-Stokes, turbulence kinetic energy and dissipation rate equations. The microscopic results obtained from the numerical experiment are integrated spatially over a unit porous structure to determine the unknown model constants.

The macroscopic turbulence model, thus established, is tested for the case of macroscopically unidirectional turbulent flow. The streamwise variations of the turbulence kinetic energy and its dissipation rate predicted by the present macroscopic model are compared against those obtained from a large scale direct computation over an entire field of saturated porous medium, to substantiate the validity of the present macroscopic model.''

It is the view of the present author that Nakayama and Kuwahara [3] have presented clearly and forcefully their case that their model is superior to that of Antohe and Lage [2], and in many respects their paper is admirable. However, there are some questionable aspects of their arguments and these are discussed in the following section. Further, there are two general questions that should be raised. First, is the turbulence discussed by Nakayama and Kuwahara true macroscopic turbulence? Second, how reliable are conclusions based on volume averaging? In the remainder of the present paper, the author presents his answers to these questions and discusses related matters, such as the way in which inertial effects should be modeled, and the nature of momentum transfer and spin-up in a porous medium.

For a review of earlier papers on macroscopic turbulence in permeable media the reader is referred to Lage [5].

2 Some Specific Comments on the Nakayama-Kuwahara Model

Having integrated the Reynolds averaged equations over a ''control volume,'' Nakayama and Kuwahara [3] obtain their momentum equation, Eq. (11). This is unexceptional. However, they then proceed to replace the last two terms of Eq. (11) by Darcy and Dupuit-Forchheimer terms to obtain Eq. (14). This replacement is a standard procedure for laminar flows, but it appears to the present author that the replacement is highly questionable in

Contributed by the Fluids Engineering Division for publication in the JOURNAL OF FLUIDS ENGINEERING. Manuscript received by the Fluids Engineering Division September 30, 1999; revised manuscript received October 11, 2000. Associate Editor: J. Katz.

the context of turbulence modeling. In the paragraph containing Eq. (14) those authors wrote, ''In the numerical study of turbulent flow through a periodic array, Kuwahara et al. [6] concluded that the Forchheimer-extended Darcy's law holds even in the turbulent flow regime in porous media.'' That too is an acceptable statement, but it does not justify the transition from Eq. (11) to Eq. (14). For one thing, Eq. (14) is substantially different from the standard Forchheimer-extended Darcy equation. Furthermore, there is a gap in the argument in proceeding from an equation for the turbulence regime in a bulk form, in which the total pressure-drop is related to the bulk fluid speed via an expression quadratic in the velocity, to an equation involving a differential expression. (The reader should note that this comment has nothing to do with whether or not differential operators are used in ''macroscopic'' or integral equations.) In summary, it seems to the present author that Nakayama and Kuwahara [3] have made an assumption of a relationship between microscopic turbulence and macroscopic drag that cannot be justified except in the gross sense that for high Reynolds number the Forchheimer term will be dominant.

Because of their assumption of periodicity when performing their numerical calculations, Nakayama and Kuwahara [3] were unable to treat eddies on a scale larger than their period length. They treated a geometry that was periodic in both the *x*- and *y*-directions with period 2H. Within a period cell, they considered solid obstacles having cross-section a square of side-length *D*, and they selected the ratio D/H so that the porosity ϕ lay between 0.2 and 0.9. That means that *D* and *H* were of the same order. In other words the period length for the numerical calculations was of the same order of magnitude as the particle diameter, and so representative of the pore scale. Eddies with a diameter greater than $2H$ cannot be accommodated on their model, simply because they are larger than the period length. In other words, global eddies (those with a diameter lager than the pore scale) were filtered out because of the assumptions about periodicity. Thus global eddies were ruled out a priori. It is true that a medium does not have to be periodic to have the Nakayama-Kuwahara model applied to it, but when the periodicity imposed is that of the pore scale then this is a severe restriction.

Further, there is a fundamental difficulty with any model in which time-averaging (Reynolds averaging) is followed by volume averaging. That procedure precludes the incorporation of the interaction between fluctuating quantities and the solid matrix of the porous medium, other than the minor effect of fluctuations in pressure and shear stresses along the interfacial solid-fluid area. This aspect was clearly stated by Antohe and Lage [2].

Also, it appears that Nakayama and Kuwahara [3] may have misinterpreted the ''zero'' turbulence conclusion (for fully developed turbulent flow) of Antohe and Lage [2]. The Antohe-Lage result says nothing about the existence or otherwise of microscopic turbulence, and its failure to do so should not be used as negative criticism of the model.

Moreover, it would have been advantageous to Nakayama and Kuwahara to recognize that the turbulence kinetic energy used in their own paper defined as a volume-average of the microscopic turbulence kinetic energy) is different from that used by Antohe and Lage (defined as the time-averaging of the square of the volume-averaged fluid velocity fluctuations).

This difference has been highlighted by the work of Pedras and de Lemos [7], and de Lemos and Pedras [8]. The analysis in these papers leads to the conclusion that the two approaches, time-averaging the volume-averaged equations and volume-averaging the time-averaged equations, lead to similar equations because of a commutative property of the two averaging operations. The authors explicitly demonstrate (Eq. (50) in [7]) that there is a difference between the expressions used to denote turbulent kinetic energy used in the two classes of models. The Pedras and de Lemos approach may be regarded as more complete, in a sense, than the Antohe-Lage approach, because clearly it has regard for pore turbulence and it does say something (but not very much) about large scale turbulence.

3 Macroscopic Turbulence in a Porous Medium

The author has over a period of some years expressed the view (Nield [9], Nield and Bejan [10]) that it is important to distinguish between turbulence in the pores of a porous medium and turbulence on a macroscopic scale (the global scale, that of the apparatus in an experiment). For example, Nield ([9], page 271) wrote that ''A further consequence of our physical argument is that true turbulence, in which there is a cascade of energy from large eddies to smaller eddies, does not occur on a macroscopic scale in a dense porous medium.'' (The physical argument is presented again below.) The author believes that subsequent investigations have shown results that are consistent with the quoted statement. For example, as Nakayama and Kuwahara [3] highlighted in the passage quoted above, the model of Antohe and Lage [2] leads to the conclusion that the only possible steady-state solution for the case considered by them is zero macroscopic turbulence kinetic energy.

The model of Nakayama and Kuwahara [3] is concerned with the effect of turbulence within the pores, and not with true macroscopic turbulence. In particular, their numerical experiments involve a model that is periodic on the pore scale, and this means that (as I have already noted) global eddies are ruled out a priori. On the other hand, the model of Antohe and Lage [2] does deal with macroscopic turbulence in a sensible fashion. Of course, as already noted above, the Antohe-Lage model says nothing about the turbulence within the pores.

This means that we have two classes of models. One class of models (that includes the Nakayama-Kuwahara model) describes the effect of turbulence within the pores. The second class, exemplified by the Antohe-Lage model, describes turbulence on a global scale. For the case of dense porous media (characterized by small values of the Darcy number, and generally with porosities less than 0.5) the first class of models will generally be the more useful for dealing with what turbulence there is, but for the case of large Darcy number (and in particular for hyperporous materials (Nield and Lage, [11]) such as metallic foams) the second class of models will be the more appropriate.

4 Limitations of the Volume-Averaging Approach

At first sight, the method of volume-averaging is a rigorous procedure, as Travkin et al. [1] claimed it is. It is indeed a rigorous procedure, but only up to the stage at which the system of equations is closed. In order to make practical progress, approximations have to be made to evaluate certain integrals, and from then on the procedure is not rigorous. It is inevitable that physical information is lost at the closure stage. (See, for example, the discussion of the ''filter'' in Sections 1.3.4 and 1.6.4 in Whitaker [12].)

In performing the closure one is guided by physical experience. In other words, the closure process is a semi-empirical matter, and the usefulness of the final model is critically dependent on the skill that one employs at the closure stage. This matter is discussed further in the next section.

5 Modeling Inertial Effects

It is relatively simple to perform averaging over terms that are linear in the dependent variables, but nonlinear terms, such as the convective (advective) inertial term $(\mathbf{V}\cdot\nabla)\mathbf{V}$ in the Navier-Stokes equation, cause difficulties. (Here $\mathbf{V}$ denotes the fluid velocity.) Even in the case of laminar flow there has been controversy over the best way to model inertial effects in a porous medium. There is agreement that these effects lead to a quadratic drag term, usually called the Forchheimer drag term, though on historical

grounds (Lage [5]) it is more accurate to call this the Dupuit-Forchheimer term. However, there has been disagreement about the coefficient of this term (Antohe and Lage [13]) and whether or not one should also include simultaneously a convective inertial term $(\mathbf{v}\cdot\nabla)\mathbf{v}$ indicated by formal volume-averaging (where $\mathbf{v}$ denotes the Darcy velocity) in the resulting momentum equation, when modeling a medium of low porosity (Nield [9]).

It was noted by Nield [14] that at least the irrotational part of this term needs to be retained in order to account for the phenomenon of choking in the high speed flow of a compressible fluid, but he suggested that the rotational part, proportional to the intrinsic vorticity, be deleted. His argument was based on the expectation that a medium of low porosity will allow scalar entities like fluid speed (the magnitude of the velocity) to be freely advected, but will inhibit the advection of vector quantities like vorticity. Nield and Bejan [10] went a step further, and suggested that even when vorticity is being continuously produced (e.g., by buoyancy) one would expect that it would be destroyed by a momentum dispersion process due to the solid obstructions.

An argument providing further support for this point of view will now be presented. There are some subtleties about the effect of the inertial terms on motion in a porous medium. The power of the total drag force (per unit volume) is equal to the rate of viscous dissipation (per unit volume); for a detailed discussion see Nield [15]. The Forchheimer drag term, although it appears to be independent of the viscosity, contributes to the viscous dissipation. The effect of inertia is mediated via a change in the pressure distribution and the velocity distribution. The flip side of the coin is that when one closes the system of equations by introducing a Forchheimer drag term one should not assume that the convective inertia term that remains in the momentum equation is identical with that obtained by formal volume-averaging. After integration, it should lead to the correct expression for the averaged kinetic energy, which involves the magnitude but not the direction of the velocity, and this means that the irrotational part of the volume-averaged convective inertial term must be unchanged, but the rotational part is not determined by the averaging process, and there is no inconsistency in setting it to zero as part of the closure process.

In the process of performing the closure after volume-averaging, it has been traditional to adjust for the contribution to the overall drag force, that includes a quadratic drag force that has a specific direction (parallel to the Darcy velocity in the case of an anisotropic medium), but to ignore the fact that one also needs to adjust for the fact that the overall moment of the force system has to be zero. It is now being suggested that an appropriate adjustment is simply to set to zero the irrotational part of the volume-averaged convective inertial term.

It has sometimes been claimed that the retention of the convective inertial term is necessary in order to account for the formation of hydrodynamic boundary layers in channel flow, and in order to estimate the entrance length, but this is not correct. The formation of such layers is primarily due to the action of viscous diffusion, and the entrance length can be estimated using the time-derivative inertial term.

6 The Lateral Transfer of Momentum, and Spin-Up in a Porous Medium

A related matter is the extent to which it is possible to transmit longitudinal momentum in a transverse direction in a dense porous medium. Nield [9] discussed the case of a special medium in which the pores consist of channels along the *x*-, *y*-, and *z*- directions. He pointed out that if one forces fluid to flow down a single *x*- channel, that will cause flow along intersecting *y*- and *z*- channels but will not produce any significant flow on the average in neighboring *x*-channels. A consequence is that, on physical grounds, one would expect that it should be difficult to produce significant motion in the bulk of a porous medium, with a fixed solid matrix, by moving just a rigid boundary. Rather, one would expect significant motion to be confined to a thin layer near the boundary. As Nield [16] showed, by consideration of a fixed circular cylinder of a porous medium surrounded by a rotating sleeve, that is indeed the form of motion predicted when one solves a momentum equation containing the Brinkman term but with the convective inertial term omitted. On the other hand, if one includes the convective inertial term then one has an equation similar to the usual Navier-Stokes equation, and this leads to the prediction that all the fluid within the porous medium will ultimately be set in motion. As far as the author is aware, no one has yet performed an experiment in order to test the prediction.

7 The Onset of Turbulence

(i) The Relationship Between Quadratic Drag and Turbulence. The topic of transition to turbulence in porous media is among the interesting topics reviewed by Masuoka [17]. He refers in particular to the experimental work discussed by Dybbs and Edwards [18], and to his own work reported by Masuoka and Takatsu [4] and by Takatsu and Masuoka [19]. Nield [20] and Antohe and Lage [13] have pointed out that the work of Masuoka and his colleagues is based on a misconception about the identity of the onset of turbulence and the Forchheimer drag term taking significantly large values. Antohe and Lage [13] have also emphasized the need to use a proper definition of Reynolds number in characterizing these phenomena.

(ii) The Detection of the Onset of Turbulence. The determination in an experiment of the critical Reynolds number at which turbulence appears is not a straightforward matter. In a personal communication to the author, Dr. J. L. Lage has pointed out that in a porous medium of conduit type, in which the pore space consists essentially of tubes of varying cross-section, there is the possibility of relaminarization, in some portions of the tubes (after divergence), of turbulence that appears in other portions (after convergence). Ideally, one would like to put probes in the narrowest part of the tubes, and of course that is difficult in practice and almost certainly has not been achieved in experiments reported to date. Also, it should be noted that the appearance of a signal chaotic in time at a single position is probably an excellent indication, but not conclusive evidence, of the onset of turbulence. One needs to observe also what is happening at a neighboring point in order to be sure that turbulence is occurring.

The Lage argument is based on the fact that, for constant volume flux through a tube, the mean velocity is inversely proportional to tube cross-section, and hence inversely proportional to the square of the tube diameter. The local Reynolds number, which involves the product of the mean velocity and the tube diameter, is thus inversely proportional to the tube diameter. That means that in the wider portions of the tube, the local Re value may drop below the critical value necessary to maintain the turbulent state. In other words, relaminarization may occur. On the same argument, the onset of turbulence is likely to occur first in those parts of the channel where the local Re is highest, namely in the narrowest part of the tubes.

A referee pointed out that while the association between high local Re and turbulence is appropriate for a tube of constant cross-section, it might not be applicable to ducts with varying cross-section. It is known that for high Re flows in aerodynamics, turbulence is seldom encountered except close to solid walls (where it can be generated). In converging sections of ducts, fluid layers close to the solid tend to run faster and flatten the time-averaged velocity profile. Consequently, less mechanical energy is converted to turbulence, because production of turbulent kinetic energy is dependent on the mean velocity gradients. In this case, in accelerated flows, relaminarization may occur. When the flow crosses an enlargement, layers close to the wall are subjected to a positive pressure gradient and tend to run slower than the core of

the flow, and separation may even occur. The referee noted that as a consequence, turbulence production is enhanced and levels of turbulent kinetic energy are increased, as found experimentally by Spencer et al. [21].

However, it is not clear to the present author to what extent results for high Re aerodynamics carry over to flow in porous media, and further investigation is desirable.

Acknowledgment

Several of the author's ideas on this subject have developed as a result of discussions/debates over the years with Dr J. L. Lage of Southern Methodist University.

References

[1] Travkin, V. S., Hu, K., and Catton, I., 1999, ''Turbulent Kinetic Energy and Dissipation Rate Equation Models for Momentum Transport in Porous Media,'' Proceedings, 3rd ASME/JSME Joint Fluids Engineering Conference, July 18–23, 1999, San Francisco, California, FEDSM99-7275, pp. 1–7.

[2] Antohe, B. V., and Lage, J. L., 1997, ''A General Two-Equation Macroscopic Turbulence Model for Incompressible Flow in Porous Media,'' Int. J. Heat Mass Transf., **40**, pp. 3013–3024.

[3] Nakayama, A., and Kuwahara, F., 1999, ''A Macroscopic Turbulence Model for Flow in a Porous Medium,'' ASME J. Fluids Eng., **121**, pp. 427–433.

[4] Masuoka, T., and Takatsu, Y., 1996, ''Turbulence Model for Flow Through Porous Media,'' Int. J. Heat Mass Transf., **39**, pp. 2803–2809.

[5] Lage, J. L., 1998, ''The Fundamental Theory of Flow Through Permeable Media: From Darcy to Turbulence,'' *Transport Phenomena in Porous Media*, D. B. Ingham and I. Pop, eds., Elsevier Science, Oxford, pp. 1–30.

[6] Kuwahara, F., Kameyama, Y., Yamashita, S., and Nakayama, A., 1998, ''Numerical Modeling of Turbulent Flow in Porous Media Using a Spatially Periodic Array,'' Journal of Porous Media, **1**, pp. 47–55.

[7] Pedras, M. H. J., and de Lemos, M. J. S., 1999, ''On Volume and Time Averaging of Transport Equations for Turbulent Flow in Porous Media,'' Proceedings, 3rd ASME/JSME Joint Fluids Engineering Conference, July 18–23, 1999, San Francisco, California, FEDSM99-7273, pp. 1–6.

[8] de Lemos, M. J. S., and Pedras, M. H. J., 2000, ''On the Definition Of Turbulent Kinetic Energy for Flow in Porous Media,'' Int. Commun. Heat Mass Transfer, **27**, pp. 211–220.

[9] Nield, D. A., 1991, ''The Limitations of the Brinkman-Forchheimer Equation in Modeling Flow in a Saturated Porous Medium and at an Interface,'' Int. J. Heat Fluid Flow, **12**, pp. 269–272.

[10] Nield, D. A., and Bejan, A., 1992/1999, *Convection in Porous Media*, Springer-Verlag, New York.

[11] Nield, D. A., and Lage, J. L., 1997, ''Discussion of a Discussion by K. Vafai and S. J. Kim,'' ASME J. Heat Transfer, **119**, pp. 195–197.

[12] Whitaker, S., 1999, *The Method of Volume Averaging*, Kluwer Academic Publishers, Dordrecht.

[13] Antohe, B. V., and Lage, J. L., 1999, ''Darcy's Experiments and the Transition to Nonlinear Flow Regime,''Proceedings, 33rd National Heat Transfer Conference, August 15–17, 1999, Albuquerque, New Mexico, NHTC99-180, pp. 1–7.

[14] Nield, D. A., 1994, ''Modelling High-Speed Flow of a Compressible Fluid in a Porous Medium,'' Transp. Porous Media, **14**, pp. 85–88.

[15] Nield, D. A., 2000, ''Resolution of a Paradox Involving Viscous Dissipation and Nonlinear Drag in a Porous Medium,'' Transp. Porous Media, in press.

[16] Nield, D. A., 1989, ''Spin-Up in a Saturated Porous Medium,'' Transp. Porous Media, **4**, pp. 495–497.

[17] Masuoka, T., 1999, ''Some Aspects of Fluid Flow and Heat Transfer in Porous Media,'' Proceedings, 5th ASME/JSME Joint Thermal Engineering Conference, March 15–19, 1999, San Diego, California, AJTE99-6304, pp. 1–14.

[18] Dybbs, A., and Edwards, R. V., 1984, ''A New Look at Porous Media Fluid Mechanics—Darcy to Turbulent,'' *Fundamentals of Transport Phenomena in Porous Media*, J. Bear and V. Carapcioglu, eds., Martinus Nijhoff Publishers, Amsterdam, pp. 199–256.

[19] Takatsu, Y., and Masuoka, T., 1998, ''Turbulent Phenomena in Flow Through Porous Media,'' Journal of Porous Media, **1**, pp. 243–251.

[20] Nield, D. A., 1997, ''Comments on 'Turbulence Model for Flow Through Porous Media','' Int. J. Heat Mass Transf., **40**, pp. 2449.

[21] Spencer, E. A., Heitor, M. V., and Castro, I. P., 1995, ''Intercomparison of measurements and computations of flow through a contraction and a diffuser,'' Flow Measurement and Instrumentation, **6**, pp. 3–14.

Discussion: "Alternative Models of Turbulence in a Porous Medium, and Related Matters" (D. A. Nield, 2001, ASME J. Fluids Eng., 123, pp. 928–931)

V. S. Travkin
Mechanical and Aerospace Engineering Department, UCLA, Los Angeles, CA 90095-1597

The paper which I authored is mentioned first by Prof. Nield [1]. I would like to make some preliminary comments about that citing in the paper by Nield, because the length of a paper which is presented to a conference like the 3rd ASME/JSME Fluids Engineering Conference in 1999, is usually restricted to 6 pages. That is the reason we could not include discussion or critics of other studies, but focused primarily on our results.

[DOI: 10.1115/1.1413247]

The paper by Antohe and Lage [2], cited by Prof. Nield, needs comments on turbulent transport in porous media. The equations derived by Antohe and Lage in their paper appeared to be based on a set of phenomenological equations that are themselves the result of assumptions and simplifications. The development of a set of equations that are rigorous does not allow one to use correlation based models developed by others that are themselves based on approximate conceptions of what the physical processes are dependent on. These models or terms in the equations already include many observed effects. After all, that was their purpose. It is inadmissible for one to include such correlations in the Navier Stokes equations, as was done by Antohe and Lage, because this results in the effects being included in the governing equations twice.

A number of serious deficiencies are found in that paper, including the following:

1 The authors initial set of equations are based on the assumption that the turbulent fluctuations and fluctuations caused by the porous medium are of the same nature. They are not, and serious error can result if they are assumed to be the same.

2 Given the above observation and other issues of development, the conclusions presented in the abstract of the paper that ''Among them, this conclusion supports the hypothesis of having microscopic turbulence, known to exist at high speed flow, damped by the volume averaging process. Therefore, turbulence models derived directly from the general (macroscopic) equations will inevitably fail to characterize accurately turbulence induced by the porous matrix in a microscopic sense,'' are not correct. Before one can reach such conclusions, the derivations of the equations upon which it is based must be valid.

Regarding the need for approximations mentioned in the first paragraphs by Prof. Nield, I appreciate and respect the desire to use approximation, but it must be a correct approximation, substantiated. When someone derives an incorrect sum of suggestions, model, governing equations and then makes an approximation of that model-it makes no sense to consider values of this ''approximation.''

In application to the VAT turbulent transport in porous media, the words ''in this review...unable to solve completely the closure problem for the VAT equations'' are not completely accurate. As a matter of fact, the papers by Shcherban et al.[3] and Primak et al. [4] were the first correct studies on VAT in turbulent transport in porous media. In these studies and others in Russian were first published two critical features:

1 basics for turbulent fields decomposition and treatment in VAT averaging [3];
2 fundamentals of averaging of nonlinear operators of class $\nabla\cdot(\nu_T\nabla\{U\}_f)$.

Since those two papers with experimental closure of VAT turbulent equations, I have published a number of papers with exact, rigorous closures (in a general interest morphologies-as capillary or globular) [5–12], as well as with approximate closures using experimental data [6,10,13–17]. In addition, we recently performed experimental studies on micro-heat exchangers, doing for the first time a data reduction methodology based completely on VAT [18]. All this is done by using the closure methods.

Over many years I've been watching the situation where people from different countries have proposed developing some "new" theoretical construction for modeling of turbulent transport in porou media. Their papers are published because there is a lack of advancement and lack of experts in this area. The mathematics and equations of VAT have yet to become part of a convenient university knowledge base and are too unfamiliar to understand or to make a close consideration. It seems one needs to blame the lack of university education plus not enough volume of solved problems.

These thoughts were behind the reason and idea of the second of our presentations at the 3rd ASME/JSME Fluids Engineering conference, "A Critique of Theoretical Models of Transport in Heterogeneous Media," [19]. This specifically addressed those issues mostly by criticizing various developments in heterogeneous and multiphase transport theories and modeling. Returning to the paper by Prof. Nield, I have no choice but to talk about those papers and studies that already were addressed in the presentation. One of them is the previous work by F. Kuwahara and A. Nakayama [20].

In this work, the Detailed Micro-Modeling Direct Numerical Modeling\(DMM-DNM)-solution of 2D problem of uniformly located quadratic rods with equal spacing in both directions is delivered and analyzed. There the Forchheimer and post-Forchheimer flow regimes were studied. This work is a good example of how DMM-DNM goals cannot be accomplished even if the solution on a microlevel is obtained completely, when the proper volume averaging theory (VAT) scaling procedures basics are not known and applied. The one structural unit periodic cell in the medium was taken for DMM-DNM. Equations were taken with constant coefficients and in phase one the VAT equation was written for the laminar regime as

$$\langle m\rangle(\rho c_p)_f\frac{\partial\tilde{T}_f}{\partial t}+\langle m\rangle(\rho c_p)_f\tilde{U}_i\nabla\tilde{T}_f$$
$$=(\rho c_p)_f\nabla\cdot\langle-\hat{T}_f\hat{u}_i\rangle_f+k_f\nabla\nabla(\langle m\rangle\tilde{T}_f)$$
$$+k_f\nabla\cdot\left[\frac{1}{\Delta\Omega}\int_{\partial S_w}T_f\vec{d}s\right]+\frac{k_f}{\Delta\Omega}\int_{\partial S_w}\nabla T_f\cdot\vec{d}s. \quad (1)$$

Adding this equation to the VAT solid phase (second phase) two temperature equation gives

$$\langle m\rangle(\rho c_p)_f\frac{\partial\tilde{T}_f}{\partial t}+\langle s_2\rangle(\rho c_p)_2\frac{\partial\tilde{T}_2}{\partial t}+\langle m\rangle(\rho c_p)_f\tilde{U}_i\nabla\tilde{T}_f$$
$$=(\rho c_p)_f\nabla\cdot\langle-\hat{T}_f\hat{u}_i\rangle_f+\nabla\cdot(k_f\nabla(\langle m\rangle\tilde{T}_f)+k_2\nabla(\langle s_2\rangle\tilde{T}_2))$$
$$+\nabla\cdot\left[\frac{k_f}{\Delta\Omega}\int_{\partial S_{12}}T_f\vec{d}s_1+\frac{k_2}{\Delta\Omega}\int_{\partial S_{12}}T_2\vec{d}s_2\right]$$
$$+\frac{k_f}{\Delta\Omega}\int_{\partial S_{12}}\nabla T_f\cdot\vec{d}s_1+\frac{k_2}{\Delta\Omega}\int_{\partial S_{12}}\nabla T_2\cdot\vec{d}s_2 \quad (2)$$

which reduces due to interface fluxes equality to

$$\langle m\rangle(\rho c_p)_f\frac{\partial\tilde{T}_f}{\partial t}+\langle s_2\rangle(\rho c_p)_2\frac{\partial\tilde{T}_2}{\partial t}+\langle m\rangle(\rho c_p)_f\tilde{U}_i\nabla\tilde{T}_f$$
$$=\nabla\cdot(k_f\nabla(\langle m\rangle\tilde{T}_f)+k_2\nabla(\langle s_2\rangle\tilde{T}_2))+(\rho c_p)_f\nabla$$
$$\cdot\langle-\hat{T}_f\hat{u}_i\rangle_f+(k_f-k_2)\nabla\cdot\left[\frac{1}{\Delta\Omega}\int_{\partial S_{12}}T_f\vec{d}s_1\right] \quad (3)$$

which has two averaged temperatures $\tilde{T}_f$ and $\tilde{T}_2$, interface surface integrated temperature $T_f(\partial S_{12})$, and two fields of fluctuations $\hat{T}_f(x)$ and $\hat{u}_i(x)$, assuming that the velocity field is also computed and known. One will write further the effective conductivity coefficients for Eq. (3) and for the one-temperature equation when the temperature equilibrium is assumed.
In the first case for the weighted temperature

$$\langle T^w\rangle=(\langle m\rangle(\rho c_p)_f\tilde{T}_f+\langle s_2\rangle(\rho c_p)_2\tilde{T}_2)/w_T, \quad (4)$$

$$w_T=\langle m\rangle(\rho c_p)_f+\langle s_2\rangle(\rho c_p)_2=\text{const}, \quad (5)$$

equation can be written as

$$w_T\frac{\partial\langle T^w\rangle}{\partial t}+\langle m\rangle(\rho c_p)_f\tilde{U}_i\nabla\tilde{T}_f=\nabla\cdot(k_f\nabla(\langle m\rangle\tilde{T}_f)+k_2\nabla(\langle s_2\rangle\tilde{T}_2))$$
$$+(\rho c_p)_f\nabla\cdot\langle-\hat{T}_f\hat{u}_i\rangle_f+(k_f$$
$$-k_2)\nabla\cdot\left[\frac{1}{\Delta\Omega}\int_{\partial S_{12}}T_f\vec{d}s_1\right], \quad (6)$$

where 3 temperatures are unknown $\langle T^w\rangle,\tilde{T}_f,\tilde{T}_2$, plus interface surface temperature integral $T_f(\partial S_{12})$, and fluctuation fields $\hat{T}_f(x)$ and $\hat{u}_i(x)$. The effective coefficient of conductivity can be looked for is

$$k^o_{\text{eff}}\langle\nabla T^w\rangle=(k_f\nabla(\langle m\rangle\tilde{T}_f)+k_2\nabla(\langle s\rangle\tilde{T}_2))+(\rho c_p)_f\langle-\hat{T}_f\hat{u}_i\rangle_f$$
$$+(k_f-k_2)\left[\frac{1}{\Delta\Omega}\int_{\partial S_{12}}T_f\vec{d}s_1\right]. \quad (7)$$

In order to avoid the complicated problem with effective conductivity coefficient definition in a multi-temperature environment Kuwahara and Nakayama [20], while performing the DMM-DNM for problem of laminar regime transport in porous medium, decided to justify the local thermal equilibrium condition

$$\langle T\rangle=\langle m\rangle\tilde{T}_f+\langle s_2\rangle\tilde{T}_2=T^*=\tilde{T}_f=\tilde{T}_2 \quad (8)$$

which greatly changes the one effective temperature equation. This equation becomes simpler with only one unknown temperature T^* and variable field $\hat{T}_f$ and writes as

$$(\langle m\rangle(\rho c)_f+\langle s_2\rangle(\rho c_p)_2)\frac{\partial T^*}{\partial t}+\langle m\rangle(\rho c_p)_f\tilde{U}_i\nabla T^*$$
$$=\nabla\cdot(k_f\nabla(\langle m\rangle T^*)+k_2\nabla(\langle s_2\rangle T^*))+(\rho c_p)_f\nabla\langle-\hat{T}_f\hat{u}_i\rangle_f$$
$$+(k_f-k_2)\nabla\cdot\left[\frac{1}{\Delta\Omega}\int_{\partial S_{12}}T_f\vec{d}s_1\right], \quad (9)$$

as the variable temperature and velocity fluctuation fields $\hat{T}_f$ and $\hat{u}_i$ should be known, although this is a problem. As long as the definition of effective conductivity coefficient is

$$k^*_{\text{eff}}\langle\nabla T^*\rangle=k_f\nabla(\langle m\rangle T^*)+k_2\nabla(\langle s_2\rangle T^*)+(\rho c_p)_f\langle-\hat{T}_f\hat{u}_i\rangle_f$$
$$+(k_f-k_2)\left[\frac{1}{\Delta\Omega}\int_{\partial S_{12}}T_f\vec{d}s_1\right], \quad (10)$$

then the effective conductivity can be calculated subject to known T^*, $\hat{T}_f$, T_f, and $\hat{u}_i$. One important issue here also is how is the temperature fluctuation $\hat{T}_f$ being calculated? By using the correct

phase temperature T_f of calculating the difference with T^*? At the same time, an important issue is that in DMM-DNM, the assumption of thermal equilibrium has no sense at all, as long as the problem has been already calculated as a two temperature problem. In this situation it is not clear what kind of temperature was used in the calculations of VAT terms and assessments of characteristics. If one temperature was used it was used instead of the already calculated two temperatures, which would be preferred. To further perform the correct estimation or calculation of effective characteristics, one needs to know what are those characteristics, in terms of definition and mathematical description of the model?

This is one more place where the DMM-DNM as it is performed now is in trouble if it does not comply with the hierarchical theory derivations and conclusions as the VAT. As shown above, only the requirement of thermal equilibrium warrants the equality of steady-state and transient effective conductivities in a two-phase medium. Consequently, if taken correctly the two-temperature model will cause more trouble in treatment and even interpretation of the needed bulk, averaged temperature (as long as this problem is already known and treated in nonlinear and temperature dependent situations), and corresponding effective conductivity coefficient(s).

Thus, comparing the two effective conductivity coefficients Eq. (7) and Eq. (10), one can assess the difference in the second term form and consequently, the value of the computed coefficients. Comparing the expressions for one equilibrium temperature and one effective weighted temperature, as well as for their effective conductivity coefficients, one can also observe the great imbalance and inequality in their definitions and computations.

Summarizing the application of DMM-DNM laminar regime approach by Kuwahara and Nakayama [20], it can be said that it is a questionable procedure to make an assumption of equilibrium temperatures when the problem was stated and computed as via DNM for two temperatures. In the calculation of the effective coefficients of conductivity, stagnant thermal conductivity k_e; tortuosity molecular diffusion k_{tor}; and thermal dispersion k_{dis}, Kuwahara and Nakayama used the questionable procedure for calculation of the latter two coefficients. They used a one cell (REV) computation for surface and fluctuation temperatures for the periodic morphology of the medium, and at the same time they used the infinite REV definition for the effective temperature gradient for their calculation. That results in the mixture of two different scale variables in one expression for effective characteristics. This is an inconsistency and if used consciously it should be stated explicitly, because it alters the results.

Returning to the question of the correct approach to turbulent transport modeling in a heterogeneous environment, I would point out that the first to really address the problem were not workers in fluid mechanics (those primarily diagnosed the problem), but in meteorology and particularly in agro-meteorology [3,4,8]. One who is interested in the field should also read first the book by Monin and Yaglom [21] who are primarily meteorologists. In that book, substantial discussion is provided on the subject of equations of kinetic energy and dissipation rate when a group of obstacles are encountered in a flow.

Nield states, ''It is the view of the present author that Nakayma and Kuwahara [22] have presented clearly and forcefully their case that their model is superior to that of Antohe and Lage [2], and in many respects their paper is admirable.'' I just want to agree with this remark by Nield about the paper of Antohe and Lage, and at the same time I am not surprised by the comment of Prof. Nield on the paper by Nakayma and Kuwahara [22]. The reason is still the same. There is no understanding of the correct averaging theory and the correct VAT equations for nonlinear problems to which those averaging operators have been applied.

Furthermore, I need to make some shorter remarks on this paper [22]. One of the biggest problems with this kind of model and a similar one by Masuoka and Takatsu [23], is that the authors cannot do the correct averaging of the right-hand side of the equations. Those equations are highly nonlinear, on both sides. The theory of half-linear conservative equations averaging is well developed in the studies by Prof. S. Whitaker, yet these authors do not refer to his work, in spite of the fact that most of their equations were developed by Whitaker many years ago and are known to a reading public.

Nakayama and Kuwahara [22] do averaging which we find questionable even in the brackets of laminar equations averaging technique. For example, they apply intrinsic averaging to vectorial functions equations. Further, in the averaged momentum equation (11) on p. 428 they incorrectly define the second

$$\frac{\partial}{\partial x_j}\left[(\nu+\nu_t)\left(\frac{\partial\{\overline{u_i}\}_f}{\partial x_j}+\frac{\partial\{\overline{u_j}\}_f}{\partial x_i}\right)\right],$$

and the third terms in r.h.s.

In the averaged equation of fluid temperature (15) they incorrectly derived the first

$$\frac{\partial}{\partial x_j}\left[\left(k_f+\frac{\rho_f c_{pf}\nu_t}{\sigma_T}\right)\left(\frac{\partial\{\overline{T}\}_f}{\partial x_j}\right)\right],$$

the second and third r.h.s. terms; in the equation of solid temperature (16) the second r.h.s. term is incorrect; in the averaged kinetic energy $\{k\}_f$ equation (20) incorrect are-the first, second, fourth and fifth r.h.s. terms and in the dissipation rate $\{\varepsilon\}_f$ equation (21)-the first, second, third, fourth and fifth r.h.s. terms are incorrect.

In their further development, these authors used those equations for numerical solution through the DMM-DNM to assess the value of turbulent viscosity of the 2D square rod medium in a cross-flow. Also, they applied a thermal equilibrium condition.

Prof. Nield is right when he speaks out about the frivolous change of a few additional terms in the right-hand side for the Darcy-Forchheimer like terms. This action is so often undertaken in many papers, and is one which is incorrect.

When Nield is writing about the interaction between fluctuating quantities and the solid matrix of the porous medium, he should be referring only to models by Masuoka-Takatsu [23] and Nakayama-Kuwahara [22], because this aspect is naturally dropped from their models. That is not relevant to the theory published by Travkin and co-authors. It is necessary to note that the statement about ''global eddies are ruled out a priori'' is inaccurate with respect to the theory published by Travkin and co-authors. There is no limitation by periodicity in this theory, but vice versa. Both scale fluctuations are allowed to exist: fluctuations for turbulence within the pore which is controlled by the pore and fluctuations of the upper scale which are controlled by the whole morphology of the medium. That means that the models of Nakayama and Kuwahara, Masuoka and Takatsu and those by Travkin and co-authors are not of the same type, as Prof. Nield writes.

In Section 4 we read about closure of the averaged equations. Prof. Nield seems to have knowledge that this closure happened to be provided only on the basis of substitution by experimental data (which is still highly reliable method as long as the data reduction is done correctly). This statement is not credible. When the closure is provided on a rigorous basis, which is actually done in some of our works [[5,7,15,24], etc.], there is no question at all about the correct form of the final governing equations. It is not to say that the closure problem for the VAT equations is solved completely. Of course, it is not even close to a final determination, but the ways and means already have substantial progress.

I question the statement ''It is inevitable that physical information is lost at the closure stage.'' I would say that, on the contrary, every detail of the microscale process can be preserved and serve as an input to the upper scale model if the closure is provided correctly, which we addressed in a few papers. In VAT closure modeling, there exists the situation when there are few method-

ologies to close the additional integral, integro-differential and differential terms in VAT equations. The most widely known and used is the method of linear approximation of fluctuation variables, introduced first and developed by S. Whitaker. The methods used in studies by Travkin and co-authors [3,4,7,10,13,24–28] are those one can use with either the two-scale modeling or experimentally obtained coefficients, for example, of resistance and heat transfer. I would not say that it is a ''semi-empirical matter.'' Some of the considerations and analysis by Prof. Nield on closure problems seem to be from guessing, because the process of closure of VAT equations, and even the existence of some terms which should be closed in nonlinear and turbulent transport equations, is unknown to most of authors whose papers we are discussing here.

As to the developments by Pedras, de Lemos and co-authors mentioned by D. Nield, I would like to make a few comments on the question of the transposition (commutativeness) of Volume-Time averaging or Time-Volume averaging. It appears from the papers co-authored by de Lemos that this question is settled in a favor of the transposability of the components of two sequences. Many factors would contradict this, for example:

1 REV (volume) averaging of Navier-Stokes equations with the large $\mathrm{Re} \geqslant 5 \cdot 10^2$ in porous media makes no sense (turbulence already appeared).

2 The closure, the solution of those lower scale turbulent equations in basic much more simple geometries is a huge area of research at the present time in the field of turbulence theory. Tens (if not hundreds) of people throughout the world are dying to find some meaningful clues. And this would be only a fraction of the problem in scaled VAT description.

3 The time averaging in turbulence modeling is connected to domain averaging. When the consequence of time→volume averaging changed for volume→time averaging, then to what domain and to what field should Reynolds averaging be applied? It is like mixing the heat and mass transport in one ''physical'' process-saying ''we have the heat-mass transport averaging (T+C).'' Mathematically it is possible, but what is the sense of that physics averaging? It means also that the enormous amount of knowledge and advancements obtained in turbulence theory could not be used because they would not be applicable to problems formulated with (volume→time) averaging in porous medium.

References

[1] Travkin, V. S., Hu, K., and Catton, I., 1999, ''Turbulent Kinetic Energy and Dissipation Rate Equation Models for Momentum Transport in Porous Media,'' *Proc. 3rd ASME/JSME Fluids Engineering Conf.*, FEDSM99-7275, San Francisco.

[2] Antohe, B. V., and Lage, J. L., 1997, ''A General Two-Euqation Macroscopic Turbulence Model for Incompressible Flow in Porous Media,'' Int. J. Heat Mass Transf., **40**, pp. 3013–3024.

[3] Shcherban, A. N., Primak, A. V., and Travkin, V. S., 1986, ''Mathematical Models of Flow and Mass Transfer in Urban Roughness Layer,'' *Problemy Kontrolya i Zaschita Atmosfery ot Zagryazeniya*, No. 12, pp. 3–10 (in Russian).

[4] Primak, A. V., Shcherban, A. N., and Travkin, V. S., 1986, ''Turbulent Transfer in Urban Agglomerations on the Basis of Experimental Statistical Models of Roughness Layer Morphological Properties,'' *Trans. World Meteorological Organization Conf. on Air Pollution Modeling and its Application*, Geneva, **2**, pp. 259–266.

[5] Gratton, L., Travkin, V. S., and Catton, I., 1994, ''Numerical Solution of Turbulent Heat and Mass Transfer in a Stratified Geostatistical Porous Layer for High Permeability Media,'' ASME Paper 94-WA-HT-41, 1994.

[6] Travkin, V. S., Gratton, L., and Catton, L., 1995, ''Modeling Technique for Closure of Transport Equations in Non-regular Globular and Capillary Porous Medium Morphology,'' *Procs. A.S.M.E./J.S.M.E. Thermal Engineering Joint Conference*, Maui, Hawaii, Vol. **3**, pp. 319–326.

[7] Catton, I. and Travkin, V. S., 1997, ''Homogeneous and Non-Local Heterogeneous Transport Phenomena with VAT Application Analysis,'' *Proceedings of the 15th Symposium on Energy Engineering Sciences*, Argonne National Laboratory, Conf.-9705121, pp. 48–55.

[8] Travkin, V. S., and Catton, I., 1994, ''Turbulent Transport of Momentum, Heat and Mass in a Two-Level Highly Porous Media,'' *Heat Transfer 1994, Proceedings of the Tenth International Heat Transfer Conference*, Brighton, U.K., **5**, pp. 399–404.

[9] Travkin, V. S., and Catton, I., 1998, ''Porous Media Transport Descriptions-Non-Local, Linear and Nonlinear Against Effective Thermal/Fluid Properties,'' Adv. Colloid Interface Sci., **76–77**, pp. 389–443.

[10] Travkin, V. S. and I. Catton, 1999, ''Compact Heat Exchanger Optimization Tools Based on Volume Averaging Theory,'' *Proc. 33rd ASME NHTC, NHTC99-246*. ASME, New Mexico.

[11] Travkin, V. S. and Catton, I., Hu, K., Ponomarenko, A. T., and Shevchenko, V. G., 1999, ''Transport Phenomena in Heterogeneous Media: Experimental Data Reduction and Analysis,'' *Proc. ASME*, AMD-233, **233**, pp. 21–31.

[12] Hu, K., Travkin, V. S., and Catton, I., 2001, ''Two Scale Hierarchical Network Model of Heat and Momentum Transport in Porous Media,'' *Proc. 35th National Heat Transfer Conference* (2001 NHTC), ASME.

[13] Travkin, V. S. and Catton, I., 1992, ''Models of Turbulent Thermal Diffusivity and Transfer Coefficients for a Regular Packed Bed of Spheres,'' *Fundamentals of Heat Transfer in Porous Media*, ASME HTD, Vol. **193**, pp. 15–23.

[14] Gratton, L., Travkin, V. S., and Catton, I., 1996, ''The Influence of Morphology upon Two-Temperature Statements for Convective Transport in Porous Media,'' Journal of Enhanced Heat Transfer, **3**, pp. 129–145.

[15] Catton, I., and Travkin, V. S., 1996, ''Turbulent Flow and Heat Transfer in High Permeability Porous Media,'' *Proc. of the Intern. Conf. on Porous Media and Their Applications in Science, Engineering and Industry*, K. Vafai and P. N. Shivakumar, eds., Engin. Foundation and Inst. Industr. Math. Sciences, pp. 333–391.

[16] Travkin, V. S., Gratton, L., and Catton, I., 1994, ''A Morphological-Approach for Two-Phase Porous Medium-Transport and Optimum Design Applications in Energy Engineering,'' *Proceedings of the Twelfth Symposium on Energy Engineering Sciences*, Argonne National Laboratory, Conf.-9404137, pp. 48–55.

[17] Travkin, V. S., Catton, I., and Hu, K., 1998, ''Channel Flow In Porous Media In The Limit As Porosity Approaches Unity,'' *Proc. ASME HTD*, Vol. **361-1**, pp. 277–284.

[18] Rizzi, M., Canino, M., Hu, K., Jones, S., Travkin, V. S., and Catton, I., (2001), ''Experimental Investigation of Pin Fin Heat Sink Effectiveness,'' accepted to the 35th ASME National Heat Transfer Conference, 2001.

[19] Travkin, V. S., and Catton, I., 1999, ''Critique of Theoretical Models of Transport Phenomena in Heterogeneous Media,'' invited presentation given at the *3rd ASME/JSME Fluids Engineering Conf.-FEDSM99-7922*, San Francisco.

[20] Kuwahara, F. and Nakayama, A., 1998, ''Numerical Modeling of Non-Darcy Convective Flow in a Porous Medium,'' *Proc. 11th Int. Heat Transfer Conf. 1998*, Vol. **4**, pp. 411–416.

[21] Monin, A. S. and Yaglom, A. M., 1965, *Statistical Hydromechanics. Mechanics of Turbulence*, Moscow, Nauka, (in Russian).

[22] Nakayama, A., and Kuwahara, F., 1999, ''A Macroscopic Turbulence Model for Flow in a Porous Medium,'' ASME J. Fluids Eng., **121**, pp. 427–433.

[23] Masuoka, T., and Takatsu, Y., 1996, ''Turbulence Model for Flow through Porous Media,'' Int. J. Heat Mass Transf., **39**, pp. 2803–2809.

[24] Travkin, V. S., and Catton, I., 1999, ''Nonlinear Effects in Multiple Regime Transport of Momentum in Longitudinal Capillary Porous Medium Morphology,'' J. Porous Media, **2**, pp. 277–294.

[25] Travkin, V. S., and Catton, I., 1995, ''A Two-Temperature Model for Turbulent Flow and Heat Transfer in a Porous Layer,'' ASME J. Fluids Eng., **117**, pp. 181–188.

[26] Travkin, V. S., Catton, I., and Hu, K., 2000, ''Optimization of Heat Transfer Effectiveness in Heterogeneous Media,'' *Proc. of the Eighteenth Symposium on Energy Engineering Sciences*, Argonne National Laboratory, 2000.

[27] Travkin, V. S., Hu, K., and Catton, I., 2001, ''Multi-variant Optimization in Semiconductor Heat Sink Design,'' accepted to the ASME-NHTC'2001.

[28] Travkin, V. S., and Catton, I., 2001, ''Transport Phenomena in Heterogeneous Media Based on Volume Averaging Theory,'' Adv. Heat Transfer, **34**, pp. 1–14.

Closure to ''Discussion of 'Alternative Models of Turbulence in a Porous Medium, and Related Matters''' (2001, ASME J. Fluids Eng., 123, p. 931)

D. A. Nield

I thank Dr. Travkin for his thoughtful discussion. I am happy to leave it to readers to decide which of his claims have merit, and I hope that these publications will inspire increased interest in the topic throughout the fluids engineering community.

Recent Mathematical Models for Turbulent Flow in Saturated Rigid Porous Media

Marcelo J. S. de Lemos
Mem. ASME
Departamento de Energia—IEME,
Instituto Tecnológico de Aeronáutica–ITA,
12228-900—São José dos Campos-SP, Brazil
e-mail: delemos@mec.ita.br

Marcos H. J. Pedras
Instituto de Pesquisa e Desenvolvimento
IP&D-UNIVAP,
12244-000-São José dos Campos-SP, Brazil

Turbulence models proposed for flow through permeable structures depend on the order of application of time and volume average operators. Two developed methodologies, following the two orders of integration, lead to different governing equations for the statistical quantities. The flow turbulence kinetic energy resulting in each case is different. This paper reviews recently published mathematical models developed for such flows. The concept of double decomposition is discussed and models are classified in terms of the order of application of time and volume averaging operators, among other peculiarities. A total of four major classes of models are identified and a general discussion on their main characteristics is carried out. Proposed equations for turbulence kinetic energy following time-space and space-time integration sequences are derived and similar terms are compared. Treatment of the drag coefficient and closure of the interfacial surface integrals are discussed. [DOI: 10.1115/1.1413243]

Introduction

On the basis of the pore Reynolds number, Re_p, the literature recognizes distinct flow regimes in porous media spanning from creeping flow ($\mathrm{Re}_p<1$) to fully turbulent regime ($\mathrm{Re}_p>300$). The mathematical treatment for high Reynolds flow has given rise to interesting discussions in the literature and remains a controversial issue.

For Re_p less than about 150, traditional analysis of flow in porous media (Darcy [1], Forchheimer [2], Brinkman [3], Ward [4], Whitaker [5], Bear [6], Vafai and Tien [7]) makes use of a Representative Elementary Volume (REV) for which transport equations are written. When the pore Reynolds number is greater than about 300, turbulence models in the literature follow two approaches. In the first one (Lee and Howell [8], Wang and Takle [9], Antohe and Lage [10], Getachew et al. [11]), governing equations for the mean and turbulent field are obtained by time-averaging the volume-averaged equations. We shall refer to those as A-L models. In the second methodology (Masuoka and Takatsu [12], Kuwahara et al. [13], Kuwahara and Nakayama [14], Takatsu and Masuoka [15], Nakayama and Kuwahara [16]), a volume-average operator is applied to the local time-averaged equation. Here, this second approach is named N-K model. A morphology-based closure has also been suggested (Travkin and Catton [17], Travkin et al. [18], Gratton et al. [19], Travkin and Catton [20], Travkin and Catton [21], Travkin et al. [22]) based on the Volume Average Theory. Use of such methodology, however, is regarded by many as of little practical use in engineering applications (Lage [23], p. 23). This third class of model will be here referred to as T-C approach. In the literature, all of these methodologies lead to different governing equations.

Motivated by the foregoing discussion, a preliminary proposal for a turbulence model for porous material was established (Pedras and de Lemos [24]). Then, a study on the different views in the literature has lead to the proposition of the *double-decomposition* idea (Pedras and de Lemos [25]) and to subsequent development of the earlier preliminary model (Pedras and de Lemos [26]). The double-decomposition concept led to a better characterization of the flow turbulent kinetic energy (Pedras and de Lemos [27]) and was a step before detailed numerical solution of the flow equations were carried out (Pedras and de Lemos [28]). Calculations were needed for adjusting the model and considered either the high Re k-ϵ closure (Rocamore and de Lemos [29]) as well as the Low Reynolds version of it (Pedras and de Lemos [28]). Full documentation of the modeling steps is detailed in de Lemos and Pedras [30], and Pedras and de Lemos [25].

Heat transfer analysis was also the subject of additional research (Rocamora and de Lemos [31,32]). One of the main motivations for this development was the ability to treat hybrid computational domains with a single mathematical tool. Hybrid systems have been calculated for the flow field (de Lemos and Pedras [33]), for nonisothermal recirculating flows in channels past a porous obstacle (Rocamora and de Lemos [34,35]) and through a porous insert (Rocamora and de Lemos [36,37]).

More specifically, in the work of Pedras and de Lemos [25,27], it was shown that the order of application of time and volume average operators was immaterial in regard to the final equations obtained for the mean flow. However, when obtaining a macroscopic transport equation for the turbulent kinetic energy, the order of application of averages will imply in a different quantity being transported. This is because there is an additional mathematical operation needed for forming the turbulent kinetic energy. This operation consists in the scalar product of the fluctuating velocity by its own transport equation. When this scalar product is taken after the volume integration process, as in A-L models (Lee and Howell [8], Wang and Takle [9], Antohe and Lage [10]), the quantity undergoing time integration is $\langle \mathbf{u}' \rangle^i \cdot \langle \mathbf{u}' \rangle^i$. Here, differently from the case of the mean flow equations, the two domains of integration are no longer independent of each other. On the other hand, when proceeding with the scalar product first at the microscopic level, with the N-K approach, a different variable is subjected to time integration $(\mathbf{u}' \cdot \mathbf{u}')$ (Masuoka and Takatsu [12], Kuwahara et al. [14], Kuwahara and Nakayama [13], Takatsu and Masuoka [37], Nakayama and Kuwahara [16]). In this second method, according to Pedras and de Lemos [27], a broader form of the turbulence kinetic energy is obtained and all microscopic effects are considered.

The objective of this paper is to classify and compare turbulence models for porous medium presented in the literature (de Lemos [38]). Proposed equations for the turbulent kinetic energy are rewritten in light of the double decomposition concept of Pedras and de Lemos [27] and the interrelationship between correspondent terms is discussed (de Lemos and Pedras [39]). Weakness and advantages of these two methodologies are discussed in

Contributed by the Fluids Engineering Division for publication in the JOURNAL OF FLUIDS ENGINEERING. Manuscript received by the Fluids Engineering Division January 18, 2001; revised manuscript received August 8, 2001. Associate Editor: L. Mondy.

an attempt to assess their practical use in engineering computation. It is expected that the contribution herein provide some insight to turbulence modelers devoted to analyze engineering systems and environmental flows which can be modeled as a porous structure having a fluid flowing in turbulent regime.

Macroscopic Fluctuating Velocity

The derivation to follow has been presented in de Lemos and Pedras [39]. To the best of the authors' knowledge, an equation for the volume-average velocity fluctuation was there derived, for the first time, in light of the double-decomposition concept of Pedras and de Lemos [40]. For clarity, some basic relationships from the double-decomposition idea are here included.

Double Decomposition. For a general fluid property, φ, the intrinsic and volumetric averages are related through the porosity ϕ as (Bear [6]),

$$\langle\varphi\rangle^i=\frac{1}{\Delta V_f}\int_{\Delta V_f}\varphi dV;\langle\varphi\rangle^v=\phi\langle\varphi\rangle^i;\phi=\frac{\Delta V_f}{\Delta V} \tag{1}$$

where ΔV_f is the volume of the fluid contained in ΔV. The property φ can then be defined as the sum of $\langle\varphi\rangle^i$ and its spatial variation within the REV, ${}^i\varphi$, as (Whittaker [5]),

$$\varphi=\langle\varphi\rangle^i+{}^i\varphi \tag{2}$$

Time fluctuations have to be considered when turbulence effects are of concern. The microscopic time-averaged equations are obtained from the instantaneous microscopic equations. For that, the time-average value of property, φ, associated with the fluid is given as:

$$\overline{\varphi}=\frac{1}{\Delta t}\int_t^{t+\Delta t}\varphi dt \tag{3}$$

where Δt is the integration time interval. The instantaneous property, φ, can be defined as the sum of the time average, $\overline{\varphi}$, plus the fluctuating component, φ':

$$\varphi=\overline{\varphi}+\varphi' \tag{4}$$

From the work of Pedras and de Lemos [27], and Rocamora and de Lemos [32], one can write for any flow property φ, combining decompositions (2) and (4),

$$\overline{\langle\varphi\rangle'}=\langle\overline{\varphi}\rangle^i \tag{5}$$

$$\langle\varphi\rangle^{i\prime}=\langle\varphi'\rangle^i \tag{6}$$

$${}^i\overline{\varphi}=\overline{{}^i\varphi} \tag{7}$$

Leading a full variable decomposition as (Pedras and de Lemos [40,41]):

$$\begin{aligned}\varphi&=\langle\overline{\varphi}\rangle^i+\langle\varphi'\rangle^i+{}^i\overline{\varphi}+{}^i\varphi'\\&=\overline{\langle\varphi\rangle^i}+\langle\varphi\rangle^{i\prime}+\overline{{}^i\varphi}+{}^i\varphi'\end{aligned} \tag{8}$$

Equation (8) comprises the *double decomposition* concept used in the development to follow. One should point out that (8) refers to any medium property over which the volume and time averaging operators are simultaneously applied. It is not restricted to fluid flow problems (e.g., compressible or incompressible, viscous or inviscid). Characterization of macroscopic fluctuation temperatures could well use the idea embodied in (8). The only limitation is the independence of *time* and *space* integration domains and, therefore, swelling, shrinking, or vibrating media are not considered within this frame work (see Pedras and de Lemos [25,27] for a discussion on the limitations of Eq. (8)). With these ideas in mind, an equation for macroscopic velocity fluctuations is shown next.

Macroscopic Velocity Fluctuation. The starting point for an equation for the flow turbulent kinetic energy is an equation for the microscopic velocity fluctuation $\mathbf{u}'$. Such a relationship can be written after subtracting the equation for the mean velocity $\overline{\mathbf{u}}$ from the instantaneous momentum equation, resulting in (Hinze [42], Warsi [43]):

$$\rho\left\{\frac{\partial\mathbf{u}'}{\partial t}+\nabla\cdot[\overline{\mathbf{u}}\mathbf{u}'+\mathbf{u}'\overline{\mathbf{u}}+\mathbf{u}'\mathbf{u}'-\overline{\mathbf{u}'\mathbf{u}'}]\right\}=-\nabla p'+\mu\nabla^2\mathbf{u}'. \tag{9}$$

Now, the volumetric average of (9) will give,

$$\begin{aligned}&\rho\frac{\partial}{\partial t}(\phi\langle\mathbf{u}'\rangle^i)+\rho\nabla+\{\phi[\langle\overline{\mathbf{u}}\mathbf{u}'\rangle^i+\langle\mathbf{u}'\overline{\mathbf{u}}\rangle^i+\langle\mathbf{u}'\mathbf{u}'\rangle^i-\langle\overline{\mathbf{u}'\mathbf{u}'}\rangle^i]\}\\&\quad=-\nabla(\phi\langle p'\rangle^i)+\mu\nabla^2(\phi\langle\mathbf{u}'\rangle^i)+\mathbf{R}'\end{aligned} \tag{10}$$

where,

$$\mathbf{R}'=\frac{\mu}{\Delta V}\int_{A_i}\mathbf{n}\cdot(\nabla\mathbf{u}')dS-\frac{1}{\Delta V}\int_{A_i}\mathbf{n}p'dS \tag{11}$$

is the fluctuating part of the total drag due to the porous structure.

Expanding further the divergent operator in (10) in light of (8), one ends up with an equation for $\langle\mathbf{u}'\rangle^i$ as,

$$\begin{aligned}&\rho\frac{\partial}{\partial t}(\phi\langle\mathbf{u}'\rangle^i)+\rho\nabla\cdot\{\phi[\langle\overline{\mathbf{u}}\rangle^i\langle\mathbf{u}'\rangle^i+\langle\mathbf{u}'\rangle^i\langle\overline{\mathbf{u}}\rangle^i+\langle\mathbf{u}'\rangle^i\langle\mathbf{u}'\rangle^i\\&\quad+\langle{}^i\overline{\mathbf{u}}{}^i\mathbf{u}'\rangle^i+\langle{}^i\mathbf{u}'{}^i\overline{\mathbf{u}}\rangle^i+\langle{}^i\mathbf{u}'{}^i\mathbf{u}'\rangle^i-\overline{\langle\mathbf{u}'\rangle^i\langle\mathbf{u}'\rangle^i}-\overline{\langle{}^i\mathbf{u}'{}^i\mathbf{u}'\rangle^i}]\}\\&\quad=-\nabla(\phi\langle p'\rangle^i)+\mu\nabla^2(\phi\langle\mathbf{u}'\rangle^i)+\mathbf{R}'\end{aligned} \tag{12}$$

Macroscopic Turbulent Kinetic Energy

The objective of this section is to derive both transport equations for k_m and $\langle k\rangle^i$ in order to compare similar terms.

Equation for $k_m=\overline{\langle\mathbf{u}'\rangle^i\cdot\langle\mathbf{u}'\rangle^i}/2$. From the instantaneous microscopic continuity equation for a constant property fluid one has,

$$\nabla\cdot(\phi\langle\mathbf{u}\rangle^i)=0\Rightarrow\nabla\cdot[\phi(\langle\overline{\mathbf{u}}\rangle^i+\langle\overline{\mathbf{u}}'\rangle^i)]=0 \tag{13}$$

with time average,

$$\nabla\cdot(\phi\langle\overline{\mathbf{u}}\rangle^i)=0 \tag{14}$$

From (13) and (14) one verifies that,

$$\nabla\cdot(\phi\langle\mathbf{u}'\rangle^i)=0 \tag{15}$$

Taking the scalar product of (10) by $\langle\mathbf{u}'\rangle^i$, making use of (13)-(14)-(15) and time averaging it, an equation for k_m will have for each of its terms (note that ϕ is here considered as independent of time):

$$\overline{\rho\langle\mathbf{u}'\rangle^i\cdot\frac{\partial}{\partial t}(\phi\langle\mathbf{u}'\rangle^i)}=\rho\frac{\partial(\phi k_m)}{\partial t} \tag{16}$$

$$\begin{aligned}\overline{\rho\langle\mathbf{u}'\rangle^i\cdot\{\nabla\cdot(\phi\langle\overline{\mathbf{u}}\mathbf{u}'\rangle^i)\}}&=\overline{\rho\langle\mathbf{u}'\rangle^i\cdot\{\nabla\cdot[\phi\langle\overline{\mathbf{u}}\rangle^i\langle\mathbf{u}'\rangle^i+\phi\langle{}^i\overline{\mathbf{u}}{}^i\mathbf{u}'\rangle^i]\}}\\&=\rho\nabla\cdot[\phi\langle\overline{\mathbf{u}}\rangle^ik_m]\\&\quad+\rho\overline{\langle\mathbf{u}'\rangle^i\cdot\{\nabla\cdot[\phi\langle{}^i\overline{\mathbf{u}}{}^i\mathbf{u}'\rangle^i]\}}\end{aligned} \tag{17}$$

$$\begin{aligned}\overline{\rho\langle\mathbf{u}'\rangle^i\cdot\{\nabla\cdot(\phi\langle\mathbf{u}'\overline{\mathbf{u}}\rangle^i)\}}&=\overline{\rho\langle\mathbf{u}'\rangle^i\{\nabla\cdot[\phi\langle\mathbf{u}'\rangle^i\langle\overline{\mathbf{u}}\rangle^i+\phi\langle{}^i\mathbf{u}'{}^i\overline{\mathbf{u}}\rangle^i]\}}\\&=\rho\phi\overline{\langle\mathbf{u}'\rangle^i\langle\mathbf{u}'\rangle^i}:\nabla\langle\overline{\mathbf{u}}\rangle^i\\&\quad+\rho\overline{\langle\mathbf{u}'\rangle^i\cdot\{\nabla\cdot[\phi\langle{}^i\mathbf{u}'{}^i\overline{\mathbf{u}}\rangle^i]\}}\end{aligned} \tag{18}$$

$$\rho\overline{\langle\mathbf{u}'\rangle^i\cdot\{\nabla\cdot(\phi\langle\mathbf{u}'\mathbf{u}'\rangle^i)\}}$$
$$=\rho\overline{\langle\mathbf{u}'\rangle^i\cdot\{\nabla\cdot[\phi\langle\mathbf{u}'\rangle^i\langle\mathbf{u}'\rangle^i+\phi\langle^i\mathbf{u}'^i\mathbf{u}'\rangle^i]\}}$$
$$=\rho\nabla\cdot\left[\phi\langle\mathbf{u}'\rangle^i\frac{\langle\mathbf{u}'\rangle^i\cdot\langle\mathbf{u}'\rangle^i}{2}\right]+\rho\overline{\langle\mathbf{u}'\rangle^i\cdot\{\nabla\cdot[\phi\langle^i\mathbf{u}'^i\mathbf{u}'\rangle^i]\}} \quad (19)$$

$$\rho\overline{\langle\mathbf{u}'\rangle^i\cdot\{\nabla\cdot(-\phi\overline{\langle\mathbf{u}'\mathbf{u}'\rangle^i})\}}=0 \quad (20)$$

$$-\overline{\langle\mathbf{u}'\rangle^i\cdot\nabla(\phi\langle p'\rangle^i)}=-\nabla\cdot\overline{[\phi\langle\mathbf{u}'\rangle^i\langle p'\rangle^i]} \quad (21)$$

$$\mu\overline{\langle\mathbf{u}'\rangle^i\cdot\nabla^2(\phi\langle\mathbf{u}'\rangle^i)}=\mu\nabla^2(\phi k_m)-\rho\phi\epsilon_m \quad (22)$$

$$\overline{\langle\mathbf{u}'\rangle^i\cdot\mathbf{R}'}\equiv 0 \quad (23)$$

where $\epsilon_m=\nu\overline{\nabla\langle\mathbf{u}'\rangle^i:(\nabla\langle\mathbf{u}'\rangle^i)^T}$. In handling (21) the porosity ϕ was assumed to be constant only for simplifying the manipulation to be shown next. This procedure, however, does not represent a limitation in deriving a general form transport equation for k_m since term (21) will require further modeling.

Another important point is the treatment given to the scalar product shown in (23). Here, a different view from the work in the Lee and Howell [8], Wang and Takle [9], Antohe and Lage [10], and Getachewa et al. [11], is considered. The fluctuating drag form $\mathbf{R}'$ acts through the solid-fluid interfacial area and, as such, on fluid particles at rest. The fluctuating mechanical energy represented by the operation in (23) is not associated with any fluid particle movement and, as a result, is here considered to be of null value. This point shall be further discussed later in this paper.

A final equation for k_m gives,

$$\rho\frac{\partial(\phi k_m)}{\partial t}+\rho\nabla\cdot[\phi\langle\overline{\mathbf{u}}\rangle^i k_m]$$
$$=-\rho\nabla\cdot\left\{\overline{\phi\langle\mathbf{u}'\rangle^i\left[\frac{\langle p'\rangle^i}{\rho}+\frac{\langle\mathbf{u}'\rangle^i\cdot\langle\mathbf{u}'\rangle^i}{2}\right]}\right\}$$
$$+\mu\nabla^2(\phi k_m)-\rho\phi\overline{\langle\mathbf{u}'\rangle^i\langle\mathbf{u}'\rangle^i}:\nabla\langle\overline{\mathbf{u}}\rangle^i-\rho\phi\epsilon_m-D_m \quad (24)$$

where

$$D_m=\rho\overline{\langle\mathbf{u}'\rangle^i\cdot\{\nabla\cdot[\phi(\langle^i\overline{\mathbf{u}}^i\mathbf{u}'\rangle^i+\langle^i\mathbf{u}'^i\overline{\mathbf{u}}\rangle^i+\langle^i\mathbf{u}'^i\mathbf{u}'\rangle^i)]\}} \quad (25)$$

represents the dispersion of k_m given by the last term on the right of (17), (18), and (19), respectively. Interesting to point out is that this term can be both of negative or positive sign.

The first term on the right of (24) represents the turbulent diffusion of k_m and is normally modeled via a diffusion-like expression resulting for the transport equation (Antohe and Lage [10], Getachewa et al. [11]),

$$\rho\frac{\partial(\phi k_m)}{\partial t}+\rho\nabla\cdot[\phi\langle\overline{\mathbf{u}}\rangle^i k_m]$$
$$=\nabla\cdot\left[\mu+\frac{\mu_{t_m}}{\sigma_{k_m}}\nabla(\phi k_m)\right]+P_m-\rho\phi\epsilon_m-D_m \quad (26)$$

where

$$P_m=-\rho\phi\overline{\langle\mathbf{u}'\rangle^i\langle\mathbf{u}'\rangle^i}:\nabla\langle\overline{\mathbf{u}}\rangle^i \quad (27)$$

is the production rate of k_m due to the gradients of the macroscopic time-mean velocity $\langle\overline{\mathbf{u}}\rangle^i$.

Lee and Howell [8], Wang and Takle [9], Antohe and Lage [10], and Getachewa et al. [11], made use of the above equation for k_m considering for $\mathbf{R}'$ (11) the Darcy-Forchheimer extended model with macroscopic time-fluctuation velocities $\langle\mathbf{u}'\rangle^i$. They have also neglected all dispersion terms that were here grouped into D_m (25). Note also that the order of application of both volume- and time-average operators in this case cannot be changed. The quantity k_m is defined by applying first the volume operator to the fluctuating velocity field.

Equation for $\langle k\rangle^i=\langle\overline{\mathbf{u}'\cdot\mathbf{u}'}\rangle^i/2$. The other procedure for composing the flow turbulent kinetic energy is to take the scalar product of (9) by the microscopic fluctuating velocity $\mathbf{u}'$. Then applying both time and volume-operators for obtaining an equation for $\langle k\rangle^i=\langle\overline{\mathbf{u}'\cdot\mathbf{u}'}\rangle^i/2$. It is worth noting that in this case the order of application of both operations is immaterial since no additional mathematical operation (the scalar product) is conducted in between the averaging processes. Therefore, this is the same as applying the volume operator to an equation for the microscopic k.

The volumetric average of a transport equation for k has been carried out in detail by de Lemos and Pedras [30], and Pedras and de Lemos [40], and for that only the final resulting equation is here presented. It reads,

$$\rho\left[\frac{\partial}{\partial t}(\phi\langle k\rangle^i)+\nabla\cdot(\overline{\mathbf{u}}_D\langle k\rangle^i)\right]$$
$$=\nabla\cdot\left[\left(\mu+\frac{\mu_{t_\phi}}{\sigma_k}\right)\nabla(\phi\langle k\rangle^i)\right]+P_i+G_i-\rho\phi\langle\epsilon\rangle^i \quad (28)$$

where

$$P_i=-\rho\overline{\langle\mathbf{u}'\mathbf{u}'\rangle^i}:\nabla\overline{\mathbf{u}}_D \quad (29)$$

$$G_i=c_k\rho\phi\frac{\langle k\rangle^i|\overline{\mathbf{u}}_D|}{\sqrt{K}} \quad (30)$$

are the production rate of $\langle k\rangle^i$ due to mean gradients of the seepage velocity and the generation rate of intrinsic k due to the presence of the porous matrix. As mentioned, Eq. (28) has been proposed by Pedras and de Lemos [40], where more details on its derivation can be found. The constant c_k was numerically determined in Pedras and de Lemos [41,44] for different media and for a wide range of porosity and Reynolds numbers. In spite of having distinct cases, a unique value of 0.28 was found to be suitable for most calculations.

Comparison of Macroscopic Transport Equations. A comparison between terms in the transport equation for k_m and $\langle k\rangle^i$ can now be conducted. Pedras and de Lemos [27] have already shown the connection between these two quantities as being,

$$\langle k\rangle^i=\langle\overline{\mathbf{u}'\cdot\mathbf{u}'}\rangle^i/2=\overline{\langle\mathbf{u}'\rangle^i\cdot\langle\mathbf{u}'\rangle^i}/2+\langle\overline{^i\mathbf{u}'\cdot{}^i\mathbf{u}'}\rangle^i/2=k_m+\langle\overline{^i\mathbf{u}'\cdot{}^i\mathbf{u}'}\rangle^i/2 \quad (31)$$

Expanding the correlation forming the production term P_i by means of (2), a connection between the two generation rates can also be written as,

$$P_i=-\rho\overline{\langle\mathbf{u}'\mathbf{u}'\rangle^i}:\nabla\overline{\mathbf{u}}_D=-\rho(\overline{\langle\mathbf{u}'\rangle^i\langle\mathbf{u}'\rangle^i}:\nabla\overline{\mathbf{u}}_D+\overline{\langle^i\mathbf{u}'^i\mathbf{u}'\rangle^i}:\nabla\overline{\mathbf{u}}_D)$$
$$=P_m-\rho\overline{\langle^i\mathbf{u}'^i\mathbf{u}'\rangle^i}:\nabla\overline{\mathbf{u}}_D \quad (32)$$

One can note that all production rates of k_m due to the mean flow constitutes only part of the general production rate responsible for maintaining the overall level of $\langle k\rangle^i$.

The dissipation rates also carry a correspondence if one expands

$$\langle\epsilon\rangle^i=\nu\overline{\langle\nabla\mathbf{u}':(\nabla\mathbf{u}')^T\rangle^i}$$
$$=\nu\overline{\langle\nabla\mathbf{u}'\rangle^i:[\langle\nabla\mathbf{u}'\rangle^i]^T}+\nu\overline{\langle^i(\nabla\mathbf{u}'):{}^i(\nabla\mathbf{u}')^T\rangle^i}$$
$$=\frac{\nu}{\phi^2}\overline{\nabla(\phi\langle\mathbf{u}'\rangle^i):[\nabla(\phi\langle\mathbf{u}'\rangle^i)]^T}+\nu\overline{\langle^i(\nabla\mathbf{u}'):{}^i(\nabla\mathbf{u}')^T\rangle^i} \quad (33)$$

Considering further constant porosity,

Table 1 Classification of turbulence models for porous media.

Model Class	Authors	General characteristics and treatment of surface integrals	Sequence of integration	Applications
A-L	Lee & Howell, 1987, Wang & Takle, 1995, Antohe & Lage, 1997, Getachewa *et al.*, 2000.	Surface integrals are not applied since models are based on macroscopic quantities subjected to time-averaging only.	Space-time	Only theory presented. Numerical results using this model are found in Chan et al., 2000.
N-K	Masuoka & Takatsu, 1996, Kuwahara *et al,* 1998, Kuwahara & Nakayama, 1998, Takatsu & Masuoka, 1998, Nakayama & Kuwahara, 1999.	Masuoka & Takatsu, 1996, assumed a non-null value in their eqn. (11) for the turbulent shear stress $\mathbf{S}_t = -\rho\overline{\mathbf{u}'\mathbf{u}'}$ along the interfacial area A_i. Takatsu & Masuoka, 1998, assume for their volume integral in eqn. (14) a different form zero value for $\mathbf{d} = (\mu/\rho + \mu_t/\sigma_k\rho)\nabla k$ at the interface A_i.	Time-space	Microscopic computations on periodic cell of square rods. Macroscopic model computations presented.
T-C	Gratton *et al.,* 1994, Travkin & Catton, 1992, 1993, 1995, 1998,Travkin *et al.,* 1993, Travkin *et al.,* 1999	Morphology-based theory. Surface integrals and volume-average operators depend on media morphology.	Time-space	Only theory, no closure for the macroscopic equation is presently available.
P-dL	Pedras & de Lemos, 2000a, 2001a, 2000b, Rocamora & de Lemos, 2000a.	Double-decomposition theory. Surface integrals involving null quantities at surfaces are neglected. The connection between ***space-time*** and ***time-space*** theories is unveiled.	Time-space	Microscopic computation on periodic cell of circular (Pedras & de Lemos, 2001b) and elliptic Pedras & de Lemos, 2001c, 200d) rods. Macroscopic computations for porous media presented. Results for hybrid domains are found in de Lemos & Pedras, 2000b and Rocamora & de Lemos, 2000b, 2000c, 2000d.

$$\langle \epsilon \rangle^i = \epsilon_m + \nu\overline{\langle^i(\nabla \mathbf{u}'):^i(\nabla \mathbf{u}')^T\rangle^i} \tag{34}$$

Equation (34) indicates that an additional dissipation rate is necessary to fully account for the energy decay process inside the R.E.V. It is worth noting that (31), (32), and (34) seems to suggest that models considering $\langle k \rangle^i$ are by far more complete than theories based on k_m.

General Classification of Turbulence Models for Porous Media

Based on the derivations above, one can establish a general classification of the models presented so far in the literature (de Lemos [38]). Table 1 classifies all proposals into four major categories. These classes are based on the sequence of application of averaging operators, on the handling of surface integrals and on the application reported so far.

The A-L models make use of transport equations for $k_m = \overline{\langle \mathbf{u}' \rangle^i \cdot \langle \mathbf{u}' \rangle^i}/2$ instead of $\langle k \rangle^i = \overline{\langle \mathbf{u}' \cdot \mathbf{u}' \rangle^i}/2$. Consequently, this methodology applies only time-averaging procedure to already established macroscopic equations (see for example Hsu and Cheng [45], for macroscopic equations). In this sense, the sequence *space-time* integration is employed and surface integrals are not manipulated since macroscopic quantities are the sole independent variables used. Application of this theory is found in Chan et al. [46].

N-K models constitute the second class of models here compiled. It is interesting to mention that Masuoka and Takatsu [12], assumed a non-null value for the turbulent shear stress, $\mathbf{S}_t = -\rho\overline{\mathbf{u}'\mathbf{u}'}$, along the interfacial area A_i in their Eq. (11). With that, their surface integral $\int_{A_i} \mathbf{S}_t \cdot \mathbf{n} dA$ was associated with the Darcy flow resistance term. Yet, using the Boussinesq approximation as in their Eq. (7), $\mathbf{S}_t = 2\mu_t \mathbf{D} - (2/3)k\mathbf{I}$, one can also see that both μ_t and k will vanish at the surface A_i, ultimately indicating that the surface integral in question is actually equal to zero. Similarly, Takatsu and Masuoka [15], assumed for their surface integral in Eq. (14), $\int_{A_i} \mathbf{d} \cdot \mathbf{n} dA$, a non-null value where $\mathbf{d} = (\mu/\rho + \mu_t/\sigma_k\rho)\nabla k$. Here also it is worth noting that $\nabla k = \overline{\mathbf{u}' \cdot (\nabla \mathbf{u}')^T}$ and that, at the interface A_i, $\nabla k = 0$ due to the non-slip condition. Consequently, also in this case the surface integral of $\mathbf{d}$ over A_i is of zero value. In regard to the average operators used, N-K models follow the *time-space* integration sequence. Calibration of the model required microscopic computations on a period cell of square rods. Macroscopic results in a channel filled with a porous material was also a test case run by Nakayama and Kuwahara [16].

The work developed in a series of papers using a morphology-oriented theory is here group in the T-C model category shown in Table 1. In this morphology-based theory, surface integrals resulting after application of volume-average operators depend on the media morphology. Governing equations set up for turbulent flow, although complicated at first sight, just follow usual volume integration technique applied to standard k-ϵ and k-L turbulence models. In this sense, time-space integration sequence is followed. No closure is proposed for the unknown surface integrals (and morphology parameters) so that practical applications of such development in solving *real-world* engineering flows is still a challenge to be overcome. Nevertheless, the developed theory seems to be mathematically correct even though additional *ad-hoc* information is still necessary to fully model the remaining unknowns and medium-dependent parameters.

Lastly, the model group named P-dL uses the recently developed *double-decomposition* theory just reviewed above. In this development, all surface integrals involving null quantities at interface A_i are neglected. The connection between space-time and time-space theories is made possible due to the splitting of the dependent variables into four (rather than two) components, as expressed by Eq. (8). For the momentum and energy equations, the double-decomposition approach has proven that either time-space or space-time order of application of averaging operators is immaterial. For the turbulence kinetic energy equation, however, the order of application of such mathematical operators will define different quantities being transported (Pedras and de Lemos [27], Rocamora and de Lemos [32]). Microscopic computation on a periodic cell of circular (Pedras and de Lemos [41]) and elliptic (Pedras and de Lemos [47]) rods were used in order to calibrate the proposed model. Pedras and de Lemos [40] further presented macroscopic computations for flow in a channel filled with a porous material. Further results for hybrid domains (*porous medium-clear fluid*) are found in de Lemos and Pedras [33] and Rocamora and de Lemos [34–36]).

Discussion and Conclusions

This paper presented the two views in the literature for characterizing the turbulence kinetic energy for flow in porous media. The two transport equations where derived in light of the double

decomposition concept and a comparison between the production and dissipation terms are presented. A general classification of all models published so far was established. The discussion below further compares the two views in the literature.

In the path followed by Lee and Howell [8], Wang and Takle [9] and Antohe and Lage [10], the drag term **R** was represented by a Darcy-Forchheimer extended model in its usual form,

$$\mathbf{R}=-\left[\frac{\mu\phi}{K}\mathbf{u}_D+\frac{c_F\phi\rho|\mathbf{u}_D|\mathbf{u}_D}{\sqrt{K}}\right] \tag{35}$$

where c_F is a constant. Time decomposition was then applied to the Darcy velocity in (35) and the 4th, 5th, 6th, and 8th terms in the divergent of (12) were neglected. A few comments on this methodology for setting up a transport equation for the flow kinetic energy seems timely.

The Darcy-Forchheimer extended model is based on average values obtained after comparing bulk flow rates to bulk pressure drops across beds of saturated media. It compares, accordingly, time-averaged quantities although a fluctuating component for the macroscopic velocity is defined and has been used throughout the development shown above. Applying then a time-decomposition operation to (35) in order to represent extra turbulent kinetic energy for the flow in a porous matrix seems to neglect the fact that such terms were proposed based on ''time-independent'' quantities. Accordingly, Eq. (35) seems to be a model for the *time-mean* drag rather than for the *instantaneous* force (11).

Also, one interesting point in the development of an equation for k_m is the treatment given to the scalar product (23). This term represents the statistical value of the fluctuating mechanical energy associated with the fluctuating drag $\mathbf{R}'$ given by (11). The fluctuating drag $\mathbf{R}'$, although different from zero, acts through the solid-fluid interface A_i and, as such, on fluid particles ''at rest.'' As a consequence, this force should not contribute to producing mechanical energy within the flow.

Accordingly, the work done by a force acting on a particle moving along a certain distance is the scalar product of this force, **F**, by the distance, $d\mathbf{r}$, such as

$$dW=\mathbf{F}\cdot d\mathbf{r} \tag{36}$$

The work rate or power is then defined as,

$$\dot{W}=\frac{dW}{dt}=\mathbf{F}\cdot\frac{d\mathbf{r}}{dt}=\mathbf{F}\cdot\mathbf{u} \tag{37}$$

or say, in Eq. (37) **u** is the velocity of the particle on which the force **F** is being applied.

Following Bird et al. [48], the microscopic (local and instantaneous) mechanical energy equation is obtained starting with the momentum Cauchy equation,

$$\rho\frac{D\mathbf{u}}{Dt}=\nabla\cdot\mathbf{T}+\rho\mathbf{g} \tag{38}$$

where **T** is the stress tensor. All terms in (38) represent forces per unit volume acting on a fluid element having velocity **u**. Following the concept embodied in (37), the mechanical energy produced by each one of these forces is given by the scalar product of (38) and the local velocity **u**,

$$\rho\frac{D}{Dt}\left(\frac{1}{2}u^2\right)=\mathbf{u}\cdot\nabla\cdot\mathbf{T}+\mathbf{u}\cdot\rho\mathbf{g} \tag{39}$$

It is clear to see that all terms in (39) vanish due to the non-slip condition at a solid stagnant wall. Text books in Fluid Mechanics (e.g., Bird et al. [48], Fox and McDonald [49]) comment that in the neighborhood of a fluid particle, stagnant solid walls cannot promote mechanical energy. Or say, solid walls can only generate mechanical energy within the flow if the wall itself is moving (e.g., a rotating turbine blade). By means of (37), this mechanical energy would be given by the scalar product of the force exerted by the wall on the fluid and the fluid particle velocity (or the velocity of the fluid particle in contact to the moving wall).

It is also clear that boundary forces modify the fluid pressure field, which, in turn, modifies fluid velocity and then the mechanical energy within the flow. However, the momentum equation in its differential form considers only the forces acting in the vicinity of a moving particle. At walls, there is no fluid movement except in the case of moving surfaces. Following this line of thought, no term derived from (35) could then contribute to either increase or decrease the overall value of the flow turbulent kinetic energy. An exception would be a moving (vibrating) porous structure and, in this case, energy would be added to the fluid. It is recognized, however, that additional terms in the *k*-equation due to the solid structure are necessary (Nakayama and Kuwahara [16]). Different proposals are made in the literature and recent work in this area is expected to improve current model assumptions (Pedras and de Lemos [27]).

Also, for a homogeneous, fully-developed unidimensional flow through a porous bed, all terms appearing in the k_m-equation and originated from the time decomposition of Darcy-Forchheimer extended model will be negative (note that all drag forces in (35) are ''negative'' and will lead to ''sink'' terms in the k_m-equation). As a consequence, the only possible solution for this case will be $k_m=0$. This, in fact, was the conclusion reached by Antohe and Lage [10]. However, Nakayama and Kuwahara [16], points out that for this same situation a certain level of turbulent kinetic energy must stay as long as the presence of porous matrix keeps generating it. This disagreement could be explained based on the fact that each work talks about a different quantity (k_m and $\langle k\rangle^i$). For flow in such infinite medium, the only generating mechanism is given by term G_i in (28) causing a non-null value for $\langle k\rangle^i$. This would be equivalent to considering the decay of turbulence behind a grid and analyzing the porous structure as a sequence of closely packed grids. Thus, mechanical energy continuously extracted from the mean flow, by gradients of *microscopic* velocity, feeds the macroscopic turbulence field. This mechanism is modeled by the generating term G_i. On the other hand, the production *P*-terms in (32), for both *k* forms, will be zero due to null gradients of the *macroscopic* mean velocity.

Applying this same reasoning to the macroscopic momentum equation including body forces (Hsu and Cheng [45]),

$$\rho\left[\frac{\partial}{\partial t}(\phi\langle\mathbf{u}\rangle^i)+\nabla\cdot(\phi\langle\mathbf{uu}\rangle^i)\right]=-\nabla(\phi\langle p\rangle^i)+\mu\nabla^2(\phi\langle\mathbf{u}\rangle^i)+\phi\rho\mathbf{g}+\mathbf{R} \tag{40}$$

where

$$\mathbf{R}=\frac{\mu}{\Delta V}\int_{A_i}\mathbf{n}\cdot(\nabla\mathbf{u})dS-\frac{1}{\Delta V}\int_{A_i}\mathbf{n}p\,dS \tag{41}$$

one verifies that the five first terms represent forces acting on fluid particles whose macroscopic mean velocity is given by $\langle\mathbf{u}\rangle^\nu$ or $\phi\langle\mathbf{u}\rangle^i$. The last term, **R**, acts on particles that are located on the interfacial area A_i, (**R** is a surface force divided by volume). If the interfacial area A_i, moves (vibrates) then the mechanical energy produced will be the scalar product of **R** and the velocity of A_i, otherwise **R** will not produce mechanical energy.

In several papers, (Vafai and Tien [7], Hsu and Cheng [45], Antohe and Lage [10], among others) **R** is modeled as a function of the Darcy velocity, $\langle\mathbf{u}\rangle^\nu$. However, that does not mean that **R** acts on particles having an average velocity $\langle\mathbf{u}\rangle^\nu$. Consider, for example, *creeping flow* around a sphere where both viscous drag, F_μ, and form drag, F_p, are obtained by integrating viscous and pressure forces, respectively, over the sphere surface. The total drag is given by,

$$F_p+F_\mu=6\pi\mu R u_\infty \tag{42}$$

where R is the radius of the sphere and u_∞ is the free stream

velocity. In spite of having the total drag described as a function of u_∞, this force acts on stagnant particles and, as such, can not produce mechanical energy within the flow. Likewise, forces $\mathbf{R}'$ (11) and $\mathbf{R}$ (41) that appear in the governing equations for porous media cannot produce mechanical energy unless the porous structure itself is allowed to move or vibrate. In this case, mechanical energy is added to the fluid via the action of the porous structure.

Acknowledgment

MJSdL is thankful to CNPq, Brazil, for their financial support during the course of this research.

References

[1] Darcy, H., 1856, *Les Fontaines Publiques de la Vile de Dijon*, Victor Dalmond, Paris.
[2] Forchheimer, P., 1901, ''Wasserbewegung durch Boden,'' Z. Ver. Deutsch. Ing. **45**, pp. 1782–1788.
[3] Brinkman, H. C., 1947, ''A calculation of the viscous force exerted by a flowing fluid on a dense swarm of particles,'' Appl. Sci. Res., **1**, pp. 27–34.
[4] Ward, J. C., 1964, ''Turbulent flow in porous media,'' J. Hydraul. Div., Am. Soc. Civ. Eng., **90** (HY5), pp. 1–12.
[5] Whitaker, S., 1969, ''Advances in theory of fluid motion in porous media,'' Ind. Eng. Chem., **61**, pp. 14–28.
[6] Bear, J., 1972, *Dynamics of Fluids in Porous Media*, American Elsevier, New York.
[7] Vafai, K., and Tien, C. L., 1981, ''Boundary and inertia effects on flow and heat transfer in porous media,'' Int. J. Heat Mass Transf., **24**, pp. 195–203.
[8] Lee, K., Howell, and J. R., 1987, ''Forced convective and radiative transfer within a highly porous layer exposed to a turbulent external flow field,'' *Proc. of the 1987 ASME-JSME Thermal Eng. Joint Conf.*, Vol. 2, pp. 377–386.
[9] Wang, H., and Takle, E. S., 1995, ''Boundary-layer flow and turbulence near porous obstacles,'' Boundary-Layer Meteorol., **74**, pp. 73–88.
[10] Antohe, B. V., and Lage, J. L., 1997, ''A general two-equation macroscopic turbulence model for incompressible flow in porous media,'' Int. J. Heat Mass Transf., **40**, pp. 3013–3024.
[11] Getachew, D., Minkowycz, W. J., and Lage, J. L., 2000, ''A modified form of the k-ϵ model for turbulent flow of an incompressible fluid in porous media,'' Int. J. Heat Mass Transf., **43**, pp. 2909–2915.
[12] Masuoka, T., and Takatsu, Y., 1996, ''Turbulence model for flow through porous media,'' Int. J. Heat Mass Transf., **39**, pp. 2803–2809.
[13] Kuwahara, F., Kameyama, Y., Yamashita, S., and Nakayama, A., 1998, ''Numerical modeling of turbulent flow in porous media using a spatially periodic array,'' J. Porous Media, **1**, pp. 47–55.
[14] Kuwahara, F., and Nakayama, A., 1998, ''Numerical modeling of non-Darcy convective flow in a porous medium,'' *Proc. 11th Int. Heat Transf. Conf.*, Kyongyu, Korea, August 23–28.
[15] Takatsu, Y., and Masuoka, T., 1998, ''Turbulent phenomena in flow through porous media,'' J. Porous Media, **3**, pp. 243–251.
[16] Nakayama, A., and Kuwahara, F., 1999, ''A macroscopic turbulence model for flow in a porous medium,'' ASME J. Fluids Eng., **121**, pp. 427–433.
[17] Travkin, V. S., and Catton, I., 1992, ''Models of turbulent thermal diffusivity and transfer coefficients for a regular packed bed of spheres,'' *Proc. 28th National Heat Transfer Conference*, San Diego, C-4, ASME-HTD-193, pp. 15–23.
[18] Travkin, V. S., Catton, I., and Gratton, L., 1993, ''Single-phase turbulent transport in prescribed non-isotropic and stochastic porous media,'' *Heat Transfer in Porous Media*, ASME-HTD-240, pp. 43–48.
[19] Gratton, L., Travkin, V. S., and Catton, I., 1994, ''Numerical solution of turbulent heat and mass transfer in a stratified geostatistical porous layer for high permeability media,'' ASME Proceedings HTD-Vol. 41, pp. 1–14.
[20] Travkin, V. S., and Catton, I., 1995, ''A two temperature model for turbulent flow and heat transfer in a porous layer,'' ASME J. Fluids Eng., **117**, pp. 181–188.
[21] Travkin, V. S., and Catton, I., 1998, ''Porous media transport descriptions–non-local, linear, and non-linear against effective thermal/fluid properties,'' Adv. Colloid Interface Sci., **76–77**, pp. 389–443.
[22] Travkin, V. S., Hu, K., and Catton, I., 1999, ''Turbulent kinetic energy and dissipation rate equation models for momentum transport in porous media,'' *Proc. 3rd ASME/JSME Joint Fluids Engineering Conference* (on CD-ROM), Paper FEDSM99-7275, San Francisco, California, 18–23 July.
[23] Lage, J. L., 1998, ''The fundamental theory of flow through permeable media from Darcy to turbulence,'' in *Transport Phenomena in Porous Media*, D. B. Ingham and I. Pop, eds., Elsevier Science, ISBN: 0-08-042843-6, 446 pp.
[24] Pedras, M. H. J., and de Lemos, M. J. S., 1998, ''Results for macroscopic turbulence modeling for porous media,'' *Proc. of ENCIT98-7th Braz. Cong. Eng. Th. Sci.*, Vol. 2, pp. 1272–1277, Rio de Janeiro, Brazil, Nov. 3–6 (in Portuguese).
[25] Pedras, M. H. J., and de Lemos, M. J. S., 1999, ''On volume and time averaging of transport equations for turbulent flow in porous media,'' *Proc. of 3rd ASME/JSME Joint Fluids Engineering Conference* (on CD-ROM), ASME-FED-248, Paper FEDSM99-7273, ISBN 0-7918-1961-2, San Francisco, California, July 18–23.
[26] Pedras, M. H. J., and de Lemos, M. J. S., 1999, ''Macroscopic turbulence modeling for saturated porous media,'' *Proc. of COBEM99-15th Braz. Congr. Mech. Eng.* (on CD-ROM), ISBN: 85-85769-03-3, Águas de Lindóia, São Paulo, Brazil, November 22–26 (in Portuguese).
[27] Pedras, M. H. J., and de Lemos, M. J. S., 2000, ''On the definition of turbulent kinetic energy for flow in porous media,'' Int. Commun. Heat Mass Transfer, **27**, No. 2, pp. 211–220.
[28] Pedras, M. H. J., and de Lemos, M. J. S., 2000, ''Numerical solution of turbulent flow in porous media using a spatially periodic cell and the low Reynolds k-ϵ model,'' *Proc. of CONEM2000–National Mechanical Engineering Congress* (on CD-ROM), Natal, Rio Grande do Norte, Brazil, August 7–11 (in Portuguese).
[29] Rocamora, Jr., F. D., and de Lemos, M. J. S., 1998, ''Numerical solution of turbulent flow in porous media using a spatially periodic array and the k-ϵ model,'' *Proc. ENCIT-98–7th Braz. Cong. Eng. Th. Sci.*, Vol. 2, pp. 1265–1271, Rio de Janeiro, RJ, Brazil, November 3–6.
[30] de Lemos, M. J. S., and Pedras, M. H. J., 2000, ''Modeling turbulence phenomena in incompressible flow through saturated porous media,'' *Proc. of 34th ASME-National Heat Transfer Conference* (on CD-ROM), ASME-HTD-1463CD, Paper NHTC2000-12120, ISBN:0-7918-1997-3, Pittsburgh, Pennsylvania, August 20–22.
[31] Rocamora, Jr., F. D., and de Lemos, M. J. S., 1999, ''Simulation of turbulent heat transfer in porous media using a spatially periodic cell and the k-ϵ model,'' *Proc. of COBEM99–15th Braz. Congr. Mech. Eng.* (on CD-ROM), ISBN: 85-85769-03-3, Águas de Lindóia, São Paulo, Brazil, November 22–26.
[32] Rocamora, Jr., F. D., and de Lemos, M. J. S., 2000, ''Analysis of convective heat transfer for turbulent flow in saturated porous media,'' Int. Commun. Heat Mass Transfer, **27**, No. 6, pp. 825–834.
[33] de Lemos, M. J. S., and Pedras, M. H. J., 2000, ''Simulation of turbulent flow through hybrid porous medium-clear fluid domains,'' *Proc. of IMECE2000–ASME–Intern. Mech. Eng. Congr.*, ASME-HTD-366-5, pp. 113–122, ISBN:0-7918-1908-6, Orlando, Florida.
[34] Rocamora, Jr., F. D., and de Lemos, M. J. S., 2000, ''Prediction of velocity and temperature profiles for hybrid porous medium-clear fluid domains,'' *Proc. of CONEM2000–National Mechanical Engineering Congress* (on CD-ROM), Natal, Rio Grande do Norte, Brazil, August 7–11.
[35] Rocamora, Jr., F. D., and de Lemos, M. J. S., 2000, ''Laminar recirculating flow and heat transfer in hybrid porous medium-clear fluid computational domains,'' *Proc. of 34th ASME-National Heat Transfer Conference* (on CD-ROM), ASME-HTD-I463CD, Paper NHTC2000-12317, ISBN:0-7918-1997-3, Pittsburgh, Pennsylvania, August 20–22.
[36] Rocamora, Jr., F. D., and de Lemos, M. J. S., 2000, ''Heat transfer in suddenly expanded flow in a channel with porous inserts,'' *Proc. of IMECE2000–ASME–Intern. Mech. Eng. Congr.*, ASME-HTD-366-5, pp. 191–195, ISBN:0-7918-1908-6, Orlando, Florida, November 5–10.
[37] Rocamora, F. D., and de Lemos, M. J. S., 2001, ''Turbulence Modeling for non-isothermal flow in undeformable porous media'', Proc. of NHTCOI, 35th Nat. Heat Transfer Conf. ASME-HTD-IY9SCD, Paper NHTC 2001-20178 ISBN: 0791835278, Anaheim, California, June 10–12.
[38] de Lemos, M. J. S., 2001, ''Modeling turbulent flow in saturated rigid porous media,'' *Proc. of NHTC'01, 35th National Heat Transfer Conference*, T15-04 Panel on Porous Media, Anaheim, CA, June 10–12.
[39] de Lemos, M. J. S., and Pedras, M. H. J., 2001, ''Alternative transport equations for turbulent kinetic energy for flow in porous media,'' *Proc. of NHTC'01, 35th National Heat Transfer Conference*, ASME-HTD-I495CD, Paper NHTC2001-20177, ISBN: 0-7918-3527-8, Anaheim, California, June 10–12.
[40] Pedras, M. H. J., and de Lemos, M. J. S., 2001, ''Macroscopic Turbulence Modeling for Incompressible Flow Through Undeformable Porous Media,'' Intern. J. Heat and Mass Transfer **44**, No. 6, pp. 1081–1093.
[41] Pedras, M. H. J., and de Lemos, M. J. S., 2001, ''Simulation of turbulent flow in porous media using a spatially periodic array and a low Re two-equation closure,'' Numer. Heat Transfer, Part A, **39**, No. 1, pp. 35–59.
[42] Hinze, J. O., 1959, *Turbulence*, McGraw-Hill, New York.
[43] Warsi, Z. U. A., 1998, *Fluid Dynamics–Theoretical and Computational Approaches*, 2nd ed., CRC Press, Boca Raton.
[44] Pedras, M. H. J., and de Lemos, M. J. S., 2001, ''Solução Numérica do Escoamento Turbulento num Meio Poroso Formado por Hastes Elípticas—Aplicação do modelo k-ϵ para baixo e alto Reynolds,'' Proc. of *COBEM01–16th Braz. Congr. Mech. Eng.* (on CD-ROM), Uberlândia, MG, Brazil, November 26–30.
[45] Hsu, C. T., and Cheng, P., 1990, ''Thermal dispersion in a porous medium,'' Int. J. Heat Mass Transf., **33**, pp. 1587–1597.
[46] Chan, E. C., Lien, F.-S., and Yavonovich, M. M., 2000, ''Numerical Study of Forced Flow in a Back-Step Channel Through Porous Layer,'' *Proc. of 34th ASME-National Heat Transfer Conference* (on CD-ROM), ASME-HTD-1463CD, Paper NHTC2000-12118, ISBN:0-7918-1997-3, Pittsburgh, Pennsylvania, August 20–22.
[47] Pedras, M. H. J., and de Lemos, M. J. S., 2001, ''Adjustment of a macroscopic turbulence model for a porous medium formed by an infinite array of elliptic rods,'' *2nd International Conference on Computational Heat and Mass Transfer*, Rio de Janeiro, Brazil, Oct. 22–26.
[48] Bird, R. B., Stewart, W. E., and Lightfoot, E. N., 1960, *Transport Phenomena*, Wiley, New York.
[49] Fox, R. W., and McDonald, A. T., 1998, *Introduction to Fluids Mechanics*, Wiley, New York, 5th ed., p. 156.

On the Mathematical Description and Simulation of Turbulent Flow in a Porous Medium Formed by an Array of Elliptic Rods

Marcos H. J. Pedras
Instituto de Pesquisa e Desenvolvimento IP&D,
UNIVAP,
12244-000, São José dos Campos, SP, Brazil

Marcelo J. S. de Lemos
Mem. ASME,
Departamento de Energia - IEME,
Instituto Tecnológico de Aeronáutica - ITA,
12228-900, São José dos Campos, SP, Brazil
e-mail: delemos@mec.ita.br

Many engineering and environmental system analyses can benefit from appropriate modeling of turbulent flow in porous media. Through the volumetric averaging of the microscopic transport equations for the turbulent kinetic energy, k, and its dissipation rate, ε, a macroscopic model was proposed for such media (IJHMT, 44(6), 1081-1093, 2001). In that initial work, the medium was simulated as an infinite array of cylindrical rods. As an outcome of the volume averaging process, additional terms appeared in the equations for k and ε. These terms were here adjusted assuming now the porous structure to be modeled as an array of elliptic rods instead. Such an adjustment was obtained by numerically solving the microscopic flow governing equations, using a low Reynolds formulation, in the periodic cell composing the medium. Different porosity and Reynolds numbers were investigated. The fine turbulence structure of the flow was computed and integral parameters were presented. The adjusted model constant was compared to similar results for square and cylindrical rods. It is expected that the contribution herein provide some insight to modelers devoted to the analysis of engineering and a environmental systems characterized by a porous structure saturated by a fluid flowing in turbulent regime.
[DOI: 10.1115/1.1413244]

Keywords: Turbulence Modeling, Porous Media, Volume-average, Saturated Flow

Introduction

A number of natural and engineering systems can be characterized by some sort of porous structure through which a working fluid permeates. Turbulent boundary layer over tropical forests and spreading of chemical contaminants through underground water reservoirs are examples of important environmental flows which can benefit form appropriate mathematical treatment. Also, fluidized bed combustors and chemical catalytic reactors are subjected to pressure loss variation due to changes in the flow regime inside the pores. In petroleum extraction, the flow accelerates toward the pumping well while crossing regions of variable porosity. Turbulent regime eventually occurs, affecting overall pressure drop and well performance. In all cases, better understanding of turbulence through adequate modeling can more realistically simulate real-world environmental and engineering flows.

Classical theory when the pore Reynolds number Re_p is less than about 150 is based on the concept of a Representative Elementary Volume - REV (Darcy [1], Forchheimer [2], Brinkman [3], Ward [4], Whitaker [5], Bear [6], Vafai and Tien [7], Whitaker [8]. For high Reynolds number ($Re_p > 300$), turbulence occurs within the pores (Prausnitz and Wilhelm [9], Mickley et al. [10] and, as such, a turbulence model is necessary in order to close the mathematical problem. For that purpose, models following the *space-time* integration sequence (Lee and Howell [11], Wang and Takle [12], Antohe and Lage [13], Getachew et al. [14], and *time-space* averaging of governing equations (Masuoka and Takatsu [15], Kuwahara et al. [16], Kuwahara and Nakayama [17], Takatsu and Masuoka [18], Nakayama and Kuwahara, [19]) have been proposed. Also suggested are morphology-oriented models which follow the *time-space* sequence and are based on the Volume Average Theory (Travkin and Catton [20], Travkin et al. [21], Gratton et al. [22], Travkin and Catton [23], Travkin and Catton [24], Travkin et al. [25]). All of these different approaches lead to different sets of governing equations and, consequently, to much debate in the literature.

Another route closer to the time-space methodology was first suggested by Pedras and de Lemos [26] prior to the proposition of the *double-decomposition* concept (Pedras and de Lemos [27–29]). This idea unveiled the connection between the space-time and time-space models. The development of this concept was a step before detailed numerical solution of the flow equations were carried out in order to establish a working version of the model (de Lemos and Pedras [30], Pedras and de Lemos [31]). Computations in a spatially periodic array of cylindrical rods using the high Re k-ε closure (Rocamora and de Lemos [32]) as well as the Low Reynolds model (Pedras and de Lemos [33,34]) were used to calibrate the introduced model constant. Heat transfer (Rocamora and de Lemos [35,36,37]) and hybrid computational domains (clear fluid-porous medium) have been also considered (de Lemos and Pedras [38]). Nonisothermal recirculating flows in channels past a porous obstacle (Rocamora and de Lemos [39,40]) and through a porous insert have been calculated (Rocamora and de Lemos [41]) using the work described in Pedras and de Lemos [31].

These two different procedures, namely *space-time* and *time-space* integration sequences, have raised interesting discussions in the literature about the proper characterization of the flow. More information on the turbulence structure under the microscopic point of view may contribute for elucidating some of the fundamental questions still pending on macroscopic modeling. One of the possibilities to gather such information is to model the topology of the porous structure and resolve the microscopic flow equation within the liquid phase. This treatment reveals the microscopic flow and was used by Kuwahara et al. [16], who adopted a spatially periodic array of square rods and by Pedras and de Lemos [34], who used cylindrical rods instead. A discus-

Contributed by the Fluids Engineering Division for publication in the JOURNAL OF FLUIDS ENGINEERING. Manuscript received by the Fluids Engineering Division January 18, 2001; revised manuscript received August 8, 2001. Associate Editor: L. Mondy.

sion on the relationship between the macroscopic and microscopic treatments is found in Pedras and de Lemos [42].

Considering available experimental work reporting the existence of turbulence in such media (Macdonald et al. [43], Kececiooglu and Jiang [44], de Lemos and Pedras [30], and Pedras and de Lemos [31], proposed a macroscopic turbulence model through the volumetric averaging of the microscopic k-ε equations. This macroscopic model, in contrast with the microscopic k-ε equations, presents two extra terms that represent extra transport/production of turbulence energy due to the presence of the solid material inside the integrated volume.

The aim of the present contribution is to adjust these new terms by numerically solving the flow field within a spatially periodic array of elliptic rods. Both low and high Re k-ε models are employed. Additional constants are determined and, with the macroscopic turbulence model so adjusted, the turbulence kinetic energy and its dissipation rate are compared with existing macroscopic flow solutions presented in the literature.

Microscopic Versus Macroscopic Turbulence

In a recent review, Lage [44], points out a distinction between *macroscopic* and *microscopic* turbulence within a porous medium. *Microscopic* turbulence was understood as the fluid regime existing within the pore whereas *macroscopic* turbulence would be the result of volume-averaging the instantaneous signal of probes distinctly located inside a REV. A more quantitative description of **macroscopic** turbulence has been proposed by Pedras and de Lemos [29], who suggested the existence of two macroscopically defined turbulence kinetic energy. The first one was formed by time-averaging the fluctuating volume-averaged velocity, $k_m = \overline{\langle \mathbf{u}' \rangle^i \cdot \langle \mathbf{u}' \rangle^i}/2$, and the second one by taking the volume integration, within the fluid phase in a REV, of the locally defined turbulence kinetic energy $k = \overline{\mathbf{u}' \cdot \mathbf{u}'}/2$. The result is then $\langle k \rangle^i = \overline{\langle \mathbf{u}' \cdot \mathbf{u}' \rangle^i}/2$. Also, a connection between k_m and $\langle k \rangle^i$ was first shown by Pedras and de Lemos [29], by means of the double-decomposition concept therein proposed.

The behavior of $\langle k \rangle^i$ as a function of porosity ϕ was numerically computed by Pedras and de Lemos [34]. In that work, the porous medium was simulated by an infinite array of circular cylinders. The compute values for $\langle k \rangle^i$ indicated that for the same Darcy velocity, or say, same volumetric mass flow rate through the bed, the overall integrated turbulence level increases with the reduction of the medium porosity (larger rod diameter). A faster fluid running through a narrower space displays steeper velocity gradients throughout the domain. Those gradients, in turn, dictate the rate at which mean flow mechanical energy is transformed into turbulence energy. Consequently, production rates of k were higher implying in higher values of $\langle k \rangle^i$ for lower porosity.

Macroscopic Equations and Numerics

Macroscopic equations for the flow turbulent kinetic energy, following both *space-time* and *time-space* integration of local instantaneous equations, have been compared in de Lemos and Pedras [46,47]. For that, their derivation will not be repeated here. There, a general classification of models presented so far in the literature was also included. Further, de Lemos and Pedras [30], and Pedras and de Lemos [31] have applied the volume-averaging operator to the microscopic k-ε equations and proposed the following macroscopic k-ε equations:

$$\rho\left[\frac{\partial}{\partial t}(\phi\langle k\rangle^i)+\nabla\cdot(\overline{\mathbf{u}}_D\langle k\rangle^i)\right] = \nabla\cdot\left[\left(\mu+\frac{\mu_{t_\phi}}{\sigma_k}\right)\nabla(\phi\langle k\rangle^i)\right] - \rho\overline{\langle \mathbf{u}'\mathbf{u}'\rangle^i}:\nabla\overline{\mathbf{u}}_D + c_k\rho\phi\frac{\langle k\rangle^i|\overline{\mathbf{u}}_D|}{\sqrt{K}} - \rho\phi\langle\varepsilon\rangle^i \quad (1)$$

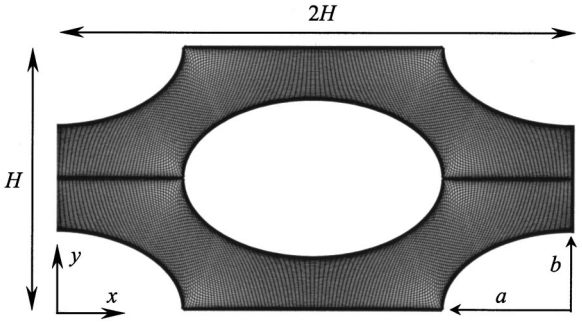

Fig. 1 Periodic cell and elliptically generated grid ($a/b=5/3$)

$$\rho\left[\frac{\partial}{\partial t}(\phi\langle\varepsilon\rangle^i)+\nabla\cdot(\overline{\mathbf{u}}_D\langle\varepsilon\rangle^i)\right] = \nabla\cdot\left[\left(\mu+\frac{\mu_{t_\phi}}{\sigma_\varepsilon}\right)\nabla(\phi\langle\varepsilon\rangle^i)\right] + c_{1\varepsilon}(-\rho\overline{\langle \mathbf{u}'\mathbf{u}'\rangle^i}:\nabla\overline{\mathbf{u}}_D)\frac{\langle\varepsilon\rangle^i}{\langle k\rangle^i} + c_{2\varepsilon}\rho\phi\left\{c_k\frac{\langle\varepsilon\rangle^i|\overline{\mathbf{u}}_D|}{\sqrt{K}}-\frac{\langle\varepsilon\rangle^{i^2}}{\langle k\rangle^i}\right\} \quad (2)$$

with,

$$-\rho\phi\overline{\langle \mathbf{u}'\mathbf{u}'\rangle^i} = \mu_{t_\phi}2\langle\overline{\mathbf{D}}\rangle^v - \frac{2}{3}\phi\rho\langle k\rangle^i\mathbf{I} \quad (3)$$

$$\mu_{t_\phi} = \rho c_\mu\frac{\langle k\rangle^{i^2}}{\langle\varepsilon\rangle^i} \quad (4)$$

where c_k, $c_{1\varepsilon}$, $c_{2\varepsilon}$, and c_μ are nondimensional constants.

For macroscopic fully developed uni-dimensional flow in isotropic and homogeneous media, the limiting values for $\langle k\rangle^i$ and $\langle\varepsilon\rangle^i$ are given by k_ϕ and ε_ϕ, respectively. In this limiting condition, Eqs. (1) and (2) reduce to:

$$\left.\begin{aligned}\langle\varepsilon\rangle^i=\varepsilon_\phi=c_k\frac{k_\phi|\overline{\mathbf{u}}_D|}{\sqrt{K}}\\ \frac{\langle\varepsilon\rangle^{i^2}}{\langle k\rangle^i}=c_k\frac{\varepsilon_\phi|\overline{\mathbf{u}}_D|}{\sqrt{K}}\end{aligned}\right\}\Rightarrow\langle k\rangle^i=k_\phi \quad (5)$$

or in the following dimensionless form,

$$\frac{\varepsilon_\phi\sqrt{K}}{|\overline{\mathbf{u}}_D|^3}=c_k\frac{k_\phi}{|\overline{\mathbf{u}}_D|^2} \quad (6)$$

The coefficient c_k was adjusted in this limiting condition and for the spatially periodic cell shown in Fig. 1. This geometry represents a model for the fine porous structure. The flow was assumed to enter through the left aperture so that symmetric and periodic boundary conditions were applied. Values of k_ϕ and ε_ϕ were obtained by integrating the microscopic flow field for Reynolds number, $\mathrm{Re}_H=|\langle\overline{\mathbf{u}}\rangle^v|H/v$, from 10^4 to 10^6. The porosity, given by $\phi=1-ab\pi/H^2$, was varied from 0.53 to 0.85.

In the numeric model, the following microscopic transport equations were used where barred quantities represent time-averaged components and primes indicate turbulent fluctuations:
Continuity equation

$$\nabla\cdot\overline{\mathbf{u}}=0 \quad (7)$$

Momentum equation

$$\nabla\cdot(\rho\overline{\mathbf{u}}\overline{\mathbf{u}})=-\nabla\overline{p}+\nabla\cdot\{\mu[\nabla\overline{\mathbf{u}}+(\nabla\overline{\mathbf{u}})^T]=\rho\overline{\mathbf{u}'\mathbf{u}'}\} \tag{8}$$

k equation

$$\nabla\cdot(\rho\overline{\mathbf{u}}k)=\nabla\cdot\left[\left(\mu+\frac{\mu_k}{\sigma_k}\right)\nabla k\right]-\rho\overline{\mathbf{u}'\mathbf{u}'}:\nabla\overline{\mathbf{u}}-\rho\varepsilon \tag{9}$$

ε equation

$$\nabla\cdot(\rho\overline{\mathbf{u}}\varepsilon)=\nabla\cdot\left[\left(\mu+\frac{\mu_t}{\sigma_\varepsilon}\right)\nabla\varepsilon\right]+[C_1(-\rho\overline{\mathbf{u}'\mathbf{u}'}:\nabla\overline{\mathbf{u}})-C_2f_2\rho\varepsilon]\frac{\varepsilon}{k} \tag{10}$$

Also, the Boussinesq's concept for Reynolds stresses is given by,

$$-\rho\overline{\mathbf{u}'\mathbf{u}'}=\mu_t[\nabla\overline{\mathbf{u}}+(\nabla\overline{\mathbf{u}})^T]-\frac{2}{3}\rho k\mathbf{I} \tag{11}$$

where the turbulent viscosity is

$$\mu_t=\rho C_\mu f_\mu\frac{k}{\varepsilon} \tag{12}$$

In the above equation set σ_k, σ_ε, C_1, C_2, and C_μ are dimensionless constants whereas f_2 and f_μ are damping functions.

The use, in this work, of the low and high Re k-ε models is justified by the fact that the turbulent flow in porous media occurs for Reynolds numbers (based on the pore) relatively low. To account for the low Reynolds effects, the following damping functions were adopted (Abe et al. [48]).

$$f_2=\left\{1-\exp\left[-\frac{(v\varepsilon)^{0.25}n}{3.1v}\right]\right\}^2\left\{1-0.3\exp\left[-\left(\frac{(k^2/v\varepsilon)}{6.5}\right)^2\right]\right\} \tag{13}$$

$$f_\mu=\left\{1-\exp\left[-\frac{(v\varepsilon)^{0.25}n}{14v}\right]\right\}^2\times\left\{1+\frac{5}{(k^2/v\varepsilon)^{0.75}}\exp\left[-\left(\frac{(k^2/v\varepsilon)}{200}\right)^2\right]\right\} \tag{14}$$

where n is the coordinate normal to the wall. The model constants are given as follows,

$$C_\mu=0.09,\quad C_1=1.5,\quad C_2=1.9,\quad \sigma_k=1.4,\quad \sigma_\varepsilon=1.3. \tag{15}$$

For the high Re model it was used the standard constants of Launder and Spalding [49].

With the assumption of macroscopic fully developed unidimensional flow, the following boundary conditions for the periodic cell (Fig. 1) were adopted:

$$\text{at the walls,}\quad \overline{\mathbf{u}}=0,\quad k=0\quad\text{and}\quad \varepsilon=v\frac{\partial^2k}{\partial n^2}, \tag{16}$$

on $x=0$ and $x=2H$ (periodic boundaries),

$$\overline{u}|_{x=0}=\overline{u}|_{x=2H},\quad \overline{v}|_{x=0}=\overline{v}|_{x=2H}, \tag{17}$$

$$k|_{x=0}=k|_{x=2H},\quad \varepsilon|_{x=0}=\varepsilon|_{x=2H}, \tag{18}$$

on $y=0$ and $y=H/2$ (symmetry planes),

$$\frac{\partial\overline{u}}{\partial y}=\frac{\partial\overline{v}}{\partial y}=\frac{\partial k}{\partial y}=\frac{\partial\varepsilon}{\partial y}=0. \tag{19}$$

where $\overline{u}$ and $\overline{v}$ are components of $\overline{\mathbf{u}}$.

The governing equations were discretized using the finite volume procedure (Patankar [50]). The SIMPLE algorithm for the pressure-velocity coupling was adopted to correct both the pressure and the velocity fields. Process starts with the solution of the two momentum equations. Then the velocity field is adjusted in order to satisfy the continuity principle. This adjustment if obtained by solving the pressure correction equation. After that, the turbulence model equations are relaxed to update the k and ε fields. This iteration sequence is repeated until convergence is achieved. Details on the numerical discretization can be found in Rocamora and de Lemos [32] and in Pedras and de Lemos [34].

For the low Re model, the node adjacent to the wall requires that $u_\tau n/v\leqslant 1$. To accomplish this requirement, the grid needs a great number of points close to the wall leading to computational meshes of large sizes. In order to minimize this problem, all calculations were made in half of the periodic cell ($2H\times H/2$) and according to the boundary condition Eq. (19). The use of the symmetry boundary condition reduces the grid to 300×100 nodes.

Table 1 Summary of the integrated results

	Medium permeability	Re_H	k-ε model	$\lvert\langle\overline{u}\rangle^v\rvert$	$\langle k\rangle^i$	$\langle\varepsilon\rangle^i$
$\phi=0.53$	$K=4.12E-05$	1.67E+04	low	2.51E-01	1.36E-02	1.26E-01
		1.67E+05	low	2.51E+00	1.09E+00	1.17E+02
		1.67E+05	high	2.51E+00	1.40E+00	1.21E+02
		1.67E+06	high	2.51E+01	1.62E+02	1.34E+05
$\phi=0.70$	$K=1.29E-04$	1.67E+04	low	2.51E-01	1.06E-02	5.72E-02
		1.67E+05	low	2.51E+00	8.16E-01	4.71E+01
		1.67E+05	high	2.51E+00	8.71E-01	4.45E+01
		1.67E+06	high	2.51E+01	9.99E+01	5.00E+04
$\phi=0.85$	$K=3.25E-04$	1.67E+04	low	2.51E-01	7.52E-03	2.83E-02
		1.67E+05	low	2.51E+00	5.48E-01	2.14E+01
		1.67E+05	high	2.51E+00	5.17E-01	1.79E+01
		1.67E+06	high	2.51E+01	7.52E+01	2.70E+04

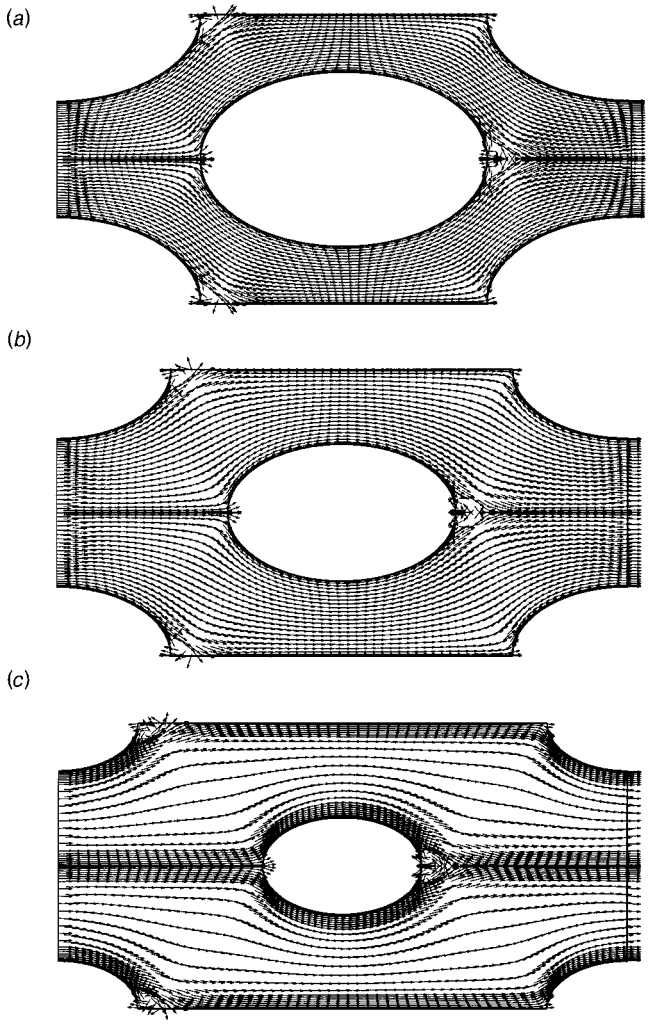

Fig. 2 Microscopic velocity field ($Re_H=1.67\times10^5$): a) $\phi=0.53$, b) $\phi=0.70$ e c) $\phi=0.85$

A highly nonuniform grid arrangement was employed with concentration of nodes close to the wall. All calculations were executed using an IBM SP2 computer.

Results and Discussion

A total of eighteen runs were carried out being six for laminar flow, six with the low Re model and six using the high Re theory. Table 1 summarizes the integrated results (volumetric averaging over the periodic cell) obtained for turbulent flow (Pedras and de Lemos [51], Pedras and de Lemos [52]. The medium permeability was calculated using the procedure adopted by Kuwahara et al. [16].

Figure 2 presents velocity fields for $\mathrm{Re}_H=1.67\times10^5$ (low Re model) and $\phi=0.53$. It is observed that the flow accelerates in the upper and lower passages around the ellipse and separates at the back. As porosity decreases maintaining Re_H constant, or say, reducing the flow passage and increasing the local fluid speed, the integrated turbulence kinetic energy, $\langle k\rangle'$, increases (see Table 1). In other words, for a fixed mass flow rate through the bed, a decrease in porosity implies in accentuated velocity gradients which, in turn, result in larger production rates of k due to steep velocity gradients within the fluid. Furthermore, the increment of the fluid momentum close to the walls as porosity is reduced, for the same $|\langle\overline{\mathbf{u}}\rangle^v|$, reduces also the size of the recirculating bubble behind the elliptic rod. This effect was verified by Pedras and de Lemos [34] for an array of cylindrical rods and by Kuwahara et al. [16], for an array of square cylinders. For the geometry here investigated, reduction of the wake region in Fig. 2 is more difficult to be visualized due the streamlined flow pattern around ellipses. Nevertheless, numerical values for $\langle k\rangle^i$ shown in Table 1 indicate a similar trend for $\langle k\rangle^i$ as a function of ϕ as in the other two arrangements used for comparison.

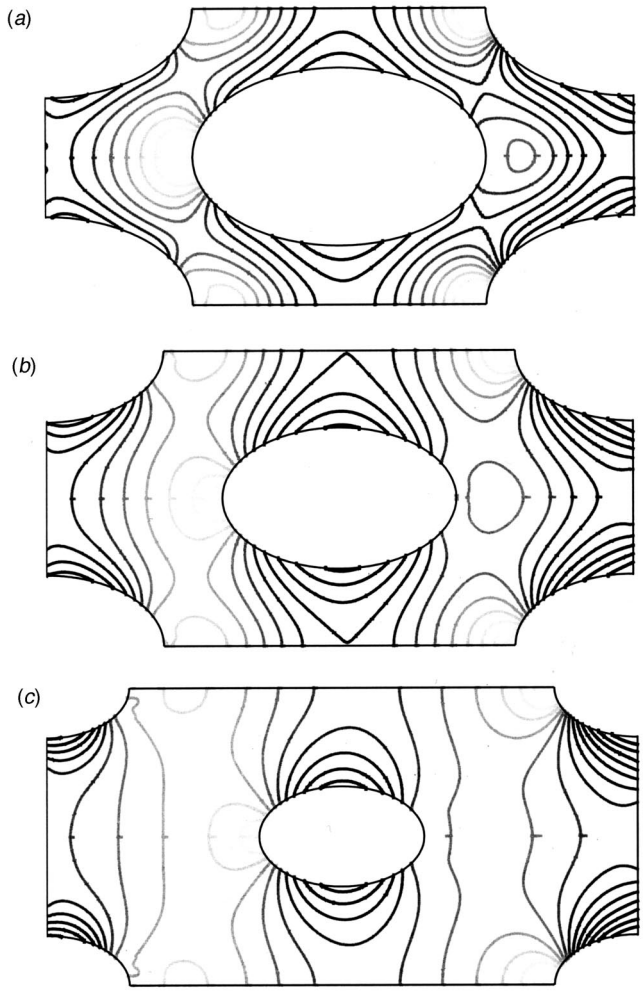

Fig. 3 Microscopic pressure field ($\mathrm{Re}_H=1.67\times10^5$): a) $\phi=0.53$, b) $\phi=0.70$ e c) $\phi=0.85$

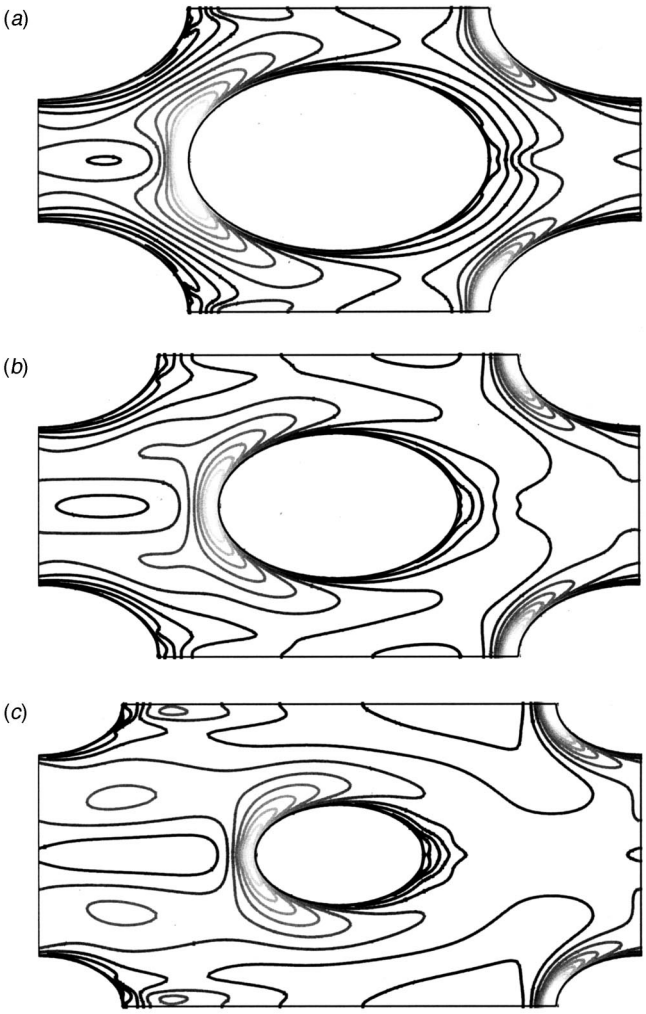

Fig. 4 Microscopic fields for k ($\mathrm{Re}_H=1.67\times10^5$): a) $\phi=0.53$, b) $\phi=0.70$ e c) $\phi=0.85$

Remainder fields for pressure, k and ε, are shown in Figs. 3, 4, and 5, respectively. It is verified that the pressure increases at the front of the ellipse and decreases at the upper and lower faces. The turbulence kinetic energy is high at the front, on the top and below the bottom of the ellipse. The dissipation rate of k presents a behavior similar to the turbulence kinetic energy.

It is also interesting to point out that for the same ϕ and Re_H the integrated values shown in Table 1 for $\langle k\rangle^i$ are lower than those obtained for square (Nakayama and Kuwahara [19]) and for cylindrical rods (Pedras and de Lemos [34]). Apparently, smoother passages in between elliptic rods contributes for reducing sudden flow acceleration within the flow, reducing then overall velocity gradients and, consequently, lowering production rates $\langle k\rangle^i$.

Pressure Gradient and Constant c_k for Elliptic Rods

The macroscopic pressure gradient based on the intrinsic pressure is obtained with the help of the following equations:

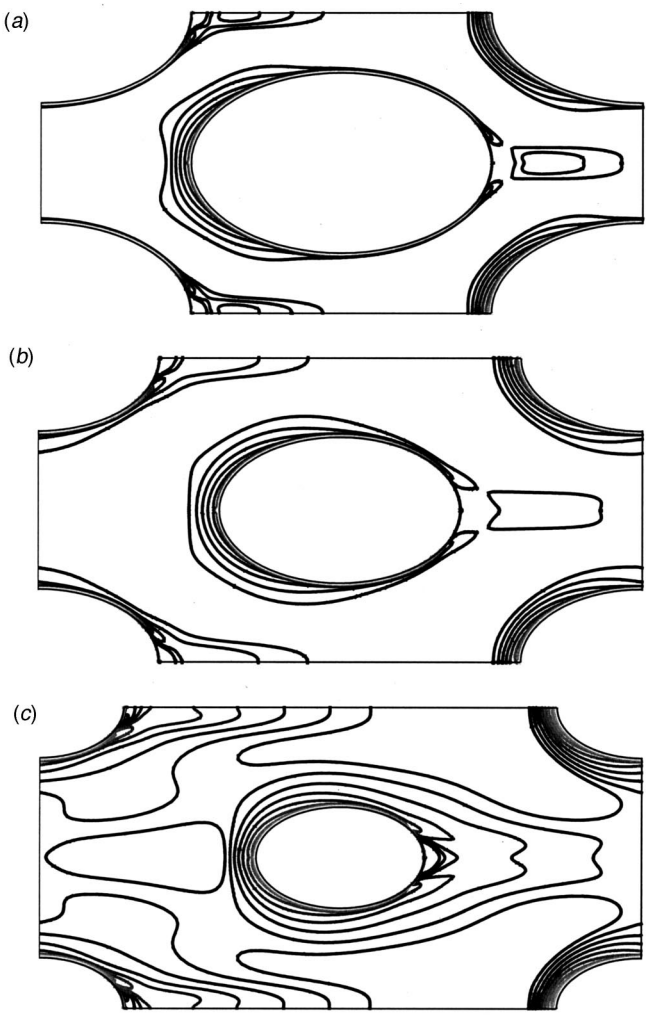

Fig. 5 Microscopic field for ε (Re_H=1.67×10^5): a) ϕ=0.53, b) ϕ=0.70 e c) ϕ=0.85

$$\frac{d\langle\overline{p}\rangle^i}{dS} = \frac{1}{2H(H/2-D/2)}\int_{D/2}^{H/2}(p|_{x=2H} - p|_{x=0})dy \qquad (20)$$

Results for the nondimensional pressure gradient versus Re_H are presented in Fig. 6, in addition to data from Kuwahara et al. [17] and Pedras and de Lemos [31], for square and cylindrical rods, respectively. Pressure gradient for elliptic rods fall lower than for square and cylindrical rods, as expected, since pressures losses over streamlined bodies are lower than those for flows where a wake region is of a larger size.

Also, for the same porosity and Reynolds number, the values for the intrinsic turbulent kinetic energy, $\langle k\rangle^i$ in Table 1 are lower than those obtained for square cylinders (Nakayama and Kuwahara [19]) and for circular rods (Pedras and de Lemos [34]). This result could be explained by recalling that, within voids formed in between the ellipses, the fluid accelerates less intensively causing lower velocity gradients and, consequently, lower production rates of k.

Once the intrinsic values of k_ϕ and ε_ϕ were obtained, they were plugged into Eq. (6). The value of c_k equal to 0.28 was found by noting the collapse of all data into the straight line shown in Fig. 7. The figure also shows data of Pedras and de Lemos [31], and Nakayama and Kuwahara [19] for cylindrical and square rods, respectively.

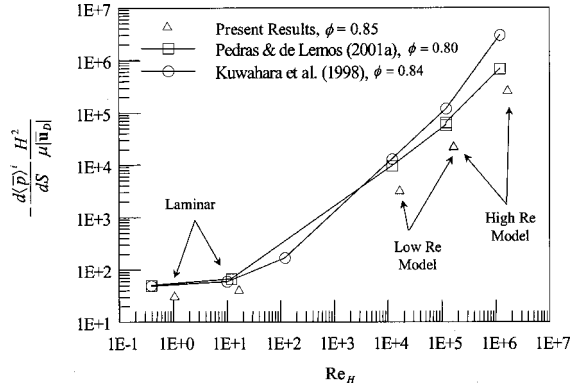

Fig. 6 Effect of Reynolds number, Re_H, on nondimensional pressure gradient

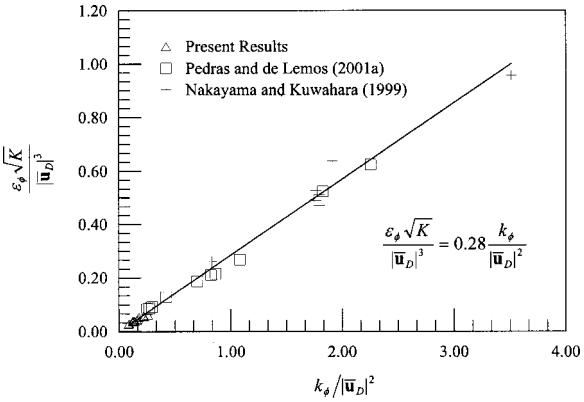

Fig. 7 Determination of value for c_k using data for different porous media, porosity and Reynolds number

Macroscopic Model Results

With the numerical evaluation of c_k, calculations using the macroscopic turbulence model above can be performed. A test case consisting in simulating the flow through a porous bed of length 10H, starting with a preselected initial conditions greater than the final asymptotic values, is now carried out. Similar test results were reported by Pedras and de Lemos [31], and Nakayama and Kuwahara [19], being the values at entrance $\langle k\rangle^i = 10k_\phi$ and $\langle\varepsilon\rangle^i = 30\varepsilon_\phi$. Figures 8 and 9 show results for $\langle k\rangle^i$ and $\langle\varepsilon\rangle^i$ along the flow. Calculations are compared with similar

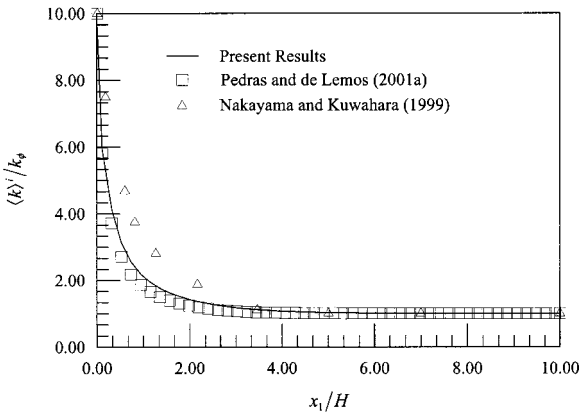

Fig. 8 Development of nondimensional turbulence kinetic energy

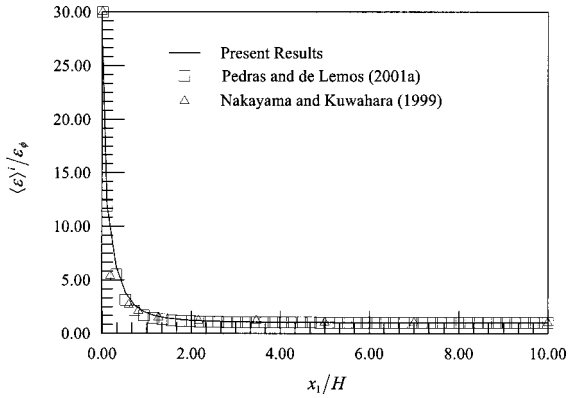

Fig. 9 Development of nondimensional dissipation rate

results of Nakayama and Kuwahara [19], for an array of square rods and with computations of Pedras and de Lemos [31] for a bed of circular cylinders. Is interesting to note that, in spite of differences on the shape of the rods, the axial decay is nearly the same in all cases indicating the coherence of the results herein with previous data published in the literature.

Concluding Remarks

This paper presented the views in the literature for characterizing turbulent flow in porous media. The equations for the flow turbulent kinetic energy were presented. A macroscopic turbulence model was adjusted for an infinite porous medium formed by spatially periodic array of elliptic rods. This adjustment was carried out by the solution of the microscopic flow field within the volume occupied by the fluid. After that, integrated flow properties were computed and the proposed model constant was determined. Then, the macroscopic model was tested comparing the numerical results of the flow in the entrance region of homogeneous isotropic porous medium with available similar results in the recent literature. Good agreement with published data was observed.

Acknowledgments

MJSdL is thankful to CNPq, Brazil, for their financial support during the course of this research.

References

[1] Darcy, H., 1856, *Les Fontaines Publiques de la Vile de Dijon*, Victor Dalmond, Paris.
[2] Forchheimer, P., 1901, ''Wasserbewegung durch Boden,'' Z. Ver. Deutsch. Ing. **45**, pp. 1782–1788.
[3] Brinkman, H. C., 1947, ''A Calculation of the Viscous Force Exerted by a Flowing Fluid on a Dense Swarm of Particles, '' Appl. Sci. Res., **A1**, pp. 27–34.
[4] Ward, J. C., 1964, ''Turbulent Flow in Porous Media,'' J. Hydraul. Div. Am. Soc. Civ. Eng. **90**, pp, 1–12.
[5] Whitaker, S., 1969, ''Advances in Theory of Fluid Motion in Porous Media,'' Ind. Eng. Chem., **61**, pp. 14–28.
[6] Bear, J., 1972, *Dynamics of Fluids in Porous Media*, American Elsevier, New York.
[7] Vafai, K., and Tien, C. L., 1981, ''Boundary and Inertia Effects on Flow and Heat Transfer in Porous Media,'' Int. J. Heat Mass Transf., **24**, pp. 195–203.
[8] Whitaker, S., 1999, *The Method of Volume Averaging*, Kluwer Academic Publishers, Dordrecht,
[9] Prausnitz, J. M., and Wilhelm, R. H., 1957, ''Turbulent Concentrations Fluctuations in a Packed Bed,'' Ind. Eng. Chem., **49**, pp. 237–246.
[10] Mickley, H. S., Smith, K. A., and Korchak, E. I., 1965, ''Fluid Flow in Packed Beds,'' Chem. Eng. Sci., **20**, pp. 237–246.
[11] Lee, K., and Howell, J. R., 1987, ''Forced Convective and Radiative Transfer Within a Highly Porous Layer Exposed to a Turbulent External Flow Field,'' *Proc. of the 1987 ASME-JSME Thermal Eng. Joint Conf.*, Vol. 2, pp. 377–386.
[12] Wang, H., and Takle, E. S., 1995, ''Boundary-Layer Flow and Turbulence Near Porous Obstacles,'' Boundary-Layer Meteorol., **74**, pp. 73–88.
[13] Antohe, B. V., and Lage, J. L., 1997, ''A General Two-Equation Macroscopic Turbulence Model for Incompressible Flow in Porous Media,'' Int. J. Heat Mass Transf., **40**, pp. 3013–3024.
[14] Getachew, D., Minkowycz, W. J., and Lage, J. L., 2000, ''A Modied Form of the k-ε Model for Turbulent Flow of an Incompressible Fluid in Porous Media,'' Int. J. Heat Mass Transf., **43**, pp. 2909–2915.
[15] Masuoka, T., and Takatsu, Y., 1996, ''Turbulence Model for Flow Through Porous Media,'' Int. J. Heat. Mass Transfer, **39**, pp. 2803–2809.
[16] Kuwahara, F., Kameyama, Y., Yamashita, S., and Nakayama, A., 1998, ''Numerical Modeling of Turbulent Flow in Porous Media Using a Spatially Periodic Array,'' J. Porous Media **1**, pp. 47–55.
[17] Kuwahara, F., and Nakayama, A., 1998, ''Numerical Modeling of Non-Darcy Convective Flow in a Porous Medium,'' *Proc. 11th Int. Heat Transf. Conf.*, Kyongyu, Korea, Aug. 23–28.
[18] Takatsu, Y., and Masuoka, T., 1998, ''Turbulent Phenomena in Flow Through Porous Media, J. Porous Media, **3**, pp. 243–251.
[19] Nakayama, A., and Kuwahara, F., 1999, ''A Macroscopic Turbulence Model for Flow in a Porous Medium,'' ASME J. Fluids Eng., **121**, pp. 427–433.
[20] Travkin, V. S., and Catton, I., 1992, ''Model of Turbulent Thermal Diffusivity and Transfer Coefficients for a Regular Packed Bed of Spheres,'' *Proc. 28th National Heat Transfer Conference*, San Diego, C-4, ASME-HTD-193, pp. 15–23.
[21] Travkin, V. S., Catton, I., and Gratton, L., 1993, ''Single-Phase Turbulent Transport in Prescribed Non-Isotropic and Stochastic Porous Media,'' *Heat Transfer in Porous Media*, ASME-HTD-240, pp. 43–48.
[22] Gratton, L., Travkin, V. S., and Catton, I., 1994, ''Numerical Solution of Turbulent Heat and Mass Transfer in a Stratified Geostatistical Porous Layer for High Permeability Media,'' ASME Proceedings HTD-vol.. 41, pp. 1–14.
[23] Travkin, V. S., and Catton, I., 1995, ''A Two Temperature Model for Turbulent Flow and Heat Transfer in a Porous Layer,'' ASME J. Fluids Eng., **117**, pp. 181–188.
[24] Travkin, V. S., and Catton, I., 1998, ''Porous Media Transport Descriptions-Non-Local, Linear and Non-Linear Against Effective Thermal/Fluid Properties,'' Adv. Colloid Interface Sci., **76-77**, pp. 389–443.
[25] Travkin, V. S., Hu, K., and Catton, I., 1999, ''Turbulent Kinetic Energy and Dissipation Rate Equation Models for Momentum Transport in Porous Media,'' *Proc. 3rd ASME/JSME Joint Fluids Engineering Conference* (on CD-ROM), Paper FEDSM99-7275, San Francisco, California, 18–23 July.
[26] Pedras, M. H. J., and de Lemos, M. J. S., 1998, ''Results for Macroscopic Turbulence Modeling for Porous Media,'' *Proc. of ENCIT98-7th Braz. Cong. Eng. Th. Sci.*, Vol. 2, pp. 1272–1277, Rio de Janeiro, Brazil, November 3-6 (in Portuguese).
[27] Pedras, M. H. J., and de Lemos, M. J. S., 1999, On Volume and Time Averaging of Transport Equations for Turbulent Flow in Porous Media, *Proc. of 3rd ASME/JSME Joint Fluids Engineering Conferernce* (on CDROM), ASME-FED-248, Paper FEDSM99-7273, ISBN 0-7918-1961-2, San Francisco, CA, July 18–25.
[28] Pedras, M. H. J., and de Lemos, M. J. S., 1999; ''Macroscopic Turbulence Modeling for Saturated Porous Media,'' *Proc. of COBEM99-15th Braz. Congr. Mech. Eng.* (on CD-ROM), ISBN: 85-85769-03-3, Águas de Lindóia, São Paulo, Brazil, November 22–26 (in Portuguese).
[29] Pedras, M. H. J., and de Lemos, M. J. S., 2000, ''On the Definition of Turbulent Kinetic Energy for Flow in Porous Media,'' Int. Commun. Heat Mass Transfer, **27**, No. 2, pp. 211–220.
[30] de Lemos, M. J. S., and Pedras, M. H. J. 2000, ''Modeling Turbulence Phenomena in Incompressible Flow Through Saturated Porous Media,'' *Proc. of 34th ASME-National Heat Transfer Conference* (on CD-ROM), ASME-HTD-I463CD, Paper NHTC2000-12120, ISBN:0-7918-1997-3, Pittsburgh, PA, August 20-22.
[31] Pedras, M. H. J., and de Lemos, M. J. S., 2001, ''Macroscopic Turbulence Modeling for Incompressible Flow Through Undeformable Porous Media,'' Int. J. Heat Mass Transf., **44**, No. 6, pp. 1081–1093.
[32] Rocamora Jr., F. D., and de Lemos, M. J. S., 1998, ''Numerical Solution of Turbulent Flow in Porous Media Using a Spatially Periodic Array and the *k-*ε Model,'' *Proc. ENCIT-98 - 7th Braz. Cong. Eng. Th. Sci.*, Vol. 2, pp. 1265–1271, Rio de Janeiro, RJ, Brazil, November 3–6.
[33] Pedras, M. H. J., and de Lemos, M. J. S., 2000, ''Numerical Solution of Turbulent Flow in Porous Media using a Spatially Periodic Cell and the Low Reynolds *k-*ε Model,'' *Proc. of CONEM2000 - National Mechanical Engineering Congress* (on CD-ROM), Natal, Rio Grande do Norte, Brazil, August 7–11 (in Portuguese).
[34] Pedras, M. H. J., and de Lemos, M. J. S., 2001, ''Simulation of Turbulent Flow in Porous Media Using a Spatially Periodic Array and a Low Re Two-Equation Closure,'' Numer. Heat Transfer, Part A, **39**, No. 1, pp. 35–59.
[35] Rocamora, Jr., F. D., and de Lemos, M. J. S., 1999, ''Simulation of Turbulent Heat Transfer in Porous Media Using a Spatially Periodic Cell and the k-ε Model,'' *Proc. of COBEM99 - 15th Braz. Congr. Mech. Eng.* (on CD-ROM), ISBN: 86-85769-03-3, Águas de Lindóia, São Paulo, Brazil, Nov. 22–26.
[36] Rocamora, Jr., F. D., and de Lemos, M. J. S., 2000, ''Analysis Of Convective Heat Transfer For Turbulent Flow in Saturated Porous Media,'' Int. Commun. Heat Mass Transfer, **27**, pp. 825–834.
[37] Rocamora Jr., and de Lemos, M. J. S., 2001, ''Turbulence Modeling For Non-Isothermal Flow in Undeformable Porous Media,'' *Proc. of NHTC'01, 35th National Heat Transfer Conference*, **ASME-HTD-I495CD**, Paper NHTC2001-20178, **ISBN: 0-7918-3527-8**, Anaheim, California, June 10–12.
[38] de Lemos, M. J. S., and Pedras, M. H. J., 2000, ''Simulation of Turbulent Flow Through Hybrid Porous Medium-Clear Fluid Domains,'' *Proc. of*

IMECE2000-ASME-Intern. Mech. Eng. Congr., ASME-HTD-366-5, pp. 113–122, ISBN:0-7918-1908-6, Orlando, FL, November 5–10.
[39] Rocamora, Jr., F. D., and de Lemos, M. J. S., 2000, Prediction of Velocity and Temperature Profiles for Hybrid Porous Medium-Clean Fluid Domains, ''*Proc. of CONEM2000—National Mechanical Engineering Congress* (on CD-ROM), Ntal, Rio Grande do Norte, Brazil, August 7–11.
[40] Rocamora, Jr., F. D., and de Lemos, M. J. S., 2000, ''Laminar Recirculating Flow And Heat Transfer In Hybrid Porous Medium-Clear Fluid Computational Domains,'' *Proc. of 34th ASME-National Heat Transfer Conference* (on CD-ROM), ASME-HTD-I463CD, Paper NHTC2000-12317, ISBN:0-7918-1997-3, Pittsburgh, PA, August 20–22.
[41] Rocamora, Jr., F. D., and de Lemos, M. J. S., 2000, ''Heat Transfer In Suddenly Expanded Flow in a Channel With Porous Inserts,'' *Proc. of IMECE2000 - ASME - Intern. Mech. Eng. Congr.,* ASME-HTD-366-5, pp. 191–195, ISBN:0-7918-1908-6, Orlando, FL, November 5–10.
[42] Pedras, M. H. J., and de Lemos, M. J. S., 1998, ''Analysis of Flow in Porous Media Via Volumetric Averaging of the Navier-Stokes Equations,'' Proc. of ENCIT98- 7th Braz. Cong. Eng. Th. Sci., Vol. 2, pp. 1278–1283, Rio de Janiero, Brazil, November 3–6 (in Portuguese).
[43] Macdonald, I. F., El-Sayed, M. S., Mow, K., and Dullien, F. A. L., 1979, ''Flow Through Porous Media: The Ergun Equation Revisited,'' Indust. Chem. Fundam. **18**, pp. 199–208.
[44] Kececiooglu, I., and Jiang, Y., 1994, ''Flow Through Porous Media of Packed Spheres Saturated With Water,'' ASME J. Fluids Eng., **116**, pp. 164–170.
[45] Lage, J. L., 1998, ''The Fundamental Theory of Flow Through Permeable Media From Darcy to Turbulence,'' in *Transport Phenomena in Porous Media,* D. B. Ingham and I. Pop, eds., Elsevier Science Ltd., ISBN: 0-08-042843-6, 446 pgs.
[46] de Lemos, M. J. S., and Pedras M. H. J., 2001, ''Alternative Transport Equations for Turbulent Kinetic Energy for Flow in Porous Media,'' Prof. of NHTC01, 35th Nat. Heat Transfer Conf. ASME-HTD-I49SCD Paper NHTC01-20177, ISBN: 0-7918-3527-8, Anaheim, California, June 10–12.
[47] de Lemos, M. J. S., and Pedras, M. H. J., 2001, ''Recent Mathematical Models For Turbulent Flow In Saturated Rigid Porous Media,'' ASME Journal of Fluids Engineering.
[48] Abe, K., Nagano, and Y., Kondoh, T., 1992, ''An Improved k-ε Model for Prediction of Turbulent Flows With Separation and Reattachment,'' Trans. Jpn. Soc. Mech. Eng., Ser. B, **58**, pp. 3003–3010.
[49] Launder, B. E., and Spalding, D. B., 1974, ''The Numerical Computation of Turbulent Flows,'' Comput. Methods Appl. Mech. Eng., **3**, pp. 269–289.
[50] Patankar, S. V., 1980, *Numerical Heat Transfer And Fluid Flow,* Hemisphere, New York.
[51] Pedras, M. H. J., and de Lemos, M. J. S., 2001, ''Adjustment of a Macroscopic Turbulence Model for a Porous Medium Formed by an Infinite Array of Elliptic Rods, *2nd International Conference on Computational Heat and Mass Transfer,* Rio de Janeiro, Brazil, October 22–26.
[52] Pedras, M. H. J., and de Lemos, M. J. S., 2001, ''Solução Numérica do Escoamento Turbulento num Meio Poroso Formado por Hastes Elíptica - Aplicação do Modelo k-ε Para baixo e Alto Reynolds,'' *Proc of COBEMOI - 16th Braz. Congr. Mech. Eng.,* (on CDROM) Uberlândia, MG, Brazil, November 26–30.

Journal of Fluids Engineering

Technical Briefs

Experimental Verification of Two New Theories Predicting Temperature-Dependent Viscosity Effects on the Forced Convection in a Porous Channel

Arunn Narasimhan
Ph.D Student

José L. Lage[1]
Mem. ASME

Department of Mechanical Engineering,
Southern Methodist University, Dallas, TX 75275-0337

D. A. Nield
Department of Engineering Science,
University of Auckland, Private Bag 92019,
Auckland, New Zealand

Dan C. Porneala
Mem ASME
Lead Research Engineer,
Research Department, Peerless Mfg. Co.,
Dallas, TX 75229

Introduction

The necessity for fundamental investigations in forced convection through porous media by fluids with temperature-dependent viscosity cannot be overstated once we take into account the lack of information on this subject [1,2]. Apart from the fundamental nature of the problem, which merits its study, many contemporary applications involving convection of fluids with temperature-dependent viscosity are hampered by this lack of understanding.

One specific application is the new microporous enhanced cold-plate design for cooling avionics [3], specifically airborne, military, phased-array radar slats. This cold-plate operates using poly-alpha-olefin oil as coolant. Poly-alpha-olefins (PAO), a class of synthetic oils commonly used in cooling military avionics, has viscosity strongly dependent on temperature. Suitability of a particular porous material for such cold-plate design or the optimization of an existing design requires an accurate prediction of the global pressure-drop across the heated channel.

The conventional procedure for predicting the pressure-drop of a fluid flowing through a porous channel using the global Hazen-Dupuit-Darcy (HDD) model (also known as the Forchheimer-extended Darcy model), fails unexpectedly, [4,5], when the fluid has temperature-dependent viscosity and the channel is heated/cooled. This inappropriateness of the global HDD model is because it is unable to capture the indirect viscosity effect on the global form-drag term.

Alternatively, new predictive models that consider the temperature dependency of viscosity were proposed recently in [4,5] and were validated against numerical results. The objective of this note, by using the experimental results for poly-alpha-olefin's (PAO) obtained with a new microporous-enhanced cold plate design for cooling avionics [6], is to verify the appropriateness of these two theoretical models as useful tools for engineering design. The verification of the models focus on the hydraulic performance of the cold-plate, in lieu of previous works [5,7] showing minimal temperature-dependent viscosity effect on the thermal performance of the cold-plate.

Nield Model

Perturbation analysis presented in [5], to predict the effects of a fluid with temperature-dependent viscosity flowing through an isoflux-bounded porous medium channel is summarized as follows. The analysis considers initially the differential HDD model, for fully developed (hydrodynamic and thermal) flow situation, with constant coefficients and temperature-dependent viscosity, namely

$$C_0 \rho K_0 u^2 + \mu(T) u - G K_0 = 0 \tag{1}$$

where C_0 and K_0 are, respectively, the form and permeability coefficients of the porous medium, ρ and μ are the density and dynamic viscosity of the fluid, u is the local longitudinal fluid Darcy speed, and the local longitudinal pressure gradient $G = dP/dx = \Delta P/L$, with L being the length of the porous channel.

The subscript "0" on the porous medium properties K and C of Eq. (1) reminds us that these quantities are obtained through experiments under isothermal condition. In this case, the fluid viscosity is uniform throughout the channel, $\mu(T) = \mu(T_{\text{in}}) = \mu_{\text{in}}$. Observe that Eq. (1) incorporates the form-drag effect of the porous medium by adding the quadratic velocity term to the Darcy equation [8]. The quadratic equation given by Eq. (1) when solved for u will result in a positive root, which will be a function of $\mu(T)$ with a solution resembling $u = F(\mu(T))$. The temperature dependency of the dynamic viscosity of the fluid can be approximated as a second-order Taylor's series expansion enabling us to express $F(\mu(T))$ as a function of T (the local unknown temperature) and a reference (known) temperature.

Assuming small change in temperature *along* the channel, for negligible longitudinal diffusion, zero-, first-, and second-order approximations were obtained for the transversal fluid speed u and temperature T, as well as for the global fluid-speed versus

[1]Corresponding author e-mail: JLL@SEAS.SMU.EDU

Contributed by the Fluids Engineering Division of THE AMERICAN SOCIETY OF MECHANICAL ENGINEERS. Manuscript received by the Fluids Engineering Division October 27, 2000; revised manuscript received May 21, 2001. Associate Editor: L. Mondy.

pressure-drop relation. The first- and second-order solutions (denoted with subscripts 1 and 2, respectively) for the global (cross-section averaged) fluid velocity are

$$U_1 = a_1 + \frac{a_2 N}{3} \tag{2}$$

$$U_2 = a_1 + \frac{a_2 N}{3} + \frac{{a_2}^2 N^2}{45 a_1} - \frac{a_2 M}{15} + \frac{a_3 N^2}{15} \tag{3}$$

where

$$a_1 = \frac{GK_0}{2\mu_w}\left[\frac{-1+\sqrt{1+4r}}{r}\right] \quad a_2 = \frac{GK_0}{2\mu_w r}\left[1 - \frac{1}{\sqrt{1+4r}}\right]$$

$$a_3 = \frac{2GK_0}{\mu_w (1+4r)^{3/2}}$$

$$r = \frac{\rho C_0 K_0^2 G}{\mu_w^2} \quad N = \frac{q'' H}{k_e}\frac{1}{\mu_w}\left(\frac{d\mu}{dT}\right)_{T_w} \quad M = \left(\frac{q'' H}{k_e}\right)^2 \frac{1}{\mu_w}\left[\frac{d^2\mu}{dT^2}\right]_{T_w} \tag{4}$$

where q'' is the surface heat flux, k_e is the effective thermal conductivity of the medium, and H is half the distance between the plates. The viscosity μ_w and its derivatives are evaluated at the reference temperature T_w, the wall temperature at the exit of the channel. Observe that when the form-drag coefficient C_0 is negligible then $r \to 0$. In this case, from Eq. (4), $a_1 = a_2 \to GK_0/\mu_w$ and the first-order solution Eq. (2) reduces to

$$U = \left(\frac{\Delta P}{L}\right)\frac{K_0}{\mu(T_{\max})}\left[1 + \frac{N}{3}\right] \tag{5}$$

a result identical to the result reported in [9], who developed a similar predictive theory for a fluid with temperature-dependent viscosity, but starting with the simpler linear Darcy flow regime, i.e., Eq. (1) replaced by $u = [K_0/\mu(T)]G$.

Narasimhan-Lage Model

Numerical simulations considering convection of a fluid with temperature-dependent viscosity through a uniformly heated, parallel-plates porous channel, and including the form-drag effects, were presented recently by Narasimhan and Lage [4]. In this work, the authors show the limitations of the global HDD model, *viz.*

$$\frac{\Delta P}{L} = \frac{\mu}{K_0} U + \rho C_0 U^2 \tag{6}$$

in accurately predicting the pressure-drop along the channel, suggesting a modification to account for the temperature-dependent viscous effects. They also showed that the global HDD model, Eq. (6), is inappropriate because it neglects indirect effects of temperature-dependent viscosity on the form-drag term of the model, a term originally believed to be viscosity-independent.

A new global model,

$$\frac{\Delta P}{L} = \zeta_\mu \left(\frac{\mu_{\text{in}}}{K_0}\right) U + \zeta_C (\rho C_0) U^2 \tag{7}$$

that accounts for the effects of temperature dependent viscosity in both drag terms of the original HDD model, was proposed.

Notice that the viscosity in Eq. (7) is evaluated at the reference inlet temperature of the channel, $\mu_{\text{in}} = \mu(T_{\text{in}})$. In addition, this model *retains* the same form, i.e., velocity dependency, of Eq. (6). The coefficients ζ_μ and ζ_C represent, respectively, the correction for the global viscous and form-drag terms due to the local effect of temperature on viscosity, which affect directly the first-order velocity term and the fluid velocity profile (via viscosity), which in turn, affects indirectly the second-order velocity term. Obviously, for no heating (uniform viscosity), $\zeta_\mu = \zeta_C = 1$ and Eq. (7) becomes identical to Eq. (6).

Predictive empirical relations for correcting the viscous and form drag terms, complementing this new algebraic (global) model, were obtained [4] as functions of the surface heat flux,

$$\zeta_\mu = \left[1 - \left(\frac{Q''}{1+Q''}\right)^{0.325}\right]\left(\frac{1}{1+Q''}\right)^{18.2} \qquad \zeta_C = 2 + (Q'')^{0.11} - \zeta_\mu^{-0.06} \tag{8}$$

with the non-dimensional heat flux Q'' given by

$$Q'' = \frac{q''}{\left(\frac{k_e}{K_0 C_0}\right)\mu_{\text{in}}}\left|\frac{d\mu}{dT}\right|_{T_{\text{in}}} \tag{9}$$

Observe from Eq. (7), the N-L model is a *direct* modification of the original *global* HDD model, Eq. (6), with the introduction of two new coefficients to capture the temperature-dependent viscosity effects on *both* of the drag terms. Apart from physical grounds that support the introduction of two coefficients (see [4] for details), the N-L model is expected to agree better with the experimental results than the global HDD model, Eq. (6), as it allows the effects of $\mu(T)$ to be accommodated in both of the drag terms.

In contrast, the perturbation model starts with the differential HDD model and arrives at a series type solution for $u(y)$ with the effects of viscosity captured in each of the terms in the series. This differential solution upon integration along y, gives the channel cross-section averaged global fluid speed U, Eq. (2) or (3). The fully developed flow situation necessary for the Nield model, although it can admit nonslug flow like profiles, does not allow changes in the velocity profile *along* the channel. This implies that the theory considers only the y-variation of viscosity, as the temperature difference *along* the channel is assumed very small. Hence, the N-L model is expected to perform better than the Nield model, especially for configurations with considerable fluid temperature variation along the channel.

Experimental Hydraulic Verification

A microporous cold-plate with a porous insert made of a compressed aluminum-alloy porous foam sandwiched (brazed) between rectangular (102×508 mm) plate sections was designed and manufactured for cooling a phased-array radar slat [3,10]. Electric heaters generating a heat flux $q'' = 0.59\,\text{V}^2$, in W/m^2, where V is the supply voltage in Volts, were used to heat the channel plates. The volumetric flow rate was varied from 0.5 to 5×10^{-5} m^3/s. Pressure measurements at the inlet P_i and outlet P_o gave the total PAO pressure-drop across the cold plate. Details of the experimental apparatus and procedure are found in [6].

The uncertainties of the PAO flow rate Q and of the experimental pressure drop ΔP are estimated following the recommendations of [11]. A conservative estimate for the uncertainty of the experimental volumetric flow rate reported in this work, U_Q/Q is 5 percent. The uncertainty of the pressure-drop across the cold-plate is equal to the precision limit $P_{\Delta P}$ because both precision pressure gages were calibrated by the manufacturer using the same equipment and procedure, hence the resulting bias limit of the pressure difference is zero. This precision limit is estimated as being equal to twice the standard deviation of several measurements, or approximately 3 percent.

The temperature dependence of the dynamic viscosity of PAOs can be modeled [3] as

$$\mu(T) = 0.1628 T^{-1.0868} \tag{10}$$

valid for $5°\text{C} \leqslant T \leqslant 170°\text{C}$. Within the same temperature range, the variations of density, specific heat and thermal conductivity of PAO are negligible.

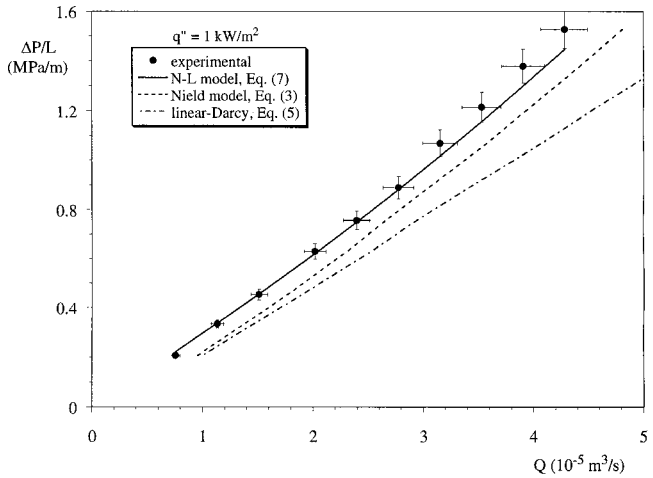

Fig. 1 Pressure drop versus volumetric coolant flow rate for $T_0=21°C$ and V=46.9 V. (Uncertainties: $U_{\Delta P}/\Delta P=3$ percent, $U_Q/Q=5$ percent)

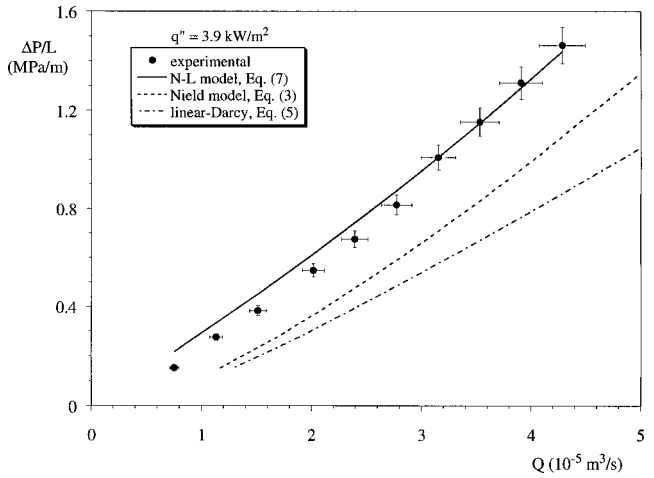

Fig. 2 Pressure drop versus volumetric coolant flow rate for $T_0=21°C$ and V=93.81 V. (Uncertainties: $U_{\Delta P}/\Delta P=3$ percent, $U_Q/Q=5$ percent)

The effective permeability K_0 and the form coefficient C_0 of the porous insert can be determined by fitting the experimental no-heating (with the heaters switched off) results with a function of the type

$$\Delta P_0=\frac{L\mu_{\text{in}}}{K_0}\frac{Q}{A_f}+L\rho C_0\left(\frac{Q}{A_f}\right)^2 \tag{11}$$

where L is the cold-plate length, equal to 0.102 m, A_f is the flow cross-section area, equal to 5.08×10^{-4} m^2, and μ_{in} and ρ are the PAO viscosity and density at 21°C, respectively, 5.95×10^{-3} kg/ms and 789.2 kg/m^3. Out of the inserts tested, as reported in [6], we focus our attention on insert no.3 (initial porosity=0.88, compression ratio=3, final porosity=0.58). Using the experimental results and Eq. (11) the permeability and form-coefficient for this insert are obtained as $K_0=4.01\times10^{-10}$ m^2 and $C_0=33.458\times10^3$ m^{-1}. This low permeability and high form-coefficient of the chosen porous medium make it particularly suitable for verifying the theoretical models *viz*. Eqs. (3) and (7), because of the negligible convective inertia and viscous diffusion effects.

It is also important to verify how well the assumption of negligible longitudinal diffusion (an assumption made by both the theoretical models) is satisfied. For the present experimental tests, using the values listed previously and $\alpha_{\text{PAO}}=8.68\times10^{-5}$ m^2/s, the minimum Péclet number, $\text{Pe}=QL/A_f\alpha$, equals 8,617 supporting the neglect of the longitudinal diffusion effect.

Results and Discussion

Figure 1 compares the experimental pressure-drop results with that predicted by the Nield model, Eq. (3), and the Narasimhan-Lage model, Eq. (7), for a reference coolant temperature $T_0=21°C$, and V=46.9 V ($q''=1$ kW/m^2). To highlight the influence of form-drag effects, predictions by the linear-Darcy model, Eq. (5), is also shown. The comparison for higher heat fluxes ($q''=3.9$ kW/m^2 and 5.8 kW/m^2) is shown in Figs. 2 and 3.

From Fig. 1 we see, for lower velocities ($Q<2\times10^{-5}$ m^3/s), both the perturbation theories, Eq. (3) and (5), agree well in their predictions. However, for higher velocities ($Q>2\times10^{-5}$ m^3/s), with the influence of form-drag gaining strength, the linear-Darcy model, Eq. (5), shows marked deviation, as expected. Both the predictions by Eqs. (3) and (5) yield smaller pressure-drop than the experimental result with the deviation of Eq. (3) being ~15%.

The N-L model, Eq. (7), as predicted in the earlier section, agrees extremely well with the experimental results for all heat fluxes (Figs. 1–3). For higher heat fluxes, the temperature distribution along the channel grows in strength making the Nield model assumption of small temperature variation along the channel invalid, leading to the systematic deviation of the second-order HDD model from the experimental results.

Conclusions

Experiments using a low permeability, high form-coefficient porous medium sandwiched inside an isoflux-bounded parallel-plate channel were performed for verifying two recent theories for predicting the global pressure-drop/fluid-velocity relationship.

The results validate the two theoretical models, subject to their respective limitations. The Nield model, Eq. (3), due to the inclusion of the form-drag effects, is definitely better than the earlier model, Eq. (5), based on the simpler Darcy equation. However, Eq. (3) is accurate only for fully developed (hydrodynamic and thermal) flow situations with very small temperature variation along the channel.

Predictions from the N-L model show excellent agreement with the experimental results for all of the heat flux values tested. However, it is worth noting here that the high-heat flux correlation for ζ_μ and ζ_C, the null-global viscous drag regime as explained in

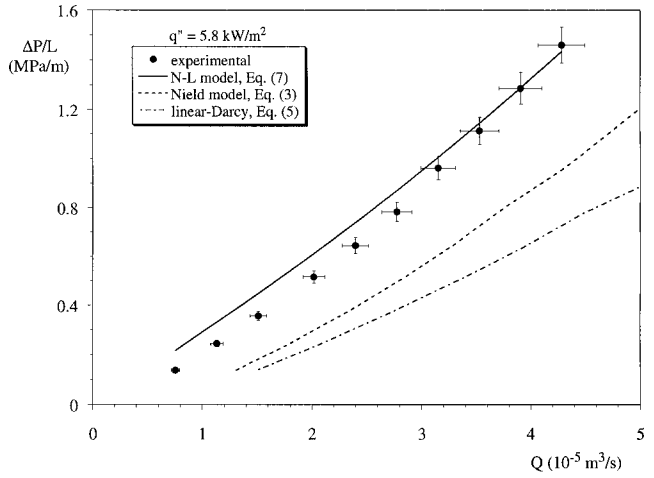

Fig. 3 Pressure drop versus volumetric coolant flow rate for $T_0=21°C$ and V=114.9 V. (Uncertainties: $U_{\Delta P}/\Delta P=3$ percent, $U_Q/Q=5$ percent)

[4], has not been tested because the experimental configuration is limited to moderate heat fluxes by the *validity range* of Eq. (10).

References

[1] Kaviany, M., 1991, *Principles of Heat Transfer in Porous Media*, Springer-Verlag, NY.

[2] Nield, D. A., and Bejan, A., 1999, *Convection in Porous Media*, 2nd ed., Springer-Verlag, NY.

[3] Lage, J. L., Weinert, A. K., Price, D. C., and Weber, R. M., 1996, "Numerical Study of a Low Permeability Microporous Heat Sink for Cooling Phased-array Radar Systems," Int. J. Heat Mass Transf., **39**, pp. 3633–3647.

[4] Narasimhan, A., and Lage, J. L., 2001, "Modified Hazen-Dupuit-Darcy Model for Forced Convection of a Fluid With Temperature-dependent Viscosity," ASME J. Heat Transfer, **123**, pp. 31–38.

[5] Narasimhan, A., Lage, J. L., and Nield, D. A., 2001, "New Theory for Forced Convection through Porous Media by Fluids With Temperature-Dependent Viscosity," ASME J. Heat Transfer, in press.

[6] Porneala, D. C., 1998, "Experimental Tests of Microporous Enhanced Cold Plates for Cooling High Frequency Microwave Antennas," Dissertation, SMU, Dallas, Texas.

[7] Narasimhan, A., and Lage, J. L., 2001, "Forced Convection of a Fluid With Temperature-dependent Viscosity Through a Porous Medium Channel," Numer. Heat Transfer, in press.

[8] Lage, J. L., & Antohe, B. V., 2000, "Darcy's Experiments and the Deviation to Nonlinear Flow Regime," ASME J. Fluids Eng., **122**, pp. 619–625.

[9] Nield, D. A., Porneala, D. C., and Lage, J. L., 1999, "A Theoretical Study, With Experimental Verification of the Viscosity Effect on the Forced Convection Through a Porous Medium Channel," ASME J. Heat Transfer, **121**, pp. 500–503.

[10] Antohe, B. V., Lage, J. L., Price, D. C., and Weber, R. M., 1997, "Experimental Determination of Permeability and Inertia Coefficients of Mechanically Compressed Aluminum Porous Matrices," ASME J. Fluids Eng., **119**, pp. 404–412.

[11] Kim, J. H., Simon, T. W., and Viskanta, R., 1993, "Journal of Heat Transfer Policy on Reporting Uncertainties in Experimental Measurements and Results," ASME J. Heat Transfer, **115**, pp. 5–6.

Effects of Pulsation on Grid-Generated Turbulence

S. Shahidinejad
Ph.D. Candidate
Mechanical Engineering Department, Sharif University of Technology, P.O. Box 11365/9567, Tehran, Iran

I. Jerphanion
Graduate Student

F. Magaud
Ph.D., Research Assistant

M. Souhar
Professor, ENSEM-INPL
e-mail: Mohamed.Souhar@ensem.inpl-nancy.fr

LEMTA-ENSEM, UMR 7563 CNRS, 2 avenue de la Foret de Haye, B.P. 160, 54504, Vandouvre Cedex, France

The effects of low frequency, large amplitude sinusoidal pulsation on grid-generated turbulence (PGGT) were experimentally studied. Two-component hot wire anemometry technique was used. Pulsation did not change homogeneous, isotropic character of grid-generated turbulence. [DOI: 10.1115/1.1412461]

1 Introduction

In contrast to stationary grid-generated turbulence (SGGT), which has been a subject of interest for about 70 years [1–4], the unsteady pulsating counterpart has not received enough attention. In periodic flows the velocity or the pressure field undergoes a well-defined oscillation at a fixed frequency and amplitude. Modeling such flows is of great engineering importance notably in the fields of aerodynamics and turbo-machinery. The present work aims at extending the existing (SGGT) data to pulsating flows to provide a better understanding of their physics. This study is a part of larger attempt to develop a new turbulence model for unsteady turbulent flows.

2 Experimental Approach

2.1 Geometric Specifications. Experiments were performed in an open circuit subsonic wind tunnel test section ($40\times40\times100$ cm), Fig. 1(*a*). A grid made of perpendicular round bars ($D=4$ mm, $M=17$ mm, $\sigma=0.45$) was used. The turbulence level, $\max|u'/U_0, v'/U_0|$, was less than 1.0% in the test section (without grid). In (SGGT) experiments U_0 was 10 m/s ($R_M=1.0\times10^4$). In all (PGGT) experiments $\overline{u}$ was 10 m/s.

2.2 Pulsation Mechanism. Sinusoidal variation in streamwise velocity, Fig. 1(*b*) was generated by means of a rotating vane set in the diffuser part of the tunnel, Fig. 1(*a*) (for more detail see [5]). The free stream was pulsated at 8.5, 13, and 20 Hz. An inductor sensor installed on the pulsating device marked the beginning of each cycle. This signal was used as a reference to determine the phase difference (φ) (with an accuracy of ±4 deg) between different data points. No phase difference in streamwise or transversal direction was found. $\overline{u}$ and $|\tilde{u}|$ decreased streamwise due to the slight divergence of the test section ($d\overline{u}/dx\approx-0.8(\mathrm{s}^{-1})$ and $d|\tilde{u}|/dx\approx-1.2(\mathrm{s}^{-1})$ along centerline axis).

2.3 Data Reduction. An X-array probe (DANTEC 55R51), relatively resistant to large amplitude pulsation, operated at constant temperature (80% overheat) by a DISA 55M01 hot wire anemometer. The data acquisition system and the dual sensor probe possessed a maximum frequency response of 3 KHz. A calibration accuracy of 5% was obtained by using an accurate Pitot tube (5–15 m/s; $\pm0.8\%$ at mid range) in the tunnel [6]. KEITHLEY DAS-1700 HR data acquisition board (16 bit precision; 8 channel) was used. The sampling frequency was 8 KHz. For each data point 480,000 samples were recorded. Data points were on the tunnel centerline axis. The experiments were reproducible within the range of accuracy of the set up.

2.4 Data Processing. Fast Fourier Transform (FFT) of the instantaneous signal was obtained (using Matlab, Ver. 5.2). In the real part plot, low frequency large peaks corresponding to the mean velocity, pulsating frequency and two or three harmonics (depending on the case) were selected to make a new vector. It should be noted that the frequencies of fluctuations were at least two order-of-magnitude higher than those of the pulsations in our experiments. In the new vector the amplitudes corresponding to higher frequencies were set to zero. The FFT^{-1} of the new vector gave the periodic component. This procedure was accomplished in full awareness of complete elimination of fluctuating parts while keeping the closest periodic form to the original signal, Fig. 1(*b*). The time average of the velocity fluctuations obtained by this method ($\overline{u'}, \overline{v'}$) was quite small as expected and was less than 5×10^{-5}. The implementation of the method on known periodic signals with added random fluctuations was quite satisfactory. The periodic part was separated with an error less than 1%. The spec-

Contributed by the Fluids Engineering Division of THE AMERICAN SOCIETY OF MECHANICAL ENGINEERS. Manuscript received by the Fluids Engineering Division August 2, 2000; revised manuscript received May 16, 2001. Associate Editor: K. M. B. Q. Zaman.

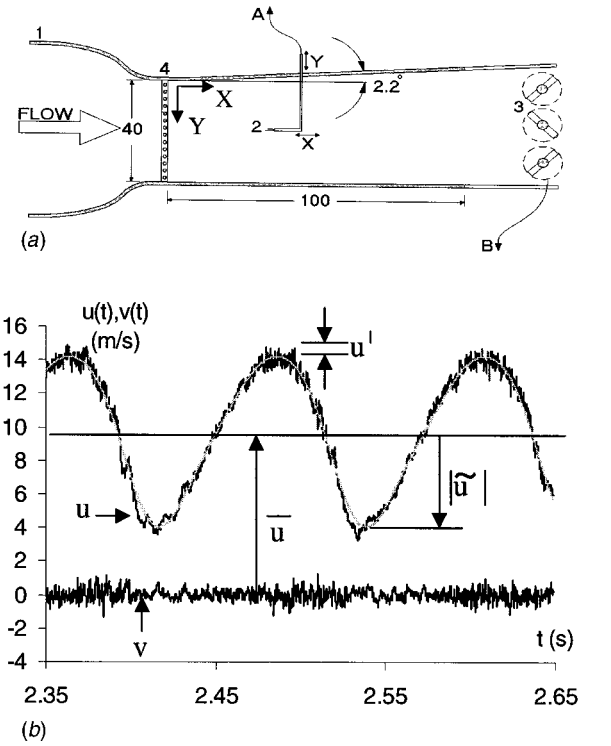

Fig. 1 (*a*) Schematic sketch of the experimental facility (dimensions in cm). 1. Wind tunnel, test section width=40 cm. 2. Hot wire probe. 3. Pulsation mechanism. 4. Grid. A: To hot wire anemometry system. B: Reference signal to data acquisition system. (*b*) A typical record of the fluctuating velocity components u, v and the corresponding periodic non-fluctuating part $\tilde{u}$ at 8.5 Hz.

tral energy of the original signal, $E_u(n)$ was compared with that of fluctuating component, $E_{u'}(n)$, Fig. 2. The area under each curve normalized the spectra. The energy of pulsation is removed without changing the high frequency character of the signal.

3 Results and Discussions

Figure 2 also provides a comparison with the $(-5/3)$ Kolmogrov law for (SGGT). The high frequency behavior and consequently the mechanism of cascading energy is the same for both (PGGT) and (SGGT). Figure 3(*a*) shows the streamwise decay of normal Reynolds stresses in (SGGT). The result, Eq. (1), was in good agreement with expected exponential decay rate [2].

$$\overline{u'^2}/U_0^2 = 0.047(X/M)^{-1.28} \tag{1}$$

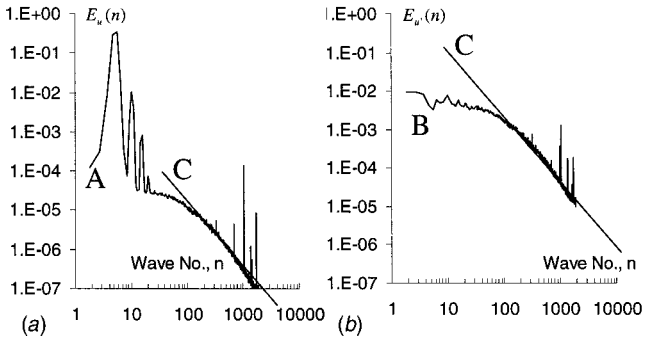

Fig. 2 Normalized power spectrum of the stream-wise velocity component at 8.5 Hz. (*a*) the original signal, (*b*) the fluctuating part. A: $E_u(n)$ B: $E_{u'}(n)$ C: $n^{-5/3}$.

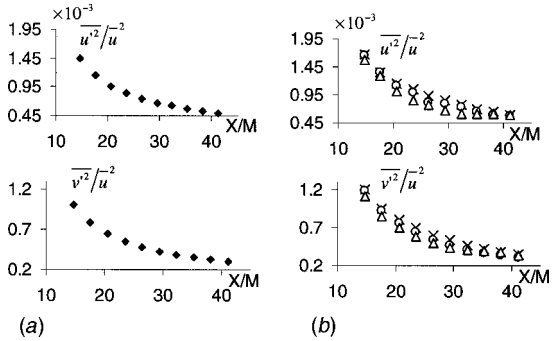

Fig. 3 Variation of normal Reynolds stresses downstream of the grid. (*a*) stationary, (*b*) pulsating flow, ×8.5 Hz, O 13 Hz, Δ 18 Hz.

The error in determination of turbulence intensities was less than 10 %. In both (SGGT) and (PGGT) homogeneity ($\overline{u'^2}=\overline{v'^2}=\overline{w'^2}$) was expected (by extrapolating) about 70-mesh size downstream of the grid in our set up, Fig. 3(*b*). The expected classical kinetic energy decay rate, [2], was obtained in (SGGT) and did not change with pulsation. The Reynolds stress ($-\overline{u'v'}$) was essentially zero, as expected, in all cases. By increasing frequency of pulsation the amplitude was decreased. Figure 4 shows streamwise variation of the energy of pulsation ($\overline{\tilde{u}\,\tilde{u}}/\overline{u}^2$) in our set up. Macro (integral) scales of turbulence were studied. Macro time scale (T) was calculated by integrating the Eulerian time correlation function $R_E(t)$, Eq. (2).

$$T=\int_0^\infty R_E(t)\,dt \tag{2}$$

It is reasonable to assume that in pulsating flows where $\overline{u} \gg u'$, the ''frozen field'' pattern as interprets the Taylor's hypothesis remains valid. Macro time scales were multiplied by the stream-wise mean velocity to obtain macro length scales Λ_u, Λ_v at each data point, Fig. 5. Despite the uncertainties that might be attributed to the instrumentation or the methods used in the calculation of scales the results are given mainly to show their order of magnitude. Maximum error of 20% should be considered for the turbulent scales. The results of stationary turbulence show that $\Lambda_u \approx 2\Lambda_v$ and are in good agreement with Compt-Bellot et al. [2]. Pulsation does not change Λ_v, but increases Λ_u (about 30%) and this effect is more pronounced farther downstream of the grid. Introducing the triple decomposition [7], Eq. (3), in the governing equations the kinetic energy equation, Eq. (4), was derived.

$$u_i(x,t)=\overline{u_i}(x,t)+\tilde{u}_i(x,t)+u_i'(x,t) \tag{3}$$

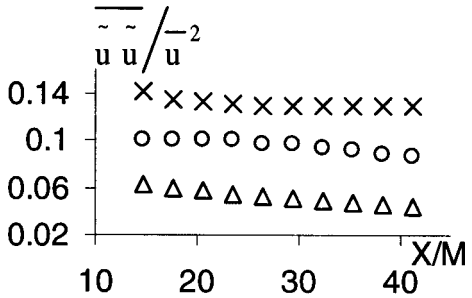

Fig. 4 Variation of normalized pulsation energy, $\overline{\tilde{u}\tilde{u}}/\overline{u}^2$ ×8.5 Hz, O 13 Hz, Δ 18 Hz

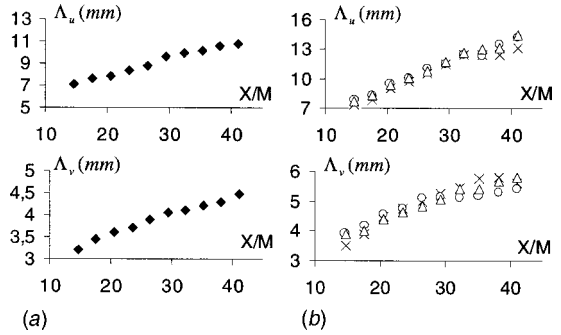

Fig. 5 Streamwise variation of macro length scales Λ_u, Λ_v. (*a*) stationary flow, (*b*) pulsating flow.

Table 1 Typical experimental values of the convection, production, diffusion and total dissipation rate at two extreme stations (X/M=14.7,41.2)

X/M	f (Hz)	$\bar{u}\frac{d\bar{k}}{dx}$	$-\overline{u^2}\frac{d\bar{u}}{dx}$	$\nu\frac{d^2k}{dx^2}$	ε
14.7	Stationary	7.53	0.01	9.86e-5	4.5
14.7	8.5	7.29	0.12	9.39e-5	7.3
14.7	13	8.70	0.07	8.6e-4	7.7
14.7	18	6.44	0.10	8.98e-5	6.5
41.2	Stationary	0.76	0.003	3.73e-6	0.5
41.2	8.5	0.74	0.04	3.38e-6	0.7
41.2	13	0.79	0.02	1.41e-5	0.7
41.2	18	0.68	0.03	3.51e-6	0.7

$$k_{,t}+\overline{u_j}k_{,j}=-\overline{u_i'u_j'}\overline{u_{i,j}}-\overline{u_i'u_j'\tilde{u}_{i,j}}-\frac{1}{2}(\overline{u_i'u_i'\tilde{u}_j}+\overline{u_i'u_i'u_j'})_{,j}$$

$$-\frac{1}{\rho}(\overline{p'u_j'})_{,j}+\nu k_{,jj}-\nu\overline{u_{i,j}'u_{i,j}'} \quad (4)$$

The second and the third terms on the right-hand side, appeared in the modified Eq. (4), represent production and diffusion due to pulsation of free stream. Table 1 shows typical experimental values of the terms in Eq. (4) at two extreme stations (X/M =14.7,41.2). Total dissipation rate (ε) is estimated as given by Eq. (5).

$$\varepsilon\approx(\sqrt{\overline{u'^2}})^3/\Lambda_u \quad (5)$$

Diffusion and production terms were negligible compared to the total dissipation rate and the convective terms in Eq. (4). Equation (6) gives the final simplified form of the *k*-equation.

$$\bar{u}\frac{dk}{dx}\approx-\varepsilon \quad (6)$$

5 Concluding Remarks

A series of experiments as an initial effort to study the pulsation effects on grid-generated turbulence was performed. Low frequency large amplitude pulsation was applied. No phase difference between data points was found. The results confirm no coupling between low frequency pulsation and high frequency turbulence. Major features of (SGGT) like isotropy, homogeneity, energy cascading phenomena, classical turbulence intensities and kinetic energy decay rates remained largely intact with pulsation. The modified *k*-energy equation was derived and simplified. Further work should be continued on documenting pulsation effects at turbulence frequencies in grid-generated turbulence and in shear flows.

Acknowledgment

This work was done in accordance with scientific cooperation program in Mechanics between France and Iran.

Nomenclature

- D = diameter of the rods in the grid (mm)
- E_u, E_u' = power spectral density function of u (or u') normalized by its total surface area (m)
- f, f_p = frequency and pulsation frequency (Hz)
- k = kinetic energy of turbulence, $k=0.5(\overline{u'^2}+\overline{v'^2}+\overline{w'^2})$ (m^2/s^2)
- M = distance between the rod centerlines in the grid (m)
- n = wave number, $n=2\pi f/\bar{u}$ (m^{-1})
- p = static pressure (pa)
- Re_M = Reynolds number based on mesh size, $Re_M=U_0M/\nu$ $R_E(t)=\overline{u(t')u(t-t')}/\overline{u'^2}$, Eulerian time correlation, averaging with respect to t'
- t, T_p = time, period of pulsation (sec)
- T = macro time scale (sec)
- U_0 = velocity in (SGGT) (m/s)
- $\bar{u}, |\tilde{u}|$ = mean velocity, pulsation amplitude in (PGGT) (m/s)
- u', v', w' = velocity fluctuations (m/s)
- X, Y = streamwise and transversal directions (m)
- ε = total dissipation rate (m^2/s^3)
- Λ_u, Λ_v = turbulent macro (integral) length scales in X and Y directions, respectively (mm)
- ρ = density (kg/m^3)
- σ = solidity, the cross-sectional of the grid to the total cross-sectional area of the test section
- u = kinematic viscosity (m^2/s)
- φ = phase difference between data points in pulsating flow (degree)

References

[1] Taylor, G. I., 1935, "Statistical Theory of Turbulence," Part I and II, Proc. R. Soc. London, Ser. A, 151–421.

[2] Comte-Bellot, G., and Corrsin, S., 1966, "The Use of a Contraction to Improve the Isotropy of Grid Generated turbulence," J. Fluid Mech., **25**, pp. 657–682.

[3] Mohamed, M. S., and LaRue, J. C., 1990, "The Decay Power Law in Grid-generated Turbulence," J. Fluid Mech., **219**, pp. 195–214.

[4] Tresso, R., and Munoz, D. R., 2000, "Homogeneous, Isotropic Flow in Grid-generated Turbulence," ASME J. Fluids Eng., **122**, pp. 51–56.

[5] Martin, M., 1969, "Contribution à l'étude de la convection thermique pulsée autour des cylinders," Ph.D. thesis, Université de Nancy, France.

[6] Bruun, H. H., 1995, *Hotwire Anemometry: Principles and Signal Analysis*, Oxford University Press, New York.

[7] Hussain, A. K. M. F., and Reynolds, W. C., 1970, "The Mechanics of an Organized Wave in Turbulent Shear Flow," J. Fluid Mech., **41**, 241–258.

Skin Friction Correlation in Open Channel Boundary Layers

Mark F. Tachie, D. J. Bergstrom, Ram Balachandar, and Shyam Ramachandran
College of Engineering, University of Saskatchewan, Saskatoon, Canada, S7N 5A9

Introduction

In near-wall turbulence research, accurate determination of the wall shear stress, τ_w, (or skin friction coefficient C_f) is of critical

Contributed by the Fluids Engineering Division of THE AMERICAN SOCIETY OF MECHANICAL ENGINEERS. Manuscript received by the Fluids Engineering Division February 17, 2000; revised manuscript received May 10, 2001. Associate Editor: J. Katz.

Table 1 Summary of experiments considered for the present correlation.

Experiment	Reynolds number	Instrumentation
Balachandar and Ramachandran [14]	$150 \leqslant Re_\theta \leqslant 500$	single-component LDA
Balachandar and Tachie [15]	$900 \leqslant Re_\theta \leqslant 2100$	single-component LDA
Tachie and Balachandar [16]	$950 \leqslant Re_\theta \leqslant 1400$	single-component LDA
Tachie et al. [9]	$1300 \leqslant Re_\theta \leqslant 2700$	single-component LDA
Tachie et al. [13]	$1000 \leqslant Re_\theta \leqslant 2300$	single-component LDA
Tachie et al. [2]	$750 \leqslant Re_\theta \leqslant 3300$	single-component LDA (with beam expansion)
Schultz and Swain [11]	$5600 \leqslant Re_\theta \leqslant 15000$	two-component LDA

importance due to its practical relevance and also because it determines the friction velocity u_τ used by most boundary layer scaling laws. A number of techniques are available to determine the wall shear stress in turbulent boundary layers. If sufficient data are obtained in the linear viscous sublayer ($y^+ \leqslant 4$), the wall shear stress can be determined from the velocity gradient at the wall. However, it is often difficult to obtain adequate data within the linear sublayer in most experiments, especially if the Reynolds number is high and instruments such as pitot-tube and cross-wire probes are used. Alternatively, a reliable estimate of the wall shear stress can be obtained by fitting polynomial to the near-wall data up to $y^+ \leqslant 15$ (George and Castillo [1], Tachie et al. [2]). In a high Reynolds number flow, where a well-defined log-region exists, the Clauser plot technique is frequently used to determine the wall shear stress. For a turbulent boundary layer, leading edge geometry as well as freestream turbulence intensity can significantly modify the skin friction characteristics. For such conditions, a formulation that does not implicitly fix the strength of the wake but rather allows its value to be optimized while ensuring a reliable estimate of u_τ was proposed by Finley et al. [3] and subsequently used by Granville [4] and Krogstad et al. [5]. At sufficiently high Reynolds numbers, the wall shear stress can also be estimated from the peak value of the Reynolds shear stress profile near the wall. Finally, on smooth surfaces wall mounted probes can be used to measure τ_w directly.

Using these methods, a number of correlations (e.g., Schultz-Grunow [6]) have been developed to allow the prediction of skin friction for practical purposes. Most of the existing correlations consider moderate to high Reynolds numbers in canonical turbulent boundary layers, whereas the focus of the present work is low to moderately high Reynolds numbers in channel flows. More recently, Osaka et al. [7] reported extensive measurements in a smooth wall turbulent boundary layer for a Reynolds number range of $800 \leqslant Re_\theta \leqslant 6300$, where Re_θ is the Reynolds number based on boundary layer momentum thickness, θ. Direct wall shear measurements were made and the skin friction correlation derived from their measurements appears to be the most reliable in the literature for the range of Re_θ they considered. Another widely referenced study of low Reynolds number boundary layer flows is that of Purtell et al. [8] who used the velocity gradient at the wall and momentum balance to infer the wall shear stress.

In the present study, we are specifically concerned with open channel flows, which show some significant similarities with canonical boundary layers studied in mechanical engineering applications (Tachie et al. [9]). In the hydraulic engineering community, it would appear that on occasion rather crude methods have been advocated for the prediction of skin friction. For example, Moody chart using the hydraulic diameter has been recommended for the prediction of the skin friction (ASCE Task Force [10]). While this may be adequate for preliminary calculations, more reliable correlations are required. Recently, Schultz and Swain [11] reported a correlation for C_f on a smooth plate in a water tunnel at moderately high Reynolds numbers. Their correlation was typically 6–9 percent higher than that given by Coles [12], and did not consider low Re_θ data.

The present study proposes a new skin friction correlation for a smooth wall boundary layer in channel flows at low to moderately high Reynolds number. The experimental data used to develop the correlation were obtained from experiments conducted in different facilities under different conditions, and cover a relatively wide range of Reynolds number ($100 < Re_\theta < 20{,}000$).

Summary of Experiments

The data used to develop the present correlation were obtained from the experiments summarized in Table 1. The studies of Tachie et al. [2,9,13], Balachandar and Ramachandran [14], Balachandar and Tachie [15] and Tachie and Balachandar [16] were conducted in the same test facility. Details of the open channel flume and the LDA system are provided in Balachandar and Ramachandran [14] and are not repeated here. These experiments also used the same laser Doppler anemometer, except for Tachie et al. [2] who used an additional beam expansion device to achieve a higher spatial resolution. The freestream velocity (U_e) in these experiments was in the range $0.01 < U_e(\text{m/s}) < 0.62$ while the background turbulence levels varied from 2.0 to 4.0 percent. The turbulence levels are typical of water channel experiments but are significantly higher than typical turbulence intensities reported in wind tunnel studies. The experiment of Schultz and Swain [11] was conducted using a two-component laser Doppler anemometer in a water tunnel at $U_e = 1.2$ to 4.0 m/s. Their turbulence intensity ranged from 2.5 to 3.0 percent.

In the first five studies summarized in Table 1, the wall shear stress was obtained from the velocity gradient at the wall ($y^+ \leqslant 6$) and the maximum uncertainty in C_f was 6 percent. In Tachie et al. [2], the high resolution LDA system together with a slight tilt of the probe towards the wall allowed measurements to be obtained down to $y^+ = 1$ in some of the tests. Both velocity gradient at the wall ($y^+ \leqslant 4$) and a fifth-order polynomial fit to the near-wall data ($y^+ \leqslant 15$) were used to determine the wall shear stress and the uncertainty in C_f was less than 3 percent. Schultz and Swain [11] considered three different methods, namely, the velocity gradient at the wall ($y^+ \leqslant 7$), Reynolds stress method and Bradshaw's method, to estimate the wall shear stress. The values of C_f determined using the velocity gradient at the wall and Bradshaw's method are used in the present work. For these methods, the uncertainty in C_f was 7 percent or less.

Results and Discussion

Figure 1 shows a plot of the skin friction coefficient (C_f) with Reynolds number (Re_θ) for the studies summarized in Table 1. The Reynolds number varied from low (150) to moderately high (15,000) values, and the range is two orders of magnitude. The skin friction correlation developed in the present work is as follows:

$$C_f = 4.13\times10^{-2} - 2.68\times10^{-2}(\log Re_\theta) + 6.528\times10^{-3}(\log Re_\theta)^2 - 5.54\times10^{-4}(\log Re_\theta)^3 \quad (1)$$

Equation (1) and 7 percent error bands at some selected values of Re_θ are shown in Fig. 1. The choice of 7 percent reflects the maximum uncertainty in C_f for the data sets used in developing

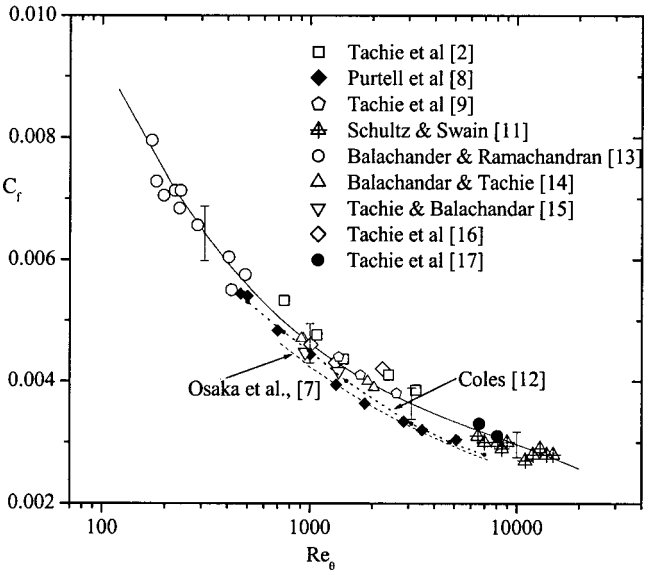

Fig. 1 Variation of skin friction coefficient with Reynolds number (solid line denotes present correlation [Eq. (1)] with ±7 percent error band; dashed line denotes correlation proposed by Osaka et al. [7] and dot-dash line denotes the correlation proposed by Coles [12])

the correlation. An assessment of goodness-of-fit using a chi-square distribution at 95 percent confidence level indicated that Eq. (1) correlates the experimental data well.

The skin friction data of Purtell et al. [8] obtained in a canonical turbulent boundary layer at $465 \leqslant Re_\theta \leqslant 5{,}100$, as well as the correlation developed by Osaka et al. [7] are also shown. In the Reynolds number range for which the data of Purtell et al. [8] and the correlation of Osaka et al. [7] overlap, there is a reasonable agreement between the experimental data and the correlation. Figure 1 also shows the data of Tachie et al. [17] obtained using pitot-tube in a wind tunnel for $U_e = 17$ m/s to 20 m/s. The turbulence intensity in the wind tunnel was 0.6 percent, which is lower than the values reported in the water channel experiments. However, the wake parameter was found to be $\Pi \approx 0.1$ and this is comparable to the values obtained in open channel flow experiments, e.g., $\Pi = 0.08 \sim 0.1$ in Tachie et al. [9]. The low value of Π in the wind tunnel experiment was attributed to leading edge effects. For this set of data, the defect profile was correlated using the formulation proposed by Finley et al. [3].

The following observations can be made from Fig. 1. The skin friction obtained in the open channel flow is comparable to the wind tunnel data reported by Purtell et al. [8] for $Re_\theta < 1000$. On the other hand, the C_f values for the wind tunnel data of Purtell et al. [8] and the correlation developed by Osaka et al. [7] are lower than the open channel data and the water channel data of Schultz and Swain [11] at higher Re_θ. The older but widely-used correlation of Coles [12] is also shown in the figure. As noted in the figure, Coles' [12] correlation describes the present data for $Re_\theta < 2000$, but would under predict the open channel data for $Re_\theta > 2000$. Furthermore, the difference between the water channel and wind tunnel data increases as Re_θ increases. For example, compared to the C_f values predicted from the correlation of Osaka et al. [7], prediction from the present correlation is 10 and 15 percent higher at $Re_\theta = 1000$ and 6000, respectively.

The similarities and differences noted above can be explained as follows. The turbulence level in the wind tunnel experiments of Purtell et al. [8] and Osaka et al. [7] is an order of magnitude lower than the water channel data. One effect of high freestream turbulence intensity on the mean flow is to reduce the wake parameter (Π) which in turn increases C_f (e.g., Hoffman and Mohammadi [18], White [19]). For the experiments conducted in open channel, the values of Π were less than 0.15. Measurements, as well as results obtained from direct numerical simulation for canonical turbulent boundary layers, showed that the values of Π are low at low Reynolds number but Π increases as the Reynolds number increases. Typical asymptotic values for Π in wind tunnel experiments varied from 0.55 to 0.62. Since values of the outer wake parameter at low Re_θ in wind tunnel do not differ much from those obtained in the open channel experiments the good agreement between the data reported by Purtell et al. [8] and the open channel data at $Re_\theta < 1000$ is to be expected even though the turbulence levels are distinctly different. On the other hand, the lower C_f values for the wind tunnel data of Purtell et al. [8] and the correlation developed by Osaka et al. [7] in comparison to the open channel data and the water channel data of Schultz and Swain [11] can be attributed to the much stronger wake components (Π) for the wind tunnel experiments.

It is interesting to observe that although the data reported by Tachie et al. [17] were obtained in a wind tunnel, they are adequately described by the present correlation but not by the wind tunnel correlation of Osaka et al. [7]. While the turbulence intensity for this experiment (i.e., Tachie et al. [17]) is similar to those reported by Purtell et al. [8], the strength of the outer wake parameter was 0.1. This is significantly lower than values obtained in wind tunnel experiments at similar Re_θ but comparable to open channel experiments as noted previously. This observation provides further evidence that the skin friction characteristics are strongly affected by the strength of the wake. Therefore, techniques such as that proposed by Finley et al. [3] that implicitly account for the role of the outer flow should be used to determine the wall shear stress.

Summary and Conclusion

A new skin friction correlation for open channel boundary layers was developed using skin friction data obtained from a variety of experiments, mostly in low Reynolds number open channel flows. The range of Re_θ varied from 150 to 15,000, which covers most of the Re_θ experiments available in the literature. The present correlation describes the existing data to within ±7 percent. It is observed that skin friction correlations developed for canonical turbulent boundary layers, e.g., Osaka et al. [7], only slightly under-predict the skin friction coefficient in open channel boundary layers at low Reynolds numbers, i.e., $Re_\theta < 2{,}000$. The level of under-prediction increases at higher Reynolds numbers.

References

[1] George, W. K., and Castillo, L., 1997, "Zero-Pressure-Gradient Turbulent Boundary Layer," Appl. Mech. Rev., **50**, No. 11, pp. 689–729.

[2] Tachie, M. F., Bergstrom, D. J., and Balachandar, R., 2000 "Mean and Fluctuating Velocity Components in Smooth and Rough Wall Turbulent Boundary Layers," 3rd International Symposium on Turbulence, Heat and Mass Transfer, Nagayo, Japan, pp. 183–189.

[3] Finley, P. J., Chong Phoe, Khoo, and Jeck Poh, Chin, 1966, "Velocity Measurements in a Thin Turbulent Wake Layer," La Houille Blanche, **21**, pp. 713–721.

[4] Granville, P. S., 1976, "A Modified Law of the Wake for Turbulent Shear Layers," ASME J. Fluids Eng., **98**, pp. 578–580.

[5] Krogstad, P. A., Antonia, R. A., and Browne, L. W. B., 1993, "Comparison between Rough- and Smooth-Wall Turbulent Boundary Layers," J. Fluid Mech., **245**, pp. 599–617.

[6] Schultz-Grunow, 1941, "New Frictional Resistant Law for Smooth Plates," NACA TM 986.

[7] Osaka, H., Kameda, T., and Mochizuki, S., 1998, "Re-Examination of the Reynolds Number-Effects on the Mean Flow Quantities in a Smooth Wall Turbulent Boundary Layers," JSME Int. J., Ser. B, **41**, No. 1, pp. 123–129.

[8] Purtell, L. P., Klebanoff, P. S., and Buckley, F. T., 1981, "Turbulent Boundary Layer at Low Reynolds Number," Phys. Fluids, **24**, No. 5, pp. 802–811.

[9] Tachie, M. F., Bergstrom, D. J., and Balachandar, R., 2000, "Rough Wall Turbulent Boundary Layers in Shallow Open Channel Flows," ASME J. Fluids Eng., **122**, pp. 533–541.

[10] ASCE Task Force, 1963, "Friction Factors in Open Channel Flows," J. Hydraulic Division, **89**, No. 2, pp. 97–143.

[11] Schultz, M. P., and Swain, G. W., 1999, "The Effect of Biofilms on Turbulent Boundary Layers," ASME J. Fluids Eng., **121**, pp. 44–51.

[12] Coles, D., 1962, "The Turbulent Boundary Layer in a Compressible Fluid," The Rand Corp., Rep. R-403-PR.
[13] Tachie, M. F., Balachandar, R., and Bergstrom, D. J., 2001, "Boundary Layer Relaxation Behind a Forward Facing Step at low Re_θ," Accepted for publication, ASME J. Fluids Eng.
[14] Balachandar, R., and Ramachandran, S., 1999, "Turbulent Boundary Layers in Low Reynolds Number Shallow Open Channel Flows," ASME J. Fluids Eng., **121**, pp. 684–689.
[15] Balachandar, R., and Tachie, M. F., 2001, "Boundary Layer-Wake Interaction in Open Channel Flows," In press: Exp. Fluids.
[16] Tachie, M. F., and Balachandar, R., 2001, "Velocity Profiles in Smooth- and Rough-Wall Turbulent Wakes," In press: Exp. Fluids.
[17] Tachie, M. F., Bergstrom, D. J., and Kotey, N. A., 1999, "Leading Edge Effects on Smooth and Rough-Wall Turbulent Boundary Layers," Mechanical Engineering Report WT99N1, University of Saskatchewan.
[18] Hoffmann, J. E., and Mohammadi, K., 1991, "Velocity Profiles for Turbulent Boundary Layers Under Freestream Turbulence," ASME J. Fluids Eng., **113**, pp. 399–404.
[19] White, F. M., 1974, *Viscous Fluid Flow*, McGraw-Hill, New York.

Particle Trajectory in Turbulent Boundary Layer at High Particle Reynolds Number

Ryoichi Kurose[1] and Hisao Makino
Research Scientist and Senior Research Scientist, Respectively, Yokosuka Research Laboratory, Central Research Institute of Electric Power Industry (CRIEPI), Yokosuka, Kanagawa 240-0196, Japan

Satoru Komori
Professor, Department of Mechanical Engineering, Kyoto University, Kyoto 606-8501, Japan

1 Introduction

Particle motions in a turbulent boundary layer are strongly related to some significant environmental problems such as desertification and air pollution, and they often occur in many industrial processes. It is, therefore, of great practical interest to investigate the particle motions both in settling the environmental problems and in designing industrial equipment.

Since lift acting on a particle is known to be affected by fluid shear and particle rotation, the effect should be taken into account in predicting the particle trajectories in a turbulent boundary layer flow. The approximate expressions for the lift on a rotating particle in a shear flow have been proposed by a number of researchers (e.g., Rubinow and Keller, [1]; Saffman [2]; McLaughlin [3]). However, most of their expressions cannot be applied to the particles with high particle Reynolds numbers of $Re_p(=|u_i-v_i|d/\nu) \gg 1$ because they are derived on the assumption that the particle Reynolds number is much less than unity ($Re_p \ll 1$). Here u_i is the fluid velocity at the center of the particle, v_i is the particle velocity, d is the particle diameter, and ν is the kinematic viscosity of the fluid. Furthermore, although not only fluid velocities but also initial particle ejection velocities and rotational speed are needed to predict the lift, it is very difficult to obtain these values in the actual turbulent boundary layer. Therefore, the effects of the fluid shear and particle rotation on the particle trajectory especially for $Re_p \gg 1$ have not yet been clarified.

In this study, we aim to numerically predict the particle trajectory in a turbulent boundary layer for high particle Reynolds numbers of $Re_p \gg 1$, and identify the effects of the fluid shear and particle rotation on the particle trajectory. To estimate the lift for $Re_p \gg 1$, recent results of Kurose and Komori [4], who provided the expressions for $1 \leqslant Re_p \leqslant 500$ by conducting the three-dimensional numerical simulations for a linear shear flow around a rotating spherical particle, were used. The initial particle ejection velocities and rotational speed required for the computations of particle trajectory were measured in a wind tunnel by means of an image processing system combined with a high-speed video system and a workstation. Wind velocities were measured by using a constant-temperature hot-wire anemometer with a miniature X-probe.

2 Experiments

Figure 1 shows test apparatus, particle-motion visualization, and air-velocity measurement systems. The test apparatus is a wind tunnel with a glass test section 5 m long (x), 0.3 m high (y), and 0.3 m wide (z). To focus on the particle behavior close to the wall, a single particle fixed by a needle on the bottom wall at a distance of 3.5 m from the entrance ($x=0$, $y=0$ and $z=0$) was carefully released by magnetically pulling out the needle in the developed boundary layer flow (Fig. 2). The particles used were polypropylene spherical particles with diameters of 500 μm and 1500 μm. The mass density ratio of the particle and fluid, ρ_p/ρ_f, is 902. As the bottom wall, rough particle beds consisting of tightly-fixed particles with the same diameter as ejected particles, which are hereafter referred to as the particle wall (Kurose and Komori [5]), were used since the prominent ejection of particles could not be observed over the smooth wall. The visualized particle motions were recorded at an interval of 0.0025 s in a high-speed video system (NAC, HSV-400), and transferred into a workstation (SUN MICROSYSTEM, SPARC STATION 10) as two-dimensional digitized frame data with $1152(x) \times 450(y)$ pixels and 256 monochrome tones. The region analyzed was 5 cm and 2 cm in x and y directions. Instantaneous streamwise and vertical air velocities in the turbulent boundary layer over the particle wall were simultaneously measured using a constant-temperature hot-wire anemometer with a miniature X-probe. The freestream wind velocity ranged from 8.4 to 15.9 m/s. The flow properties over the 500 μm dia and 1500 μm dia particle walls are listed in Table 1, where U_δ is the freestream wind velocity, δ is the boundary-layer thickness, Re_δ is the Reynolds number defined by $Re_\delta=\delta U_\delta/\nu$, δ^* is the displacement thickness, u^* is the friction velocity, and d^+ is the nondimensional particle diameter in

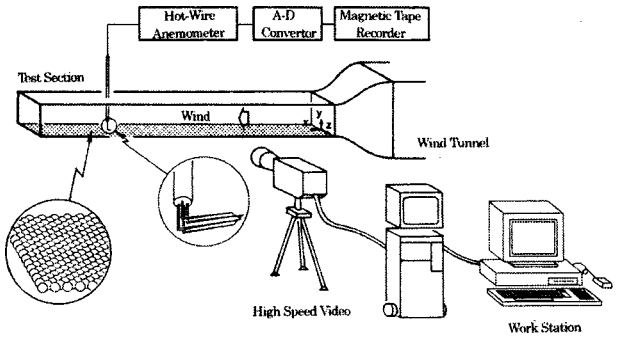

Fig. 1 Test apparatus, particle-motion visualization, and air-velocity-measurement systems

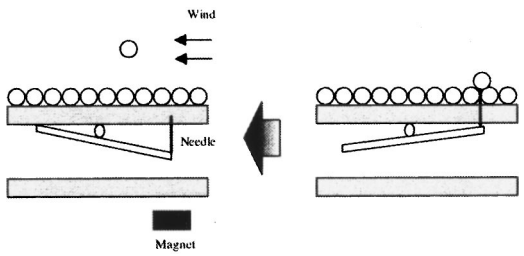

Fig. 2 Particle fixation and release system

Table 1 Flow properties

Wall	U_δ [m/s]	δ [m]	Re_δ [-]	δ^* [m]	u^* [m/s]	d^+ [-]
	8.4	0.0762	4000	0.0267	0.33	11.0
	10.2	0.0755	48100	0.0264	0.40	13.3
500 μm	12.1	0.0748	56600	0.0262	0.48	16.0
	14.0	0.0747	65400	0.0261	0.55	18.3
	15.9	0.0746	74100	0.0261	0.62	20.7
	8.4	0.0861	45200	0.0301	0.36	33.8
	10.2	0.0860	54800	0.0301	0.45	42.2
1500 μm	12.1	0.0853	64500	0.0299	0.53	49.7
	14.0	0.0848	74200	0.0297	0.62	58.1
	15.9	0.0843	83800	0.0295	0.72	66.6

wall unit defined by $d^+ = du^*/\nu$. The particle visualization and analysis were conducted for 200 particles for each particle diameter and each freestream wind velocity.

3 Results and discussion

Figures 3(a), (b), and (c) show the typical time records of the horizontal and vertical positions, x_p and y_p, velocities, v_x and v_y, and accelerations, a_x and a_y, for the 500 μm dia particle and $U_\delta = 15.9$ m/s. The particle rolls on the wall with small collisions with the roughness right after the release, and it suddenly ejects markedly at a certain point (referred to as ejected position) indicated by an arrow in Fig. 3(*a*). At this point, v_y, a_x, and a_y begin to increase rapidly. The similar trends were also observed for the other cases with different particle diameter of 1500 μm and different wind velocities, and the ejection positions for the same particle diameter and the same wind velocity tend to be almost the same despite the existence of roughness.

Figure 4 shows the ensembly averaged values of the horizontal positions of particle ejections, $\langle x_p^E \rangle$, and horizontal and vertical

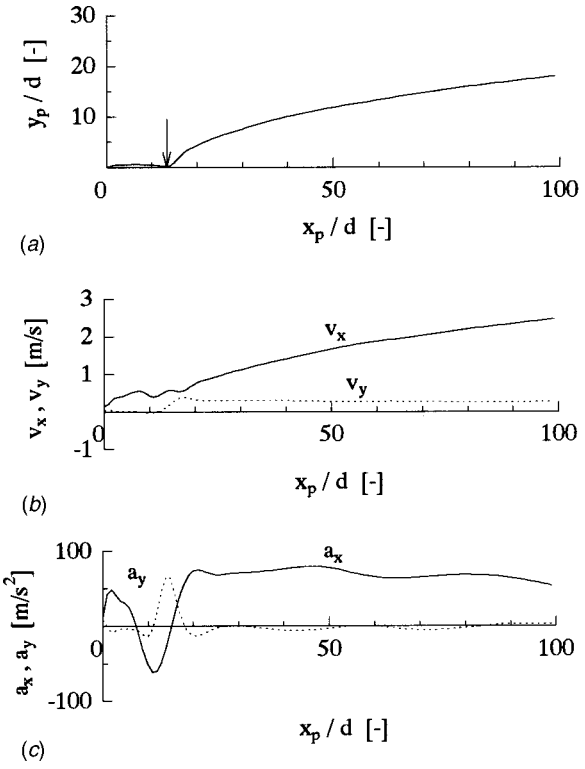

Fig. 3 Typical time records of the horizontal and vertical positions, velocities and accelerations (500 μm dia particle, $U_\delta = 15.9$ m/s): (*a*) positions; (*b*) velocities; (*c*) accelerations.

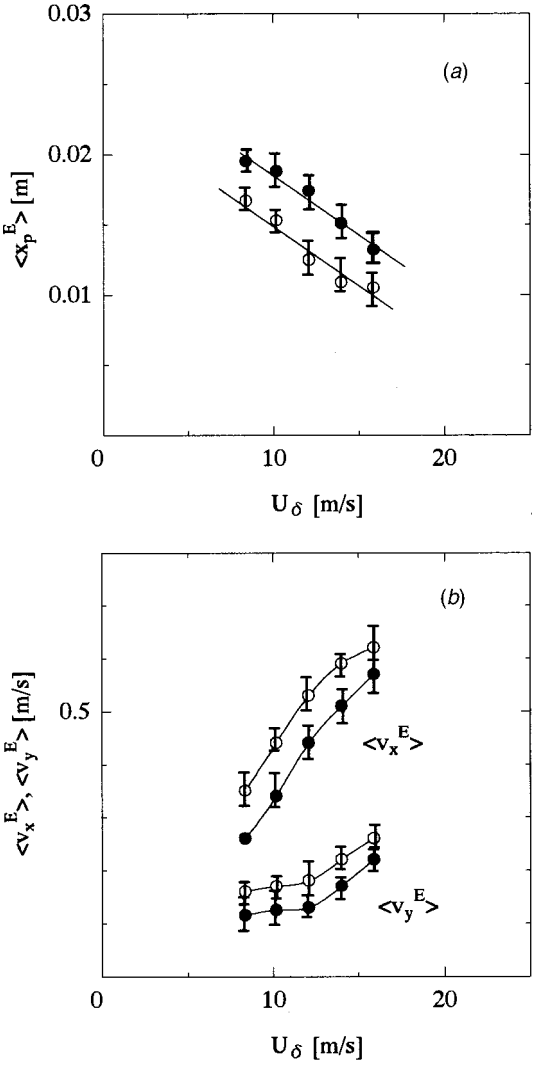

Fig. 4 Ensembly averaged values of horizontal ejection position and horizontal and vertical velocities: (*a*) horizontal ejection position; (*b*) horizontal and vertical ejection velocities; ○, 500 μm dia particle; ●, 1500 μm dia particle.

velocities of the ejected particles, $\langle v_x^E \rangle$ and $\langle v_y^E \rangle$, at the ejected positions against the freestream wind velocity, U_δ. The values of $\langle x_p^E \rangle$ for 1500 μm and 500 μm dia particles decrease in proportion to U_δ with the same inclination, and $\langle x_p^E \rangle$ for the 500 μm dia particle is less than that for the 1500 μm dia particle. On the other hand, the values of $\langle v_x^E \rangle$ and $\langle v_y^E \rangle$ increase with increasing U_δ, and the ejection velocities for the 500 μm dia particle are larger than those for the 1500 μm dia particle. The particle ejection velocity, $\langle V^E \rangle (= (\langle v_x^E \rangle^2 + \langle v_y^E \rangle^2)^{1/2})$, is estimated to be $1.13\,u^*$ for the 500 μm dia particle and $0.83\,u^*$ for the 1500 μm dia particle, respectively. Here u^* is estimated from the distributions of the Reynolds stress. Both values of $\langle V^E \rangle$ are less than those given in the previous studies (e.g., $1.8\,u^*$ by White and Schulz [6], $3.3\,u^*$ by Araoka and Maeno [7], $3.5\,u^*$ and $4.4\,u^*$ by Nalpanis et al. [9] and $5.8u^*$ by Willetts and Rice [8]) because, in the present study, the analyzed region is confined to the small area close to the wall. The particle Reynolds numbers Re_p at the beginning of the big ejection were 200-300 for the 500 μm dia particles and 300-500 for the 1500 μm dia particles.

The particle rotational speeds of $x-y$ plane were measured by analyzing the visualized frames of a white particle with the half part painted in black. The 500 μm dia particle was too small to

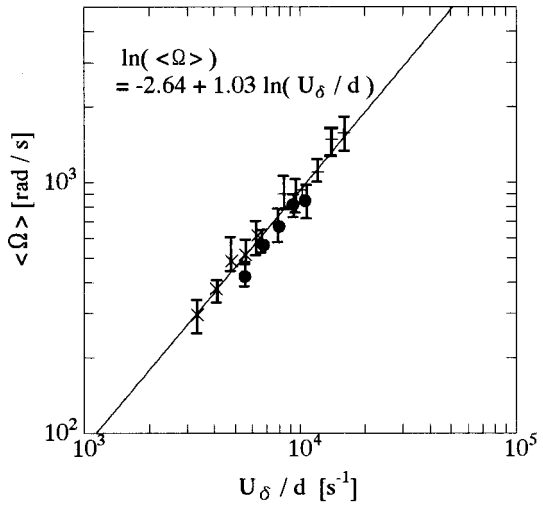

Fig. 5 Correlation between mean angular rotational speed and free-stream wind velocity divided by particle diameter: ●, 1500 μm dia particle; ×, 2500 μm dia particle; +, 1000 μm dia particle.

observe, therefore, the visualizations were carried out for 1500 μm and 2500 μm dia particles over the 1500 μm dia particle walls and 1000 μm dia particles over the 500 μm dia particle wall. Figure 5 shows the correlation between the ensembly averaged value of the angular rotational speed, $\langle\Omega\rangle$, and freestream wind velocity divided by the particle diameter, U_δ/d. It is found that $\langle\Omega\rangle$ monotonously increases with increasing U_δ/d and it is approximated by

$$\ln(\langle\Omega\rangle) = -2.64 + 1.03 \ln\left(\frac{U_\delta}{d}\right). \tag{1}$$

From this expression, the particle rotational speed for the 500 μm dia particle will also be evaluated.

To investigate the effects of fluid shear and particle rotation on the particle trajectory, computations of the trajectory of the ejected particle were carried out for the 500 μm dia particle for $U_\delta = 15.9$ m/s. The two-dimensional equation for the motion of a particle used is

$$m_p\left(\frac{dv_i}{dt}\right) = \frac{1}{8} C_D \pi d^2 \rho_f |u_j - v_j|(u_i - v_i) \tag{2}$$

where C_D is the drag coefficients, u_i the wind velocities at the center of the particle, m_p the particle mass, ρ_f the air density. The virtual mass and Basset history forces were neglected, since Nalpanis et al. [9] mention that these forces are negligible above a distance over one or two particle sizes from the wall. The Stokes number defined by $\mathrm{St} = (\rho_p/\rho_f)(d/2)^2 U_\delta/\nu\delta$ and the particle response time defined by $\tau_p = (2/9)(\rho_p/\rho_f)(d/2)^2/\nu$ were 750 and 0.78, respectively. The lift force acts on a solid particle in the vertical direction by fluid shear and particle rotation was estimated by

$$f_L = \frac{1}{8} C_L \pi d^2 \rho_f |u_i - v_i|(u_x - v_x) \tag{3}$$

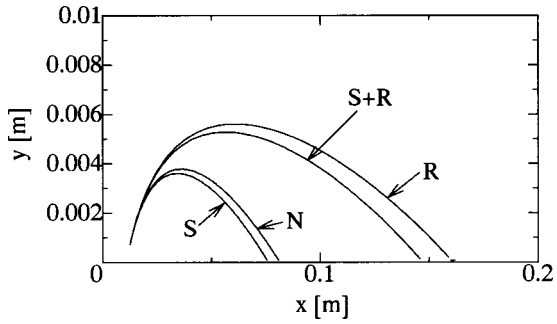

Fig. 6 Comparison of predicted particle trajectories. Arrows S, R, S+R and N mean the predictions with effect of fluid shear, with effect of particle rotation, with both effects and without both effects.

Here, C_L is the lift coefficient, and the value can be obtained from the expressions of Kurose and Komori [4] as functions of the particle Reynolds number for $1 \leqq \mathrm{Re}_p \leqq 500$, dimensionless fluid shear rate for $0 \leqq S^*(=(u_x - v_x)S/(d/2)) \leqq 0.4$ and dimensionless angular rotational speed for $0 \leqq \Omega^*(=(u_x - v_x)\Omega/(d/2)) \leqq 0.25$, where S and Ω are the dimensional fluid shear rate and angular particle rotational speed. The effects of the fluid shear and particle rotation on C_D were ignored, and the value of C_D was given using the approximate expressions of Morsi and Alexander [10] as a function of the particle Reynolds number of Re_p. The values of u_x, u_y, and S were obtained from the air velocity measurement, and Ω was estimated from expression (1) ($\Omega = \langle\Omega\rangle$). The trajectories can be calculated by integrating Eq. (2) with (3) forward in time, and the calculations were repeated until that particle ejected from the bottom wall again reaches the bottom wall. The initial particle positions, x_p and y_p, and particle ejection velocities, v_x and v_y, were set to the ensembly averaged values in Fig. 4. Figure 6 shows the particle trajectories. The fluid shear and particle rotation act to decrease and increase the horizontal length and the maximum height of the trajectory, respectively, and the effect of the particle rotation is stronger than that of the fluid shear. This means that the effect of the particle rotation should be taken into account in predicting the particle trajectory in the turbulent boundary layer, especially for high particle Reynolds numbers.

References

[1] Rubinow, S. I., and Keller, J. B., 1961, "The transverse force on a spinning sphere moving in a viscous fluid," J. Fluid Mech., **11**, pp. 447–459.

[2] Saffman, P. G., 1965, "The lift on a small sphere in a slow shear flow," J. Fluid Mech., **22**, pp. 385–400 (and Corrigendum, 1968, **31**, p. 624).

[3] McLaughlin, J. B., 1991, "Internal migration of a small sphere in linear shear flows," J. Fluid Mech., **224**, pp. 261–274.

[4] Kurose, R., and Komori, S., 1999, "Drag and lift forces on a rotating sphere in a linear shear flow," J. Fluid Mech., **384**, pp. 183–206.

[5] Kurose, R., and Komori, S., 2001, "Effects of particle roughness on turbulence structure in a boundary layer flow," Int. J. Multiphase Flow, **27**, pp. 673–683.

[6] White, B. R., and Schulz, J. C., 1977, "Magnus effect in saltation," J. Fluid Mech., **81**, pp. 497–512.

[7] Araoka, K., and Maeno, N., 1981, "Dynamical behavior of snow particles in the saltation layer," *Proc. 3rd Symp. On Polar Met. & Glaciology*, Mem. Natl Inst. Polar Res., Tokyo, Vol. 19, pp. 253–263.

[8] Willetts, B. B., and Rice, M. A., 1985, "Intersaltation collisions," *Proc. Initl Workshop on the Physics of Blown Sand 1*, pp. 83–100, Mem. 8, University of Aarhua, Denmark.

[9] Nalpanis, P., Hunt, J. C. R., and Barrett, C. F., 1993, "Saltating particles over flat beds," J. Fluid Mech., **251**, pp. 661–685.

[10] Morsi, S. A., and Alexander, A. J., 1972, "An Investigation of particle trajectories in two-phase systems," J. Fluid Mech., **55**, pp. 193–208.